OUT-OF-PLANE RETROFITTING OF MASONRY WALL USING ENGINEERED CEMENTITIOUS COMPOSITES

Saeed Pourfalah Bazkiani

Submitted for the degree of Doctor of Philosophy

Heriot Watt University

School of Energy, Geoscience, Infrastructure and Society

March 2017

ABSTRACT

The contribution of infill masonry walls to the overall behaviour of frame structures has been acknowledged through numerous published experimental and numerical investigations. Both the in-plane and out-of-plane response of such walls have a significant effect on the overall structural performance of frames and can be subjected to a range of in-plane and out-of-plane actions (e.g. wind, earthquakes, impact and blast loads) characterised by different time-histories, loading-frequencies and intensities. Infill walls are particularly vulnerable to the application of loads in the out-of-plain direction and often sustain significant damage (in the form of cracking) which can result in failure and collapse. It is interesting to note that after sustaining a certain level of damage due to the load applied in the out-of-plane direction, an infill wall can no longer contribute to the in-plane response of a frame. In an attempt to enhance the overall behaviour of infill walls, present work sets out to develop a method for improving the out-of-plain behaviour of such elements. This is achieved through the use of a thin layer of engineered cementitious composite (ECC) which is fully or partially bonded on the face of the wall which is in tension (opposite to the face on which the out-of-plane action is applied) or on both faces of the wall.

For this purpose, an ECC mix is initially developed employing materials available in the UK. Its behaviour is then established experimentally under increasing loading rates and temperatures. This material is then used to strengthen a series of beam-like masonry specimens under different loading rates by conducting a series of static and dynamic 4-point bending tests. The test data obtained is then employed to develop a numerical model of the problem at hand capable of realistically predicting the experimentally established behaviour through the use of nonlinear dynamic finite element analysis. Both, experimental and numerical studies, reveal that in all cases considered the use of ECC resulted in a significant enhancement of the out-of-plain behaviour of the specimens in terms of strength, stiffness and ductility. Furthermore, the specimens with a partially bonded ECC layer performed better compared to those with a fully ECC layer. In addition, the performance of these specimens under impact load was further enhanced when adding a second layer on the other face of the specimen. Finally, a parametric numerical investigation is conducted to assess the effect of a range of parameters (associated with the boundary conditions imposed onto the specimen, the properties of the materials involved, the geometry of the specimen and loading rate) on the behaviour of the specimens.

ACADEMIC REGISTRY
Research Thesis Submission

Name*:*	**Saeed Pourfalah Bazkiani**		
School/PGI:	**School of Energy, Geoscience, Infrastructure and Society**		
Version: *(i.e. First, Resubmission, Final)*	**Final submission**	Degree Sought (Award and Subject area)	**PhD in Civil Engineering**

Declaration

In accordance with the appropriate regulations I hereby submit my thesis and I declare that:

1) the thesis embodies the results of my own work and has been composed by myself
2) where appropriate, I have made acknowledgement of the work of others and have made reference to work carried out in collaboration with other persons
3) the thesis is the correct version of the thesis for submission and is the same version as any electronic versions submitted*.
4) my thesis for the award referred to, deposited in the Heriot-Watt University Library, should be made available for loan or photocopying and be available via the Institutional Repository, subject to such conditions as the Librarian may require
5) I understand that as a student of the University I am required to abide by the Regulations of the University and to conform to its discipline.

* *Please note that it is the responsibility of the candidate to ensure that the correct version of the thesis is submitted.*

Signature of Candidate*:*	Saeed Pourfalah	Date:	

Submission

Submitted By *(name in capitals):*	**Saeed Pourfalah Bazkiani**
Signature of Individual Submitting:	
Date Submitted:	

For Completion in the Student Service Centre (SSC)

Received in the SSC by (name in capitals):			
Method of Submission (Handed in to SSC; posted through internal/external mail):			
E-thesis Submitted ***(mandatory for final theses)***			
Signature:		Date:	

Table of Contents

List Of Tables

List of Figures

List of symbols and abbreviations

2-D	:	Two dimensions
3-D	:	Three dimensions
ASTM	:	American Society for Testing and Materials
BS	:	British standard
CEM I	:	Cement type 1
COV	:	Coefficient of Variation
E	:	Young's modulus
ECC	:	Engineered cementitious composites
FE	:	Finite element
GPa	:	Giga Pascal
h	:	Height of specimens
H13ECC	:	Hybrid engineered cementitious composites with 6 mm steel fibres
H6ECC	:	Hybrid engineered cementitious composites with 6 mm steel fibres
HECC	:	Hybrid engineered cementitious composites
HSD camera	:	High speed digital camera
I	:	Moment of inertia
I-R delay	:	Impact peak to reaction peak delay
kN	:	Kilo Newton
LVDT	:	Linear Variable Differential Transformer
M	:	Moment
min	:	Minute
mm	:	Millimetre
MPa	:	Mega Pascal
NLFEA	:	Non-linear finite element analysis
PE	:	Poly ethanol
PVA	:	Poly vinyl ethylene

R/I ratio	:	Reaction to impact load ratio
t	:	Time
URM	:	Unreinforced masonry
ε_{crack}	:	Strain of cracking
ε_{max}	:	Maximum strain
σ_{crack}	:	Stress of crack
σ_{max}	:	Maximum stress

Chapter 1: Introduction

1.1 Background

When designing frame structures, it is common practice not to include the infill walls in the models used for structural analysis purposes, as they are considered to be essentially non-load bearing elements (Hak, 2014). In doing so, the stiffness and strength contribution of the latter elements, as well as their interaction with the structural elements of the frame, are fully ignored. Worldwide it has been observed that damages or failures sustained by infilled frame structures are associated with the majority of recorded fatalities and injuries. It is also interesting to note that when reviewing the costs for repairing damages sustained by various structures during earthquakes the majority of these costs (about 80%) are associated with damages sustained by infill walls (Tiedeman 1980). Based on the above, it is not surprising that an increasing interest has been observed concerning the investigation of the effect of infill walls on the structural performance of frame structure over the last decade.

The available experimental and numerical information clearly shows that existing infill walls significantly contribute to the redistribution of the internal actions developing within the structural elements of the frame, resulting in the redirection of the loads towards other regions of the structure (Abrams et al., 1996, Mehrabi et al., 1996, Murty and Jain, 2000). This redistribution can cause an increase in the overall stiffness and load carrying capacity of the frame. However, it can also cause the development of stress concentrations in other regions of the structure (e.g. joint area, or at specific regions along the length of the beams or columns) never intended to undertake the internal actions which develop due to the additional loads transferred through the infill walls (Chrysostomou and Asteris, 2012, Davidson et al., 2005). The latter actions can potentially lead to localised cracking or even unpredictable (and in many cases brittle) modes of failure (i.e. short-column mechanism).

Apart from the in-plane behaviour of infill walls, the out-of-plane behaviour can also have a significant effect on the structural performance of frames. The out-of-plane motion can cause an infill wall to sustain damages or even collapse. After sustaining a certain level of damage, an infill wall can no longer contribute to the response of the frame structure with its in-plane stiffness. As a result, FEMA-306 recommends the calculation of the capacity of masonry infill walls associated with an out-of-plane response under seismic

excitation whereas EC8 specifically states that appropriate measures should be taken in order to prohibit partial or total out-of-plane collapse of slender masonry infill walls.

During the last decades, the out-of-plane behaviour of masonry walls has been experimentally and numerically investigated (Griffith and Vaculik, 2007, Cavaleri et al., 2009) under static and dynamic (ranging from earthquake to impact and blast) loading. Based on these studies, the out-of-plane response is characterized by limited ductility and is dependent on the slenderness and strength of the subjected wall (Bruneau, 1994). It is also interesting to note that when infill walls are restrained at their boundaries by the surrounding structural elements of the frame (beams, columns) they can develop additional out-of-plane resistance due to arching-effects (Abrams et al., 1996, Dawe and Seah, 1989). Infill walls can be subjected to a range of actions in the out-of-plane direction ranging from static to seismic loads (characterized by low and intermediate loading rate) (See Figure 1.1) to extreme loading condition under blast and explosion (see Figure 1.2) (characterized by high loading rate and intensities).

Figure 1.1. Out of plane failure of infill walls in earthquake (http://db.concretecoalition.org/building/135)

Therefore it is essential to design masonry walls resilient to out-of-plane loads involving seismic, impact, and blast loading in order to enhance public safety (see Figure 2.1) as well as structural integrity and resistance. Several retrofitting methods have been already used to improve the out-of-plane performance of infill walls. The most common method is the use of external reinforcement in the form of mesh in combination with cement render (Hutchison et al., 1984, Karantoni and Fardis, 1992, Abrams and Lynch, 2001, Sheppard and Tercelj, 1980, ElGawady et al., 2004). The external reinforcement can also be provided in a form of metal/fibre reinforced polymer straps that are glued directly onto the wall surface (Taghdi, 1998, Carney and Myers, 2003). In developing countries,

polymeric bands, commonly used in packaging, have also been used to create a mesh around a wall to retain its structural integrity during a seismic event (Sathiparan and Meguro, 2011). While these methods can improve the out-of-plane behaviour of a masonry wall, their application is characterized by a series of problems such as increasing mass of the building, they interfere with architecture façade of building, high cost, and poor performance at high temperature.

Figure 1.2. Out of plane Failure of infill walls subjected to blast (Ward, 2004)

Work described in this thesis presents an experimental, analytical and numerical investigation to introduce a more efficient method of strengthening masonry walls against out-of-plane loads. The proposed method uses fibre reinforced cementitious composite called Engineered Cementitious Composites (ECCs) which is characterized by ductile, strain-hardening behaviour under tension and high tensile strain capacity, typically in up to 5% (Figure 1.3). This high tensile strain capacity is mainly due to the ability of this material to form multiple closely-spaced fine cracks with width less than 100 micron. These features have been all possible due to the systematic tailoring of the fibre (typically about 2% fibre), matrix, and interface properties of the composite. Existing studies documented that the ECC layer(s) can improve the out-of-plane behaviour of masonry beams (Davidson et al., 2005, Dehghani et al., 2015, Kyriakides et al., 2012). The application of a thin ECC layer has been found to enhance load carrying capacity and improved ductility of the masonry walls. Also the use of ECC layer changed the failure mode of the masonry walls from a brittle catastrophic failure to ductile failure (Dehghani et al., 2015, Kyriakides et al., 2012). The behaviour of ECC-retrofitted walls under concentrated, distributed, quasi-static and low velocity projectile impact load revealed

that not only can the ECC layer increase ductility and load carrying capacity of masonry walls but also safeguard against fragmentation due to impact (Maalej et al., 2010). However, in all studies local failure of ECC layer, without development of uniform cracking along the entire ECC layer length was observed. This highlights that the full potential of ECC layer has not been utilized before failure.

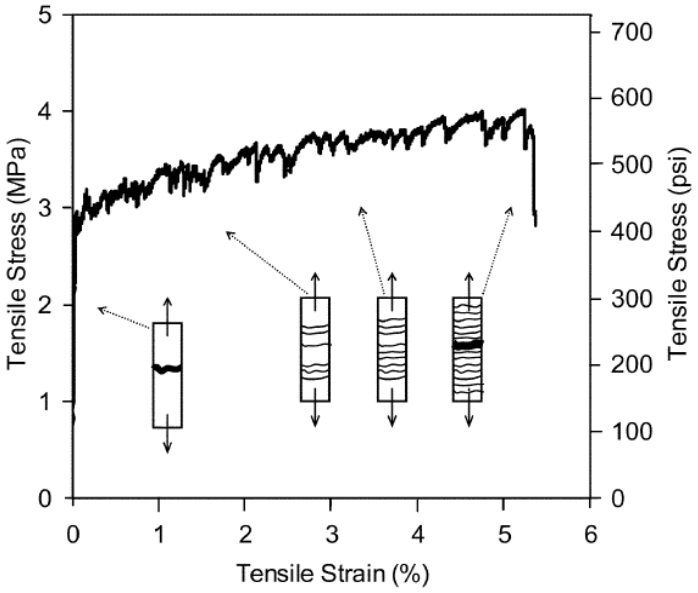

Figure 1.3. Typical tensile stress–strain curve development of ECC. (Yang et al., 2007)

This research assesses the effect of a thin layer of ECC attached to one or both sides of a masonry wall on the out-of-plane resistance, stiffness, ductility and energy dissipation capacity of retrofitted walls. Furthermore, it is expected that this layer(s) will reduce fragmentation due to application of impact loads imposed laterally on the surface of the walls. This research also explores the possibility of using a new technique (partially bonded ECC layer) to retrofit masonry infill walls against out-of-plane loads. The idea of partial bonded ECC layer was inspired by research that presented the influence of an interface defect on the performance of concrete repair (Li et al., 2000). It was found that partial debonding of ECC layer from the concrete beam leads to the development of multiple cracks in the ECC layer. This study uses the same concept to improve the efficiency of ECC-retrofitted masonry walls against out-of-plane loads.

Figure 1.4 shows a fully bonded ECC-retrofitted masonry wall. In the full bond ECC-retrofitted wall, ECC is directly applied to the surface of the masonry wall. Therefore the ECC layer fully bonds to the masonry wall throughout its entire surface. However, in the partially bonded ECC-retrofitted masonry wall, the central area of the masonry wall is

debonded from ECC and only the perimeter of the masonry walls are bonded with the ECC layer (Figure 1.4 b). To reduce the size of samples and simplify the test setup needed for conducting experiments, a strip of both walls were selected for tests (beam- like samples) which are presented in Figures 1.4c and d. The sample size, specification and loading methods are presented later on in the relevant chapter (Chapter 4).

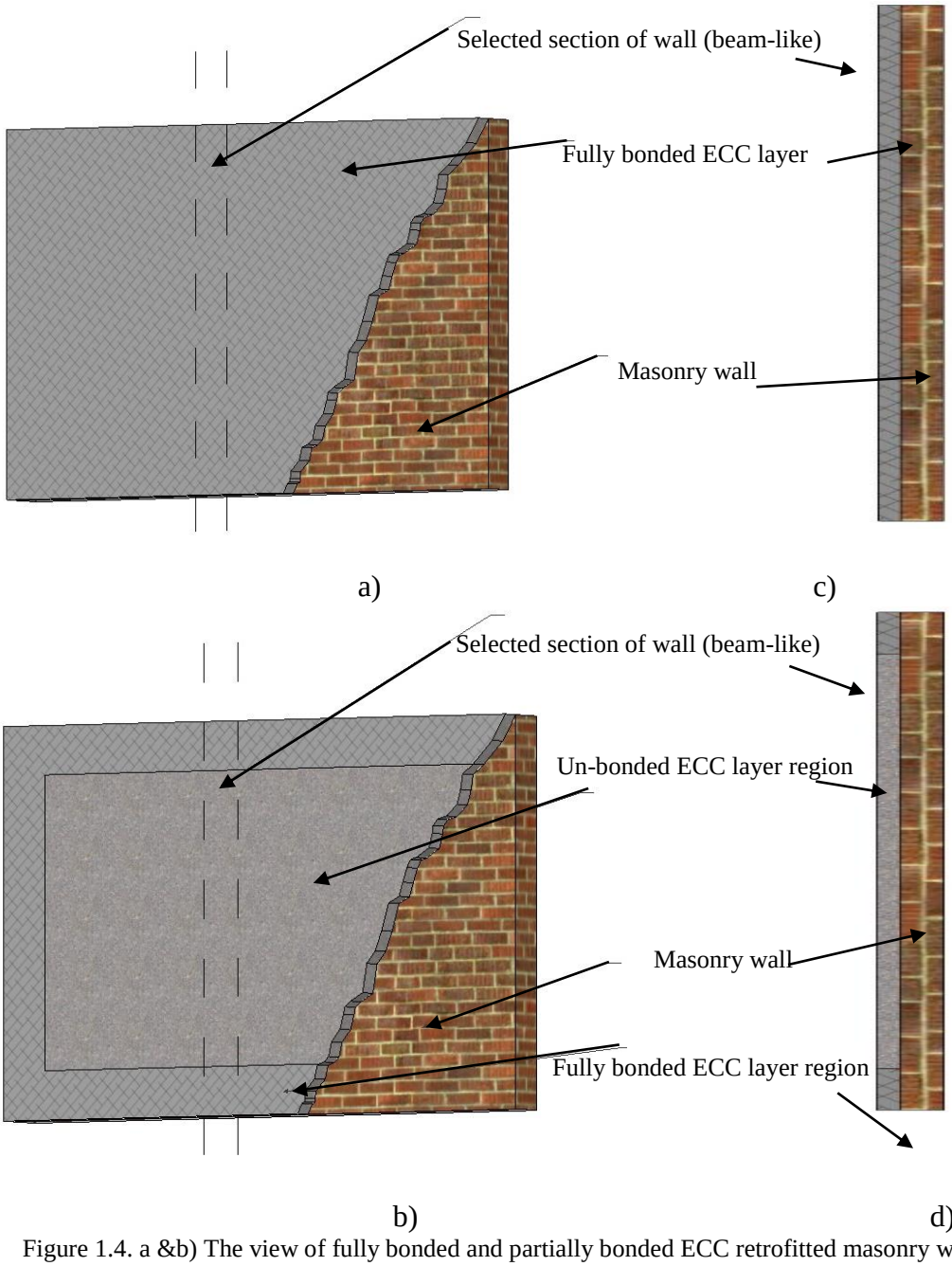

Figure 1.4. a &b) The view of fully bonded and partially bonded ECC retrofitted masonry walls respectively c &d) side view of selected section of fully and partially bonded ECC retrofitted masonry walls respectively (beam-like specimens)

1.2 Problem statement

During the life of a building, infill walls can be subjected to a range of out-of-plane loads. The out-of-plane strength and ductility of an infill wall is very limited and often causes sustaining significant damage and collapse. Using an ECC layer is one of the retrofitting methods to improve the out-of-plane performance of infill walls. Recently a series of studies were carried out on the ECC-retrofitting masonry walls. However, all of them use full bonded ECC layer or even enhanced the bond toward ECC layer. Therefore, these experiments exhibited local failure in the vicinity of the brick-mortar interface in the ECC layer. This issue is due to (i) the using of a thick layer of ECC that leads to compression failure in masonry beam or (ii) the development of a strong bond between ECC layer and brickwork which leads to localized failure in the vicinity of the brick-mortar interface in masonry walls.

Recently a study reported that in the partially bonded ECC layer connected to a concrete beam a uniform crack propagation was observed in the ECC layer within the un-bonded area (Li et al., 2000). This idea can be applied along the case of ECC-retrofitted masonry infills to improve their performance against out-of-plane loads. Using a partially bonded ECC can prevent local failure of the ECC layer and improve the ECC-retrofitted masonry ductility against out-of-plane loads. This study attempts for the first time to utilize a partial bonded ECC layer in unreinforced masonry walls aiming to avoid local failure of the ECC layer.

1.3 Research aim and objectives

The primary aim of this research is to propose the partially bonded ECC layer as a new technique for retrofitting masonry infill walls against a range of out-of-plane loads including quasi-static, elevated and impact loads. This is done to increase the out-of-plane ductility and to take full advantage of the ECC layer. The objectives of this research include:

1. To use materials available locally in the UK to develop ECC/HECC and identify the best mix proportions.
2. To evaluate the mechanical behaviour of ECC/HECC at high temperatures and elevated loading rate.

3. To assess the mechanical properties of the individual components of retrofitted masonry infill walls involving ECC, mortar and brick as well as the behaviour of the brick-mortar and brick-ECC interface.

4. To study the behaviour of ECC-retrofitted masonry specimens under different loading rate including static, elevated and impact loads.

5. To study the influence of the bond developing between the masonry beam and ECC layer on the behaviour of ECC-retrofitted specimens under different loading rates including static, elevated and impact loads.

6. To develop and validate a finite element (FE) model in order to study the flexural behaviour of masonry infill walls and conduct a parametric study to assess the effects of different parameters on the performance of retrofitted specimens including different loading rates, different temperatures, different support conditions, different lengths different mechanical properties of brick and mortar.

1.4 Contents of the thesis

Chapter 2 reviews the available information of the field observations and experiments about the behaviour of masonry wall subjected to out-of-plane load. This is followed by a concise review of the available literature concerning the performance of masonry walls subjected to out-of-plane high loading rate. A review of the published experimental, numerical and analytical studies investigating the out-of-plane retrofitting methods of masonry walls is then presented. Next, a brief history of the development of ECC material and its application are provided accompanied by description of ECC behaviour under different loading rates and temperatures. Then a critical review of the use of ECC for retrofitting the masonry walls is given comparing the benefits of this method with other available retrofitting methods. Finally a short discussion is provided identifying the gaps in the state of the art.

Chapter 3 presents the procedure followed for developing ECC at Heriot-Watt University. First, a brief discussion is presented on the different materials and mixtures used to develop the ECC followed by a series of tests (four-point bending and compression test)

carried out for selecting the optimum mixture. Results obtained from uniaxial tensile tests carried out on the dog-bone ECC specimens are presented assessing the selected mixture strain hardening behaviour under quasi-static and elevated uniaxial tension. Finally, the behaviour of ECC at elevated temperature is studied by conducting a series of compression and four-point bending tests (a range of temperatures between 20˚C to 600˚C were considered).

Chapter 4 focuses on experimental study of the behaviour of retrofitted beam-like masonry specimens under low-rating load. First the properties of the material used in the experiments are assessed by a series of small-scale tests including a compression test on brick, mortar and brickwork to characterize the compression properties of material, the brick-mortar and brick-ECC shear tests to characterize the brick-mortar interface and the brick-ECC interface properties and brick-mortar tensile test to characterize the brick-ECC interface properties. Then the performance of beam-like masonry specimens retrofitted by an ECC layer (including fully bonded and partially bonded retrofitting techniques) subjected to four-point bending load is studied. The main aim of this study was to investigate the full bond and partial bond ECC retrofitting techniques under quasi-static and elevated loading rate. To explain the results of ECC-retrofitted specimens an analytical study carried out and obtained predictions are compared by experiments and discussed.

In chapter 5 results of the impact test carried out to study the behaviour of masonry specimens retrofitted with ECC are presented. Four-point bending tests carried out to study the behaviour of the masonry specimens retrofitted with ECC subjected to high-rate loading. First, the results obtained from specimens retrofitted by one layer ECC attached to the tensile face of specimens discussed are followed by the results of masonry specimens retrofitted with two layers of ECC attached on both (tensile and compression) faces. A high-speed digital camera (HSD camera) was used to track the movement of impactor and the specimens through the loading process. Based on the data acquired, the displacement, velocity, contact force, time, history and strain of the specimens are obtained. The data provided was used to study the specimen’s behaviour under high-rate loading.

In chapter 6, a non linear finite element analysis (NLFEA) is developed to investigate the experiments presented in Chapters 3, 4 and 5. The predictions of NLFEA are validated against the counterpart test results. Following the validation of the NLFEA model, a parametric study is carried out to assess the effects of a series of parameters on the behaviour of the ECC retrofitted specimens and the obtained predictions are presented and discussed. Theses parameters include the variation of the mechanical properties of materials used in the experiments, the ECC bond condition, the boundary condition of retrofitted masonry specimens, the size of retrofitted masonry walls and the increasing of loading rate and temperature.

Chapter 7 presents the conclusions obtained from the experimental and numerical studies carried out in the previous chapters followed by a series of recommendations for further research.

1.5 References

ABRAMS, D. & LYNCH, J. 2001. Flexural behavior of retrofitted masonry piers. KEERC-MAE Joint Seminar on Risk Mitigation for Regions of Moderate Seismicity,.

ABRAMS, D. P., ANGEL, R. & UZARSKI, J. 1996. Out-of-plane strength of unreinforced masonry infill panels. *Earthquake spectra,* 12**,** 825-844.

BRUNEAU, M. 1994. State-of-the-art report on seismic performance of unreinforced masonry buildings. *Journal of Structural Engineering,* 120**,** 230-251.

CARNEY, P. & MYERS, J. J. 2003. Shear and flexural strengthening of masonry infill walls with FRP for extreme out-of-plane loading. Proceedings of the Architectural Engineering Institute 2003 Annual Meeting, 246-250.

CAVALERI, L., FOSSETTI, M. & PAPIA, M. 2009. Modeling of out-of-plane behavior of masonry walls. *Journal of structural engineering,* 135**,** 1522-1532.

CHRYSOSTOMOU, C. & ASTERIS, P. 2012. On the in-plane properties and capacities of infilled frames. *Engineering structures,* 41**,** 385-402.

DAVIDSON, J. S., FISHER, J. W., HAMMONS, M. I., PORTER, J. R. & DINAN, R. J. 2005. Failure mechanisms of polymer-reinforced concrete masonry walls subjected to blast. *Journal of Structural Engineering*. 52**,** 95-102

DAWE, J. & SEAH, C. 1989. Out-of-plane resistance of concrete masonry infilled panels. *Canadian Journal of Civil Engineering,* 16**,** 854-864.

DEHGHANI, A., FISCHER, G. & ALAHI, F. N. 2015. Strengthening masonry infill panels using engineered cementitious composites. *Materials and Structures,* 48**,** 185-204.

ELGAWADY, M., LESTUZZI, P. & BADOUX, M. 2004.A review of conventional seismic retrofitting techniques for URM. 13th international brick and block masonry conference, Citeseer, 1-10.

GRIFFITH, M. & VACULIK, J. 2007. Out-of-plane flexural strength of unreinforced clay brick masonry walls. *TMS Journal,* 25**,** 53-68.

HAK, S. 2014. Out-of-plane Experimental Response of Strong Masonry Infills. 2nd European Conference on Earthquake Engineering and Seismology. Hrvatska znanstvena bibliografija i MZOS-Svibor.

HUTCHISON, D., YONG, P. & MCKENZIE, G. 1984. Laboratory testing of a variety of strengthening solutions for brick masonry wall panels, 8th WCEE. *San Francisco, USA***,** 575-582.

KARANTONI, F. V. & FARDIS, M. N. 1992. Effectiveness of seismic strengthening techniques for masonry buildings. *Journal of Structural Engineering,* 118**,** 1884-1902.

KYRIAKIDES, M., HENDRIKS, M. & BILLINGTON, S. 2012. Simulation of unreinforced masonry beams retrofitted with engineered cementitious composites in flexure. *Journal of Materials in Civil Engineering,* 24**,** 506-515.

LI, V. C., HORII, H., KABELE, P., KANDA, T. & LIM, Y. 2000. Repair and retrofit with engineered cementitious composites. *Engineering Fracture Mechanics*, 65**,** 317-334.

MAALEJ, M., LIN, V., NGUYEN, M. & QUEK, S. 2010. Engineered cementitious composites for effective strengthening of unreinforced masonry walls. *Engineering Structures,* 32**,** 2432-2439.

MEHRABI, A. B., BENSON SHING, P., SCHULLER, M. P. & NOLAND, J. L. 1996. Experimental evaluation of masonry-infilled RC frames. *Journal of Structural Engineering,* 122**,** 228-237.

MURTY, C. & JAIN, S. K. 2000. Beneficial influence of masonry infill walls on seismic performance of RC frame buildings. Proceedings of the 12th World Conference on Earthquake Engineering, Auckland, New Zealand.

SATHIPARAN, N. & MEGURO, K. 2011. Seismic behavior of low earthquake-resistant arch-shaped roof masonry houses retrofitted by PP-band meshes. *Practice Periodical on Structural Design and Construction,* 17**,** 54-64.

SHEPPARD, P. & TERCELJ, S. 1980. The effect of repair and strengthening methods for masonry walls. 7th World Conference on Earthquake Engineering, 255-262.

TAGHDI, M. 1998. *Seismic retrofit of low-rise masonry and concrete walls by steel strips,* University of Ottawa (Canada).

WARD, S. P. 2004. Retrofitting existing masonry buildings to resist explosions. *Journal of performance of constructed facilities,* 18**,** 95-99.

YANG, E.-H., YANG, Y. & LI, V. C. 2007. Use of high volumes of fly ash to improve ECC mechanical properties and material greenness. *ACI Materials Journal,* 10, 49-59.

Chapter 2: Literature review

2.1 Introduction

In the present chapter, a review is carried out on the available information concerning the out-of-plane behaviour exhibited by unreinforced masonry (URM) walls when subjected to static, seismic, impact and blast loads. This information is either (i) recorded in the field, (ii) measured from experiments conducted in the laboratory or (iii) produced from numerical studies which employ nonlinear finite element analysis. The aim of this review is to study the behaviour and assess the vulnerability of URM infill walls against out-of-plane loads and try to identify the effect of the applied loading rate on the exhibited response. Various retrofitting methods developed for strengthening URM walls in the out-of-plane direction are also presented and discussed. Emphasis is then focused on assessing the potential benefits stemming from the use of engineered cementitious composite (ECC) for strengthening URM walls in the out-of-plane direction. The behaviour of ECC under different loading rates and temperatures is initially studied and its ability to be used for the strengthening of URM walls under different loading conditions is assessed on the basis of the available information obtained from experimental and numerical studies.

2.2 Main characteristics of the out-of-plane behaviour of URM walls

The available experimental and numerical data clearly shows that existing infill walls act predominantly as equivalent diagonal struts within the openings of a frame. These "struts" undertake a portion of the applied (horizontal) loads and redirect them to other regions of the structure, thus offering relief to certain structural elements of the RC frame. This results in a significant redistribution of the internal actions developing within the structural elements of the frame. Although this redistribution can result in an increase of the overall stiffness and load carrying capacity of the frame it can also lead to the development of stress concentrations in certain regions of the structure (e.g. joint area, or at specific regions along the length of the beams or columns) which potentially causing localised cracking or even unpredictable (and in many cases brittle) modes of failure (i.e. short-column mechanism) (Chrysostomou & Asteris 2012).

Apart from the in-plane behaviour of infill walls, the out-of-plane behaviour also has a significant effect on the structural performance of RC frames since out-of-plane motion can potentially cause an infill wall to sustain significant damages or even collapse. Consequently, after sustaining a certain degree of damage, infills can no longer contribute to the response of the RC frame with their in-plane stiffness. During the last decades, the out-of-plane behaviour of masonry walls has been experimentally and analytically investigated (Griffith et al. 2007, Cavaleri et al. 2005 & 2009) under static and dynamic loads. Furthermore, many studies indicate that infill panels restrained by frames can develop significant out-of-plane resistance due to the development of arch action and that the out-of-plane strength of a masonry infill wall is mainly dependent on its slenderness. FEMA-306 recommends the calculation of the capacity of masonry infill walls in connection with their out-of-plane failure under seismic excitation. EC 8 (Code, 2005) states that the capacity and stiffness of the infill walls should be taken into consideration during structural analysis, while at the same time accounting for the high uncertainties related to the behaviour of the infill walls. Furthermore, EC8 suggests that appropriate measures should be taken in order to avoid brittle failures and premature disintegration of the infill walls, as well as the partial or total out-of-plane collapse of slender masonry walls.

Drawing from observation after earthquakes and experiments, the behaviour of infill masonry walls is affected by a range of parameters which include the shape and size of the building, the number of the storeys (Magenes, 2006, Russell and Ingham, 2010); the construction method and materials of wall and the dimensions of the walls considered (Housner, 1963, Sorrentino et al., 2006, Lam et al., 2000, Sorrentino et al., 2008, Derakhshan, 2011). The support conditions imposed can also significantly affect the behaviour of URM walls. The distribution of the internal stresses developing within the wall as well as the resulting crack patterns is largely dictated by the support condition imposed (Vaculik, 2012). One-way spanning walls (supported only at two opposite sides) undergo uniaxial bending in the horizontal or vertical direction (Drysdale et al., 1994, McDowell et al., 1956) resulting in the development of cracking parallel to the supports and the axes of internal bending. The behaviour of two-way spanning walls, which include any type of wall supported on at least one vertical and one horizontal edge, is biaxial bending and the associated crack patterns are presented in Figure 2.1 & 2.2 (Griffith et al., 2007)

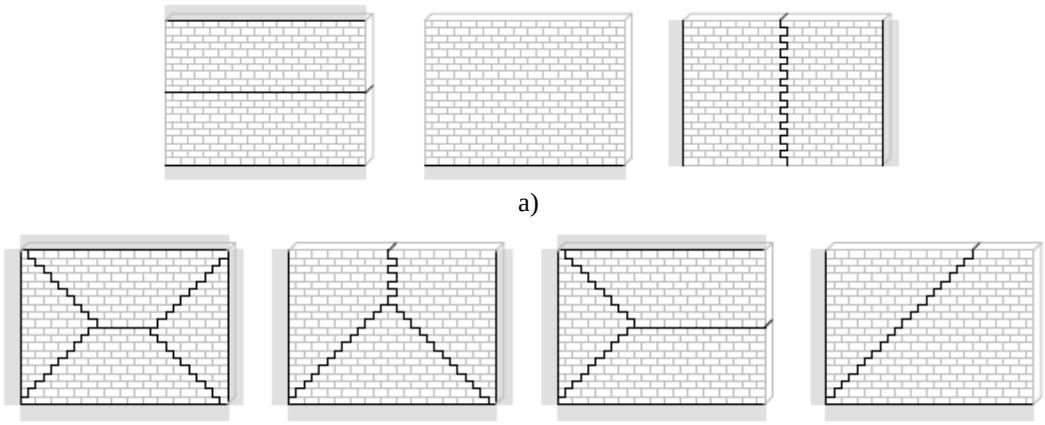

a)

b)

Figure 2.1. a) Vertically and horizontally spanning one-way walls, b) Various types of support shapes and associated out-of-plane flexural cracking pattern (Griffith et al., 2007)

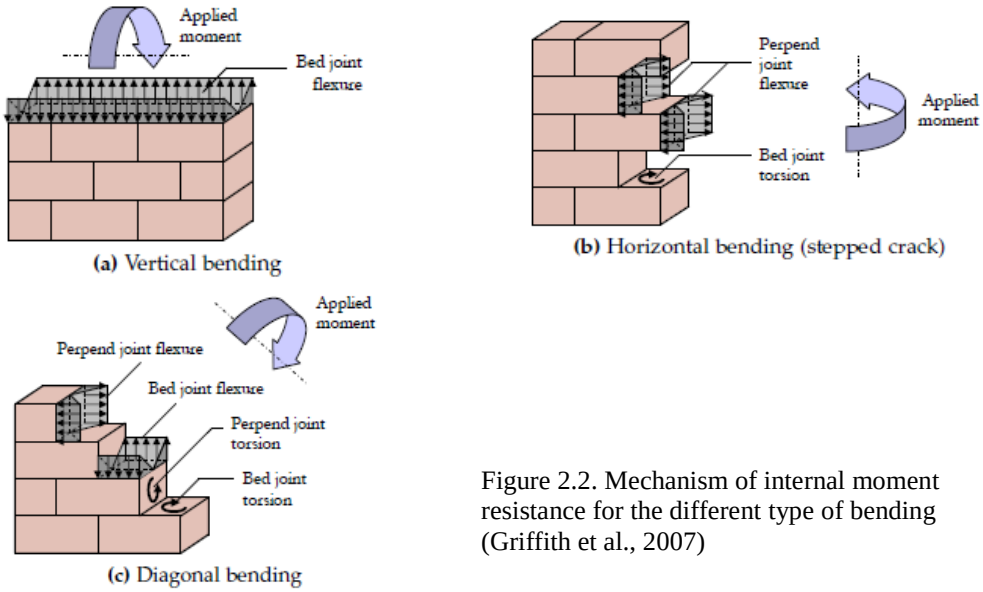

Figure 2.2. Mechanism of internal moment resistance for the different type of bending (Griffith et al., 2007)

2.3 Main characteristics of the out-of-plane loads for URM walls

A wide range of out-of-plain load ranging from creep and shrinkage to blast can be imposed on masonry infill walls. The corresponding strain rates associated with the aforementioned loads are shown in Figure 2.3 (Micallef et al., 2014). Dynamic action such as earthquakes can be significantly more destructive than to static loads due to the inertia force or the resonance effects developing on structures which results in a range of failure modes such as spalling and scabbing or shear plugs due to punching shear failure. The action of loads characterised by higher rates of loading is associated with blast and explosion that URM walls are not designed to withstand. Therefore explosions are one of the major threats to URM walls due to the low flexural capacity and the brittle mode of failure. In fact the failure of URM walls was reported as a major cause of damage and

loss of human life by the Federal Emergency Management Agency (Myers et al., 2004). Four different levels of damage level exhibited by URM walls as a result of blast loading are considered by the US Department of Defence presented in Table 2.1 depending on the level of damage sustained (Criterion, 2002). Table 2.2 lists the equivalent force at different threat levels.

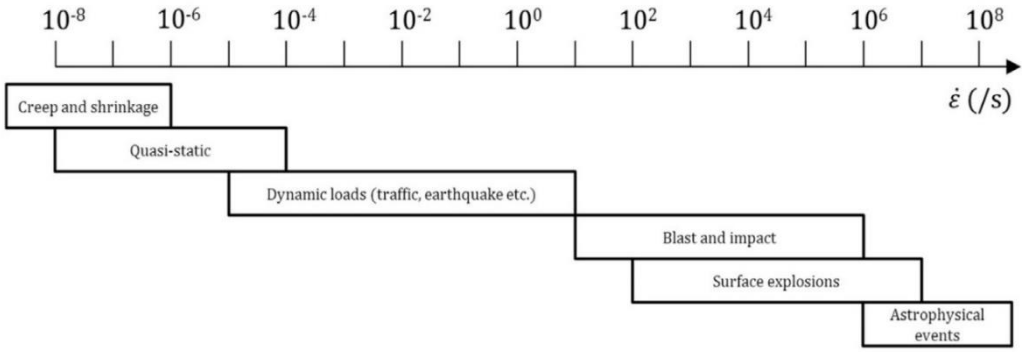

Figure 2.3. Strain rate range of concrete for various load source (Micallef et al., 2014)

Table 2.1: Levels of damage to tested URM Walls (Criterion, 2002)

Level	Damage Level	Damage Description	Performance Description
I	Failure	Wall falls out of test frame.	Wall crumbles and scattered debris.
II	Heavy Damage	Damage that definitely affects load capacity of wall. Wall will not survive same blast load.	Visible wide-open cracks or significant shear cracks, and damage to FRP retrofit. Small debris close to the wall.
III	Light Damage	Damage that does not affect load capacity but additional damage will be observed under same blast load.	Hairline to wider cracks at mortar joints or hairline shear cracks.
IV	No Damage	No damage affecting load capacity of wall.	Hairline cracks in mortar joints.

Table 2.2: Anti-terrorism/force protection design parameters (Criterion, 2002)

Threat level	Weapon(TNT) (kg)	Standoff distance (m)	Tool	Blast pressure (kPa)
High	450	24	2250 kg truck	379
Medium	225	24	1800 kg car	214
Low	99	24	1800 kg car	124
Minimum	22.5	24	1800 kg car	55

2.4 Examples of out-of-plane failures of masonry walls from field observations

Masonry is extensively used to construct infill and load bearing walls because it is available locally in many parts of the world and is an affordable material. It is estimated that more than 70% of the buildings worldwide are constructed from masonry (Matthys

and Noland, 1989). Recent seismic events have demonstrated that URM walls are extremely vulnerable in the out-of-plane direction (Cavaleri et al., 2009, Griffith and Vaculik, 2007) due to their low tensile strength and their brittle nature (Tiedeman, 1980). Based on field observations after major seismic events in L'Aquila (Italy, 2009), Lorca (Spain, 2011) and Emilia (Italy, 2012) considerable damages have been recorded in URM walls associated with their out-of-plane response (see Figure 2.4) (Hak et al., 2014). It has been established that damages or failures exhibited by infill masonry walls in frame structures are largely responsible for the majority of recorded fatalities and injuries (Tiedeman, 1980). It is also interesting to note that when reviewing the costs for repairing damages sustained by various structures during earthquakes it has been estimated that approximately 80% of these costs are associated with damages sustained by the infill walls (Tiedeman, 1980).

Figure 2.4. Examples-of-out of plane masonry failure at earthquake (Emilia, Italy 2012) (Hak et al., 2014)

After the Abruzzo region earthquake (Oyarzo-Vera and Griffith, 2009) it was observed that a common mode of failure exhibited in masonry historical building is related to the out-of-plane failure of masonry walls (Figures 2.5 a & b). In the case of modern frame structures, the most common failure mode was associated with failure of masonry infill panels and exterior masonry panels. It was also observed (Bazzurro et al., 2009) that damage was sustained by URM infill walls in reinforced concrete (RC) buildings. The level of damage varied from small cracks to the total collapse of the infill walls with minor or no damage exhibited to the RC structural elements (beam columns). It is interesting to note that in some cases RC buildings completely lost their masonry infill walls at their lower storeys (Figure 2.5 c). Due to the extensive damage caused to the infill walls and internal partition walls repair costs were high as was the risk of injury and fatality (due to the resulting debris) (Figure 2.5 d). Similarly, after the Christchurch earthquake (Dizhur et al., 2011) it was also observed that the out-of-plane collapse of URM walls was the most common mode of failure associated with buildings. In addition, many two-storey buildings lost their entire front façades or upper storey masonry walls

(Figure 2.6 a). Two characterised types of out-of-plane wall failures presented in Figure 2.6 b, c (Dizhur et al., 2011).

It is interesting to note that the damage sustained by URM walls due to their out-of-plane response during earthquakes may significantly affect the in-plane behaviour of these elements in terms of stiffness and load-carrying capacity (Bruneau, 1994). The combination of in-plane and out-of-plane forces can affect the URM walls. When in-plane shear cracks develop in URM walls, out-of-plane resistance of these walls substantially reduces. Therefore the possibility of out-of-plane failure increases in the URM wall (Figure 2.7 c). Finally, the lack of proper anchorage for masonry infill walls can increase the chance of out of plane failure (see figure 2.7 a & b).

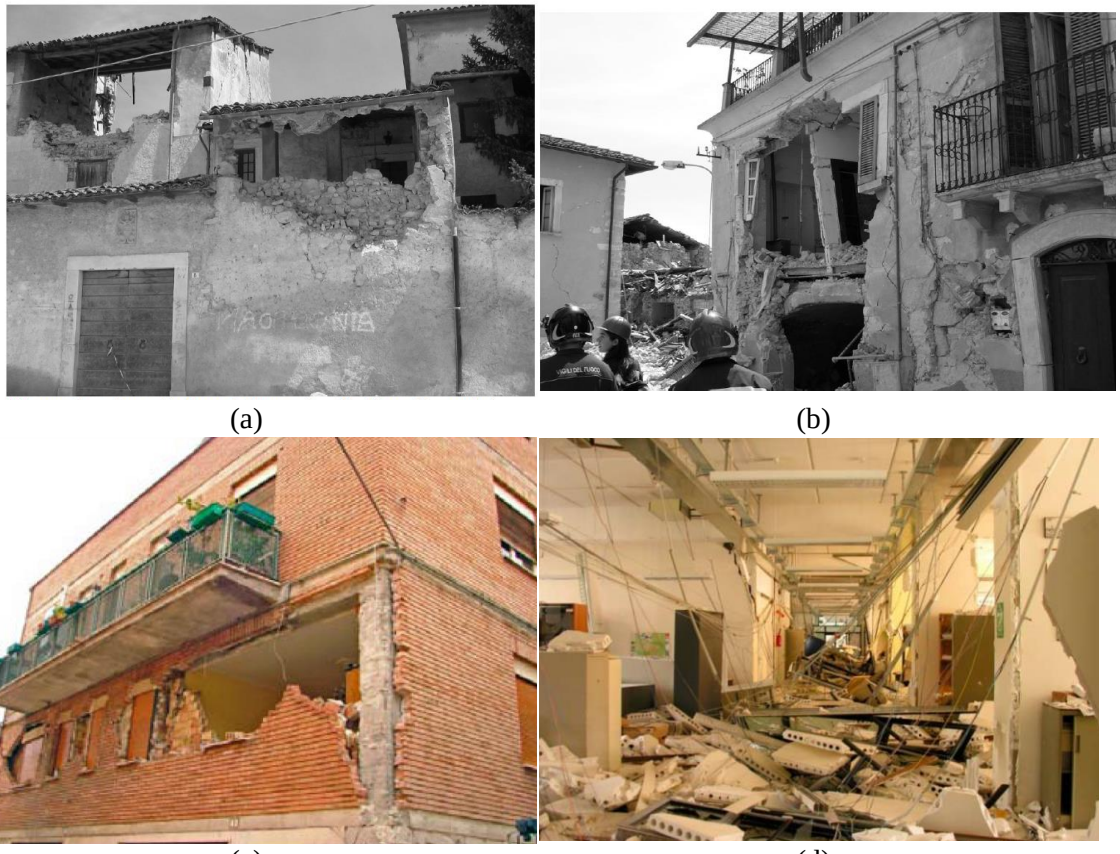

(a) (b)

(c) (d)

Figure 2.5. Examples of out-of-plane collapses of (a,b) external URM walls of traditional masonry structures (San Gregorio, Onna) (Oyarzo-Vera and Griffith, 2009) (c) infill walls and (d) internal partition walls (Bazzurro et al., 2009)

(a) (b)

(c)

Figure 2.6. a) out-of-plane failure of the facade of building b) one-way out-of-plane failure of masonry walls c) two-way out-of-plane failure of masonry walls (Dizhur et al., 2011)

(a) (b) (c)

Figure 2.7. a) out-of-plane failure of URM top story wall (San Francisco, Loma Prieta earthquake) b) failure of church gable (Watsonville, Loma Prieta Earthquake), c) combined out-of-plane/pounding failure (Santa Cruz, Loma Prieta Earthquake) (Bruneau, 1994).

Masonry walls subjected to the out-of-plane high rate loading are vulnerable as they exhibited a brittle mode of failure followed by the production of projectiles debris. The debris from the shattered masonry walls due to an explosion caused extensive damages to the vicinity (Bangash, 2006). Such concern arose from an attack on the World Trade

Centre on 26th February 1992 where masonry infill walls collapsed and the resulting debris caused several causalities and extensive damage to nearby structures (Bangash, 2006) (Figure 2.8).

Figure 2.8. Out-of-plane failure of masonry infill walls in blast explosion (Bangash, 2006)

2.5 Investigating the behaviour of URM walls

The behaviour of URM walls can be assessed experimentally, numerically (through the use of linear finite element analysis) and through the use of simplified assessment methods.

2.5.1 Experimentally established behaviour of URM walls

A wide range of experimental investigations has been conducted to date studying the behaviour of small-scale masonry specimens or full-scale masonry walls under static, earthquake and high rate loading conditions (the latter being associated with impact and blast problems). Different types of test have been conducted for achieving the loading conditions mentioned above including static flexural test, shake table tests, drop weight and blast tests (Hashemi, 2007). Tests investigating the behaviour of URM specimens can mainly be categorised into three groups:

(i) URM walls subjected to uniform or concentrated quasi-static loads applied perpendicular to the wall through the use of inflatable air-cushions or airbags or hydraulic actuators.

(ii) Unreinforced masonry infills subjected to the out-of-plane impact generated by drop weight.

(iii) URM walls subjected to a sudden pressure wave generated from an explosion.

The behaviour of one-way infill masonry walls commonly investigated under static distributed load applied in the out-of-plane direction through the use of the experimental setup presented in the figure 2.9a (FURTADO et al. 2007). The infill walls were placed within the RC frames that was supported latterly by an independent secondary steel frame (see figure 8). The masonry infill wall specimens had a height of 2.3m, a width of 4.20m and a thickness of 0.06m. The out-of-plane load was applied in the form of displacement increments (displacement control) through the use of an air cushion that was inflated via a hydraulic system. The air cushion was positioned between the wall and reaction steel frame (see figure 2.9 a). The specimens were able to undertake a maximum load of 81.2kN exhibiting a displacement of 0.022m at the centre of the panel. During the testing cracks propagated diagonally at the mid-span of the walls as well as at the boundaries between the infill wall and RC frame (see Figure 2.9 b). The damages in the boundaries contributed to the poor performance of out-of-plane performance of specimens.

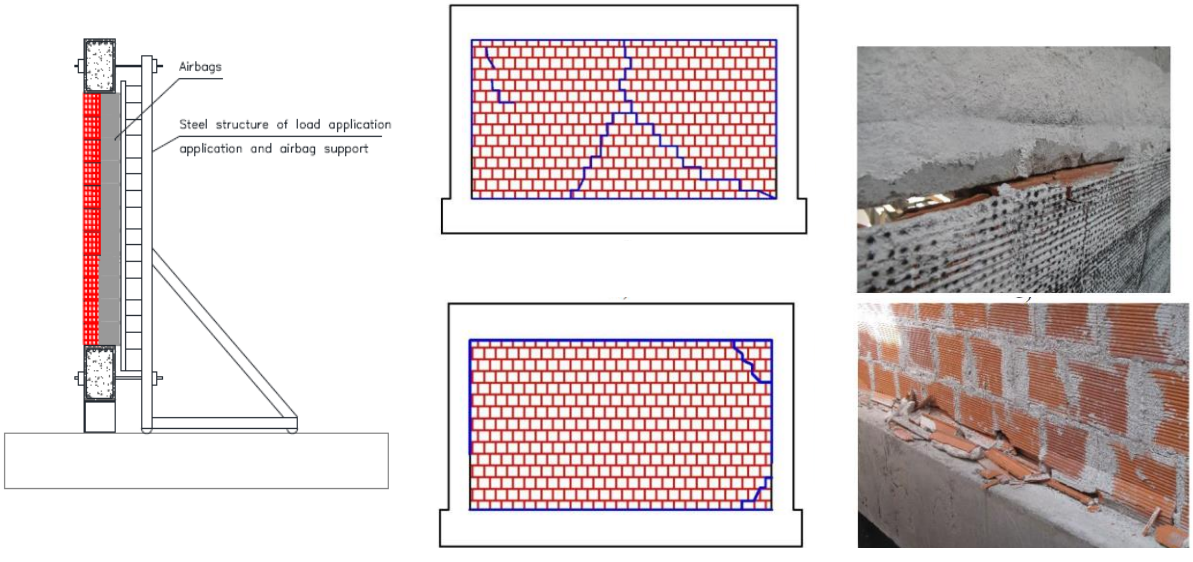

Figure 2.9. a) test set up b) the crack patterns developed after loading (Furtado et al. 2007)

A similar test setup was employed to investigate the out-of-plane behaviour of eight full-scale URM walls under quasi-static loading (Griffith and Vaculik, 2007). Two of these specimens were solid (with no openings) whereas as the remaining six walls had an

opening (see Figure 2.10 a, b). The load was applied onto the face of the wall through the use of a system of air cushions placed between the specimens and a reaction frame (see Figure 2.10 c). Some specimens were also subjected to axial compression prior to the application of the out-of-plane load. Different boundary conditions were imposed through the use of different detailing at the supports (see Figures 2.10 a).

After testing, only a few visible cracks were observed at the vertical edges of the walls in combination with extensive diagonal cracking (see figure 2.10 d). It was observed that increasing values of axial loading could approximately double the out-of-plane strength and stiffness of walls. This was due to the increase of the axial vertical compressive stress on the walls. It reported that the walls with openings had greater strength than solid walls because the length of diagonal cracks contributing to the wall resistance was mostly unaffected by the opening while higher pressure was required to generate the corresponding amount of external work. In addition, the walls which were un-supported at their top edge exhibited less strength and stiffness prior to collapse due to lack of axial compressive stress associated by the confinement that would have been provided if the wall was essentially supported on the top edge. Furthermore, walls with larger width to height ratios appear to have been less influenced by the boundary conditions imposed along the restricted edge and as a result exhibit lower strengths.

Wall Geometry and Support Conditions (dimensions in "mm")	Wall	Pre-compression σ_v
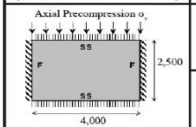	1	0.10 MPa
	2	0 MPa
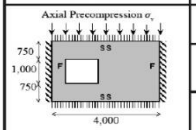	3	0.10 MPa
	4	0.05 MPa
	5	0 MPa
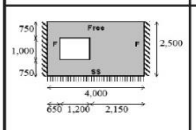	6	N/A Top edge is unsupported.
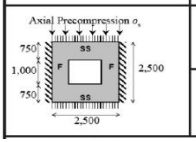	7	0.10 MPa
	8	0 MPa

a

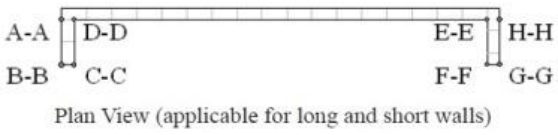

Plan View (applicable for long and short walls)

b

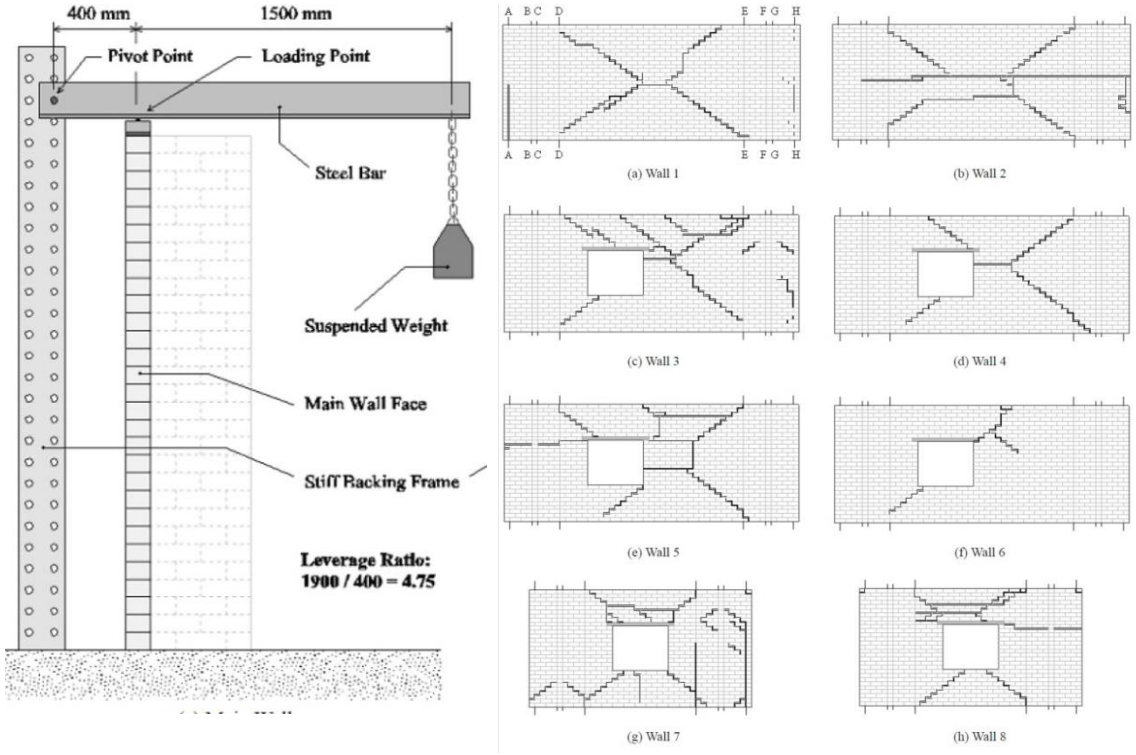

Figure 2.10. a,b) Walls geometry and plan views of walls respectively c) test setup d) Crack patterns developing after loading (Griffith and Vaculik, 2007)

Another experimental setup used to study the out-of-plane behaviour of masonry walls is presented in figure 2.11a (Derakhshan, 2011). In this case, eight full-scale wall specimens, built with solid clay bricks, with different thicknesses and heights were subjected to different levels of axial loading. An out-of-plane distributed quasi-static load was then applied onto the face of masonry walls through the use of hydraulic jacks connected with air cushions (see Figures 2.11b). The top support, between the wall and supporting frame (see Figure 2.11a) was considered to act as a pin. In all cases considered a horizontal crack was observed approximately at a certain height from the wall base (see Figure 2.12a). The cracks were associated with the failure at the brick-mortar interface (Fig 1.12b). It was observed that with increasing values of axial loading the walls exhibited higher values of strength and stiffness.

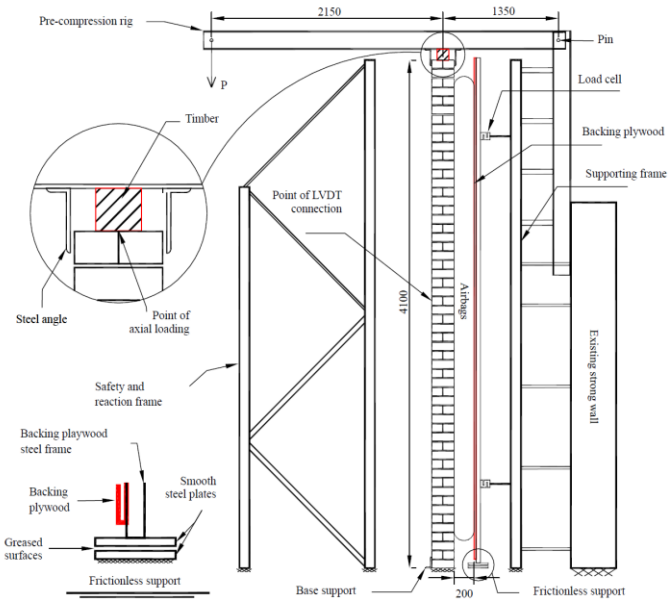

a)

b)

Figure 2.11 a) Latter view of the test setup b) air bag position (Derakhshan, 2011)

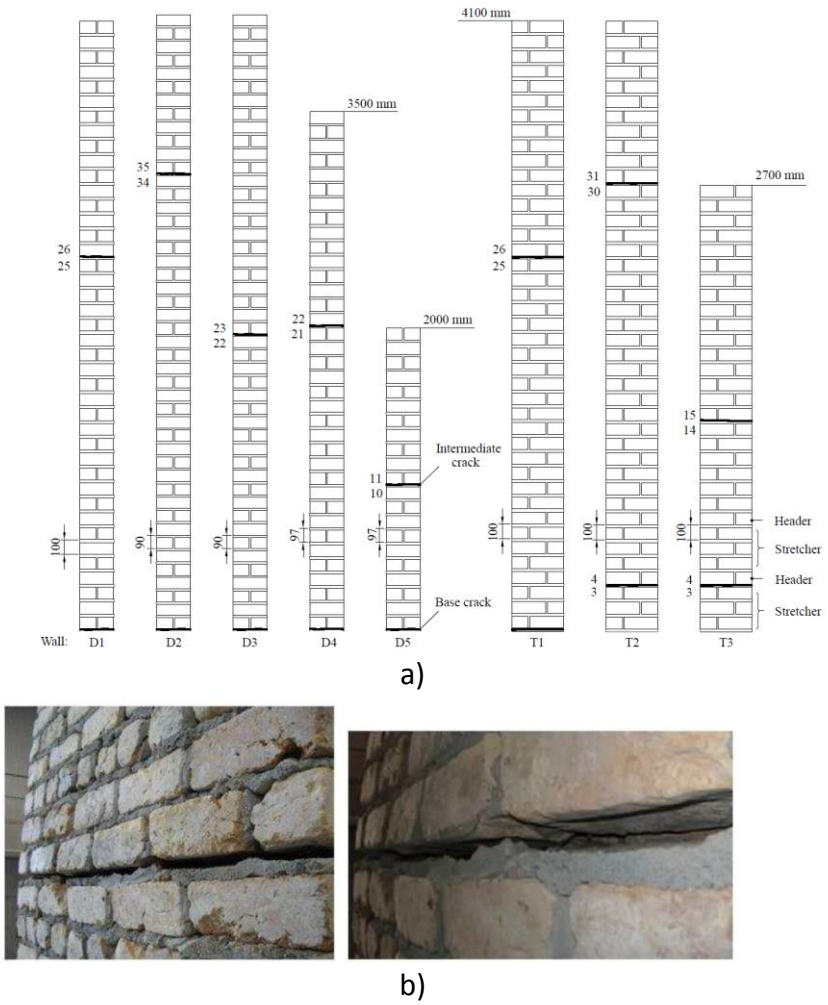

Figure 2.12. a) cracking development after applying the horizental load , b) crack patten in walls at failure (Derakhshan, 2011)

A series of tests were carried out on full scale, single storey RC frames with masonry infills (Hak et al., 2014). Initially, an in-plane load (resulting in 0.0, 1.0, 1.5 and 2.5% drift) was applied to the top beam of RC frame. This was then followed by the application of an out-of-plane concentrated load applied monotonically to failure at the centre of the infill wall surface through the use of a hydraulic actuator. The crack profile forming on the surface of the wall is shown in Figure 2.13 and is the same as that shown for the case of two-way support walls observed in out-of-plane failure. It was characterised by the opening of horizontal crack at mid-height of the panel following by diagonal cracks towards the corners of the infill walls. It was observed that the failure mechanism was drastically affected by the level of damage sustained during the application of the in-plane horizontal load. The crack forming after applying in-plane loads is presented in Figures 2.13 a, b & c. The variation between the level of in-plane load applied and the out-of-plane strength of infill walls is presented in Figure 2.13d.

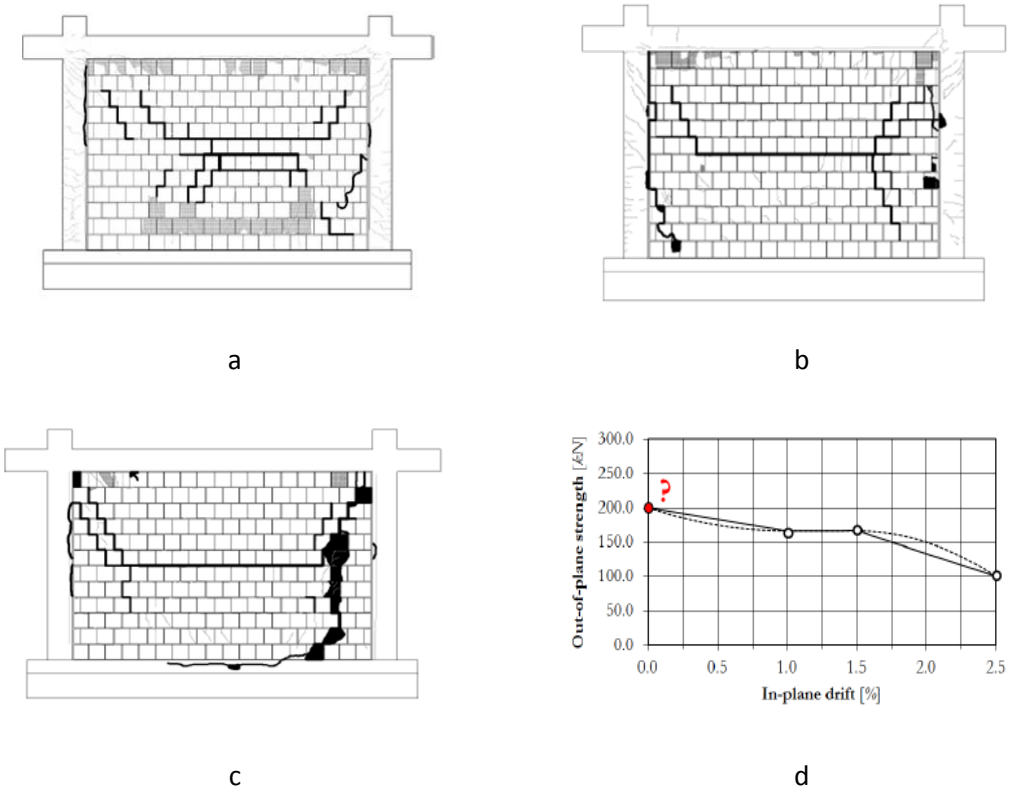

Figure 2.13. Crack patterns exhibited (grey in-plane and black out of plane) at a) 2.5% drift, b) 1.5% drift. c) 1% drift; d) in-plane and out-of-plane strength relationship (Hak et al., 2014).

The drop-weight set-up presented in figure 2.14 was used in order to investigate the performance of URM walls when subjected to low velocity impact (Gilbert et al., 2002). A spherical drop hammer was used to apply the impact force. The impact load was applied over an area (impact region) of 400x400 mm whereas the drop-mass was allowed to fall from a height of 500 mm in order to create the loading conditions with the collision of a car. The main variables considered were the wall thickness (200 to 440 mm), wall length (5000 to 9150 mm) , unit type (weak concrete block 12 N/mm, Strong concrete block 37 N/mm2 and solid class B clay engineering block 134 N/mm2) , strength of wall (dry laid weak blocks, mortar bonded weak block, mortar bonded strong block and mortar bonded solid brick), the impact location (close to end of the wall or in mid-point) and the end conditions (fixed or pinned).

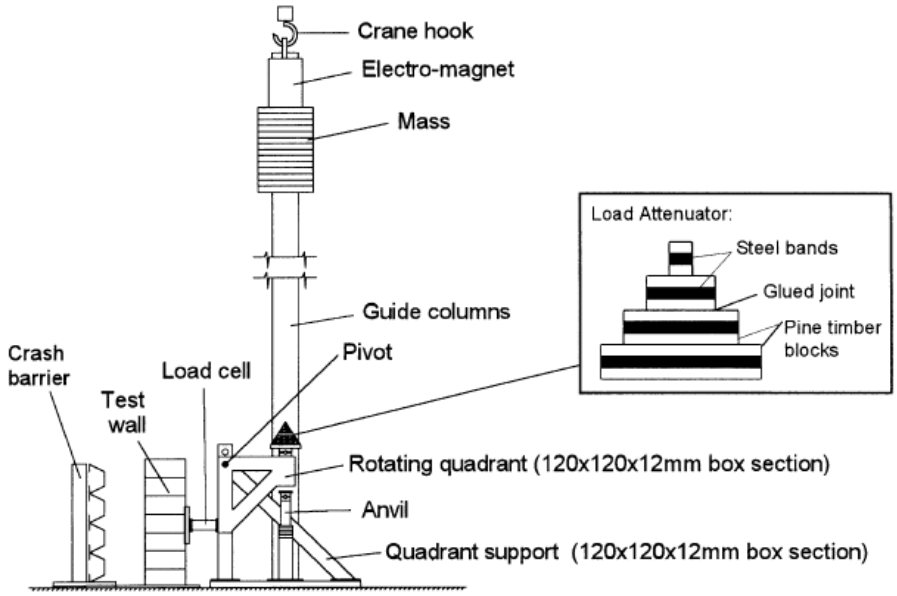

Figure 2.14. Drop weight test set up (Gilbert et al., 2002)

Figure 2.15 shows the crack patterns forming on different URM walls constructed from blockwork and brickwork respectively. For all walls considered, failure was associated with the formation of cracks. Wall length was found to effect the failure mode. Short walls without fix ends tended to form vertical cracks at the impact area (Figure 2.15). Long walls or short walls with fix ends exhibited a vertical crack at the impact area and vertical or diagonal cracks near either sides. The wall thickness was found to influence the out-of-plane impact resistance. Thicker walls exhibited higher load carrying capacity. The thickness of walls did not affect ranking profile significantly. Strong concrete and brick walls exhibited different failure modes compared to weaker walls. The strong unit walls resulted in the developing of diagonal rather than vertical cracking.

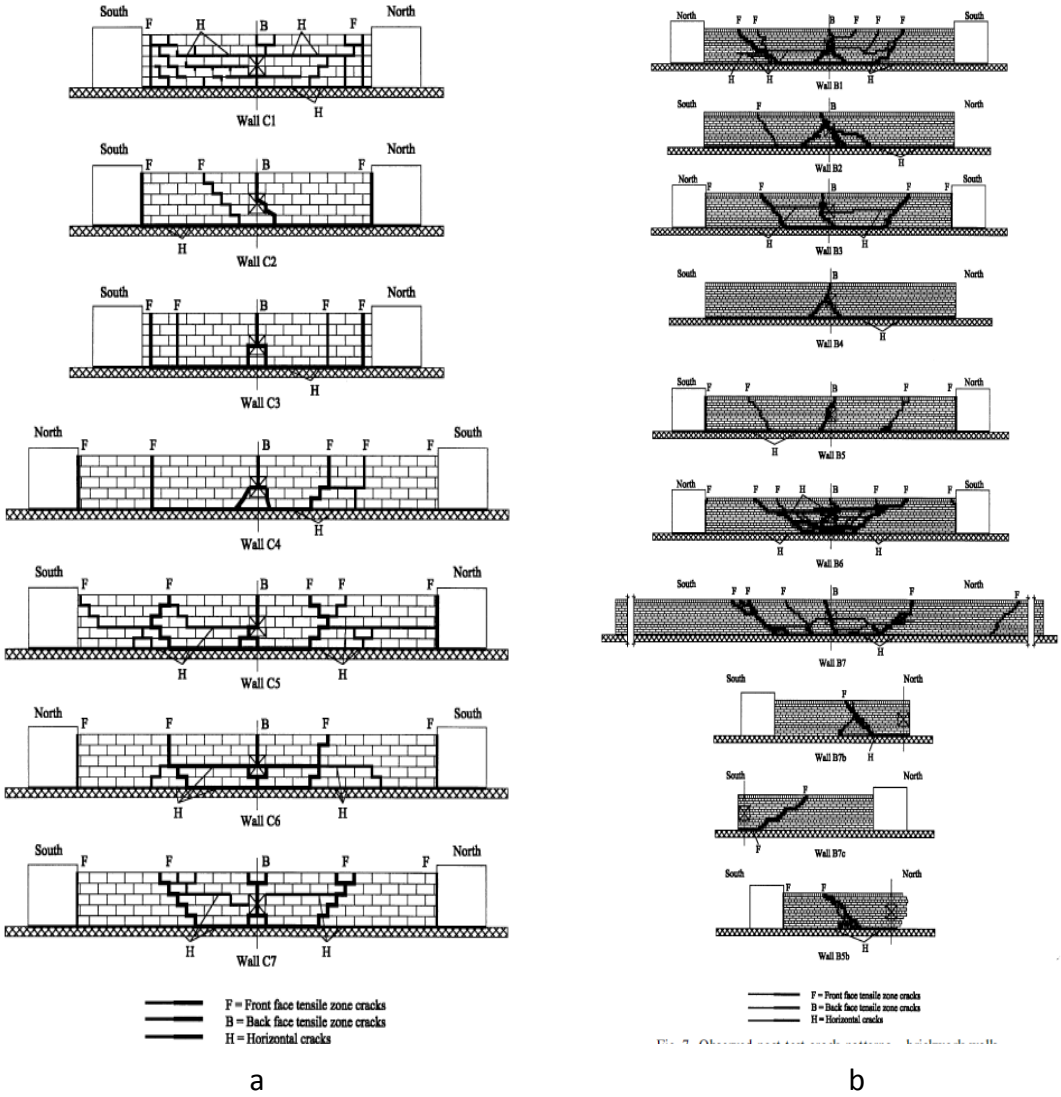

Figure 2.15.Crack patterns developing on URM wall specimens constructed from: (a) blockwork and (b) brickwork (Gilbert et al., 2002)

The behaviour of masonry infill and its failure mode at blast tested by the full-scale 2.24m x 1.22m walls with different thicknesses of 0.1m and 0.2m (Myers et al., 2004). A steel frame was designed for boundary condition of walls and was connected to walls at top and bottom. The blast test placed at the US Army base and conducted with military explosive range. It observed the blast resistance capacity of URM walls was typically dominant by their tensile capacity. The URM wall failed under out-of-plane mode in the maximum tensile region. Walls experienced vertical and horizontal cracks during the blast at mid-height of walls and also some vertical cracks in the middle of walls (Figure 2.16).

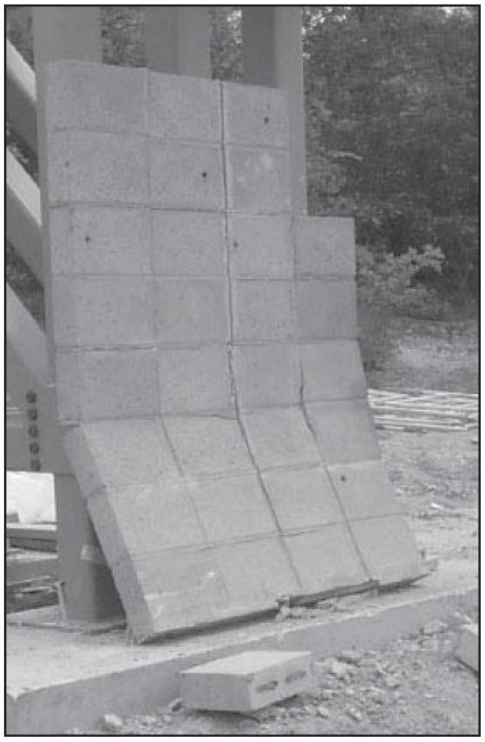

Figure 2.16. Failure of wall at blast peak pressure 1254 kPa (Myers et al., 2004)

The localised damage and fragmentation of the masonry wall subjected to explosion was investigated for the case of two 1.2m x 1.5m x 0.24m URM wall specimens subjected to different blast loads characterised by different intensities (Shi et al., 2016). The edges of the subject walls were connected to the members (beam and columns) of a concrete frame. The blast load was generated via the detonation of 1kg or 6kg of explosive material (TNT) located 0.4m away from centre of the walls. When using 1kg of TNT it was noted that the damage associated with spalling exhibited on the interior face of the wall specimen was more significant than that sustained by the exposed face of the wall (see Figure 2.17 a,b), with debris being scattered at a distance of up to 11.7m from the specimen. The size and shape of the fragments produced varied. It is interesting to notice that the sharper and finer fragments were projected furthest (Figure 2.17 e). The results of the first test indicated a very high level of risk, associated with potentially lethal debris with high initial velocities being generated without the collapse of the masonry wall. The use of 6 kg of TNT increased the intensity of the generated blast load resulting in localised collapse at the centre of the wall, (Figure 2.17 c, d). It is interesting to note the lack of spalling towards the supports due to the brittle nature of the mode of failure exhibited by the wall under high loading rates.

a

b

c

d

(b) Splashed fragments

e

Figure 2.17 (a) Front and (b) rear faces of the URM wall after first test (1kg TNT) accompanied by (c) the front and (d) rear faces of the wall after the second test (6kg TNT) e) debris produced during the first test (Shi et al., 2016)

The performance of the URM walls was studied when subjecting the 2m x 2m x 0.45m URM wall specimens fixed along their bottom edge (see Figure 2.18 a) to blast loads with different intensities (Ahmad et al., 2014). Different amounts of TNT (4 kg, 6 kg, 8 kg, 10 kg, 12 kg and 14kg) were used to conduct a series of tests. The charges were placed 3m away from the centre of the walls. It was observed that the wall was able to maintain its integrity (in spite the development of some cracking) when subjected to a blast load generated by using 6kg of TNT (Figure 2.18 c). The use of larger amounts of TNT resulted in the development of horizontal cracking in the middle of the walls. When using 12 kg of TNT, the level of horizontal cracking exhibited was non-reparable (Figure 2.18 d), whereas when using 14 kg of TNT, the wall fully collapsed.

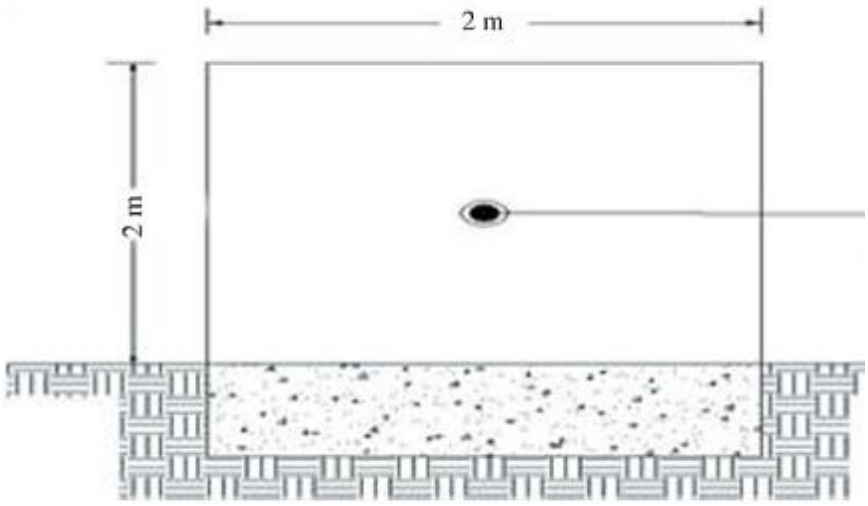

a)

b)

c) d)

Figure 2.18 a)The walls dimensions and support condition, b) the blast wave propagation, c) wall after explosion of 6kg charge d) wall after explosion of 12kg charge (Ahmad et al., 2014)

2.5.2 Numerical studies

Due to the difficulties, limitations and the high costs associated with the experimental investigation of URM walls experiments under high rate loading of experimental tests, the behaviour of subjected walls are investigated through the use of nonlinear finite element (NLFEA) analysis. The use of NLFEA models can provide more detail for the description of the behaviour of masonry infill walls as well as the effect of a wide range of parameters. The NFE models result calibrated and compared to a counterparts experimental tests. These models are then used to predict the behaviour of masonry structures at different loads.

2.5.2.1 Modelling of masonry infill walls

The different models employed for simulating masonry infill walls can be as follows (Asteris et al., 2013):

i) One-phase model: (Figure 2.17). This is the simplest approach for modelling masonry walls as the masonry (consisting of the masonry units, mortar and interface is available) (Timoshenko et al., 1959) is modelled as a homogenous and isotropic continuum. Such models can be used for the analysis of large-scale masonry structures (Asteris et al., 2013). However, this approach is not appropriate for detailed stress analysis of small-scale specimens, especially when considering the influence of the brick-mortar interface (Asteris et al., 2013).

ii) Two-phase model: In this approach the masonry units and mortar are lumped and modelled together, whereas the bricks interface is modelled by discontinuing elements (Figure 2.19 c) (Asteris et al., 2013). This approach can reduce the computation power required while providing a more accurate representation of the masonry walls compared to one-phase model. However after cracking of URM walls occurs the accuracy of these models decreases (Hashemi, 2007).

iii) Three-phase model: based on experimental observation after the crack initiation in URM infills, the out-of-plane strength and behaviour of URM walls depend on the compressive strength of masonry because of the arch action of the URM walls (Hashemi, 2007). Three-phase methods represent the masonry units and the mortar layer in the joints by continuum elements whereas the brick-mortar interface is

presented by interfaces elements (Figure 2.19d) (Eremin et al., 1956, McDowell et al., 1956, Angel et al., 1994, Klinger et al., 1997, Dawe and Seah, 1989). Though this approach provides more accurate results compared to the experimental data (Dawe and Seah, 1989) the level of computation cost associated with the solution of such a problem is intensive and the application of this approach is usually limited to small laboratory specimens (Asteris et al., 2013).

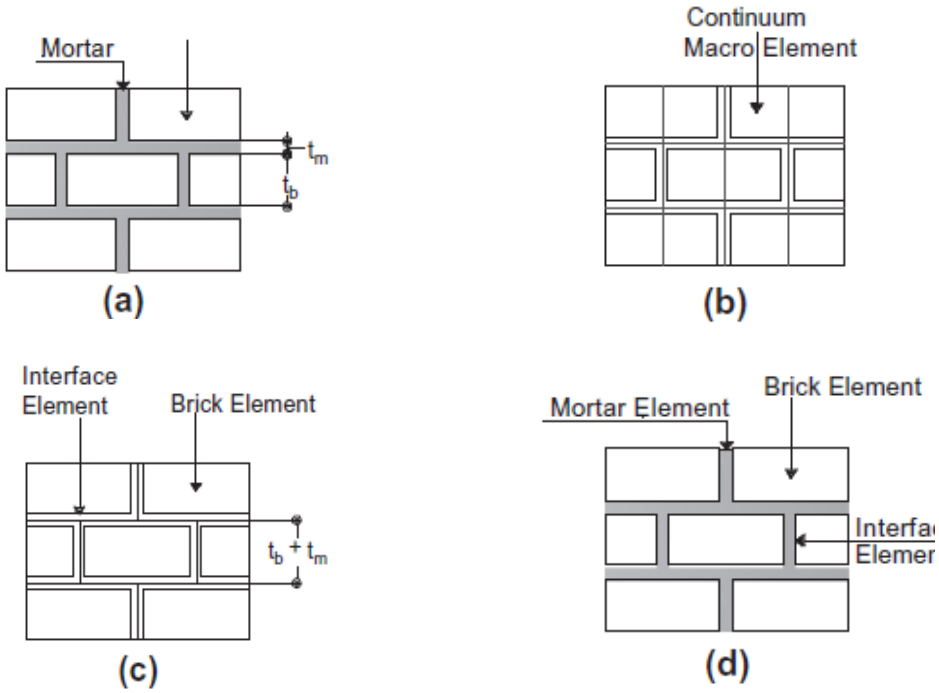

Figure 2.19. Masonry different models, a) masonry sample b) one phase model c) two phases model d) three phases model (Asteris et al., 2013)

2.5.2.2 Smeared crack approach

The localized failure associated with cracking happens when the stress developing in a given part of the FE models (brick unit, mortar) corresponds to a point in the principal stress space that lies outside the surface defining the failure criterion for material. The plane of the crack is normal to the direction in which the largest tensile stress. In the smeared-cracking model approach, the cracks are smeared out in a continuum fashion and the concrete becomes orthotropic or transversely isotropic after the occurrence of the first crack (Asteris et al., 2013).

2.5.2.3 Discrete element method

The discrete element method is associated with interfaces (jointed) failure. The changes in contact forces are traced with time during the calculation process. The equations of dynamic equilibrium for each element/block in this method are repeatedly solved until the laws of contact and boundary conditions are satisfied. Furthermore, in this method the elements/blocks can be split-up based on the assumed joints failure-criteria during the calculation process. Due to its capability to explicitly represent the motion of multiple, intersecting discontinuities, the discrete element method is particularly suitable for the analysis of discontinuity such as the masonry walls in which a significant part of the deformation is due to relative motion between the blocks (Asteris et al., 2013). The discrete element models developed for masonry structures under static and dynamic loads (Mohebkhah and Tasnimi, 2007, Mohebkhah et al., 2008).

2.5.2.4 Nonlinear finite element solution procedure

The NFEA solution strategy has usually been developed independently from the material models adopted and shows the following characteristics (Asteris et al., 2013):

i) It employs an iterative procedure based on well-established numerical techniques such as the Newton–Raphson method in order to account for the stress redistributions during which the crack formation and closure checks, as well as convergence checks, are carried out simultaneously in each iteration (Figure 2.20).
ii) It adopts an implicit or explicit integration scheme to solve numerically the governing equation of motion in the case of dynamic problems.

2.5.2.5 Calibration of numerical models against the experimental tests

It is a common practice that the mechanical properties employed to define the constitutive models adopted from the results of small-scale compressive, tensile and shear tests on masonry prisms, masonry units and mortar specimens, as these tests are simple, inexpensive and easy to carry out. However, this approach may contain some errors due to the scatter characteristic of the masonry material properties, the different curing conditions in the laboratory and the field, the fact that small-scale tests may not be representative of large scale structural problems and the effect of some parameters in large structures (i.e. boundary conditions and the structures shape and size) may significantly affect the behaviour of masonry structures (Sarhosis, 2016). As a result, it is recommended that the results obtained from large-scale experiments are considered (Figure 2.20) to identify the material properties (Sarhosis and Sheng, 2014).

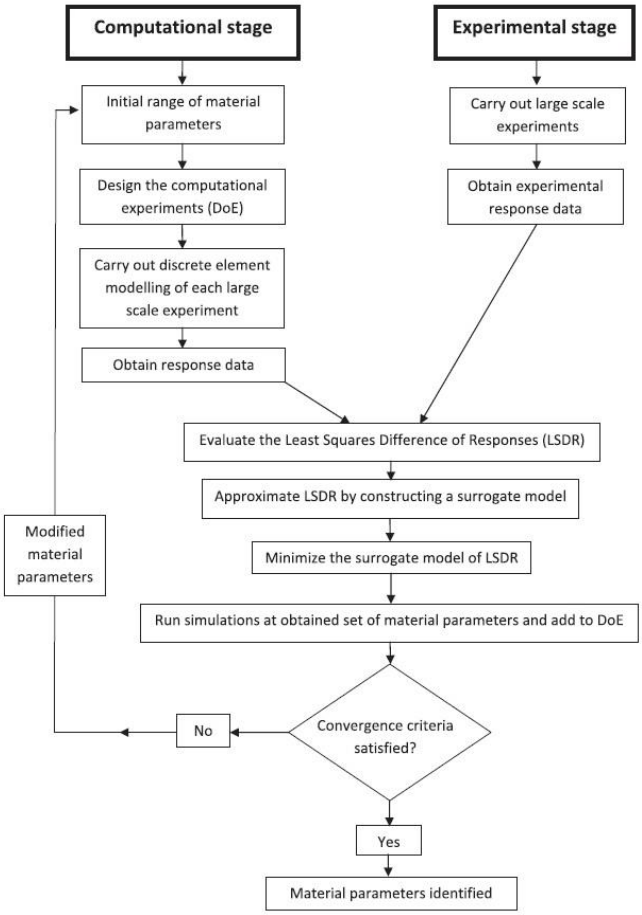

Figure 2.20. Schematic chart for the identification of material properties (Sarhosis and Sheng, 2014)

2.5.2.6 Numerical case study for masonry walls under out-of-plane loads

The out-of-plane behaviour of URM infills walls is studied by NFEA method by adopting a one-phase approach (Hashemi, 2007) under force controlled pushover analysis (Figure 2.21). The infill wall behaviour was assessed under different boundary (fixed and pinned) conditions for the case of two-way infill walls (four sides of the wall were connected to columns and beams) and one-way infill walls (only top and bottom edges of the wall were connected to beams). It was observed that when assessing URM infill using fixed connection the NFEA overestimates the stiffness of URM walls in out-of-plane direction compare to experimental data. The comparison of the predicted results with their experimental counterparts revealed that that NFEA model predicts better the out-of-plane behaviour of infill walls when considering the URM walls with side released (Figure 2.22).

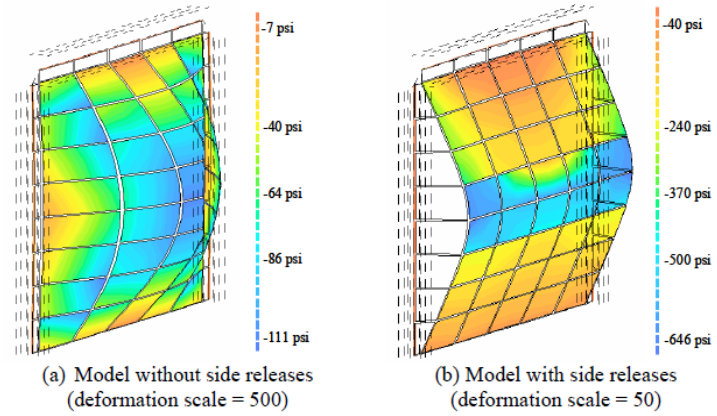

Figure 2.21.Exaggerated deformed shapes of FE models subject to uniform out-of-plane pressure (Hashemi, 2007)

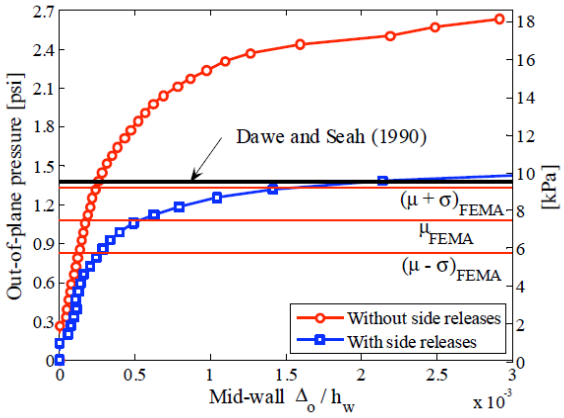

Figure 2.22. Out-of-plane FE pushover analysis results compared with empirical approaches (Hashemi, 2007)

The two-phase approach (the linear elastic solid elements for masonry unit and contact interface model for the brick-mortar interface) was used to model masonry walls under impact load (Burnett et al., 2007). It was observed that the magnitude of the applied loading impulse had a significant influence on the failure mode and displacement–time response. For example, diagonal front face cracks were not observed at 90% of the impulse while at 110% resulted in diagonal cracks forming closer to the point of impact and crack widths becoming larger (Figure 2.23). It was observed that parameters consisting of the base friction, fracture energy, joint failure stress need to be calibrated. Change in these parameters results in a significant change of the predicted response of NFEA. The mesh size, time step and penalty stiffness had a significant influence on the overall response of a wall model when a reasonably fine mesh is employed.

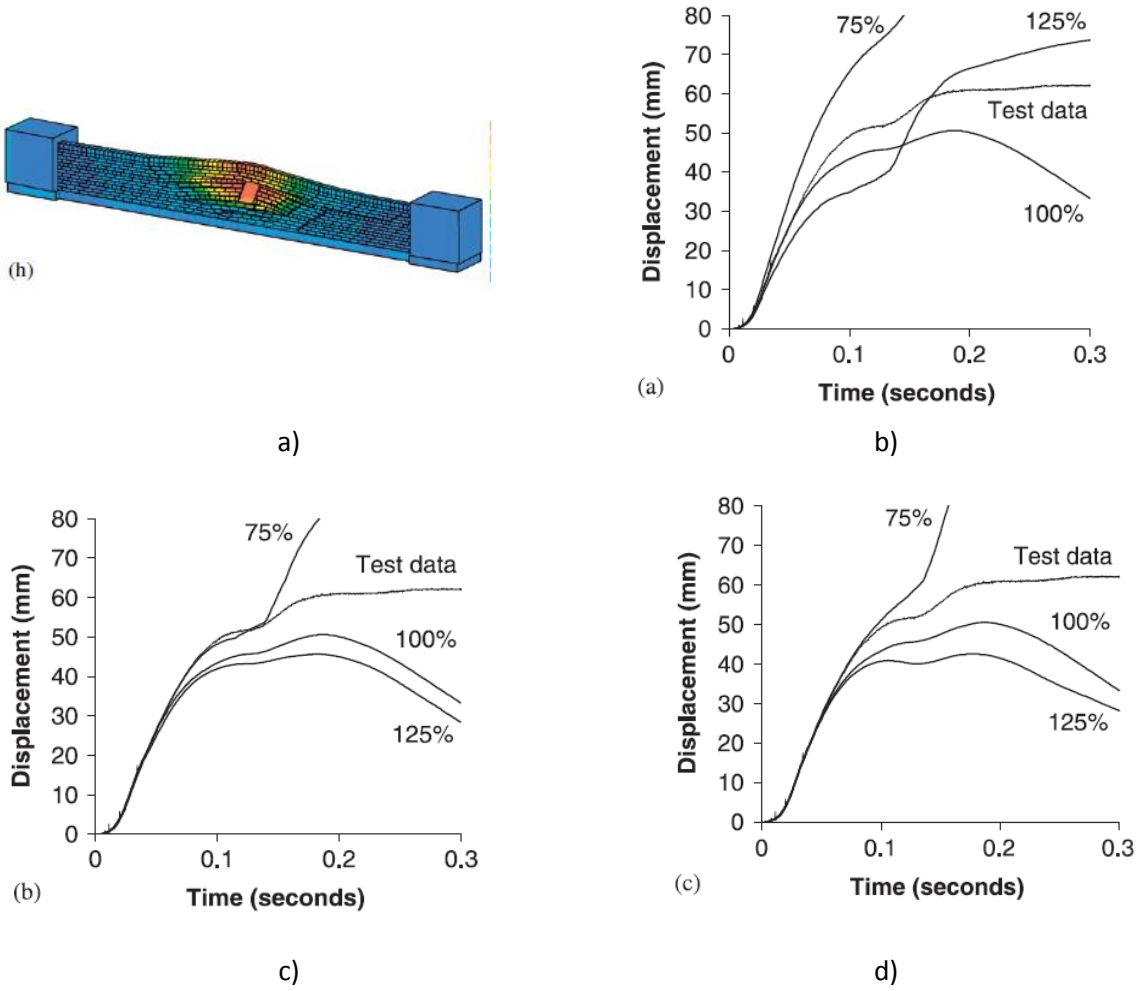

Figure 2.23. a) numerically predicted out-of-plane displacement, the influence of b) base friction, c) fracture energy, d) joint failure stress (Burnett et al., 2007)

2.6 Methods for strengthening URM walls

Considering the weak performance of URM walls under out-of-plane loads, it is essential to use retrofitting methods to enhance their out-of-plane behaviour in terms of strength, stiffness, ductility.

2.6.1 Concrete layer and steel mesh

A series of methods have been developed by forming a layer of concrete/mortar and with a reinforcement mesh on the masonry surface.

Forrocement method: This method involves the use of several layers of reinforcing mesh with fine diameter bars and reinforcement ratios of 3-8% and a mortar layer with a thickness of 10-50 mm (Figure 2.24). The mortar can be casted or sprayed through the mesh with a covering thickness of about 5 mm. The mechanical properties of the

retrofitted wall highly depend on the mesh properties (ElGawady et al., 2004). The main parameters in this method are associated with the quantity of the steel mesh and quality of mortar layer.

Figure 2.24. Retrofitting of a URM building using mesh and micro-concrete (ElGawady et al., 2004).

Reinforced plaster: In this method, a layer of mortar plaster should be applied over a mesh of steel reinforcement (see figure 2.25). The direction of steel bar can be horizontal, vertical or diagonal and the plaster is applied manually in this method (ElGawady et al., 2004).

Figure 2.25. Reinforced plaster method for improving the torsional moment of a single story masonry building (Tasnimi and Rezazadeh, 2012).

Shotcrete: The concrete sprayed on the surface of masonry wall reinforced with a layer of a steel mesh. This method is more convenient and economical compared to the methods mentioned earlier (Figure 2.26). Normally the thickness of the shotcrete layer is about 60 mm and the reinforcement provided is in the form of a welded wire fabric with a minimum steel ratio placed mainly for crack control. In order to improve the transfer of the shear stresses at the interface between the masonry and the shotcrete layer a series of dowels can be installed in the wall (ElGawady et al., 2004).

Figure 2.26. applying shotcrete (ElGawady et al., 2006)

Advantages and disadvantages: Main advantages of the latter three methods are associated with the low cost required for their application, the durable and uniform behaviour exhibited by the strengthened walls, they require locally available material, and they significantly improve the in-plane strength as well as the out-of-plane stability and energy dissipation. However, the main disadvantages of these methods are related to the increase in the mass of structures, they require surface preparation prior to their application, they affect the aesthetic view of the building, they require finishing of the surfaces formed after retrofitting and a relatively long time is needed for their applications (ElGawady et al., 2004).

2.6.2 External steel reinforcement

Steel straps can be used as external reinforcement to improve the behaviour of URM infill walls. The steel reinforcement (sheets) are attached to the USM walls and connected to the existing framework (figure 2.27). Then steel straps can secure the URM infill wall position and increase the load carrying capacity in the out-of-plane direction (Ward, 2004).

Figure 2.27. Steel stud reinforcement wall and window (Ward, 2004)

Advantages and disadvantages: The advantages of the use of external steel strips is associated with the fact that its application requires minimum surface preparation, it achieves a durable and uniform behaviour of strengthened URM walls, improves the out-of-plane strength and the energy dissipation exhibited by the strengthened URM walls. Some disadvantages are associated with the time-consuming and complicated procedure of installation, the high costs, the increase in the mass of the structure, and the fact that the use of such strips can affect the aesthetic view of the building (Ward, 2004).

2.6.3 Fibre reinforced polymer (FRP)

FRP usually made from glass, carbon, aramid fibres are often used (in the form of straps) instead of steel sheets and plates in order to enhance the in-plane and out-of-plane behaviour of URM walls. This type of materials are lighter than steel, they have higher strength and are non-corrosive. This method can be applied quickly and is non-intrusive. (Buchan and Chen, 2007). The FRP strips usually are bonded onto the surface of the URM wall with epoxy resin and can improve in-plane and out-of-plane strength of URM walls (Mosallam, 2007).

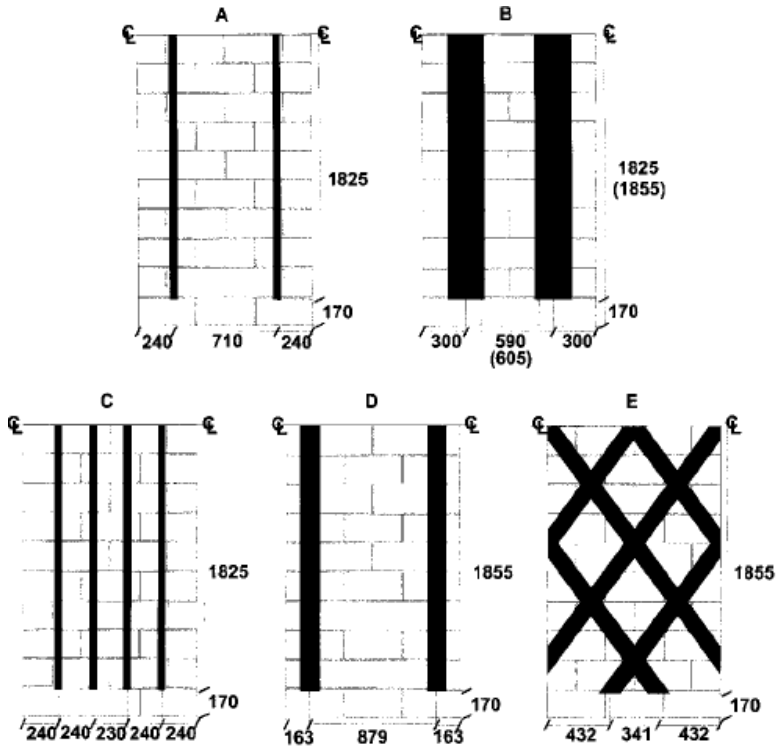

Figure 2.28. Different patterns of FRP on URM wall (Albert et al., 2001)

Advantages and disadvantages: The use of this method does not add mass to the structure, it caused less disturbance, the material used are readily available, highly durable and have tailored mechanical properties. The main disadvantages of this method include the finishing that is required after retrofitting, the high cost of FRP, poor performance at high temperatures, very sensitive to ultra-violet rays and behaviour of URM walls retrofitted with FRP is linear and non-ductile (Mosallam, 2007).

2.6.4 Elastomeric Spray

The use of elastomeric spray is a relatively new method and employs a polyurea-based coating of up to 15 mm thick applied directly to the surface of an existing masonry wall. Once dry, the coating forms a tensile membrane-enhancing the flexural capacity of the masonry significantly reducing spalling (Ward, 2004). The coating is relatively inexpensive, but the wall surface must be prepared very thoroughly and considerable attention must be paid to the cleanliness of the masonry surface (Figure 2.29). The system has been exposed to blast pressures of up to 35 psi and impulses of 215 psi-ms successfully reducing spalling. For load-bearing walls and masonry infills with windows,

it may be necessary to fit a secondary component to the internal face in order to redistribute the loads around critical areas.

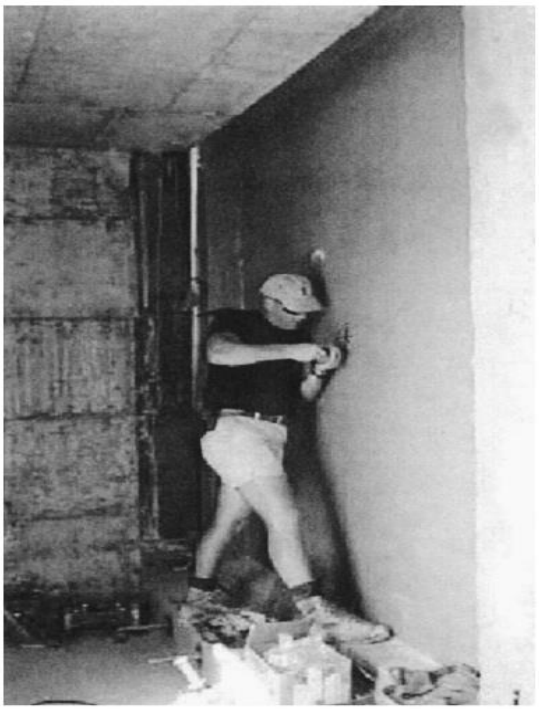

Figure 2.29. Elastomeric spray applied to URM wall (Ward, 2004)

2.6.5 Geotextiles

Geotextile are developed by the geotechnical industry for the stabilisation of weak soils (Figure 2.30). Tests where geotextiles have been secured to the internal face of masonry walls and subjected to blast loads have been conducted (Ward, 2004). The fabrics commercial names include Aramid, Kevlar, and Geofabric are usually glued to the internal face of the masonry wall. In doing so, they act as a net system catching masonry fragments from entering the building avoid causing further damages and injuries (Figure 2.30). While effective, considerable attention must be paid in order to secure the fabric top and bottom or ensuring there is an effective bond between the fabric and the masonry. Further, special arrangements must be made for load-bearing walls and walls with windows.

Figure 2.30. Anchored geotextiles secured to building frame acting as a catcher system (Ward, 2004)

2.6.6 Comparison of different retrofitting method of URM walls

For retrofitting of URM building the designer should choose the appropriate method according to structure requirement. Table 2.3 summarised the advantages and disadvantages of retrofitting methods mentioned earlier (Amiraslanzadeh et al.).

Table 2.3: Advantages and disadvantages of different retrofitting methods (Amiraslanzadeh et al.)

Method	Advantage	Disadvantage
Shotcrete, Ferrocement, Reinforcement plaster	Low cost, durable and uniform behaviour, Locally available material, improve in-plane strength, improve out of plane stability, Improve energy dissipation	High mass, require surface treatment, affect the aesthetic view of the building. Require finishing, high disturbance, long process, reduce the volume of building
Steel straps external reinforcement	Surface preparation is minimal, durable and uniform behaviour, improve the out of plane strength, improve energy dissipation	The installation process is long and complicated. The technic is expensive, increase mass, affect aesthetic view of building, fragmentation problem at blast
FRP	No added mass, Low disturbance, Available materials, Improves shear and flexural strength, Improves in-plane and out-of-plain behaviour	Affect architecture, Require finishing, High cost. Poor performance at high temperature, very sensitive to ultra-violet rays. Linear stress-strain curve.
Elastomeric Spray, Geotextiles	No debris. No added mass. Improve out of plane behaviour	Very limited data. Expensive, high technology needed

2.7 Retrofitting of URM walls using the engineered cementitious composites

2.7.1 An introduction to ECC and its application

Engineered Cementitious Composites (ECC) is a fibre reinforced composite that exhibits ductile, strain-hardening behaviour under tension. This composite has a high tensile strain capacity (up to 3-5%), which is achieved due to the formation of a large number of microcracks (crack width <100 micron)(Li, 2003) (Figure 2.31). The first version of ECC was developed by Li and Leung in 1992 (Li and Leung, 1992). This early version of ECC used poly ethanol (PE) fibres with a fibre volume contents of about 2%. During the past two decades, various types of ECC have been developed, including self-compacting ECC (Kong et al., 2003), sprayable ECC (Kim et al., 2003), high-early strength ECC (Wang and Li, 2006, Li and Wang, 2007), light-weight ECC (Wang and Li, 2003), green ECC (Li et al., 2004, Lepech et al., 2008), self-healing ECC (Herbert and Li, 2012, Li and Herbert, 2012, Li and Yang, 2007), pigmentable ECC (Yang et al., 2012), ix) high volume fly-ash ECC (Wang and Li, 2007), PVA-ECC(Li et al., 2001). Figure 2.31 shows the typical stress-strain curves describing the behaviour of PVA-ECC under tension.

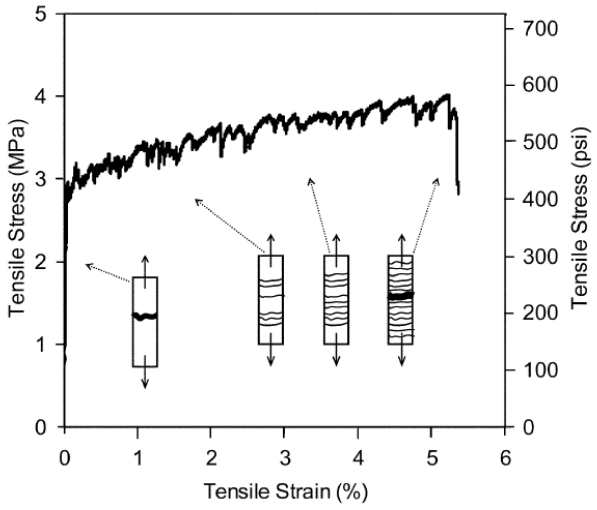

Figure 2.31. Typical tensile stress–strain curve development of ECC. (Yang et al., 2007)

The subject material has also been successfully produced in various countries, including Japan (Kanda et al., 2006), Germany (Mechtcherine et al., 2011a), South Africa (Song and Van Zijl, 2004), Denmark (Lárusson et al., 2010, Lárusson et al., 2013), Netherlands (Zhou et al., 2010), New Zealand (Lin et al., 2014), UK, Turkey (Şahmaran et al., 2013), Malaysia (Altwair et al., 2012), Singapore (Ahmed and Maalej, 2009, Zhang et al., 2014), China (Yuan et al., 2014), Brazil (Tonoli et al., 2010), Iran (Halvaei et al., 2014) and India

(Patodi and Kulkarni, 2012). All of these studies have shown that ECC is a ductile material in which the mixture can be adjusted to achieve a desirable, strain hardening tensile property. Table 2.4 lists all ECC mixtures that have been successfully developed around the world. In general, these mixtures typically contain cement, fly-ash, water, fine sand and, if necessary, a viscosity modifying agent. Different ECC mixtures summarised by the author are based on the mixture proportion of fly-ash used of low, moderate, and high volume content. The ECC in Japan (Kanda et al., 2006), for example, contains a low amount of fly-ash, but high water-to-binder ratio (W/B). The ECCs developed in the USA, Turkey, Iran, India, Germany and Malaysia (Halvaei et al., 2014, Li, 2003, Şahmaran et al., 2013) utilize moderate amounts of fly-ash (typically the fly-ash-to-cement ratio is between 1.0 to 1.2), and the water-to-binder ratio (w/b) is between 0.22-0.33. In the high volume fly-ash ECC, the fly-ash-to-cement-ratio is typically greater than 2.0.

Table 2.4: ECC mixture in different countries.

Fly Ash Content	Country	Cement	Fly Ash	Sand	W/B	PVA
Low	New Zealand	1	0.3	0.8	0.36	2
	Singapore	1	0.12	0.55	0.5	2
	Japan	1	0.4	0.8	0.5	2
Moderate	USA (M45)	1	1.2	0.8	0.25	2
	Turkey	1	1.2	0.8	0.27	2
	Iran	1	1.2	0.8	0.25	2
	India	1	1.0	1	0.22	1.5
	Germany	1	1.2	1	0.28	2
	Malaysia	1	1.2	0.8	0.33	2
High	Africa	1	1.7	1.4	0.36	2
	UK	1	2.8	0.6	0.28	2
	USA (High volume fly ash)	1	2.2	2.2	0.28	2

Key characteristics of ECC behaviour include high fatigue resistance under cyclic loads, the development of multiple uniformly distributed fine cracks (with widths that are very narrow and not easily visible) (Rokogo and Kanda, 2005). Due to these unique aspects of ECC behaviour, the subject material has been used in various applications: (i) building and repairing bridge decks, (ii) retrofitting of the surface of dams (iii) surface repairing of irrigation channels, (iv) retrofitting of retaining walls, (v) retrofitting of railways, (vi) the construction of structural members of skyscrapers to absorb earthquake energy (see

Figure 2.32) (Rokugo et al., 2009). In addition to the above more potential markets are available for ECC as its use can increase the life cycle of infrastructures and subsequently reduce the construction cost in the long term.

Figure 2.32 a) Dam retrofitting application b) retaining wall retrofitting application c) bridge retrofitting application d) improving the seismic behaviour of a tower (Rokugo et al., 2009).

2.7.2 Behaviour of ECC under different loading rates

The general uniaxial tensile behaviour of ECC under quasi-static load was measured on coupon specimens at 28 days after being produced as presented in Figure 2.33 (Kong et al., 2003). The ultimate tensile strain of the ECC measured varied from 3% to 5% for specimens. During the test, a large number of microcracks with very fine crack spacing (2–5 mm) and small average crack width of 0.08 mm were observed in specimens (figure 2.33).

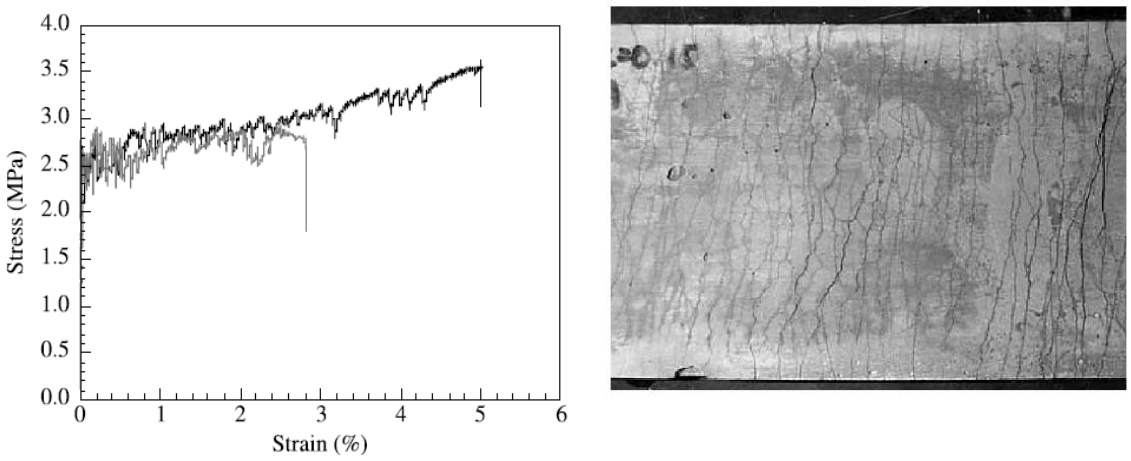

a b

Figure 2.33. a) The stress-strain curves of ECC specimens under uniaxial tensile test (Kong et al., 2003) b)The crack pattern formed on the ECC specimens during tensile test (Kong et al., 2003)

The ECC behaviour under high loading rates showed a reduction in the tensile strain capacity by about 80% at strain-rates higher than 10^{-4} s^{-1} compared to those mentioned under quasi-static loading rate, while the tensile strength increases by about 70% under high loading rates (Yang and Li, 2006). It was found that the chemical bond between the PVA fibres and ECC matrix affected the ductility of ECC at high loading rates more than other parameters (i.e. fibre modulus of elasticity, matrix toughness).

Other studies investigated the behaviour of ECC under strain rates ranging from 10^{-6} s^{-1} to 10^{-3} s^{-1} and also from 10 s^{-1} to 50 s^{-1} where it was subjected to uniaxial tensile loading (Mechtcherine et al., 2011b). When strain rates increased from 10^{-6} s^{-1} to 10^{-3} s^{-1} the test data obtained showed a 22% increase in tensile strength while the strain capacity of ECC decreased by 47%. Furthermore, it is interesting to note that the developing cracking was

less distributed while the width of the cracks forming increased with higher loading rates. At strain rates $50s^{-1}$ the tensile strength of the ECC specimens increased by 53% and strain capacity increased by 163% compared to their counterpart established at a strain rate of $10s^{-1}$. The observed increase in the value of strain capacity under these loading rates is attributed to the change of fibre failure mode. Although at lower strain rates the increase in chemical bond caused the fibres to rupture with average pull out a range of 300 microns, at higher strain rates the fibre pull out range increased from 0.5 to 2.5 mm. This increase was caused by local plastic deformation of the fibres (Figure 2.34).

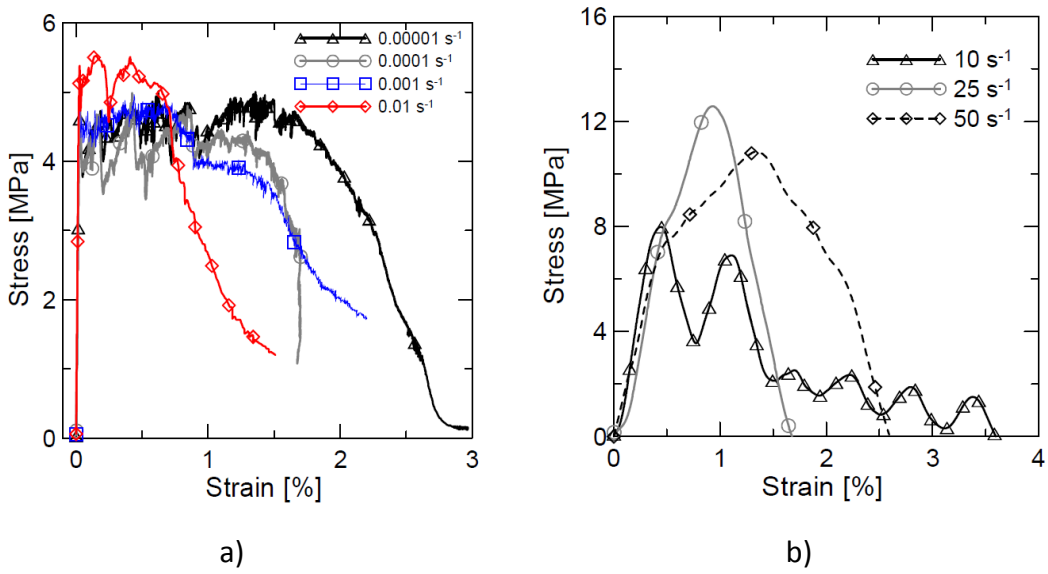

Figure 2.34. Stress-strain curves obtained from the tensile test of ECC dog-bone specimens under different loading rate a) from 10^{-6} s^{-1} to 10^{-3} s^{-1} b) from 10 s^{-1} to 50 s^{-1} (Mechtcherine et al., 2011b).

2.7.3 Effect of temperature on ECC

Despite the widespread applications of ECC, studies about its behaviour under increasing temperatures are very limited. One study about the behaviour of ECC at high temperature (up to 800 ˚C) (Şahmaran et al., 2011, Sahmaran et al., 2010) revealed that PVA fibre can decrease the degree of spalling and increase the compressive strength of ECC under high temperature (about 50% at 400°C is) (Figure 2.35). They also found that a higher content of fly-ash in ECC mix proportion (FA/C=2.2 compare to FA/C=1.2) improves the compressive strength of ECC (about 10%) at high temperature.

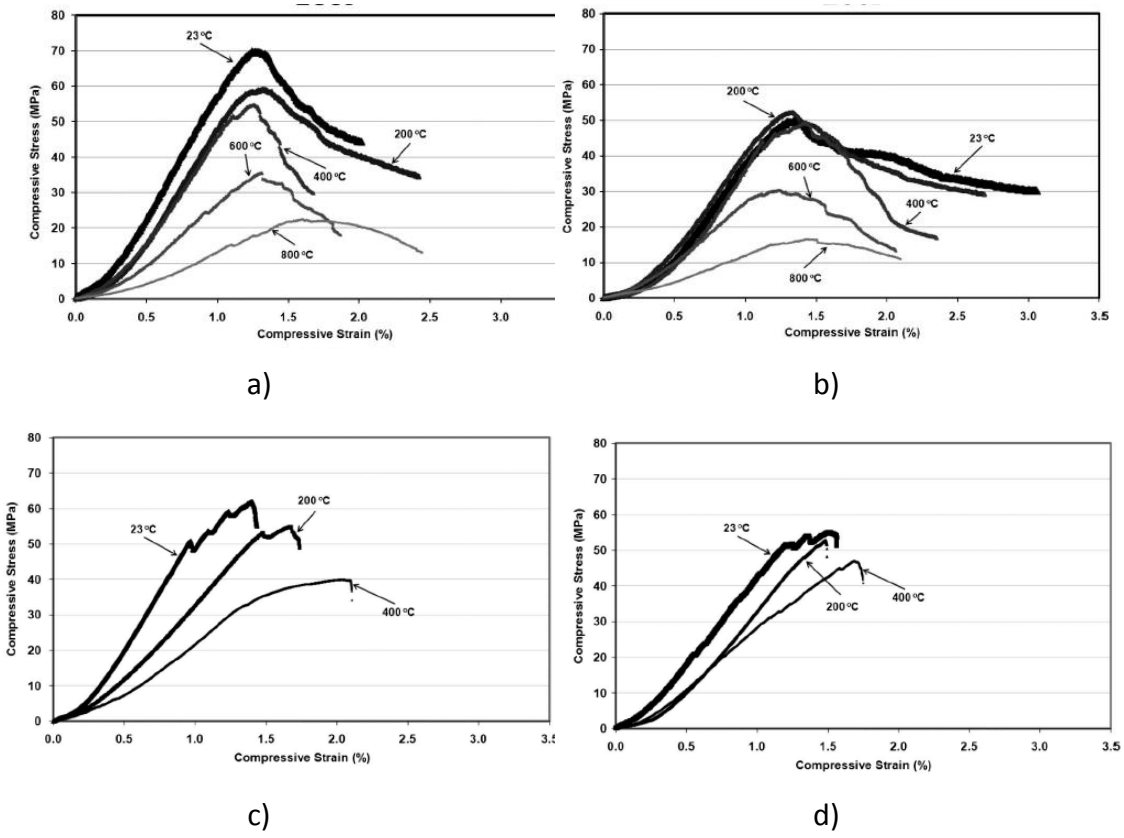

Figure 2.35. Effect of elevated temperatures on compressive stress-strain curves of ECC and ECC matrix mixtures a & c) ECC1 with FA/C= 1.2 with and without PVA fibre respectively, b & d) ECC2 with FA/C= 2.2 with and without PVA fibre (Şahmaran et al., 2011, Sahmaran et al., 2010)

Tests conducted to investigate the tensile strength of ECC during and after fire (Mechtcherine et al., 2012) reveal that when temperature increased up to 100°C the tensile strain capacity of ECC increased while tensile strength of ECC decreases. When ECC is subjected to high temperature (of up to 100°C), the strain capacity increases possibly due to the reduction of the bond interface of PVA fibre and ECC matrix (Figure 2.36). It is observed that the crack width at 60°C is bigger than that established under 20˚C which results in an increase in tensile strain capacity. Also due to the reduction of bond strength between the fibre and matrix, longer fibre free length can develop and higher elastic and plastic deformation of fibre occur. However, at 150°C, it was found that the ability of ECC to form multiple cracks diminished due to the deterioration of the fibre mechanical properties.

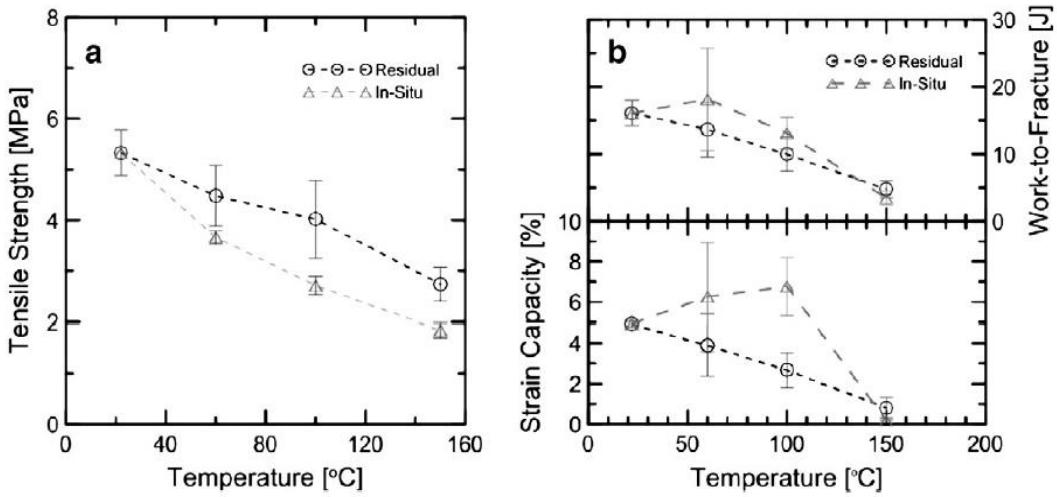

a) b)

Figure 2.36. Effect of temperature on the residual and in situ mechanical properties of ECC (a) uniaxial tensile strength and (b) strain capacity and work of fracture (Mechtcherine et al., 2012)

Finally, tests carried out to investigate the effect of high temperatures on the compressive strength of ECC (Shang and Lu, 2014) revealed that until 200°C the compressive strength of ECC increases (less than 5%). Furthermore, the effect of elevated temperatures did not decrease the compressive strength until 400°C. However, beyond 400°C the compressive strength of ECC decreases drastically (more than 40%).

2.7.4 Combined high temperature and high loading rate effect on the tensile behaviour of ECC

The research on the combined effect of high temperature (20 ˚C to 150˚C) and high strain rates ($10^{-5}s^{-1}$ to $10^{-2}s^{-1}$) on the tensile behaviour of ECC is presented in Figure 2.37 (Mechtcherine et al., 2012). It observed the tensile strength of ECC under combined high temperature and high loading rate decreases continuously from 20 ˚C to 150˚C for all strain rates ranging from 10^{-5} s^{-1} to 10^{-2} s^{-1}. However, ECC under the strain rate of 10^{-2} s^{-1} has higher (about 25%) tensile strength compare to that established at 10^{-5} s^{-1}. The tensile strain capacity of ECC for all strain rates increases when temperature increased from 20 ˚C to 100˚C and then at temperature beyond 150˚C the strain hardening capacity decreased drastically.

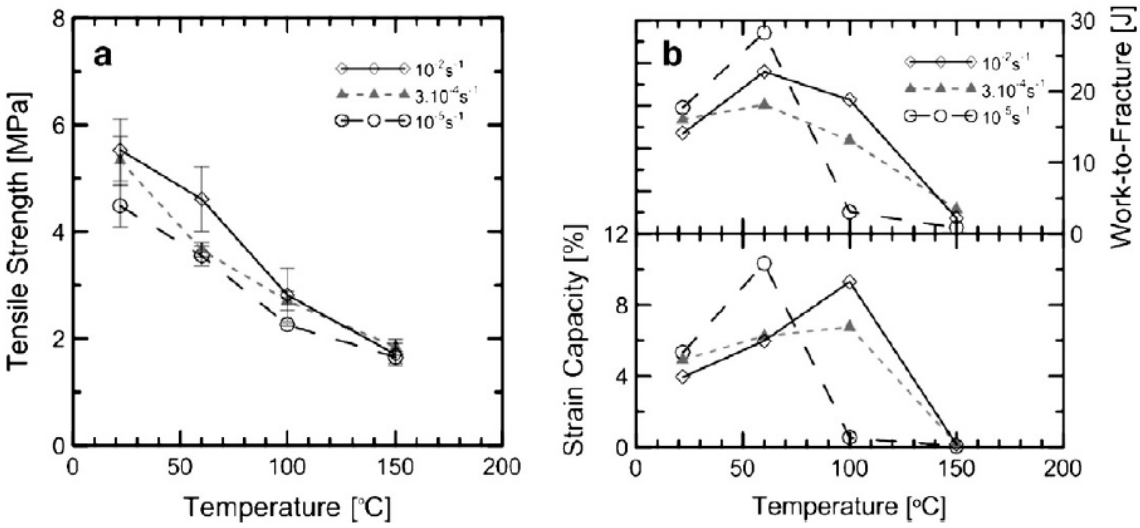

a) b)

Figure 2.37. Effect of temperature and strain rate on the in-situ mechanical properties of ECC: (a) uniaxial tensile strength and (b) strain capacity and work-to-fracture (Mechtcherine et al., 2012)

2.7.5 Hybrid ECC (HECC)

Hybrid fibre ECC (HECC) is a combination of high-modulus fibres (normally steel fibres) and low-modulus fibres (such as Polyethylene (PE) or Polyvinyl Alcohol fibres (PVA)). Initially, HECC was developed to achieve the desired balance between the ultimate strength and the strain capacity of material required for the construction of impact and blast-resistant structures (Maalej et al., 2005) (Figure 2.38 a). The flexural behaviour of HECC with different volume fractions of high-modulus fibres (between 0.5% to 1.5% steel fibre by volume) and low modulus fibres (between 0.6% to 1.5% PVA fibre by volume) investigated to optimize the critical fibre volume fraction of high-modulus fibres and low-modulus fibres, in order to achieve strain hardening behaviour in tension (Ahmed et al., 2007). It was observed that the low-modulus fibres (PVA fibres) affect the tensile strain capacity of hybrid fibre composites, while high-modulus fibres (steel fibres) influence the ultimate tensile strength. The effects of the length of low-modulus fibres (12mm and 18mm PE fibre) on the strain hardening behaviour of the HECC investigated (Ahmed and Maalej, 2009). It observed the increase of length of low-modulus fibres (PE fibres) by 1.5 times increases in tensile strain capacity by about 6 times and improves the multiple cracking behaviour of hybrid fibre composites (Figure 2.38 b)

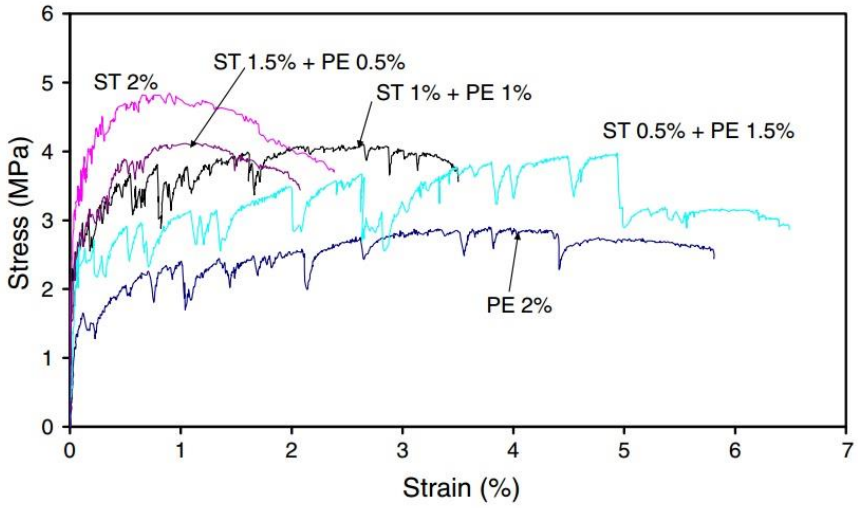

a)

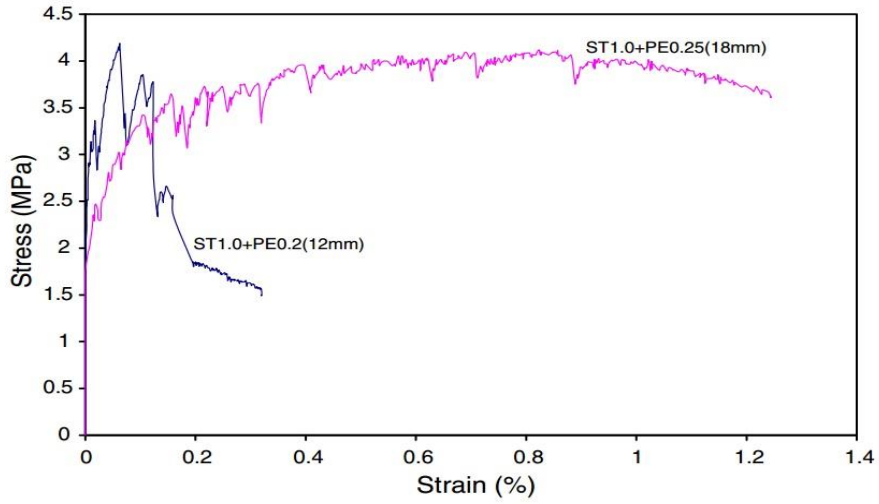

b)

Figure 2.38. a) Stress-strain curves obtained from mono fibre and hybrid fibres reinforced ECC under uniaxial tensile test b) Stress-strain curves obtained from 12mm and 18mmPE fibres on HECC behaviour under uniaxial tensile test (Ahmed and Maalej, 2009)

Other studies on the behaviour of HECC reveals that the higher the high-modulus fibres content (steel fibres) resulted in the higher compressive strength, Young's modulus, ultimate flexural strength and flexural strain. However, the increase in high-modulus fibres content (steel fibres) was found to decrease the ultimate strain capacity (Hermes et al., 2012). Also, it was observed that using a larger amount of low-modulus fibres (more than 1.75% PVA fibre by volume) does not increase tensile strain capacity.

2.7.6 Behaviour of HECC under different loading rates

The behaviour of HECC (with 0.5% steel and 1.5% PVA fibres by volume) under uniaxial tensile tests subjected to different strain rates ranging from $2x10^{-6}$ s^{-1} to $2x10^{-1}$ s^{-1} was studied by (Maalej et al., 2005). It observed the HECC specimens strain capacity reduced by about 25% whereas the tensile strength of specimens increased about 75% under elevated loading rates compared to their counterparts subjected for the case of lower loading rates. Other studies carried out on the tensile behaviour of HECC with two different hybrid mix proportions of (i)1.5% PVA and 0.5% steel fibre by volume and (ii) 1.75% PVA and 0.58% steel fibre by volume under different loading rates from $1x10^{-5}$ s^{-1} to $1x10^{-1}$ s^{-1} (Soe et al., 2013). It is observed for both HECC mixtures that the strain capacity reduced about 20 times whereas the maximum tensile strength increased about 2 times under elevated loading rates compared to their counterparts subjected to lower loading rates (Figure 2.39).

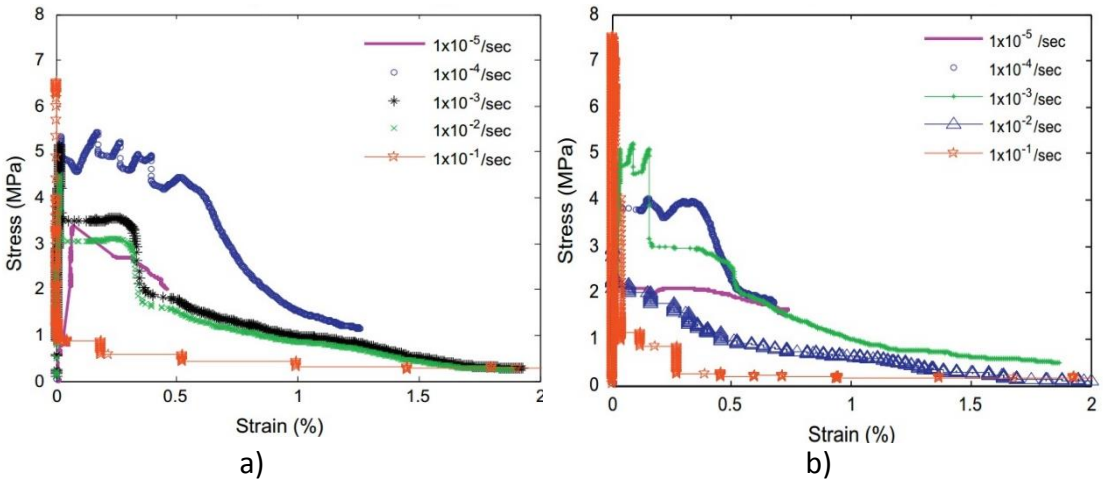

Figure 2.39. Stress-strain curves of HECC under different loading rate a) 1.5% PVA and 0.5% steel fibre b) 1.75% PVA and 0.58% steel fibre (Soe et al., 2013)

2.7.7 Effect of temperature on HECC

As discussed earlier (section 2.7.3) the performance of ECC at elevated temperatures especially over than 100 ˚C is highly affected due to the reduction of mechanical properties of the low-modulus fibres (PVA fibre). In the HECC the high-modulus fibres (steel fibres) are less vulnerable to high temperatures as the melting temperature of steel is 1400˚C compared to 230˚C for PVA. Though there is not any study on the behaviour of HECC at high temperature a study conducted on the hybrid fibre reinforced concrete under elevated temperatures (up to 900˚C) revealed that hybrid steel fibres can reduce the spalling, improve the ductility of the specimens, absorb more energy during flexural testing and improve the integrity of the samples (Ding et al., 2012). Steel fibres can reduce the gradient of thermal stress inside the specimens (due to high thermal conductivity) and

limit the development of thermal stress cracks. It observed that steel fibre at high temperatures can transfer tensile stresses across the cracks thus resulting in HECC with higher flexure toughness, load carrying capacity and fracture energy at high temperatures compared to ECC which included only low-modulus fibres reinforced concrete (Figure 2.40).

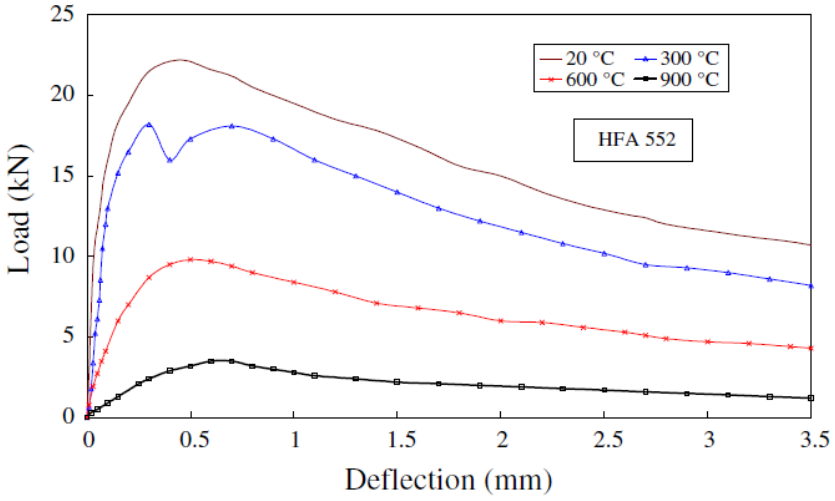

Figure 2.40. Comparison of performance of hybrid reinforced concrete at different temperatures (Ding et al., 2012)

2.7.8 Examples of experiments using ECC panels against blast and impact load.

The blast resistance performance of four 2000mm x 1000mm hybrid ECC panels were compared with 2000mm x 1000mm x 100mm mild steel reinforced concrete panels under impact load (Zhang et al., 2005). The hybrid ECC specimen thickness was 75mm and 100 mm. The impact was achieved by a hemi-spherical nose shaped projectile with a mass of 45 kg and a height of 4 m (Figure 2.41 b). The specimens lay down on a rectangular mounting frame and was considered to be simple supported along its four edges (Figure 2.41 a). The RC panels and 75 mm thick HECC panels were subjected to consecutive impact loads until failure while the 100mm thick HECC panels were subjected to 10 consecutive.

In the RC panels scabbing was observed after the second impact and after the fourth impact the panels perforated (Figure 2.41 c,d,e). However, for both 75mm and 100mm thick HECC panels only some micro cracks were observed after the tenth impact. The 75mm thick panel failed after seventeen impacts (Figure 2.41 f,g,h,I,j). After being perforated by the drop hammer, the ECC specimen did not collapse and was characterised by significant redual load-carrying capacity. The crater exhibited on the rear face of of the ECC specimen was around 140 mm compared to the diameter of 450~500 mm

exhibited by the RC panel. The debris produced during impact testing by the 75mm hybrid ECC were substantially lower compared to those produced by the RC panels. Figure 2.42a and b presents the debris produced by the RC panel after the second impact and by the 75mm thick hybrid ECC panel after the seventeenth impact respectively.

a)

b)

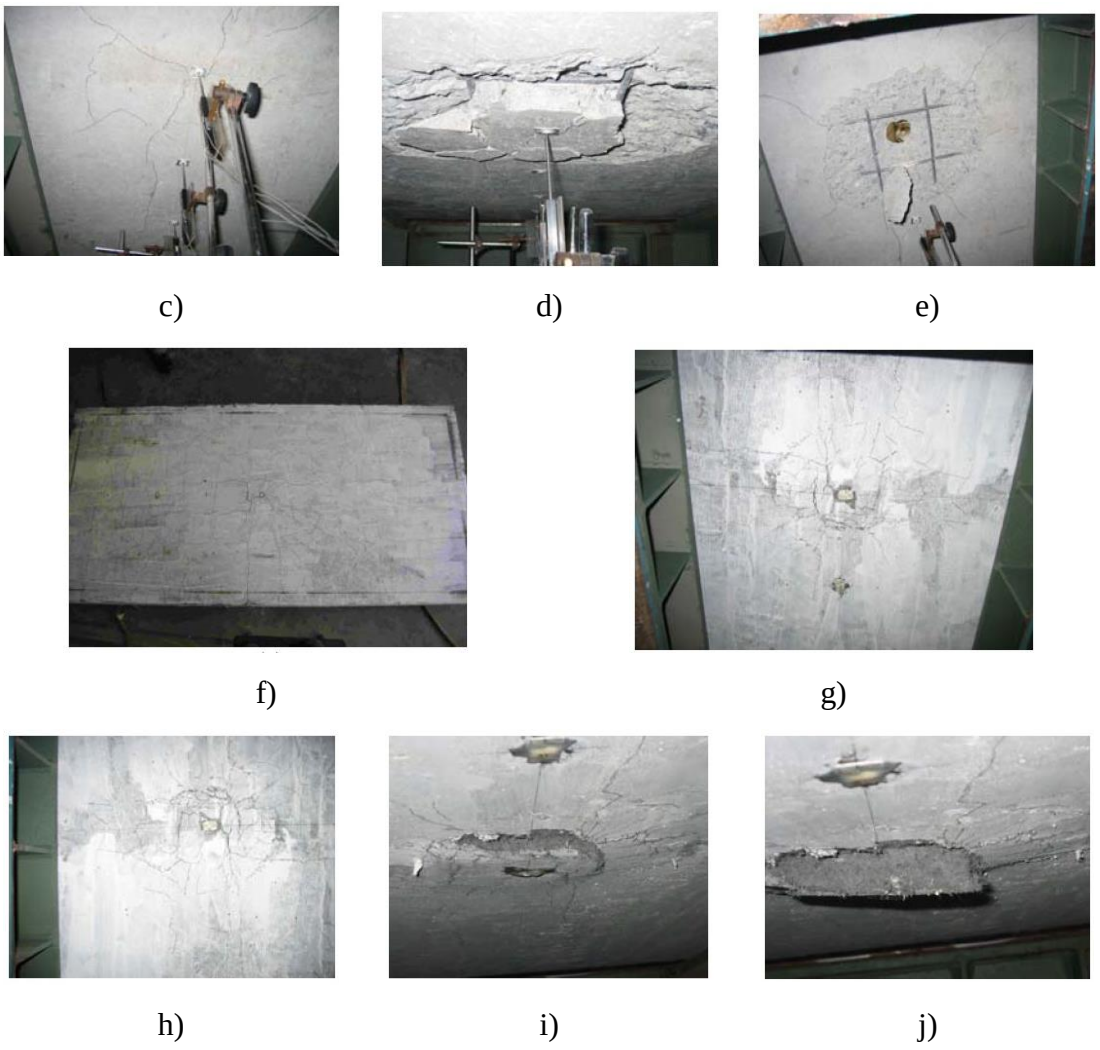

c) d) e)

f) g)

h) i) j)

Figure 2.41 a)Mounting frame b) impact hammer c,d,e) the rear face of RC panel after first, second and third impact respectively, f) 75mm thick HECC panel after 10 impacts g) 100mm thick HECC panel after 10 impacts h,I,j) the rear face of 75mm thick HECC panel after 11th , 14th , 16th impact respectively (Zhang et al., 2005)

a) b)

Figure 2.42 a) debris produced after second impact of RC panel, b) debris produced after 17th impact on the 75mm thick HECC panel (Zhang et al., 2005)

A series of 300 x170 mm panels made of HECC with different thickness ranging from 55 mm to 150 mm were impacted by a small-mass (15 g) ogive-nose projectile launched by

a compressed-helium gas of different speed ranging from 300mm/s to 750 mm/s (Figure 2.43) (Maalej et al., 2005). It was found that the HECC increased the integrity of specimens, reduced fragmentation, spalling and damages due to projectile debris, increased energy absorption allowing a better distribution of microcracking in the damaged zone compared to its counterparts when using regular concrete.

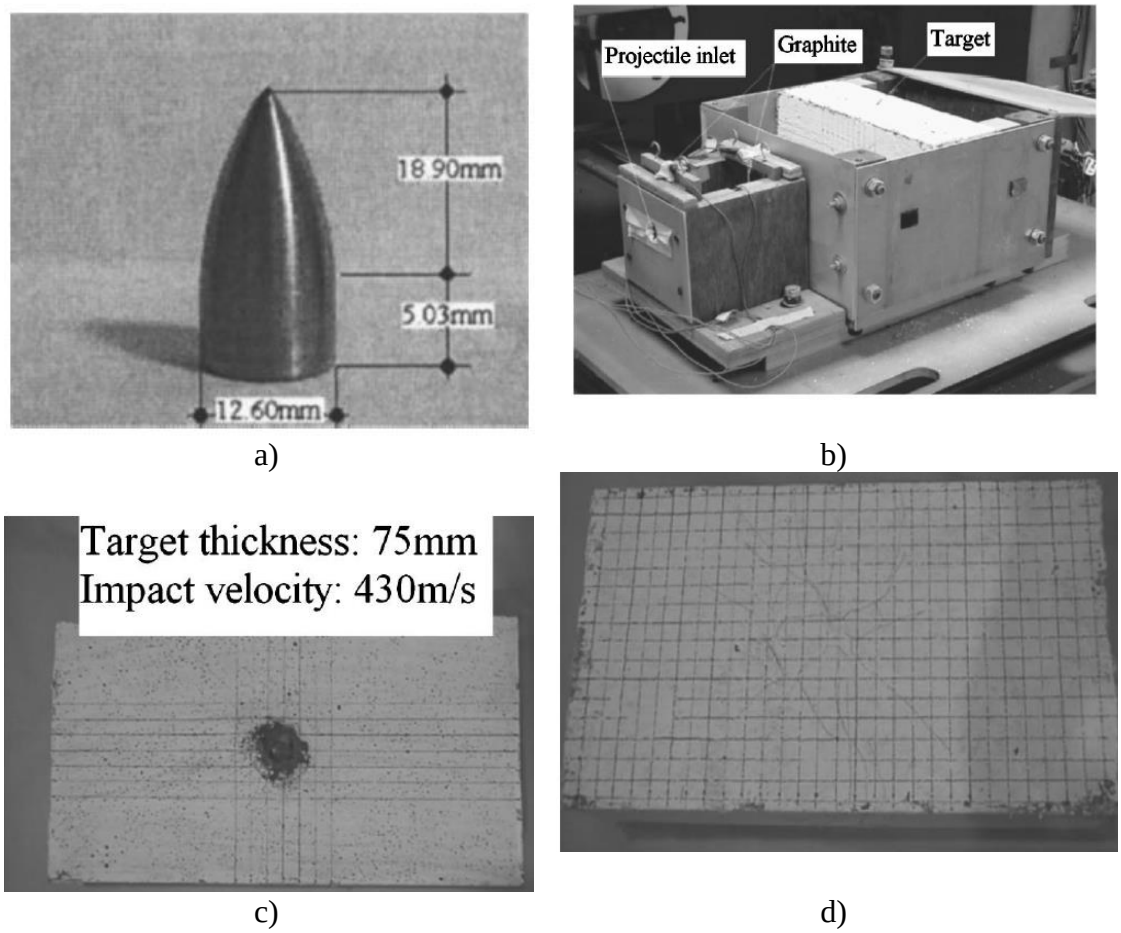

a) b)

c) d)

Figure 2.43. a) Ogive-nose projectile, b) test setup, typical damage on specimens c) front face d) rear face (Maalej et al., 2005)

2.7.9 Examples of experiments using ECC for retrofitting masonry walls

A series of tests have been carried out to investigate the potential benefits stemming from the use of ECC layer for retrofitting masonry infill walls and enhancing their out-of-plane behaviour under different loading rates.

A study on the out-of-plane behaviour of masonry beam-like specimens retrofitted with ECC on their bottom face (acting in tension) using 2% PVA fibre by volume under four point bending is presented in Figure 2.44 (Dehghani et al., 2015). The load was applied monotonically to failure in the form of displacement increments (displacement control)

at a rate of 0.3 mm/min. Three specimens were considered in these tests: (i) a plain masonry beam-like specimen essentially consisting of a stack of 11 bricks, (ii) the same beam-like specimens with a 20mm thick layer of ECC on the tensile side and (iii) the beam-like specimens with a 20 mm thick layer of ECC on tensile side and a bonding agent between ECC and masonry to avoid any delamination between ECC layer and the masonry beam.

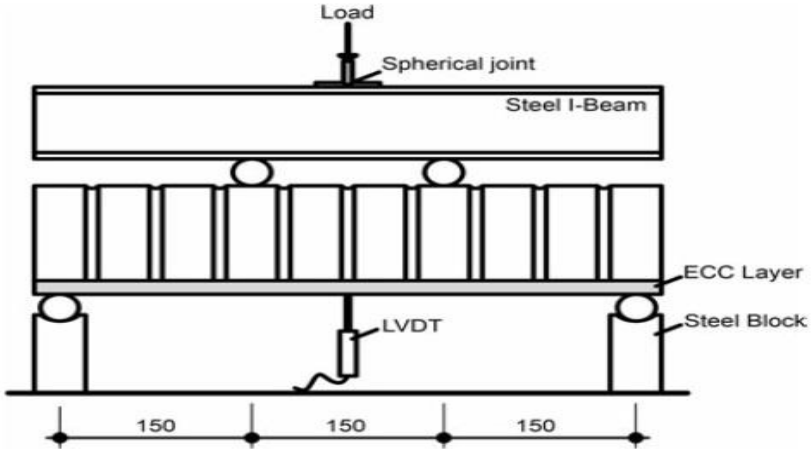

Figure 2.44. Four-point bending test setup (Dehghani et al., 2015)

In the case of the plain masonry specimens failure occurred in joints (forming between the bricks) within the middle third of the span at an average load of 5 kN and a coresponding mid-span deflection of 0.2 mm. The nature of failure reported as a brittle catastrophic failure as the specimen abruptly lost its load-carrying capacity. On the other hand, in the case of the retrofitted specimens, the first crack happened in the ECC layer at a load of 20 kN. At the same time, the maximum deflection of the samples increased from 25 to 30 times compared to unreinforced masonry specimens. In both cases of the retrofitted specimens, no delamination was observed between the ECC layer and masonry units (bricks) while at the same time multiple cracks formed in the ECC layer central span near the failure point of masonry beams (Figure 2.45 a). The specimens with the bonding agent showed more consistent behaviour in the inelastic region (Figure 2.45 b).

a)

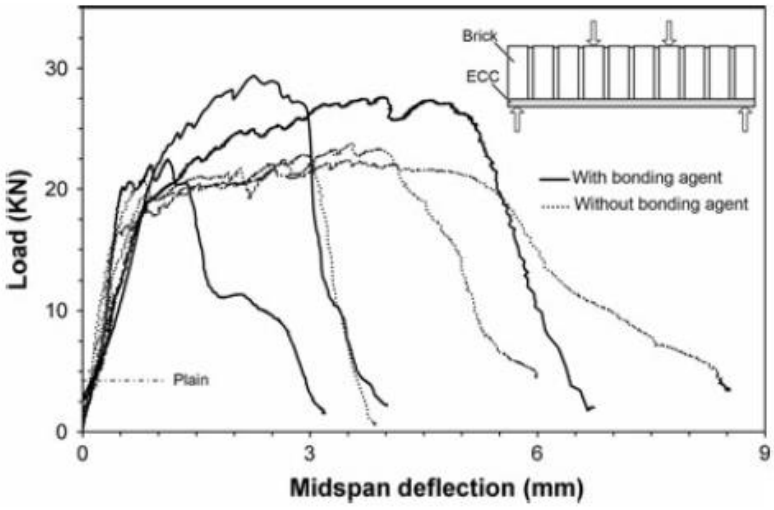

b)

Figure 2.45. a) Flexural response of the masonry beams b) The typical failure mode of retrofitted specimens and multiple cracking in the ECC layer (bottom view) (Dehghani et al., 2015)

The behaviour of retrofitted masonry walls with ECC using 0.5% steel and 1.5% polyethylene fibres were investigated under different out-of-plane loading rates (Maalej et al., 2010). The specimens dimensions were 1000 mm x1000 mm x100 mm including a plain masonry wall, a retrofitted specimen with a 34mm thick layer of ECC with an 8 mm diameter steel mesh applied either on the tensile face or both faces of the wall. Three types of loading cases were considered (a) concentrated quasi-static load, (b) distributed quasi-static load and (c) low-velocity projectile impact load (Figure 2.46).

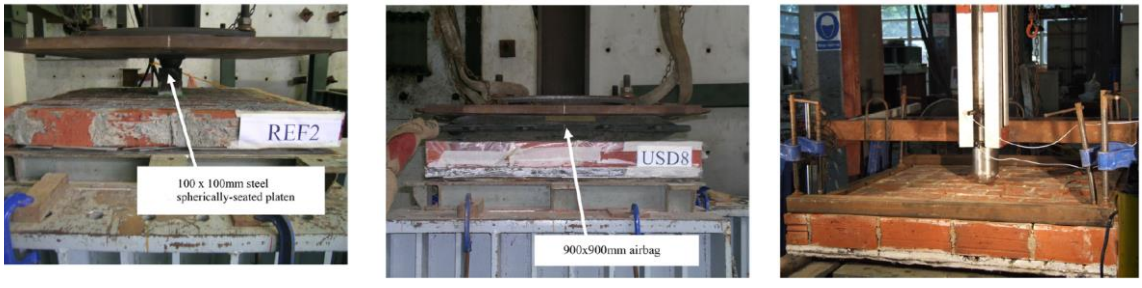

a b c

Figure 2.46. Test setup a) concentrated load b) distributed load c) impact load (Maalej et al., 2010)

The concentrated quasi-static load was applied monotonically to failure (in the middle of the face of the wall) in the form of displacement increments (displacement control) at a

rate of 0.1mm/min. The distributed load was applied in the form of load increments (load control) at a rate of 1.5kN/min. It was observed that the ECC retrofitted walls with or without the steel mesh exhibited a very good stress and crack distributions (see Figures 2.47 a&b). Only in the ECC layer with steel mesh the cracks were less dense compared to the cracks developing in the unreinforced ECC layer as the stresses were mostly distributed through the steel mesh (Figure 2.47 c&d). The plain masonry wall failed in a brittle manner at a very low load. The specimens strengthened with one layer of ECC under concentrated and distributed loads exhibited compression failure in the masonry at the ultimate limit state due to the high tensile strain capacity of the ECC layer which allowed the specimens to exhibit high ductility. Punching failure was exhibited in the masonry wall retrofitted with a single ECC layer which was reinforced with a steel mesh under concentrated loading. The specimens strengthened with (i) two layers of ECC (on both faces of the wall) which were reinforced by a steel mesh and tested under a point load and (ii) a single and double layer of ECC with steel mesh under distributed load exhibited a shear de-bounding observed on ECC layer. It observed that under all loading regimes the ECC-retrofitted specimens without steel reinforcement exhibited higher deflection (between 3-6 times) compare their steel reinforced counterparts. However, the steel reinforced specimens under all loading regimes had about 2 times higher load bearing capacity compared to their counterparts without steel reinforcement.

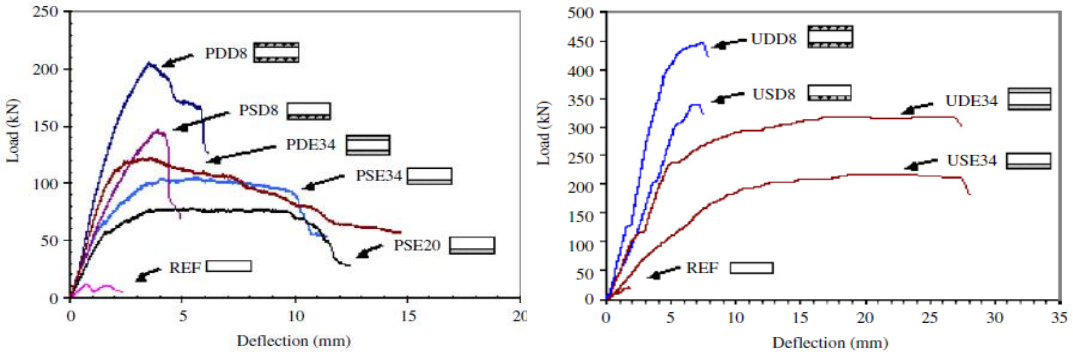

a b

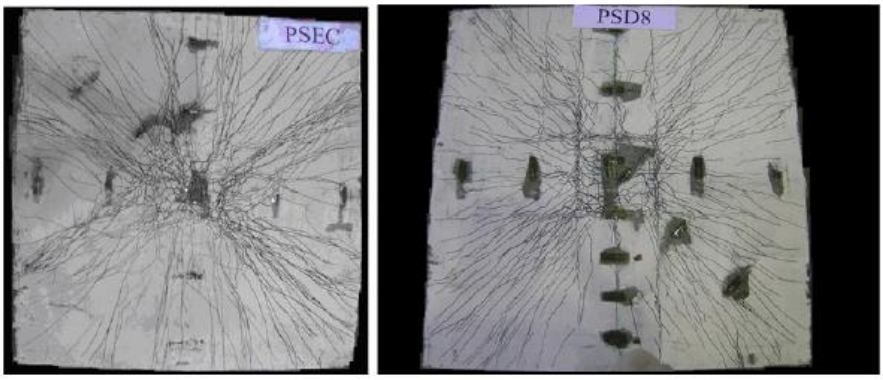

c d

Figure 2.47. Load-deflection responses of wall components a) concentrated load, b)Distributed load; the typical cracking pattern of the ECC-strengthening layers c) without steel mesh, d) with steel mesh (Dehghani et al., 2015).

Low velocity impact was achieved by dropping a spherical projectile of 51 kg from a height of 4m presented in Figure 2.48 c (Maalej et al., 2010). The plain masonry wall failed during the first impact exhibiting a sudden and brittle failure mode. The drop-mass perforated the wall during impact and the latter was shattered into several parts. All ECC retrofitted walls were able to withstand multiple impacts before perforation (Figure 2.48 a&b). The single layer ECC tolerated 5 impacts, single layer ECC with steel mesh tolerated 9 impacts, double layer ECC tolerated 9 impacts and double layer ECC with steel mesh tolerated 18 impacts. Also no fragments were observed in all of the ECC retrofitted specimens (Figure 2.48 c, d, e & f). Figure 2.48 b shows that the indention depth and crater size of the reinforced wall decreased when adding the 8 mm steel mesh in the ECC layer. Double layer ECC walls exhibited higher penetration resistance with lesser indention depth and smaller crater size compared with the single layer ECC. This was due to the absorption of the impact energy by the ECC layer that protected the brittle masonry layer. It was also observed that the ECC retrofitted walls without steel mesh exhibited multiple very denser cracking. On the other hand, in the case of the ECC retrofitted walls with a steel mesh the cracks where concentrated near steel mesh.

Overall it was concluded that under quasi-static loads that ECC layer can improve the out of plane resistance of masonry walls by increasing the ultimate load capacity by 6.5 to 22 times and the maximum deflection by 4.2 to 15.9 times. The use of the steel mesh can increase the ultimate load carrying capacity by 40%-60% while reducing the deflection capacity of the specimen by about 17%-74%. Finally, under impact loading the ECC retrofitted wall can resist multiple impacts. Also, fragmentation due to impact reduced significantly.

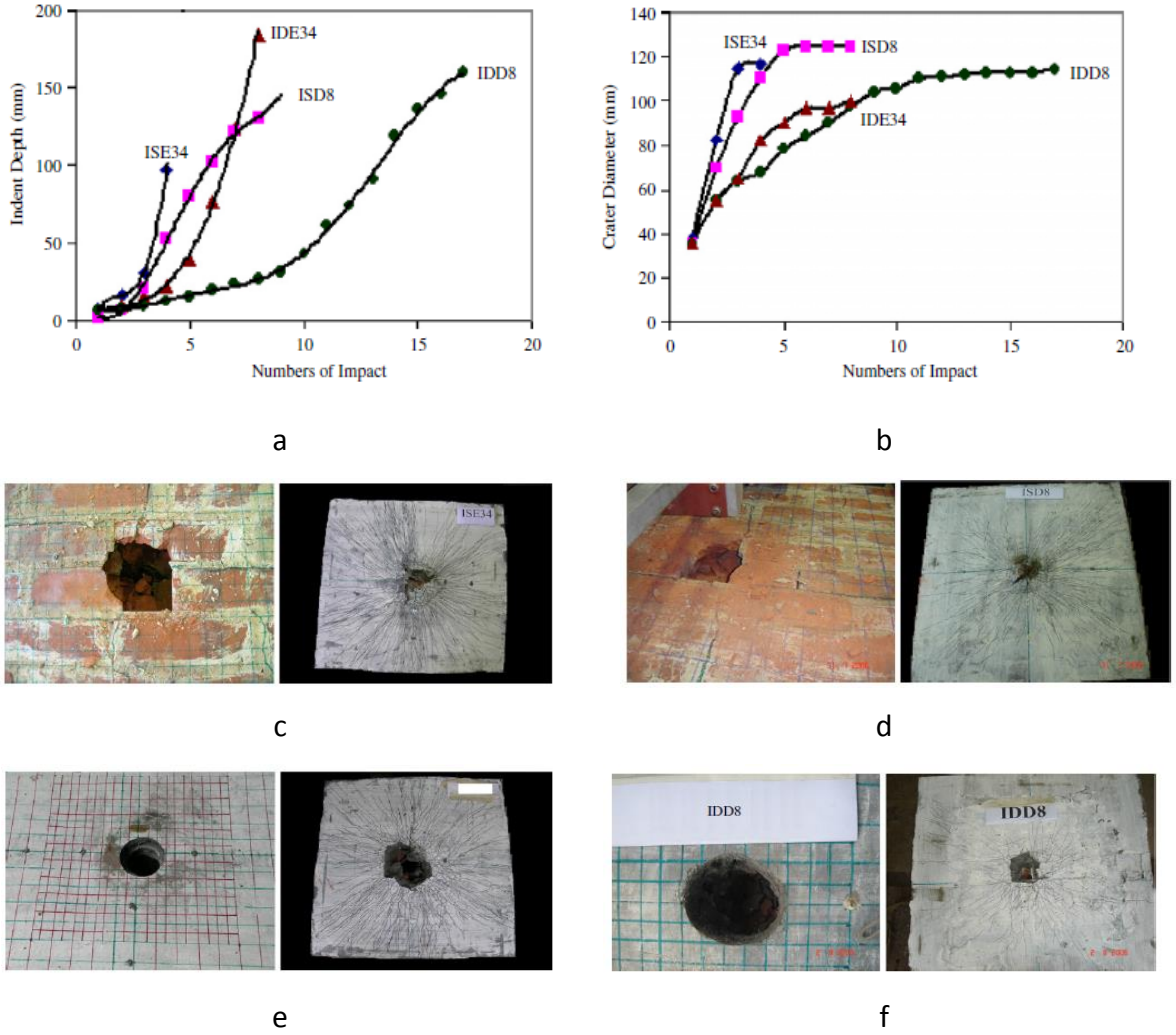

Figure 2.48. a) The plot of indent depth development and b) crater diameter impact after perforation, specimens at failure c) one layer ECC, d) one layer ECC with mesh, e) double layer ECC f) double layer ECC with mesh (Maalej et al., 2010).

Another study was carried out on the seismic behaviour of ECC-retrofitted masonry infills in non-ductile reinforced concrete frames (Kyriakides and Billington, 2008). In the case of out-of-plane force, five different beam-like specimens were tested (consisting of a stack of 9 bricks) under quasi-static four-point bending test. These specimens were strengthened by applying a 13 mm thick ECC layer (a) cast directly onto the masonry, (ii) connected onto the masonry wall through the use of stich dowels, (iii) steel reinforced ratio 0.125% of volume ECC layer, (iv) steel reinforced ratio 0.125% of volume ECC layer and connected onto the masonry through the use of stich dowels and (v) steel reinforced 1% of volume ECC layer. The load was applied monotonically to failure in the form of displacement increments at a rate of 0.005mm/sec. Some plain masonry specimens were also tested for the purpose of comparison (Figure 2.49). The average load carrying capacity of the specimens was 472 N and exhibited a brittle mode of failure.

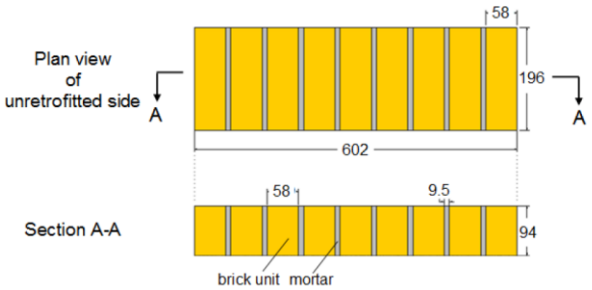

Figure 2.49. Plain masonry specimens (Kyriakides and Billington, 2008)

In the specimens retrofitted with a 13 mm ECC layer the load carrying capacity increased about 5 times and the deflection was substantially enhanced compared to plain masonry specimens (Figure 2.50). At the ultimate limit state the specimens exhibited multiple cracking in the ECC layer below the mortar joint at the central region (between points which loads were applied) This proved that the ECC layer in this region of the specimen had entered its tensile strain hardening region (Figure 2.55 a).

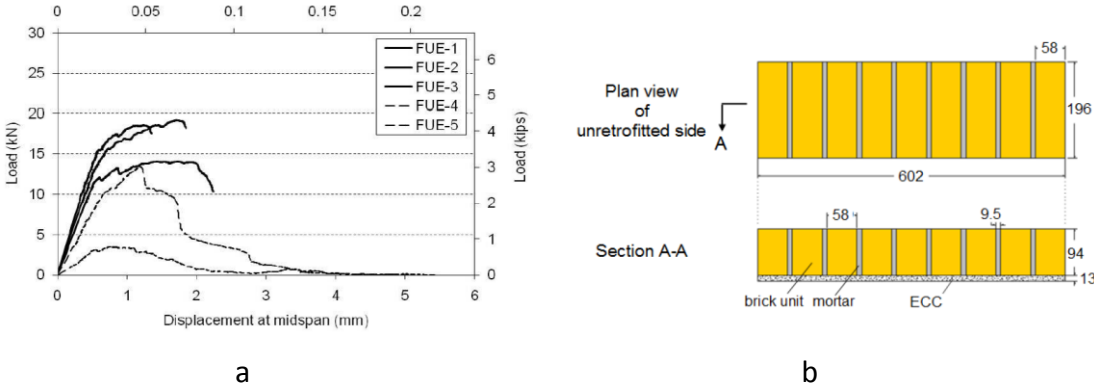

Figure 2.50.A) load-displacement responses of ECC used to retrofit masonry beams b) specimens with 13 mm ECC (Kyriakides and Billington, 2008)

When retrofitting with a 13mm thick ECC layer with stich dowels the response of the specimens was similar to previous tests and only the initial stiffness was higher than the former test (Figure 2.51). The failure mode exhibited at the ULS was the same with previous tests and multiple cracking developed in the ECC layer below the mortar joint at the mid-span happened (Figure 2.55 b).

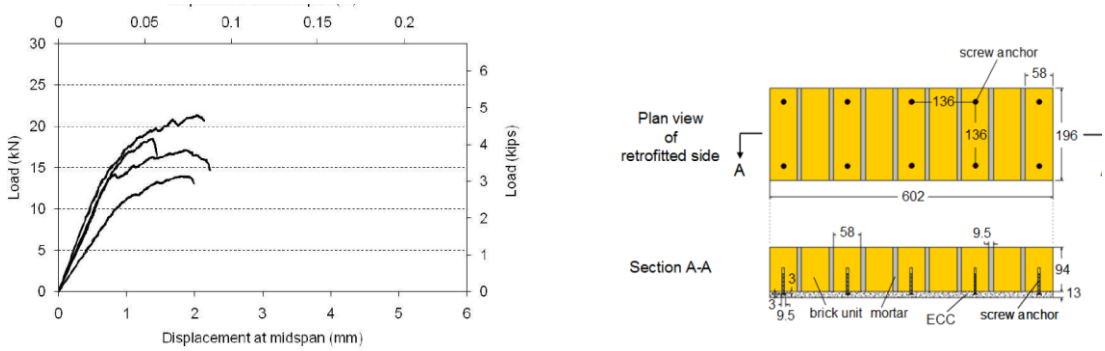

a b

Figure 2.51. a) load-displacement responses of ECC with stich dowels used to retrofit masonry beam b) specimens with 13 mm ECC and dowels (Kyriakides and Billington, 2008)

When retrofitting with a 13mm thick ECC layer with a 0.125% steel reinforcement the poor bond between ECC layer and masonry surface observed caused sliding of masonry over the ECC layer. The specimens had less load bearing capacity compared to the previous tests (Figure 2.52). The failure mode exhibited was associated with delamination of the ECC layer, then failure in mortar interface occurred in the masonry beams (Figure 2.55 c).

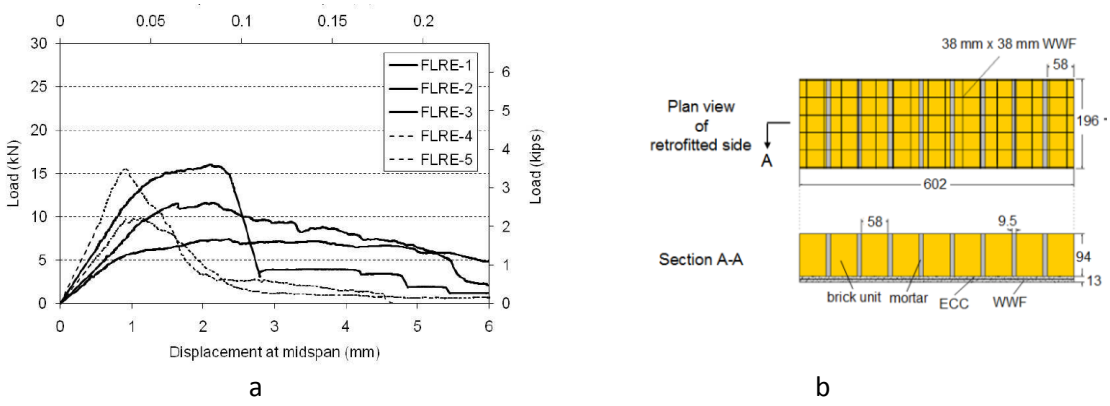

a b

Figure 2.52. a) Load-displacement responses of ECC with 0.125% reinforcement used to retrofit masonry beams b) specimens with 13 mm ECC and 0.125 steel reinforcement (Kyriakides and Billington, 2008)

When retrofitting with a 13mm thick ECC layer with 0.125% steel reinforcement and stich dowels the deflection of the specimens increased by 100%-117% and the load carrying capacity increased by about 25% compared to the former test (Figure 2.53). The failure mode exhibited a uniform crack pattern in the central span of ECC layer due to partial delamination of the ECC layer from the masonry (Figure 2.55 d).

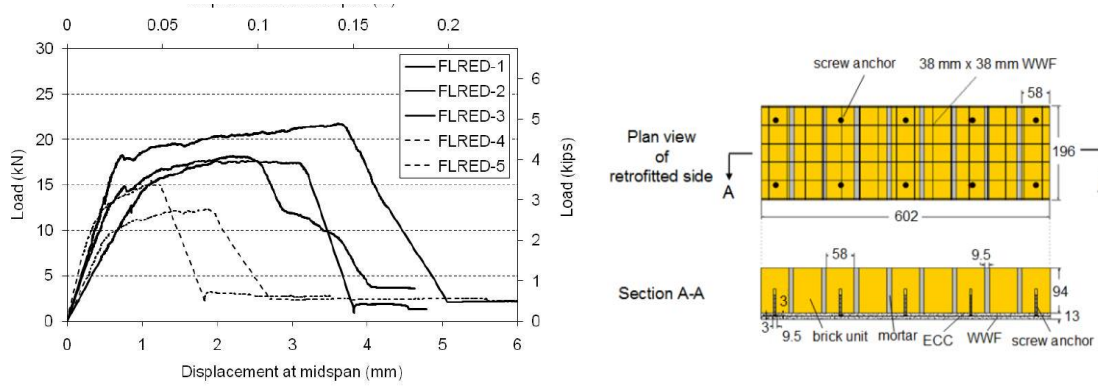

a b

Figure 2.53. Load-displacement responses of ECC with 0.125% reinforcement and stich dowels used to retrofit masonry beams b) specimens with 13 mm ECC with 0.125% reinforcement and stich dowels (Kyriakides and Billington, 2008)

Finally, when retrofitting with a 13mm thick ECC layer with 1% steel reinforcement and stich dowels the ultimate load capacity of specimens increased compared to the previous test and caused the development of shear cracks in the brick units (Figure 2.54). The failure mode exhibited the delamination of ECC layer from the part of the masonry beam located outside of the constant moment region followed by brick failure (Figure 2.55 e&f).

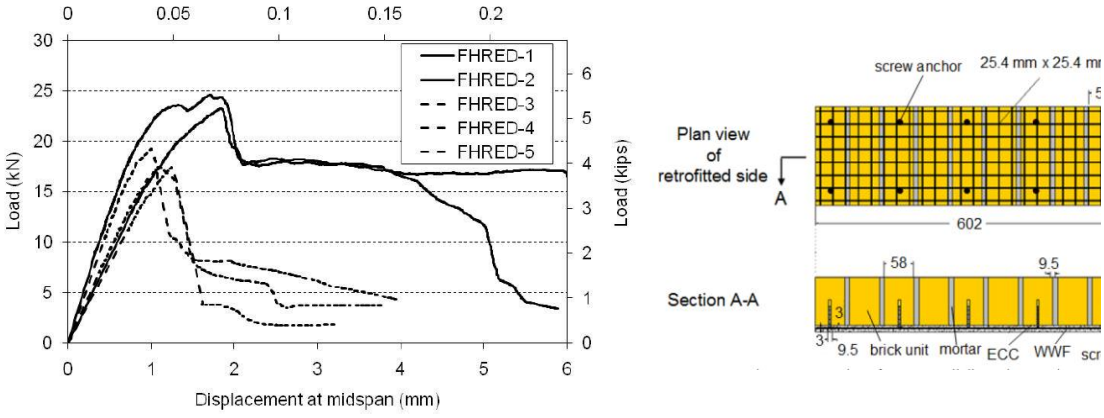

a b

Figure 2.54. a) Load-displacement responses of ECC with 1% reinforcement and dowels b) specimens with 13 mm ECC with 1% reinforcement and stich dowels (Kyriakides and Billington, 2008)

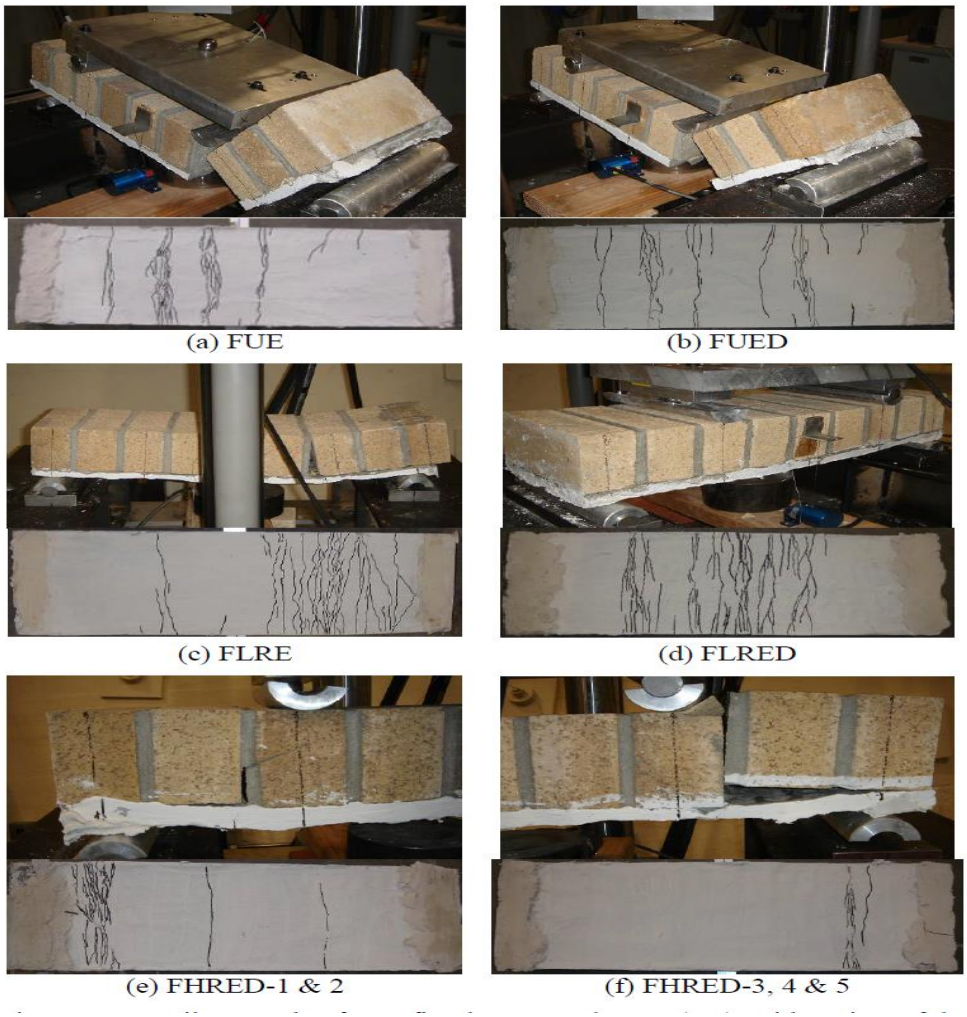

Figure 2.55. Failure mode of retrofitted masonry beams a) 13 mm ECC layer b) 13 mm ECC layer and dowels c) 13 mm ECC layer and 0.125% steel reinforcement d) 13 mm ECC layer and 0.125% steel reinforcement and dowels e&f) 13 mm ECC layer and 0.125% steel reinforcement d) 13 mm ECC layer and 1% steel reinforcement and dowels. (Kyriakides and Billington, 2008)

It was concluded that the plain masonry beams under four-point bending exhibited a brittle form of failure in the brick-mortar interface close to the point at which the load is applied. When strengthening is carried out through the use of a 13 mm thick ECC layer applied on the face of the masonry beam-like specimen which is in tension, the load carrying capacity increased by approximately 35 times (compared to that established for the case of the unstrengthened specimens), and the beams failed in a highly ductile manner (unlike the unstrengthened specimen that exhibited brittle failure). When delamination suddenly happened between the ECC layer and the masonry surface more cracks developed in the ECC layer and the displacement of specimens increased by almost two times. The differences in the load-carrying capacity, ductility and stiffness established for the different groups of retrofitted masonry beams were mainly attributed to the brick-mortar adhesion area size, the brick-mortar bond strength of the masonry

joints, the variability in the ductile response of the ECC layer and the ECC masonry bond quality.

2.7.10 Retrofitting through the use of a partially unbonded ECC layers

Kunieda et al. suggested a new technic of retrofitting for ductile surface coating repair material (Kunieda et al., 2004). They found that normally repair coating materials are required to follow the crack opening motion of main members under so-called zero-span elongation. This phenomenon causes local failure in ECC repair layer and prevents uniform crack distribution in the ECC layer. Therefore an un-bonded ECC layer near the crack zone in the main member can improve the crack distribution in ECC layer. A 30mm thick ECC layer was applied on a 100x100x400 mm concrete beam-like specimen involving un-cracked concrete beam, pre-cracked concrete beam and pre-cracked concrete beam with a 50mm unbounded length of ECC near crack (Figure 2.56).

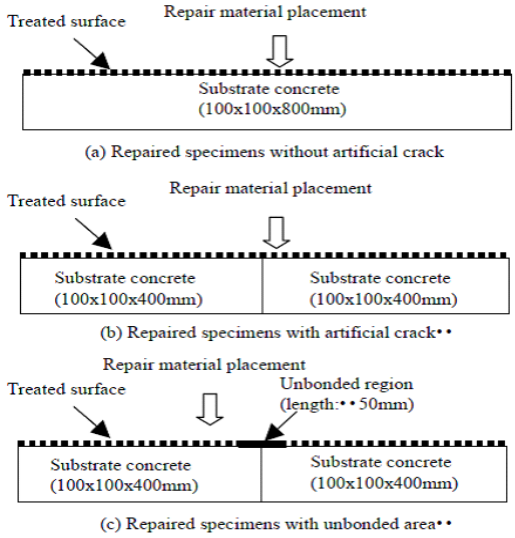

Figure 2.56. Repaired specimens (Kunieda et al., 2004)

It was observed that the specimens with the un-bonded region, fractured after 5% strain at the ECC layer in the bottom of repaired specimens rather than 3% strain in other cases (Figure 2.57). It observed that when the ECC layer is bonded to the concrete beam the cracking exhibited in the ECC layer is more localised close to the pre-crack section of the concrete beam. In contract when the ECC layer is unbonded a uniform fine cracking is exhibited in the ECC layer.

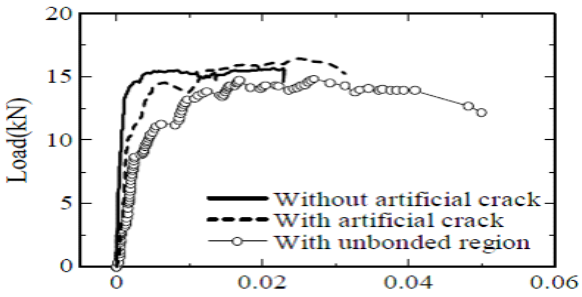

a

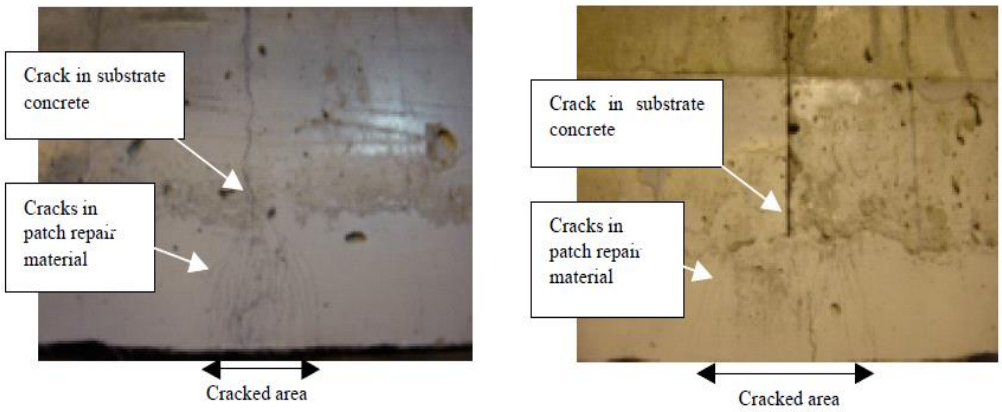

b c

Figure 2.57. a) Strain at specimen bottom; crack pattern of repaired specimen b) bonded c) unbonded (Kunieda et al., 2004)

Next, a simulation was carried out to investigate the load-displacement behaviour when strain capacity of the ECC layer varies from 1% to 6%. The results reveal a dramatic improvement in load-displacement curves for unbonded specimens compared to bonded specimens especially when the ECC layer had higher strain capacity (Figure 2.58).

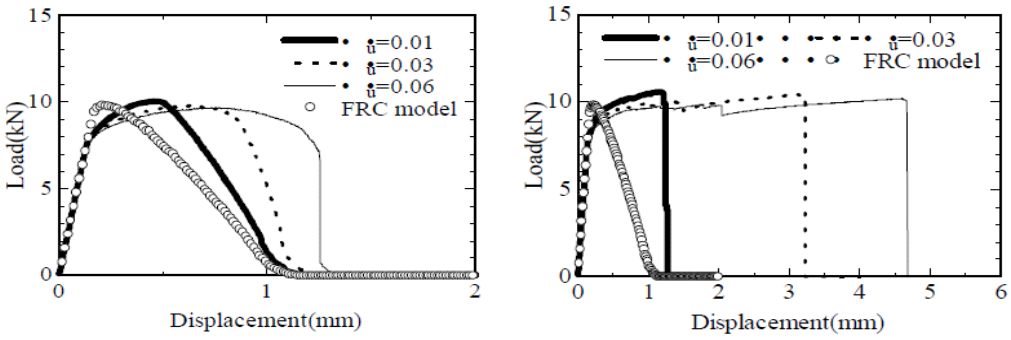

a b

Figure 2.58. Load displacement responses (modelling) a) bonded b) unbonded models (Kunieda et al., 2004)

Another study investigated three different repair materials for retrofitting concrete beams involving plain concrete, FRC and ECC as an external coating (Li et al., 2000). The beams were tested under four point flexural loading (Figure 2.59). To simulate an interface

defect they used a tape with the very smooth surface to prevent bonding between the base concrete at the interface. Also, a notch was included in the concrete beam. Figure 2.59 shows a view of the post-failure cracks. At failure for the concrete repair material (concrete/concrete) the load dropped suddenly and the specimen broke into two halves (Figure 2.60). At failure of the FRC repair material (FRC/concrete) the cracks bridged by the steel bars and the load drop gradually as the cracks propagated. At failure of the ECC repair specimen (ECC/concrete) a series of cracks developed in ECC layer, the load initially increased followed by very gradual and ductile strain hardening failure.

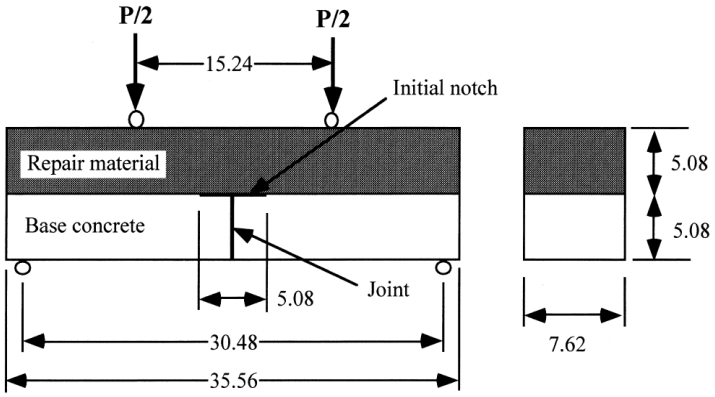

Figure2. 1 Test Setup (Li et al., 2000)

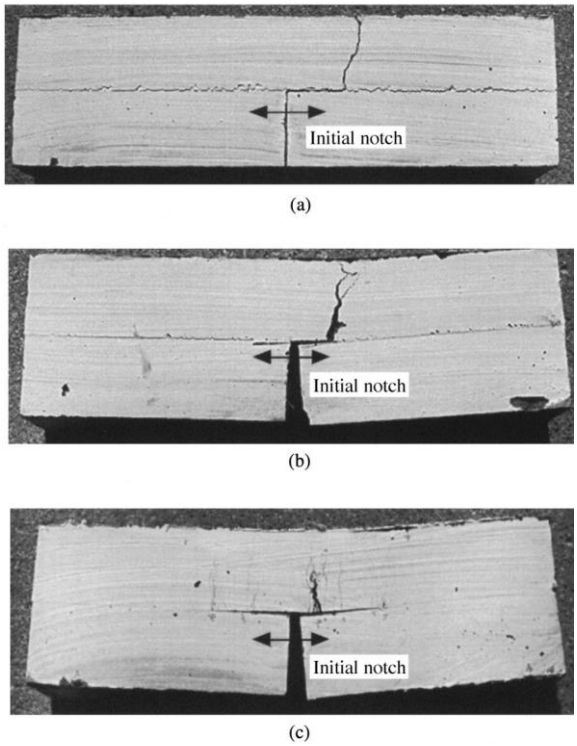

Figure 2.59. Failure mode of a) concrete/concrete, b) FRC/concrete and c) ECC/concrete beams (Li et al., 2000)

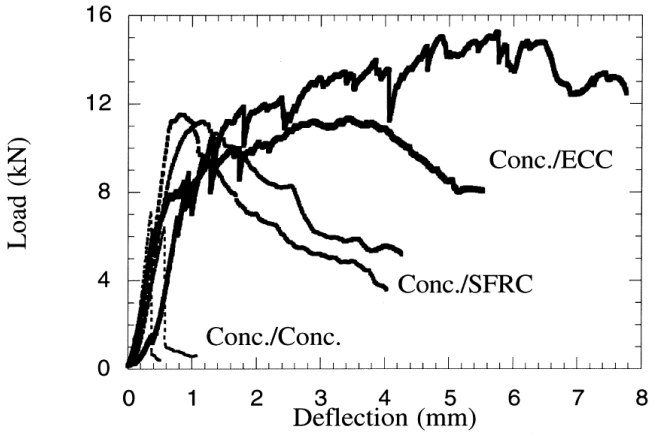

Figure 2.60. load-deflection of the retrofitted beams (Li et al., 2000)

2.8 Conclusion

The studies on the out-of-plane behaviour of URM walls subjected to static, seismic, impact and blast loads revealed the weak performance of masonry walls including brittle failure, limited load bearing capacity and ductility. The failure of URM walls in the incidents such as earthquake or blast explosion resulting in producing debris which were reported as a major source of destruction and causalities. Different retrofitting methods have been developed for strengthening URM walls in the out-of-plane direction. However, all methods exhibited some disadvantages which limited their applications. A new method which uses ECC for strengthening URM walls in the out-of-plane direction has been introduced recently. The behaviour of ECC-retrofitted masonry walls subjected to different loading rates exhibited significant improvement in the out-of-plane direction. In the event such as earthquake, explosion and blast the masonry wall can be subjected to the combined actions of elevated loading rate and temperature. However, there is no comprehensive study which assesses the behaviour of ECC-retrofitted masonry walls under combined elevated loading rate and temperature. A novel idea of partial debonding of the ECC layer from the masonry wall exhibited promising results to enhance the masonry walls behaviour. However, this technique is not assessed under elevated loading rate and temperature.

2.9 References

AHMED, S. & MAALEJ, M. 2009. Tensile strain hardening behaviour of hybrid steel-polyethylene fibre reinforced cementitious composites. *Construction and Building Materials*, 23**,** 96-106.

AHMED, S. F., MAALEJ, M. & PARAMASIVAM, P. 2007. Analytical model for tensile strain hardening and multiple cracking behavior of hybrid fiber-engineered cementitious composites. *Journal of materials in civil engineering,* 19**,** 527-539.

ALBERT, M. L., ELWI, A. E. & CHENG, J. R. 2001. Strengthening of unreinforced masonry walls using FRPs. *Journal of Composites for Construction,* 5**,** 76-84.

ALTWAIR, N. M., JOHARI, M. M. & HASHIM, S. S. 2012. Flexural performance of green engineered cementitious composites containing high volume of palm oil fuel ash. *Construction and Building Materials,* 37**,** 518-525.

ANGEL, R., ABRAMS, D. P., SHAPIRO, D., UZARSKI, J. & WEBSTER, M. 1994. Behavior of reinforced concrete frames with masonry infills. University of Illinois Engineering Experiment Station. College of Engineering. University of Illinois at Urbana-Champaign.

ASTERIS, P., COTSOVOS, D., CHRYSOSTOMOU, C., MOHEBKHAH, A. & AL-CHAAR, G. 2013. Mathematical micromodeling of infilled frames: state of the art. *Engineering Structures,* 56**,** 1905-1921.

BANGASH, T. 2006. *Explosion-resistant buildings: design, analysis, and case studies*, Springer Science & Business Media.

BAZZURRO, P., ALEXANDER, D., CLEMENTE, P., COMERIO, M., SORTIS, A., FILIPPOU, F., GORETTI, A., JORJANI, M., MOLLAIOLI, F. & MOSALAM, K. 2009. The Mw= 6.3 Abruzzo, Italy, Earthquake of April 6, 2009. *Learning from Earthquakes, EERI Special Earthquake Report*.

BRUNEAU, M. 1994. State-of-the-art report on seismic performance of unreinforced masonry buildings. *Journal of Structural Engineering,* 120**,** 230-251.

BUCHAN, P. & CHEN, J. 2007. Blast resistance of FRP composites and polymer strengthened concrete and masonry structures–A state-of-the-art review. *Composites Part B: Engineering,* 38**,** 509-522.

BURNETT, S., GILBERT, M., MOLYNEAUX, T., BEATTIE, G. & HOBBS, B. 2007. The performance of unreinforced masonry walls subjected to low-velocity impacts: Finite element analysis. *International Journal of Impact Engineering,* 34**,** 1433-1450.

CAVALERI, L., FOSSETTI, M. & PAPIA, M. 2009. Modeling of out-of-plane behavior of masonry walls. *Journal of structural engineering,* 135**,** 1522-1532.

CODE, P. 2005. Eurocode 8: Design of structures for earthquake resistance-part 1: general rules, seismic actions and rules for buildings.

CRITERION, U. F. 2002. DoD Minimum Antiterrorism Standards for Buildings. Washington.

DAWE, J. & SEAH, C. 1989. Out-of-plane resistance of concrete masonry infilled panels. *Canadian Journal of Civil Engineering,* 16**,** 854-864.

DEHGHANI, A., FISCHER, G. & ALAHI, F. N. 2015. Strengthening masonry infill panels using engineered cementitious composites. *Materials and Structures,* 48**,** 185-204.

DERAKHSHAN, H. 2011. *Seismic assessment of out of plane loaded unreinforced masonry walls.* ResearchSpace@ Auckland.

DING, Y., AZEVEDO, C., AGUIAR, J. & JALALI, S. 2012. Study on residual behaviour and flexural toughness of fibre cocktail reinforced self compacting high performance concrete after exposure to high temperature. *Construction and Building Materials,* 26**,** 21-31.

DIZHUR, D., INGHAM, J., MOON, L., GRIFFITH, M., SCHULTZ, A., SENALDI, I., MAGENES, G., DICKIE, J., LISSEL, S. & CENTENO, J. 2011. Performance of masonry buildings and churches in the 22 February 2011 Christchurch earthquake. *Bulletin of the New Zealand Society for Earthquake Engineering,* 44**,** 279-296.

DRYSDALE, R. G., HAMID, A. A. & BAKER, L. R. 1994. *Masonry structures: behavior and design*, Prentice Hall.

ELGAWADY, M., LESTUZZI, P. & BADOUX, M. 2004. A review of conventional seismic retrofitting techniques for URM. 13th international brick and block masonry conference. Citeseer, 1-10.

ELGAWADY, M., LESTUZZI, P. & BADOUX,. 2006. Retrofitting of masonry walls using shotcrete. 2006 NZSEE Conference, Paper,.

EREMIN, A., COHEN, E. & LAING, E. 1956. Discussion of "Arching Action Theory of Masonry Walls,". *Journal of the Structural Division***,** 27-40.

FURTADO, A., RODRIGUES, H. & ARÊDE, A. 2002. Evaluation of the effect of masonry infill walls presence in existing RC structures: Numerical and experimental study.

GILBERT, M., HOBBS, B. & MOLYNEAUX, T. 2002. The performance of unreinforced masonry walls subjected to low-velocity impacts: experiments. *International journal of impact engineering,* 27**,** 231-251.

GRIFFITH, M. & VACULIK, J. 2007. Out-of-plane flexural strength of unreinforced clay brick masonry walls. *TMS Journal,* 25**,** 53-68.

GRIFFITH, M. C., VACULIK, J., LAM, N., WILSON, J. & LUMANTARNA, E. 2007. Cyclic testing of unreinforced masonry walls in two-way bending. *Earthquake Engineering & Structural Dynamics,* 36**,** 801-821.

HAK, S., MORANDI, P. & MAGENES, G. 2014. Out-of-plane Experimental Response of Strong Masonry Infills. 2nd European Conference on Earthquake Engineering and Seismology.

HALVAEI, M., JAMSHIDI, M. & LATIFI, M. 2014. Application of low modulus polymeric fibers in engineered cementitious composites. *Journal of Industrial Textiles,* 43**,** 511-524.

HASHEMI, S. A. 2007. *Seismic evaluation of reinforced concrete buildings including effects of masonry infill walls,* University of California, Berkeley.

HERBERT, E. & LI, V. 2012. Self-healing of engineered cementitious composites in the natural environment. *High Performance Fiber Reinforced Cement Composites 6.* Springer.

HERMES, P., ZHANG, Y., SOE, K. & BELL, J. 2012. Material Properties of a New Hybrid-Fiber Engineered Cementitious Composite. Advanced Materials Research, Trans Tech Publ, 433-438.

HOUSNER, G. W. 1963. The behavior of inverted pendulum structures during earthquakes. *Bulletin of the seismological society of America,* 53**,** 403-417.

KANDA, T., TOMOE, S., NAGAI, S., MARUTA, M., KANAKUBO, T. & SHIMIZU, K. 2006. Full scale processing investigation for ECC pre-cast structural element. *Journal of Asian Architecture and Building Engineering,* 5**,** 333-340.

KIM, Y. Y., KONG, H.-J. & LI, V. C. 2003. Design of engineered cementitious composite suitable for wet-mixture shotcreting. *Materials Journal,* 100**,** 511-518.

KLINGER, R., RUBIANO, N. R. & BHASHANDY, S. 1997. Evaluation and analytical Verification of shaking table data from infilled frames. *The Masonry Society Journal,* 15**,** 33-41.

KONG, H.-J., BIKE, S. G. & LI, V. C. 2003. Development of a self-consolidating engineered cementitious composite employing electrosteric dispersion/stabilization. *Cement and Concrete Composites,* 25**,** 301-309.

KUNIEDA, M., KAMADA, T., ROKUGO, K. & BOLANDER, J. 2004. Localized fracture of repair material in patch repair systems. International Conference on Fracture Mechanics of Concrete Structures, Colorado, 765-772.

KYRIAKIDES, M. & BILLINGTON, S. 2008. Seismic retrofit of masonry-infilled non-ductile reinforced concrete frames using sprayable ductile fiber-reinforced cementitious composites. *14 WCEE*.

LAM, N., WILSON, J., CHANDLER, A. & HUTCHINSON, G. 2000. Response spectrum modelling for rock sites in low and moderate seismicity regions combining velocity, displacement and acceleration predictions. *Earthquake engineering & structural dynamics,* 29**,** 1491-1525.

LÁRUSSON, L. H., FISCHER, G. & JÖNSSON, J. 2010. Mechanical interaction of Engineered Cementitious Composite (ECC) reinforced with Fiber Reinforced Polymer (FRP) rebar in tensile loading. *Advances in Cement-based Materials (ACM2009)*.

LÁRUSSON, L. H., FISCHER, G. & JÖNSSON, J. 2013. Prefabricated floor panels composed of fiber reinforced concrete and a steel substructure. *Engineering Structures,* 46**,** 104-115.

LEPECH, M. D., LI, V. C., ROBERTSON, R. E. & KEOLEIAN, G. A. 2008. Design of green engineered cementitious composites for improved sustainability. *ACI Materials Journal,* 105**,** 567-575.

LI, V. C. 2003. On engineered cementitious composites (ECC). *Journal of advanced concrete technology,* 1**,** 215-230.

LI, V. C. & HERBERT, E. 2012. Robust self-healing concrete for sustainable infrastructure. *Journal of Advanced Concrete Technology,* 10**,** 207-218.

LI, V. C., HORII, H., KABELE, P., KANDA, T. & LIM, Y. 2000. Repair and retrofit with engineered cementitious composites. *Engineering Fracture Mechanics,* 65**,** 317-334.

LI, V. C., LEPECH, M., WANG, S., WEIMANN, M. & KEOLEIAN, G. 2004. Development of green engineered cementitious composites for sustainable infrastructure systems. Proceedings of the International Workshop on Sustainable

Development and Concrete Technology, Beijing, China, May 20-21, 2004. Center for Transportation Research and Education Iow, 181.

LI, V. C. & LEUNG, C. K. 1992. Steady-state and multiple cracking of short random fiber composites. *Journal of Engineering Mechanics,* 118**,** 2246-2264.

LI, V. C. & WANG, S. 2007. High Early Strength Engineered Cementitious Composites. Google Patents.

LI, V. C., WANG, S. & WU, C. 2001. Tensile strain-hardening behavior of polyvinyl alcohol engineered cementitious composite (PVA-ECC). *ACI materials Journal,* 98.

LI, V. C. & YANG, E.-H. 2007. Self healing in concrete materials. *Self Healing Materials.* Springer.

LIN, Y.-W., WOTHERSPOON, L., SCOTT, A. & INGHAM, J. M. 2014. In-plane strengthening of clay brick unreinforced masonry wallettes using ECC shotcrete. *Engineering Structures,* 66**,** 57-65.

MAALEJ, M., LIN, V., NGUYEN, M. & QUEK, S. 2010. Engineered cementitious composites for effective strengthening of unreinforced masonry walls. *Engineering Structures,* 32**,** 2432-2439.

MAALEJ, M., QUEK, S. T. & ZHANG, J. 2005. Behavior of hybrid-fiber engineered cementitious composites subjected to dynamic tensile loading and projectile impact. *Journal of Materials in Civil Engineering,* 17**,** 143-152.

MAGENES, G. 2006. Masonry building design in seismic areas: recent experiences and prospects from a European standpoint. Proceedings of the First European Conference on Earthquake Engineering and Seismology, Geneva, Switzerland, 3-8.

MATTHYS, H. & NOLAND, L. 1989. Proceedings of an international seminar on evaluation, strengthening and retrofitting masonry buildings. *TMS, Colorado, USA.*

MCDOWELL, E., MCKEE, K. & SEVIN, E. 1956. Arching action theory of masonry walls. *Journal of the Structural Division,* 82**,** 1-8.

MECHTCHERINE, V., DE ANDRADE SILVA, F., MÜLLER, S., JUN, P. & TOLEDO FILHO, R. D. 2012. Coupled strain rate and temperature effects on the tensile behavior of strain-hardening cement-based composites (SHCC) with PVA fibers. *Cement and Concrete Research,* 42**,** 1417-1427.

MECHTCHERINE, V., MILLON, O., BUTLER, M. & THOMA, K. 2011a. Mechanical behaviour of strain hardening cement-based composites under impact loading. *Cement and Concrete Composites,* 33**,** 1-11.

MECHTCHERINE, V., SILVA, F. D. A., BUTLER, M., ZHU, D., MOBASHER, B., GAO, S.-L. & MÄDER, E. 2011b. Behaviour of strain-hardening cement-based composites under high strain rates. *Journal of Advanced Concrete Technology,* 9**,** 51-62.

MICALLEF, K., SAGASETA, J., RUIZ, M. F. & MUTTONI, A. 2014. Assessing punching shear failure in reinforced concrete flat slabs subjected to localised impact loading. *International Journal of Impact Engineering,* 71**,** 17-33.

MOHEBKHAH, A. & TASNIMI, A. 2007. Seismic behavior of brick masonry walls recommended by IS-2800: experimental and numerical approaches. Proc. of the 5th Conf. on Seismology and Earthquake Engineering.

MOHEBKHAH, A., TASNIMI, A. & MOGHADAM, H. 2008. Nonlinear analysis of masonry-infilled steel frames with openings using discrete element method. *Journal of Constructional Steel Research,* 64**,** 1463-1472.

MOSALLAM, A. S. 2007. Out-of-plane flexural behavior of unreinforced red brick walls strengthened with FRP composites. *Composites Part B: Engineering,* 38**,** 559-574.

MYERS, J. J., BELARBI, A. & EL-DOMIATY, K. A. 2004. Blast resistance of FRP retrofitted un-reinforced masonry (URM) walls with and without arching action. *The Masonry Society Journal,* 22**,** 9-26.

OYARZO-VERA, C. & GRIFFITH, M. C. 2009. The Mw 6.3 Abruzzo (Italy) Earthquake of April 6th 2009: On Site Observations. *Bulletin of the New Zealand Society for Earthquake Engineering,* 42**,** 302.

PATODI, S. & KULKARNI, C. 2012. Performance evaluation of hybrid fiber reinforced concrete matrix. *International Journal of Engineering Research and Applications (IJERA),* 2**,** 1856-1863.

ROKOGO, K. & KANDA, T. 2005. Recent HPFRCC R&D Progress in Japan. Proceedings of International Workshop on HPFRCC in Structural Applications. Honolulu: HPFRCC.

ROKUGO, K., KANDA, T., YOKOTA, H. & SAKATA, N. 2009. Applications and recommendations of high performance fiber reinforced cement composites with

multiple fine cracking (HPFRCC) in Japan. *Materials and structures,* 42**,** 1197-1208.

RUSSELL, A. P. & INGHAM, J. M. 2010. Prevalence of New Zealand's unreinforced masonry buildings. *Bulletin of the New Zealand Society for Earthquake Engineering,* 43**,** 182.

ŞAHMARAN, M., BILICI, Z., OZBAY, E., ERDEM, T. K., YUCEL, H. E. & LACHEMI, M. 2013. Improving the workability and rheological properties of Engineered Cementitious Composites using factorial experimental design. *Composites Part B: Engineering,* 45**,** 356-368.

SAHMARAN, M., LACHEMI, M. & LI, V. C. 2010. Assessing mechanical properties and microstructure of fire-damaged engineered cementitious composites. *ACI Materials Journal,* 107.

ŞAHMARAN, M., ÖZBAY, E., YÜCEL, H. E., LACHEMI, M. & LI, V. C. 2011. Effect of fly ash and PVA fiber on microstructural damage and residual properties of engineered cementitious composites exposed to high temperatures. *Journal of Materials in Civil Engineering,* 23**,** 1735-1745.

SARHOSIS, V. 2016. Optimisation procedure for material parameter identification for masonry constitutive models. *International Journal of Masonry Research and Innovation,* 1**,** 48-58.

SARHOSIS, V. & SHENG, Y. 2014. Identification of material parameters for low bond strength masonry. *Engineering Structures,* 60**,** 100-110.

SHANG, X. & LU, Z. 2014. Impact of High Temperature on the Compressive Strength of ECC. *Advances in Materials Science and Engineering.*

SOE, K. T., ZHANG, Y. & ZHANG, L. 2013. Material properties of a new hybrid fibre-reinforced engineered cementitious composite. *Construction and Building Materials,* 43**,** 399-407.

SONG, G. & VAN ZIJL, G. 2004. Tailoring ECC for commercial application. Proceedings of the 6th RILEM symposium on fiber-reinforced concretes (FRC)—BEFIB, Citeseer, 20-22.

SORRENTINO, L., MASIANI, R. & DECANINI, L. D. 2006. Overturning of rocking rigid bodies under transient ground motions. *Structural Engineering and Mechanics,* 22**,** 293-310.

SORRENTINO, L., MASIANI, R. & GRIFFITH, M. C. 2008. The vertical spanning strip wall as a coupled rocking rigid body assembly. *Structural Engineering and Mechanics,* 29**,** 433-453.

TASNIMI, A. & REZAZADEH, M. 2012. Experimental and numerical study of strengthened single storey brick building under torsional moment. *International Journal of Civil Engineering,* 10.

TIEDEMAN, H. 1980. A statistical evaluation of the importance of non-structural damage to buildings. Proc., 7th World Conf. on Earthquake Engrg, 617-624.

TIMOSHENKO, S., WOINOWSKY-KRIEGER, S. & WOINOWSKY-KRIEGER, S. 1959. *Theory of plates and shells*, McGraw-hill New York.

TONOLI, G., SAVASTANO, H., FUENTE, E., NEGRO, C., BLANCO, A. & LAHR, F. R. 2010. Eucalyptus pulp fibres as alternative reinforcement to engineered cement-based composites. *Industrial crops and products,* 31**,** 225-232.

VACULIK, J. 2012. Unreinforced masonry walls subjected to out-of-plane seismic actions.

WANG, S. & LI, V. 2003. Lightweight Engineered Cementitious Composites (ECC). PRO 30: 4th International RILEM Workshop on High Performance Fiber Reinforced Cement Composites (HPFRCC 4),. RILEM Publications, 379.

WANG, S. & LI, V. C. 2006. High-early-strength engineered cementitious composites. *ACI materials journal,* 103.

WANG, S. & LI, V. C. 2007. Engineered cementitious composites with high-volume fly ash. *Materials Journal,* 104**,** 233-241.

WARD, S. P. 2004. Retrofitting existing masonry buildings to resist explosions. *Journal of performance of constructed facilities,* 18**,** 95-99.

YANG, E.-H., GARCEZ, E. & LI, V. C. 2012. Development of pigmentable engineered cementitious composites for architectural elements through integrated structures and materials design. *Materials and structures,* 45**,** 425-432.

YANG, E.-H., YANG, Y. & LI, V. C. 2007. Use of high volumes of fly ash to improve ECC mechanical properties and material greenness. *ACI Materials Journal,* 104.

YANG, E. & LI, V. C. 2006. Rate dependence in engineered cementitious composites. International RILEM Workshop on High Performance Fiber Reinforced Cementitious Composites in Structural Applications. RILEM Publications SARL, 83-92.

YUAN, F., PAN, J. & WU, Y. 2014. Numerical study on flexural behaviors of steel reinforced engineered cementitious composite (ECC) and ECC/concrete composite beams. *Science China Technological Sciences,* 57**,** 637-645.

ZHANG, Z., QIAN, S. & MA, H. 2014. Investigating mechanical properties and self-healing behavior of micro-cracked ECC with different volume of fly ash. *Construction and Building Materials,* 52**,** 17-23.

ZHOU, J., QIAN, S., BELTRAN, M. G. S., YE, G., VAN BREUGEL, K. & LI, V. C. 2010. Development of engineered cementitious composites with limestone powder and blast furnace slag. *Materials and Structures,* 43**,** 803-814.

Chapter 3 Development of ECC mixture and investigation of ECC material behaviour

3.1 Introduction

This chapter presents an experimental program aiming at (a) developing an ECC mixture (with PVA fibre) produced from materials available in the UK and then two hybrid ECC (HECC) mixtures (including both PVA and steel fibres) (b) establishing ECC and HECCs behaviour under different loading rates and temperatures. Initially, the behaviour of ECC is established under ambient temperatures (20˚C) by conducting a series of compression, flexural and tensile tests. An appropriate mixture is selected (exhibiting the best material behaviour in terms of workability, strength and ductility) and used for the experimental study presented in Chapters 4 and 5 and for calibrating the parameters of the material models employed in the numerical study in Chapter 6. Then two different HECC mixtures are developed based on the ECC mixture and their behaviour is assessed under ambient temperatures (20˚C) by conducting a series of compression and tensile tests. The behaviour of ECC and HECC are also investigated experimentally under increasing temperatures by conducting a series of flexural and compression tests. This is essential, as it is not uncommon for such materials to be subjected to a combination of actions associated with high loading rates (e.g. generated by earthquakes, explosions and collisions) and elevated temperatures (e.g. as a result of fires that occur either during or immediately after the application of dynamic actions mentioned previously). Tables 3.1 and 3.2 provide an outline of the tests carried out at ambient and elevated temperatures respectively.

Table 3.1: Material tests carried out at ambient temperature (20 ˚C)

Type of test	Material type	ID	W/B	Loading rate (mm/min)	Number of tests
Compression test	ECC	SEC22	0.22	1	3
		SEC25	0.25	1	3
		SEC28	0.28	1	3
		SEC32	0.32	1	3
Bending test	ECC	SEB22	0.22	1	3
		SEB25	0.25	1	3
		SEB28	0.28	1	3
		SEB32	0.32	1	3
Tensile test	ECC	SET	0.28	1	5
	HECC	SH6T	0.28	1	5
		SH13T	0.28	1	5
	ECC	EET	0.28	400	5

Table 3.2: Material tests carried out under elevated temperatures

Type of test	Material type	ID	Temperature (˚C)	Number of tests
Compression test	ECC	20EC	20	2
		200EC	200	2
		400EC	400	1
		600EC	600	1
	HECC (PVA & 6mm steel fibres)	20H6C	20	1
		200H6C	200	2
		400H6C	400	1
		600H6C	600	1
	HECC (PVA & 13 mm steel fibres)	20H13C	20	1
		200H13C	200	1
		400H13C	400	1
		600H13C	600	1
Bending test	ECC	20EB	20	2
		60EB	60	2
		100EB	100	2
		150EB	150	1
		200EB	200	1
		400EB	400	1
	HECC (PVA & 6mm steel fibres)	20H6B	20	1
		60H6B	60	2
		100H6B	100	1
		200H6B	200	2
		400H6B	400	2
		600H6B	600	1
	HECC (PVA & 13 mm steel fibres)	20H13B	20	1
		60H13B	60	2
		100H13B	100	2
		200H13B	200	2
		400H13B	400	1
		600H13B	600	1

Figure 3.1a shows the labelling system assigned to the different specimens (presented in Tables 3.1) when subjected to different test and loading rates. The first letter in Figure

3.1(a) refers to the rate of loading (S: 1 mm/min, E: 400 mm/min). The second letter refers to the type of material E= ECC, H6= HECC (PVA & 6mm steel fibres) H13= HECC (PVA &13mm steel fibres). The third letter refers to the type of test carried out C: compression, B: flexural, T: tensile test. The fourth letter refers to the water to binder ratio (W/B) used in the mixes (i.e. 0.22, 0.25, 0.28, 0.32). The final number corresponds to specimen number. Figure 3.1 b shows the labelling system assigned to the different specimens (presented in Tables 3.2) when subjected to the different tests under different temperatures. The first letter refers to the temperature to which the specimen were subjected prior to testing (20˚C, 60˚C, 100˚C, 200˚C, 400˚C, 600˚C). The second letter refers to the type of material E= ECC, H6= HECC (PVA & 6mm steel fibres) H13= HECC (PVA &13mm steel fibres). The following letter defines the type of test carried out (C: compression, B: bending) and the final number refers to the specimen number.

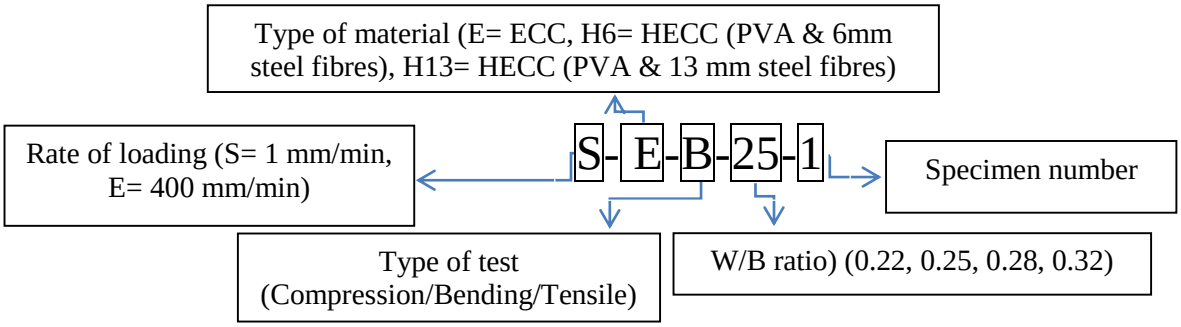

(a)

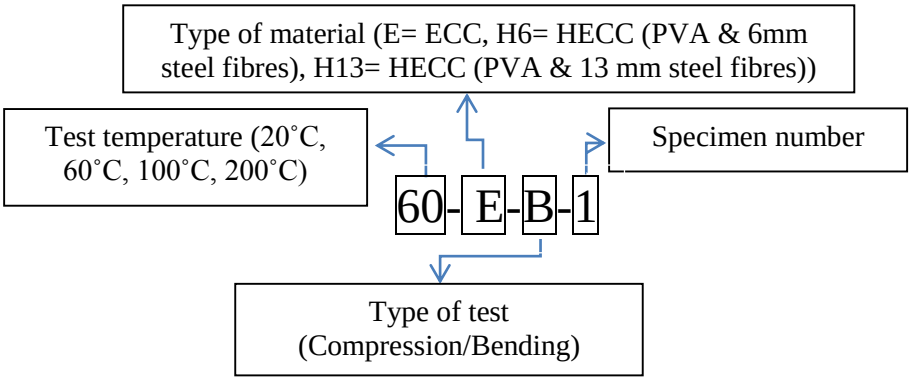

(b)

Figure 3.1. Labelling system adopted for tests carried out under increasing (a) loading rates and (b) temperatures.

3.2 Development of ECC mix

ECC was initially produced by cement, water, fine silica and sand as well as filler and fibres (Li and Leung, 1992). Fly ash – a by-product of industry obtained by burning coal–

was used to partially replace cement in ECC mix in order to make it more environmentally friendly (sustainable) (Yang et al., 2007). For the present study Cem I 52.5 is chosen as the most appropriate option for the ECC mix (this is pure cement - in order to avoid the additional influence of the presence of mineral admixtures found in other CEM types - which is readily available in the UK). Two types of fly ash (EN 450 and Superpozz SV80), available in the UK market, were tried. The use of Superpozz resulted in better workability and as a result was selected for the final mix. A series of different silica sands (i.e. DA 110, DA 80F, AF 100, M6, M300, AFA100, RH110, HST95, M10, M400) and limestone powders (i.e. TRUCARB UF, TRUCARB 298 and TRUCARB 295) were also tried. After a series of trial mixes, RH110 was selected for the final mixture based on the observed workability. Superplasticizer GELENUIM ACE 499 was also used. A viscose agent (RheoMATRIX 110) and an air entraining admixture (MICRO-AIR 119) were also used in the trial mixes, however, as their use did not improve the workability of the mixture significantly, they were eliminated from the final mix. Two types of polyvinyl alcohol (PVA) (REC15, Kuraray) fibre were used (Table 3.3) with a density of 1300 kg/m3. The 12 mm PVA fibres were ultimately used as the resulting mixture presented better strain hardening behaviour. The surface of the PVA fibres was coated with a proprietary oiling agent (1.2% by weight) to reduce any excessive fibre-matrix chemical bond.

Table 3.3: Fibres properties

Fibre ID	Length (mm)	Nominal Diameter (mm)	Tensile strength (MPa)	Modulus of Elastisity (GPa)
St 6	6	0.15	3000	210
St 13	13	0.15	3000	210
PVA8	8	0.04	1600	14
PVA12	12	0.04	1600	14

To develop the ECC some preliminary tests were carried out on the fresh properties of ECC which are presented in Appendix 1. Then a series of mixes were produced with a fixed fly-ash-to-cement ratio of 1.8 and and a fine silica sand to cement ratio of 0.6. Water/binder ratios of 0.22, 0.25, 0.28 and 0.32 were studied to find the best mix proportion (Table 3.4). A high range water reducing (HRWR) admixture was used at rate of about 1%. Standard 12mm long Polyvinyl Alcohol (PVA) fibre was used at a dosage of 2% by volume (Figure 3.2).

Table 3.4: The ECC mixture proportions

Mixture ID	Water(kg/m^3)	Cement(kg/m^3)	Fly-ash(kg/m^3)	Silica sand(kg/m^3)	PVA (kg/m^3)	HRWR (kg/m^3)
ECC M1	303	491	885	299	26	4.9
ECC M2	330	471	848	289	26	4.7
ECC M3	356	454	817	273	26	4.5
ECC M4	386	430	775	264	26	4.3

a b

Figure 3.2. a) Materials used for producing one litre of ECC b) 8-litre Hobart planetary mixer

3.2.1 Mixing process

A 8-litre Hobart planetary motion mixer was used to produce the PVA-ECC (see Figure 3.3) by adopting the following mixing procedure:

Step 1: The cement, fly-ash, and silica sand are mixed manually for 1 min.

Step 2: Approximately 80% of the water is added to the mixture and mixed at low speed (61 rpm) for 1 min.

Step 3: The superplasticizer (HRWR) is gradually added (over a period of 20 sec). Mixing continues for an additional 1 min.

Step 4: The remaining water is added, and the matrix is then mixed for another 2.5 min at high speed (113 rpm).

Step 5: The fibres are added in small amounts to the rotating mixer for 1 min at low speed. After introducing all the fibres, the ECC is mixed for 4.5 min at high speed and then for 30 sec at a low speed in order to reduce the entrapped air.

3.2.2 Casting and curing

The fresh ECC was cast in moulds in order to form prismatic (beam) specimens with dimensions of 20x40x170 mm for flexural testing and some cubes (50mmx50mmx50mm) for compression testing. Following casting, the moulds were covered with a plastic film (to avoid water evaporation) and left for 24 hours. The specimens were demoulded and then immersed in water in a curing tank at 20±3^{o}C for 28 days until the testing date.

3.2.3 Compression tests

A compressive machine (Avery-Denison 3000 kN) was used for establishing the compressive strength of the ECC cube specimens (see Figure 3.3). The load was gradually applied in the form of load increments (load-control) at a rate of 37 kN/min in accordance with ASTM C109. The apparatus measured maximum compressive strengths of the specimens which are presented in Figure 3.4 in relation to the water to binder ratio (W/B). It is observed that with increasing W/B ratios the compressive strength of ECC reduces. It is interesting to note that although the experimental results are characterised by some variation, a clear trend emerges concerning the effect of W/B on the compressive strength.

Figure 3.3. Avery-Denison 3000 kN compression test machine

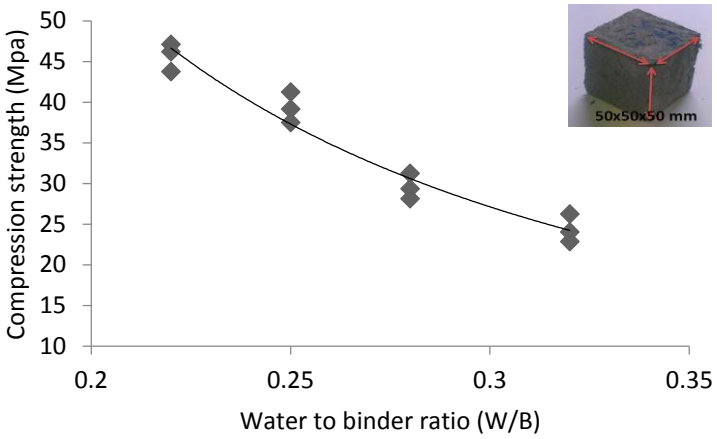

Figure 3.4. Compressive strength vs W/B ratio curves for the different ECC mixture

3.2.4 Bending test

Figure 3.5 shows the four-point bending test setup used to assess the behaviour of the ECC prismatic specimens in flexural. The specimens were tested using a 100kN INSTRON universal testing machine (Figure 3.5). The load was applied in the form of displacement increments (displacement controlled) at a rate of 1 mm/min. The load applied was measured using a 100kN load cell mounted on the loading head. Each specimen was tested as a simply supported beam with a clear span of 150 mm. The position at which the two point loads were applied along the span of the specimen is presented in Figure 3.5. The vertical deflection and the vertical displacement was measured at the loading head.

a)

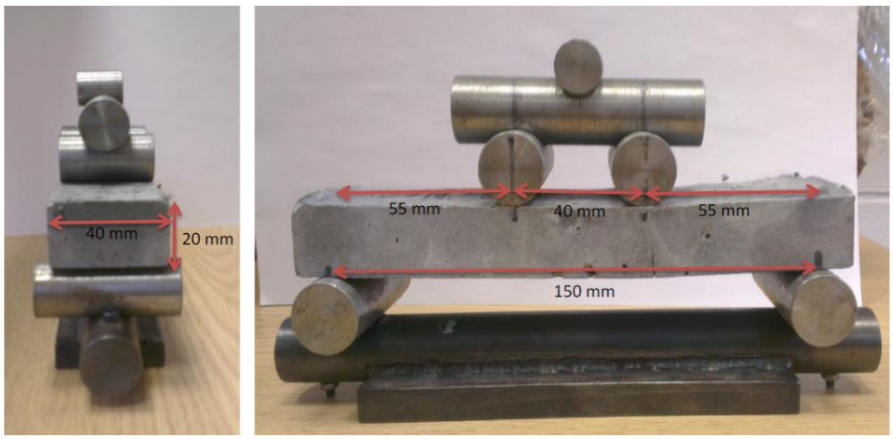

b)

Figure 3.5. a) 100kN INSTRON universal testing machine b) test setup of four-point bending specimens.

Results of the bending test for each group of specimens are shown in Figure 3.6. The SB22 series (W/B=0.22) exhibited very limited deflection. Specimens SB25, SB28 and SB32 exhibited more ductile behaviour respectively as their W/B ration increased. To compare the results obtained from bending test (see Figure 3.6) and select the best mixture four parameters were considered: (i) maximum load carrying capacity, (ii) maximum deflection (at maximum load), (iii) the load at which the first crack observed (start of strain hardening branch) and (iv) the number of cracks developing along the central span of the specimen.

Figure 3.7 a reveals that the first crack in the specimens has a clear relation to the W/B ratio. The increase of W/B ratio in the ECC mix results in the development of cracking earlier in the loading process (as a result the increase of W/B leads to a reduction in the load at which the first crack develops). This is due to the reduction of the strength of the ECC matrix discussed in section 3.2.3. It can be observed from Figure 3.7 b that the load bearing capacity for all specimens not affected very significantly by increasing the W/B ration. The maximum load is associated with the friction developing between the fibres and ECC matrix which not appeared to be dependent on the W/B ratio. Figure 3.7 c demonstrates the relation between ductility of specimens and W/B ratio. The ductility exhibited a direct relation with the W/B ratio, whereas W/B increases the ductility of specimens enhances. The main reason for increase in ductility is the increasing the number of cracks developing in the central span of specimens. Figure 3.7 d shows that increasing the W/B ratio resulting in increase of the crack numbers which developed in the central region of specimens. The number of cracks developed in the specimens

exhibits the strain hardening behaviour of specimens. The increase of the W/B ratio reduces the strength and toughness of the ECC matrix resulting in more cracks formation.

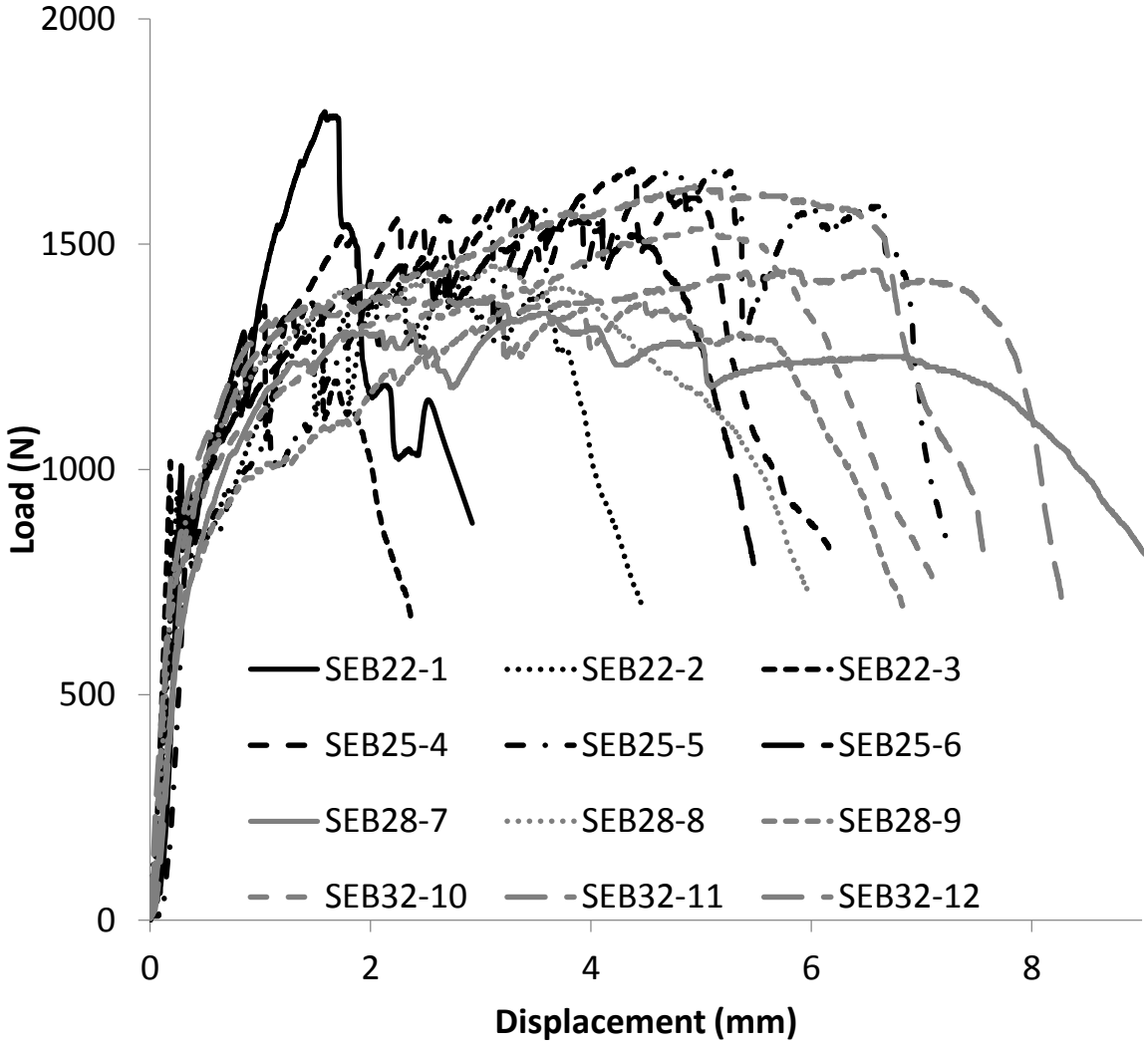

Figure 3.6. Four- point bending load-deflection curves for SEB22, SEB25, SEB28 and SEB32 series.

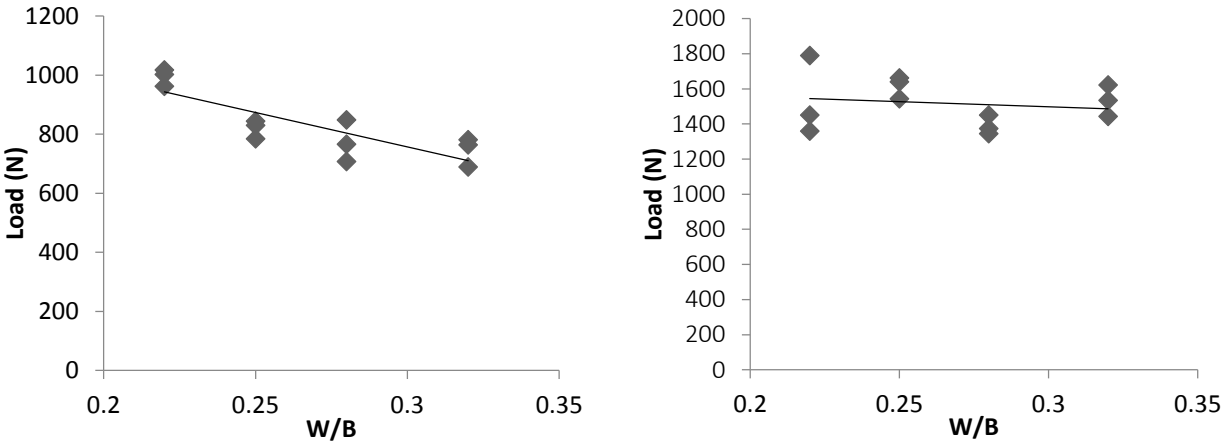

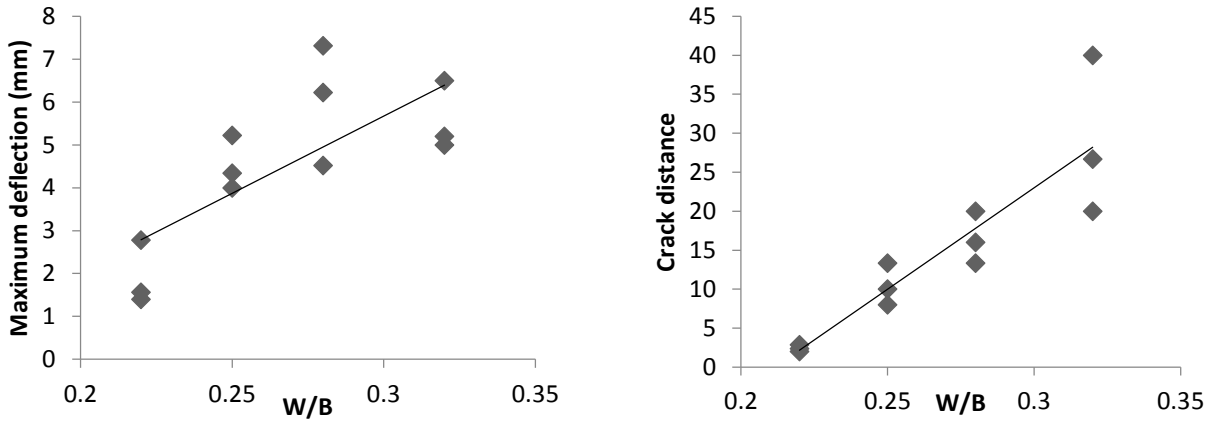

(c) (d)

Figure 3.7. Results from four-point bending tests carried out on SEB22, SEB25, SEB28 and SEB32 series expressing the variation of a) the load at which the first crack develops (b) maximum load capacity (c) Maximum deflection and (d) the number of cracks developing along the mid-span region of the specimen with respect to the W/B ratio

From the analysis of the test data associated with the bending and compression tests presented in Figures 3.4 and 3.7 it emerges that the mix associated with specimen ECC M3 (W/B = 0.28) has the best mix proportion. This mixture had a compressive strength higher than 30 MPa at 28 days while exhibiting appropriate deflection and crack number resulting in strain hardening behaviour. The HECC material is also developed based on the selected ECC mix proportion presented in Table 3.5. For both H6ECC and H13ECC 12mm Polyvinyl Alcohol (PVA) fibre was used at a dosage of 1.75 % by volume and steel fibres were used at a dosage of 0.75 % by volume. It should be mentioned that in HECC mixtures the percentage of PVA fibre is reduced to keep the total fibres percentage (including PVA and steel fibres) 2.5% which makes HECCs more cost-efective for potential applications.

Table 3.5: The finalised ECC and HECC mixture proportions

Mixture ID	Water (kg/m^3)	Cement (kg/m^3)	Fly-ash (kg/m^3)	Silica sand (kg/m^3)	PVA fibre (kg/m^3)	Steel fibre (kg/m^3)	HRWR (kg/m^3)
ECC	356	454	817	273	26	-	4.5
H6ECC	354	451	817	273	22.75	58.86	4.5
H13 ECC	354	451	817	273	22.75	58.86	4.5

3.2.5 Tensile tests

A series of uniaxial tensile tests are then conducted on the selected mixture of ECC, H6ECC and H13ECC (presented in Table 3.5) according to Japan's recommendation for ECC tensile testing. The mixing procedure adopted for preparing the ECC used in this series of tests is the same as that described in section 3.2.2. Dog-bone specimens (see

Figure 3.8) were selected for conducting the tensile tests. The load applied during the tensile test was measured through the use of a 100 kN load cell while two pneumatic grips were used to support the specimen on both sides (Figure 3.8 a). The dimensions of the specimens are presented in Figure 3.8 c. Two Linear variable differential transformers (LVDTs), each one positioned on one side of the sample were used to measure the relative displacement on the 80 mm central span demonstrated in Figure 3.8 b. During testing the subject specimens exhibited deformation, cracking and ultimately failure along the narrow (middle) portion of the specimens. The measurement obtained from this narrow region (80 mm central part) is considered to describe the material behaviour of ECC in tension and can be used to derive the material properties of ECC. The load was applied in displacement increments (displacement control) either at a rate of 1 mm/min or 400 mm/min.

a) b)

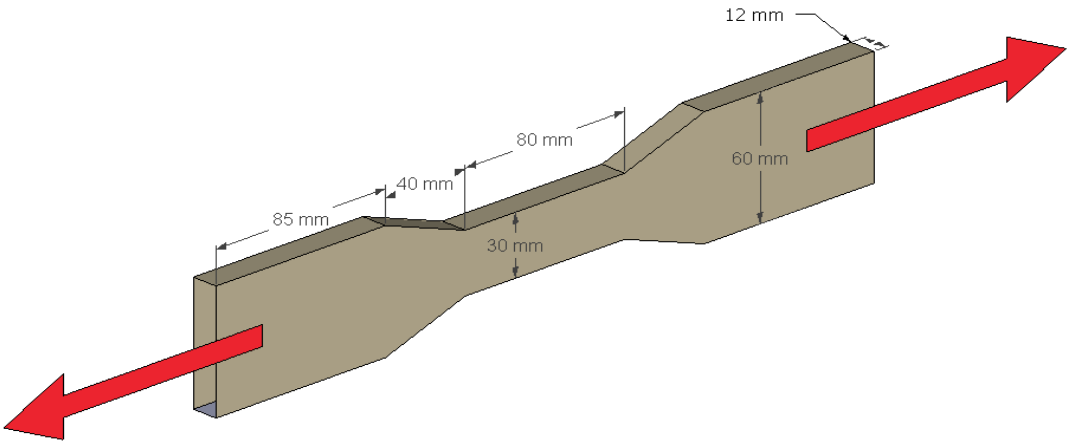

c)

Figure 3.8 . a) 100kN INSTRON universal testing machine with pneumatic grips b) Dog-bone tensile test setup c) Dog-bone tensile test dimensions

Results obtained from the uniaxial tensile tests conducted on the ECC dog-bone specimens expressing the variation of the stress (the load divides by cross section of 30mm x 12mm) developing along the narrow region of the specimens and the strain (displacement divide by 80 mm length of central span) are represented in Figure 3.9. The stress–strain curves describe material behaviour undet uniaxial tension and consists of three different branches: (i) a linear elastic branch which starts when loading process initiates and ends when the first cracking occurs (ii) the strain hardening branch which is a plateau including a series of fluctuations due to the propagation of the cracks in the specimens (iii) finally the descending branch initiating after the peak stress is obtained resulting in failure when localized crack happens in specimens.

The average material properties of ECC established on the basis of these curves for different rates of applied loading are summarised in Table 3.6. The stress and strain values at first cracks, the modulus of elasticity (E) are calculated based on the initial elastic branch describing the ECC behaviour. The peak stress and the corresponding strain are obtained from the strain hardening branch. For the case of the ECC specimens under quasi-static load (SET series) a maximum (peak) stress of 3.8 MPa and a strain capacity (corresponding to maximum stress) of 3.5% was measured. All specimens of the SET series exhibited strain hardening behaviour and uniform crack distribution along the central part of specimens (see Figure 3.10). In the case of the ECC specimens under elevated loading rate (EET series), a maximum (peak) stress of 5.2 MPa and a strain capacity of 2.2% were recorded. The latter specimens demonstrated a strain hardening

behaviour with uniform crack distribution in the narrow middle portion, though the number of cracks were less than those observed in the SET series.

A comparison of the test data obtained from the specimens included in the SET and EET series (Figure 3.9) reveals that the behaviour of ECC is strain rate sensitive (i.e. the material properties of ECC are dependent on the rate of deformation). The peak stress developed by the specimens of the EET series was about 36% higher than that of the SET Series. Furthermore, the strain capacity of EET series was reduced by 38% compared to that of the SET Series. The comparison of crack propagated on the specimens of the SET and EET series (Figure 3.10) shows a reduction in cracks number in EET series compared to the SET series due to increasing the loading rate.

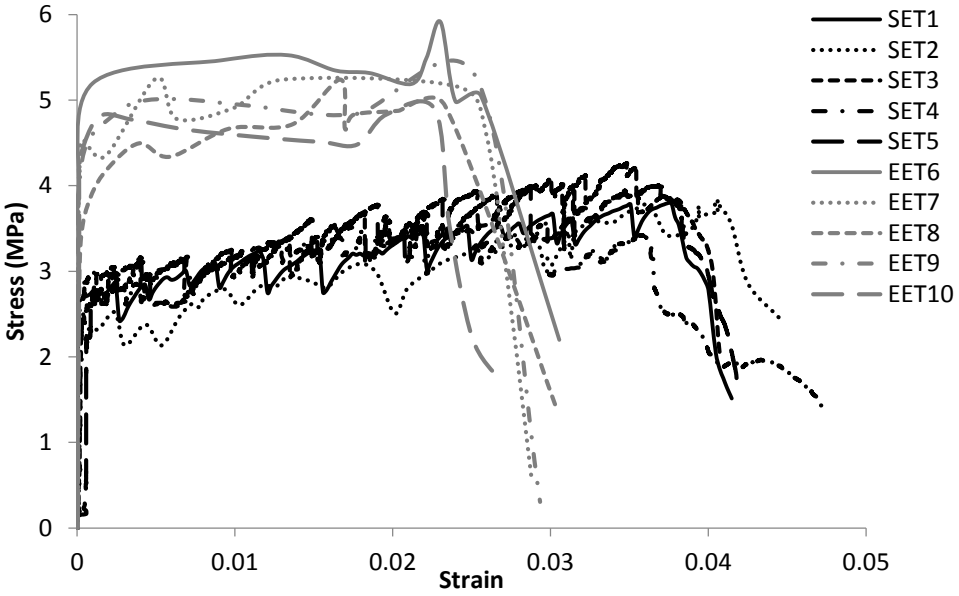

Figure 3.9. Tensile test stress-strain curves for SET and EET series

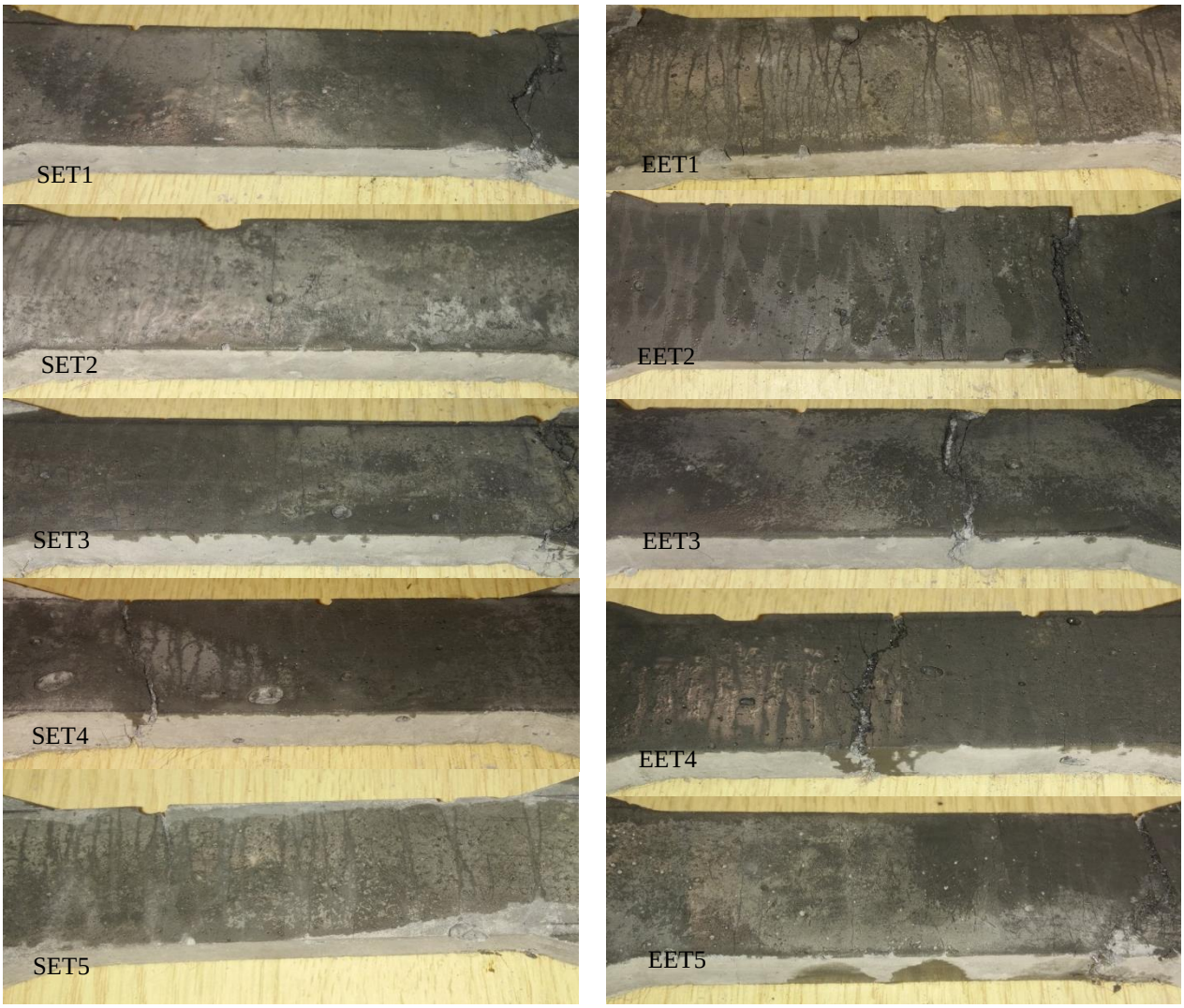

Figure 3.10. Failure crack patterns at the tensile test of dog-bone specimens a) under a displacement rate of 1 mm/min and (b) under a rate of 400 mm/min.

Stress-strain results obtained from the uniaxial tensile tests conducted on the HECC dog-bone specimens are presented in Figure 3.11. As in the case of the ECC the stress–strain curves describe material behaviour under uniaxial tension characterised by three different branches: (i) initial ascending elastic branch, by ii) plateau strain hardening branch iii) descending branch of curves resulting in failure. The average material properties of ECC established on the basis of these curves are summarised in Table 3.6. For the case of the specimens included on 6 mm steel fibres (SH6T series) a maximum (peak) stress of 4.3 MPa and a strain capacity (corresponding to maximum stress) of 3 % was measured. All specimens of the SH6T series exhibited strain hardening behaviour and uniform crack distribution along the central part of specimens (see Figure 3.12). In the case of specimens included, the 13 mm steel fibres (SH13T) series, a maximum (peak) stress of 4.7 MPa

and a strain capacity of 2.5% were recorded. The latter specimens demonstrated a strain hardening behaviour while exhibiting uniform crack distribution in the narrow middle portion. However, the number of cracks were less than the SH6T series.

A comparison between the test data obtained from the specimens of the SET series (ECC) presented in Figure 3.9 and SH6T (HECC with 6 mm steel fibres) and SH13T series (HECC with 13 mm steel fibres) presented in Figure 3.11 reveals that the behaviour of ECC is more ductile than HECCs. The peak stress developed by the specimens of the SH6T and SH13T series were 13% and 22% higher than that obtained from the specimens of the SET Series respectively. The strain capacity of SH6T series and SH13T were 16% and 40% less compared to the SET series respectively. The comparison of the cracking profile development on the specimens (Figure 3.12) shows a reduction in crack numbers for those included in the SH13T series compared to those developing in the specimens included in the SH6T series due to the use of a 13 mm length steel fibre in SH13T compared to the 6 mm length steel fibre in SH6T. It observed that the longer steel fibre (13 mm compared to 6 mm) resulted in reduction of the ductility of SH13T about 20% while increasing the strength 21% compared to SH6T series.

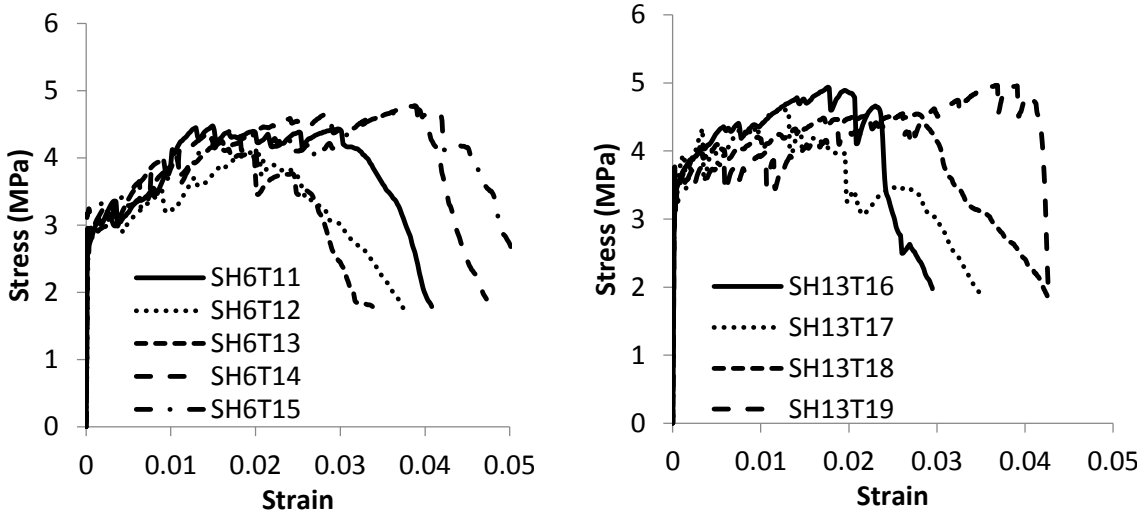

Figure 3.11. Tensile test stress-strain curves for a) SH6ET and b) SH13ET series

Table 3.6: Average tensile test results for specimens

ID	loading rate (mm/min)	Stress at first crack (MPa)	Strain of first crack	E (GPa)	Max stress (MPa)	Max strain
SET	1	2.75	0.000180	15.4	3.85	0.035
EET	400	4.16	0.000144	30.6	5.22	0.022
SH6T	1	2.89	0.000191	15.1	4.36	0.030
SH13T	1	3.32	0.000179	18.5	4.71	0.025

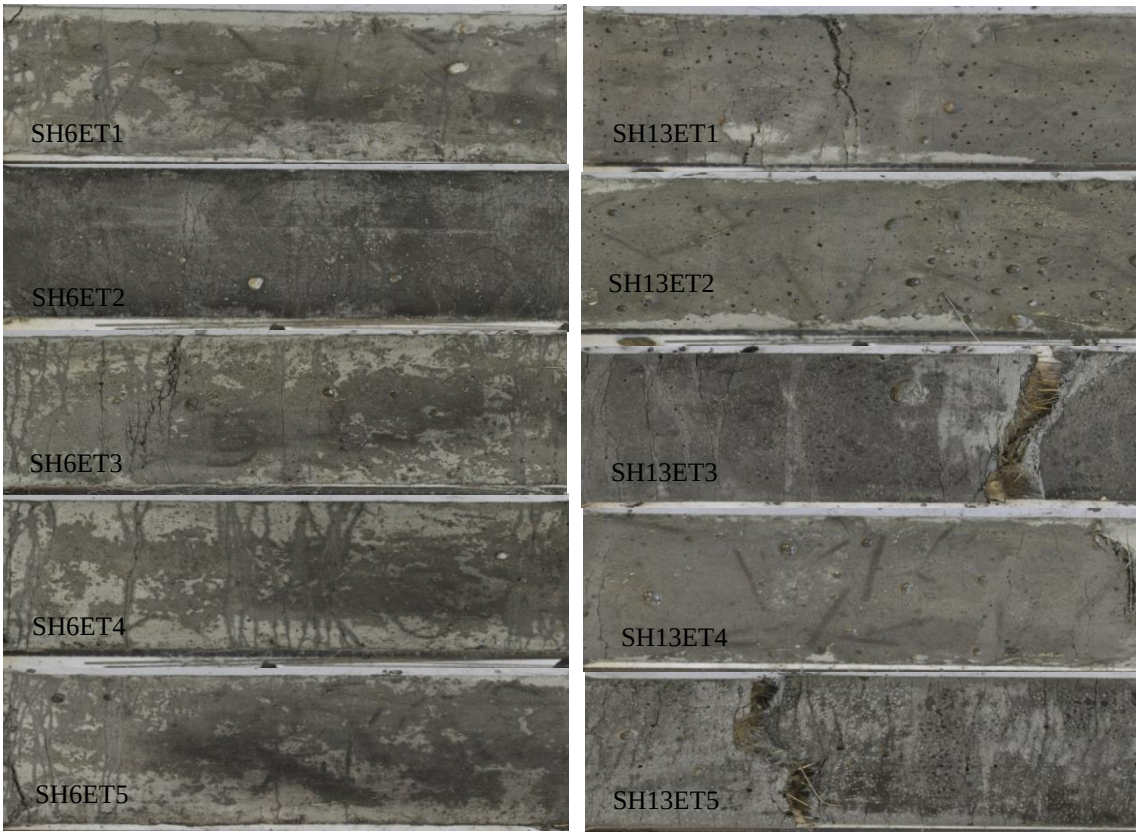

a) SH6T series b) SH13T series

Figure 3.12. Failure crack patterns along the central span of dog-bone specimens under uniaxial tensile load a) SH6T series (b) SH13T series.

3.3 Mechanical properties of ECC and HECCs at elevated temperature

In an attempt to establish the effect of temperature on the behaviour of ECC and HECCS a series of prismatic specimens were prepared for testing under compression and flexure tests as discussed in section 3.2.3 and 3.2.4 respectively (Figure 3.13 c&d). The ECC was mixed and casted as described in section 3.2.1 and 3.2.2. After demoulding, the specimens were immersed in water (in a curing tank) at 20±3^{o}C for 21 days and then cured for one

week in the laboratory environment out of water (20±3ºC and 60% humidity) for 7 days prior to testing to reduce the possibility of spalling under high temperature when the specimens pores are full of water. The specimens were tested at Edinburgh University using a 600kN INSTRON universal testing machine with an integrated heating chamber to run in-situ tests at high temperature (Figure 3.13 a). The samples were initially put in a furnace and the temperature was increased at a rate of 10ºC per minute until the target temperature was attained (Figure 3.11). The temperature then remained constant for 30 minutes. Then tests were carried out while the specimens remained heated on the target temperature inside the heating chamber. The heating regime followed is presented in Figure 3.13

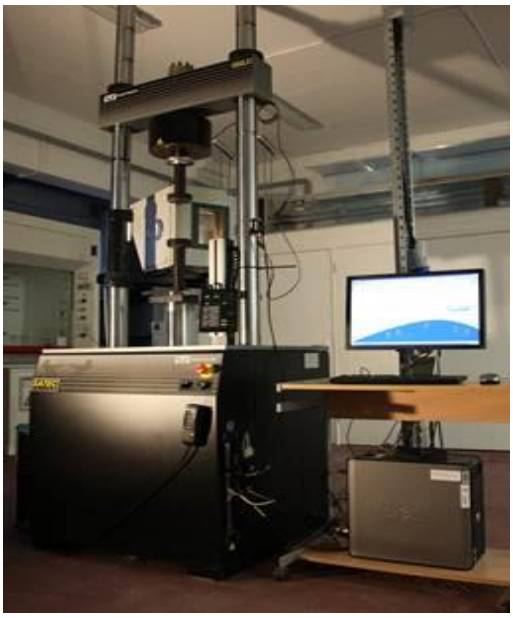

a

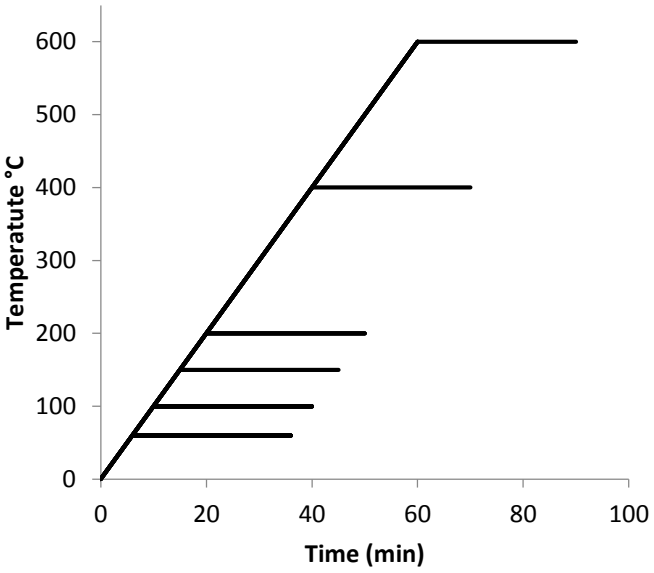

b

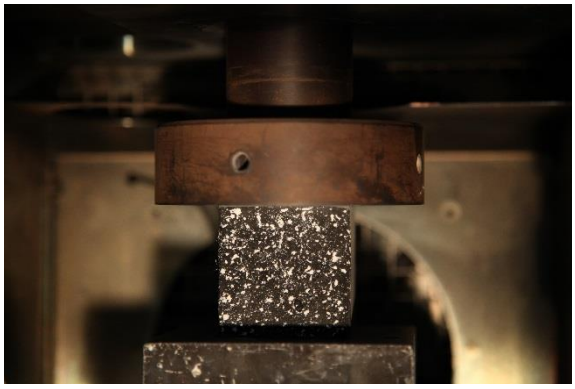

c

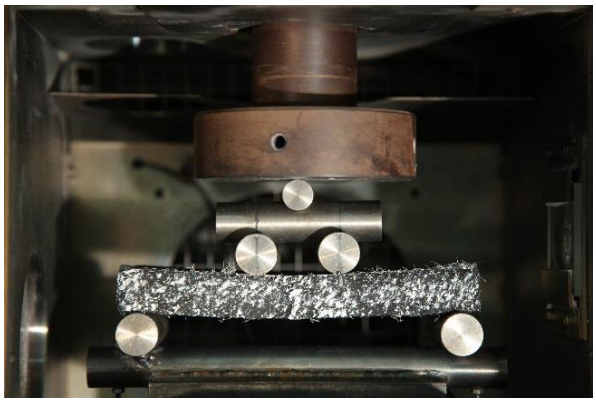

d

Figure 3.13. a) Instron 600 kN testing machine with integrated heating chamber b) Heating regime adopted for specimens c) a compression specimens test setup inside heating chamber d) a four-point bending test set up inside heating chamber

3.3.1 Compression test

During testing the compressive load was applied in the form of displacement increments (displacement control) at rate of 1 mm/min and the specimens were subjected to a maximum 5% compression strain. Figure 3.14 shows the compression stress-strain curves measured for each specimen. The stress-strain curved describing the behaviour of the ECC specimens under uniaxial compression after being subjected to temperatures between 20ºC to 600ºC. The stress–strain curves comprised of: i) an initial ascending branch starting when the load was applied and continued until peak load was attained followed by ii) a strain softening descending branch ultimately leading to failure associated with extending cracking resulting in the loss of load carrying capacity. The compression strength (defined by the peak stress value in the stress-strain curve) at 20°C temperature was measured for ECC, H6ECC and H13 ECC at approximately 38.8 MPa, 40.1MPa and 45MPa. These results are 21%, 25% and 40% higher than the counterparts measured in section 3.2.3. The main reason for this difference is the different curing methods adopted on these specimens were cured out of water for the last 7 days of the curing period. It is reported that dry concrete tends to show higher strength than saturated concrete due to the decreased internal hydrostatic pressure within the process (Bushlaibi and Alshamsi, 2002).

Table 3.7 presents the effect of temperature on various aspects of the specimen's behaviour in terms such as the maximum stress and associated modulus of elasticity (E) (is calculated based on stress and strain at peak point). At 20˚C the compression strength of ECC, H6EC and H13ECC series are close to each other in spite of some variations observed in the results. A reduction in the strength was observed when increasing the temperature for all specimens (Figure 3.15a). In the case of ECC series of specimens subjected to temperatures equal to 200˚C, 400˚C and 600˚C the compression strength decreased by 6%, 10% and 25% respectively compared to their counterpart measured under ambient temperature (20 ˚C). In the case of the H6ECC series specimens subjected to temperatures equal to 200˚C, 400˚C and 600˚C a 6%, 11% and 33% reduction in compression strength was observed respectively compared to their counterpart under ambient temperature (20 ˚C). The compression strength of the H13ECC specimens subjected to 200˚C, 400˚C and 600˚C reduced by 14%, 27% and 35% respectively compared to their counterpart under ambient temperature (20 ˚C). Figure 3.15b shows

the effect of the temperature on the modulus of elasticity of the specimens. For all specimens a reduction in the modulus of elasticity was observed with increasing temperatures.

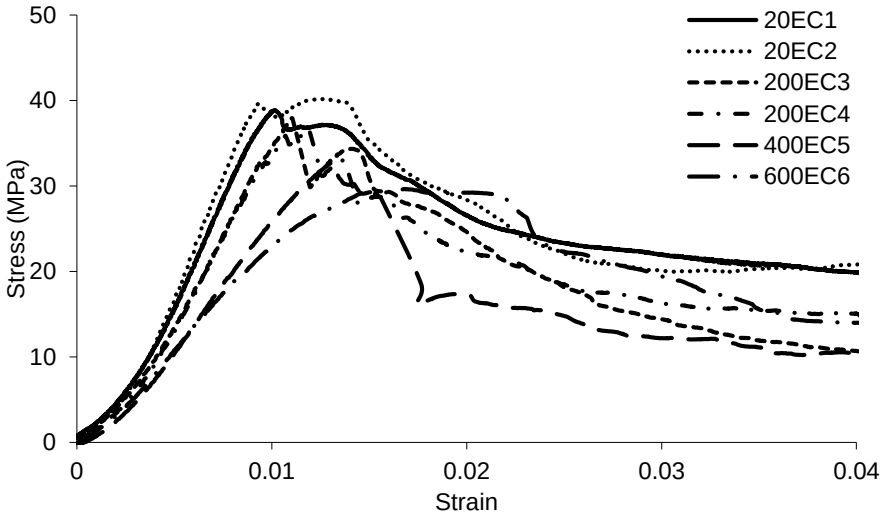

a)

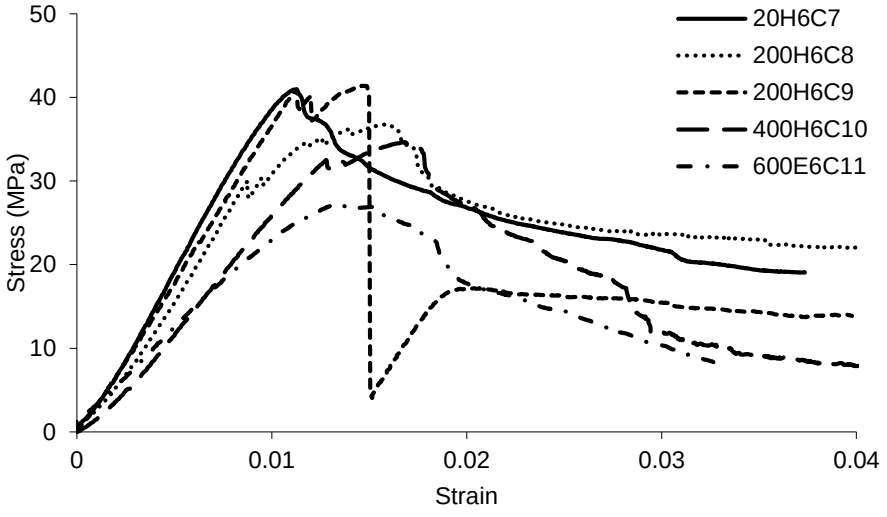

b)

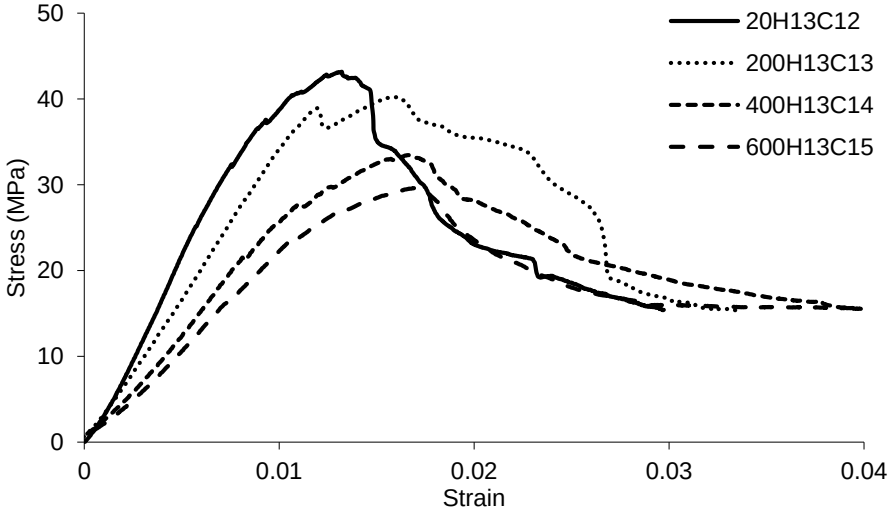

c)

Figure 3.14. Experimentally established stress-strain curves at different temperatures a) ECC specimens, b) H6ECC specimens, c) H13ECC specimens

Table 3. 1 The Average compression test results for specimens

Specimens ID		Temperature (˚C)	Stress (MPa)	Strain	E (GPa)
ECC	20EC	20	38.8	0.00965	40.2
	200EC	200	36.15	0.0096	37.6
	400EC	400	35.1	0.013	27.0
	600EC	600	29.2	0.015	19.4
H6ECC	20EC	20	40.1	0.01	40.1
	200EC	200	38.45	0.01	38.4
	400EC	400	32	0.013	24.6
	600EC	600	27.2	0.0135	20.1
H13ECC	20EC	20	45	0.0118	38.1
	200EC	200	38.5	0.012	32.0
	400EC	400	32.8	0.0154	21.2
	600EC	600	29.5	0.0168	17.5

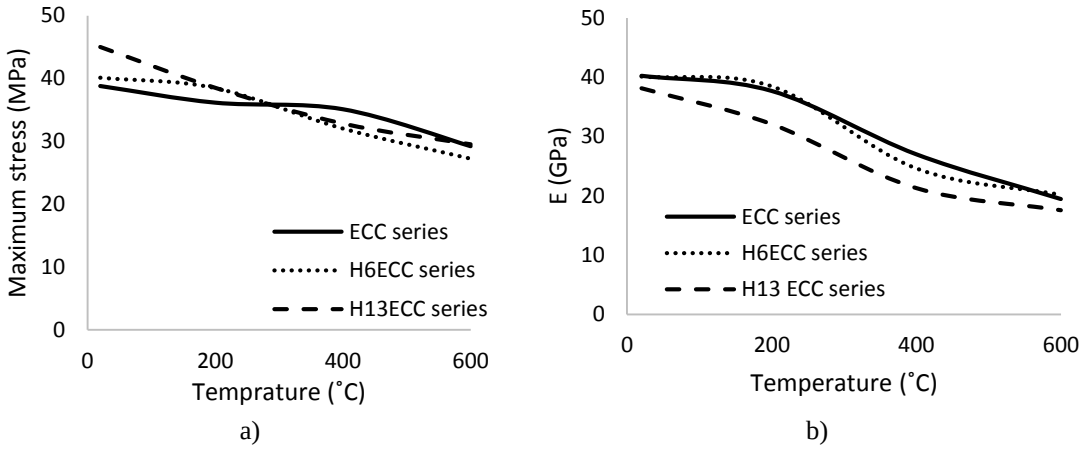

a) b)

Figure 3.15. Effect of temperature on the specimens a) Maximum load, b) Modulus of elasticity

The weight of all specimens were measured before they were subjected to high temperature and the compression tests. After carrying out the tests the specimens cooled down for an hour and then the weight of specimens (including the main body and debris produced during the tests) were measured. Figure 3.16a compares the total weight of the specimens before and after subjecting them to high temperatures. At 200°C about 10% of the weight of all specimens decreased compared to their counterpart measured under ambient temperature (20 ˚C) mainly due to evaporation of the moisture content. At 400°C and 600°C the specimens lost about 12% and 14% of their weight respectively compared to their counterpart under ambient temperature (20 ˚C) mainly due to evaporation of PVA fibre. Figure 3.16 b presents the percentage of debris produced during testing from the specimens when subjected to high temperatures. In the case of the ECC series of

specimens subjected to 200 ˚C, 400 ˚C and 600 ˚C temperature 2%, 21% and 30% of specimen's weight were lost in the form of debris during tests respectively. However, in both H6ECC and H13ECC series specimens subjected to 200 ˚C, 400 ˚C and 600 ˚C temperature only 2%, 3% and 8.5% of specimen's weight respectively were lost in the form of debris during tests. It is interesting to observe that both H6ECC and H13ECC specimens produced less debris when subjected to high temperature compared to the ECC specimens. Considering the combined action of high loading rates and elevated temperatures (in explosion or blast events) the integrity of the structure members is very important as projectile debris are repeatedly reported as a major source of causalities (Wightman and Gladish, 2001, Taber et al., 2006, Freiwald, 1972, Cooper et al., 1983). Figure 3.17 shows the six surfaces of the cubes specimens subjected to compression tests at failure for the ECC, H6ECC and H13ECC series. It is evident that the H6ECC and E13ECC specimens exhibited a higher level of integrity at high temperatures compared to the ECC specimens due to the introduction of steel fibres in their mixtures.

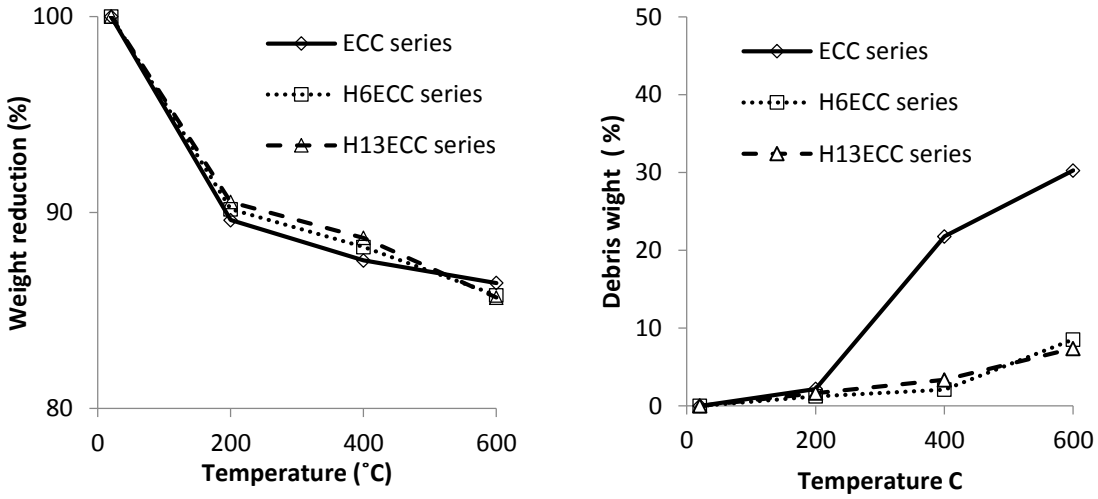

a) b)

Figure 3.16. a) Comparison of specimens' weight before and after subjected to high temperature b) percentage of debris separated from specimens when subjected to high temperature

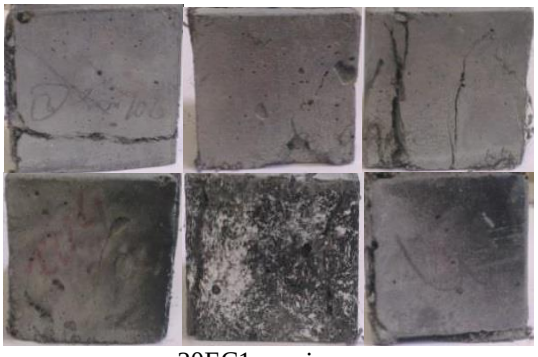

20EC1 specimen

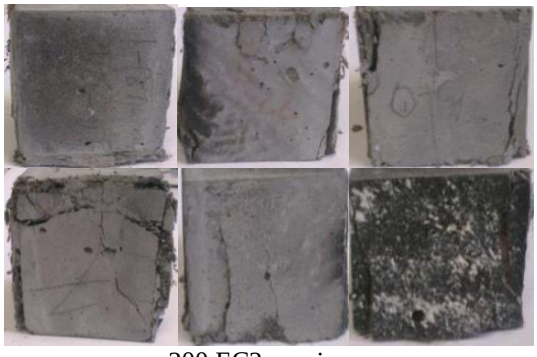

200 EC2 specimen

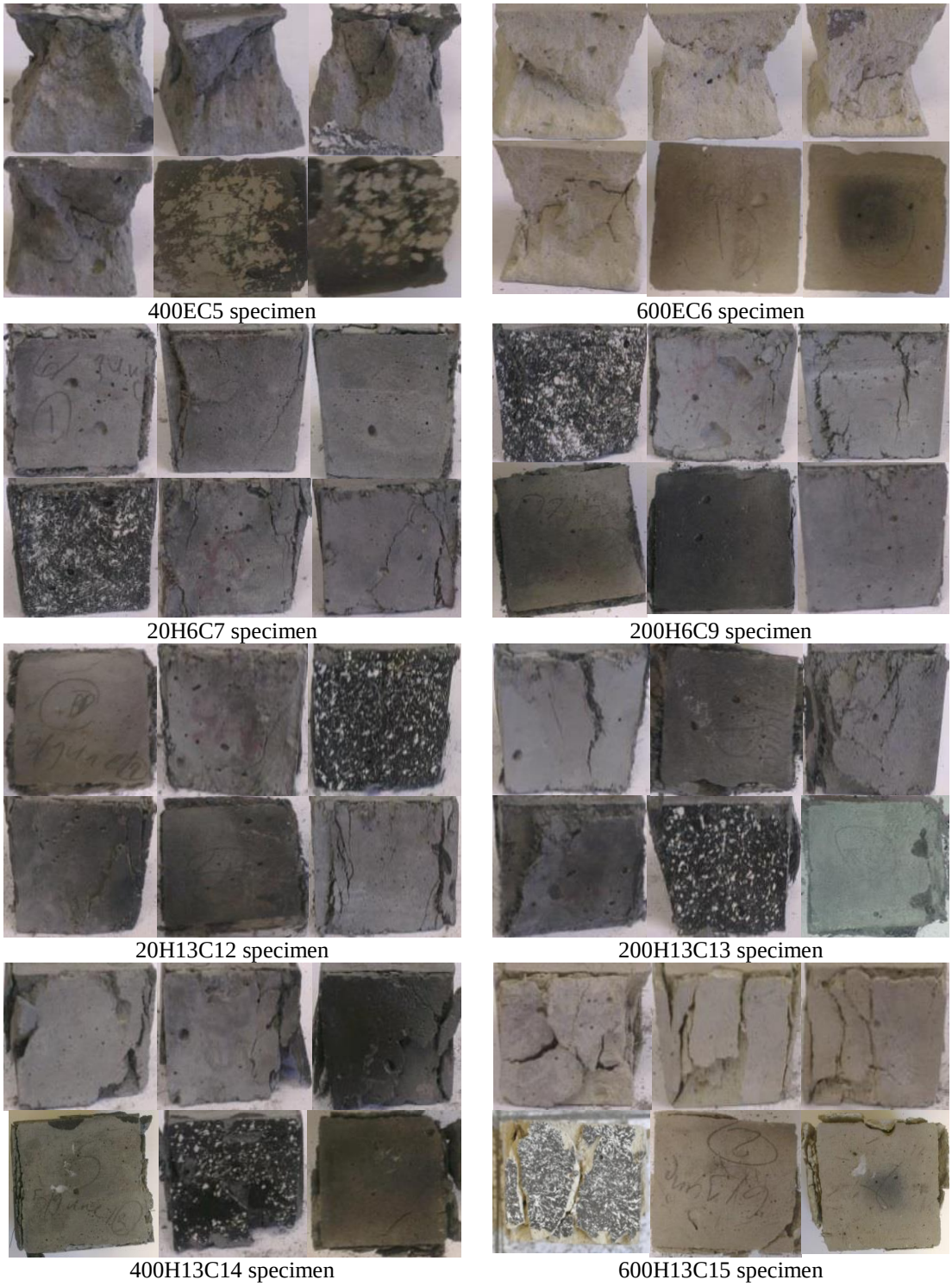

400EC5 specimen 600EC6 specimen

20H6C7 specimen 200H6C9 specimen

20H13C12 specimen 200H13C13 specimen

400H13C14 specimen 600H13C15 specimen

Figure 3.17.Failure crack patterns of 6 faces of cube specimens at compression test under different temperature

3.3.2 Bending test

Flexural tests were carried out as described in section 3.2.4. Figure 3.18 shows the results of the flexural test (in terms of load-deflection curves) for all samples at a rate of 1 mm/min. It observed that the ductility of ECC specimens (EB series), H6ECC specimens

(H6B series) and H13ECC specimens (E13B series) increased with increasing temperatures up to 100˚C and all specimens exhibited a strain hardening behaviour. By increasing temperature beyond 100 ˚C a strain softening behaviour was observed resulting in a sudden drop in the level of ductility exhibited by specimens. At 400 ˚C the E6B and E13B series specimens exhibited a brittle failure, whereas both H6B and H13B exhibited limited ductility and strain softening behaviour up to 600 ˚C. To compare the results of the bending tests (Figure 3.18) five parameters were considered: (i) the load carrying capacity (peak-load), (ii) maximum deflection (corresponding to peak load), (iii) the load at which the first crack was observed, (iv) the number of cracks developing along the central span of the specimen and (v) crack width developing along the central span of the specimen.

Figure 3.19a presents that the first crack in the specimens has a clear relation to the temperature to which they were subjected. The increase in temperature resulted in the development of cracking earlier in the loading process up to 100 ˚C (as a result the increase in temperature leads to a reduction in the load at which the first crack develops) up to 100 ˚C which is due to the reduction of toughness of ECC matrix. Where subjecting to temperatures beyond 100 ˚C the first crack load is almost constant for all series. It can be observed from Figure 3.19 b that the maximum load bearing capacity of specimens decreased with increasing the temperatures up to 100 ˚C, then it is constant for temperature up to 600 ˚C. The maximum load is related to the interaction between fibres and the ECC matrix which decreased due to the reduction of the modulus of elasticity of PVA fibre and the chemical bond between the PVA fibre and the ECC matrix. Both of these reductions (mentioned above) resulted in decreasing of load carrying capacity of specimens. Figure 3.19 c demonstrates the relation between ductility and temperatures. Increasing temperatures up to 100˚C results in enhancement of the ductility of ECC specimens (EB series). Then the ductility of the specimens decreases when subjected to temperature of 150°C and the behaviour of specimens changes to strain softening behaviour. In the EB series at 200 ˚C the specimens exhibit a brittle failure in the absence of PVA fibres which were burnt at this temperature. However, both H6B and H13B present the strain softening behaviour and some ductility up to 600°C due to the presence of steel fibres. The change of ductility of the specimens at different temperatures is related to two parameters (i) the number of cracks and (ii) the crack width developing in the central span. Figure 3.19 d indicates that the visible crack number reduced continuously

with increasing the temperatures up to 100 ˚C. Finally from 150˚C the behaviour of ECC and HECCs changed to strain softening and only one crack was observed in all series of specimens subjected to 150˚C and higher temperatures (Figure 3.20). Figure 3.19 e shows the crack width under different temperatures. For the EB series at 20°C the average crack width was 50μ in the central span while for the H6B and H13B series the average crack width was 40μ in the central span (Figure 3.22). Along the crack resulting in failure the PVA fibres pulled out of about 500μ (Figure 3.21). At 60°C the average crack width increased to 400μ (more than 6 times) for the EB specimens while for the H6B and H13B series the average crack width was about 70 μ. For all series the PVA fibres pull out about 3000 μ at the crack resulting in failure. It shound be mentioned that 60˚C is a glass transient temperature for PVA for which 80 percent of the modulus of elasticity of PVA fibres reduces. The reduction of the modulus of elasticity of PVA fibres increases the crack width in the EB series (Redon et al., 2001). However for both H6B and H13B series the steel fibre limited the crack width of specimens. At 100°C the average crack width for EB series was 750μ compared to 200μ for both H6B and H13B series specimens. At the crack resulting in failure the PVA fibres pull out about 5000 μ for all series. At 150°C only one crack (localized crack) was observed in all series and at the crack resulting in failure the PVA fibres pulled out up to 6000 μ. It is interesting to observe that at this temperature (150°C) the mode of failure exhibited by the specimens was associated with the pulling out (and not the fracturing) of the PVA fibres. However, for temperatures below 150°C failure of the specimen was associated with the rupture of the PVA fibres. It was noted that the diameter of the PVA fibres also was less than about half of that recorded at normal temperatures. At this temperature the PVA fibre loses its ability to bridge the cracks and therefore cannot transfer the tensile stressed developing normal to the plane of the crack. At 200°C fibres burned (the dark colour of fibre is presented in figure 3.21) and a brittle behavior was observed in the EB series. However both H6B and H13B present more ductile strain softening behaviour compared to the EB specimens. At 400°C the PVA fibres were not observed anymore on the only localized cracking (Figure 3.21) resulting in brittle behaviour in the EB series. However, in both H6B and H13B steel fires pulled out and ductile strain softening behaviour was observed. Finally, at 600 °C both H6B and H13B exhibited a strain softening behaviour. It is interesting to notice that both 6mm steel fibre in the H6B specimens and the 13 mm steel fibre in the H13B specimens ruptured, whereas at lower temperatures all steel fibres exhibited pull-out behaviour without rupture (Figure 3.21). In the case of the H6B specimens the 6 mm steel

fibres exhibited about 0.5mm pull-out prior to rapture compared to 13 mm steel fibres (included in the H13B specimens) which exhibited about 0.2mm pull-out prior to rapture (see Figure 3.23). The rapture of the steel fibres at 600°C can be attributed to yield strength of steel fibre which reduces about 60% at 600°C compared to that that at 20°C. Furthermore, the thermal expansion of the steel fibres (which have a thermal expansion coefficient two times higher than that of the ECC matrix) which results in an increase of the bond forming between the steel fibre and the surrounding ECC matrix. This increase in bond results in a reduction of the pull-out behaviour allowing the fibres reach their fracture tensile strength. When the length of steel fibre increases the anchorage length of fibre on either side of the plane of the crack increases resulting in higher resistance against pull-out behaviour.

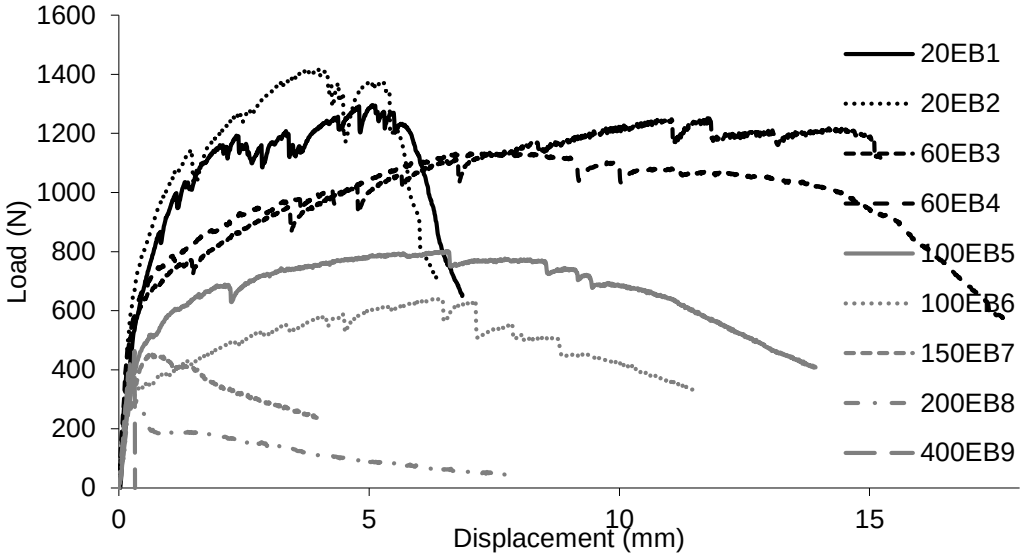

a)

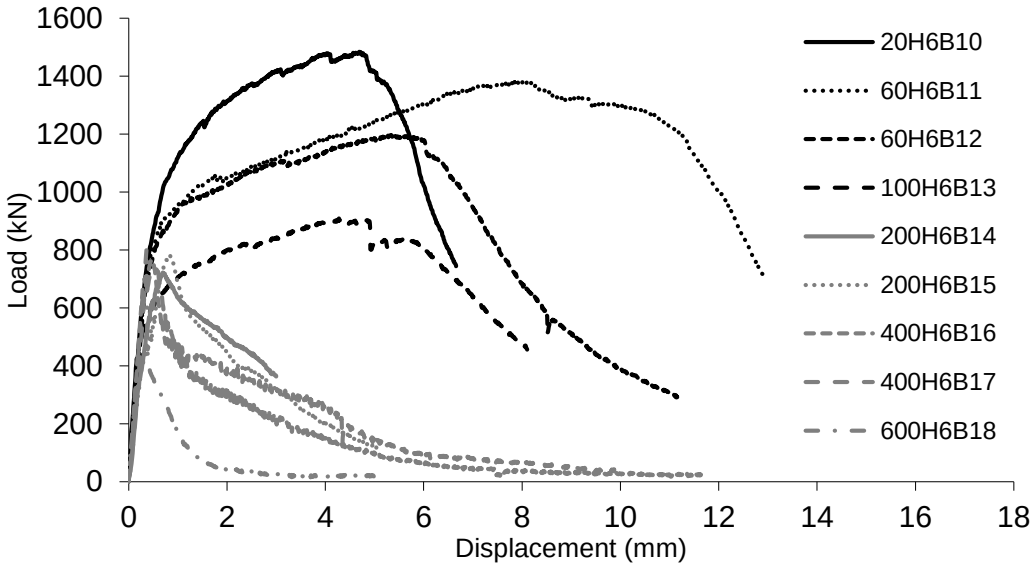

b)

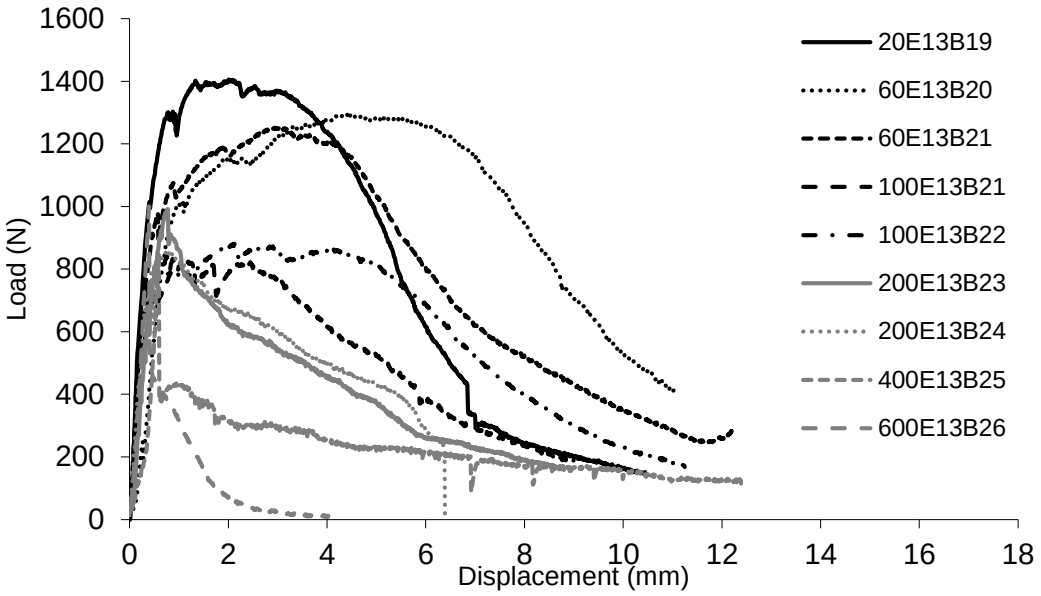

c)

Figure 3.18. Four-point bending load-deflection curves for a) EB series b) H6B series c) H13B series

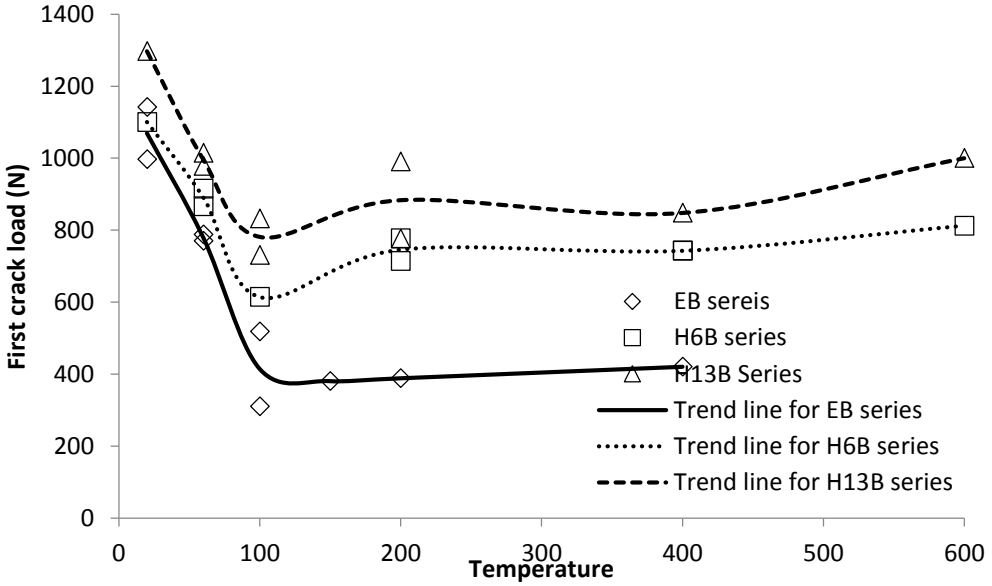

a)

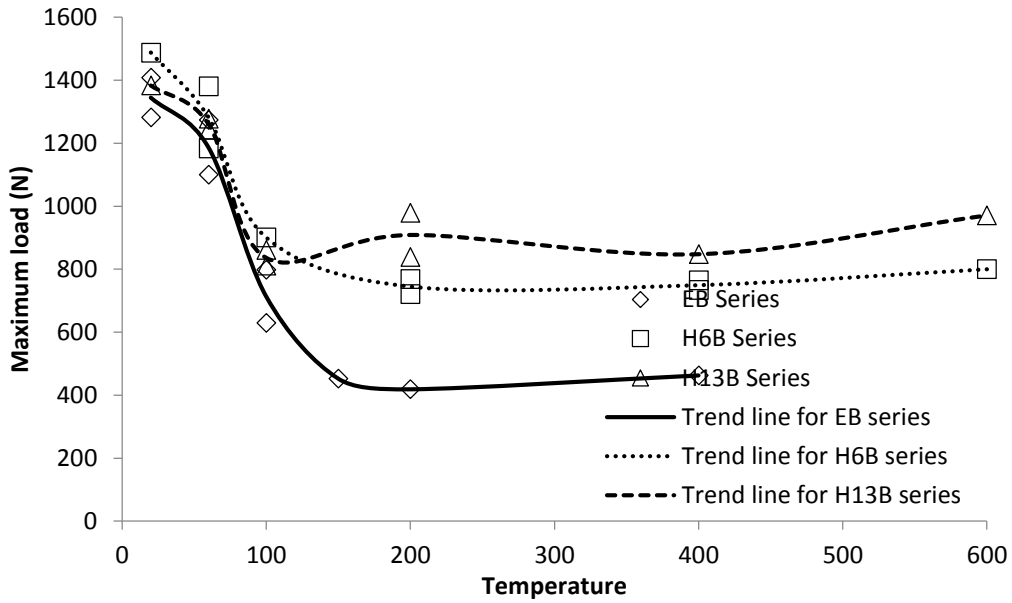
Maximum load (N)
Temperature
EB Series
H6B Series
H13B Series
Trend line for EB series
Trend line for H6B series
Trend line for H13B series

b)

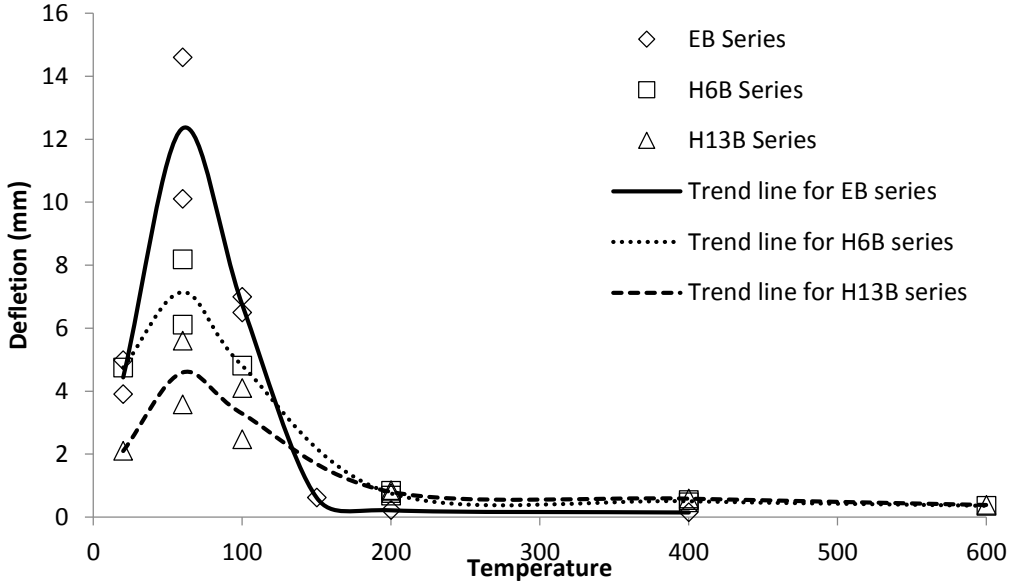
Defletion (mm)
Temperature
EB Series
H6B Series
H13B Series
Trend line for EB series
Trend line for H6B series
Trend line for H13B series

c)

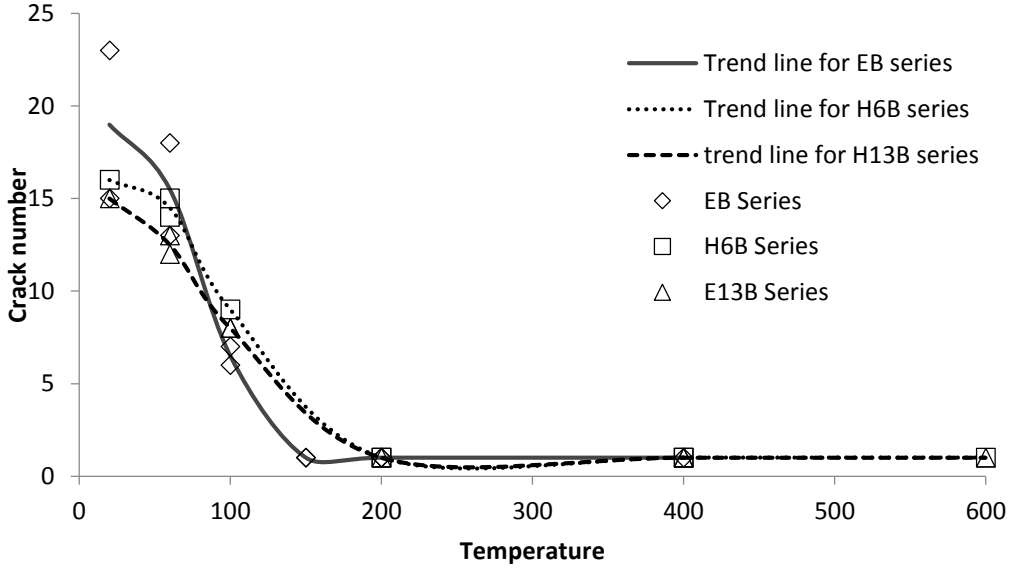
Crack number
Temperature
Trend line for EB series
Trend line for H6B series
trend line for H13B series
EB Series
H6B Series
E13B Series

d)

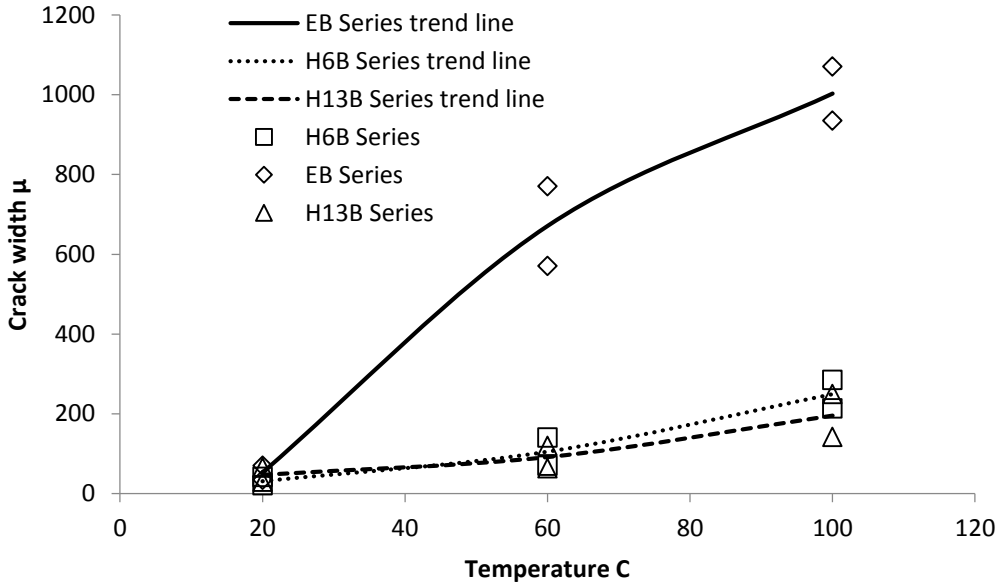

e)

Figure 3.19. Four-point bending test results for EB series under high temperature a) first crack load vs temperature curve b) maximum load capacity vs temperature curve c) maximum deflection vs temperature curve d) Visible crack number in the midspan vs temperature curve e) the crack width vs temperature curve

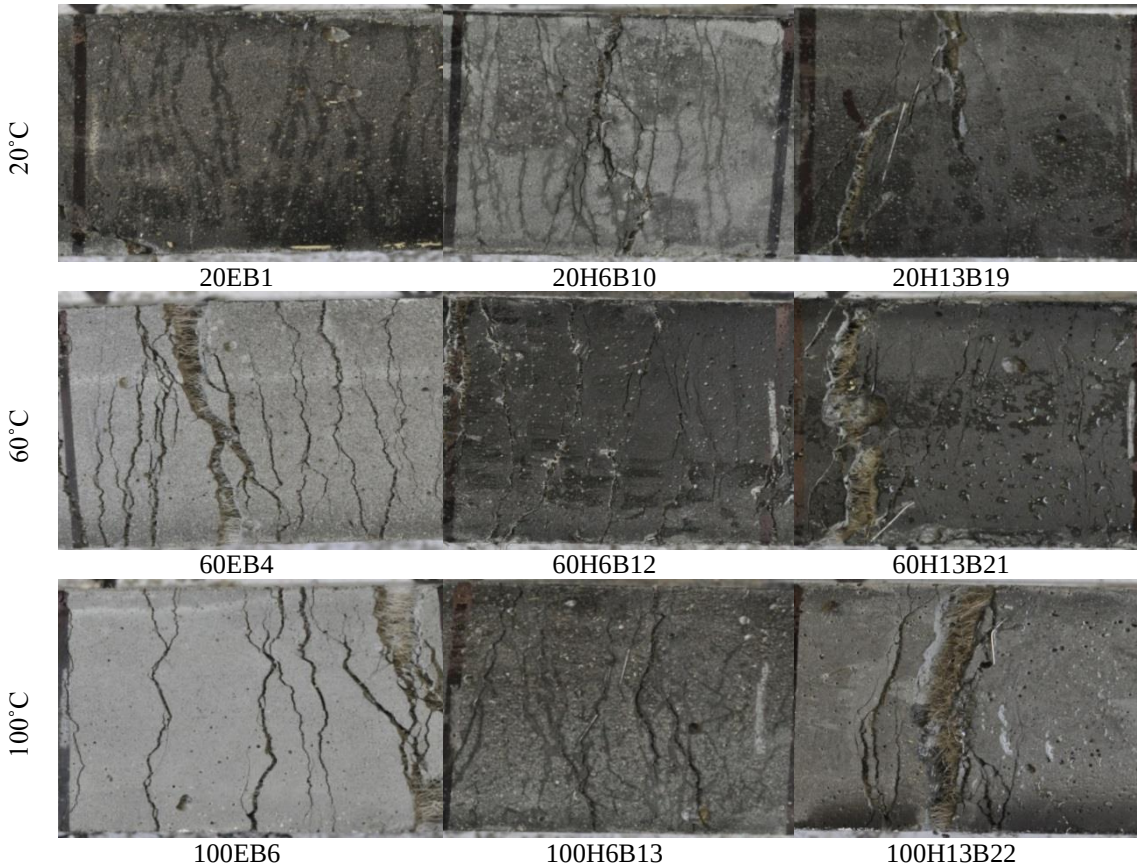

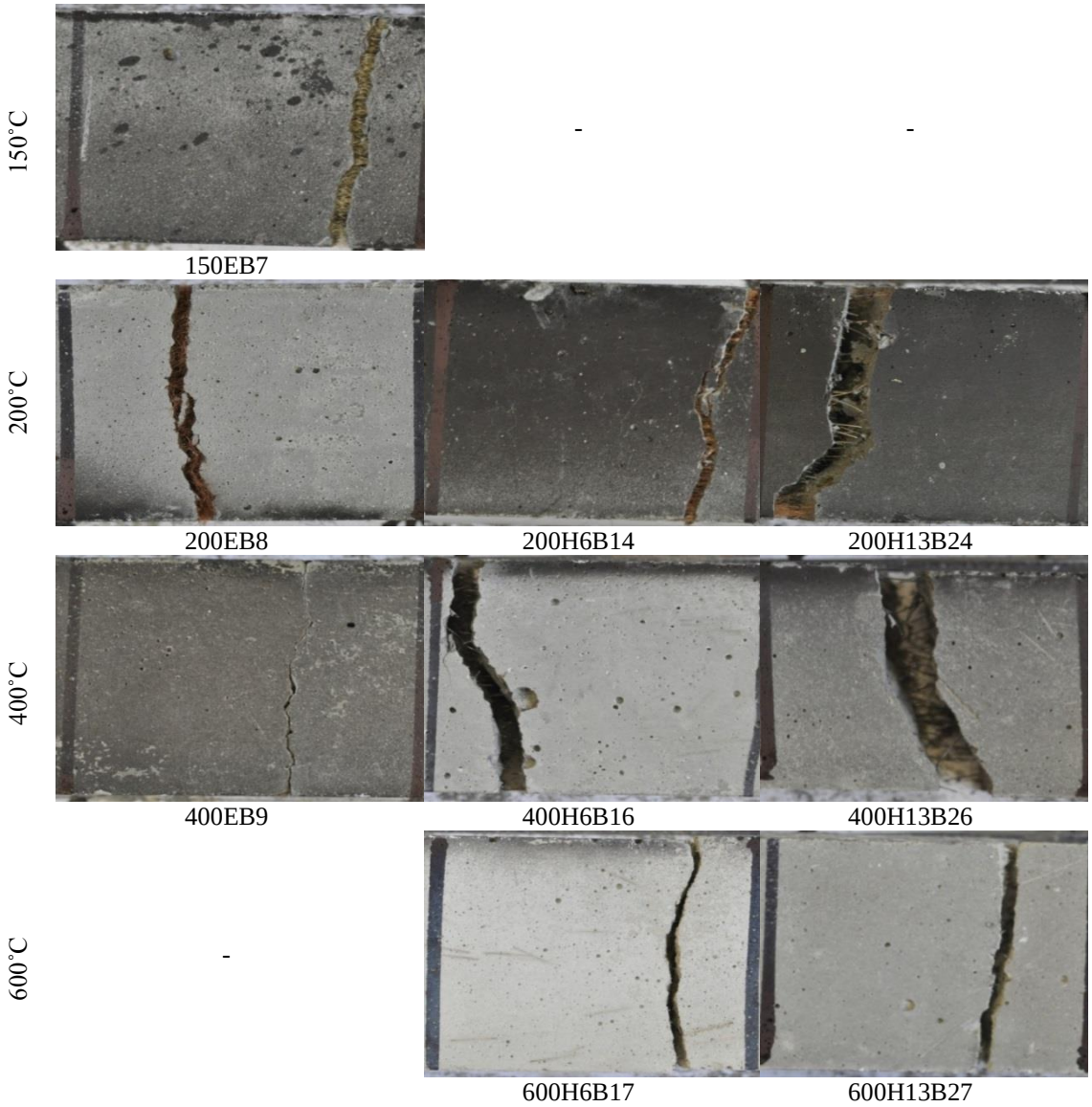

Figure 3.20. Failure crack patterns at bending test along 40mm of central span

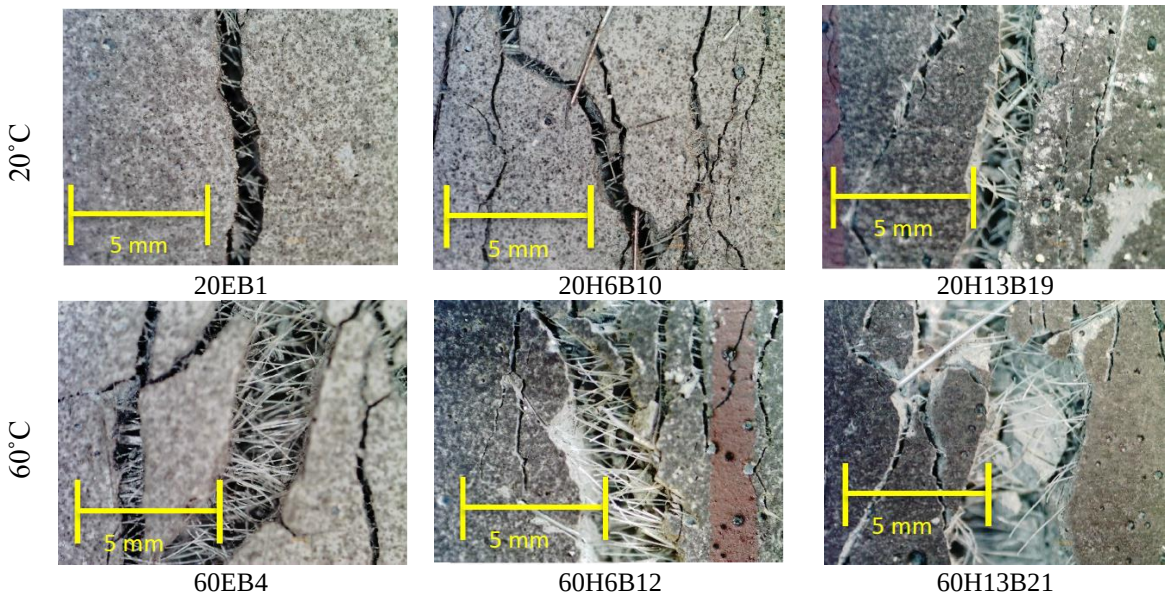

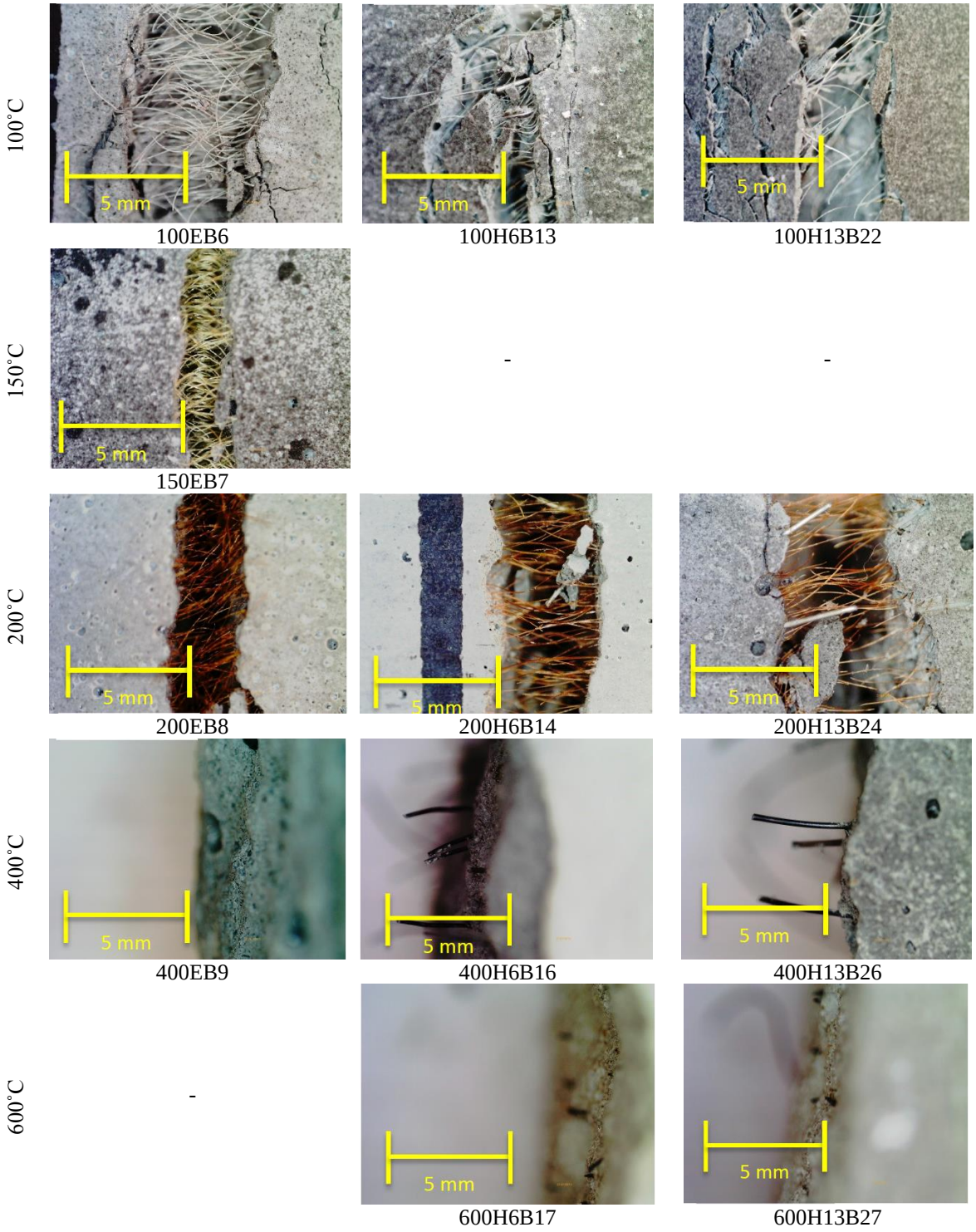

Figure 3.21. Local failure crack at bending test for specimens

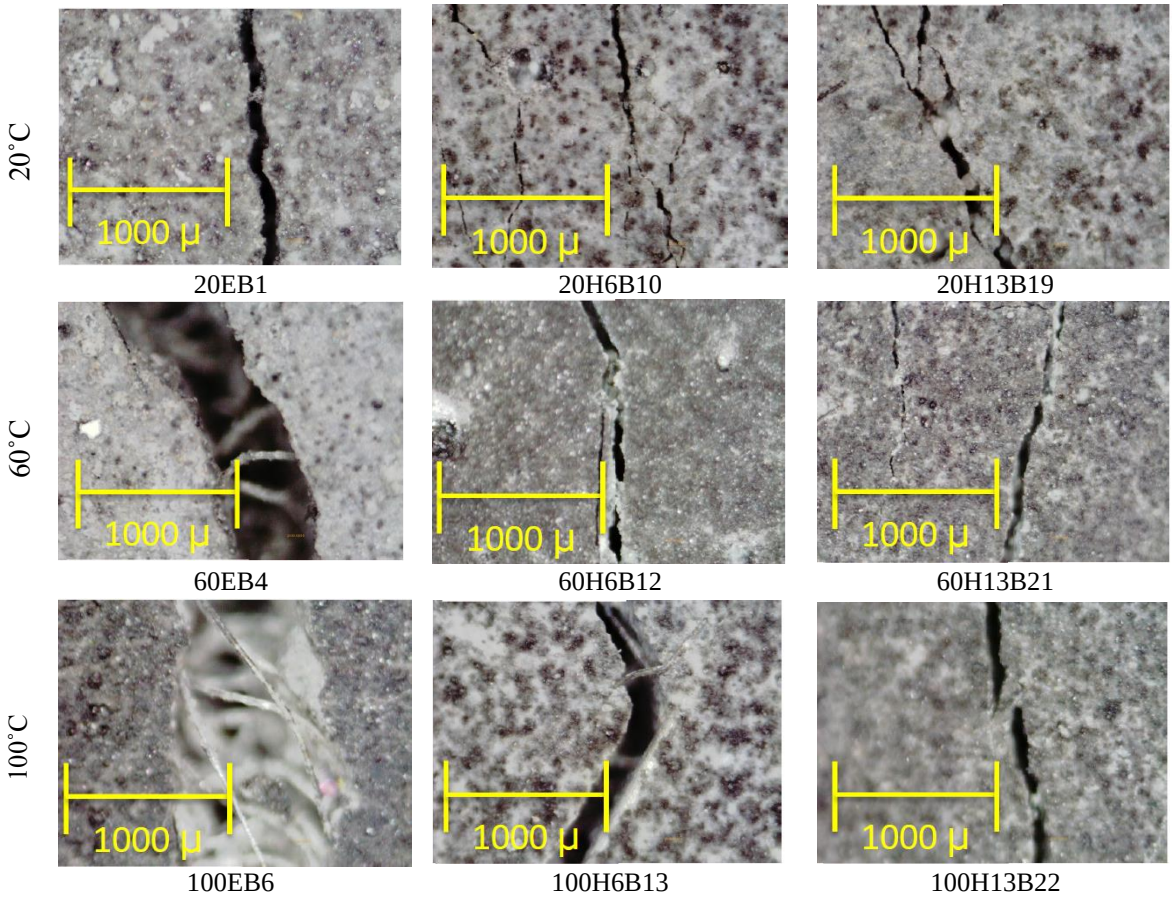

Figure 3.22. Typical crack width at bending test when multiple crack distribution happened in specimens

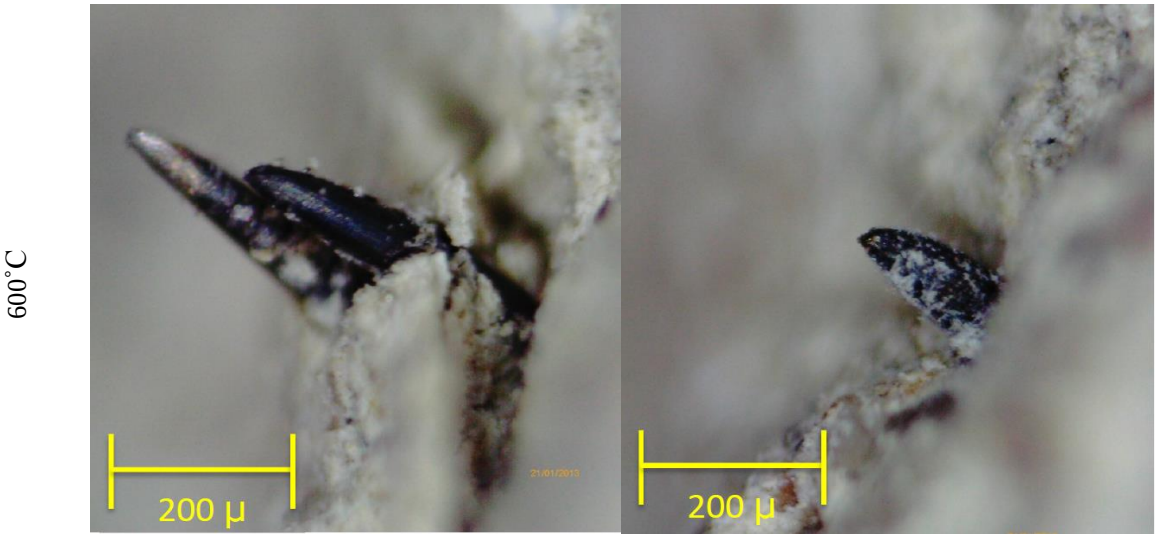

Figure 3.23. Typical steel fibres behaviour at bending test under 600 ˚C

3.4 Conclusions

In order to develop the ECC mixture through the use of materials available in the UK a series of compression, four-point bending and uniaxial tensile tests were carried out. After

finalising the ECC mixture a series of tests were conducted to establish the ECC material behaviour in tension and compression under different loading rates and temperatures. Based on the experimental investigation and the data obtained the following conclusions are drawn:

- The ECC mix proportions selected were a fly-ash-to-cement ratio of 1.8, a water/binder ratio of 0.28 and Fine silica sand to cement ratio of 0.6.

- The resulting ECC material under unixaial tension exhibited a strain hardening ductile behaviour with about 3.5% strain capacity under quasi-static load (1 mm/min). This ECC mixture can improve ductility of masonry walls under out-of-plane loads.

- At elevated loading rate (400 mm/min) the strain capacity of ECC decreased by 38% while the maximum load capacity increased by about 36% compared to their counterparts established under the lower loading rate (1mm/min) considered. This proves that the material behaviour of ECC is dependent of the strain-rate. It is observed under increasing values of loading rate the strain capacity reduces but the strength increases under increasing strain rates.

- A comparison between behaviour of ECC and HECCs under uniaxial tensile tests reveals that the steel fibres can increase the tensile strength of specimens (a 13% and 22% enhancement for H6ECC and H13EC compared to ECC specimens respectively) while decrease the ductility of specimens (a 16% and 40% reduction for H6ECC and H13EC compared to ECC specimens respectively).

- It is observed that under elevated temperatures up to 600 ˚C the compression behaviour of ECC and HECCs are similar therefore steel fibre would not significantly affect the compressive behaviour of HECCs. At 200˚C the compression strength of specimens do not show important change, whereas at 400 ˚C and 600 ˚C a 14% and 25% reduction was observed respectively in the value of the compression strength of specimens.

- Considering the weight of the debris produced during testing under uniaxial compression (under 5% compression strain) reveals that the steel fibre can increase the integrity of the specimens. At 600 ˚C only 7% debris produced by HECCs

specimens compare to 30% in the ECC specimens. However, it found that the length of steel fibre is not important as both H6ECC and H13ECC produced same amount of debris.

- Due to the use of PVA fibre in ECC and HECC, any spalling was not observed in specimens subjected to elevated temperatures up to 600 ˚C during compression and bending tests.

- It is observed at flexural tests under elevated temperatures of up to 100˚C the ductility of ECC, H6ECC and H13 ECC increased, namely 300%, 150% and 200% at 60˚C and 150%, 20% and 150% at 100 ˚C respectively compared to their counterparts results under 20 ˚C. It was documented that enhancing the ductility of ECC and HECCs up to 100˚C is related to the increasing the crack width in the specimens due to the reduction of the modulus of elasticity of the PVA fibres. However, further increasing the temperature results in brittle failure of the ECC specimens and a change in the behaviour of HECC to strain softening with limited ductility.

- It is observed under flexural tests at 60 ˚C and 100 ˚C steel fibres can limit the crack width exhibited by HECCs specimens about 500% compared to ECC counterpart specimens. However, steel fibres do not affect the number of cracks in HECCs specimens compared to ECC. Any meaningful difference was not observed between crack width of H6ECC and H13ECC subjected to high temperatures up to 100 ˚C.

- At flexural tests the load bearing capacity of all specimens continuously decreased by increasing the temperature up to 100 ˚C and was constant under further temperature. However, the load bearing capacity of HECCs was 100% more than ECC subjected to 100 ˚C to 600 ˚C.

- At flexural tests it was observed at 150 ˚C the failure mode of PVA fibres changed from rupture to pulling out resulting in the change of behaviour of ECC and HECC from strain hardening to strain softening behaviour. In the case of steel fibres at 600 ˚C the steel fibres mode of failure changed from pulling out to rupture in the H6ECC and H13ECC specimens.

- A comparison between H6ECC and H13ECC behaviour under tensile test reveals that the ductility of H6ECC is about 20% more than H13ECC. The behaviour of H6ECC under flexural tests also exhibited 100% more ductility under 20 ˚C, 60 ˚C and 100 ˚C. It can be concluded that shorter steel fibre (6 mm compare to 13 mm) provides better ductility under different temperatures.

3.5 Reference

BUSHLAIBI, A. H. & ALSHAMSI, A. M. 2002. Efficiency of curing on partially exposed high-strength concrete in hot climate. *Cement and concrete research,* 32**,** 949-953.

COOPER, G. J., MAYNARD, R. L., CROSS, N. L. & HILL, J. F. 1983. Casualties from terrorist bombings. *Journal of Trauma and Acute Care Surgery,* 23**,** 955-967.

FREIWALD, D. 1972. Approximate Blast Wave Theory and Experimental Data for Shock Trajectories in Linear Explosive-Driven Shock Tubes. *Journal of Applied Physics,* 43**,** 2224-2226.

LI, V. C. & LEUNG, C. K. 1992. Steady-state and multiple cracking of short random fiber composites. *Journal of Engineering Mechanics,* 118**,** 2246-2264.

REDON, C., LI, V. C., WU, C., HOSHIRO, H., SAITO, T. & OGAWA, A. 2001. Measuring and modifying interface properties of PVA fibers in ECC matrix. *Journal of Materials in Civil Engineering,* 13**,** 399-406.

TABER, K. H., WARDEN, D. L. & HURLEY, R. A. 2006. Blast-related traumatic brain injury: what is known? *The Journal of neuropsychiatry and clinical neurosciences,* 18**,** 141-145.

WIGHTMAN, J. M. & GLADISH, S. L. 2001. Explosions and blast injuries. *Annals of emergency medicine,* 37**,** 664-678.

YANG, E.-H., YANG, Y. & LI, V. C. 2007. Use of high volumes of fly ash to improve ECC mechanical properties and material greenness. *ACI Materials Journal,* 104.

Chapter 4 Assessing the behaviour of masonry beam-like specimens under static loading

4.1 Introduction

This chapter provides a detailed description of the results of an experimental programme designed to investigate the behaviour of masonry beam-like specimens (essentially consisting of a stock of bricks connected with mortar joints and strengthened with a layer of ECC as shown later on in Figure 4.14) under static and elevated loading rates. Initially, three series of tests were conducted to establish the fundamental mechanical properties of the individual materials used in four-point bending tests used (brick, mortar ECC) as well as their interaction. These include compression tests to obtain the compressive strength of brick and mortar, triplet shear tests to determine the shear strength of the brick-mortar and brick-ECC interfaces and crossed brick couplet tests to obtain the bond strength of the brick-mortar. Test results are used to establish the input parameters necessary for the analytical study presented in section 4.4 and to calibrate the parameters in the numerical study presented in Chapter 6. 15 masonry beam-like specimens (consisting of a stack of 10 bricks) are then tested under four-point bending to assess the ability of a thin ECC layer to enhance their out-of-plane performance. The ECC layer was fully or partially bonded to the masonry specimens and the loading rates were 1mm/min and 200mm/min. Tables 4.1 and 4.2 provide a summary of the experimental programme.

Table 4.1: Tests for establishment material properties

Type of test	ID	Specimen type	Relevant standard	Number of tests
Compression tests	CB	Brick	ASTM C67-14	4
	CM	Mortar	ASTM C109	4
	CBM	Brickwork	ASTM C1314-14	5
Triplet shear tests	SBM	Brick/mortar triplet	BS EN 1052-3:2002	5
	SBE	Brick/ECC triplet	BS EN 1052-3:2002	4
Crossed brick tensile tests	TBM	Brick/mortar couplet	ASTM C952-12	5

Note: For ID, see Figure 4.1(a).

Table 4.2: Four-point bending tests

Specimen type	ID	Loading rate (mm/min)	Number of tests
Brickwork beam	SN	1	2
	EN	200	2
Brickwork beam retrofitted with an ECC layer fully bonded to the beam soffit	SF	1	3
	EF	200	3
Brickwork beam retrofitted with an ECC layer partially bonded to the beam soffit	SP	1	2
	EP	200	3

Note: For ID, see Figure 4.1(b).

Figure 4.1 shows the labelling system assigned to the different types of specimens presented in Tables 4.1 and 4.2. The first letter in Figure 4.1(a) refers to the type of test (C: compression, S: shear, T: tensile tests), the second letter to type of material (B: brick, M: mortar), the third letter to the material between two adjacent interfaces (M: Mortar, E: ECC) and the number at the end to specimen number. The first and second letters shown in Figure 4(b) refer to the rate of loading (S: 1 mm/min, E: 200 mm/min) and bond arrangement (F: Full bond, P: Partial bond, N: No bond (or no ECC)). The number at the end refers to the specimen number.

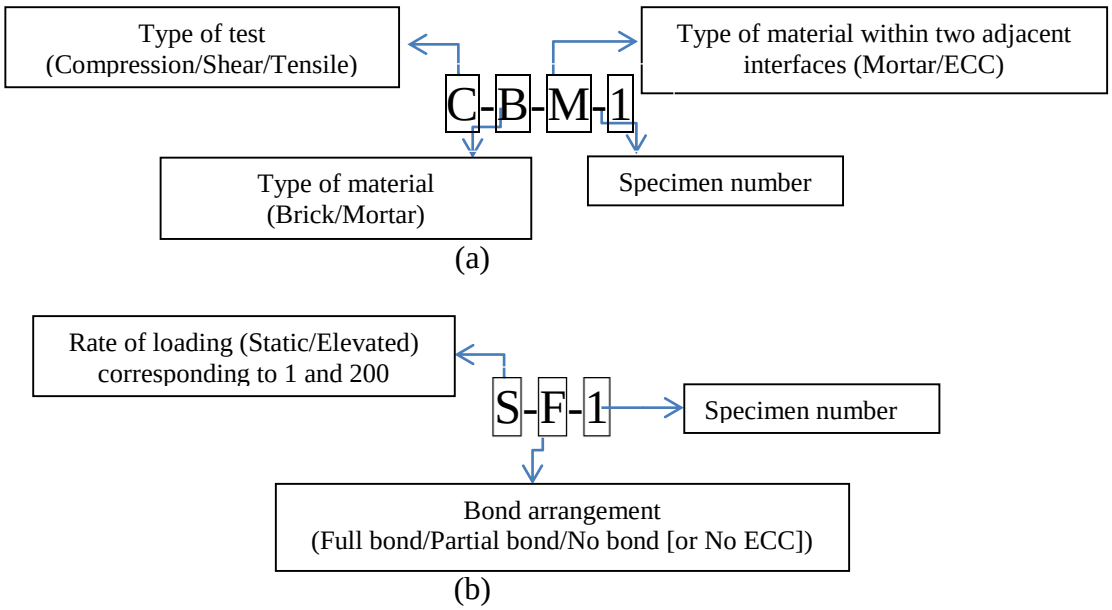

Figure 4.1. Labelling system used in (a) Part 1 and (b) Part 2 test programme.

4.2 Part 1: Material tests

A series of tests are initially conducted to determine the mechanical properties of the individual materials used to produce the specimens subjected to four-point bending testing and their interaction. These tests include: (i) compression tests on the brick, mortar and brickwork specimens (see figure 4.2), (ii) shear test on brick-mortar and brick-ECC specimens (see figure 4.7) and (iii) tensile test on the brick-mortar couplet (see figure 4.12).

4.2.1 Compression tests

4.2.1.1 Compression tests conducted on brick units

Four Class B Engineering solid bricks (BS EN 771-1) with dimensions of 100×102×65 mm were tested in compression in accordance with ASTM C67-14. The main purpose of the tests was to determine the compressive strength and modulus of elasticity of the brick units. Prior to testing, all bricks were dried in an oven at 110ºC for 24 hours and then were cooled down to the room temperature for four hours. Each brick was then capped with 3mm thick fast hardening cement. Once the cement had set (about 30 minutes), the brick was positioned in a 3000kN Avery-Denison testing machine (Figure 3.3), with the bed (100×102 mm) surface aligned to the direction of loading. Two Linear Variable Displacement Transducers (LVDTs) were placed at each side of the brick to measure the relative displacements of the top and bottom loading plates. Loading was carried out in a load-controlled mode at a rate of 200 kN/min.

Figure 4.2 shows the stress-strain curves for the four specimens. The brick unit exhibited a linear behaviour up to 60Mpa and high strength followed by a brittle and sudden failure mode under compressive load. The average compressive strength of the bricks was found to be 60 MPa with a coefficient of variation (COV) 5.1%, whereas the average modulus of elasticity was found to be 35 GPa with COV = 4.4%.

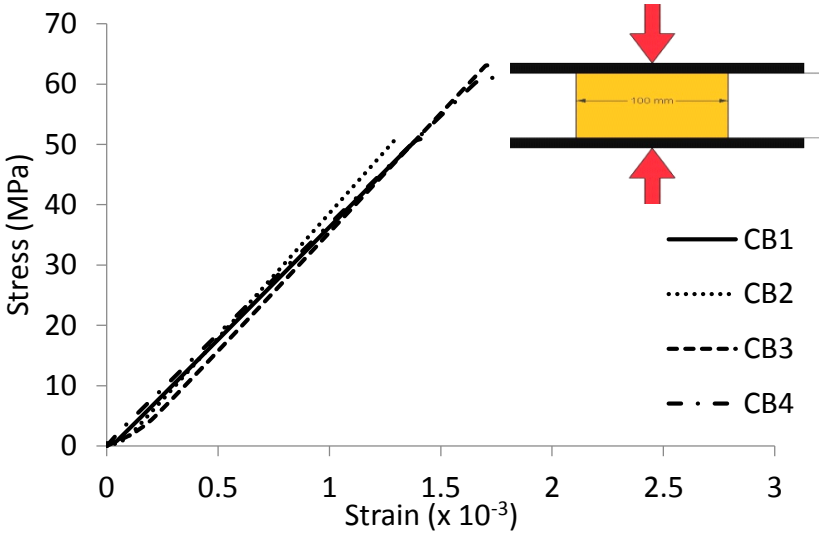

Figure 4.2. Compressive stress-strain curves for the engineering bricks

4.2.1.2 Compression tests on mortar

M12 mortar (BS EN 998-2:2010) specimens were made with CEM I 52.5N Portland cement and a fine silica sand of mean particle size 120 μm. The sand-to-cement ratio was kept constant at 3 and the water-to-cement ratio at 0.85 (both by mass).

Five mortar cylinders were tested in accordance with ASTM C109. The mortar was mixed using a ten litter Hobart planetary motion mixer and casted in the mounds with a diameter of 300mm x 150mm. After 24 hours, the specimens were demoulded and then cured for 28 days in a water tank. The same preparation, testing machine and instrumentation to those described in Section 4.2.1.1 were used. Loading was carried out in a load controlled mode at a rate of 15 MPa/min.

Figure 4.3 shows the stress-strain curves for the five mortar cubes. Specimens had essentially linear behavior followed by sudden brittle failure. The mean compressive strength of the mortar was found to be 22 MPa with COV= 6.4%, whereas the average modulus of elasticity was 11 GPa with COV=4.3%.

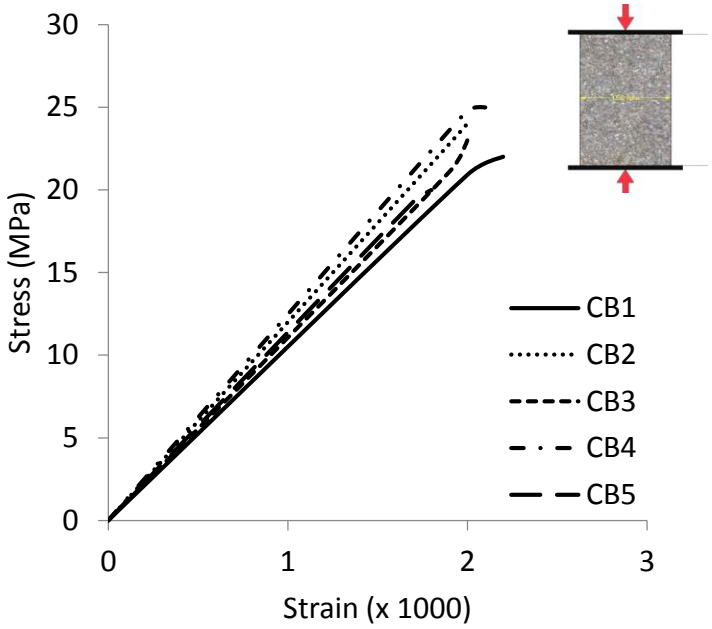

Figure 4.3. Compressive stress-strain curves for the mortar M12

4.2.1.3 Compression tests of masonry specimens

Five masonry specimens with dimensions of 102×210×275 mm were tested in compression in accordance with ASTM C1314-14. The brickwork comprised of four bricks and three 5mm thick mortar joints and they were all produced from the same batch (Figure 4.4). All bricks were firstly submerged in water for 24 hours and their surface was then dried off prior to fabrication of the specimens. The specimens were then covered with damp hessian and plastic sheets for 28 days.

Prior to testing the top face of the specimen was capped in accordance to ASTM C1552 using a 3mm thick layer of fast-hardening cement. Two LVDTs were mounted at each side of the specimen with a gauge length of 210 mm. Figure 4.4a and b present the dimensions of the specimen and test setup employed respectively. The tests were carried out using a 3000kN Avery-Denison testing machine under a loading rate of 150 kN/min.

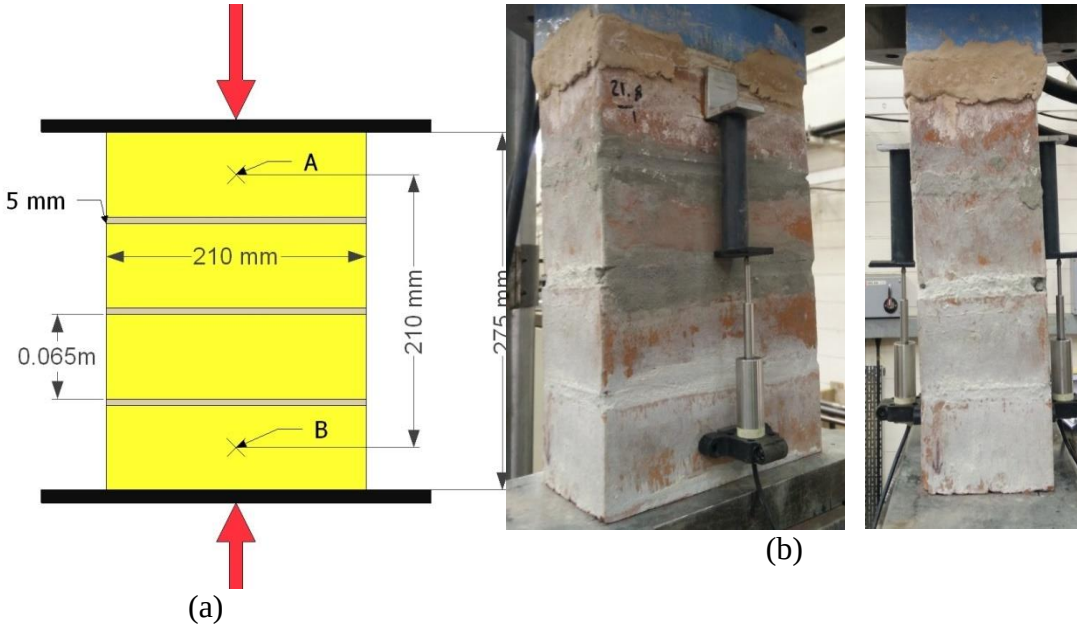

Figure 4.4. Brickwork compression test: (a) dimensions of specimen, (b) test setup

The stress-strain curves presented in Figure 4.5 reveal that the specimens considered exhibited linear behaviour followed by a brittle failure once the peak load was attained. During testing, it was observed that vertical cracks developed before complete or partial face delamination (as indicated in ASTM C1314-14) occurred. The specimens finally failed in a very brittle manner (see Figure 4.6 for the state of the specimens after failure). The mean compression strength of the masonry was 27 MPa with COV= 23.4% and the mean modulus of elasticity was 16 GPa with COV= 15.7%.

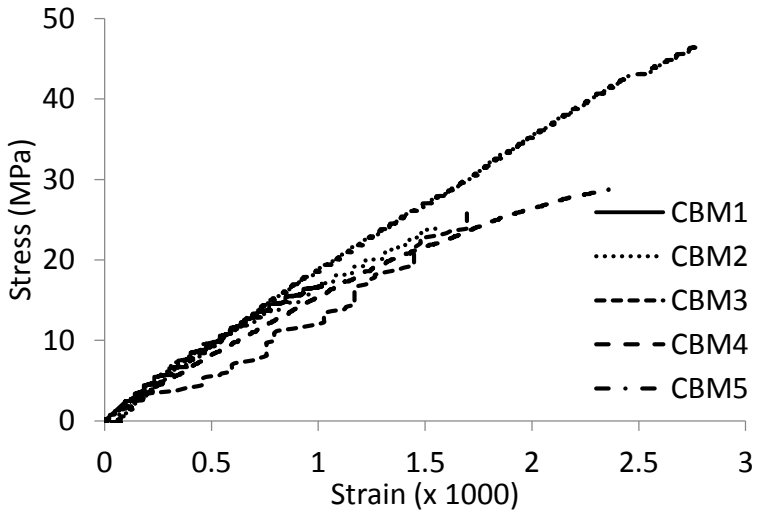

Figure 4.5. Compressive stress-strain curves for the masonry brickworks

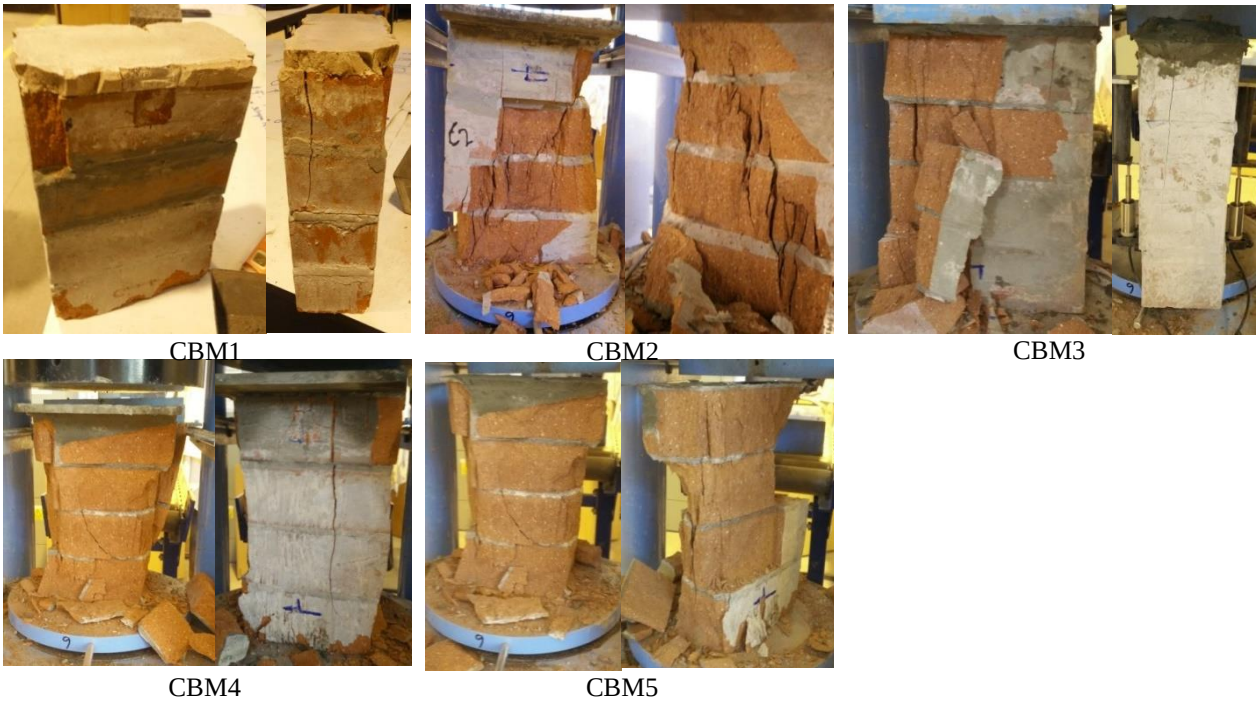

Figure 4.6.Failure modes exhibited by the masonry prisms

4.2.2 Triplet shear tests

Five brick/mortar and four brick/ECC triplets were tested to BS EN 1052-3:2002. The brick/mortar (SBM) triplets comprised three bricks and two 5mm thick mortar sandwiched between two bed (102 x 210 mm) surfaces. The brick/ECC (SBE) triplets had the same number of bricks and joints, but with the stretcher (65 x 210 mm) surface of the bricks being bonded, replicating the actual condition of part 2 tests presented in the second half of this chapter. The thickness of the ECC joint was made to be 15mm. The same test preparation and curing condition as those described in Section 4.2.1.2 were used.

Figure 4.7 shows the details of the triplet specimens and test setup used to carry out the shear tests. The tests were carried out using a 500kN INSTRON testing machine at a crosshead rate of 0.2 mm/min. The load was applied to the middle brick at two points at a distance of approximately 14 mm from the edge of the brick. The two outer bricks were also supported at the same distance from the edge of the joint. Three 12 mm thick steel plates with plan dimensions of 65×100 mm were placed on the contact point of the brick, in order to distribute the load uniformly to the brick. Four 12 mm steel bars were also placed both at load and support points. Two LVDTs were placed at each side of the specimen to measure the vertical displacement.

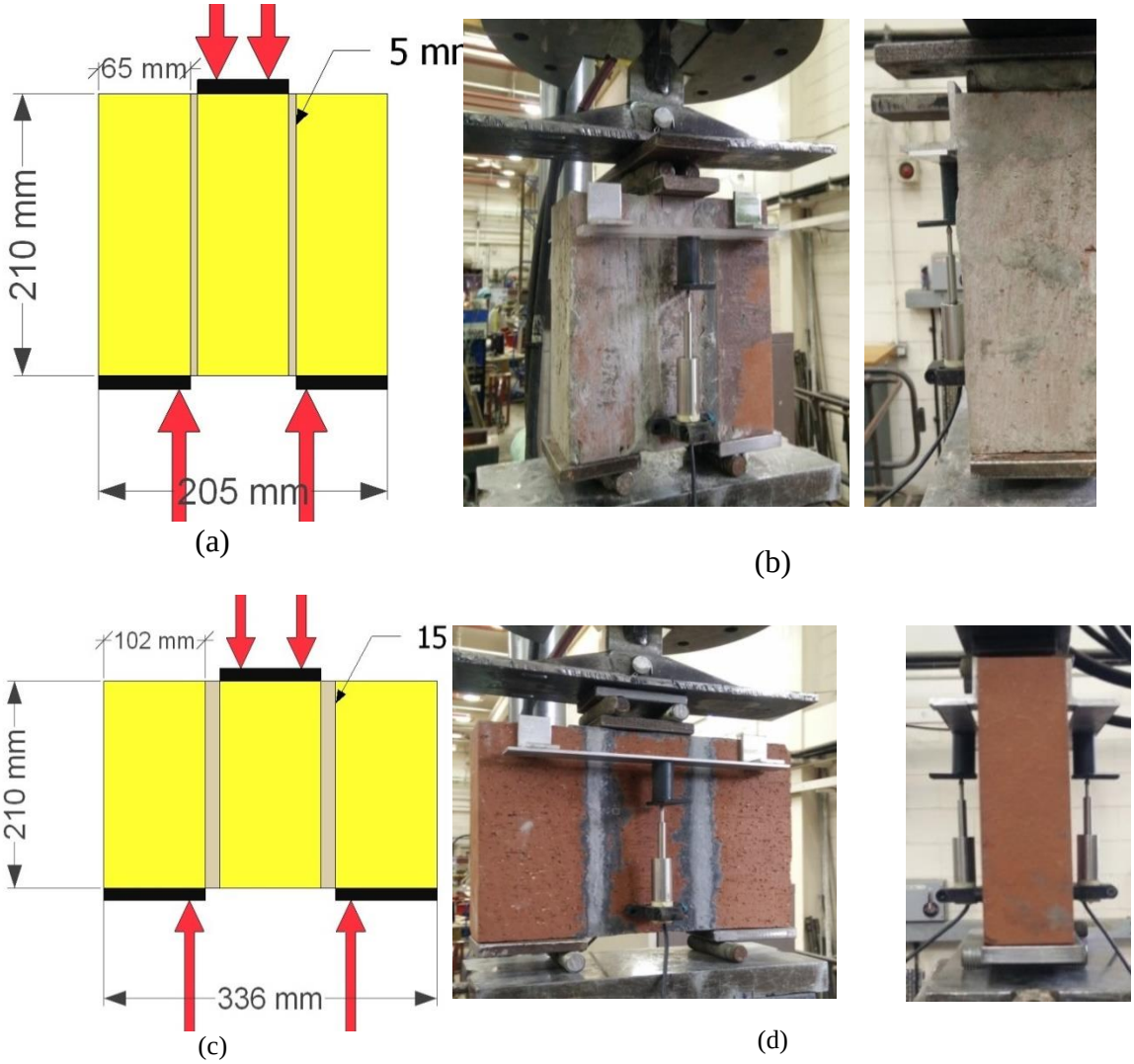

Figure 4.7. Triplet shear test: (a) dimensions of SBM specimen, (b) test setup for SBM specimens, (c) dimensions of SBE specimens, (d) test setup for SBE specimens

Figure 4.8 shows the stress-strain curves for the brick/mortar (SBM) triplets. Specimens presented a uniform and linear shear behavior and sudden failure. The mean shear strength was found to be 0.68 MPa with COV= 19.7%. Figure 4.9 shows the state of the specimens after failure. As can be seen, failure happened only in the brick-mortar interface on one face according to BS EN 1052-3:2002.

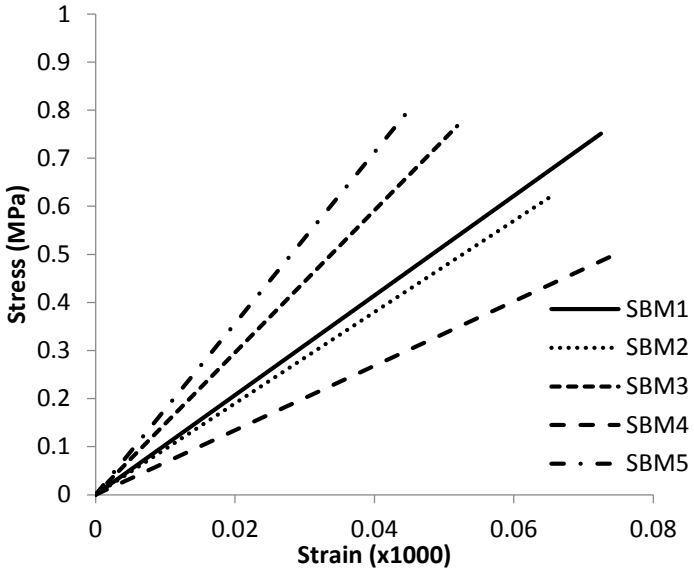

Figure 4.8. Shear stress-strain curves for the SBM specimens

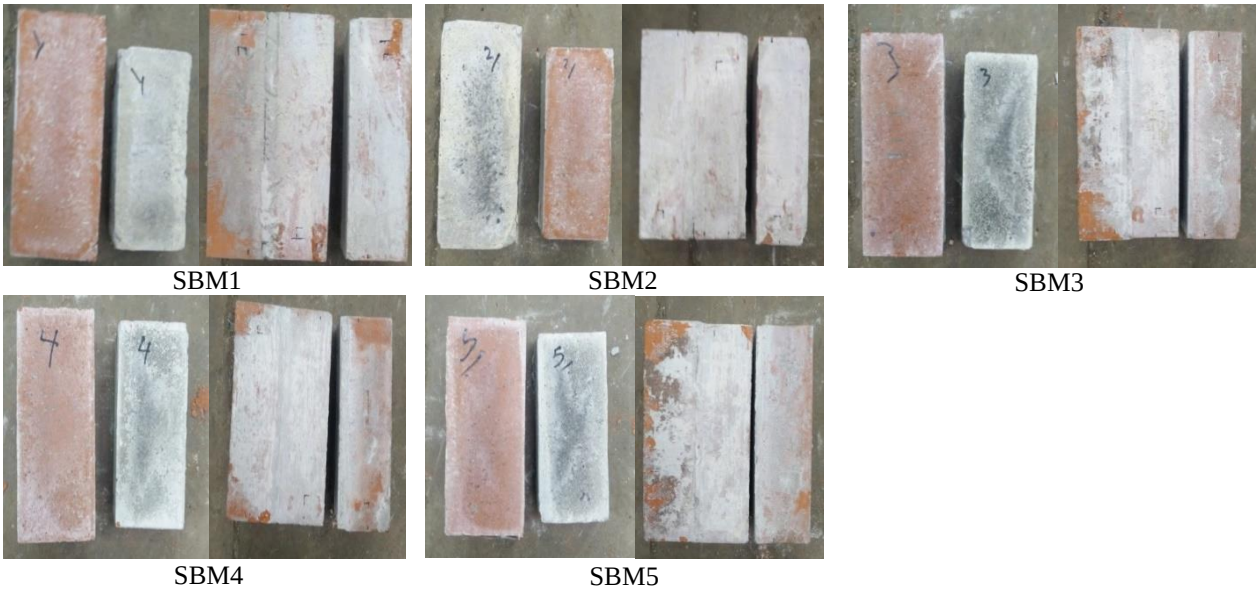

Figure 4.9. SBM specimens at failure under shear load

Figure 4.10 shows the stress-strain curves for the brick/ECC (SBE) triplets. Specimens presented a uniform and linear shear behavior and sudden failure. The mean shear strength was found to be 1.13 MPa with COV= 14%. Figure 4.11 shows the state of the specimens after failure. Most of the specimens' failure happened in the brick-mortar interface on one face according to BS EN 1052-3:2002. However, the SBE2 specimen's failure happened at the middle brick.

Considering that in a masonry wall the top and bottom face (vertical to the wall surface) of the brick is in contact with mortar whereas the side faces of the bricks (parallel to the facade of the wall) are in contact with ECC, the arrangement/configuration of the SBM

and SBE specimens is different (see Figures 4.9 and 4.11). More specifically, the specimen SBM tests were executed on the top sides of brick faces (see Figure 4.9) whereas the SBE tests were conducted on the front side faces of brick (see Figure 4.11). The results obtained show that the mean shear strength of the brick/ECC interface is approximately twice that of the brick/mortar (1.31 vs 0.68 MPa). The main reasons which explain the higher shear strength of SBE specimens are:

1- Fresh ECC is a self-compact and highly workable mortar while M12 mortar is not self-compact mortar. Therefore fresh ECC could fill the bricks gap better than mortar.

2- The mix proportion of ECC involved less water to cementations material rather than M12 mortar. The water to binder (composition of cement and fly ash) ratio in ECC was 0.28. However the water to cement ration of M12 mortar was 0.85 which is three times higher than ECC.

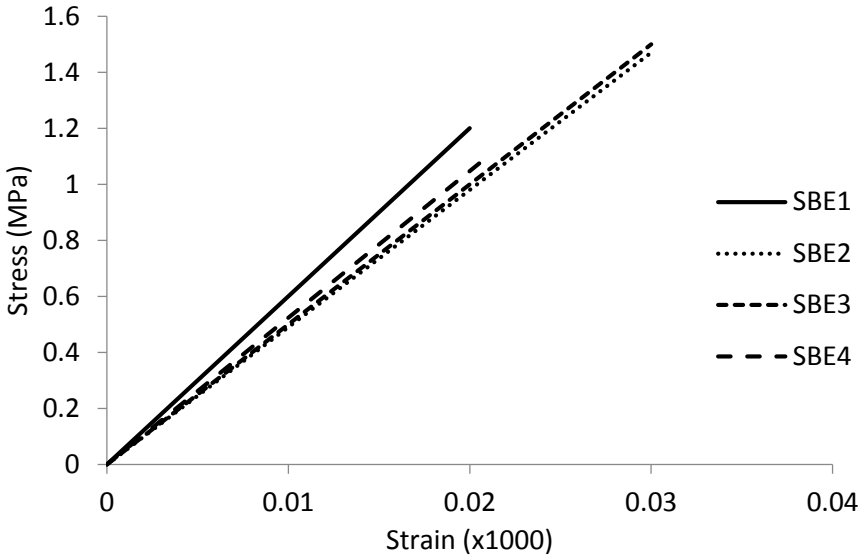

Figure 4.10. Shear stress-strain curves for the SBE specimens

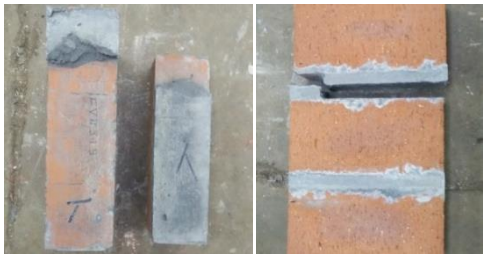

SBE1

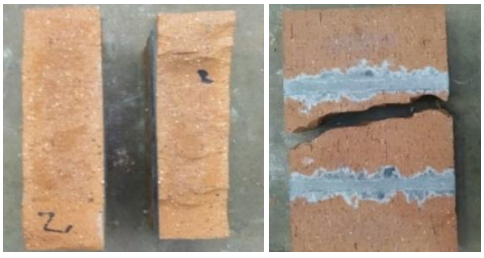

SBE2

SBE3 SBE4

Figure 4.11. SBE specimens at failure under shear load

4.2.3 Crossed brick couplet tests

Five crossed bricks couplet tests were carried out to obtain the bond strength of brick/mortar interface in accordance to ASTM C952-12. Each couplet was joined with an approximately 5 mm thick mortar which was flush with the sides of the bottom brick. Figure 4.12 shows the details of specimens and test setup used to carry out the couplet tests. The same test preparation and curing condition to those described in Section 4.2.1.2 were used.

Each couplet was supported at three points using two M20 steel bolts placed at one side of the brick and one M20 bolt placed at the other side of the brick. The same bolt arrangement was used for the loading points. To minimize eccentricity, three steel ball bearings were placed on the top of loading bolts underneath the spreader plate. The tests were performed using a 500kN INSTRON testing machine at a crosshead displacement rate of 1 mm/min.

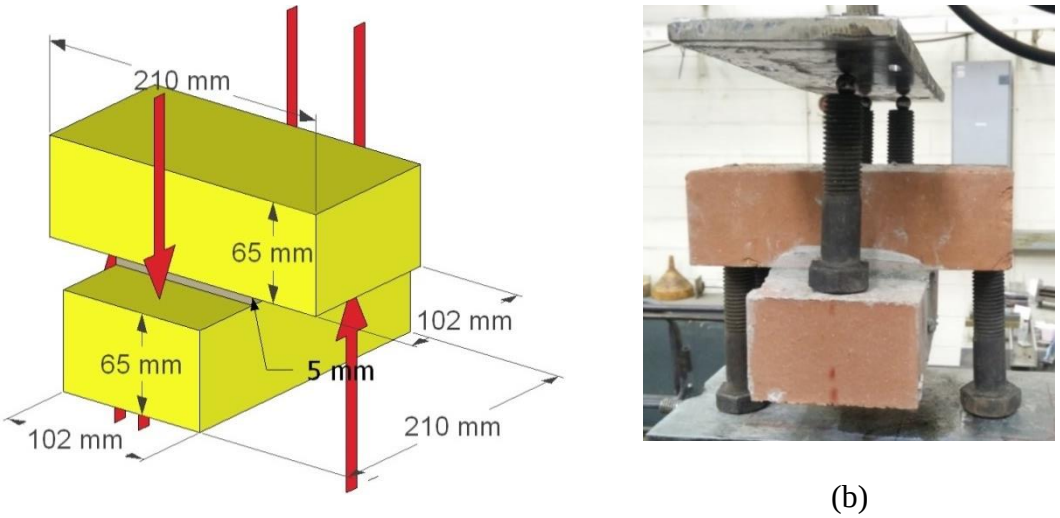

(a) (b)

Figure 4.12. Crossed brick couplet tests: (a) dimensions of specimen, (b) test setup

Table 4.3 presents the results of the couplet tests. The average tensile strength of masonry prism is 0.4 Mpa with COV 4.6%. Figure 4.13 shows the specimens after failure. All samples failed at the interface between the mortar and upper brick, in accordance with failure mode described in ASTM C952-12.

Table 4.3: Results of crossed brick couplet tests

ID	Bond tensile strength (MPa)
TBM1	0.40
TBM2	0.43
TBM3	0.42
TBM4	0.41
TBM5	0.38
Average	0.41

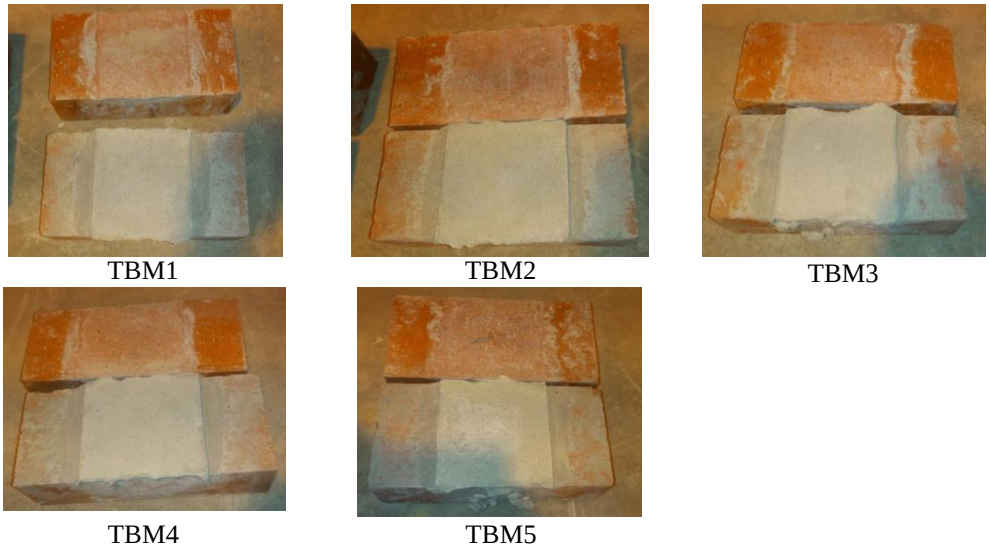

Figure 4.13. Crossed brick couplet tests specimens at failure under tension

4.3 Four-point bending tests on masonry beam-like specimens

4.3.1 Test programme

The second part of the experimental programme involved the flexural testing of 15 beam-like brickworks, which can be arranged into the following three main groups:

(1) Four non-retrofitted brickwork beams (N series): This set of specimens had no ECC reinforcement and served to benchmark the out-of-plane performance of masonry infills.

(2) Six brickwork beams retrofitted with a 15 mm thick of ECC layer fully bonded to the tension (bottom) face of the beam (F series).

(3) Five brickwork beams retrofitted with a 15 mm thick of ECC layer partially bonded to the tension (bottom) face of the beam (P series).

In each group, half of the specimens were tested at a loading rate of 1 mm/min (quasi-static) and the other half were tested at an elevated rate of 200mm/min, aiming to study the behaviour of ECC and its effect on the suggested retrofitting performance.

Each brickwork comprised of ten bricks and nine 5-10 mm thick mortar joints, forming a beam-like specimen with dimensions of 740×210×102 (thick) mm. N series brickworks were directly tested to failure, whereas F and P series brickworks were retrofitted with a 15mm thick ECC which was bonded to the bottom surface of the beams (see Figure 4.14). The properties of brick, mortar and ECC used to construct the four-point tests are presented in section 4.2.

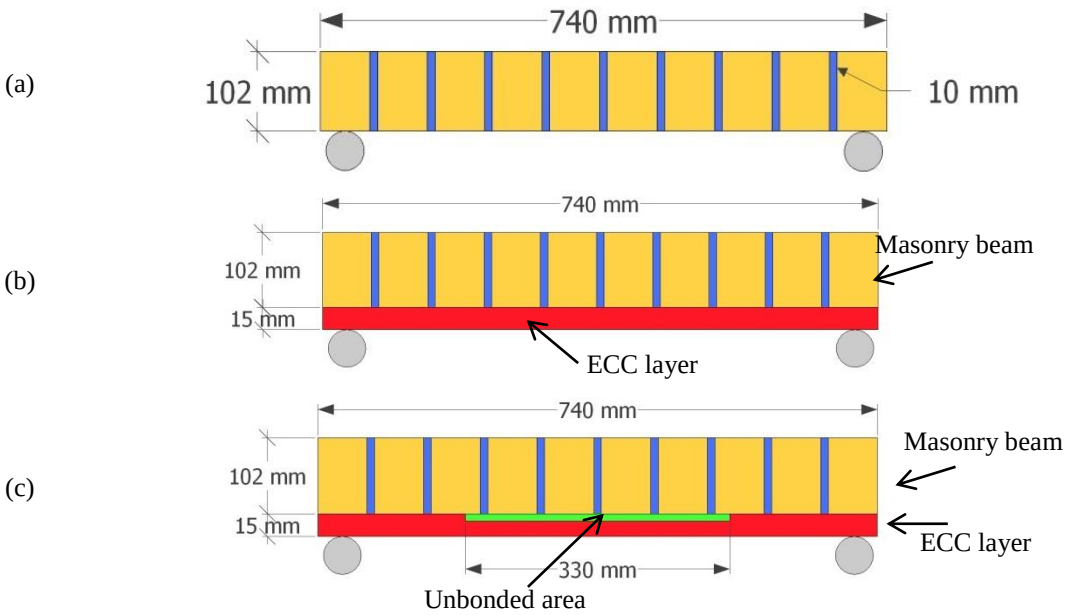

Figure 4.14. Four-point bending test (a) N series, (b) F series (c) P series

4.3.2 Fabrication and test setup

Fabrication. Each brick unit was firstly submerged in water for 24 hours. The bricks were then removed and wiped off with a damp cloth to remove excessive surface moisture prior

to bonding. The brick units were then stacked vertically, with mortar being laid between two bed surfaces. The top brick was then tamped down to form approximately 5-10 mm thick joint. The joint surfaces were then made flush with the bricks, with the exception of the first two outer joints of the retrofitted brickwork beams where a groove with a depth of approximately 5-10 mm was made to enhance the brick/ECC bond interface (see Figure 4.15 b). This process was repeated until ten brick units were stacked with a total of nine joints in between (see Figure 4.15). A timber framework was used to aid the fabrication process and produce test specimens with consistent geometry in terms of height/length and shape (flat and straight). This consistency was considered important not only to minimize the variations in the measurement obtained during tests but also to ensure that the effect of any torsional forces would be minimized during testing. Upon completion of the fabrication process, the specimens were left in the laboratory for 14 days to cure. This marked the completion of the fabrication process of the first series of non-retrofitted brickwork beams (N series).

In the other two series of specimens (F and P series), after the completion of the process described above the brickwork beams were laid down flat on the floor (tensile surface faced upward) prior to ECC casting (see Figure 4.15). A timber mould was then constructed around the perimeter of the top surface of each beam, creating a mould with internal dimensions of 740×210×15 mm. At their perimeter the moulds were sealed using a plaster to ensure that there would be no leakage of the ECC. Duct-tape was fitted to the middle third of the tensile surface of the partially bonded specimens (P series, see Figure 4.15), in order to prevent bonding of the brick with the 15 mm thick ECC layer. The surface of the brickworks was wetted immediately prior to ECC casting to minimize the absorption of water from the ECC layer to the brick, which could alter the tensile properties of the ECC.

Once all moulds were ready for casting, ECC was produced in a batch of 6 litres using the same mixing procedure presented in section 3.2. Upon completion of the mixing process, the mixing bowl was lifted manually to slowly pour the ECC from one end of the top surface of the brickwork to the other end (see Figure 4.15). The ECC was self-compacting, so vibration was unnecessary, but it still required the top surface to be troweled to ensure a level, flat surface across the top of the timber mould. The surface

was tapped in places to ensure no significant air bubbles remained before covering the free surface of the ECC layer with a plastic sheet. After about a day, the timber moulds were removed and the ECC layer was then covered with damp hessian and plastic sheeting. All specimens were left to cure for a further 21 days prior to testing.

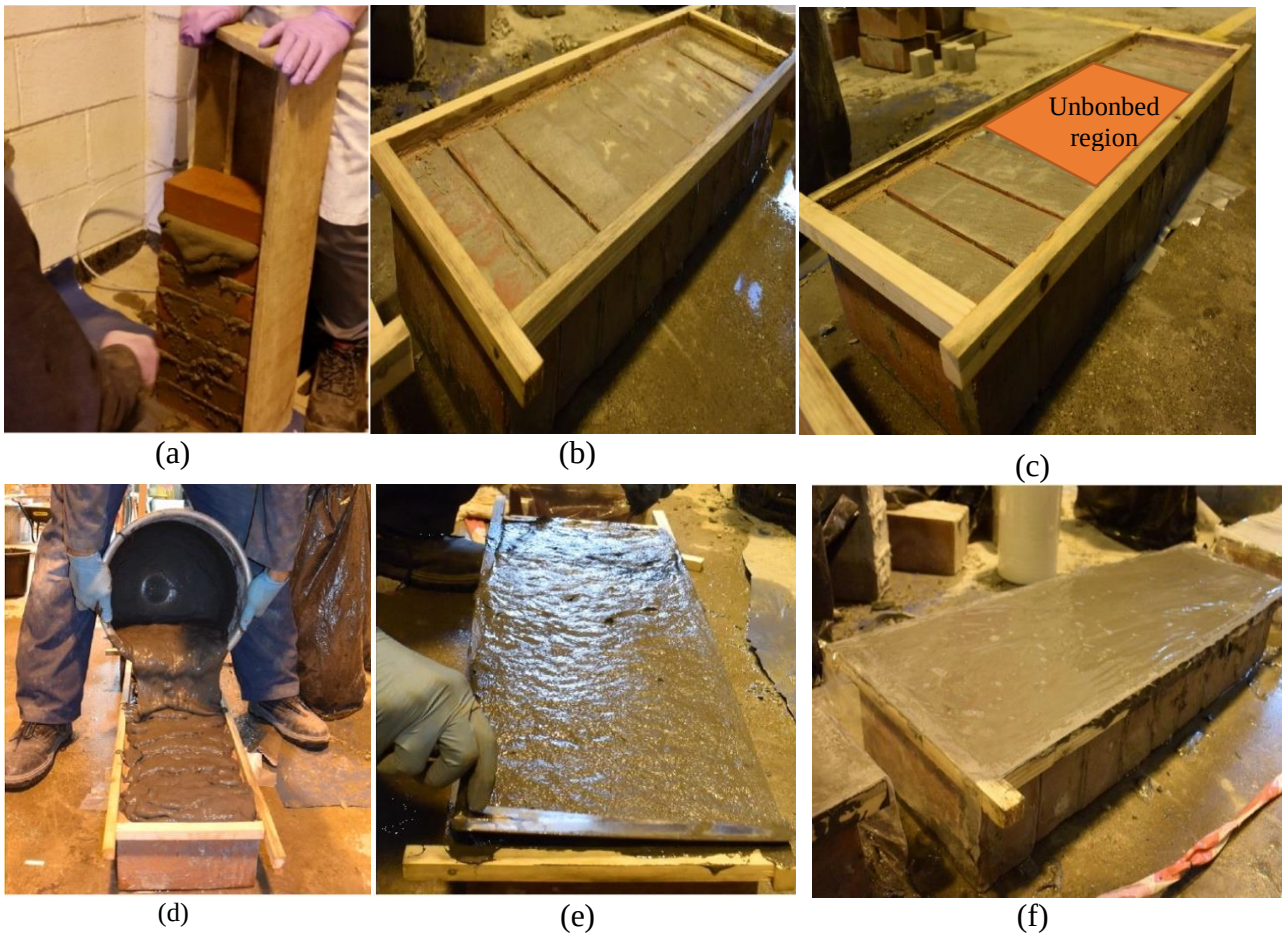

Figure 4.15. Specimens building procedure: a) building the masonry beam, b) fabrication of the wooden mould for F series, c) fabrication of the wooden mould for P series, d) casting the ECC, e) leveling the ECC layer surface, f) covering of the ECC layer by a plastic film

Test setup. Figure 4.16 shows the four-point bending test setup used for this experimental programme. The setup consisted of three main elements: i) four rectangular hollow sections (100 x 200 mm) which were welded together to form a stiff base upon which specimens were supported; ii) two roller supports placed at approximately 660 mm apart; and iii) a specially designed two-point loading apparatus. The use of the two roller supports and the loading head would facilitate adjustment of the testing rig to the deformities that would be present in the sample through fabrication. This would allow for

the specimen to be loaded vertically and thereby minimizing the risk of premature failure due to torsion induced forces. The loading apparatus has two transverse spreader elements that can be adjusted along the longitudinal axis of the specimen to deal with inherent variations in the length of the beam. The base and the loading apparatus were connected to the existing jaws of a 500kN INSTRON testing machine. Loading was applied in a displacement controlled mode until failure. The distance between the two point loads was 210 mm (see Figure 4.16).

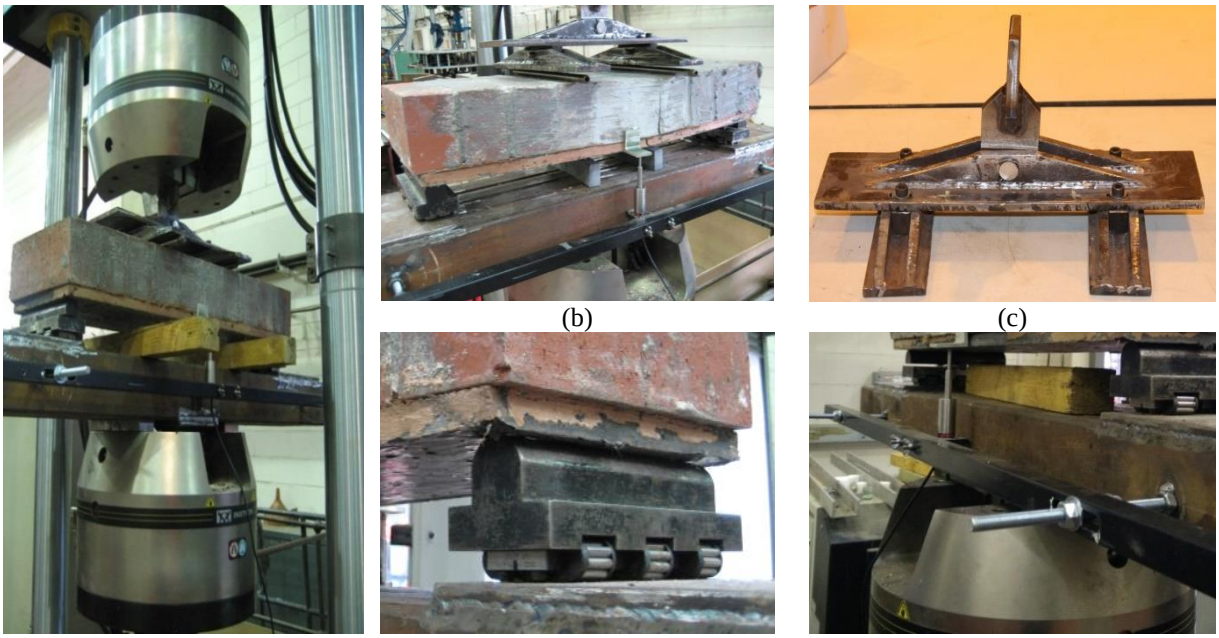

Figure 4.16. Four-point bending test setup a) Instron machine, b) Loading rig, supports and LVDT positions, c) loading rig d) support e) LVDT holder

Instrumentation. Two LVDTs were used to measure the average of the beam's midspan vertical deflections. In order to obtain true deflection readings for the LVDTs and eliminate the effect of support settlement, the LVDTs were mounted on two hollow square sections which were installed and independently supported on each side of the base steel beam below the centre of the two supports (see Figure4.16). The LVDTs were connected to a data acquisition system that documented the results. At the quasi-static 1 mm/min loading rate, the sampling rate was set constant at 10 Hz, whereas at the rate of 200 mm/min, the rate was set at 100 Hz.

4.3.3 Results of non-retrofitted brickworks (N series)

The load-deflection curves for non-retrofitted brickwork beams (SN1, Sn2, EN8 and EN9) are compared in Figure 4.17. The results show that the load carrying and deflection capacities of the brickwork beams somewhat increase with increasing rates of loading. The SN beams, tested at a rate of 1 mm/min, showed an average load-carrying capacity of 1.2 kN and deflection capacity of 0.06 mm, whereas the EN series beams, tested at a rate of 200 min/min, exhibited average load-carrying and displacement capacities of 2.3 kN and 0.11 mm, respectively. Both increased by a factor of about 1.9. The enhancement of the load carrying capacity can be attributed to the inertia force arising from the increased rates of loading, apart from the variations of material properties. In all specimens, failure was sudden and brittle, resulting from the formation of a flexural crack which rapidly extended upwards, leading to a complete loss of strength. Overall, the results highlight the fact that while the brickwork performed well when subjected to in-plane loading (e.g. compression load; see Section 4.2.1.2), it is vulnerable when subjected to out-of-plane forces.

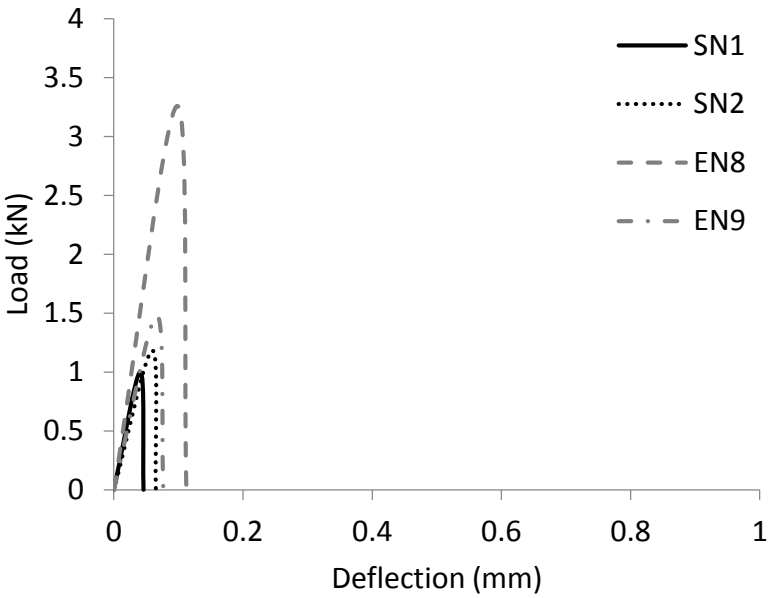

Figure 4.17. Four- point bending load-deflection curves for SN and EN series

The crack patterns after failure are presented in Figure 4.18. It is evident that only one crack can be observed at one of the brick/mortar interfaces over the central span (at the fourth/fifth/sixth mortar joint). This finding reiterates the results of couplet tests presented in Section 4.2.1.4 that the brick/mortar interface is indeed the weakest link in the

brickwork specimens considered used in this study and that the bond strength of the brick/mortar interface is much weaker than the tensile strength of the brick itself.

Figure 4.18. Failure crack patterns at non retrofitted beams a) SN1, SN2 under a displacement rate of 1 mm/min and (b) EN8 under a rate of 200 mm/min.

4.3.4 Results of retrofitted brickworks: Full bond (F series)

The load-deflection curves describing the behaviour of the six ECC-retrofitted brickwork beams are compared in Figure 4.19, with the results of N-series specimens. SF series corresponds to specimens that were tested at the rate of 1 mm/min, whereas EF series refers to those tested at a rate of 200 mm/min. It is evident from the load-deflection curves presented in Figure 4.19 that all specimens exhibited a linear elastic response until crack initiation, followed by a plateau (horizontal region in the load-deflection curve associated with the strain-hardening behaviour of ECC) before finally a softening behaviour (associated with the descending branch of the load-deflection curves) ultimately leading to failure. With the exception of Beam EF10 which exhibited only a very short plateau followed by a more gradual failure. The plateau resembles the tensile strain-hardening response of the ECC as presented previously in Figure 3.9. During the deflection hardening process, it was observed that four to five brick/mortar interfaces (joints) over the central region fractured, which was also accompanied by the formation of multiple micro-cracks in the ECC layer underneath. In some places, delamination was also observed close to the cracked regions, causing more multiple cracks to form in the ECC

layer toward the middle of the brick. The crack widths appeared to increase throughout the loading process, making them more visible with increasing level of deflection.

Regarding the results of the SF specimens shown in Figure 4.19, it is evident that the use of the ECC layer significantly improves the stiffness, strength and deformability of the brickworks specimens under out-of-plane loading. Crack initiation appears to occur at an average load of 12.9 kN, which is approximately ten times higher than that of the non-retrofitted specimens (SN series). The average load and deflection capacities were found to be 12.9 kN and 3.9 mm (approximately 10 and 64 times higher times than those of SN series specimens, respectively). The increase in load and deflection capacities can be attributed to the additional strength provided by the ECC layer and are also indicative of the strain hardening characteristics of the ECC.

The test results also indicate that the response of the retrofitted brickwork specimens was significantly influenced by the rate of loading applied. It is evident that increasing the loading rate from 1 mm/min to 200 mm/min resulting in an increase of both first cracking load and load carrying capacity by 36%, from approximately 13 kN to 18 kN. The EF series specimens still exhibited deflection hardening response. The deflection of EF series with the mean deflection corresponding to the maximum load was ranging from 3.9 mm to 1.4 mm. It is anticipated that the increase in load capacity and the decrease in the deflection capacity is attributed primarily to the strain-rate dependence of the ECC presented in Section 3.9, signifying that the ECC matrix toughness used in this study is more rate dependent than the fibre and fibre/matrix bridging properties. The increase in first cracking can be associated with both inertia effects and material rate dependency as just aforementioned. More detailed discussions about this phenomenon will be presented in Chapter 6 when investigating the subject problem numerically via NLFEA.

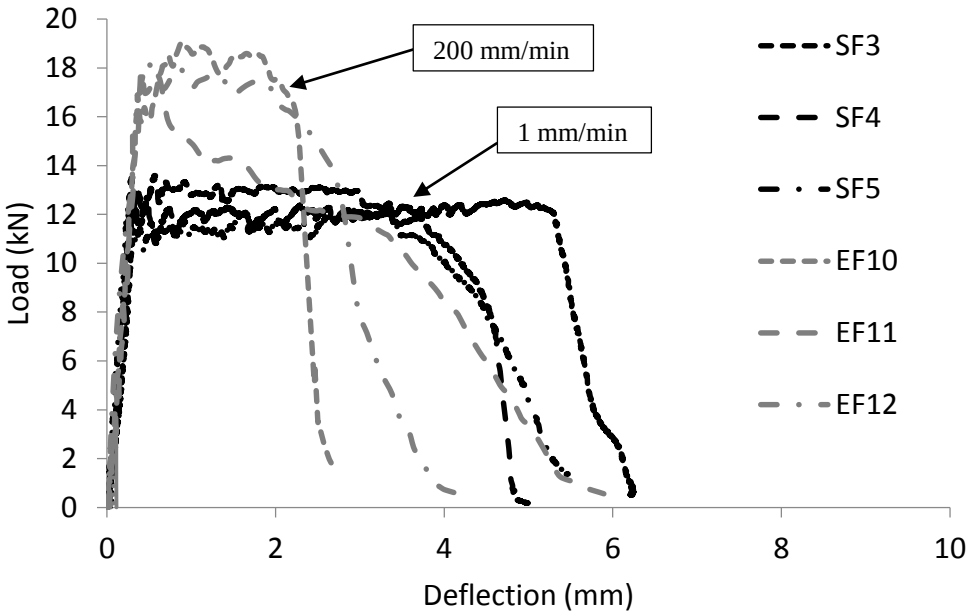

Figure 4.19. Four- point bending load-deflection curves for SF and EF series.

Figure 4.20 shows the crack patterns forming across the central span of the bottom surface of the brickworks, with the brick/mortar interface marked in red for ease of identification. The surface was slightly wetted to facilitate crack identification. A thin film was then placed on the wetted surface to allow the crack marking. Note that in some cases the crack width was very small and the sketches presented may not indicate the full extent of actual cracking. It is evident from Figure 4.20 that the entire brick/mortar interfaces in the center span were fractured, resulting in the formation of a number of micro-cracks close to the fractured brick/mortar interface regions. It is interesting to note that the width of the isolated cracked regions lies within the range of 20-40 mm. This can be associated with the fact that these cracks originally initiated from the tip of the fractured brick/mortar interfaces that were in contact with the ECC. These cracks then propagated downward over an angle of approximately -45 to 45^{o} to the vertical (see Figure 4.24). Given that the thickness of the ECC layer is about 15 mm, these cracks would, therefore, extend over a width of approximately 30 mm at the soffit. Apart from this possible crack formation, some other vertical micro-cracks can also form due to the deterioration of the bond between the brick and the ECC.

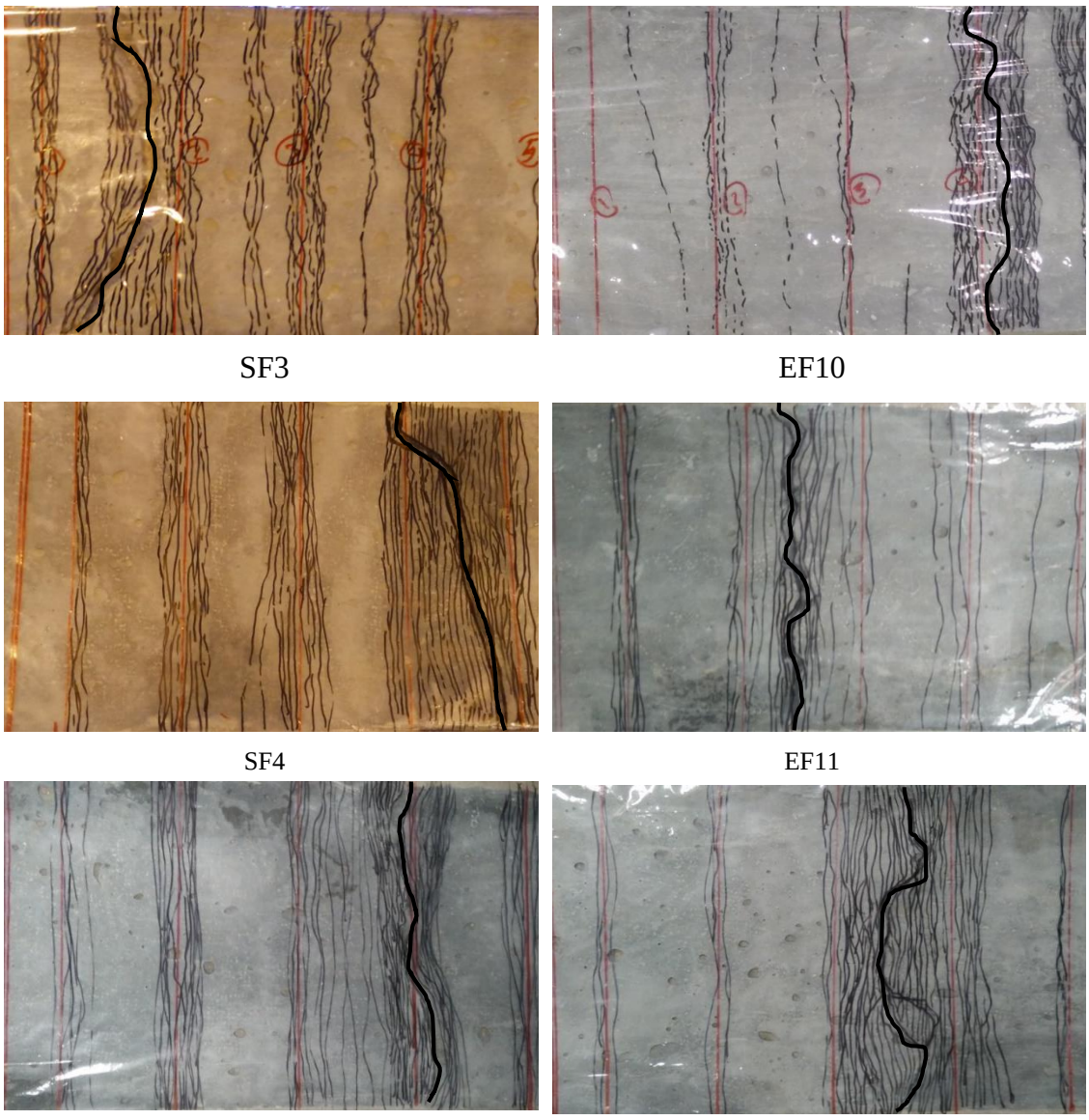

Figure 4.20. Failure crack patterns on the tensile face of Beams SF3, SF4, SF5 under a displacement rate of 1 mm/min and (b) Beams EF10, EF11 and EF12 under a rate of 200 mm/min.

With reference to Figure 4.20, it is also evident that the number of the micro-cracks close to the brick/mortar interface exhibited by the EF series specimens is consistently lower than that of the SF series specimens and hence appears to be less uniform. This can be associated with the rate-dependent behaviour of ECC which at elevated loading rate exhibits less number of cracks as observed in ECC material tests presented in Figure 3.9. Given the width of the micro-cracks of the two series of specimens is comparable, the smaller number of cracks exhibited by the EF series specimens is consistent with the apparent decrease in ductility experienced by this series of specimens prior to failure (see Figure 4.19).

Furthermore, it is interesting to note that while the micro-cracks initiated in the ECC layer underneath the brick/mortar interface region (joint), some cracks extended towards the middle of one of the bricks in the midspan and propagated across the width of the specimen in an irregular pattern (see Figure 4.20 -Specimens SF3, SF4, EF11 and EF12). This is due to bond deterioration in the brick/ECC interface. It was for this reason that the influence of bond was studied as one of the main parameters in the experimental programme. The results are presented in the next section.

4.3.5 Results of retrofitted brickworks: Partial bond (P series)

The load-deflection responses of the six specimens retrofitted with an ECC layer partially bonded to the tension surface are compared in Figure 4.21, with the results of N-series specimens to assess the contribution of the ECC layer. SF series specimens were subjected to a displacement rate of 1 mm/min, whereas EF series specimens to a rate of 200 mm/min. It is evident from Figure 4.21 that all specimens display an initial linear-elastic response, up to first cracking followed by a deflection hardening response. The deflection hardening process is primarily due to the formation of multiple micro-cracks in the ECC layer.

The SP specimens exhibited an increase in first cracking and peak load of approximately 7 times and 9 times respectively. The N series peak load was 1.2 kN compared to SP series first crack load and peak load 8.7 kN and 10.9 kN, respectively. The enhancement in displacement capacity is more significant, from 0.06 mm to 6.59 mm (about 110 times). Similar to the SP series specimens, the EP series specimens also display an increase in both first cracking and peak loads by about 6.5 times from 2.3 kN to 14.4 and 14.9 kN, respectively. This series of specimens also display a significant increase in ductility from about 0.11 mm to 4.05 mm (approximately 35 times).

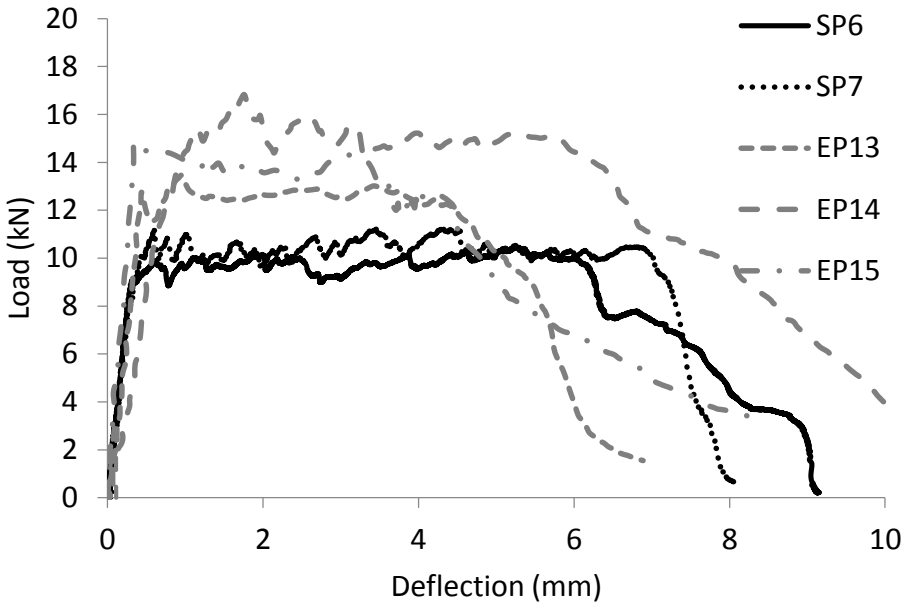

Figure 4.21. Four- point bending load-deflection curves for SP and EPseries.

Figure 4.22 displays the failure crack pattern developed across the central region of the ECC layer for the two rates of loading considered. Widespread fine multiple cracking was observed in all specimens regardless of the location of the brick/mortar interface and the rates of loading considered. As such, unlike the multiple-cracks in the F (full bond) series specimens, the cracks in P series specimens form vertically and perpendicular to the applied tensile stress (see Figure 4.24). Furthermore, since the micro-cracks can now form at any location within the middle unbonded region of the specimens, this results in a dramatic increase in crack numbers. This finding offers an explanation as to why the displacement capacity of these P series specimens appears to be higher than that of the F series specimens. Though, the micro-cracks distributed uniformly in the unbonded central span irrespective of the rates of loading considered in this study, a reduction in the number of the micro-cracks can be observed over the two rates of loading tested. The reduction in cracking density with increasing loading rate can be once again attributed to the rate dependent behaviour of ECC (see Section 3.2.5), resulting primarily from the rate dependence of the chemical bond between the PVA fibre and the ECC matrix.

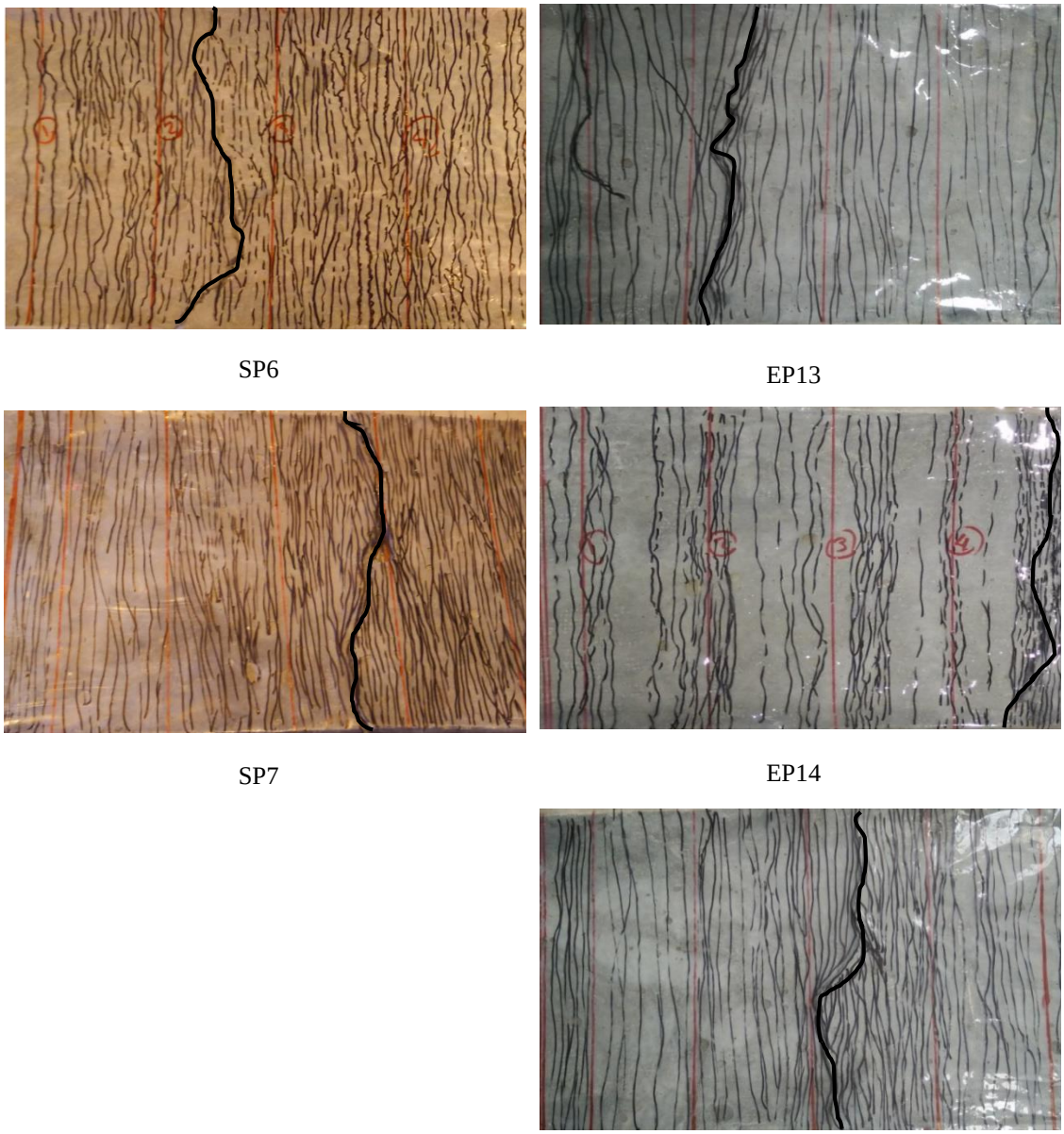

Figure 4.22. Failure crack patterns on the tensile face of Beams SF6 and SF7 under a displacement rate of 1 mm/min and (b) Beams EF13, EF14 and EF15 under a displacement rate of 200 mm/min.

4.3.6 Effect of bond arrangement

The load-deflection responses for all brickwork beams tested in this chapter are presented in Figure 4.23, with the summary of the first cracking and maximum loads as well as the deflection corresponding to the maximum load presented in Table 4.4. It is evident that both SF and SP series specimens have considerably better performance that SN series specimens. However, the SF series beams outperform the SP series beams by 18% in terms of the maximum load capacity and 49% in terms of the first cracking load. The

potential reasons for this difference are discussed in next section. Concerning the deformability, it is clear that both SF and SP series beams display much ductile out-of-plane response (respectively, about 65 times and 110 times higher than that of the SM series beams). The higher value of ductility exhibited by the SP series samples can be attributed to the more uniform crack distribution along the middle unbonded region of specimens. The higher ductility of the SP series beams highlights the benefit of partially de-bonding the ECC layer in applications where out-of-plane ductility is of primary concern.

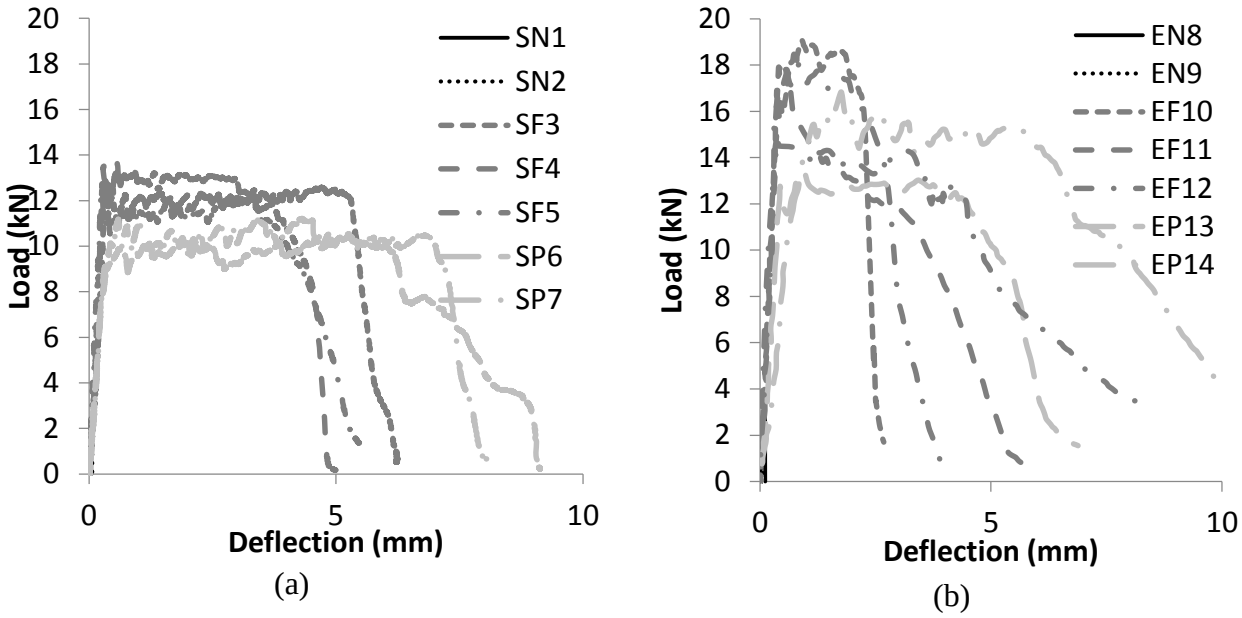

Figure 4.23. Comparison of the load-deflection responses of the brickwork beams subjected to a crosshead rate of (a) 1 mm/min and (b) 200 mm/min.

Figure 2.24 presents the typical crack pattern on the front face of the specimens exhibited by the fully bonded specimens compared to that developing on the partially bonded specimens. The red lines define the central portion of the span of specimens (which in the case of the partially bonded specimens coincides with the unbonded region) and black lines represent the cracks. As it is discussed in the sections 4.3.4 and 4.3.5 the cracks in the fully bonded specimens propagate downward at an angle (between -45 and 45o to the vertical). However, the cracks in the partially bonded specimens develop perpendicular to the applied tensile stress in the ECC layer. It is interesting to note that the same crack patterns are observed for both loading rates (low and elevated) considered.

a)

b)

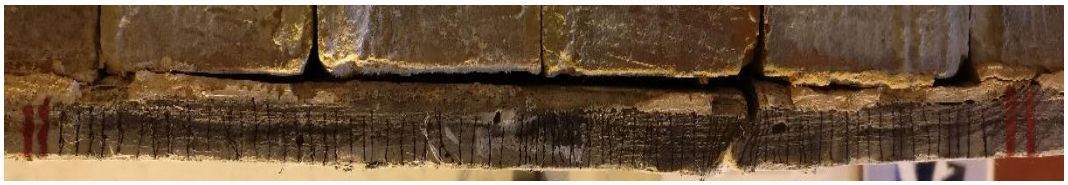

Figure 4.24. Comparison of the crack pattern distributed in the front face of ECC layer within the central span a) fully bonded b) partially bonded specimens.

The figure 4.25 presents the typical internal face of ECC layer for the full bond and partial bond specimens after failure. It is documented that in the full bond specimens the thickness of ECC layer beneath the mortar joints (including the brick mortar interface) is about 2 mm thicker than rest of ECC layer. This is due to penetration of fresh ECC in the mortar layer pores. However, in the partial bond specimens the layer of plastic tape used to isolate the fresh ECC from masonry beam and ECC layer within this area is completely smooth and did not fill the gaps in the masonry beams.

a)

b)

Figure 4.25. Internal face of ECC layer a) full bond b) partial bond

Table 4.4 provides a summary of results obtained from the non-retrofitted, fully bonded and partially bonded retrofitted specimens when subjected to loading rates of 1mm/min and 200mm/min. These results are discussed in section 4.5 to explain the behaviour of specimens and the exhibited cracking process. Furthermore, the results are used in Chapter 6 to calibrate the finite element models developed.

Table 4.4: Summary of the four-point tests

Loading rate (mm/min)	ID	Average thickness (mm)	First cracking load (kN)	Average of first cracking load (kN)	Maximum load (kN)	Average of maximum load (kN)	Deflection at the maximum load (kN)	Average deflection at the max load (kN)
1	SN	-	1.1	1.2	-	-	0.05	0.06
		-	1.3		-		0.07	
	SF	16.88	13.5	12.9	13.9	12.9	3.02	3.89
		16.12	12.8		12.6		5.21	
		15.67	12.5		12.2		3.43	
	SP	15.42	9.2	8.7	11.2	10.9	7.15	6.59
		14.78	8.2		10.6		6.02	
200	EN	-	3.0	2.3	-	-	0.15	0.11
		-	1.5		-		0.08	
	EF	16.38	18.1	17.7	18.2	18.4	1.91	1.43
		16.17	17.9		17.9		0.57	
		15.57	16.9		19.1		1.82	
	EP	15.89	14.9	14.4	14.5	14.9	3.27	4.05
		15.48	12.8		13.3		3.73	
		14.93	15.5		17.0		5.16	

4.4 Conclusions

Regarding the observations and analytical study the following conclusions can be drawn:

- Retrofitting of masonry walls with ECC can substantially improve their performance in terms of ductility, stiffness and load carrying capacity.

- The level of the bond achieved between the ECC layer and the masonry specimens is a very important parameter in the retrofitting of masonry beams. The ductility of the masonry beams retrofitted with the partially bonded ECC layer when subjected to static or elevated loading rates is approximately 1.5 to 2 times more than the fully bonded specimens. This was observed in both cases of loading rate considered herein (1mm/min and 200mm/min).

- The partially bonded specimens (subjected to static or elevated loading rates) exhibit ductile behaviour due to the multiple cracking developing in the un-bonded region of the ECC. The cracks in the fully bonded specimens (subjected to static or elevated

loading rates) developed near the brick-mortar interface regions (joints) over the centre span of the specimens. In the case of partially bonded specimens, a more uniform crack pattern was observed, indicating a better utilization of the ECC strengthening layer.

- Considering the response of the retrofitted specimens, it is predicted that the strains (and hence the cracking) in the ECC layer in the un-bonded region is more distributed, hence resulting in larger deformation.

- Cracking in the full bonded specimens developed mainly near the brick-mortar interfaces within the central span. Cracks direction in fully bonded specimens is diagonal and increases the strength of full bond specimens. Cracking in the partially bond specimens were distributed uniformly in the middle third (unbended) span. Cracks direction in partially bonded specimens is vertical to tensile load.

- The fully bonded beams exhibited a 66% increase in the first cracking load and a 33% increase in the maximum load capacity when subjected to elevated loading rates compared to their counterparts recorded under equivalent static loading. The partially bonded specimens exhibited a 36% increase in the first crack load a 42% in strength. This reveals that the load bearing capacity of the specimens under elevated loading rates improved in all cases. It is considered that this change in the recorded behaviour is linked to the strain rate sensitivity of the material properties of ECC.

- The fully bonded beams and partially bonded beams exhibited a 66% and 35% reduction in deflection when subjected to elevated loading rate compared to their counterparts recorded under equivalent static loading. This behaviour presents the rate dependence behaviour of ECC with increasing loading rate which was discussed in section 3.2.5. However, the fully bonded beams exhibited a reduction of ductility about 3 times higher than that of partially bonded beams. This shows that the fully bonded beams are more vulnerable when subjected to elevated loading rates compare to partially bonded beams. This vulnerability is due to the concentration of stress near the brick-mortar interface whereas in the partially bonded beams the stress in the ECC layer is distributed uniformly.

- The crack pattern exhibited by fully bonded and partially bonded series had similar characteristics under both cases of loading rates considered. However, the number of cracks developing decreased with increasing loading rates. The same behaviour was observed in the case of the ECC dog-bone specimens discussed in section 3.2.5. The reduction of the crack number observed in the case of the elevated load rate resulted in a reduction of ductility.

Chapter 5: Drop weight testing of masonry specimens retrofitted with ECC

5.1 Introduction

In this chapter the results obtained from drop-weight tests carried out on masonry beam specimens, identical to those considered in Chapter 4, are presented and discussed. The experimental investigation aims at assessing the level of enhancement in structural performance achieved in the out-of-plane behaviour of the subject specimens under impact loading through the use of:

- A single ECC layer added to the bottom (tensile) surface of the masonry specimens.
- Two ECC layers, one on the top (compressive) and a second on the bottom (tensile) surface of the masonry specimens

The experimental (drop-weight) setup and the methodology employed for studying the behaviour of the retrofitted masonry specimens is initially presented. The method employed for the preparation of the specimens is the same as that employed in Chapter 4. This is followed by a presentation of the data recorded during testing, describing certain important aspects of the dynamic response exhibited throughout the loading process. These aspects include the time history of the contact and reaction forces generated as well as the displacement and acceleration of the drop-weight and certain points along the element span. Emphasis is also focused on recording the deformation and cracking profiles exhibited throughout the loading process up to failure. The results are then analysed and discussed in relation to their counterparts established under equivalent static loading (presented in chapter 4) in order to determine the effect of loading rate on the exhibited behaviour.

Two different type of impact loads are applied in these tests: high and low intensity impact loads. High intensity impact loads (H series) are generated when using two 210mm x 20mm x 5mm steel pads in the impact region between the drop-mass and masonry specimen. Low intensity impact loads (L series) are generated when two 210mm x 40mm x 20mm timber pads are used. In all tests conducted the impactor was dropped from a height of 300 mm. This loading process was repeated until the residual load-carrying capacity of the specimens was exhausted and the specimens essentially collapsed. After

each impact the crack patterns of the specimens were recorded. Table 5.1 shows the number of blows (impacts) required for each specimen to collapse (i.e. to fully lose its load-carrying capacity) and a summary of the main characteristics of each test.

Table 5.1: Impact case studies retrofitted specimens.

Specimens name	Impacts number	Number of ECC layer	Level of bond between ECC and masonry	Impact load	Average Impact per group
HFO4	3	One layer	Full bond	H-series	1.75
HFO2*	2				
HF07	1				
HFO1*	1				
LFO8†	2			L-Series	2
LFO11	2				
HPO5†	3		Partial bond	H-series	1.67
HPO6	1				
HPO3*	1				
LPO9	4			L-series	3.5
LPO10†	3				
HFT14	4	Two layer	Full bond	H-series	3
HFT12	2				
LFT16	3			L-series	2.67
LFT21	3				
LFT19	2				
HPT13	2		Partial bond	H-series	2
HPT15	2				
LPT18	4			L-series	3
LPT17†	3				
LPT20	2				

* Data logger results are missing
† HSD camera results are missing

Figure 5.1 shows the terminology used for describing each case study considered in relation to the main characteristics of the retrofitting method adopted and the intensity of the impact load applied. The first letter is associated with the intensity of the impact load imposed: H and L are associated with high and low intensity impact respectively. The second letter describes whether the ECC layer attached to the bottom face of the specimen is fully or partially bonded to the masonry: F denotes full bond and P partial bond. The

third letter is related to the number of ECC layer(s) applied onto the specimen. The letter O is associated with one layer being applied to the lower (tensile) face of the specimens whereas T denotes the use of a second layer applied at the upper face of the specimen. Finally, the number at the end refers to the number of the sample considered. Table 5.1 categorizes the tests carried out in Chapter 5 in four groups depending on the retrofitted method adopted (i.e. the use of one or two layers of ECC) and the intensity of the impact load applied and the bond level.

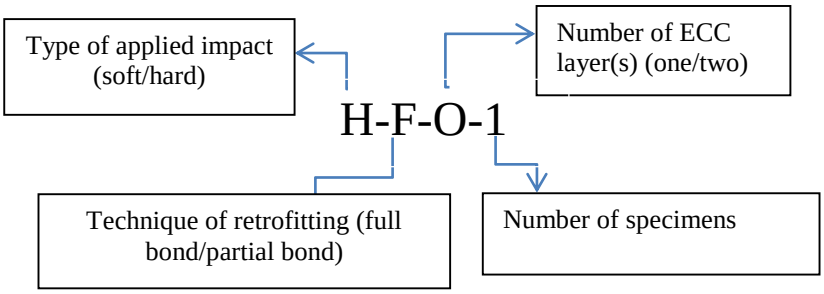

Figure 5.1. The terminology of different specimens.

5.2 Specimens preparation

The properties of the materials used, the dimensions of the specimen and the fabrication method adopted were presented in section 4.3 when discussing the quasi-static tests. In the case of the retrofitted specimens with a fully bonded layer of ECC, the latter was directly applied onto the moist brick face forming a 15mm thick layer. When retrofitting through the use of a partially bonded layer of ECC, a packaging tape was applied on the middle third span of the brick surface (see Figure. 4.26) to prevent bonding with the ECC layer. The curing process was carried out as in the case of the retrofitted specimens tested under static loading described in section 4.3. Upon completion of the application of the first ECC layer (see Figure 4.27), the specimens were covered with damp hessian and a plastic sheet (Figure 4.28) and left to cure for 21 days leading to testing. Specimens requiring a second layer of ECC were turned over after three days in order to cast the second layer of ECC on the other face of masonry beam. After casting the second ECC layer, the samples were covered with damp hessian and plastic sheeting and left to cure for 21 days leading to testing.

5.3 Test setup and instrumentation

Figure 5.2 shows the drop-weight setup available at the structure's lab at Heriot-Watt University which is employed for the present study. It is capable of applying different rates and intensities of impact loading depending on the weight of the drop-mass used

and the height from which it is released. All of the specimens are simply supported and subjected to multiple impact tests until failure/collapse (complete loss of load-carrying capacity) is observed. The impact rig consists of the main steel framework, the specimens' supports and the impactor (drop-mass). To study the specimens' behaviour under impact loading, the displacement time history exhibited at certain points along the element span and the impact and reaction forces generated have been measured throughout the loading process through the use of a high-speed digital camera and a number of dynamic load cells. In addition the deformation profile and the crack patterns exhibited by the specimens at different stages of the loading proces are also monitored.

Steel framework: The framework for the impact rig has been assembled at Heriot Watt University structural laboratory. Solid steel beams have been used in constructing the framework that supports the specimen and a truss supporting a guide rail for delivering (guiding) the drop weight to the predefined impact area of the specimen (Figure 5.3). The frame was bolted to the concrete slab beneath the rig.

Loading system: This system includes an electronic winch, a steel mass (drop weight), a load cell, a spreader beam and two loading plates which allowed the impact load to be applied on two locations along the element span. At each load point a steel pad was used to effectively distribute the load on the impact region effectively (see Figure 5.4) in order to minimise the development localised damage. Guide rails supported by a steel truss are used to deliver the drop weight to the prescribed impact region. An electronic winch was used to release the drop weight from a specific height. On the top, the steel mass (drop-weight) was connected to the winch and at the bottom it was connected to a dynamic load cell (Figure 5.4 b) which had a maximum load capacity of 600 kN. A spreader beam was used to transfer the concentrated impact load to two points along the specimen span (4-point bending test). The spreader beam consists of a solid steel prism with dimensions of 260mm x 60mm x 60mm welded on top of a plate 240mm x 200mm x 20 mm and two bars (200mm diameter). This was used in order to apply the imposed load in the form of two concetrated loads (uniformly distributed along the width of the specimen) at two locations symetrically positioned in respect to the specimen midspan (Figure 5.4 a). The distance between two concentrated loads was 210mm. The total weight of impactor (steel mass), load cell and load spreader was 47 kg.

Figure 5.2. Overview of impact test's instrumentation.

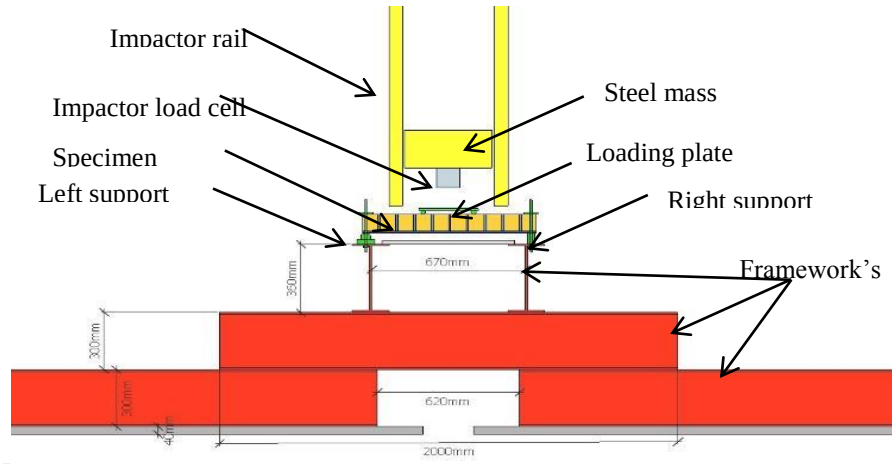

Figure 5.3. Impact framework.

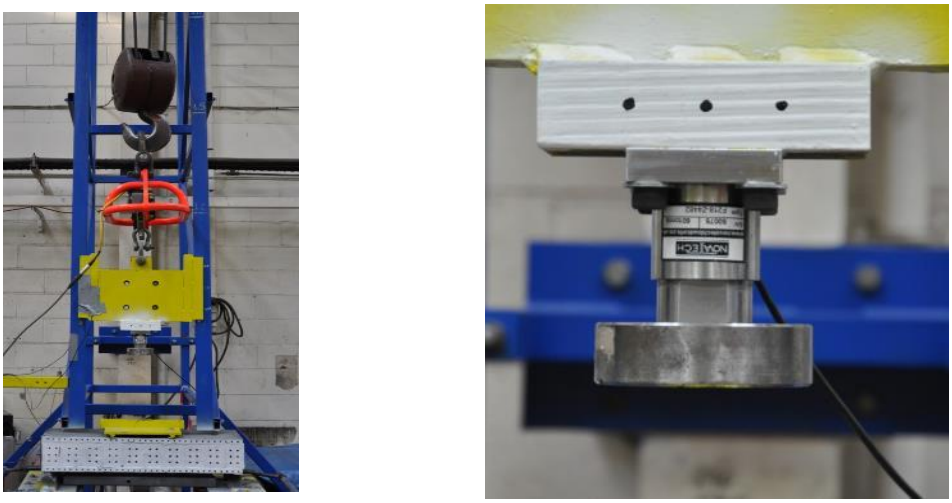

(a) (b)

Figure 5.4 a) Impactor set up and load spreader b) load cell.

Supports: The supports were designed in order to minimise the effect of uplift after the specimen being subjecting to impact loading (see Figure 5.5). At the right support two load cells were placed beneath the specimens in order to measure the reaction force

generated throughout the drop-weight test. Each load cell can measure a maximum load of 200 kN; therefore the support can measure a reaction force of up to 400 kN. To avoid localized damage being exhibited close to the support a 210 x 20 x 5 mm steel plate was inserted between the load cells and specimens. The supports were designed to allow some rotation and horizontal displacement while effectively restricting uplift through the use of two vertical steel ties (see Figure 5.5 b &c). The distance between the supports (the clear span of specimens) was 660mm.

Data Acquisition system: A digital data acquisition system was used to record data from the load cells (Micro Analog2-FE-MM40 data acquisition system made by Fylde Electronic Laboratories Ltd). A sampling frequency rate of 70 KHz was used for each channel. A trigger connected to the impactor initiated the data acquisition system one second prior to the impactor coming into contact with the specimens. Then the data was continuously recorded until end of the tests.

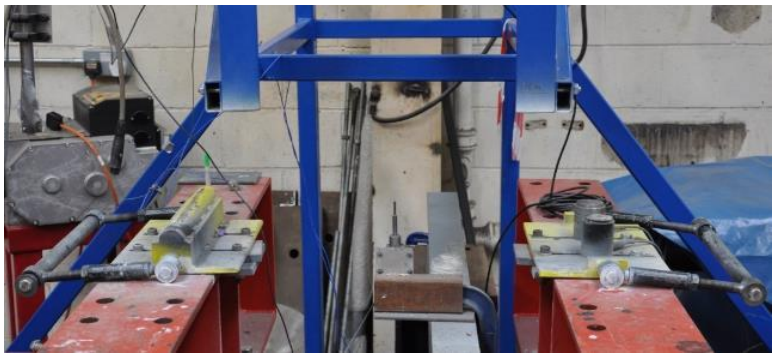

a)

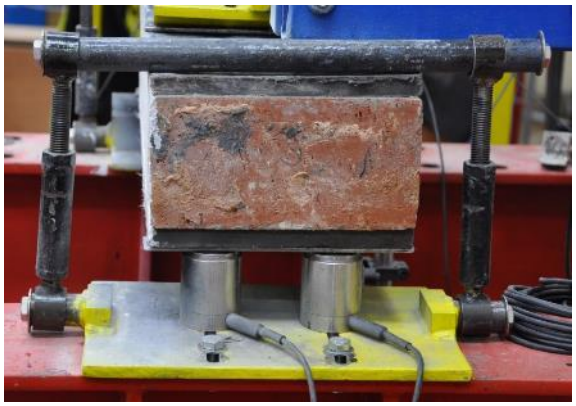

b) c)

Figure 5.5. (a) Arrangement of the supports, (b) right and (c) left support

High speed digital (HSD) camera: A HSD camera has been used in order to record and observe in detail various aspects of specimen's behaviour throughout the testing process such as the deformation profiles at different stages of the test, the variation with time of

the vertical and horizontal displacement of specific points (marked with dots on the specimens surface) along the element span and other moving components of the loading system, the cracking process and the failure mode ultimately exhibited. The HSD camera was set to capture 4000 frame per second (fps) throughout the duration of the drop-weight test. A trigger was connected to the HSD camera to initiate it approximately half a second prior to impact. After triggering the camera continuously records the frames for three seconds. In order to digitise the photographic evidence appropriate contrast between the dots and the surface of specimens is required. This was achieved by painting white the front side of specimens facing the HSD camera. Then a grid of black dotes are marked on the white surface through the use of a stencil sheet (template). These dots (see Figure 5.8) provided a clear target to track the vertical and horizontal deflection of samples through the loading process.

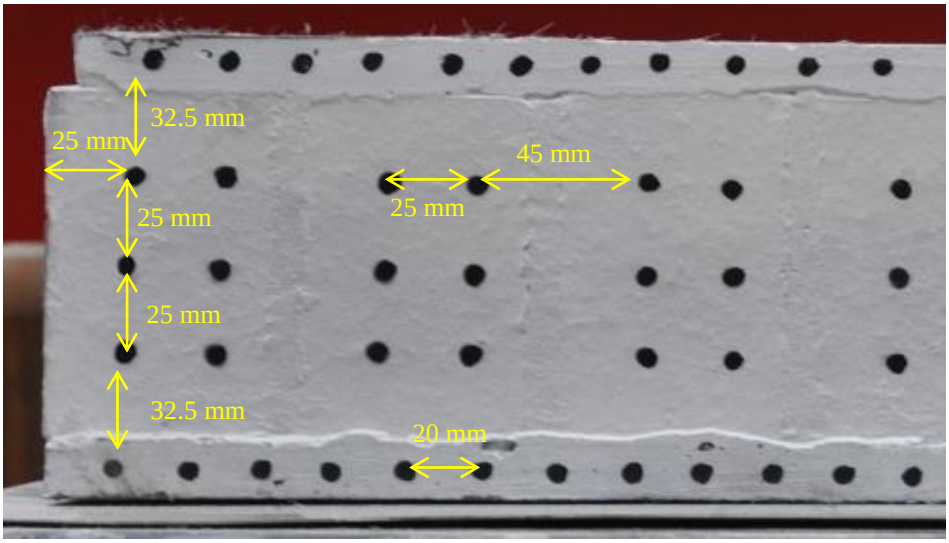

(a)

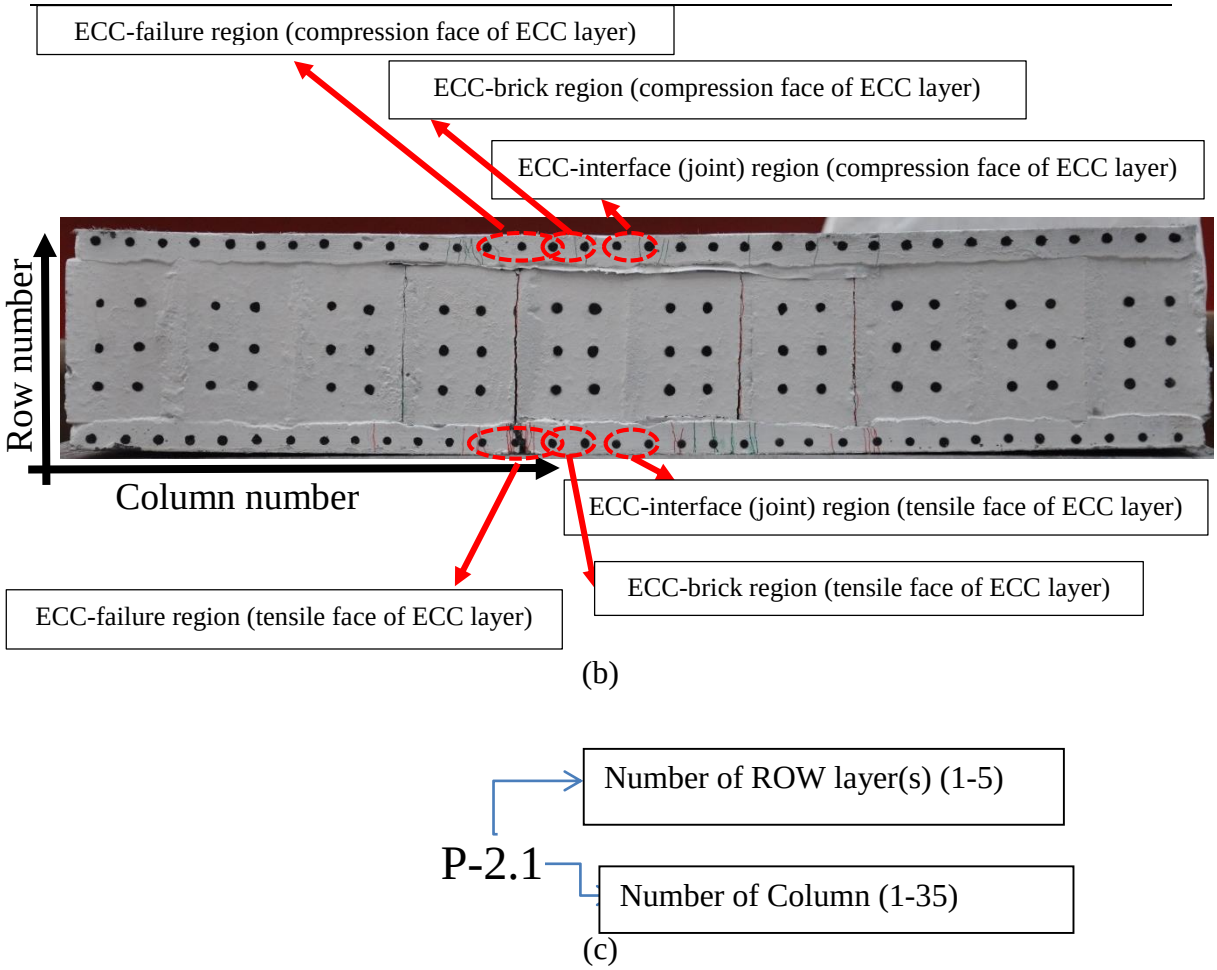

Figure 5.6 (a,b) Arrangement of dots (targets) used for monitoring purposes on the surface specimens and (c) relevant terminology adopted for identification purposes

To identify the different points along the element span studied during each test a specific name was assigned to each point depending on its location. Figure 5.6 (c) shows the terminology that is used for identifying the location of the different points marked in the form of a grid on the surface of each specimen. The first number represents the row to which the point belongs. A total of 5 rows of dots were marked on the specimen surface. The bottom row (located within the ECC layer) is considered as the first row, the three next rows are marked on the bricks while the fifth row being marked within the top ECC layer. The next number presents the column number of the points. The column close on the left end of the specimens is considered to be the first column and the numbering increases from left to right. Figure 5.7 shows the number of points marked on the surface of the specimen facing the HSD camera.

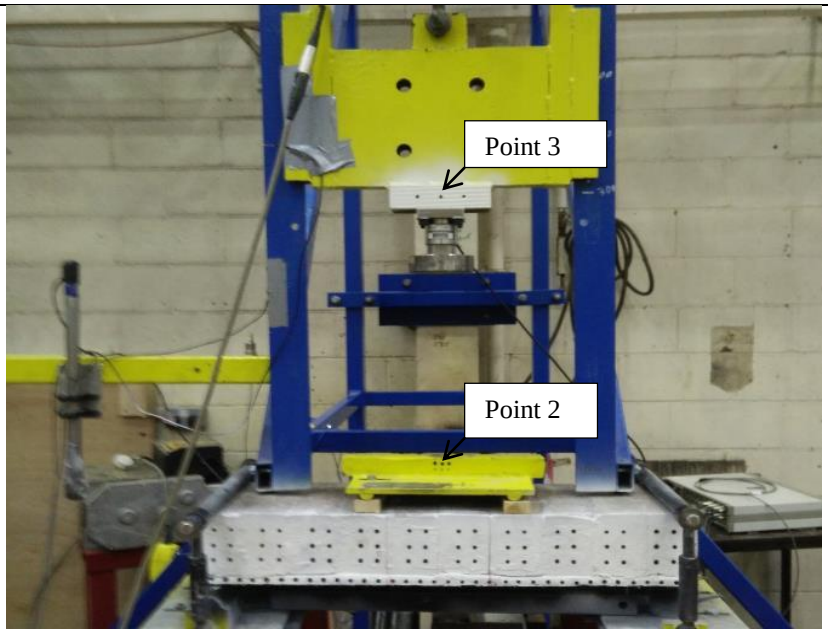

Figure 5.7: Impact and reaction force time-histories

5.4 Impact and reaction force time-histories

The impact force time history was obtained from the load cell located on the impactor (see Figure 5.4) whereas the reaction force time history was obtained from load cells located on the right support (see Figure 5.5). The reaction force measured was then multiplied by two in order to obtain an estimate of the total reaction force (generated at both supports) of specimens. It is assumed that due to the symmetry characterising the loading and support condition of the specimens the reaction force recorded at each support are equal. Emphasis will be focussed on the following parameters established from the recorded time histories of the impact load and reaction forces:

i) *R/I ratio*: the ratio between the maximum reaction force and the maximum impact load.

ii) *I-R delay*: the delay measured between the time at which the maximum impact load is attained and the time at which the maximum reaction force is recorded. This parameter is associated with time required for the stress wave generated at impact region to reach the specimen supports.

iii) *Initial loading rate*: The rate at which the impact load is applied immediately after initial contact. Its value is determined from the initial slope of the curve describing the time history of the impact force.

iv) *Average loading rate*: The average rate at which the impact load is applied defined as the ratio between the maximum impact load and the time required for the impact load to achieve this value.

The values of the above parameters are presented in the Tables 5.2-5.4

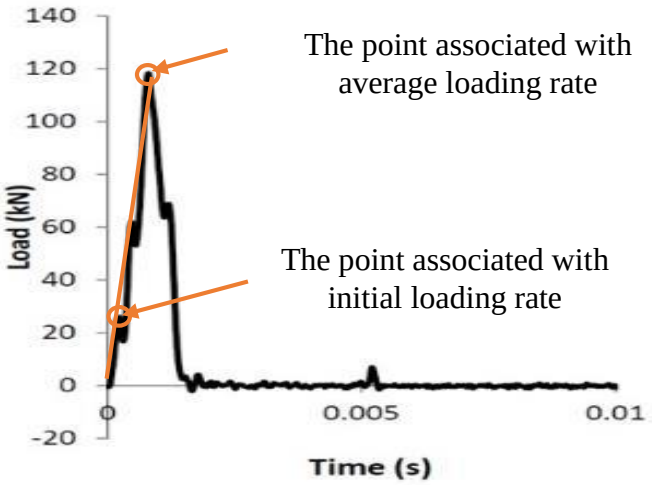

Figure 5.8. The locations of peak load associated with initial and average loading rate

5.4.1 Impact and reaction force time-histories of specimens with one layer ECC

Figure 5.9 presents the time histories of the impact load and reaction forces generated during testing of specimens retrofitted with one layer of ECC. The results obtained from the data logger during tests are summarised in the Table 5.2. For the case of the fully bonded specimens subjected to high intensity impact loading (HFO series) the impact force, presented in Figure 5.9, increases rapidly to a maximum force of approximately 120kN. It is interesting to notice that the form of the curves describing the time-history of the impact force is characterised by one major wave with multiple (namely three) peaks, possibly associated with multiple secondary impacts being exhibited throughout the loading process. The maximum load sustained is usually associated with the middle peak. The time history of the reaction forces presented for the same specimens is characterised by multiple (three) peaks, the intensity of which decreases with time. The number of peaks identified in the impact load-time history is equal to those observed waves in the reaction force time history.

It is interesting to note that when the specimens are subjected to consecutive drop tests the form of the impact (contact) force generated during each impact is similar, however,

the form of the reaction forces changes and the peak load generated gradually reduces with every consecutive drop-tests. As a consequence it can be suggested that the impact (contact) force is more associated with the developing inertia forces whereas the reaction forces are associated with the resistance and the integration of the structural form considered. The ratio between maximum impact (contact) force and reaction force (I/R ratio) are presented in table 5.2. In specimens subjected to consecutive drop tests, it is observed that this ratio (I/R) reduces with every consecutive drop-tests. This is mainly due to the reduction of reaction forces generated during each consecutive drop test while the peak value and time history of the impact force remained essentially unchanged.

Furthermore, it is interesting to observe the delay between the impact and reaction forces (I-R delay) (see Table 5.2). This is probably associated with the fact that the problem at hand is a wave propagation problem within a nonlinear (and discontinuous) medium (depending on the level of damage sustained). More specifically during contact between the drop-weight and the specimen, stress-waves are generated which propagate away from the impact region towards the supports. As a result the delay between the time histories of the impact and reaction forces is associated with the time required for these waves to reach the supports. Furthermore, it is interesting to notice that with every consecutive impact the above delay increases due to the increasing level of damage sustained and the cracking developing which reduces the speed with which the wave travels away from the impact region through the specimens towards the supports.

The curves in Figure 5.9 presents the time histories of the impact load and reaction forces generated by partially bonded specimens while subjected to high intensity impact loading (HPO series). As in the case of the HFO specimens the time history of impact loads is characterised with one major waves including three main peaks. The maximum impact load is associated with second peak of the wave and about 120 kN. The time history of the reaction force generated by the HPO specimens exhibited the multi waves with single peak, the intensity of which decreased with time. It is observed that the delay between the impact and reaction forces (I-R delay) (see Table 5.2) in the HPO series is less than that established for the HFO series when subjected to consecutive impacts. This reveals the level of damage sustained in HPO series (resulting in the reduction of the speed of the stress waves traveling within specimens) is less than that sustained in the HFO series.

Another parameter that is important to notice is the variability characterising the behaviour exhibited of the specimens included in both the HFO and HPO series. This parameter is associated with the number of consecutive drop-tests that the specimens are able to undertake prior to losing their load-carrying capacity. Some specimens are able to tolerate 3 drop-tests whereas other specimens collapse after a single drop test. This variation is attributed to the variability characterising the properties of the materials used in the specimens (i.e. brick, mortar, ECC) and their interfaces. Furthermore the imperfection in the fabrication process of specimens can affect the behaviour exhibited under high loading rates and intensities not observed however under static loading.

The results obtained from the specimens included in LFO series (see figures 5.10) reveal that the form of the impact load time history is characterised by three major waves with multiple distinct peaks with a the maximum value of about 80 kN. As in the case of the HFO series, when the specimens are subjected to consecutive drop tests the time-history of the impact load generated during each impact is similar. The curves describing the time-history of the reaction loads exhibited by the LFO series is also characterised by multiple waves, the intensity of which reduces with time. Similar observations, in terms of the reduction of peak values of the reaction force are made as in the case of the specimens included in the HFO series however, it is interesting to notice that the difference between the peak values of the impact load and the associated reaction force generated during the first impact tests is much smaller, denoting a lower level of damage being sustained during testing.

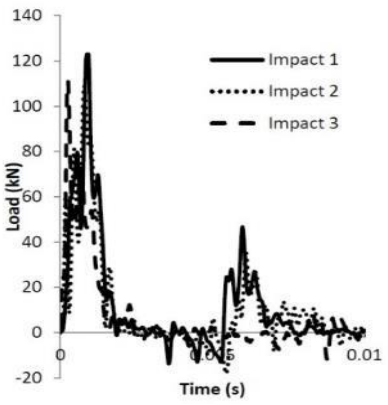

a)

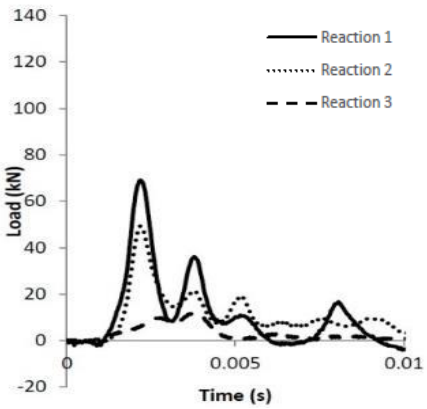

HFO4 b)

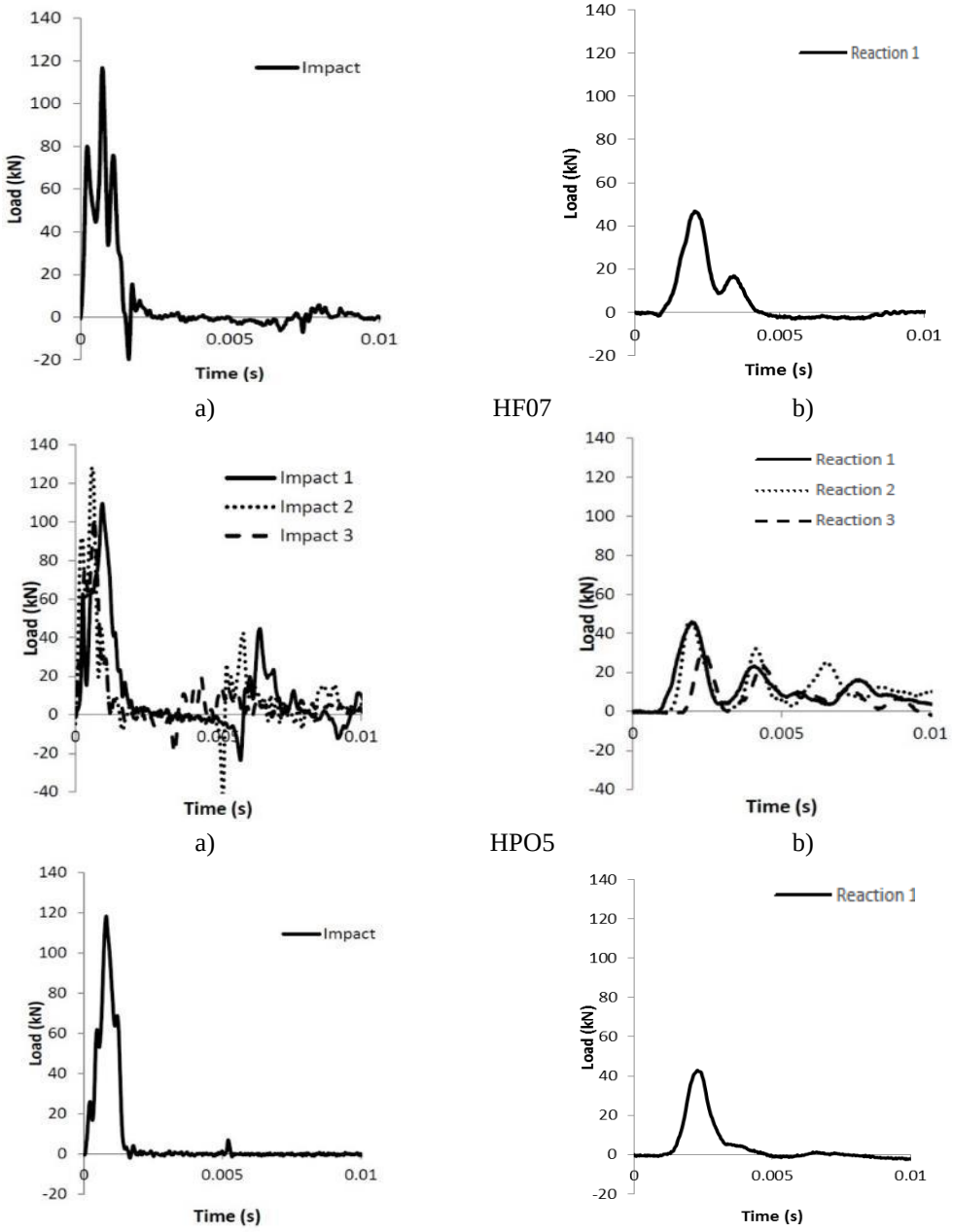

Figure 5.9: Time histories of (a) Impact and (b) Reaction forces generated when subjecting specimens with one fully (HFO) or partially (HPO) bonded layer of ECC to high intensity impact loading

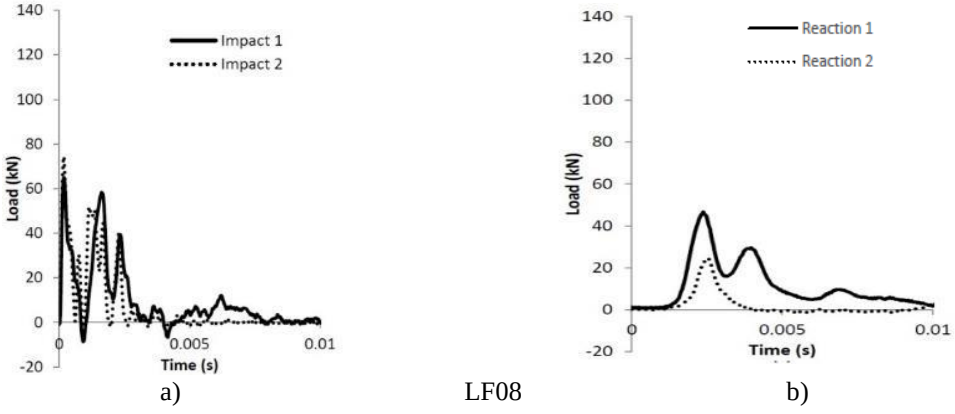

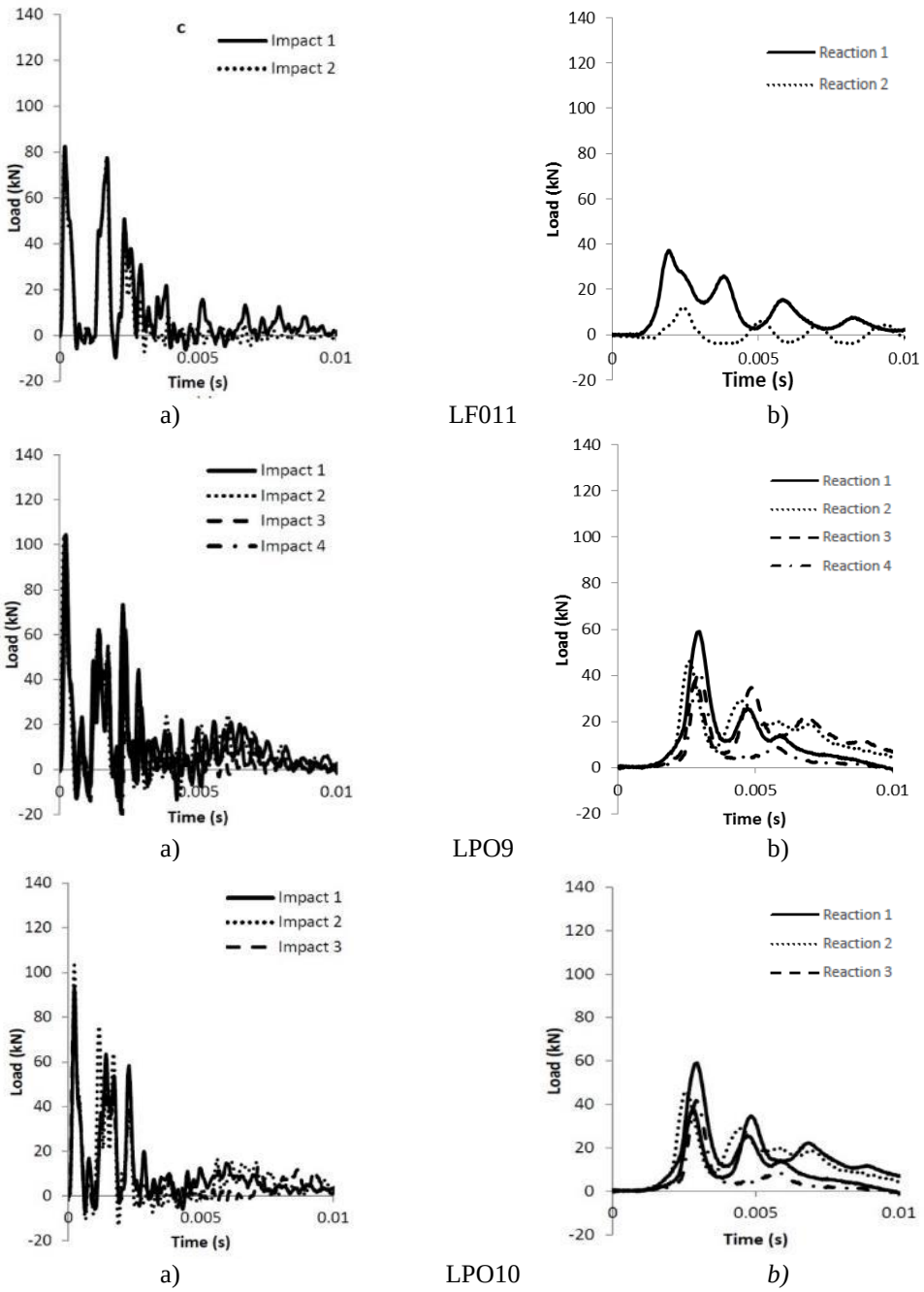

Figure 5.10. Time histories of (a) Impact and (b) Reaction forces generated when subjecting specimens with one fully (LFO) or partially (LPO) bonded layer of ECC to high intensity impact loading

The results obtained from the specimens included in the LPO series (see figures 5.10) reveal that the form of the impact load time history is characterised by multiple waves (namely 3) with one or two peaks. A maximum load of 100kN was observed which is higher than that recorded by the specimens included in the LFO series. Therefore, it is observed that the LPO series undertakes higher values of impact loading. The form of the time-history of the reaction forces developing at the supports of the LPO specimens are also characterised by multiple waves each having a single peak, the intensity of which reduces with time. It is interesting to notice that the difference between the peak values

of the impact load and the associated reaction force is lower than that established for the specimens included in the HPO series but higher than that observed in the LFO series. Furthermore, the LPO specimens are capable of undertaking a larger number of impacts (see Table 5.1) and therefore appear to be capable of absorbing the impact energy more effectively.

5.4.2 Impact and reaction force time-histories of specimens with two layers ECC

The results describing the time histories of the impact load and reaction forces generated during testing of the specimens retrofitted with two layers of ECC are presented in Figure 5.11 and their main aspects are summarised in Table 5.3. For the masonry specimens retrofitted with two fully bonded ECC layers subjected to high intensity impact loads (HFT series) the impact force (Figures 5.11) increases rapidly to a maximum value of approximately 100kN. The maximum load sustained by HFT series is about 20% less than that of the maximum load of the HFO series. Due to the presence of the ECC layer in the compression face of the specimens the form of the curve describing the time-history of the impact load is different from that recorded when conducting drop-weight test on the specimens without the ECC layer in the compression face. It is observed that the form of curves describing the time-history of the impact force is characterised by two major waves with multiple (two to five) peaks. The maximum load sustained is usually associated with the first peak of the first wave.

The time history of the reaction forces recorded from the HFT specimens is characterised by a single wave with multiple peaks (one to six), the intensity of which decreases with time. It is worth noticing that the form of the curve describing the time history of the reaction forces is different to that of their counterparts established from the HFO series. A more gradual reduction in the intensity of reaction forces with time is observed compared to the HFO series. These changes in the form of the impact loads and reaction forces can be attributed to the ECC layer in the compression face of specimens through which the impact loads are applied onto the specimen. The introduction of the ECC layer results in a more flexible impact region (as the modulus of elasticity of ECC is lower than that of the bricks) and allows a better distribution of the load onto the specimens.

As in the case of HFO series, the HFT specimens are subjected to consecutive drop tests. The intensity of the impact load (contact force) generated during each impact is similar, while the intensity of the reaction forces changes as its peak load gradually reduces with every consecutive drop-test. It is observed that the I/R ratio reduces with every consecutive drop-test. However the I/R ratio for the specimens which are presented in table 5.3 is higher compared to that established for the HFO series. This can be attributed to the lower level of damage sustained by the HFT series compared to that exhibited by the HFO specimens during each consecutive drop. It is interesting to notice that the HFT specimens exhibited a longer delay between the peak value of the impact load and the peak value of the reaction force (I-R delay) (see Table 5.3) compared to their counterparts established for the case of the HFO specimens. This can be attributed to the introduction of the second layer of ECC at the top of the specimens which appears to transfer the impact energy to masonry beams. As a result the time required for these waves to reach the supports increased when using the second layer of ECC. Furthermore, it is observed that with every consecutive impact the above delay increases due to the increasing level of sustained damage which reduces the travelling speed of the stress wave travelling from the impact region towards the supports, similar to what was observed for the case of the HFO specimens.

Figure 5.11 shows the time histories of the impact load and reaction forces measured during HPT tests. As in the case of the HFT series, the time history of the impact loads for the HPT series is characterised by two waves with multiple peaks. However the time history of the impact loads were different compared to those of the HPO series due to the addition of the top ECC layer. The maximum impact load sustained by the specimens is associated with the first peak of the second wave. It is about 100 kN as in the case of HFT series but 20% less than that recorded in the HPO series. The time history of the reaction loads recorded during the HPT series impact test is characterised by a single waves with multiple peaks, the intensity of which decreasing with time. It is interesting to notice that the case of which the reaction force reduces is smaller than that observed during both HFT and HPO series tests. Compared to HPO series the HPT specimens exhibited longer delay in I-R delay which as discussed above is due to redistribution of impact load by top layer ECC.

The results obtained from LFT series specimens are presented in Figures 5.12. It is observed that the form of the impact load time history is characterised by three major waves each characterised by several distinct peaks (two or three) with a maximum value of 90 kN, usually exhibited in the first peak of the first wave. As in the case of the HFT series, when the LFT specimens are subjected to consecutive drop-tests. The form of the curve describing the time-history of the impact load generated during each impact is similar. However, it is different compared to that recorded by the HPO series. The peak load of the specimens is 10 % more than the LFO series. The form of the curves describing the time-history of the reaction forces developing at the supports of the LFT specimens are characterised by a single wave with multiple peaks. The intensity of each peak reduces with time as in the case of HFT series. As in the case of the HFT series, similar observations in terms of reduction of the peak reaction force are made in the LFT specimens. However, it is interesting to notice that the reduction of the intensity of reaction load is more gradual compared to the LFO series which reveals a lower level of damage being sustained during testing.

It is observed that the value of I/R during first impact for the LFT series is less than that established for the LFO series. However, the reduction of the I/R ratio in the cases of consecutive impacts is far less than the LFO series which exhibit lower level of damage and cracks in the specimens. The I-R delay coefficient is same as the HFT series but greater than the HFO series due to redistribution of load in the top layer ECC.

In the case of the LPT series (see figures 5.12) the time histories of the impact load generated during the tests is characterised by multiple waves (two major waves) with multiple peaks (two or three). Usually the first peak of the first wave is associated with the maximum peak load which is about 90 kN. The maximum impact load is the same as that established in the LFT series but 10% higher than that recorded by the specimens included in the LFO series.

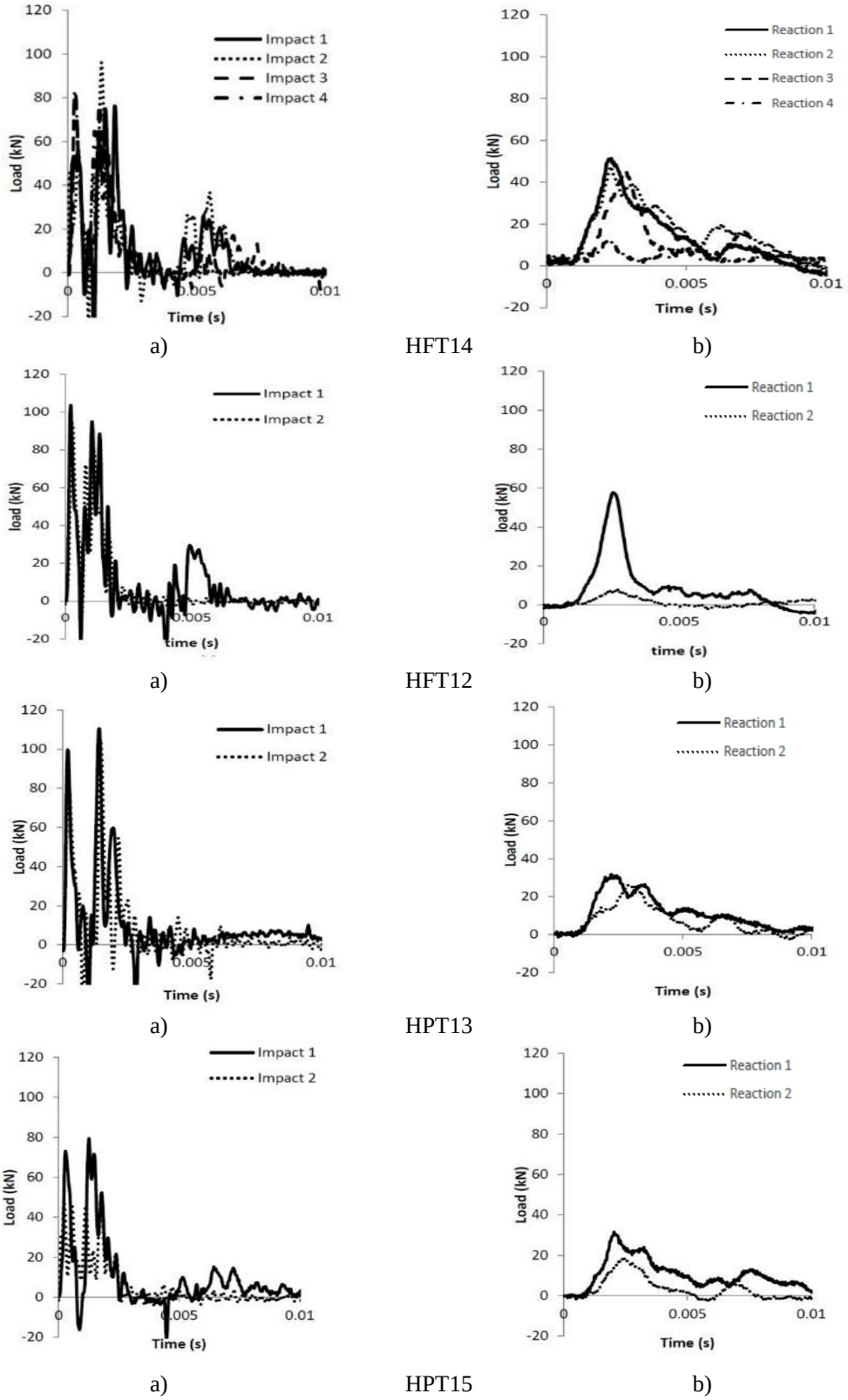

Figure 5.11 Time histories of (a) Impact and (b) Reaction forces generated when subjecting specimens with two fully (HFT) or partially (HPT) bonded layers of ECC to high intensity impact loading

The form of the time-history of the reaction forces developing at the supports of the LPT specimens are characterised by single waves with multiple peaks, the intensity of which

reduces with time. The curves describing the value of the reaction force with time is similar as that observed in the LFT series specimens but different to those recorded in LPO series due to addition of the top layer of ECC. It is interesting to notice that the R/I ratio is higher than those generated by the specimens included in the HFT series, as the LPT specimens are capable of undertaking a larger number of impacts (see Table 5.1) and absorbing the impact energy more effectively. The I-R delay in the case of the LFT series is lower than HFT series denoting a lower level of damage being sustained during testing. This also increased the capacity of specimens to undertake a larger number of impacts.

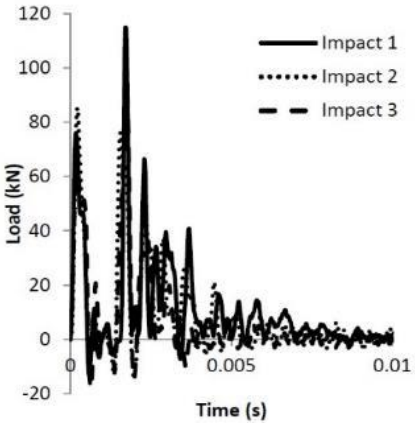

a)

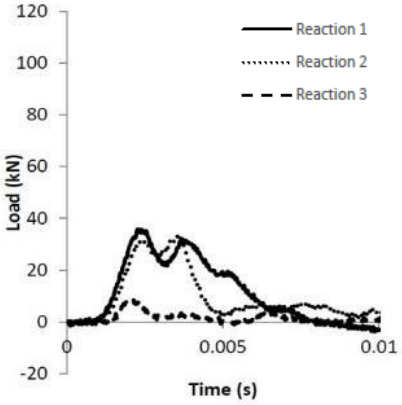

LFT16 b)

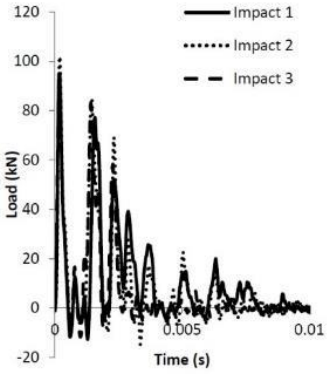

a)

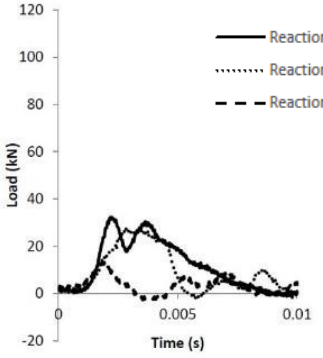

LFT21 b)

(Fig 5.12 continues to the next page)

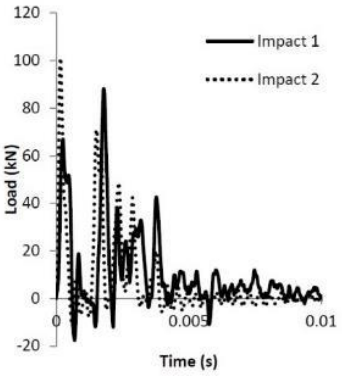

a)

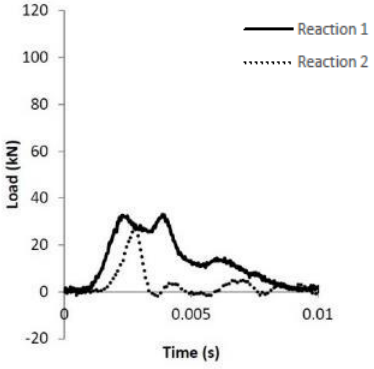

LFT19 b)

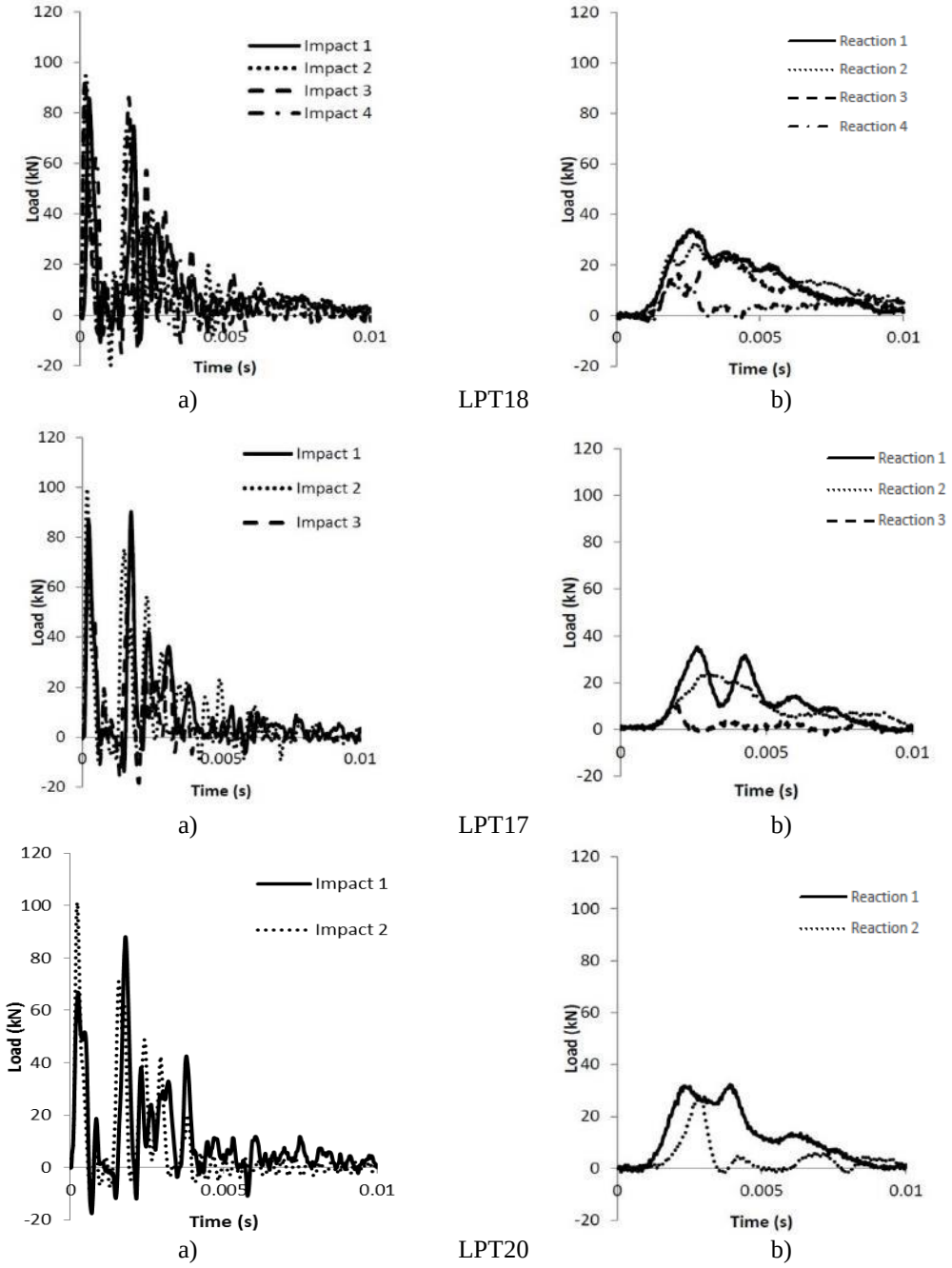

Figure 5.12 Time histories of (a) Impact and (b) Reaction forces generated when subjecting specimens with two fully (LFT) or partially (LPT) bonded layers of ECC to high intensity impact loading

5.5 Acceleration time history of the HS camera

In this section the impact load is calculated through the use of the photographic evidence recorded by the HSD camera in order to compare with the data recorded by the load cells. The photographic data can be used to compensate for the cases in which the data obtained from the accusation is missing. To achieve this the movement of the two points on the

impactor (namely point 2 and point 3, see Figure 5.7) is recorded and the acceleration time history they exhibited during testing is calculated (see Figure 5.8). For this reason the second derivative with respect to time of the vertical component of the displacement (i.e. vertical acceleration) exhibited by points 2 and 3 is calculated. The accelerations obtained from point 3 exhibited a high fluctuation due to friction between the steel mass and rail used for guiding the impactor, whereas the acceleration time history obtained from point 3 exhibited significantly less fluctuation. Therefore the acceleration time history obtained from point 2 is selected for this study.

The maximum impact load is then estimated through the use of the acceleration time histories by multiplying the acceleration peak value α_{max} with the mass of the impactor in accordance to Eq. 5.1. The total mass of the impactor m_i including the steel mass, load cell and spreader measured 47 kg.

$$F = m_i \cdot a_{max} \qquad Eq\ 5.1$$

5.5.1 Acceleration time history of specimens with one layer ECC

Figure 5.13 presents the time histories of the acceleration measured during each drop weight test conducted on the specimens retrofitted with one layer ECC. The results obtained from the HS camera records during each test, are summarised in the Table 5.2. For the case of the fully bonded specimens subjected to high intensity impact loads (HFO series) the acceleration time histories are presented in figure 5.9 increases rapidly to a maximum peak value equal to approximately 120kN (Table 5.2). It is interesting to observe that the acceleration results (obtained from the HS camera) can be used to provide estimates of the maximum impact load close to its counterparts recorded by the load cells for all drop-tests with the exception of those resulting in failure (collapse) of the specimens. In the latter cases the acceleration results underestimate the maximum value of the impact load obtained from the load cells by about 50%.

It is observed that at the time (during the loading process) at which the specimens are about to fail (collapse) the impactor's acceleration reduces to about 50% then the specimen fails instantly whereas in the rest of drop-tests (not resulting in collapse of the specimen) the motion of the specimens causes several secondary impacts between the

steel mass and the specimens. It is interesting to notice that the time-history of the acceleration is characterised by one major wave with a single peak followed by a series of secondary minor waves possibly associated with multiple contact between steel mass and specimens. It is interesting to note that when the specimens are subjected to consecutive drop tests (HFO2, HFO4) the form of the acceleration time history generated during each impact is similar apart from the last impact. As a consequence it can be suggested that during the initial collision between the impactor and the specimen the acceleration represents the impact (contact) force.

Figure 5.13 presents the time histories of the acceleration for the specimens included in the HPO series. As in the case of the fully bonded specimens, the time history of the acceleration is characterised with one major wave including one peak. The maximum impact load is associated with the peak value of the acceleration recorded and is calculated equal to 110 kN. It is interesting to observe that the acceleration results can provide predictions of the maximum impact load close to that recorded by the load cell for all drop-tests considered. However, as in the case of the HFO specimens, in the case of the drop tests resulting to failure of the specimens the acceleration calculated from the photographic evidence underestimates by about 50% the value of the maximum impact load compared to that established from the load cells. It is interesting to notice that as in the case of the HFO series, when the specimens were subjected to consecutive drop tests (HPO5) the form of the acceleration time history generated during each impact is similar apart from last drop-test resulting in the collapse of the specimen.

Figure 5.13. Time histories of acceleration exhibited by the impactor when subjecting specimens with one fully (HFO) or partially (HPO) layer ECC to high intensity impact loading

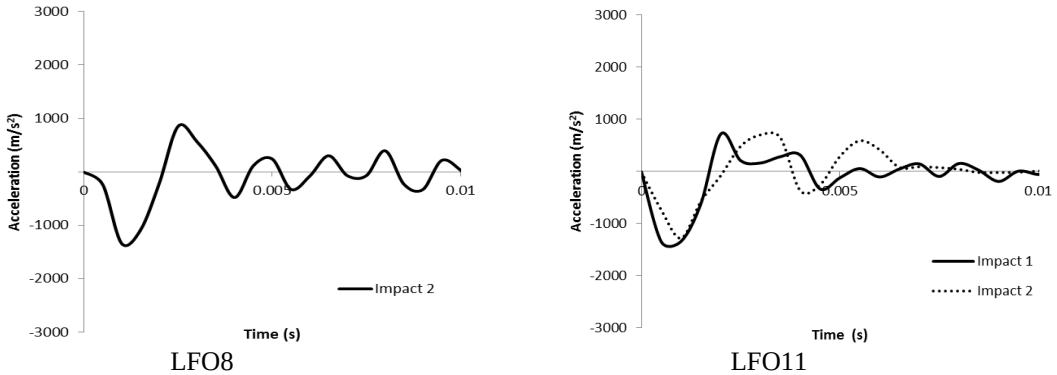

LFO8 LFO11

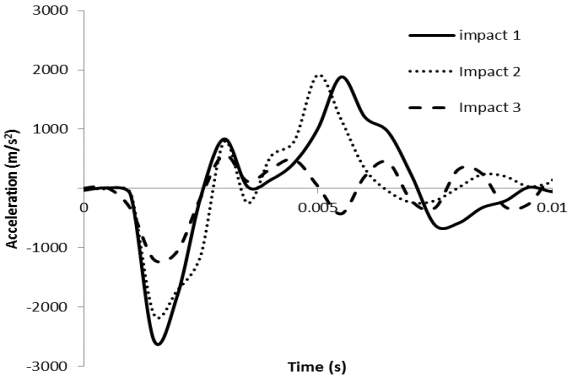

HFO4

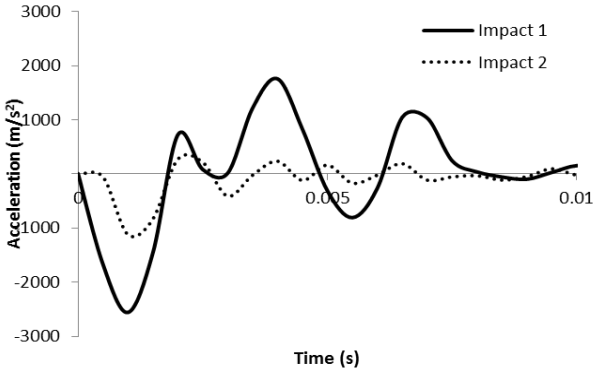

HFO2

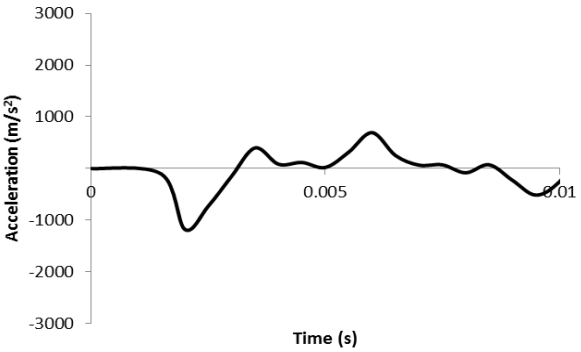

HFO7

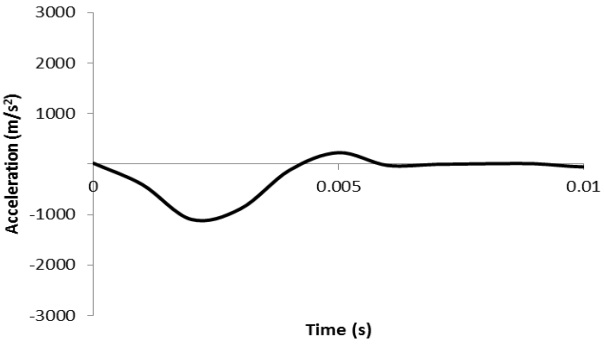

HFO1

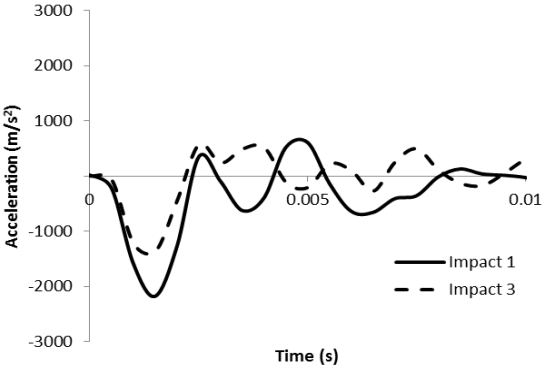

HPO5

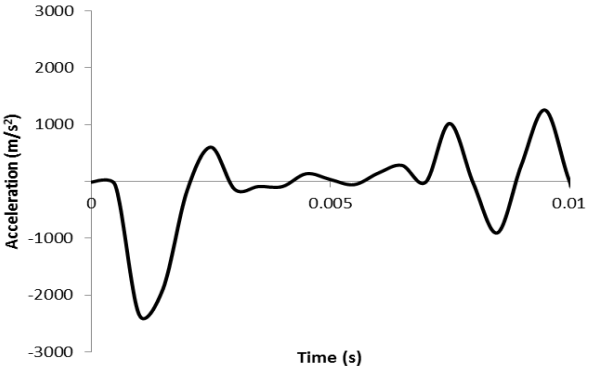

HPO6

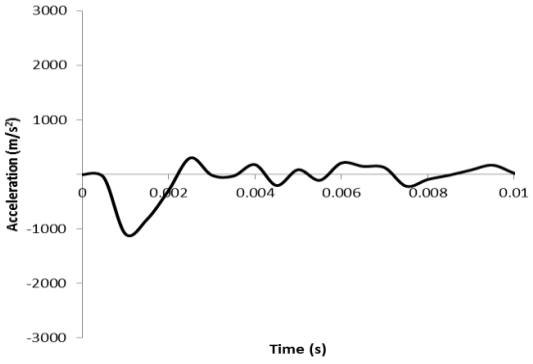

HPO3

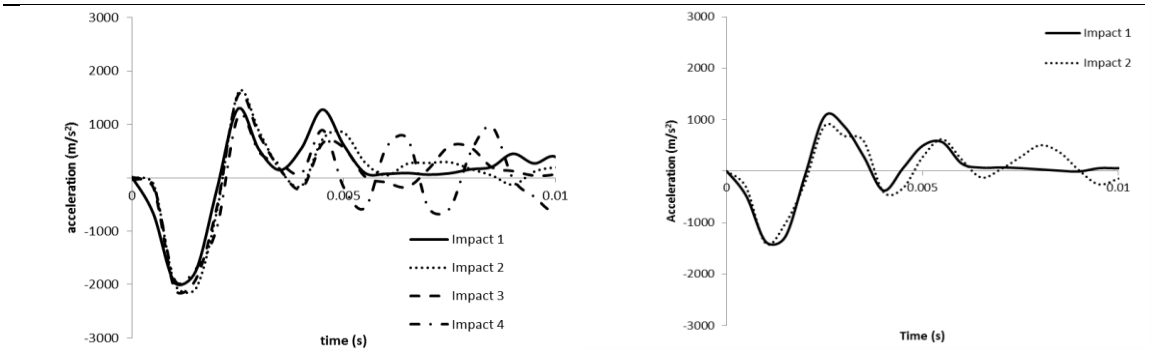

LPO9 LPO10

Figure 5.14. T Time histories of (a) Impact and (b) Reaction forces generated when subjecting specimens with one fully (LFO) or of partially (LPO) layer ECC to low intensity impact loading

Figure 5.14 demonstrates histories of the acceleration for the LFO series. As in the case of the fully bonded specimens, the acceleration time histories calculated from the photographic evidence are characterised by one major wave including one peak. The maximum impact load is associated with the peak value of the acceleration time history and its value is determined to be about 110 kN. It is interesting to observe that the acceleration results can provide estimates of maximum impact loading close to that recorded by the load cell for all drop-tests considered. However, as in the case of the HFO specimens the drop-tests resulting in failure (collapse) of the specimens underestimate by about 50% the value of the maximum impact load established by the load cells. It is interesting to notice that as in the case of the LFO specimens, when the specimens are subjected to consecutive drop tests (LFO11) the form of the acceleration time history generated during each impact is similar apart from last drop test resulting in the collapse of the specimen.

The results obtained from the specimens included in LPO series (see figures 5.14) reveals that the form of the acceleration time history is characterised by one major wave with one peak and a maximum value equivalent to approximately 60 kN. As in the case of the fully bonded specimens, the time history of the acceleration is characterised with one major wave including one peak. The maximum impact load is associated with the peak value of the acceleration recorded and is calculated equal to 95 kN. It is interesting to observe that the acceleration results underestimate the maximum impact load by 25% compared to that recorded by the load cell for all drop-tests considered. It is interesting to notice that as in the case of the LPO series, when the specimens were subjected to consecutive drop tests (LPO9) the form of the acceleration time history generated during each impact is close in all cases.

5.5.2 Acceleration time history of specimens with two layers ECC

To measure the acceleration time history of the impactor and use this to calculate the impact load imposed onto the specimen the same strategy employed in the section 5.5.1 is used herein. The acceleration is measured at point 2 (see Figure 5.8) and the total weight of the impactor was 47kg. The acceleration time histories calculated from the photographic evidence from each drop tests conducted on the specimens retrofitted with two layers ECC are presented in Figure 5.15 and summarised in the Table 5.3. For the case of the specimens with fully bonded layers of ECC subjected to high intensity impact loads (HFT series) the acceleration records are presented in Figure 5.15 increases rapidly to a maximum peak value of acceleration which when multiplied by the mass of the impactor is equivalent to a maximum peak load of approximately 100kN. It is observed that the acceleration time-history is characterised by one major wave with a single peak. It is interesting to note that when the specimens are subjected to consecutive drop tests the form of the acceleration time histories calculated during each drop-test (apart from those resulting in collapse of the specimens) are similar. However, the values of the maximum impact load calculated from the acceleration surpass that established from the load cells by up to 25%. The predicted results for the maximum load of the HFT specimens is about 35% less than the HFO series when subjected to the same loading conditions which is in agreement to its counterpart established from the load cells which reveal a reduction of about 30%.

Figure 5.15 shows the acceleration time histories measured in the case of the HPT specimens. The maximum peak load and equivalent load are summarised in Table 5.3. As in the case of the HFT specimens the time history of acceleration is characterised by one wave with one peak. The maximum impact load calculated based on the peak value of the acceleration is about 85 kN. It is interesting to notice that the latter value is close to that recorded by the load cells for all drop-tests considered which is about 80 kN. It is also interesting to note that as in the case of the HFO series, when the HPT specimens were subjected to consecutive drop tests the form of the acceleration time history generated during each impact is similar apart from the last drop-test resulting in the collapse of the specimen.

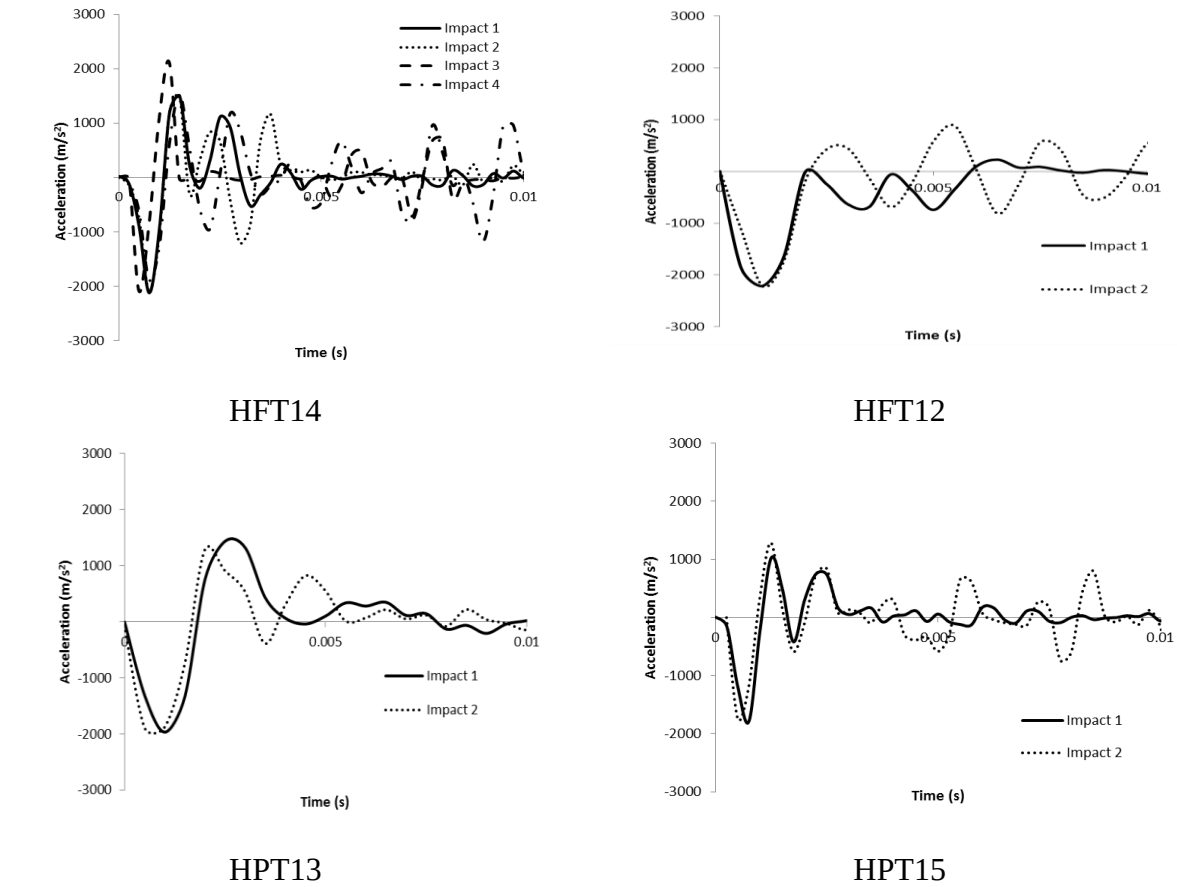

Figure 5.15. Time histories of acceleration generated when subjecting specimens with two fully (HFT) or partially (HPT) bonded layers ECC to high intensity impact loading

The curves describing the acceleration time histories obtained from the LFT specimens are presented in Figure 5.16 and their main aspects are summarised in Table 5.4. It is observed that the form of the acceleration time histories is characterised by one major wave including one distinct peak with a maximum value equivalent equal to approximately 100 kN. It is observed that the difference between the calculated value of the maximum impact load and that established from the load cells is about 10%. As in the case of the HFT specimens, when the LFT specimens are subjected to consecutive drop tests the form of the acceleration time history generated during each impact is similar.

The acceleration time histories established for the case of the LPO specimens (see Figures 5.12) are characterised by multiple (two or three) waves with a single peak. The peak acceleration value of the first wave is associated with the maximum impact load which is equivalent to approximately 100 kN (see Table 5.4). The maximum calculated load is the same as that recorded by the specimens included in the LFT series. However, the

calculated maximum impact load is 10 % higher compared to that established by the load-cells.

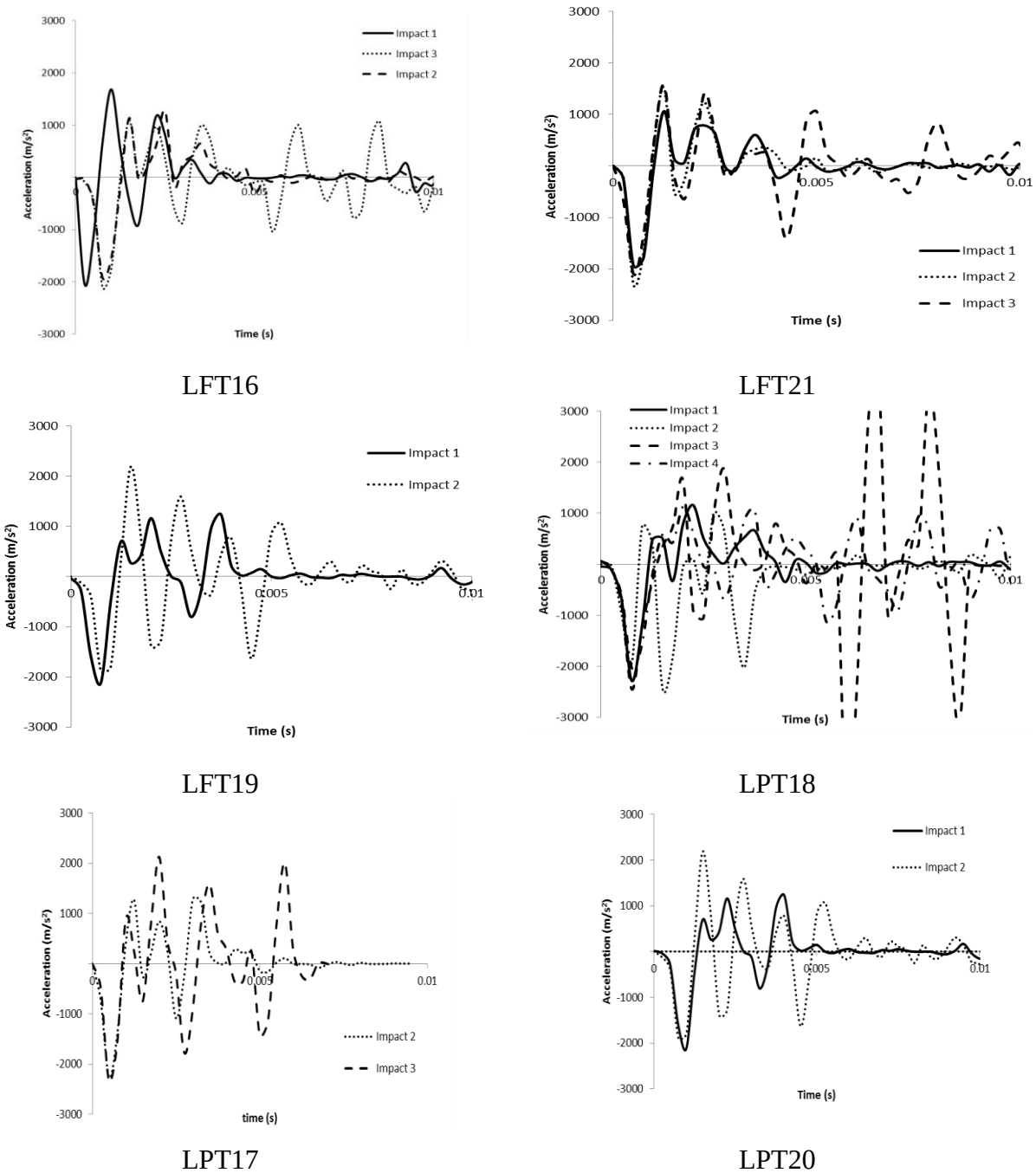

Figure 5.16. Time histories of (a) Impact and (b) Reaction forces generated when subjecting specimens with two fully (LFT) or partially (LPT) bonded layers of ECC to low intensity impact loading

5.6 Displacement time history obtained from HS camera

The vertical displacement exhibited at the mid-span region of the specimens is recorded through the use of the HS camera. Emphasis is focused on points $P_{1.17}$ and $P_{1.18}$ which are

located in the middle of tensile face of the ECC layer (see Figure 5.7). On the basis of the time histories established the maximum and residual values of the displacement are established. However, for the case of the drop test resulting in the failure (collapse) of specimens these values could not be established.

5.6.1 Displacement time history of specimens with one layer ECC

Figures 5.17 shows the displacement time histories measured during testing of the specimens retrofitted with one layer ECC under high intensity impact loading. The results obtained from the HS camera records during the tests are summarised in the Table 5.2. For the case of the fully bonded specimens subjected to high intensity impact loads (HFO series) the deflection time history is presented in Figure 5.17. The maximum deflection is 3.5 mm to 10 mm and then reduces by 5% to 30% and stabilises at 3.5mm to 6.5 mm (Table 5.2). However, for impacts resulting in failure of the specimens the displacement continuously increased due to the collapse of the specimen. The difference between the peak and residual deflection represents the flexible behaviour of the specimens under impact load. It is interesting to observe that in the case of the specimens subjected to consecutive drop-tests the gradient of history of displacement is similar. This is associated with the property of ECC layer which can absorb energy of impacts without sustaining permanent damage.

Figure 5.17 demonstrates histories of the displacement for the HPO series and is summarised in Table 5.2. The time history of displacement which is available for one consecutive impact characterised with a rapid increase to maximum deflection of about 3.8 mm and then stabilised at 1.1 mm which represent a 70% reduction of deflection. It is interesting to notice that the specimens exhibited 250% more reduction of residual deflection compared to the HFO series. This fact reveals that the ECC layer ductile capacity is employed more effectively in the partially bonded specimens compared to the fully bonded counterparts. Similar to the HFO series the specimens subjected to consecutive impacts- which represent the same form of impact load- exhibited the close gradient in displacement time-history curves which represent the specimen’s ability to absorb the multiple impacts without sustaining damages or localized cracks.

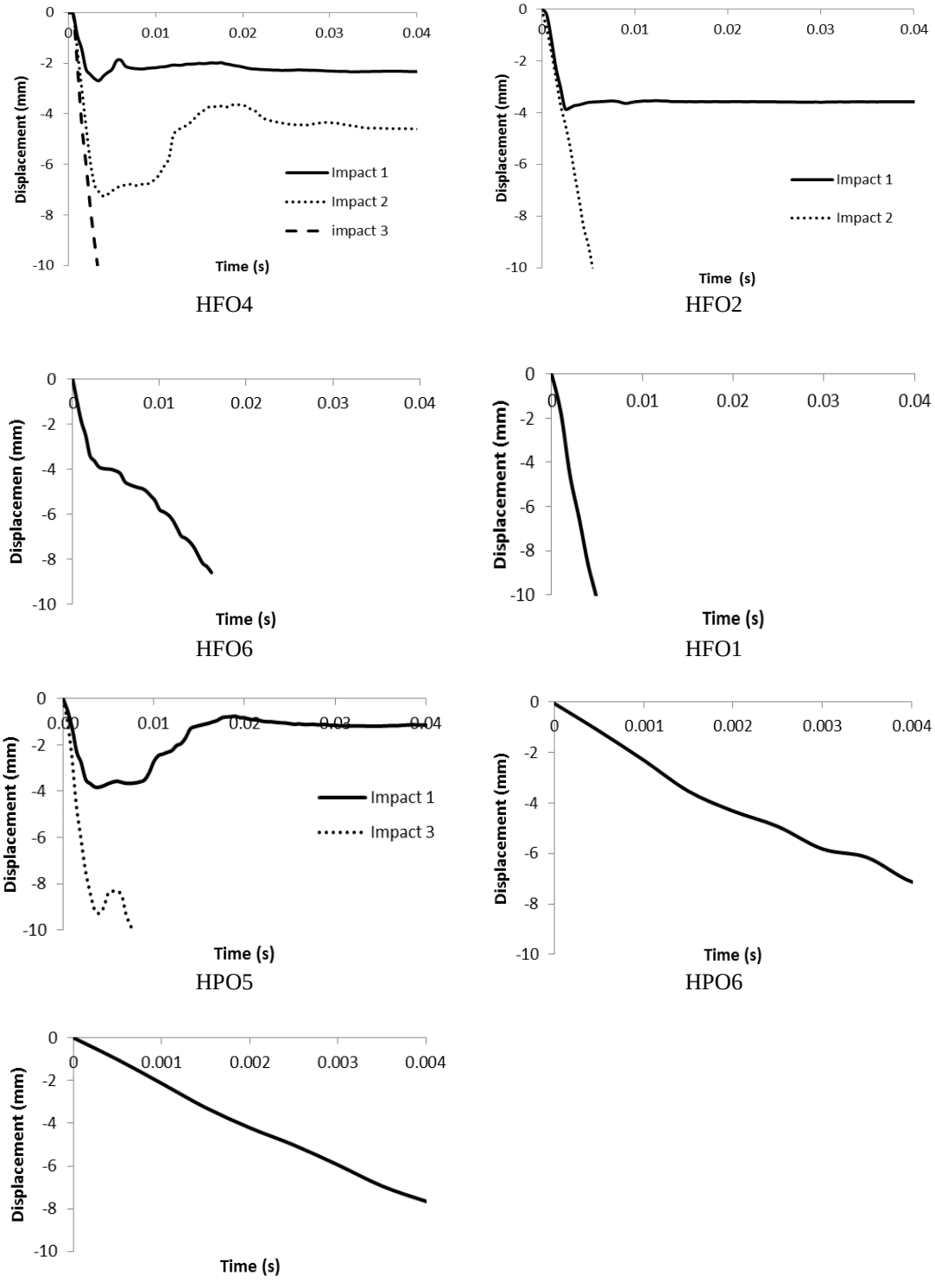

Figure 5.17. Displacement time histories established for the case of specimens strengthened with a fully (HFO) and partially (HPO) bonded layer of ECC under high intensity impact loading

The curves describing the time histories of the deflection measured while conducting drop-weight tests on the LFO specimens are presented in Figure 5.18 whereas their main aspects (i.e. maximum and residual value of displacement) are summarised in Table 5.2.

These curves show that the deflection increases rapidly to a maximum peak value approximately equal to 2.5 mm which then reduces by only about 5% finally stabilising at 2.39mm (Table 5.2). This reduction is associated to the level of damage (extent of cracking) sustained by the specimens. It is observed that the specimens (LFO11) subjected to consecutive impacts the form of the curves describing the displacement time-history are similar to each other same in the case of the HFO series.

Figure 5.18 shows the displacement time histories established for the case of the LPO specimens and the main aspects (the maximum and residual values of the displacement) of these curves are summarised in Table 5.2. From these curves it is observed that the displacement increases rapidly to a maximum value between 8.5 and 11.5 mm and then reduces, stabilising at a value (residual value) of 4 mm resulting in a reduction of deflection of up to 65% of the maximum value. It is interesting to notice that as in the case of the HPO series, that the residual displacement established after drop-weight testing is approximately 70% less compared to the peak value. Additionally, the LPO series exhibited lower values of residual displacement compared to that established for the case of the LFO series. This suggests that the LPO specimens are capable of sustaining less damage while more effectively absorbing impact energy and exhibited a higher level of structural integrity compared to their LFO counterparts. As in the case of the LFO specimens, when the LPO specimens are subjected to consecutive drop tests the gradient of the displacement time-history curves increased after each impact which is associated with development/extension of cracking in the specimens. Table 5.1 shows that that the LPO specimens could tolerate on average three impacts compared to the LFO series which could tolerate on average two impacts.

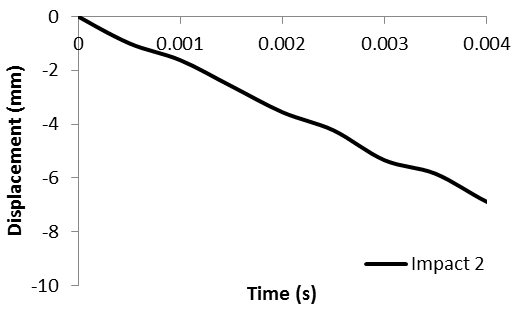

LFO8

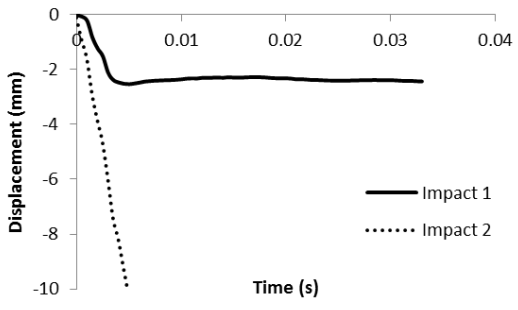

LFO11

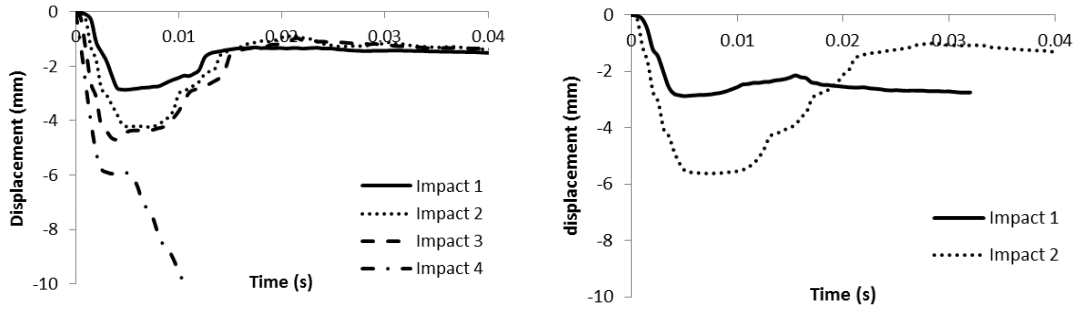

LPO9 LPO10

Figure 5.18. Displacement time histories established for the case of specimens strengthened with a fully (LFO) and partially (LPO) bonded layer of ECC under low intensity impact loading

5.6.2 Displacement time history of specimens with two layers ECC

The same methodology adopted in section 5.6.1 is used herein to calculate the deflection of the specimens retrofitted with two layers of ECC. Emphasis is focused on establishing the average displacement of points $P_{1.17}$ and $P_{1.18}$ (see Figure 5.7) on the side surface of the specimens. The curves describing the displacement time histories obtained from the HFT specimens are presented in Figure 5.19 and the main aspects of these curves are summarised in the Table 5.4. These curves reveal a rapid increase of displacement to a peak value in the range of 3 to 6.5 mm. The displacement then reduces finally stabilising at 2.81 to 5.5 mm which represents a 10% reduction in displacement in relation to the peak value (see Table 5.2) which is within the range of values calculated for the HFO series (5%-30%). It is interesting to observe that the specimens subjected to consecutive impacts the gradient of the displacement time history curves increases after each impact which represents the level of damages sustained by specimens.

Figure 5.19 shows the curves describing the displacement time histories obtained from drop-weight tests conducted on HPT specimens whereas the main aspects of these curves are summarised in Table 5.3. The displacement time histories reveal a rapid increase in displacement to maximum value ranging between 3.2 to 4.2 mm followed by a 10% reduction and ultimately stabilising at 2.7 to 4.2 mm (residual displacement). It is interesting to notice that the specimens exhibited the same level of reduction in deflection compared to that established in the case of the HFT specimens. However, this reduction was lower than that of the HPO series. The HPT specimens subjected to consecutive impacts exhibited similar displacement time-history curves.

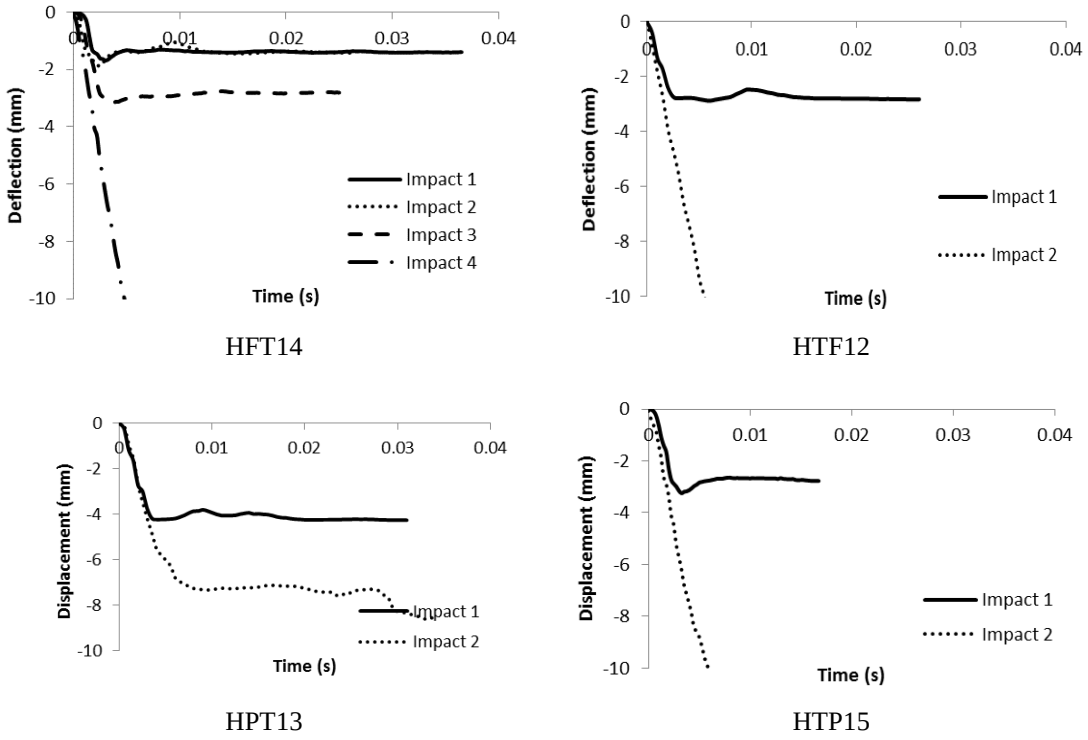

Figure 5.19 Displacement time histories obtained from specimens strengthened with fully (HFT) and partially (HPT) bonded layers of ECC subjected to high intensity impact loading

Figure 5.20 presents the curves describing the displacement time histories obtained from drop-weight tests conducted on LFT specimens and the main aspects of these curves are summarised in Table 5.4. Based on the form of these curves it is observed that the displacement increases rapidly reaching a maximum value in the range of 1.5 to 6 mm then reducing by about 10%, ultimately stabilised at a value of 1.4 to 5.5 mm (residual displacement). As in the case of the HFT series, LFT specimens exhibited a 10% reduction after attaining the maximum deflection, however this reduction is higher than that exhibited by the LFO series. It is observed that the specimens subjected to consecutive impacts exhibit similar displacement time-histories.

The results obtained from the LPT series (see Figure 5.20) exhibited displacement time histories characterised by a rapid increase to maximum value approximately equal between 2 and 12 mm then reducing by 10% to 20% and finally stabilising at 1.5 to 10 mm (residual displacement). The observed reduction in displacement is less than that established for the case of the LPO series whereas it is significantly higher than that recorded in the case of the LFT series. It is observed that specimens subjected to

consecutive impacts exhibited similar displacement time histories and were able to consistently withstand an average of 3 impacts (see Table 5.1).

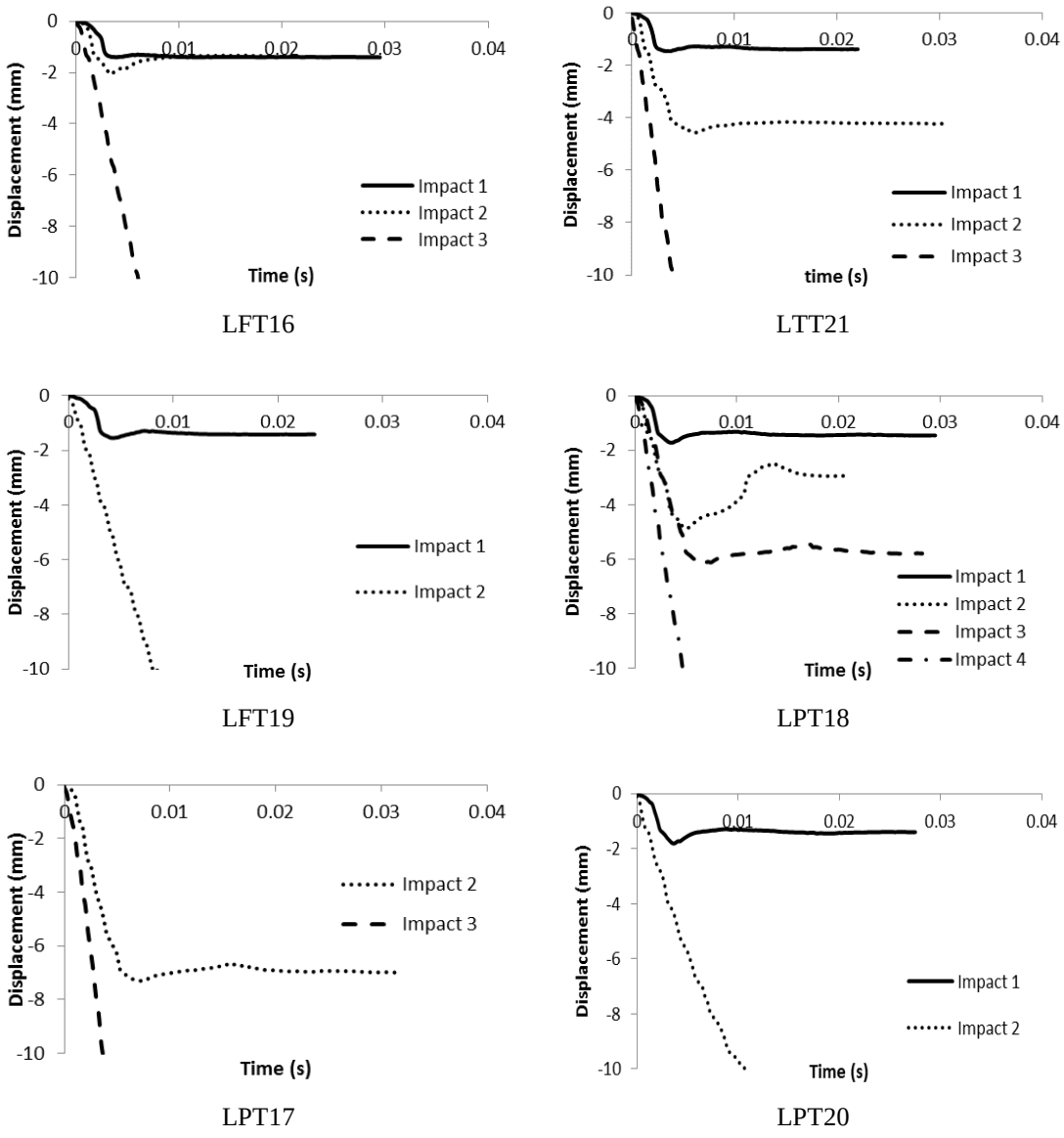

Figure 5.20. Displacement time histories obtained from specimens strengthened with fully (LFT) and partially (LPT) bonded layers of ECC subjected to low intensity impact loading

5.7 Strain and strain rate history obtained from the high speed camera

The strain time history exhibited at certain locations of the specimens are established on the basis of the displacement data obtained from the HS camera. It is observed that the distribution of strain in the ECC layer located in tensile face can provide significant information concerning the general performance of the specimens. Therefore, the strain time history exhibited at 3 critical regions of the ECC layer is investigated. These regions

include: (i) the area beneath the joints between the bricks (brick-mortar interface), (ii) the area beneath the bricks and (iii) the area at which failure occurs in the ECC layer. To calculate the strain in these three regions the horizontal displacement between different neighbouring points presented in Figure 5.7 are investigated. It was assessed that that the best points that can represent the strain distribution in the ECC layer beneath the joints (brick-mortar interface) located between point between points $P_{1.15}$ and $P_{1.16}$ (see Figure 5.7). The strain is calculated as the ratio between relative horizontal displacement (ΔL) between the latter two points divided by their initial distance which was 20 mm (see Eq2).

$$\varepsilon = \frac{\Delta L}{L} \qquad \text{Eq 5.2}$$

The strain of the ECC layer beneath the brick is investigated and points $P_{1.17}$ and $P_{1.18}$ are selected to represent the ECC-brick region. The strain time history is calculated in the same manner as that employed for points $P_{1.15}$ and $P_{1.16}$ (see Figure 5.7). Finally, the strain of the region at which failure ultimately occurs is calculated at different points as the ECC layer failed in different places usually within the central span (see Section 5.8). Therefore for each case considered the relative horizontal displacement of two points in either side of the plain of the crack resulting in failure of the ECC layer is studied. The strain is calculated in same fashion which explained for points $P_{1.15}$ and $P_{1.16.}$

As ECC has exhibited a strain rate sensitive behaviour when subjected to different loading rates (see section 3.2.5) the strain rate of the three regions mentioned above are investigated. For this reason the slope of strain time history is calculated in accordance to Eq.3.

$$\frac{d\varepsilon}{dt} = \frac{\varepsilon_2 - \varepsilon_1}{t_2 - t_1} \qquad \text{Eq 5.3}$$

The maximum values of strain and strain rate for all regions considered are summarised in the Table 5.2. However, in the case of drop-weight tests resulting in the failure of the specimens the maximum strain at the failure point could not be calculated.

For the specimens retrofitted with two layers ECC the strain and strain rate of the ECC layer at the lower face of the specimens are calculated in the same manner described earlier. Then the strain in the top ECC layer is calculated for the same areas (cross-

sections) for which strain and strain rate were calculated in the bottom ECC layer. Therefore, for region beneath the joints (brick-mortar interface) and beneath the bricks between points $P_{5.15}$ and $P_{5.16}$ (see figure 5.7) as well as $P_{5.17}$ and $P_{5.18}$ selected respectively. Furthermore, for regions at which failure ultimately occurs two points in the top ECC layer corresponding to points on either side of the cross-section at which the plain of the crack resulting in failure of the bottom ECC layer are selected. The rest of the calculations are the same to those conducted for the bottom ECC layer. The maximum values of strain and strain rate are summarised in the Tables 5.3 and 5.4. As in the previous part, in the case of drop-weight tests resulting in the failure of the specimens the maximum strain at the failure point could not be calculated.

Figure 5.21 shows the terminology that is used to name the strain and strain rate figures presented in this chapter. The first number presents the number of impact load. The next letter presents the locations with which the strain and strain rates calculated correspond to, the ECC layer attached to the bottom face of the specimens (acting in tension) is represented by T whereas the ECC layer at the top of the specimens (acting in compression) is represented by C. The last letter is left blank for when calculating strains whereas the letter R is used when calculating strain rates

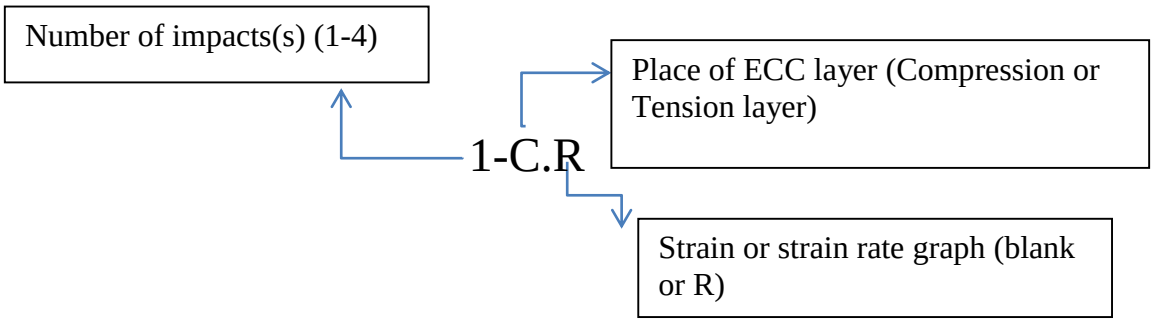

Figure 5.21. Terminology used to name the strain and strain rate graphs in the following section

5.7.1 Strain and strain rate time history of specimens with one layer ECC

Figures 5.22 presents the curves describing the time histories of the strain and strain rate exhibited during drop-weight testing of specimens retrofitted with one layer ECC. The results obtained from HSD camera during the tests and are summarised in the Table 5.2. For the case of the specimens strengthened by a fully bonded ECC layer and subjected to high intensity impact loads (HFO series) the strain in the joint region increases rapidly to a maximum peak value of approximately 2%. It is interesting to notice that the curve describing the time-history of the strain is characterised by one major wave with multiple

(up to 5 peaks) peaks. The maximum value of strain is usually associated with the middle peak of the wave. It is interesting to notice that the form of the curve describing the strain time history is similar to that observed by the curves describing the variation of the impact loads with time (see Section 5.4.1). It is interesting to notice that several cracks in the joint region were observed during impact testing (Section 5.8). The strain rate in this region reached values of up to $20s^{-1}$ during the tests.

For the curve describing the variation of strain with time in the failure region of the specimens was characterised by a single wave with one peak. The strain in the failure region of the specimens developed with the same gradient as that exhibited in the joint region. However, with every consecutive impact the strain in the failure region increased (up to 8%) before the specimen finally collapsed while level of strain in other regions of the ECC layer remained almost the same. The strain rate in this region reached $120s^{-1}$ during testing. In the ECC region beneath the brick the values of strain calculated were very small. It is interesting to note that no cracking developed in this region of the specimens. The strain rate in this area region was also very small.

Figure 5.22 presents the curves describing the time histories of the strains and strain rates exhibited by the HPO specimens. As in the case of the specimens with the fully bonded layer of ECC the form of the curve describing the variation with time of strain in the joint region is characterised by one major wave with multiple peaks which is the same as the time history curves of impact loads applied on the specimens. The maximum value of strain is associated with the middle peak of the wave and is equal to about 1%. The strain rate of specimens reached a maximum value of $15s^{-1}$.

The curve describing the variation of strain with time in the failure region of specimens is characterized by a single wave with multiple peaks. It is interesting to see the strain-rate in the failure region of specimens was higher compared to that observed at the joint region. When subjecting the specimens to consecutive impact the strain in the failure region increased (by approximately 6%) with every impact before collapse. At the same time the level of strain in other regions of ECC layer remained almost the same. The strain rate in failure region reached to $78s^{-1}$ during the tests.

In the ECC region beneath the brick the strain time history was characterised by a single wave with multiple peaks and a maximum value of about 1%. It is interesting to see the strain time history in the ECC layer below the bricks was similar to that associated with the joint region. The maximum strain rate of specimens ECC-brick region was about $20s^{-1}$. It is interesting to note that the maximum values of strain in both the joint and failure regions is less than those established during the tests conducted on the HFO specimens (about 100% and 25% respectively) whereas the maximum strain values in the brick region remained essentially the same (about 1%). This suggests that the strain distribution in the unbonded region of the ECC layer in the HPO specimens is more uniform than in the fully bonded ECC layer of the HFO specimens thus suggesting that the cracking sustained in the ECC layer of the HPO specimens is more distributed. Also the maximum strain rate exhibited by the HPO specimens is lower than that exhibited by the HFO series (see Table 5.2) which reduced the likelihood of the HPO specimens exhibiting sudden (brittle) failure. As a result the HFO specimens appear to be able to undertake the applied impact load more effectively.

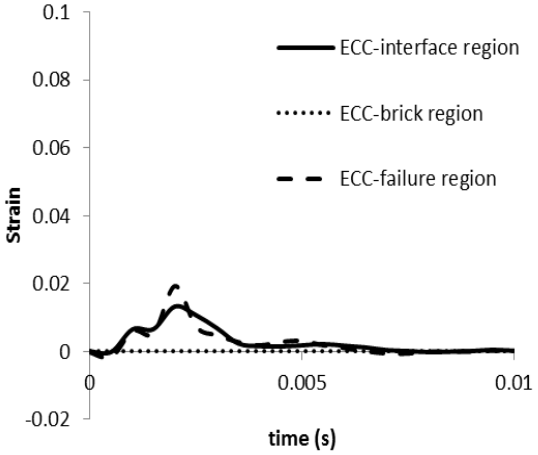

1T, HFO4

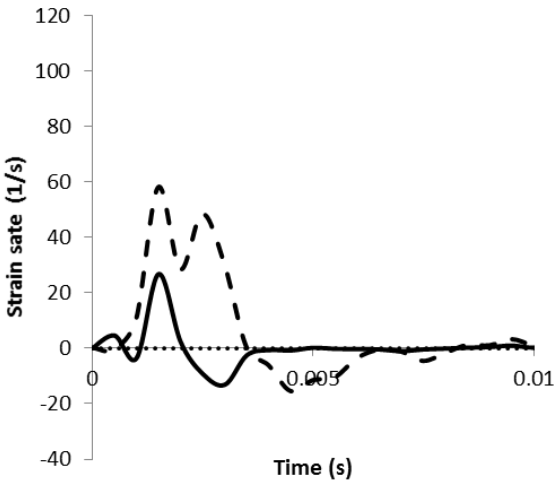

1TR, HFO4

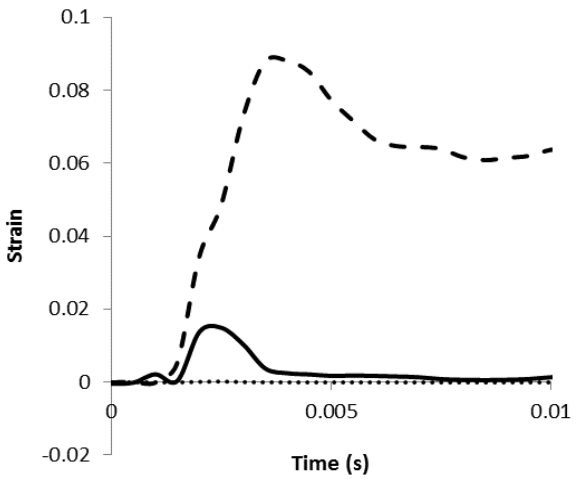

2T, HFO4

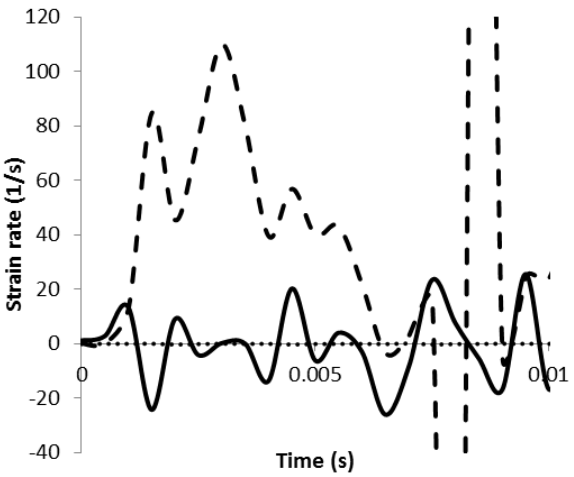

2TR, HFO4

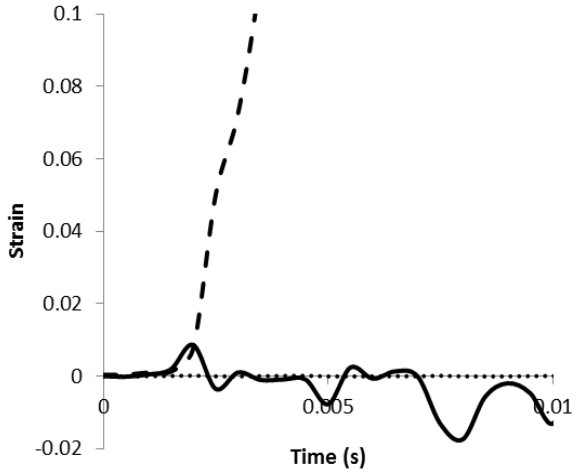

3T, HFO4

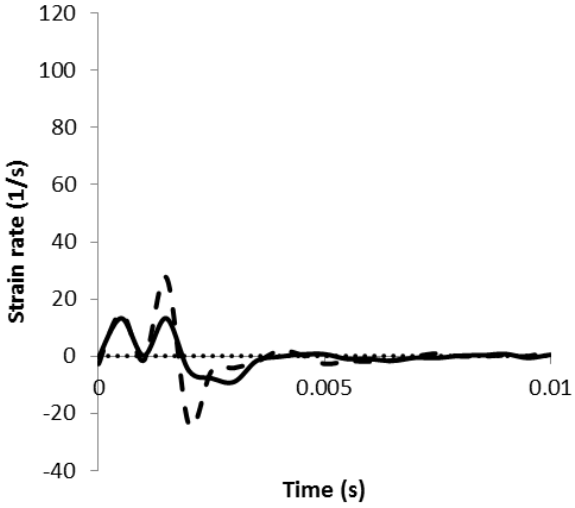

3TR, HFO4

HFO4

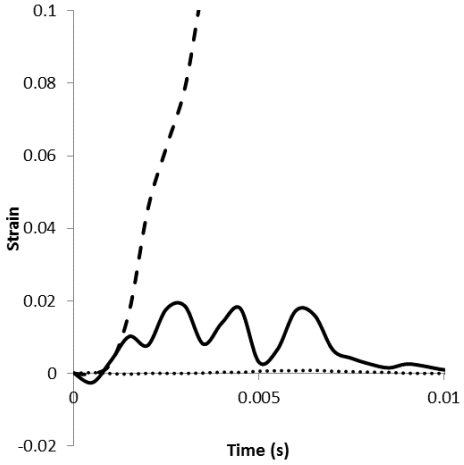

1T, HFO2

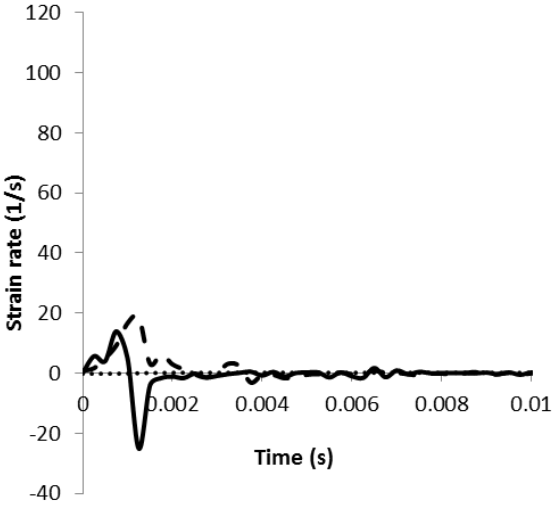

1TR, HFO2

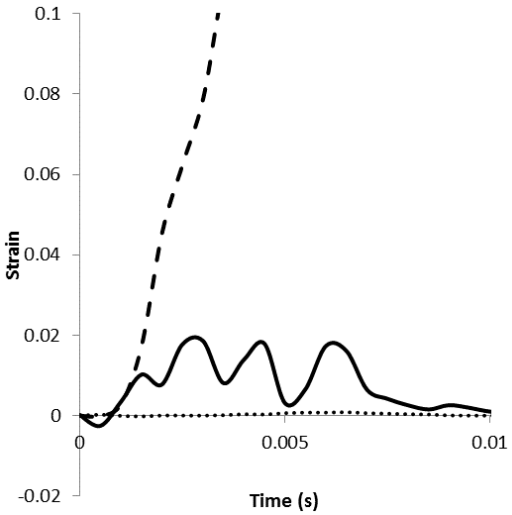

2T, HFO2

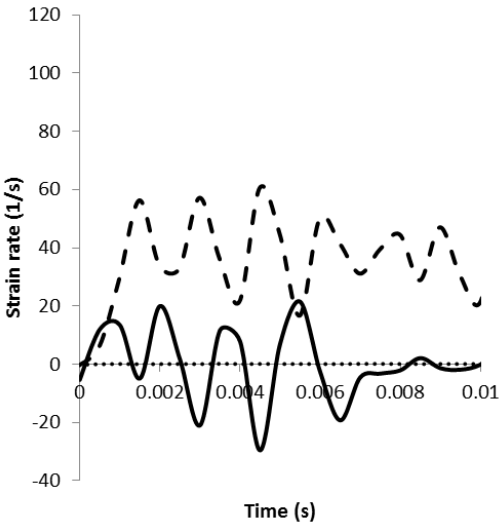

2TR, HFO2

HFO2

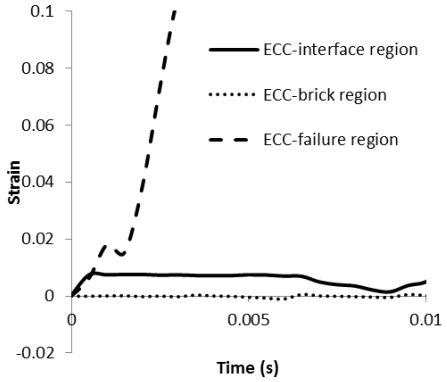

1T, HFO7

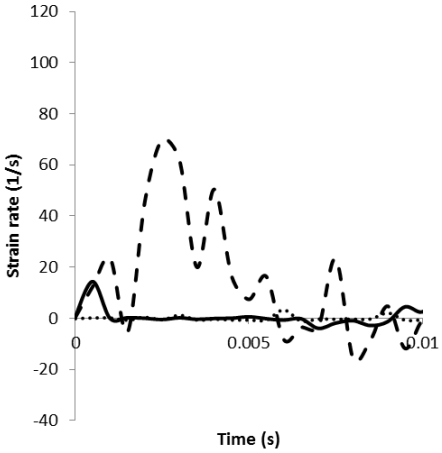

1TR, HFO7

HFO7

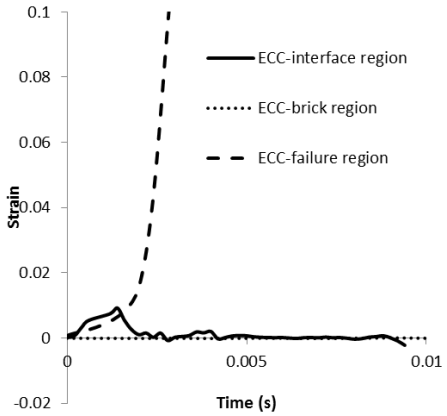

1T, HFO1

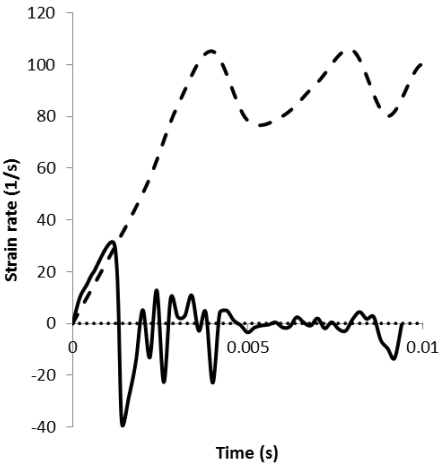

1TR, HFO1

HFO1

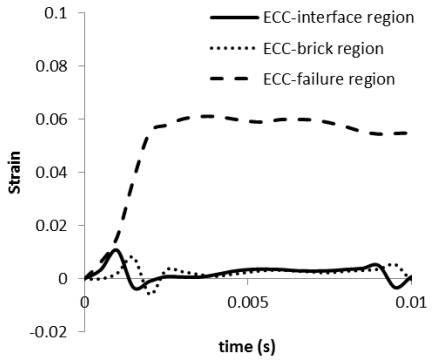

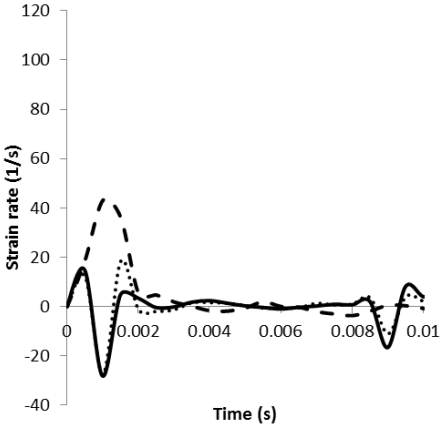

1T, HPO5 1TR, HPO5

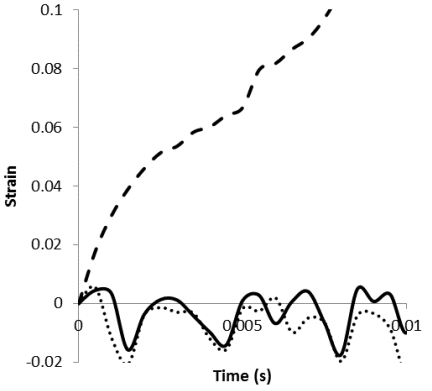

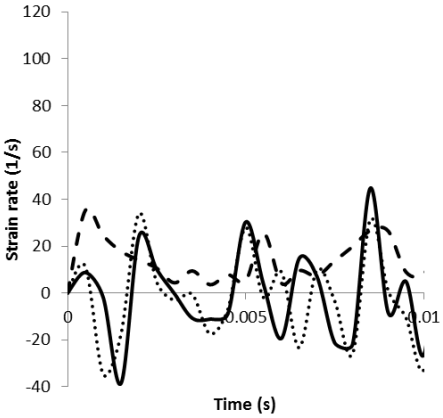

2T, HPO5 2TR, HPO5

HPO5

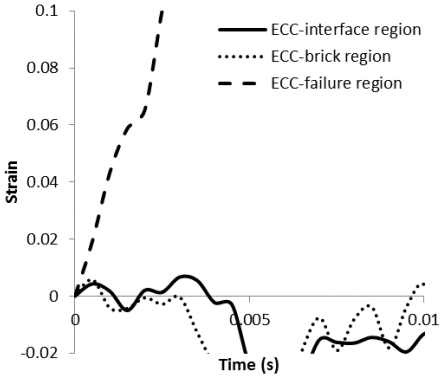

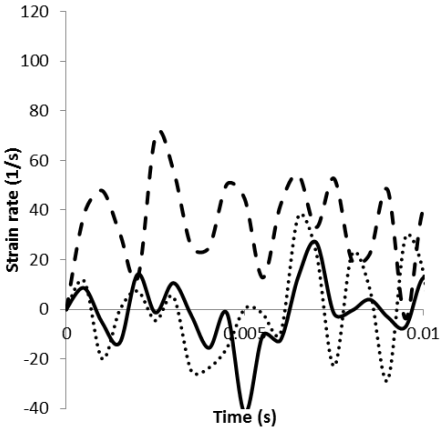

1T, HFO6 1TR, HFO6

HFO6

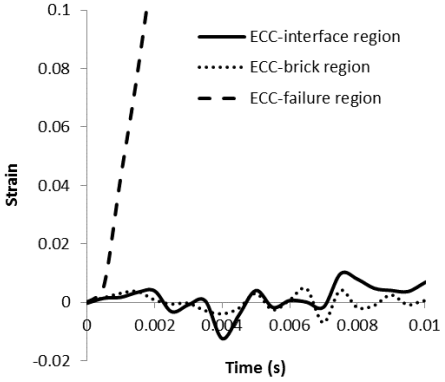

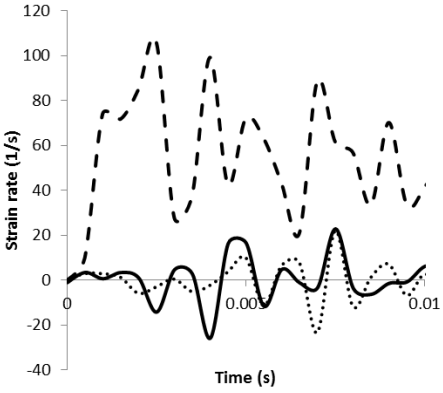

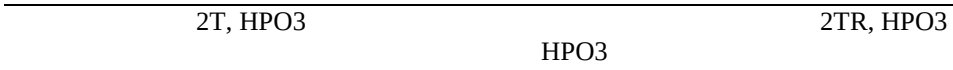

Figure 5.22. Strain (T) and strain rate (TR) time histories obtained from specimens strengthened with fully (HFO) and partially (HPO) bonded layer of ECC subjected to high intensity impact loading

Figures 5.23 shows the curves describing the time histories of the strain and strain rate of LFO specimens with their main aspects being summarised in the Table 5.2. For the LFO series the curves associated with strain in the joint region are characterised by multiple waves with multiple peaks with the middle peak of the first wave being associated to the maximum strain value (approximately 1%). It is interesting to note that the form of the curve describing the strain time history is similar to the curve describing the variation of impact loading with time (see Section 5.4.1). The strain rate in this region reached a maximum value of $10s^{-1}$ during the tests.

The curve describing the variation of strain with time in the failure region of the specimens is characterised by a single wave with multiple peaks of up to 3.5%. It is interesting to notice that, as in the case of the HFO series, the strain curves for the failure region of the specimens are similar (in terms of gradient) to those associated with the interface region until the peak strain value of the latter region is attained. The strain rate in the failure region reached a peak value of $120s^{-1}$ during testing. It is interesting to notice that the strain and strain rate exhibited by the ECC in the region beneath the brick were very small (as in the case of the HFO series).

The time histories of the strain and strain rate sustained by the LPO specimens (see Figure 5.23) are characterised by multiple waves with multiple peaks (as was the case of impact loading). The maximum strain value exhibited by the specimens is associated with the middle peak of first wave and about 3%. The maximum value of strain rate was about $20s^{-1}$.

The strain time history of specimens exhibited in the failure region is characterized by a single wave with multiple peaks. It is interesting to see that the strain in the failure region of specimens developed at a rate higher than that in the joint region. Under consecutive impacts the strain in the failure region increased up to 7.1% during each impact prior to failure. The strain rate in this region reached a maximum value of $90s^{-1}$.

In the ECC region beneath the brick the strain time history is characterised by waves with multiple peaks (as in the ECC-interface region) with a maximum value of about 1%. The strain rate exhibited by the specimens was about $20s^{-1}$. It is interesting to observe that, as in the case of the LPO series, a uniform strain distribution is exhibited by the unbonded region of the ECC layer of the specimens compared to the fully bonded ECC layer of the LFO series. In the LPO series uniform strain distribution which is observed at the ECC layer caused to higher resistance against the impact loads in specimens compared to the LFO series.

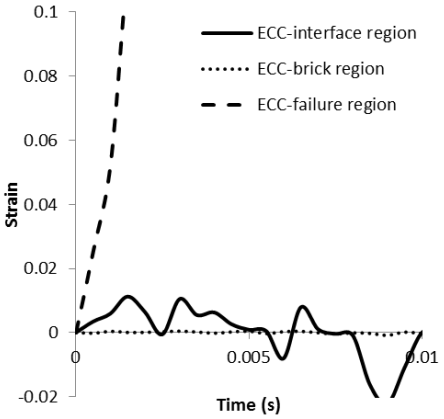

1T, LFO8

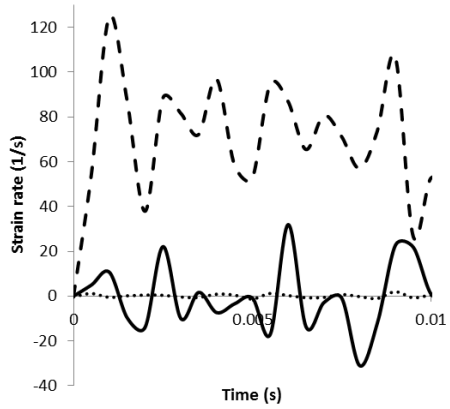

1TR, LFO8

LFO8

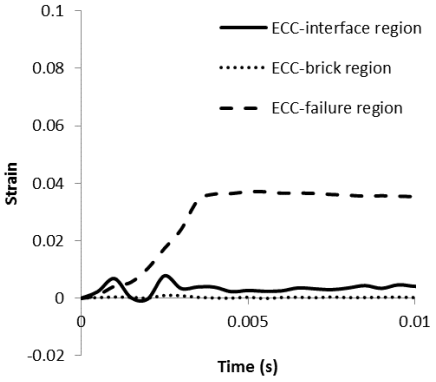

1T, LFO11

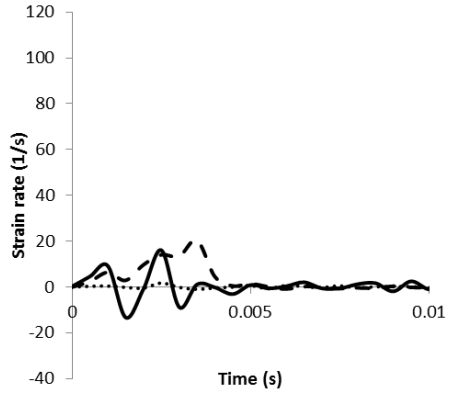

1TR, LFO11

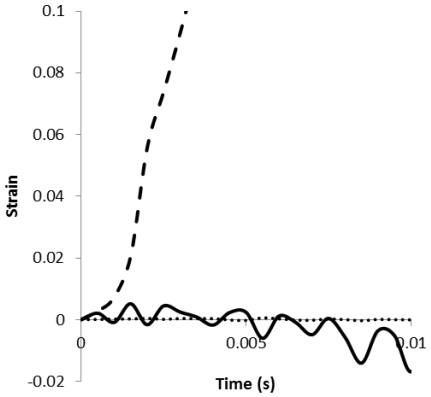

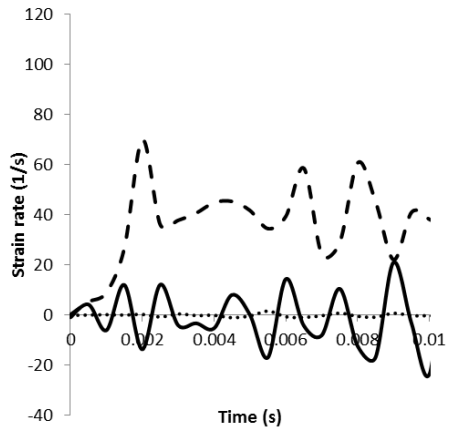

2T, LFO11

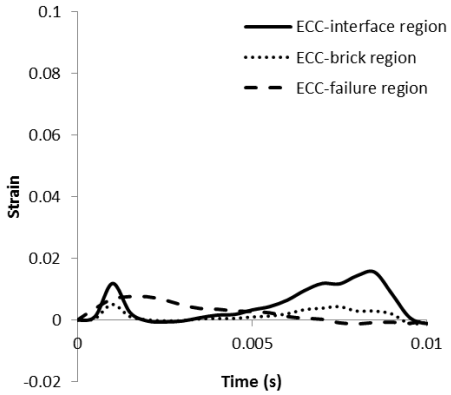

2TR, LFO11

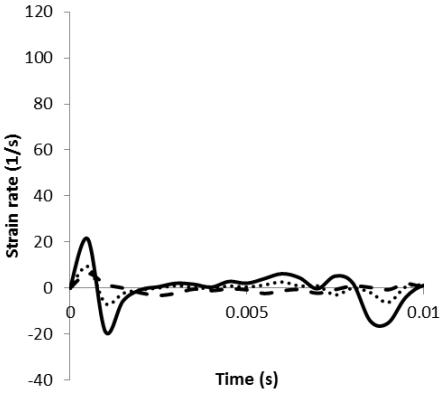

LFO11

1T, LPO9

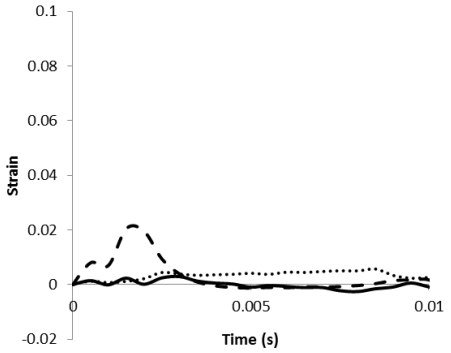

1TR, LPO9

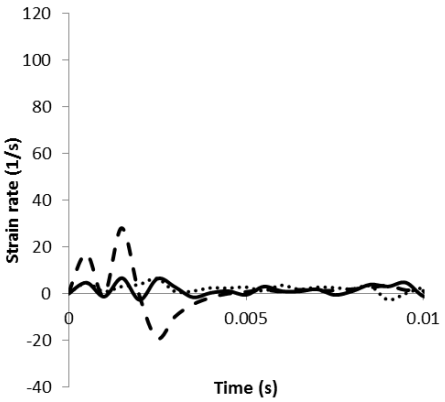

2T, LPO9

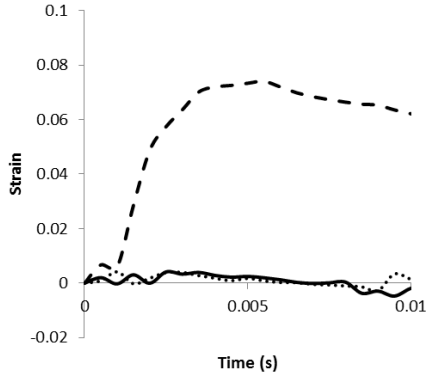

2TR, LPO9

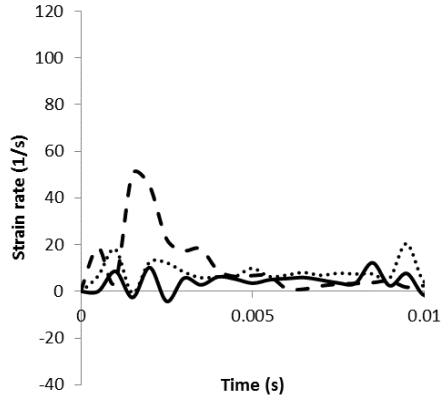

3T, LPO9

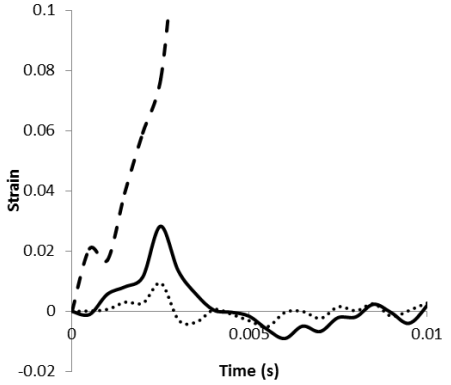

3TR, LPO9

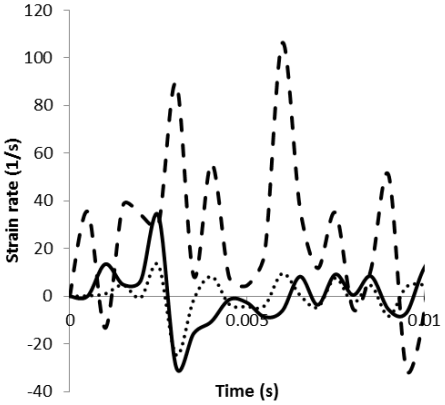

4T, LPO9

4TR, LPO9

LPO9

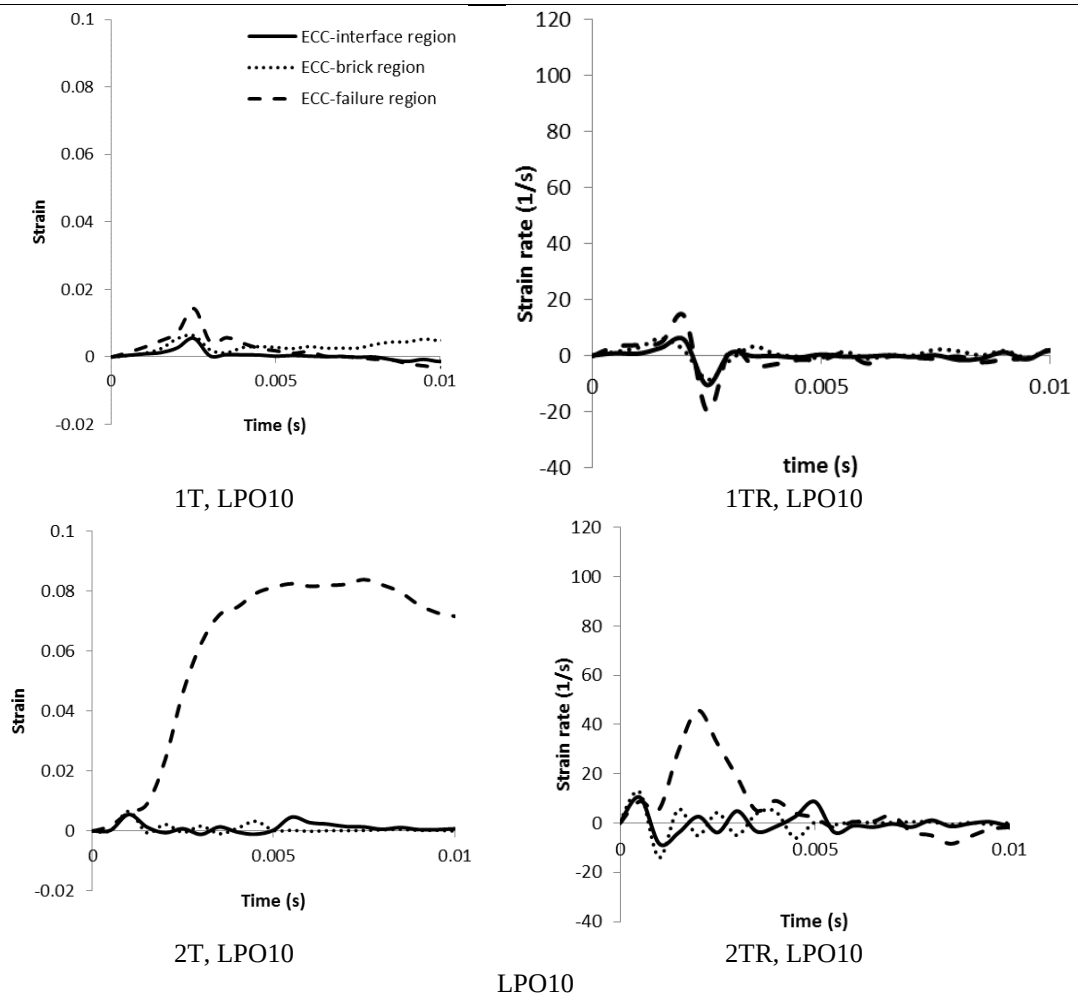

Figure 5.23. Strain (T) and strain rate (TR) time histories obtained from specimens strengthened with fully (LFO) and partially (LPO) bonded layer of ECC subjected to low intensity impact loading

5.7.2 Strain and strain rate time histories of specimens with two layers ECC

The curves describing the time histories of the strain and strain rate generated during testing of specimens retrofitted with two layers ECC are presented in Figure 5.24 and the main aspects of these curves are summarised in Table 5.3. For the tensile face of the HFT series the curves describing the variation of strain in the ECC-interface region (Figure 5.6) consists of a single wave with multiple peaks (similar to those associated with the impact load time history) with a maximum strain of about 1%. The strain rate in this region was about $10s^{-1}$ during the testing. The properties of the strain time history is similar to that established for the specimens included in the HFO series.

The curves describing the time history of the strain in the failure region of the ECC layer in tension is characterised by a single wave with multiple peaks. The strain in the failure

region increases with every consecutive impact up to 8% before failure occurs whereas the level of strain in the other regions considered along the tensile face of the ECC layer remained almost constant. The strain rate in this region reached a maximum value of $20s^{-1}$ which is approximately 600% less than that established in the HFO series. In the tensile face of the ECC layer beneath the brick the values of strain established were very low whereas the strain rate was about 5 s^{-1}.

The strain time history in the ECC-interface region (see Figure 5.6) of the top ECC layer subjected to compression of HFT is characterised by a single wave with multiple peaks and sustained a maximum value of approximately 0.5%. The maximum value of strain rate in this region was about $10s^{-1}$. It is interesting to notice that the strain in the ECC-interface region (see Figure 5.6) of the top ECC layer (subjected to compression) had the same properties with the lower ECC layer subjected to tension.

The curve describing the variation of strain with time in the failure region of the compression face formed a single wave with multiple peaks. The strain in this region was almost constant during consecutive impacts. It is interesting to notice that the maximum strain in the top ECC layer acting in compression was about 1% which caused local failure in the ECC layer. The strain rate in this region reached to $15s^{-1}$. The strain exhibited in the region of the top ECC layer between two consecutive joints (above a brick) was very small as in the case of the lower ECC layer (acting in tension). The strain rate exhibited at this region was about 5 s^{-1}.

Figure 5.24 presents the curves describing the time histories of the strain and strain rate exhibited by the bottom ECC layer of the HPT specimens (acting in tension). As in the case of the HPO specimens the time history of strain in the joint region was characterised by one major wave with several peaks. The maximum strain exhibited is this region was about 0.5% whereas the associated strain rate attained a maximum value of $15s^{-1}$.

The curve describing the time history of the strain exhibited in the failure region of the specimens is characterized by a single wave with multiple peaks. When subjected to consecutive drop-tests the maximum value of strain increased by up to 1.5% with every impact before ultimately failing. The strain rate in this region obtains a maximum value of $78s^{-1}$. The time history of the strain exhibited in the lower ECC layer (acting in tension)

below a brick (between two consecutive joints) is characterised by a single wave with multiple peaks attaining a maximum value of about 0.5%. It is interesting to see that the strain values exhibited in this region are similar to those exhibited by the bottom ECC layer below the joint region. The maximum value of the strain rate in ECC-brick region was about $20s^{-1}$. It is interesting to note that the maximum strain in the bottom ECC layer (tensile face) ECC-interface and ECC-failure regions is less than their counterparts exhibited by the HFT specimens (about 80% and 30% respectively) due to the uniform distribution of strain in the bottom ECC layer. Also it is interesting to notice that the strain exhibited in the failure region is 75% less than the HPO series.

Figure 5.24 shows the time history of the strain exhibited in the ECC-interface region on the top layer ECC (compression face) of the HPT series is characterised by a single wave with multiple peaks attaining a maximum value of 0.2%. It is interesting to notice that the strain in top ECC layer (acting in compression) have the same properties with the bottom ECC layer (acting in tension). The strain in the top ECC layer is about 50% less than its counterpart exhibited by the HFT specimens. This reveals that the unbonding the ECC layer in specimens can reduce the risk of localized failure in the top layer ECC (compression face) due to uniform strain distribution. The strain rate in this region was about $10s^{-1}$ during the tests.

The time history of the strain exhibited in the top ECC layer (in the cross-section at which failure is exhibited in the bottom ECC layer) is characterised by a single wave with multiple peaks attaining a maximum value of 0.3%. This value remains essentially the same for every impact when the specimens are subjected to consecutive drop-tests. It is interesting to notice that the strains in the top ECC layer were more effectively distributed compared to the HFT specimens. As a result the localised failure in the compression face of ECC was not observed when specimens failed. The strain rate in this region was approximately $5s^{-1}$. In the top ECC layer the strain in ECC-brick region (between two consecutive joints) was about 0.3% same as ECC-interface region. The strain rate of this region was approximately 5 s^{-1}. It is interesting to observe that unbonding the ECC layer in compression face resulting in the uniform distribution of strain.

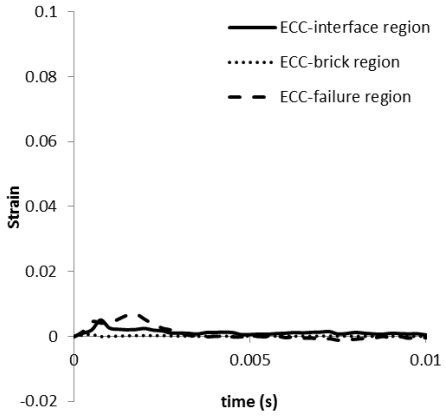

1T, HFT14

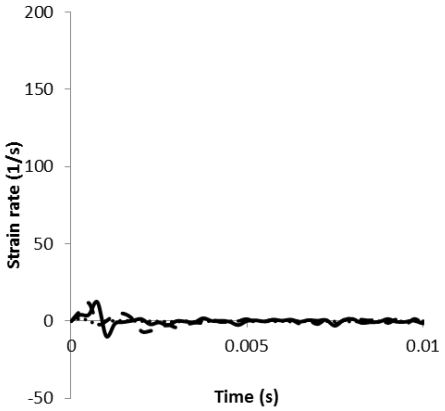

1TR, HFT14

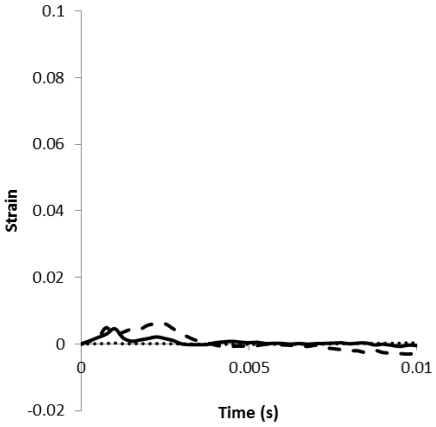

2T, HFT14

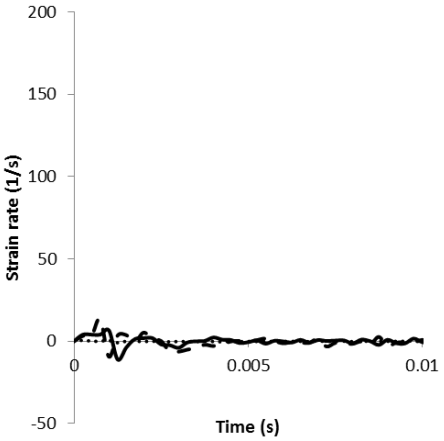

2TR, HFT14

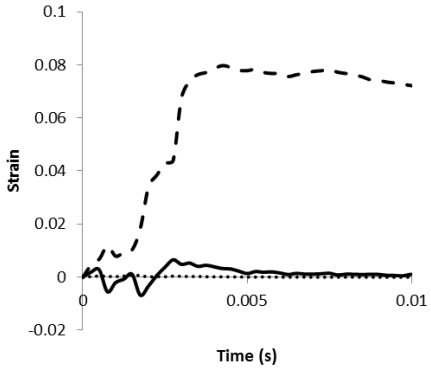

3T, HFT14

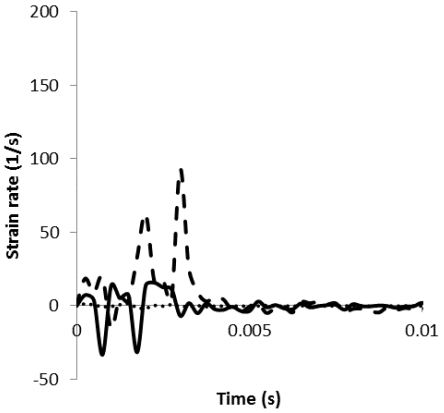

3TR, HFT14

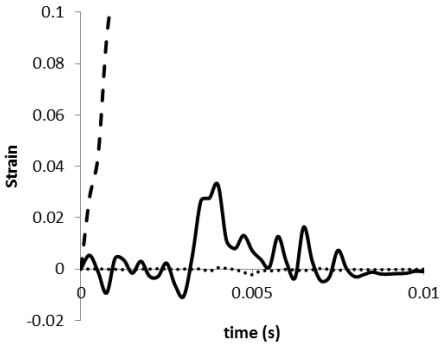

4T, HFT14

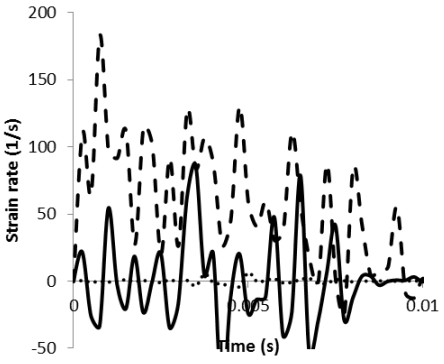

4TS, HFT14

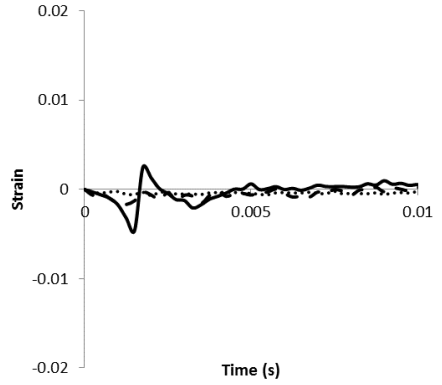

1C, HFT14

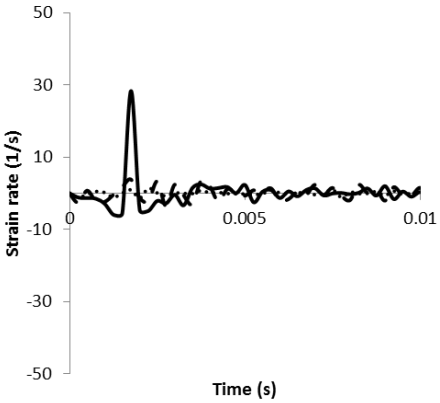

1CR, HFT14

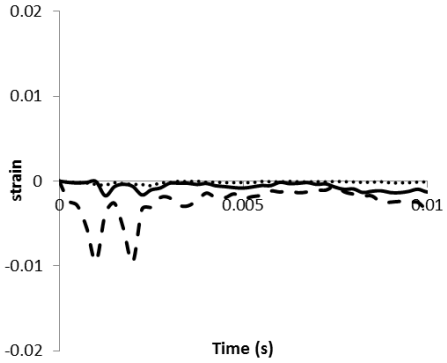

2C, HFT14

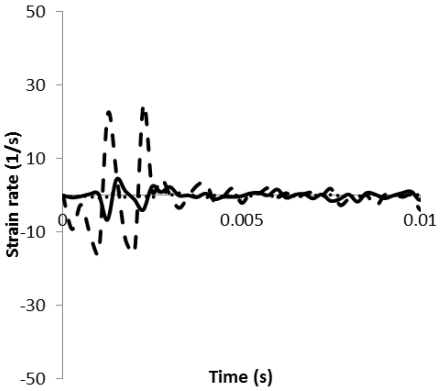

2CR, HFT14

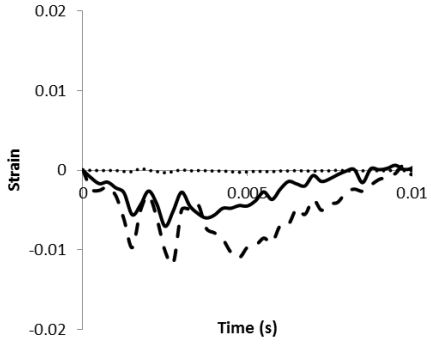

3C, HFT14

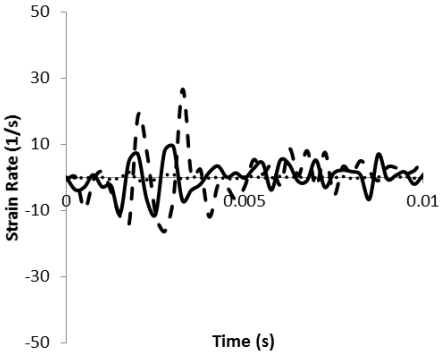

3CR, HFT14

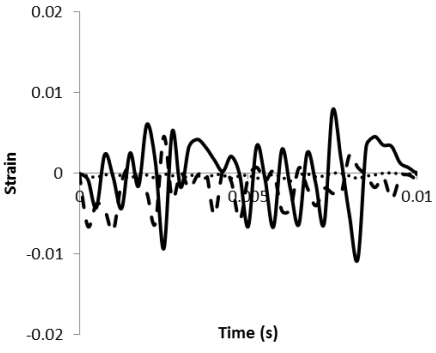

4C, HFT14

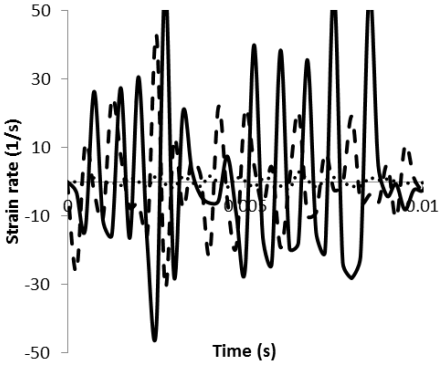

4CR, HFT14

HFT14

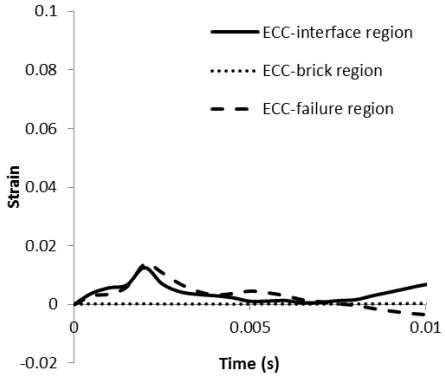

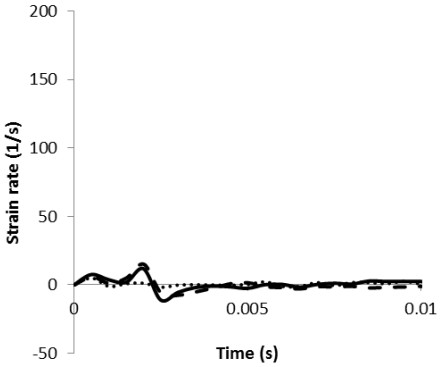

1T, HFT12

1TR, HFT12

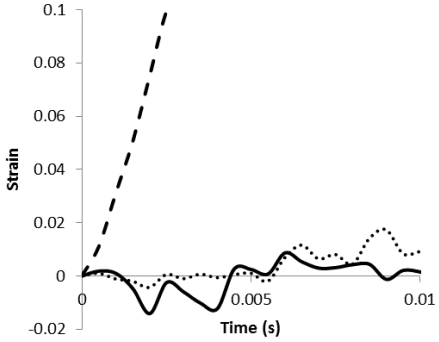

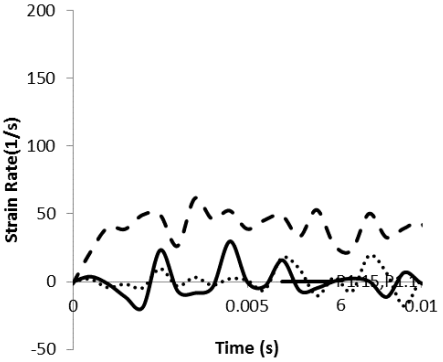

2T, HFT12

2TR, HFT12

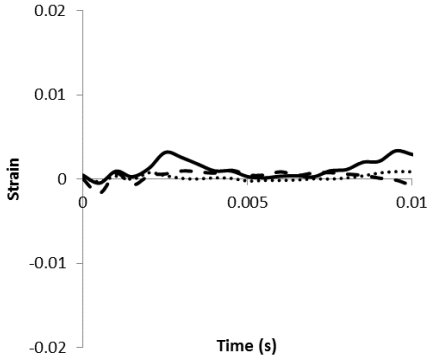

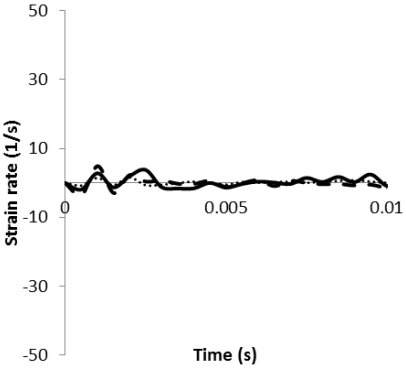

1C, HFT12

1CR, HFT12

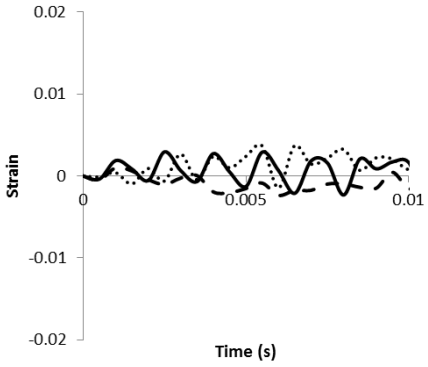

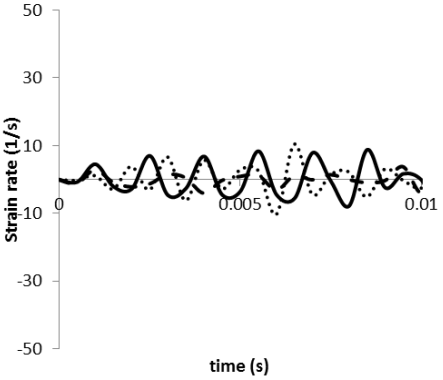

2C, HFT12

2CR, HFT12

HFT12

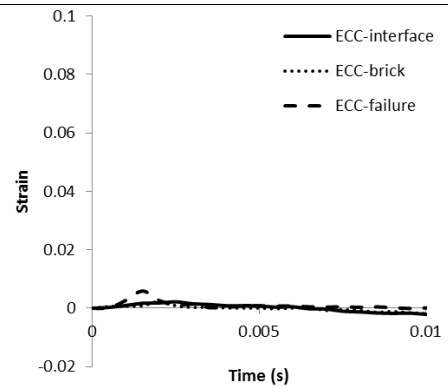

1T, HPT13

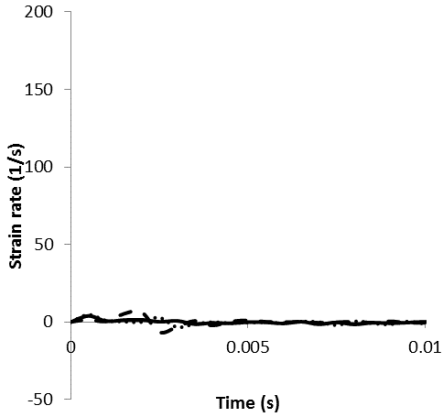

1TR, HPT13

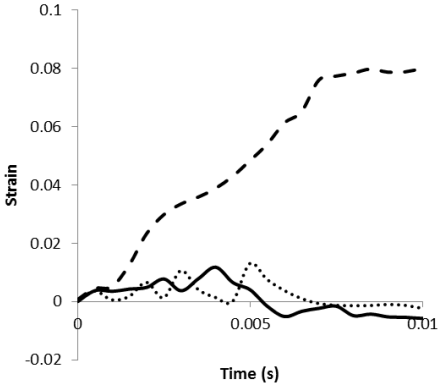

2T, HPT13

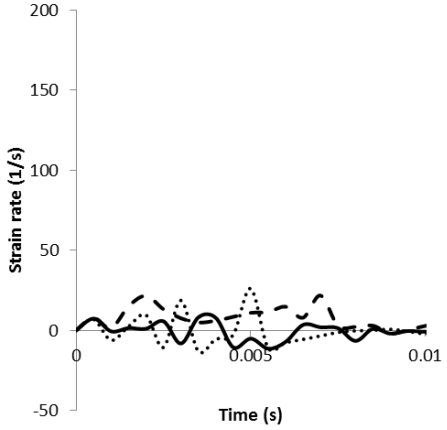

2TR, HPT13

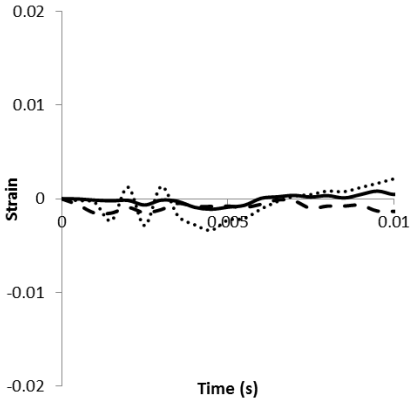

1C, HPT13

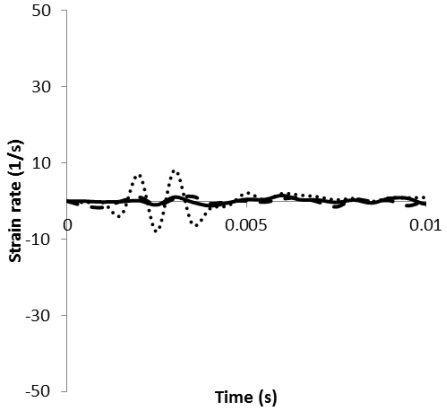

1CR, HPT13

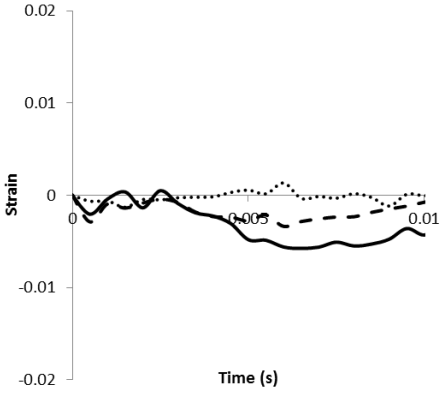

2C, HPT13

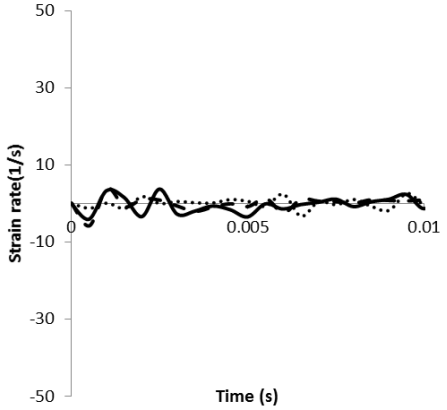

2CR, HPT13

HPT13

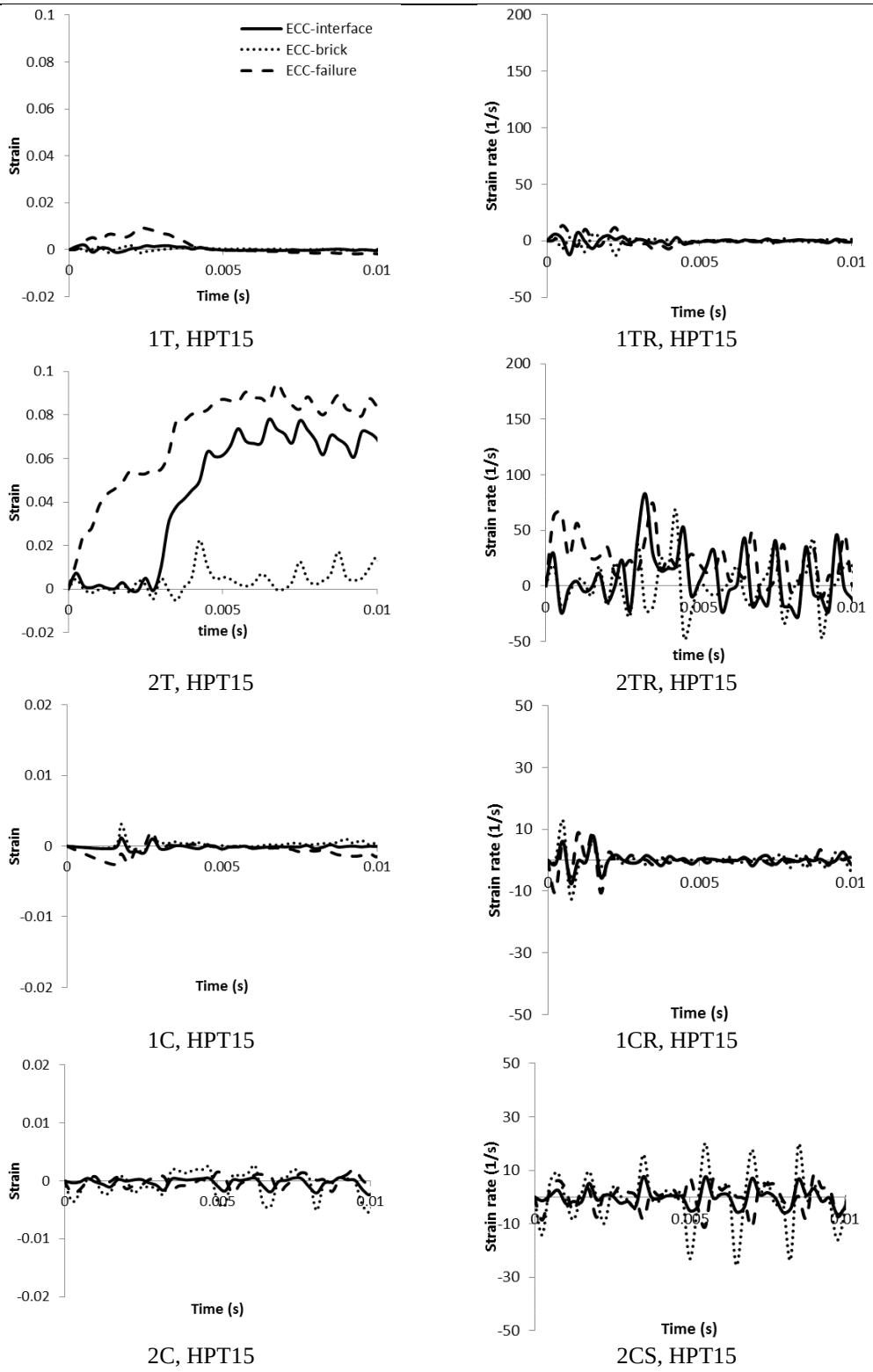

Figure 5.24. Strain (T & C) and strain rate (TR & CR) time histories obtained from specimens strengthened with fully (HFT) and partially (HPT) bonded layers of ECC subjected to high intensity impact loading

Figure 5.25 presents the curves describing the time histories of the strain and strain rate exhibited at different locations of the LFT specimens the main aspects of which are summarised in Table 5.4. The curves describing the time histories of the strain exhibited

in the bottom ECC layer (acting in tension) in the joint region (forming between two consecutive bricks) is characterised by a single wave with multiple peaks. It is noticed that the form of strain time history curves is different compared to the counterpart impact load applied on specimens. The maximum strain sustained by this region was about 1% and the maximum strain rate was about 10 s^{-1}. The form of the time history of the strain is similar with that established when considering the HFT specimens.

In the failure region of the bottom ECC layer the strain time history was characterised by a single wave with multiple peaks. When subjected to consecutive drop tests the strain maximum value of strain increased with every impact up to 3.5% before ultimately failing whereas the strain in other regions of the bottom ECC layer was remained essentially constant with every consecutive impact. The strain rate in the failure region reached a maximum value of 30s^{-1}. In the region of the bottom ECC layer beneath a brick (between two consecutive joints) the strains exhibited were very small whereas the strain rate was about 10 s^{-1}.

The strain time history in the top ECC layer at the joint region (forming between two consecutive bricks) of the LFT specimens is characterised by a single wave with multiple peaks attaining a maximum value of about 0.5%. The strain rate achieved in this region was about 15s^{-1}.

The strain time history exhibited in the top ECC layer at the cross-section at which failure occurs in the bottom ECC layer is characterised by a single wave with multiple peaks. The strain in this region was almost constant during consecutive impacts. It is interesting to notice that the maximum strain was about 0.4%. This reveals that in the LFT series the top ECC layer did not failed during impact in contrast with what was observed in the HFT series. The strain rate in this region reached a maximum value of 15s^{-1}. In the top ECC layer above the brick (between two consecutive joints) the strain values established were small whereas the strain rate was about 10 s^{-1}.

Figure 5.25 presents the curves describing the time histories of the strain and strain rate exhibited at different locations along the bottom ECC layer of the LPT specimens. The time history of the strain exhibited in the joint region is characterised by one major wave with multiple peaks as in the case of the HPT specimens. It is interesting to notice that

the form of strain time history is similar to that describing the variation of impact load applied onto the specimens (see section 5.4.2). The maximum value attained by the specimens is about 2% whereas the maximum value of strain rate was $47s^{-1}$.

The time history of the strain exhibited in the failure region of specimens is characterized by a single wave with multiple peaks. The maximum value of the strain increases up to 5.2% with every consecutive drop tests before failure ultimately occurs. The strain rate in this region reached a maximum value of $100s^{-1}$. The strain time history of the bottom ECC layer below two consecutive joints (ECC-brick region) is characterised by a single wave with multiple peaks attaining a maximum value of about 3%. It is interesting to see that the strain exhibited in the ECC-brick region is higher than that exhibited in the ECC-joint region of the LPT specimens. The strain rate of ECC-brick and ECC-interface regions reached up to $60s^{-1}$. It is interesting to note that level of maximum strain in the bottom ECC layer (acting in tension) reached 2% resulting in very ductile behaviour being exhibited by the specimens.

Figure 5.24 shows the strain time history exhibited by the top ECC layer (acting in compression) in the joint (interface) region (forming between consecutive bricks) of the LFT specimens is characterised by a single wave with multiple peaks attaining a maximum value of about 0.4%. It is interesting to notice that the strain exhibited in the top ECC layer at the joint region was similar to that exhibited in the bottom ECC layer in the same region. The strain rate in this region was about $10s^{-1}$.

The curves describing the variation of strain with time exhibited on the top ECC layer at the cross-section at which failure is exhibited in the bottom ECC layers is characterised by a single wave with multiple peaks. When subjected to multiple drop tests the maximum value of strain (0.4%) remains almost constant with every impact. The strain rate exhibited in this region was about $5s^{-1}$. In the region of the top ECC layer forming between two consecutive joints (brick region) the maximum values of strain was about 0.6% which is higher than the values established in the ECC-interface region. The strain rate of this region was about 5 s^{-1}. It is interesting to observe that unbonding the top ECC layer (compression face) resulting in the uniform distribution of strain which can reduce the risk of localized failure due to the concentration of strain. Due to uniform distribution of strain in the tensile face up to 3% and in the compression face up to 0.6% LPT series

specimens presented best impact resistance properties (see Table 5.1) compared to all other series.

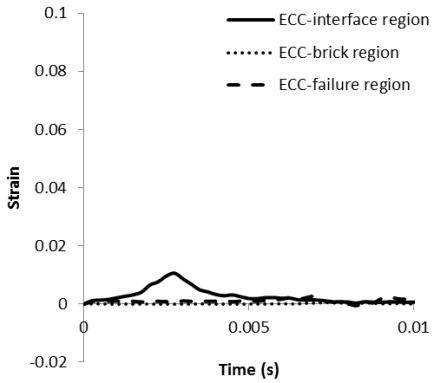

1T, LFT16

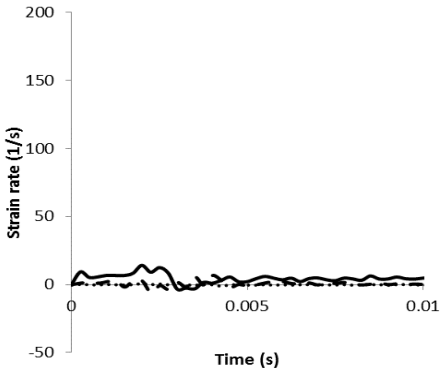

1TR, LFT16

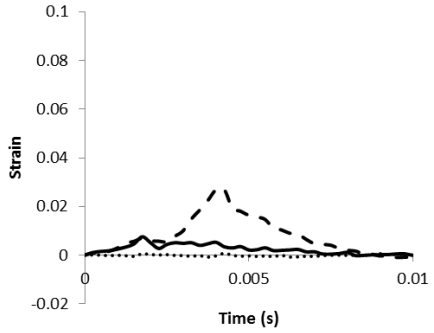

2T, LFT16

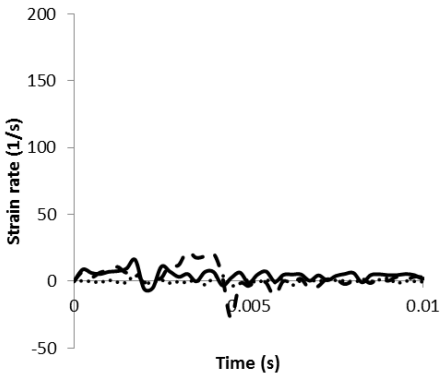

2TR, LFT16

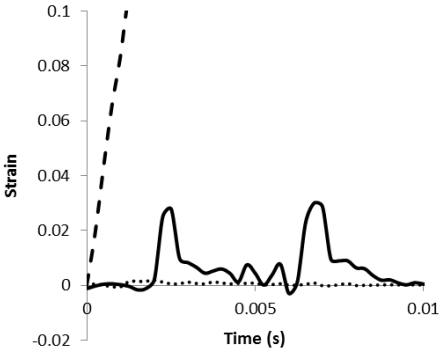

3T, LFT16

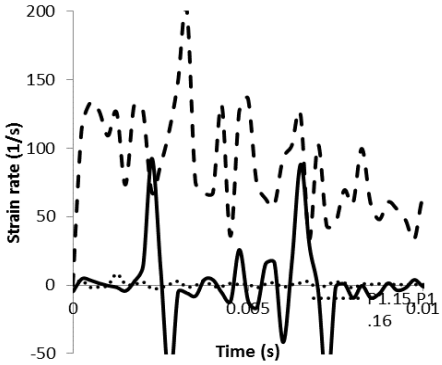

3TR, LFT16

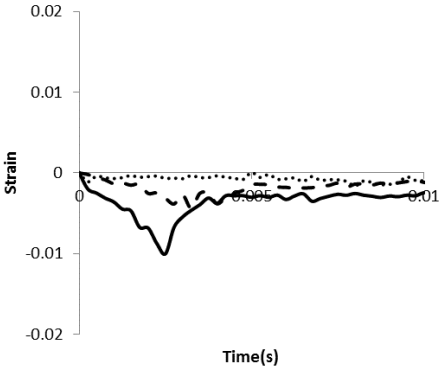

1C, LFT16

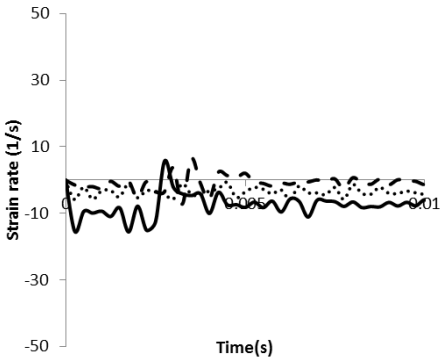

1CR, LFT16

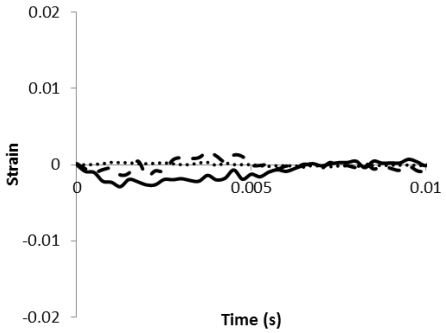

2C, LFT16

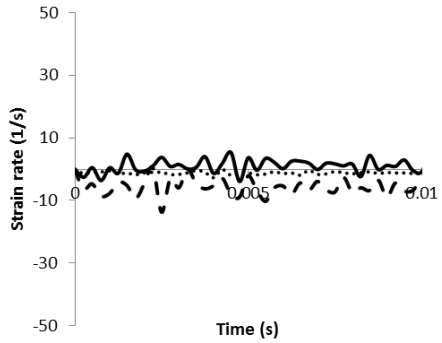

2CR, LFT16

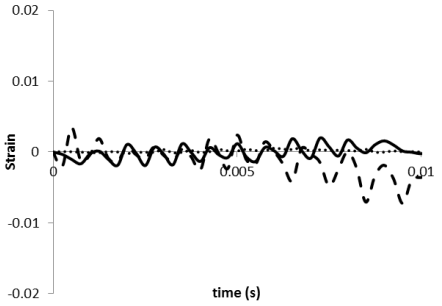

3C, LFT16

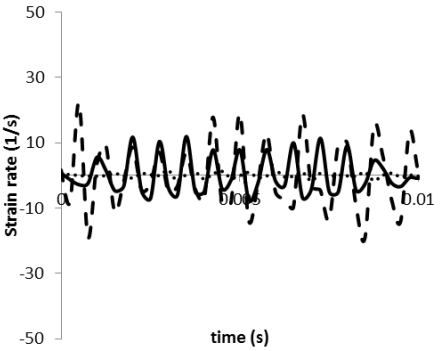

3CR, LFT16

LFT16

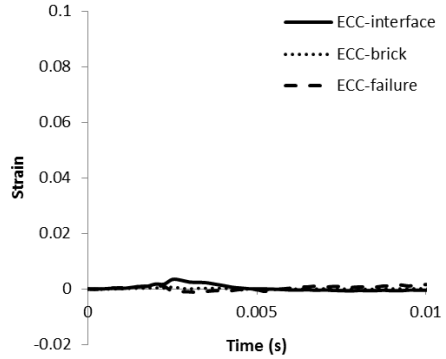

1T, LFT21

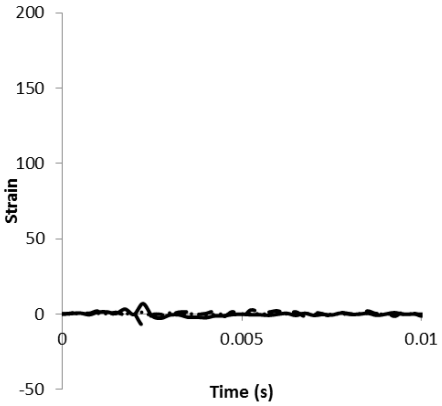

1TR, LFT21

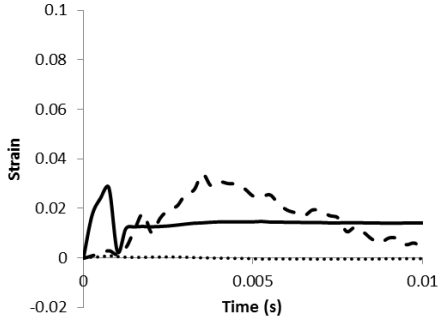

2T, LFT21

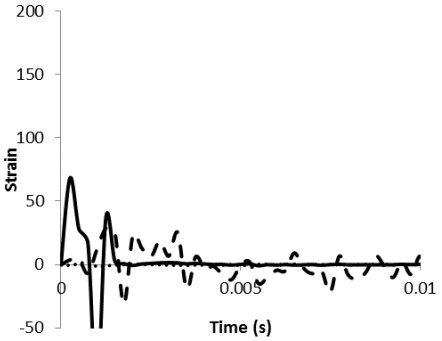

2TR, LFT21

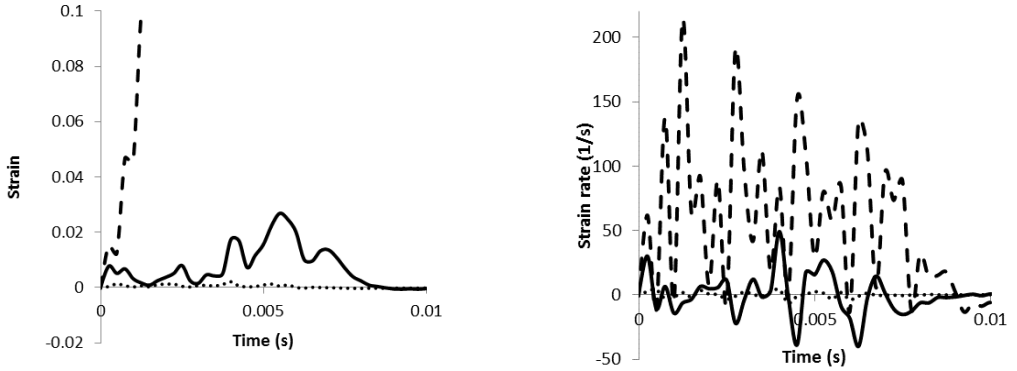

3T, LFT21 3TR, LFT21

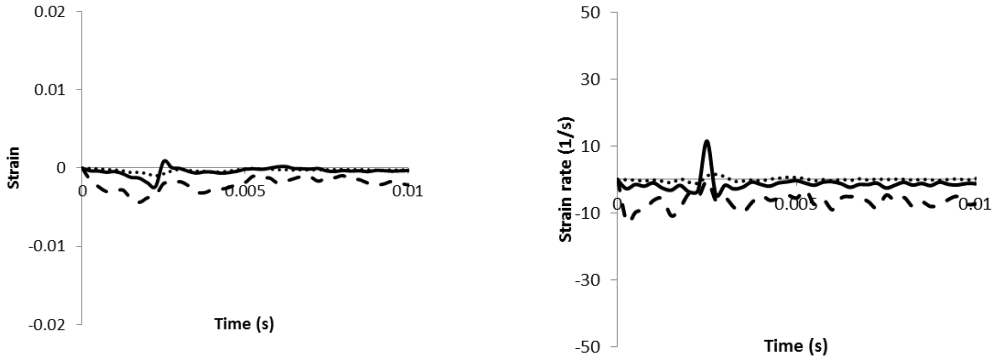

1C, LFT21 1CR, LFT21

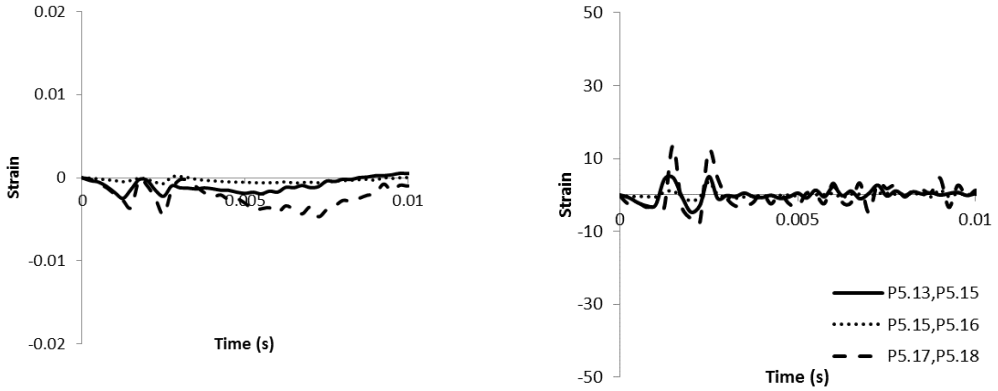

2C, LFT21 2CR, LFT21

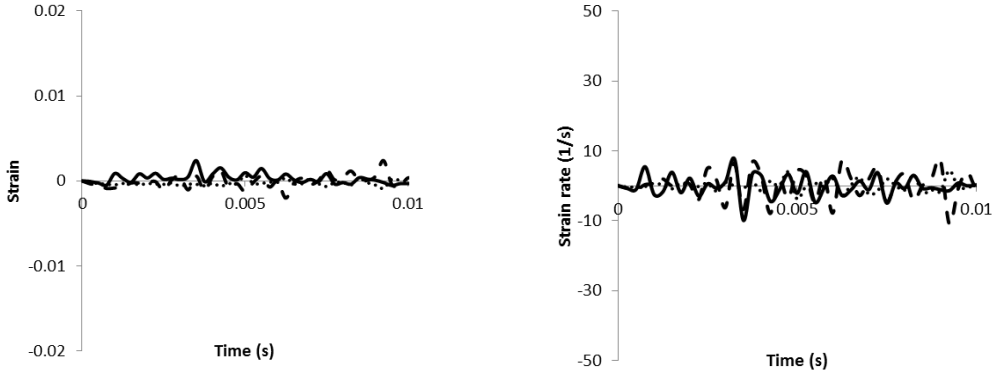

3C, LFT21 3CR, LFT21

LFT21

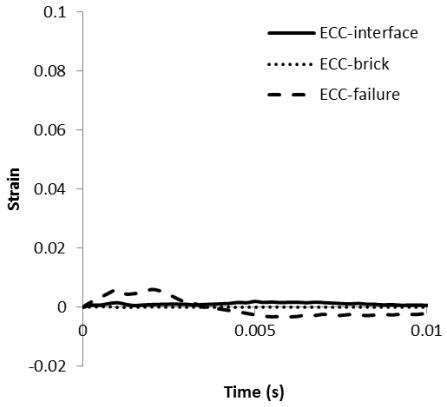

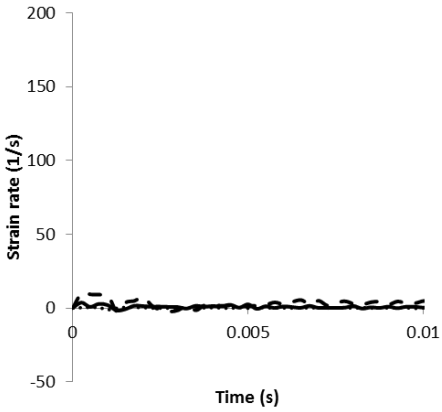

1T, LFT19 1TR, LFT19

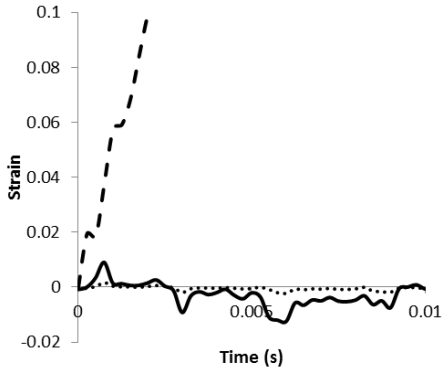

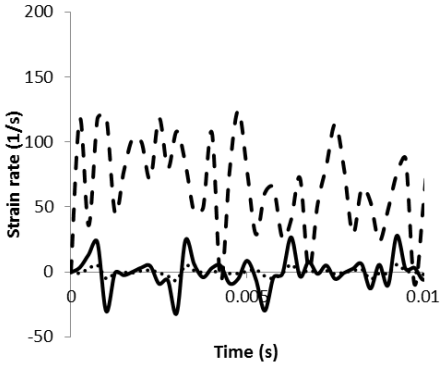

2T, LFT19 2TR, LFT19

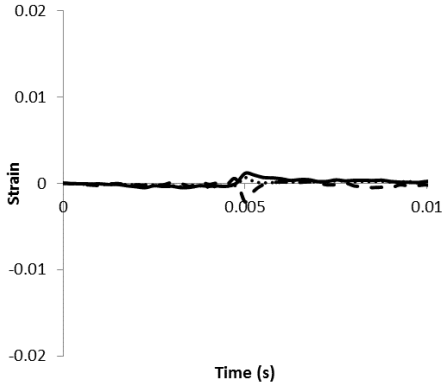

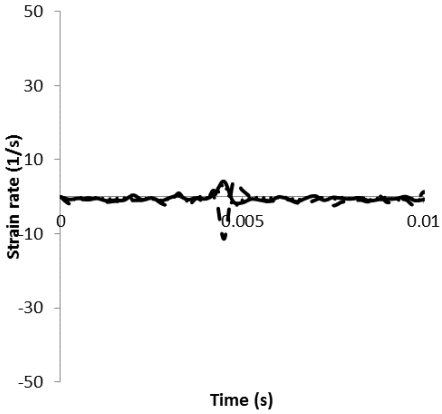

1C, LFT19 1CR, LFT19

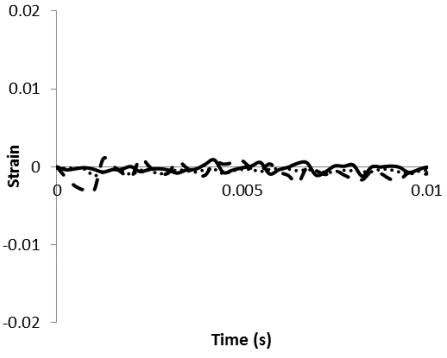

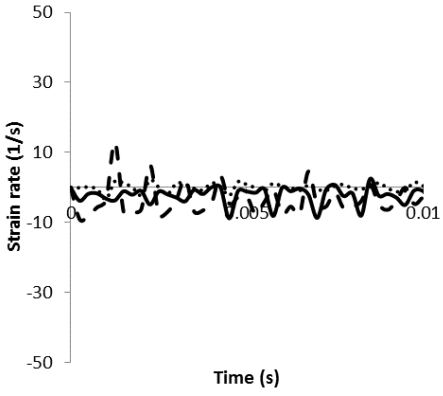

2C, LFT19 2CR, LFT19

LFT19

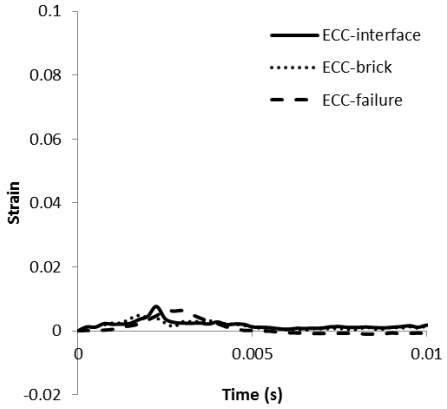

1T, LPT18

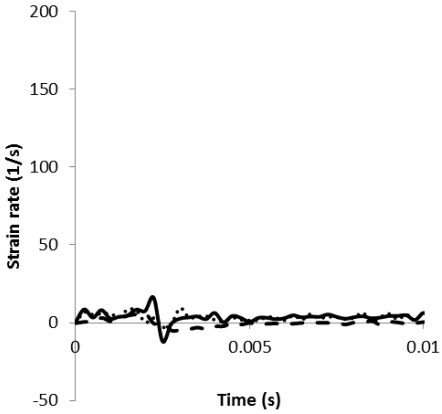

1TR, LPT18

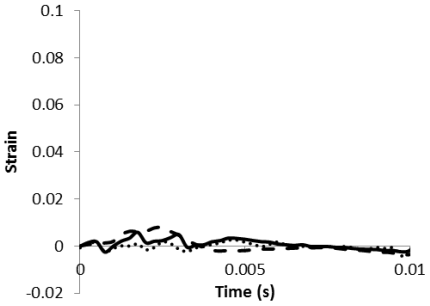

2T, LPT18

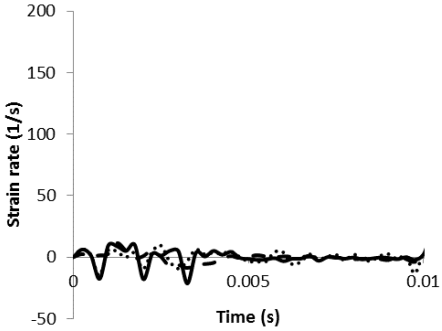

2TR, LPT18

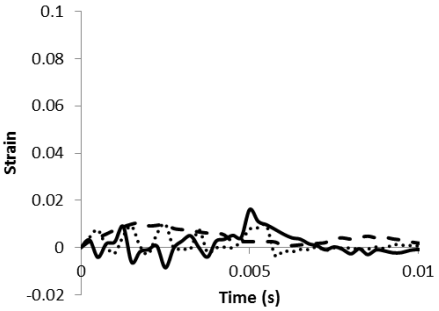

3T, LPT18

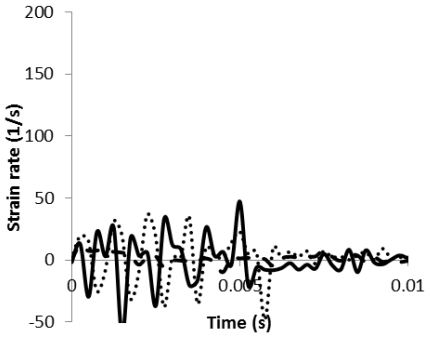

3TR, LPT18

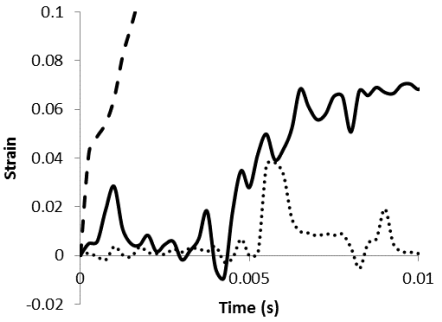

4T, LPT18

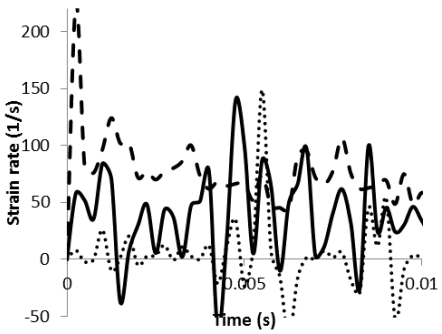

4TR, LPT18

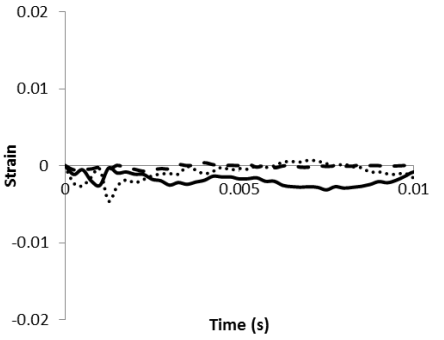

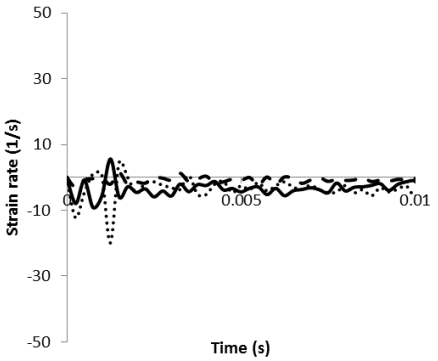

1C, LPT18 1CR, LPT18

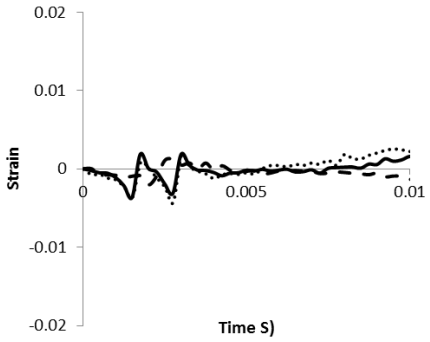

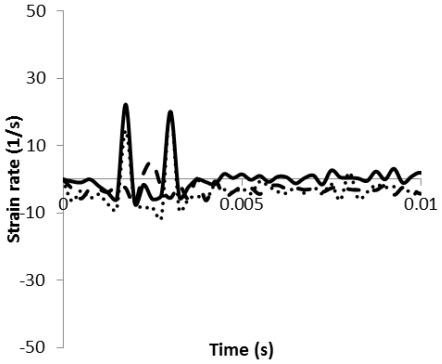

2C, LPT18 2CR, LPT18

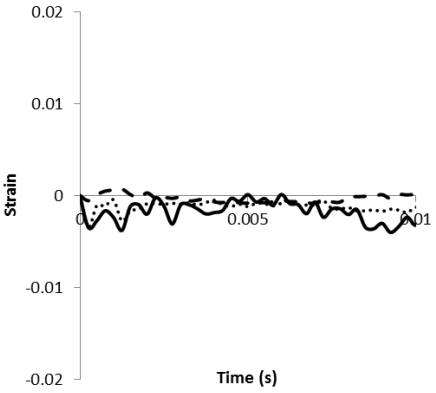

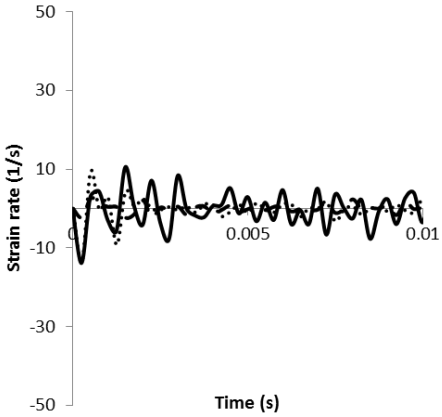

3C, LPT18 3CR, LPT18

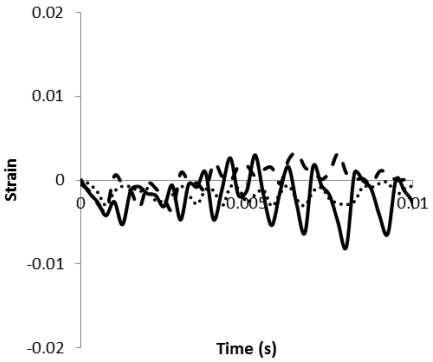

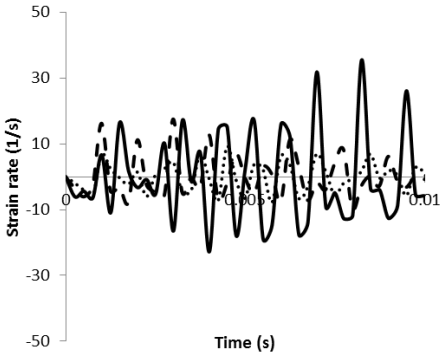

4C, LPT18 4CR, LPT18

LPT18

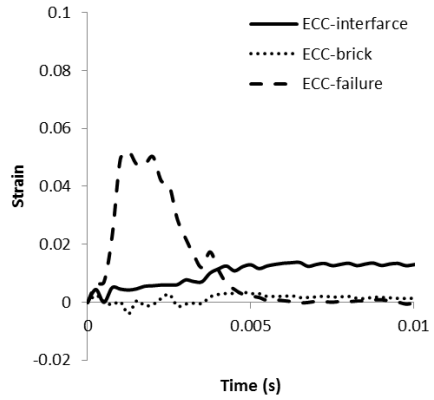

1T, LPT17

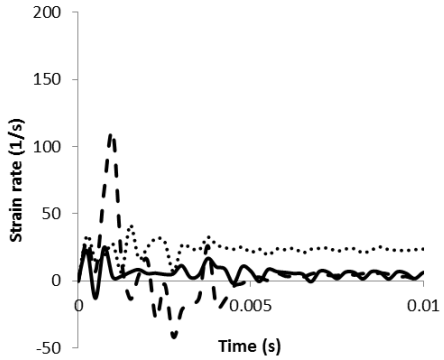

1TR, LPT17

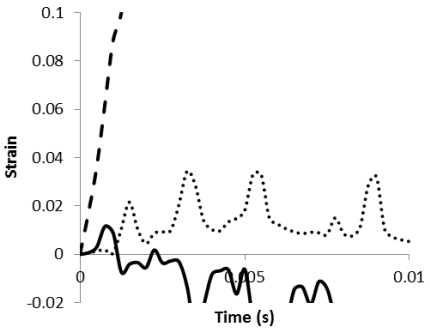

2T, LPT17

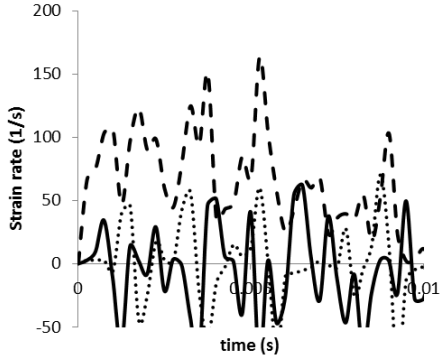

2TR, LPT17

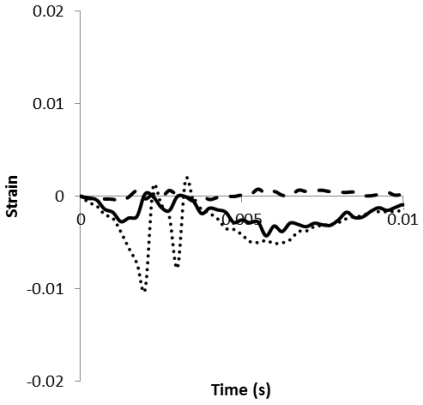

1C, LPT17

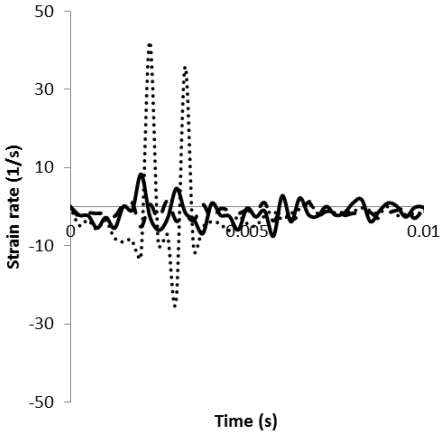

1CR, LPT17

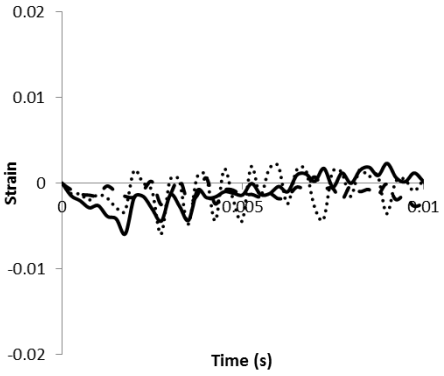

2C, LPT17

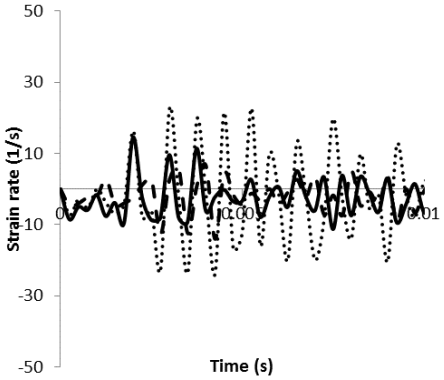

2CR, LPT17

LPT17

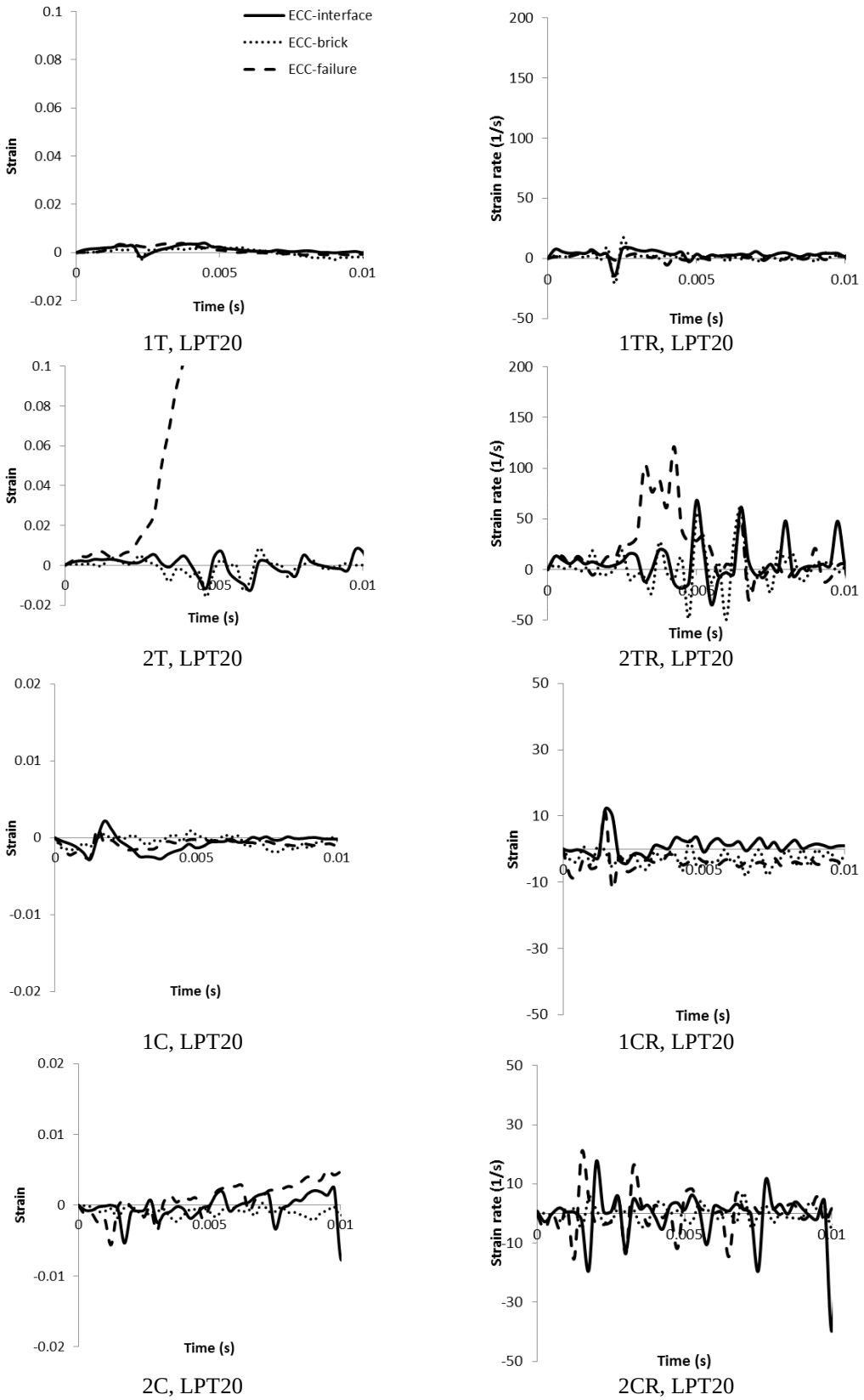

Figure 5.25. Strain (T & C) and strain rate (TR & CR) time histories obtained from specimens strengthened with fully (LFT) and partially (LPT) bonded layers of ECC subjected to low intensity impact loading

Table 5.2: The results of fully and partially bonded retrofitted specimens with one layer ECC to high and low intensity impact loading

			specimen		HFO4			HFO2		HFO7	HFO1	HPO5			HPO6	HPO3	LFO8		LFO11		LPO9				LPO10		
			Number of impacts	Unit	1st	2nd	3rd	1st	2nd	1st	1st	1st	2nd	3rd	1st	1st	1st	2nd	1st	2nd	1st	2nd	3rd	4th	1st	2nd	3rd
Results obtained from data logger	Impactor	Peak point	Load	kN	123	108	111	-	-	116	-	109	128	102	118	-	64.1	74.3	82.1	79.9	101.3	105	103	104.5	99.2	103.2	81.1
			Time	ms	0.86	0.68	0.22	-	-	0.73	-	0.92	0.58	0.67	0.81	-	0.17	0.16	0.17	0.16	0.19	0.17	0.22	0.22	0.22	0.22	0.19
			Loading rate	kN/ms	143	159	503	-	-	159	-	118	221	152	146	-	377	464	483	499	533	615	468	475	451	469	427
		Initial loading rate		kN/ms	338	486	435	-	-	469	-	361	457	375	312	-	377	464	483	499	533	615	468	475	451	469	427
	Reaction		Load	kN	68.77	49.3	12	-	-	45.9	-	44.7	45.5	29.6	42.9	-	46.7	24.7	37	11.58	58.7	46	37.9	41	38.7	33.1	25.2
			Time	ms	2.1	2.2	3.7	-	-	2	-	1.87	2.01	2.32	2.2	-	2.3	2.5	1.91	2.41	2.57	2.8	2.88	2.9	2.85	2.88	3.08
	Impact load & reaction relation		R/I		0.56	0.46	0.11	-	-	0.39	-	0.4	0.35	0.29	0.36	-	0.72	0.33	0.45	0.14	0.57	0.44	0.36	0.39	0.39	0.32	0.31
			I-R delay	ms	1.24	1.52	3.48			1.27		0.95	1.43	1.65	1.39		2.13	2.34	1.74	2.25	2.38	2.63	2.66	2.68	2.63	2.66	2.89
Results obtained from HS camera	Strain in tension		ECC-brick	%	0.011	0.01	0.01	0.017	0.01	0.01	0.012	0.8	-	0.3	0.62	0.42		0.11	0.03	0.01	0.5	0.1	0.42	0.9	0.69	0.52	
			ECC-interface	%	1.33	1.49	0.86	1.7	1.9	0.73	0.85	1.1	-	0.29	0.56	0.48	-	1.1	0.68	0.31	1.2	0.14	0.4	2.9	0.64	0.65	-
			ECC-failure	%	1.92	8.79	-	3.26	-	1.74	-	6.1	-	-	-	-		-	3.6	-	0.76	2	7.1	-	1.49	-	-
	Strain rate in tension		ECC-brick	s-1	0.11	0.12	0.11	0.04	0.03	0.04	0.12	14	-	14	19	4.2		0.6	1	0.4	9.1	4.8	18	4.9	5.1	12	-
			ECC-interface	s-1	15.2	28	16.7	14	13.5	16.2	32	16	-	13	14	4.1	-	10.7	9.1	5.3	21.4	4.7	18	13	5.77	11	-
			ECC-failure	s-1	16.2	58	84	18	33.2	23.5	105	48	-	38	48	78		124	10.5	67.3	7.2	17	50	89	15.1	48	-
	Deflection		max	mm	2.69	7.19	-	3.58	-	-	-	3.8	-	-	-	-		-	2.51	-	2.86	4.11	4.68	-	2.85	5.68	-
			residual	mm	2.03	4.59	-	3.52	-	-	-	1.17	-	-	-	-	-	-	2.39	-	1.44	1.31	1.3	-	2.83	1.24	-
	Acceleration		HS camera	m/s^2	2561	2180	1197	2557	1113	1230	1180	2176	-	1371	2346	1092	-	1342	1342	1281	1921	2080	2089	1921	1951	1923	-
			Equivalent force	kN	120.3	102	56.2	120.2	52.3	57.8	55.46	102.2	-	64.4	110.2	51.3		63	63	60.2	90	97.7	98.1	90.2	91.6	90.3	-

Table 5.3: The results of fully and partially bonded retrofitted specimens with two layers ECC to high intensity impact loading

			specimen		HFT14				HFT12		HPT13		HPT15	
			Number of impacts	Unit	1st	2nd	3rd	4th	1st	2nd	1st	2nd	1st	2nd
Results obtained from data logger	Impactor	Peak point	Load	kN	55.6	56.3	81	84	103.5	93.9	99.6	78	73	48
			Time	ms	0.39	0.4	0.2	0.28	0.22	0.28	0.19	0.22	0.28	0.22
			Loading rate	kN/ms	142	140.7	405	312	472	335	524	354	260	218
		Initial loading rate			286	450	405	312	472	350	524	418	361	284
	Reaction		Load	kN	50	47.3	44	12	57.7	7.7	30.9	26	30	17.8
			Time	ms	2.29	2.3	2.77	2.3	2.57	2.74	2.3	2.9	2.1	2.52
	Impact load & reaction relation		R/I		0.62	0.49	0.54	0.14	0.56	0.08	0.27	0.24	0.41	0.34
			I-R delay	ms	1.9	1.9	2.57	2.02	2.35	2.46	2.11	2.68	1.82	2.3
Results obtained from HS camera	Strain in tension		ECC-brick	%	0.05	0.037	0.036	0.098	0.02	0.12	0.23	0.44	0.51	-
			ECC-interface	%	0.5	0.46	0.28	0.5	1.21	0.1	0.26	0.43	0.1	0.68
			ECC-failure	%	0.68	0.49	7.8	-	1.32	-	0.59	-	0.19	0.74
	Strain rate in tension		ECC-brick	(s^{-1})	4	3.2	3.8	2.7	4.9	2	3.95	7.6	13.4	-
			ECC-interface	(s^{-1})	12.3	4	7.3	11.1	5.9	1.8	4.9	7.6	4.1	19.1
			ECC-failure	(s^{-1})	11.6	13.6	18.7	-	7.5	-	6.3	-	5.8	29
	Strain in compression		ECC-brick	%	0.047	0.043	0.017	0.044	0.033	0.01	0.021	0.021	0.26	0.21
			ECC-interface	%	0.46	0.17	0.56	0.38	0.32	0.049	0.22	0.009	0.032	0.35
			ECC-failure	%	0.16	0.97	0.97	0.65	0.17	0.051	0.14	0.028	0.33	0.034
	Strain rate in compression		ECC-brick	(s^{-1})	2.6	2.2	1.1	1.6	1.9	0.2	0.3	4	10.5	8.1
			ECC-interface	(s^{-1})	5.9	6.7	4.2	14	0.9	1.4	3.8	1.3	1.29	14.1
			ECC-failure	(s^{-1})	2.3	15.6	9.6	26	3.4	1.6	1.6	5.7	1.28	2.3
	Deflection		Max	mm	1.68	1.87	3.08	-	2.89	-	4.23	-	3.2	-
			residual	mm	1.37	1.38	2.83	-	2.81	-	4.23	-	2.77	-
	Acceleration		HS camera	m/s^2	2115	2118	2085	1882	2215	2213	1875	1850	1874	1738
			Equivalent force	kN	99.4	99.5	97.9	88.4	104.1	104	88.1	86.9	88	81.6

Table 5.4: The results of fully and partially bonded retrofitted specimens with two layers ECC to low intensity impact loading

			specimen		LFT16			LFT21			LFT19		LPT18				LPT17			LPT20	
			Number of impacts	Unit	1st	2nd	3rd	1st	2nd	3rd	1st	2nd	1st	2nd	3rd	4th	1st	2nd	3rd	1st	2nd
Results obtained from data logger	Impactor	Peak point	Load	kN	76.1	85.3	66.9	94.6	101.4	92.2	66.9	101.2	85.8	94.7	93.7	53.1	87.3	99.3	78.3	66.9	101.1
			Time	ms	0.168	0.22	0.224	0.168	0.19	0.16	0.25	0.16	0.3	0.19	0.16	0.28	0.22	0.16	0.16	0.25	0.22
			Loading rate	kN/ms	452	386	304	563	531	576	398	6.31	286	498	585	189	396	620	489	267	459
		Initial loading rate			452	386	304	563	531	576	398	6.31	286	498	585	189	396	620	489	267	459
	Reaction		Load	kN	35	31	9.4	31	27.2	13.1	32.3	26.4	34	24	15	12	33.4	23.7	9.8	31.7	27.2
			Time	ms	2.54	2.38	2.01	2.12	3.3	1.93	2.49	2.85	2.5	1.8	2	1.9	2.68	3.16	1.84	2.35	2.8
	Impact load & reaction relation		R/I		0.35	0.34	0.09	0.32	0.26	0.14	0.4	0.26	0.39	0.25	0.16	0.17	0.38	0.23	0.12	0.47	0.26
			I-R delay	ms	2.37	2.16	1.79	1.95	3.11	1.77	2.24	2.69	2.2	1.61	1.84	1.62	2.46	3	1.68	2.1	2.58
Results obtained from HS camera	Strain in tension		ECC-brick	%	0.013	0.083	0.054	0.08	0.05	0.06	0.06	0.02	0.76	0.19	0.31	2.84	-	0.49	1.16	0.32	0.64
			ECC-interface	%	1.06	0.69	0.43	0.23	2.83	0.77	0.15	0.91	0.48	0.18	0.75	0.91	-	0.25	2.17	0.17	0.07
			ECC-failure	%	0.28	2.61	-	0.21	3.42	-	0.6	-	0.62	0.76	1.05	-	-	5.2	-	0.27	0.3
	Strain rate in tension		ECC-brick	(s^{-1})	0.27	0.8	1.5	1.01	68	11.9	3.7	23	8.5	6.2	13.6	58.2	-	25	34.3	2.3	13
			ECC-interface	(s^{-1})	9.2	7.1	8.6	1.54	3.2	4.3	1.2	10.6	6.7	6.5	19.3	7.9	-	31	46.8	3.7	4.5
			ECC-failure	(s^{-1})	1.97	2.2	-	2	3.1	-	10.5	-	3.12	2.6	11.9	-	-	111	-	7.6	12.8
	Strain in compression		ECC-brick	%	0.02	0.019	0.021	0.035	0.089	0.087	0.021	0.038	0.22	0.36	0.34	0.42	-	0.23	0.59	0.21	0.56
			ECC-interface	%	0.44	0.21	0.14	0.19	0.27	0.089	0.023	0.28	0.24	0.35	0.35	0.3	-	0.1	0.39	0.18	0.11
			ECC-failure	%	0.38	0.11	0.26	0.39	0.36	0.091	0.022	0.3	0.21	0.1	0. 18	0.18	-	0.05	0.14	0.28	0.13
	Strain rate in compression		ECC-brick	(s^{-1})	5.8	2.6	0.8	3.6	3.2	1.44	0.7	4.2	8.1	0.95	13.7	6.1	-	5.8	8.5	8.5	5.3
			ECC-interface	(s^{-1})	15.4	3.1	2.88	2.1	0.45	1.2	1.9	4.3	3.1	6.4	13.6	7.3	-	13	7.3	3.7	2.1
			ECC-failure	(s^{-1})	2.1	6.3	8.42	12.6	3.3	1.6	1.8	9.1	6.2	5.7	6.1	4.2	-	3.4	6.2	2.6	3.4
	Deflection		Max	mm	1.36	2.04	-	1.38	4.53	-	1.55	-	1.72	4.97	6.11	-	-	7.2	-	1.8	-
			residual	mm	1.35	1.36	-	1.37	4.18	-	1.42	-	1.45	2.95	5.62	-	-	6.9	-	1.45	-
	Acceleration		HS camera	m/s^2	2040	2110	1920	2108	2316	2187	2112	1891	2446	2035	2423	2530	-	2337	2340	2119	1886
			Equivalent force	kN	95.8	99.1	90.2	99	108	102	99.2	88.8	114	95.6	113.8	118.9	-	109.8	109.9	99.5	88.6

5.8 Crack patterns exhibited throughout the loading process

In order to observe the overall behaviour of the specimens and to establish weak points along the element span as well as the failure mode ultimately exhibited by the specimens, the crack patterns developing throughout the loading process are recorded:

i) Through the use of a HS camera: The crack patterns and deformation profiles are presented at four different stages of the loading process: 1ms, 2ms, 3ms and 4ms after the initial contact of the drop weight with the specimen (see Appendix 2).

ii) After each drop-test the specimens were inspected carefully and the crack patterns marked on the front face of the specimens (see Figures 5.26 to 5.29). For specimens subjected to consecutive impacts, the crack patterns exhibited after the first, second, third and fourth drop tests are marked with red, green, blue and black colours respectively.

iii) After failure of specimens the crack pattern on the ECC layers of specimens are marked and documented (see Figure 5.26 to 5.29)

5.8.1 Crack patterns of specimens with one layer ECC

Figure 5.26 presents the crack pattern of the HFO specimens after each consecutive drop test and after failure. The development of the cracks through each drop weight test was recorded through the use of a HS camera and are presented in Appendix 2. The crack patterns obtained from the LFO series are presented in Figure 2.26 as well as in Appendix 2. Both the HFO and LFO series exhibited the same behaviour. The first cracks developed and propagated in the ECC-interface regions specially within the central span of masonry beam (fourth, fifth and sixth interfaces), then cracks initiated in the adjacent ECC layer beneath the interfaces (joints) until ultimately failing (the red lines marked on the ECC layer show the location of the interfaces (joints)- see Figure 5.26 b). These locations are the weakest sections of the retrofitted masonry beams. In some specimens of the HFO series a few cracks developed in the brick beneath the load spreader due to the development of high stress concentrations in this area however, in the LFO series these

bricks remained intact during testing. However, the bond between the bricks and the ECC layer remained intact during impact testing and delamination was not observed. Therefore the strengthened masonry beam-like specimens appeared to work as a composite member. It is interesting to notice that the cracks in the tensile (bottom) ECC layer were concentrated in the region adjacent to the joints (forming between the bricks) of the masonry beam and extended locally the ECC layer. It is worth mentioning that the ECC layer adjacent to the bricks (spanning between two consecutive joints) remained almost intact, free of cracking. It is also interesting to observe that the crack patterns results are in agreement with the strain data presented in Section 5.7 which showed high concentrations in the ECC layer close to interface (joint) region whereas the strains exhibited in the other parts of the ECC layer were significantly less than the ECC-interface regions. It is interesting to note that when the specimens were subjected to consecutive impacts the form of the crack patterns within the ECC layer remained constant while the number and width of the cracks forming close to the joint regions increased. A comparison of the crack patterns developing in the specimens included in the HFO and LFO series revealed that the number of crack in both series are close to each other.

Figure 5.27 depicts the crack pattern developing on the specimens included in the HPO and LPO series respectively whereas a more detailed description concerning the propagation of the cracks throughout the loading process is presented in Appendix 2. As in the case of the fully bonded specimens cracking initiated at the interfaces (joints) within the central span of masonry beam-like specimens. The cracks then propagated in the ECC layer randomly within the central (un-bonded) span regardless of the location of the joints (the red lines marked on the ECC layer represent locations of the joints -see Figure 5.26). This revealed that the partially bonded specimens can perform better than the fully bonded specimens under impact loading. As in the case of the HFO series in some HPO specimens a few cracks developed in the brick beneath the loading points due to the high stress concentrations developing in this area. However, in the LPO series the bricks remained intact in contrast to HPO series. It is interesting to observe that bricks within the central span, not bonded to the ECC layer (especially the two middle bricks), dislocated from their initial position during testing resulting in the failure of the ECC layer. It is interesting to notice that the cracks the bottom ECC layer are uniformly distributed within the central (un-bonded) span of the subject layer. This was then

followed by the development of localized cracking in a random place within the central span which resulted in failure of the ECC layer. It is interesting to observe that the ECC layer adjacent to the bricks (between two consecutive joints) was uniformly cracked in contrast to HFO and LFO series. The distribution of the cracks is in line with the strain distribution described in Section 5.7 with the strain being the same at different locations along the ECC layer. It is observed for the case of the specimens subjected to consecutive drop tests the crack patterns remained similar but the number and width of the cracks increased within the ECC layer. A comparison between the cracks patterns of the specimens included in the HFO and LFO series reveals that the number of cracks developing on specimens subjected to low intensity impact loading in more than high intensity impact load.

HFO4

a)

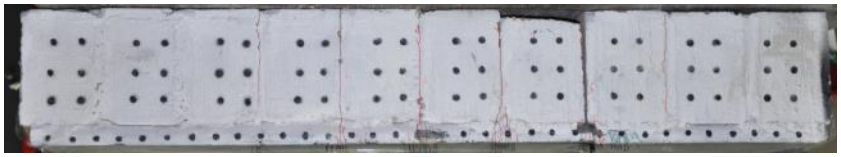

b)

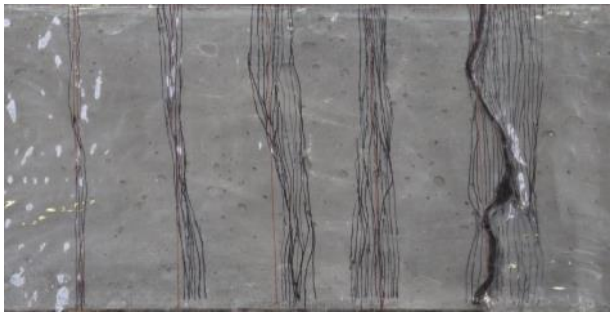

HFO7

a)

b)

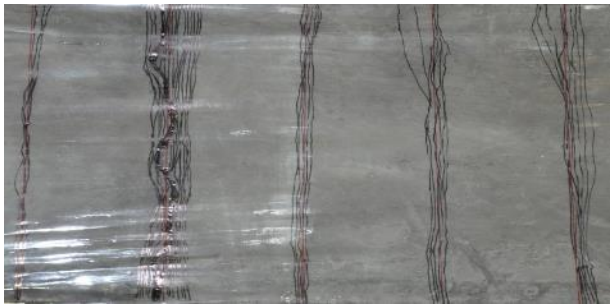

HFO2

a)

b)

LFO1

a)

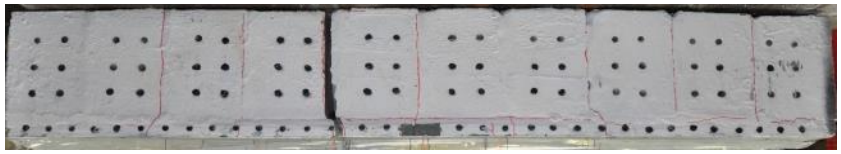

b)

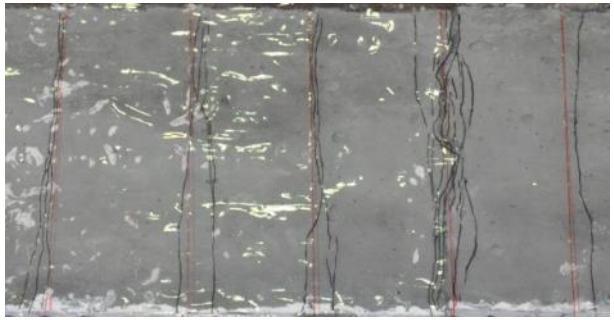

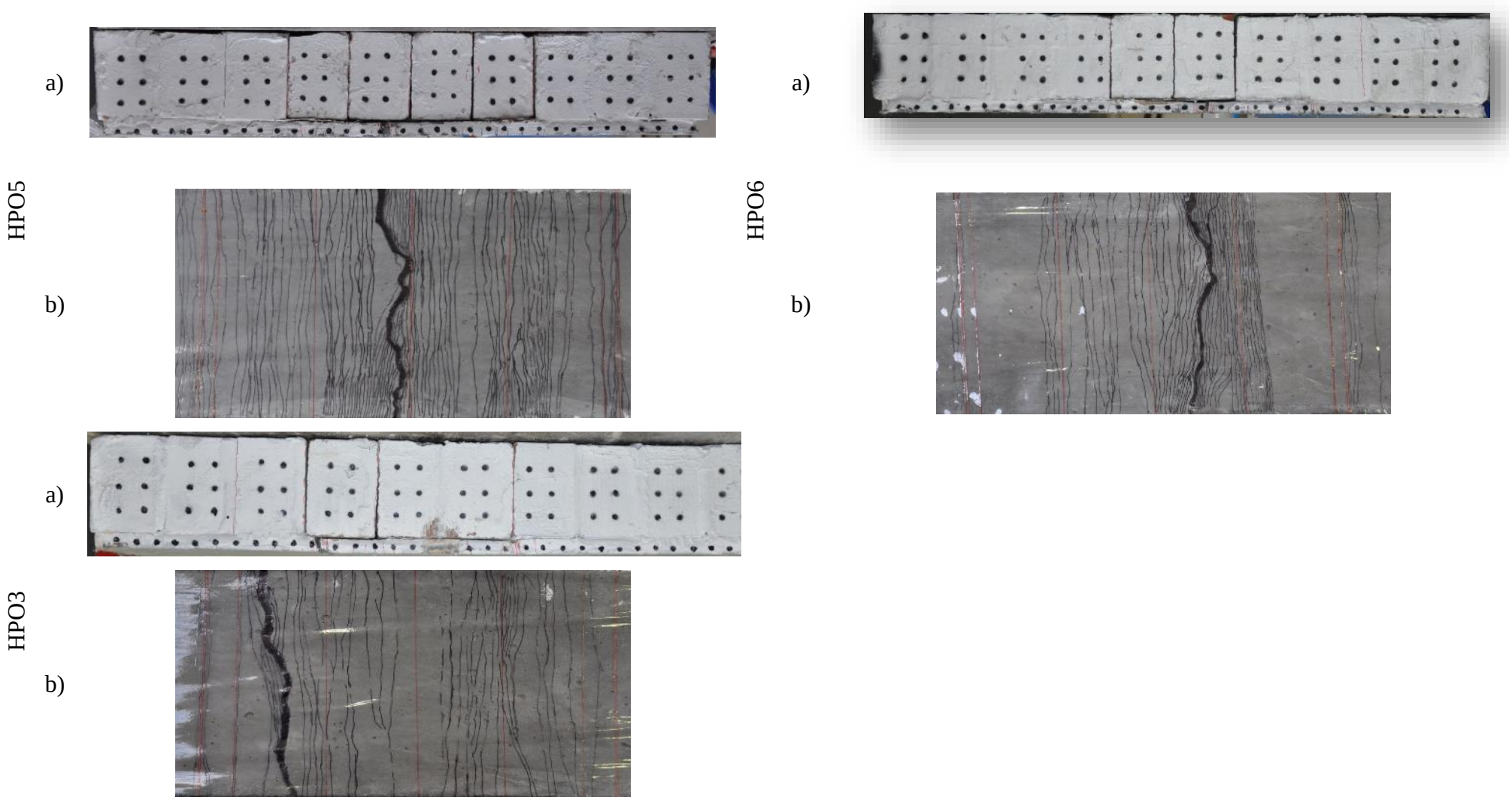

Figure 5.26. The crack patterns developing when subjecting specimens strengthened with a fully (HFO) and partially (HPO) bonded ECC layer to high intensity impact loading a)front face b) bottom ECC layer

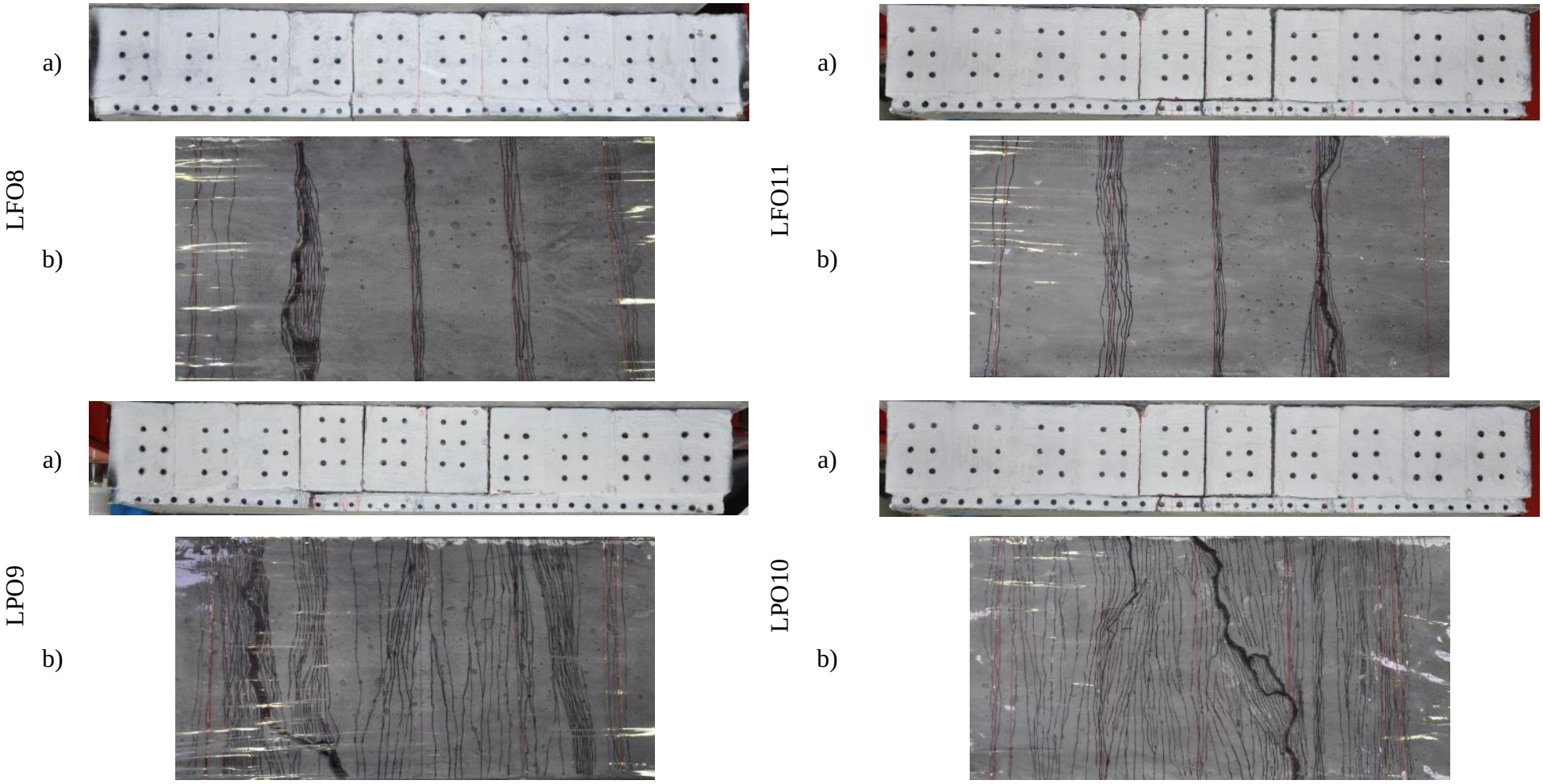

Figure 5.27. The crack patterns developing when subjecting specimens strengthened with a fully (LFO) and partially (LPO) bonded ECC layer to low intensity impact loading

a) front face b) bottom ECC layer

5.8.2 Crack pattern of specimens with two layers ECC

Figures 5.28 and 5.29 present the crack patterns exhibited by the specimens included in the HFT and LFT series after failure. A more detailed description of the cracking process exhibited by specimens throughout the loading process is presented in Appendix 2. Both the HFT and LFT specimens exhibit very similar behaviour to that exhibited by the HFO and HPO series. The first cracks developed at the interfaces (joint) regions (forming between consecutive bricks) within the central span of the masonry beam (fourth, fifth and sixth interfaces) (see Appendix 2 LFT series), and then cracks begin to develop in the bottom ECC layer (acting in tension) beneath of interfaces (joints) until ultimately failure occurs (the red lines marked on the ECC layer represent the locations of the joints - see Figures 5.28 b and 5.29b). When the localized crack developed in the bottom ECC layer (beneath one of central joints), the top ECC layer (acting in compression) cracked and failed at the same location (on the top of the cross-section at which the bottom ECC layer failed in tension). It is interesting to observe that in the case of the specimens retrofitted with two layers of ECC the weakest section is the interfaces forming between the brick units (joints). It is observed that in both the HFT and LFT series the top ECC layer absorbed the impact loads and prevented the formation of cracks on the brick beneath the load points in contrast with what was observed in the case of the HFO series. The bond forming between the bricks and the ECC layer remained intact during impact testing. It is interesting to notice that the cracks in the bottom ECC layer are concentrated in the region adjacent to the joints between the brick units which then gradually extend locally within the bottom ECC layer. When localised crack begin to form in the top ECC layer (in compression) along the same cross-section where failure occurs in the bottom (tensile ECC) layer. It worth mentioning that the ECC layer below the bricks (between two consecutive joints) remains almost intact and free of cracking. It is interesting to observe these crack patterns are in agreement with the strain measurements and distribution discussed in the Section 5.7 which described a high concentration of strain in the ECC layer close to the joint region whereas the values of strains exhibited in other parts of the ECC layer were much lower. It is interesting to note that when the specimens were subjected to consecutive drop tests the form of the crack pattern was constant while the number and width of the cracks increased within the ECC layer in the adjacency of interfaces. A comparison between the HFO and LFO series crack pattern reveals that the number of crack at in both cases are similar.

Figures 5.28 and 5.29 presents the crack patterns exhibited by the specimens included in the HPT and LPT series respectively whereas a more detailed description of the cracking process exhibited throughout the loading process is presented in Appendix 2. The crack patterns are characterised by a series of cracks initiating at the interfaces (joints) forming between the brick units within the central span. Cracking then starts developing randomly along the central (unbonded) span of the bottom ECC layer regardless to the location of the joints (the red lines in the face of ECC layer represent place of interfaces- see Figures 5.28 b and 5.29 b). The top ECC layer cracked and failed in a cross-section other than that at which the bottom ECC layer failed. This reveals that the partially bonded specimen can absorb more effectively the impact energy compared to the fully bonded specimens. As in the case of the HFT and LFT series, the top ECC layer absorbed the impact energy and prevented cracking of brick beneath the load point. It is interesting to observe that bricks within the central span were confined between the two ECC layers that prevented any dislocation/movement of the brick units during impact. It is interesting to notice that the cracks in the bottom ECC layer are uniformly distributed along the central (unbonded) span of subject layer. At failure localized cracking developed in a random location within the central span leading to tensile failure of the layer followed by the development of a series of cracks in the top ECC layer at random locations. The distribution of cracks is in line with strain measurements provided in Section 5.7 which revealed a uniform strain distribution along the un-bonded length of the ECC layer. It is observed in the specimens subjected to consecutive drop test exhibited the same form of crack patterns while the number and width of the cracks increased. A comparison between the HFO and LFO series reveals that the form and number of crack developing is the same in both cases.

HFT14

a)

b)

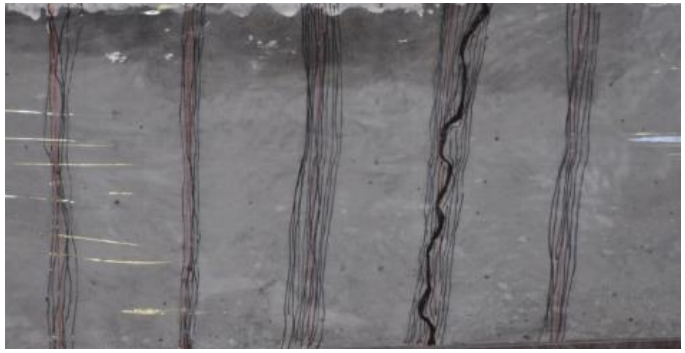

c)

HFT12

a)

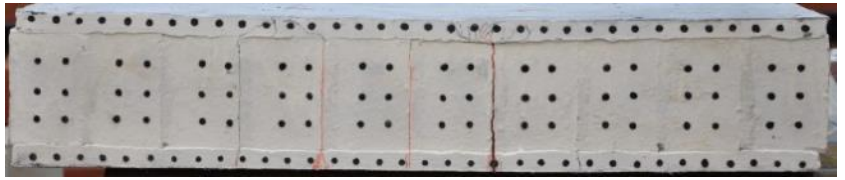

b)

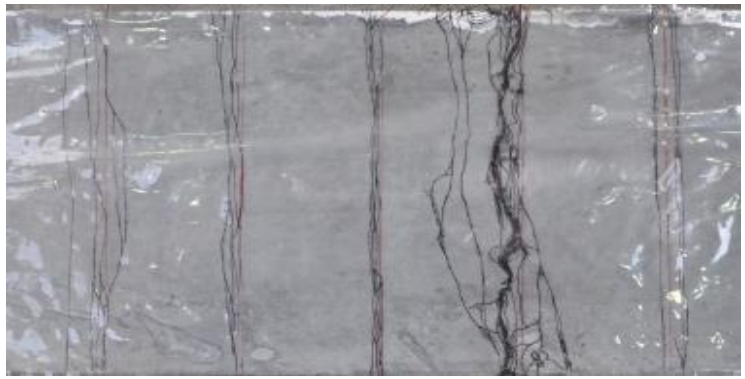

c)

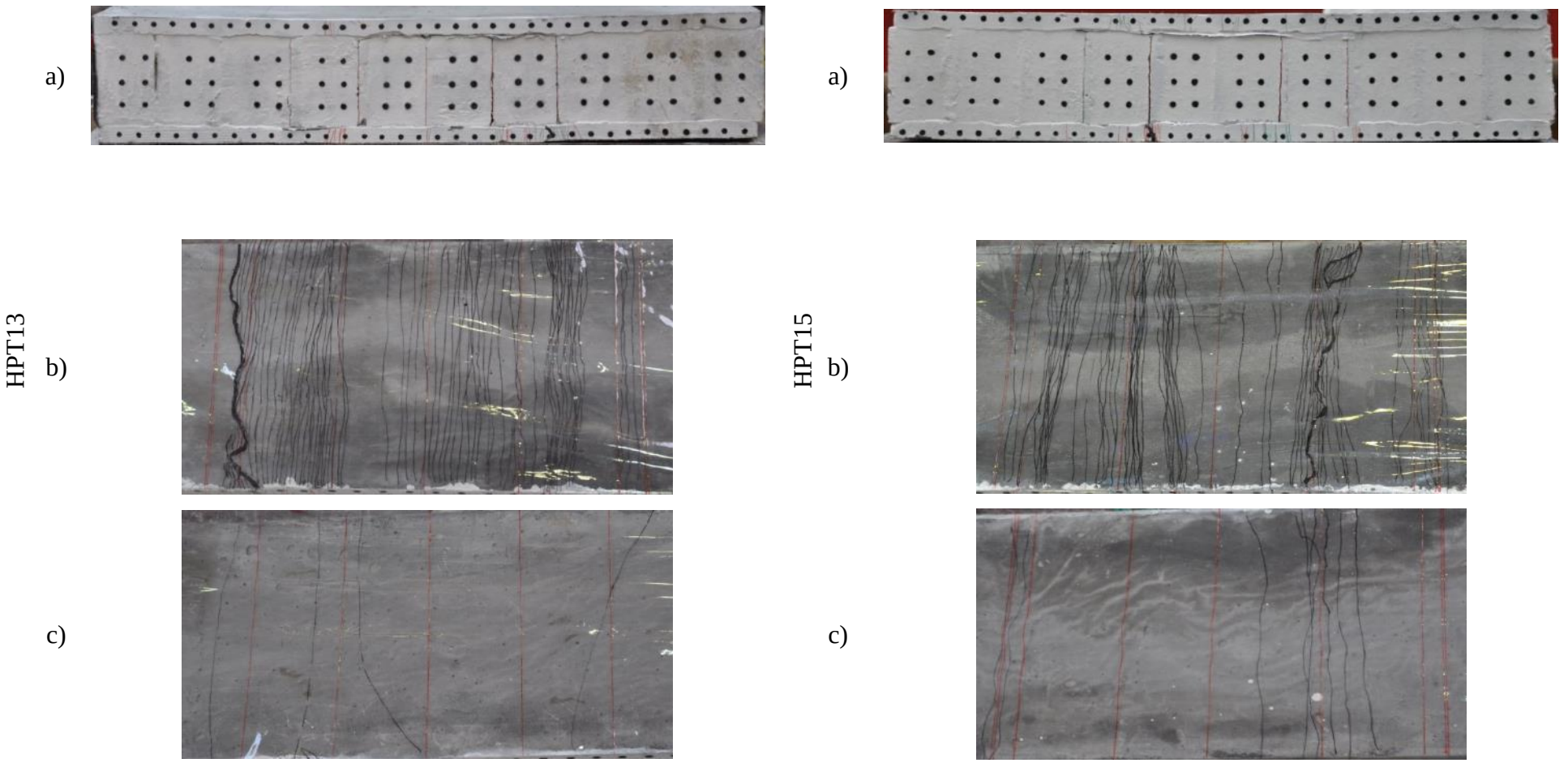

Figure 5.28 The crack patterns developing when subjecting specimens strengthened with two fully (HFT) and partially (HPT) bonded ECC layers to high intensity impact loading a) front face b) bottom ECC layer c) top ECC layer

LFT16

a)

b)

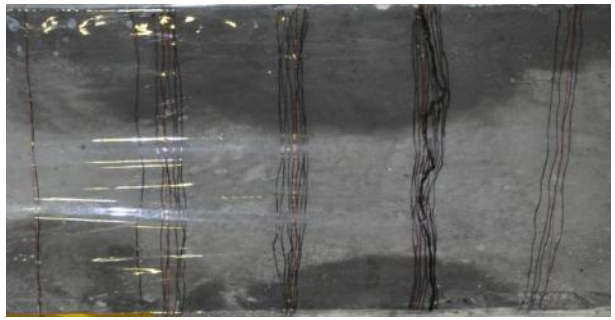

c)

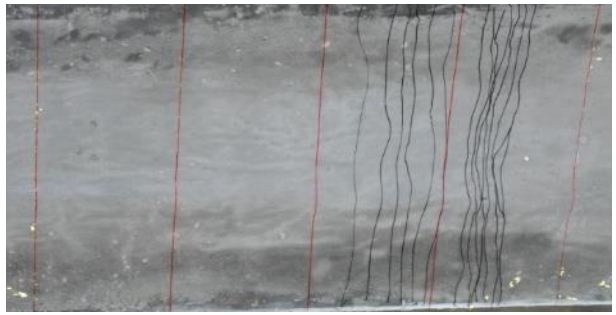

LFT19

a)

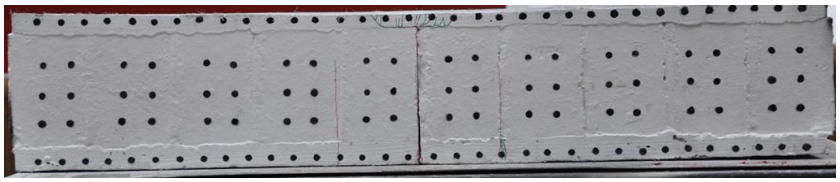

LFT21

a)

b)

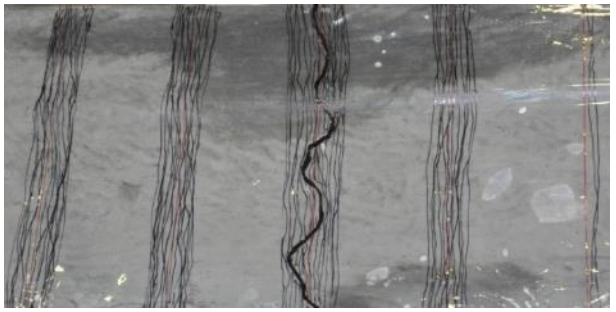

c)

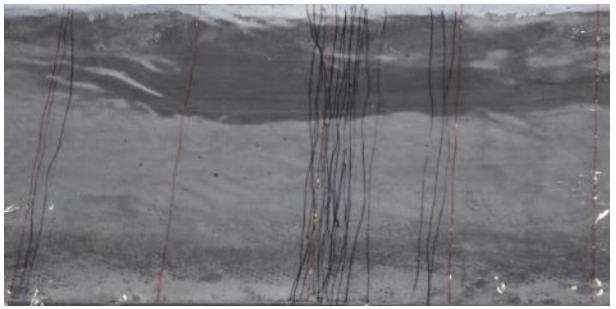

LPT18

a)

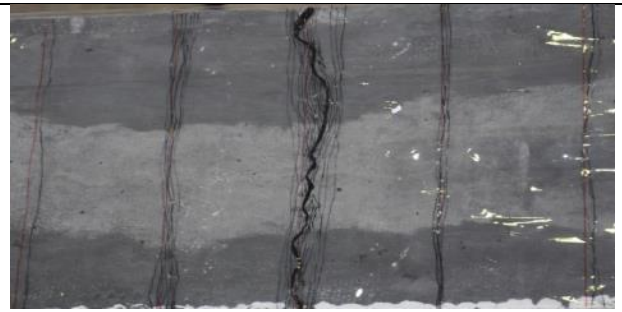

b)

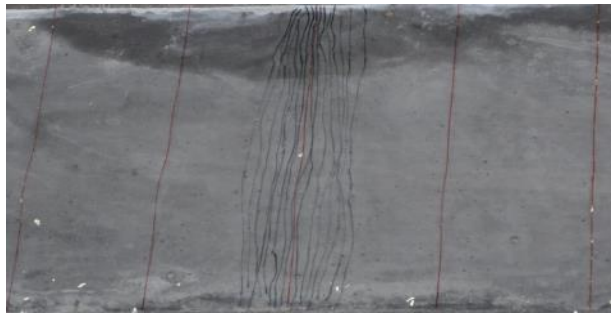

c)

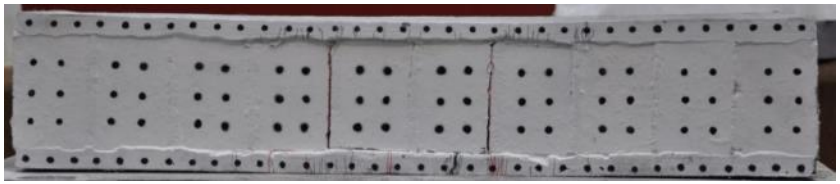

a)

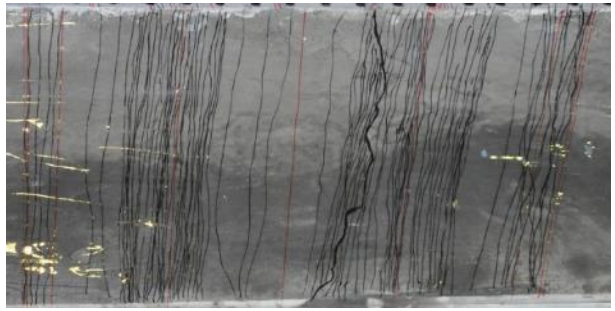

b)

LPT17

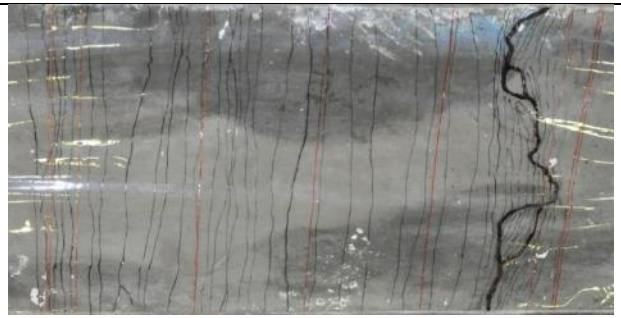

b)

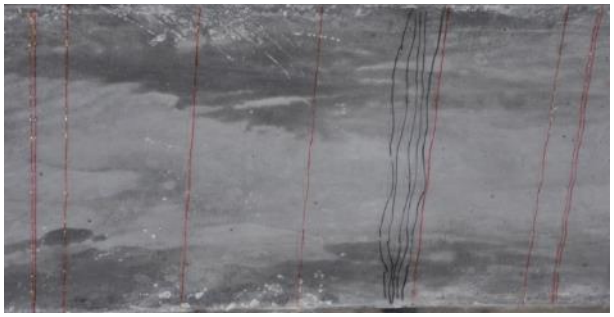

c)

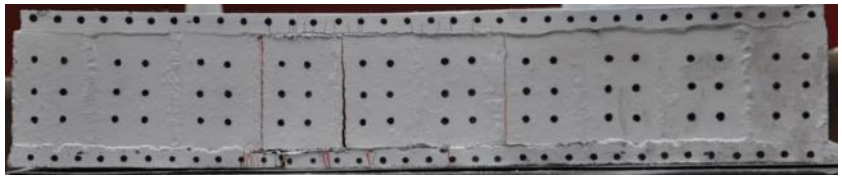

a)

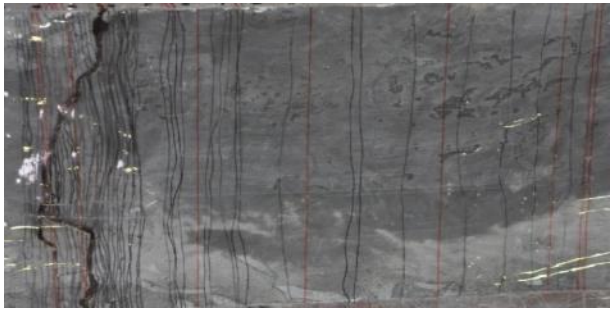

b)

LPT20

c) 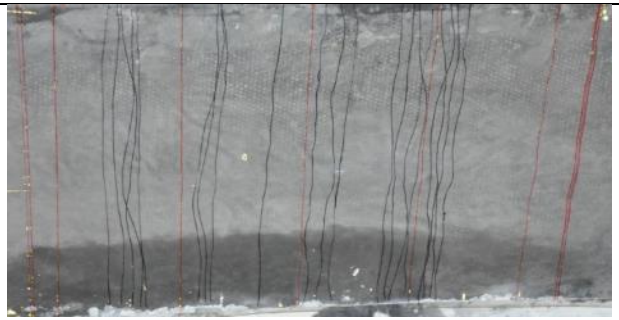 c) 

Figure 5.29 The crack patterns developing when subjecting specimens strengthened with two fully (LFT) and partially (LPT) bonded ECC layers to low intensity impact loading a) front face b) bottom ECC layer c) top ECC layer

5.9 Discussion:

In the previous sections the time history of the impact and reaction forces generated during drop weight testing as well as the variation of (i) the acceleration of the drop weight, (ii) the displacement, strain and strain rate of certain points along the specimen span and (iii) the crack process exhibited at different stage of the loading process are presented and discussed for the HFO, HPO, LFO, LPO, HFT, HPT, LFT and HPT test series. In this section a comparison between the different responses exhibited by the specimens recorded during the impact tests is presented in an attempt to elucidate the ability of the strengthening methods adopted to enhance certain aspects of the behaviour of the masonry specimens.

5.9.1 Comparison of impact loads applied on the specimens

Two types of impact loading are considered: high intensity and low intensity impact loading (see Section 5.3). Though test condition introduced to the specimens was same for all drop-tests conducted (as the same mass was dropped from the same height) the various aspects of the behaviour exhibited by the different groups of specimens were characterised by significant differences. When high intensity impact loading was applied on the specimens strengthened with a fully or partially bonded single layer of ECC (HFO and HPO series) the impact loads time history was characterised by a single wave with multiple peaks and a short duration of approximately 2ms (for whole wave). The initial and average (peak load divided by the time required to attain it) loading rates exhibited were 400 kN/ms, and 200kN/ms respectively (see Table 5.2) and the maximum peak load was 120 kN. However, for the case of low intensity loading applied onto specimens strengthened with one layer of ECC (LFO and LPO series) the time history of the impact force generated was characterised by multiple waves with single peaks. The duration of the impact load was 4 ms (for whole waves) with an initial and average loading rate of approximately 450 kN/ms and a maximum load of 100kN. Though the loading rate established during low intensity drop-weight testing is higher than that recorded in the case of high intensity impact testing whereas the duration of impact wave during each drop weight test and the peak load were about 200% and 20% lower respectively.

In the case of the specimens retrofitted with two layers of ECC subjected to high intensity drop-weight testing the time history of the impact load generated was characterised by multiple waves with multiple peaks, a short duration of approximately 2ms, an initial and average loading rate of 400kN/ms and 300 kN/ms respectively and a maximum load of 80 kN (see Table 5.3). In the case of low intensity drop weight testing the time history of the impact load was characterised by multiple waves with multiple peaks, a duration of 4 ms, an initial and average loading rate of 400kN/ms and a maximum impact load of 80 kN (see Table 5.4). It is interesting to note that the impact load time history generated during each consecutive drop test were similar. This suggests that the impact load generated is associated with the inertia forces developing during the collision of the drop-weight on the specimens rather than the structural resistance offered by the specimen itself.

5.9.2 Comparison of reaction loads obtained from specimens

The main characteristics of the reaction load generated are summarised in Tables 5.2-5.4. The R/I ratio (i.e. peak impact load and peak reaction force ratio) established reduced with every consecutive drop test. This parameter is associated with the resistance of specimens against impact load and reduced as the level of damage sustained increased in specimens with every impact. However, the I-R delay (duration between maximum impact and reaction force) increased with every consecutive drop test. This parameter is associated with the time required for the stress wave generated at the impact region to reach the supports of the specimens. This parameter increased as level of damage (cracking) increased in the specimens. In the case of the specimens strengthened with a fully bonded layer the average rate at which R/I ratio reduces and the I-R increases with every consecutive drop-test is higher than that observed for the case of the specimens with partially bond ECC layers. Both these parameters reveal that the rate of developing of cracking in the case of the partially bond specimens is slower than fully bonded counterparts. It is interesting to notice that partially bonded specimens exhibited higher structural integrity and resistance against the impact load as the level of damage sustained in the specimens was lower that that was observed in the fully bonded specimens.

5.9.3 Effect of bond arrangement on the specimens behaviour

The deflection exhibited at different points along the element span provides information concerning the deformability of specimens and their ability to absorb impact energy during drop weight testing. However, it was not possible to fully measure these values when the specimens the drop-weight tests results in failure/collapse of the specimens. The maximum deflections recorded in the mid-span of specimens with one layer ECC were 3.5mm -10mm, 3.8mm, 2.5mm and 8.5mm-11.5mm for HFO, HPO, LFO and LPO series respectively. The maximum deflections recorded in the mid-span of specimens with two layer ECC were 2.8mm-5.5mm, 3.2mm-4.2mm, 1.5mm, 5.5mm and 2mm-12mm for HFT, HPT, LFT and LPT series. All specimens presented a ductile behaviour when subjected to impact load. The partially bonded specimens exhibited approximately 40% higher deflection compared to fully bonded specimens, however it was not possible to measure the exact total value of deflection during tests. The residual deflection of the specimens retrofitted with one layer of ECC exhibited 5%-30%, 70%, 5% and 65% reduction (in relation to the maximum deflection) for the HFO, HPO, LFO and LPO series. The residual deflection of specimens retrofitted with two layers ECC exhibited 10%, 10%, 10%, 10-20% reduction (in relation to the maximum deflection) for the case of the HFT, HPT, LFT and LPT series respectively. It is interesting to notice that partially bonded specimens exhibited more reduction of residual deflection compared to that established for the case of the fully bonded specimens. This fact reveals that the partially bonded specimens utilize more effectively the benefits offered by the ECC layer(s) compared to fully bonded counterparts. In the unbonded region of the ECC layer the more uniform distribution cracking is observed thus allowing the specimens to absorb impact energy more effectively and with less damage.

Using the information recorded about the crack propagation and strain distribution exhibited during testing it is possible to derive conclusions about the specimens' behaviour under impact loading. In the case of the fully bonded specimens the strain exhibited in the bottom (tensile) ECC layer below the brick (between two consecutive joints) was almost very small in all cases. In contrast, the strain exhibited by the bottom ECC layer below the joint (i.e. interface between two bricks) reached a maximum value up to 3%. The crack patterns recorded also reveal that for the case of the fully bonded specimens the full strain capacity of the ECC layer is not utilised by these specimens. In

the case of the partially bonded specimens a more uniform distribution was observed throughout the span of the unbonded region of the ECC layer with a maximum value of 3%. The crack pattern also verifies the above findings suggesting that the partially bonded specimens were able to more effectively absorb the impact energy while at the same time utilising more effectively the benefits that the ECC material has to offer.

In the specimens retrofitted with one layer ECC two problems were observed under impact loading. First, localised cracking develops in the bricks below the point of loading under high intensity loading and then, in the case of the partially bonded specimens, the bricks located in the central span dislocate after the application of the impact resulting in failure of ECC layer. However, both these problems were rectified when using the second layer ECC at the top of the specimens. Specimens with a second layer of ECC exhibited a more consistent response while being able to undertake a larger number of consecutive impact loads (blows) before collapsing (see Table 5.1).

In all specimens retrofitted with ECC layer(s) and subjected to impact load debris (moving at high speed) were not observed during the impact tests (see Appendix 2). This fact reveals that the ECC layer can act as a net effectively catching any debris produced during the impact. The integrity of the structure members is very important in explosion or blast events as projectile debris are repeatedly reported as a major source of causalities (Wightman and Gladish, 2001, Taber et al., 2006, Freiwald, 1972, Cooper et al., 1983). It is observed that the ECC layer(s) with any bond arrangement can stop projectile debris being formed.

5.9.4 Comparison between the behaviour exhibited under static and impact loading

The results obtained from tests conducted on specimens strengthened with one layer of ECC under static loading (see Table 4.4) revealed a load-bearing capacity of 13 kN and 11 kN and a maximum mid-span deflection of ECC layer of 4 mm and 7mm for the case of fully and partially bonded specimens respectively. During drop-weight testing a maximum reaction force of 45 kN and a deflection of 5mm was established for the case of fully bonded specimens with one layer of ECC. A maximum reaction force of 45 kN and a maximum deflection of 7 mm was exhibited by the specimens with one partially bonded layer of ECC0. An average of two consecutive drop tests were conducted before

the specimens finally collapsed. It is interesting to notice that the load bearing capacity of ECC retrofitted specimens increased by about 4 times under impact loading compared to that established under equivalent static loading while the deformability of the specimens under impact loading was similar to that exhibited under static loading.

As discussed in Chapter 3 (see Figure 3.9) ECC is a strain rate dependent material (its properties are dependent on the strain rate). Very limited information is presently available in the literature about the behaviour of ECC under high loading rates. Available data report that at strain rates of $10s^{-1}$ the ductility of ECC is 70% lower compared to that established under static testing while the load bearing capacity of ECC increased by about 200%. At strain rates of $50s^{-1}$ the ductility of the specimens is still 70% lower than that exhibited under static loading while the load bearing capacity of ECC increased by about 300%.The loading rate measured in the ECC layer during the impact tests was between 10 s^{-1} to 100 s^{-1} for specimens at the bottom ECC layer. The specimens' behaviour under impact loading presented the same trend as reported in the literature which suggests the load bearing capacity of specimens increases while the ductility is close to static counterpart.

It is interesting to observe that the strain time histories and crack pattern exhibited under impact load are similar to those exhibited under static loading. Both the HFT and LFT specimens exhibited values of strain and crack profiles in the bottom ECC layer below the joint region similar to those established during equivalent static loading presented in Chapter 4 (see Section 4.20). HPO and LPO exhibited a uniform strain and crack distribution within the central (un-bonded) span which is similar to their static counterparts (see Figure 4.22). However, the number of visible cracks under impact loading for all specimens was less than static counterparts.

5.10 Conclusions

Regarding the observations and data obtained from the data logger and HSD camera following conclusions can be drawn:

- The use of ECC layer(s) resulted in an increase of the specimens strength, ductility and deformability while prohibiting the generation of debris. The ECC layer essentially act as a net that stops the production of debris due to impact load.

- It is observed that under high and low intensity impact loading the form of the curve describing the time history of the contact force generated in the impact region is characterised by certain differences depending on the properties of the interface between the impactor and the specimens, the method adopted for applying the ECC layers and the speed with which the impactor strikes the specimen. High intense impact loads are characterised by a maximum value of 120KN and 80kN for specimens retrofitted with one and two layers of ECC respectively as well as very short duration of 2 ms. Low intensity impact loads are characterised by a maximum value of 100kN and 80kN for specimens retrofitted with one layer and two layers of ECC respectively as well as very short duration of 4 ms. .

- It is interesting to notice that under consecutive drop-tests the impact load generated is largely associated with the impact energy and inertia force and was less affected by the specimens' ability to resist the impact load. On the other hand the reaction forces generated is associated with the level of damage sustained by the specimen during testing.

- When strengthening the specimens with a second layer of ECC the performance of specimens significantly enhanced. The dislocation of bricks in partially bonded specimens during impact testing was limited by the top ECC layer and failure of bricks below the points of loading was not observed. On average 3 impacts were sustained by the specimen before the specimen with 2 layers of ECC collapsed unlike the specimens strengthened with one layer of ECC which were able to undertake on average 2 impacts. Also, the variability observed in the specimens behaviour during impact testing reduced and specimens exhibited more consistent performance when the second layer of ECC was applied in top of specimens.

- The level of bond achieved between the ECC layer and masonry surface is an important parameter in retrofitting of masonry walls against impact loading. The ductility of the masonry beams retrofitted with an ECC layer partially bonded to the specimen when subjected to impact load is higher (approximately 40%) compared to fully bonded counterparts specimens. This was observed in both cases of impact loads (high and low intense impact).

- The behaviour of the partially bonded specimens (subjected to high and low intense impact loads) exhibit more ductile characteristics due to the multiple and distributed cracking developing in the un-bonded region of the ECC layer. The cracks in the fully bonded specimens (subjected to high and low intense impact) developed near the brick-mortar interface regions (joints) over the centre span of the specimens. In the case of partially bonded specimens, a more uniform crack pattern was observed, indicating a better utilization of the ECC layer.

- It is demonstrated that the strains (and hence the cracking) in the ECC layer in the un-bonded region is more distributed, potentially resulting in larger deformation compared to fully bonded specimens.

- Strengthening the masonry specimens with one layer of ECC enabled them to undertake levels of applied loading significantly higher than the load-carrying capacity established under equivalent static loading. A comparison between behaviour of specimens exhibited under impact loading and equivelant static loading reveals that the load carrying capacity of the specimens increased by about 4 times while their response exhibits more ductility characteristics. It also allowed the specimens in some cases to undertake more than one drop-tests (blows) before collapsing.

5.11 References

COOPER, G. J., MAYNARD, R. L., CROSS, N. L. & HILL, J. F. 1983. Casualties from terrorist bombings. *Journal of Trauma and Acute Care Surgery,* 23**,** 955-967.

FREIWALD, D. 1972. Approximate Blast Wave Theory and Experimental Data for Shock Trajectories in Linear Explosive-Driven Shock Tubes. *Journal of Applied Physics,* 43**,** 2224-2226.

TABER, K. H., WARDEN, D. L. & HURLEY, R. A. 2006. Blast-related traumatic brain injury: what is known? *The Journal of neuropsychiatry and clinical neurosciences,* 18**,** 141-145.

WIGHTMAN, J. M. & GLADISH, S. L. 2001. Explosions and blast injuries. *Annals of emergency medicine,* 37**,** 664-678.

Chapter 6: Finite element modelling

6.1 Introduction

The experimental studies presented in Chapters 4 and 5 show that the benefit stemming from the use of ECC for retrofitting the masonry specimens considered in the preceeding chapters under static and dynamic actions in the out-of-plane direction include: (i) an increase in load-bearing capacity, deformability and ductility, as well as (ii) a change in the mode of failure from fully brittle to ductile. The experiments also showed that the behaviour exhibited under high loading rates considerably differs compared to that established under equivalent static loading. However, the test data often cannot provide a detailed description of specimen's behaviour (e.g. stress-strain distribution during the loading process, the effect of the interaction of specimens and apparatus etc.). Also the effect of a wide range of parameters on the specimens' behaviour (i.e. elevated temperature effect) has not been investigated in detail experimentally.

Due to the limitations characterising the available experimental data and in order to investigate in more detail the behaviour exhibited by the subject specimens, non-linear finite element analysis (NLFEA) is employed. This is achieved through the use of ADINA, a finite element analysis package capable of conducting static and dynamic nonlinear analysis. The package allows users to define appropriate constitutive models describing the behaviour of the relevant materials, including brick, mortar, ECC and their interfaces. The aim of this numerical investigation is to develop models capable of realistically predicting the behaviour of the retrofitted masonry specimens. A number of preliminary models are developed to initially calibrate the various parameters necessary in order to fully define the individual constitutive models employed for describing the behaviour of the materials used for the construction of the masonry specimens and their interaction. The latter parameters are then employed for the development of more intricate models capable of predicting the behaviour of the retrofitted masonry specimens investigated experimentally in chapters 4 and 5 respectively.

A series of two-dimensional (2-D) FE models are developed to simulate the experiments carried out on brick units as well as mortar and ECC specimens in order to establish their behaviour under uniaxial compression and/or tension. Interface models are developed based on the data obtained from the shear, compression and tensile tests presented in

Chapter 4 in order to describe the interaction exhibited between the various materials consisting of the retrofitted masonry specimens. The latter models are calibrated through the use of the data obtained from the tests conducted on small scale masonry specimens in Sections 4.2.2 and 4.2.3 to establish bond characteristics between brick–mortar under compression, tension and shear and between brick-ECC under tension and shear.

Once the individual material and interface models have been appropriately calibrated, they are used to form more advanced models representing the masonry beam-like specimens studied experimentally under static and dynamic (impact) loading in chapters 4 and 5 by conducting a series of four point bending tests. Initially, 2D detailed FEA models are developed to simulate the retrofitted and non-retrofitted masonry beam specimens subjected to quasi static flexural tests. The latter models were then simplified in order to reduce the computational cost and the number of parameters required for their definition. After validating the numerical predictions against the test data presented in Chapters 4 and 5 the simplified models are used to study the effect of a number of parameters. These parameters are associated with the variability of the properties of the material or interfaces relevant to the specimens considered, the load and boundary conditions imposed, the geometry of the specimens, the different retrofitting techniques employed and the rate of loading. It should be noted that the effect of the latter parameters on the response of retrofitted masonry specimens has not been investigated in detail to date.

Table 6.1 presents the list of simulations initially carried out to calibrate the models describing material and interface behaviour. These models are calibrated against available experimental data presented and discussed in Chapter 4. Table 6.2 presents a summary of the detailed and simplified models developed for predicting the behaviour of the masonry beam specimens presented in Chapters 4 and 5 subjected to four point static and dynamic bending tests. Table 6.3 presents the different parameters which are considered in the parametric investigation. These include the loading rate and intensity, the variation in mechanical properties of the masonry walls units, the geometry and length of the specimens and the boundary conditions.

Table 6.1: Calibration models developed for calibrating material and interface behaviour

Type of model	ID	Relevant experiment
Brick unit	MCB	Compression test - see Section 4.2.2
Mortar	MCM	Compression test - see Section 4.2.3
ECC	MTE	Tensile test - see Section 3.4.2
Brick-mortar interface	ITBM	Tensile test - see Section 4.2.7
Brick-mortar interface	ISBM	Shear test - see Section 4.2.5
Brick-mortar interface	ICBM	Compression test- see Section 4.2.4
Brick-ECC interface	ISBE	Shear test - see Section 4.2.6

Table 6.2: Models representing masonry specimens

Type of model	ID	Relevant experiment	Load
Non-retrofitted masonry beam	SDM	Section 4.3.3	Static load
Detail model of retrofitted masonry beam with one fully bonded layer of ECC	SDFO	Section 4.3.4	
Detail model of retrofitted masonry beam with one partially bonded layer of ECC	SDPO	Section 4.3.5	
Simplified model of retrofitted masonry beam with one fully bonded layer of ECC	SSFO	Section 4.3.4	
Simplified model of retrofitted masonry beam with one partially bonded layer of ECC	SSPO	Section 4.3.5	

Table 6.3 parametric study

Parametric study	Parameters Considered
Effect of 2nd layer ECC at top of masonry beams	Fully bonded, partially bonded
Variation of material and interface properties	ECC (effect of elevated temperature up to 600 ˚C)
	Brick fc=60MPa to fc=10MPa
	Mortar fc=22MPa to fc=7MPa
Effect of specimen length	740mm to 3000mm
Boundary condition	Pinned-pinned & fixed-fixed specimens
Loading rate	1,200 to 1,200,000 kN/s

Figure 6.1a describes the terms used for identifying the different groups of models mentioned in Table 6.1. The first letter indicates whether the model describes material (M) or interface (I) behaviour. The second letter is associated with the type of loading considered (i.e. letters C, S, T and F are associated with compression, shear, tension and flexure loading respectively). The third letter refers to the type of material considered

(letters B and M are associated with brick and mortar respectively). When considering interface models the fourth letter refers to the second material considered (letters M and E are associated with mortar and ECC respectively). Finally, a number presents number of samples. In Figure 6.1 (b) the first letter shows the rate of loading on simulations. The second letter presents the type of models, for the detailed model D and simplified model S are chosen. The third letter refers to different masonry beams. The masonry presented by M, full bond ECC F and partial bond P. The next letter presents the number of ECC layer one layer ECC demonstrated by O and two layers by letter T. Finally a number presents number of samples.

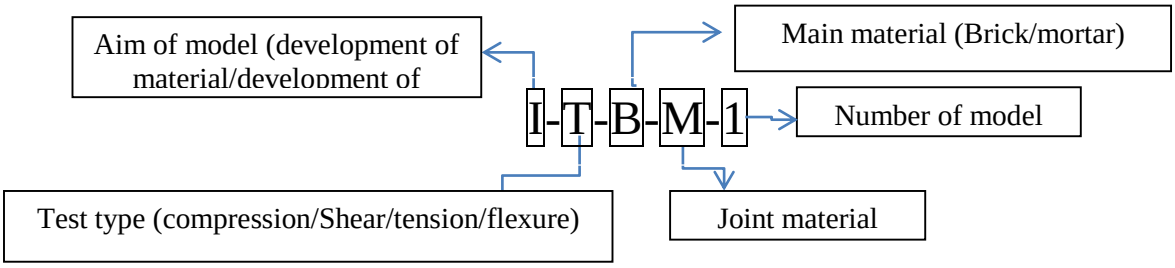

(a)

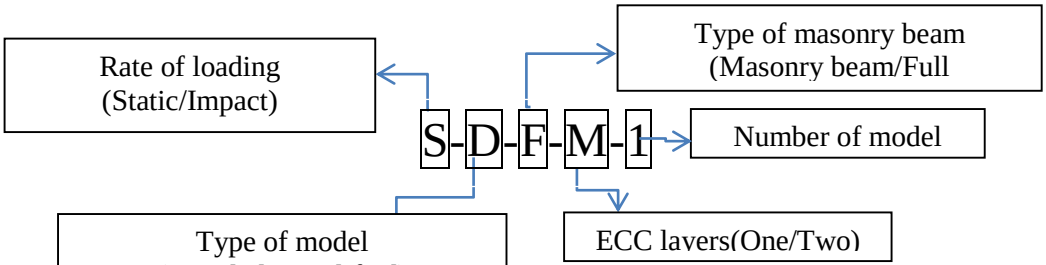

(b)

Figure 6.1 Labelling system used in (a) part 1 and (b) part 2 numerical programme

6.2 Part 1 Calibration of material and interface models

6.2.1 Main characteristics of ADINA

ADINA (ADINA 9.0.1) has been found capable of realistically predicting the response of a wide range of structural configurations under static and dynamic loading. The subject package is capable of carrying out three-dimensional (3-D) static and dynamic nonlinear finite element analysis (NLFEA) while realistically accounting for the nonlinearities

characterising the behaviour of the materials involved. When studying structural response under dynamic actions the equation of motion is solved numerically through the use of an implicit Newmark integration scheme. The choice of 3D dynamic NLFEA is dictated by (a) the nonlinear behaviour of the various materials involved (i.e. brick, mortar) under triaxial stress conditions, which invariably develop prior to local failure (i.e. cracking), (b) the introduction of non-homogeneity and stress redistribution after the occurrence of cracking and (c) the development of significant inertia forces (ADINA Manual, 2012).

Material Modelling: The following material models are employed in ADINA capable of describing the behaviour of the materials involved and their interaction (ADINA Manual, 2012):

- *Concrete material model*: Although the model is entitled "concrete model", the basic constitutive characteristics are such that the model can also be useful when representing other materials (i.e. brick). The basic material characteristics are tensile cracking failure at a maximum, relatively small principal tensile stress, compression crushing failure at high compression and strain softening from compression crushing failure to an ultimate strain, at which the material totally fails. The uniaxial stress-strain data curve of material under compression and tension and shear retention are the important input for this material.

- *Plastic-multilinear material models*: this model can be used with large displacement and large strain formulations. This material uses a nonlinear plastic uniaxial stress-strain data input under tension provided in tabular form which is used for modelling ECC behaviour in this study.

- *Nonlinear elastic material model*: this model can be used with the large displacement and large strain formulations. This material uses a nonlinear elastic uniaxial stress-strain data input under compression and tension in tabular form which used for modelling ECC behaviour.

- *Cohesive interface*: the cohesive interface can be employed to model the separation of zero thickness interfaces, such as laminated composites, bonded interfaces. The cohesive element is composed of top and bottom surfaces with initially zero thickness. The cohesive element uses a bilinear constitutive law that relates the traction to the

relative displacement at the element mid-surface. Initially linear elastic behaviour followed by the initiation and evolution of damage is assumed. After the onset of damage, the strength of the cohesive element are gradually reduced to zero in its softening envelope. Shear and tension strength and stiffness are main inputs in this element.

Nonlinear Solution Strategy: During each time step the equation of motion governing the nonlinear dynamic problem considered is solved as a sequence of equivalent static problems through the use of the Newmark family of approximation methods (ADINA Manual, 2012). At the beginning of each iteration and based on the values of displacement, velocity and acceleration obtained from the previous iteration, the effective stiffness and load matrix are calculated and an equivalent static problem is formulated. The equivalent static problem is solved through an iterative procedure based on the Newton-Raphson method (ADINA Manual, 2012). During the solution process of the equivalent static problem every Gauss point is checked to determine whether loading or unloading takes place and to establish whether any cracks close or form. Depending on the results of the previous checks, changes are introduced to the stress-strain matrices of the individual finite elements and to the global stiffness matrix representing the structure investigated. Convergence is checked locally at each Gauss point and once the values of the strain and the corresponding stress increments are less than the small predefined value (i.e. convergence criterion) then convergence is accomplished and the solution can move on to the next time step. When the convergence criterion is not achieved, the residual forces are calculated and are then re-imposed onto the FE model of the specimens investigated until convergence is finally achieved (ADINA Manual, 2012).

Modelling of Cracking: Cracking is considered either through the (fixed) smeared crack approach or via failure of the cohesive interface model. The smeared-crack approach is adopted for modelling cracking in materials including brick unit and mortar layer. A crack forms when the stress developing in a given part of the structure corresponds to a point in the principal stress space that lies outside the predefined failure surface of the concrete material. This is then followed by an immediate loss of load-carrying capacity in the direction normal to the plane of the crack. At the same time, the shear stiffness is also reduced drastically to a small percentage (about 5 to 10%) of its previous value (before the occurrence of the crack). However, it is not set to zero in order to minimize the risk of numerical instability during the execution of the solution procedure, as explained

elsewhere. It should be noted that each integration point can develop up to three cracks (in three different dimensions). In the case of the cohesive interface elements the cracks happened in the discrete element fashion and after the interfacial normal or shear tractions reach their respective tensile or shear strengths, the strength is gradually reduced to zero.

6.2.2 Brick behaviour under uniaxial compression

The present model MCB is developed based on the experimental data presented in section 4.2.1.1. The behaviour of the brick units under uniaxial compression is essentially modelled through the use of the concrete material (ADINA Manual, 2012). The compression strength $(f_{c,b})$ is established experimentally equal to 63 MPa and the modulus of elasticity 35 GPa (see Section 4.2.1.1). The tensile strength $(f_{t,b})$ is presently assumed to be 10% of $f_{c,b}$ (Beall, 1993) and the Poisson ratio (v) is considered equal to 0.15 (Rots, 1997). A shear reduction factor of 0.1 is used however the influence of this coefficient is not expected to have a significant effect on the predicted response of the masonry units since in all experiments conducted the brick units did not crack. The density of the brick unit was measured at 2000 kg/m^3. Figure 6.2 shows the stress-strain curve adopted in order to describe the behaviour of brick units under uniaxial tension and compression.

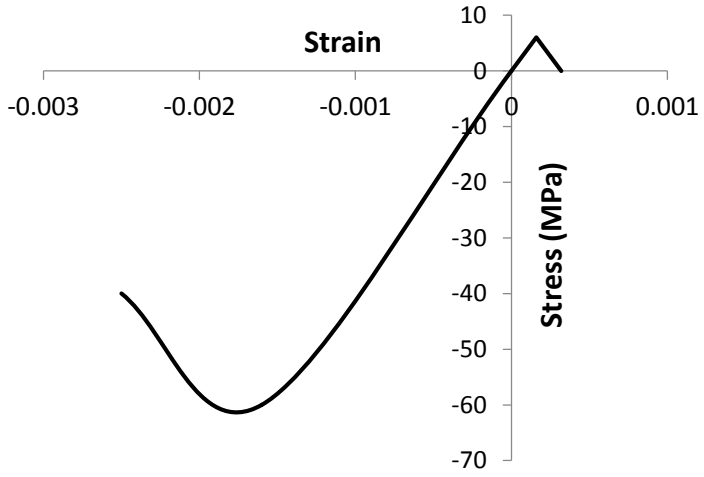

Figure 6.2 Stress-Strain curve employed for describing the behaviour of brick units under uniaxial tension and compression.

In order to validate the material model presently employed for describing the behaviour of the brick units in compression and tension, the 2-D plane-stress model showed in Figure 6.3 is employed. This model consists of a prismatic specimen representing the brick unit and two steel plates positioned on the top and bottom face of the prism. The

steel plates are assumed to behave elastically throughout the loading process. The dimensions of steel plates are 20x100 mm and brick 100x65 mm with a thickness of 100 mm. A 10 x 15 4-node mesh with dimensions of 10mm x 4.15 mm is used for the brick model. The pinned supports assigned to bottom steel layer. The load is applied in the form of load increments on the top of the specimen. The predictions obtained from the model are presented in the form of stress-strain curves (see Figure 6.4.) are in good agreement with the experimental data both in terms of stiffness and strength. The FE model predicts the modulus of elasticity 37 GPa which is close to mean value obtained from experiments 35 GPa. The predicted compressive strength obtained from the MCB model is 52 MPa which underestimate the experimental results with the average compressive strength of 60 MPa. (Section 4.2.1.1).

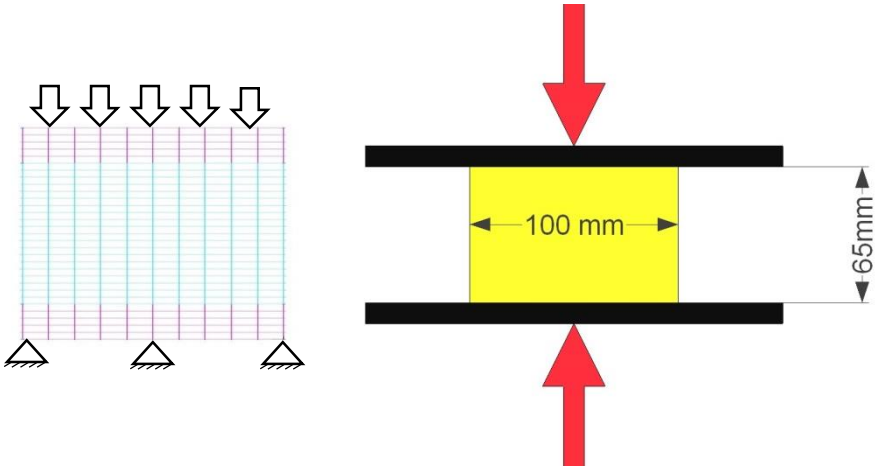

Figure 6.3 FE model for compression test accompanied by its experiment

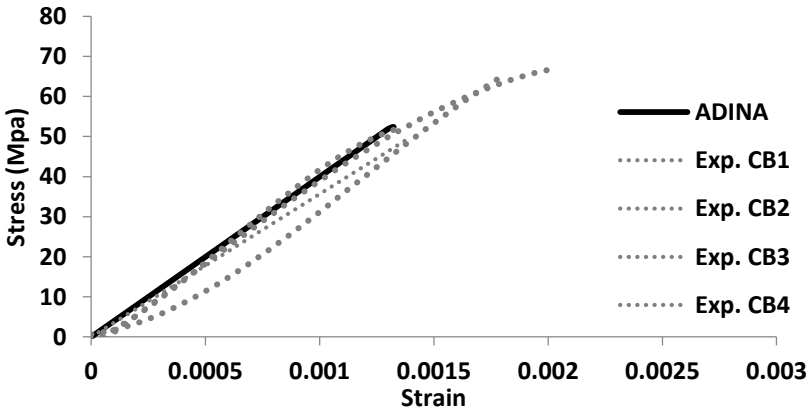

Figure 6.4 Comparison of stress-strain curves predicted numerically and established experimentally for describing the behaviour of the brick units in compression

6.2.3 Mortar behaviour under uniaxial compression,

The model MCM is developed based on experimental data presented in the section 4.2.1.2. The behaviour of the mortar under uniaxial compression is essentially modelled through the use of the concrete material model (ADINA Manual, 2012). The compression strength *($f_{c,b}$)* measured 20 MPa and the modulus of elasticity 10 GPa in section 4.2.1.2. The tensile strength *($f_{t,b}$)* is assumed equal to 10% of the compression strength (Rots, 1997) and the Poisson's ration (*v*) of mortar supposed 0.15 (Rots, 1997). A shear reduction factor 0.1 is used however the influence of this coefficient is not expected to have any significant effect in the masonry specimens since in all experiments conducted the mortar did not fail. The density of mortar measured about 2000 kg/m3. Figure 6.5 shows the stress-strain curve adopted in order to describe the behaviour of mortar under uniaxial tension and compression.

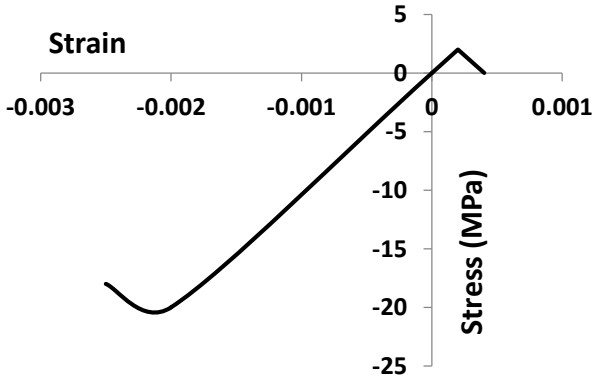

Figure 6.5 Stress-strain curve describing the behaviour of bricks under uniaxial compression and tension

In order to validate the material model presently employed for describing the behaviour of the mortar specimen in compression and tension the 2-D plane stress model presented in Figure 6.6 is employed. This model representing the mortar and two steel plates are positioned on the top and bottom face of the model. The steel plates are assumed to behave elastically throughout the loading process. The dimensions of the steel plates are 200x200 mm and mortar cylinder 150 mm x 300 mm. A 10 x 30 4-node mesh with dimensions of 15 mm x 10 mm is used for the mortar model. The roller supports assigned to the bottom steel layer. The load is applied in the form of load increments on the top of the specimen. The result obtained from the model presented in the form of stress-strain curves (see Figure 6.7) are in good agreement with the experimental data both in terms of stiffness and strength. The MCM model predicts the modulus of elasticity 12.5 GPa and

compressive strength 25 MPa which are close to mean value obtained from experiments 11 GPa for modulus of elasticity and 22 for compressive strength (Section 4.2.1.2)

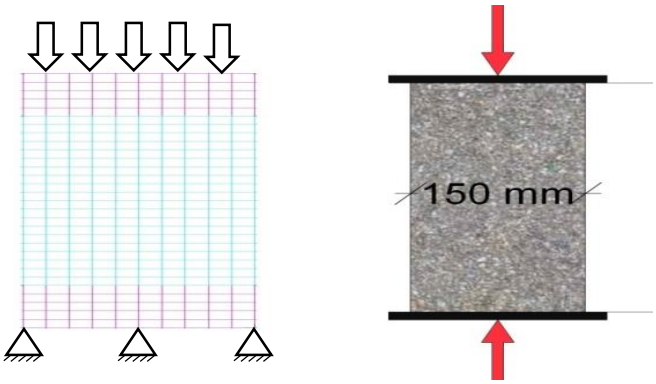

Figure 6.6 FE model for compression test accompanied by its experiment

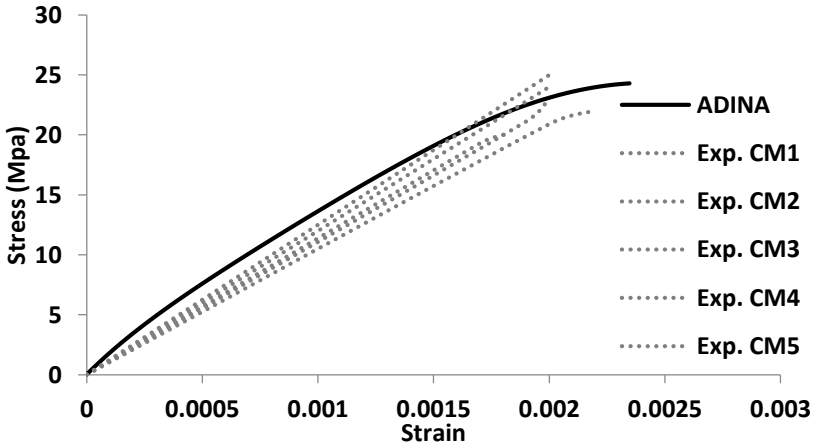

Figure 6.7 Comparison of stress-strain curves predicted numerically and established experimentally for describing the behaviour of the brick units in compression

6.2.4 ECC behaviour under uniaxial tension

The ECC (MTE) is modelled as a multi-linear plastic material (ADINA Manual, 2102). The properties of ECC have been established during the tensile tests conducted on the ECC dog-bone specimens described in section 3.2.5. The density and the poison ratio of ECC are assumed equal to 2000 kg/m3 and 0.15 respectively (Billington and Yoon, 2003). The tensile behaviour of ECC is described by the tri-linear stress-strain curve presented in Figure 6.8. The first portion of the curve is defined up to the yield point; the latter point being associated with the initial development of cracking. The second portion of the curve, between the yield point and the point at which peak-stress is attained, is associated with the development of cracking distributed throughout the length of the

specimen. The third and final portion of the curve is associated with failure of the fibres and loss of load-bearing capacity. Initial cracking occurs at a strain of 0.00018 and a stress of 2.8 MPa. The peak stress is equal to 3.75 MPa and its corresponding strain is 0.035. Failure (associated with softening and loss of load-bearing capacity) occurs at a strain of 0.04.

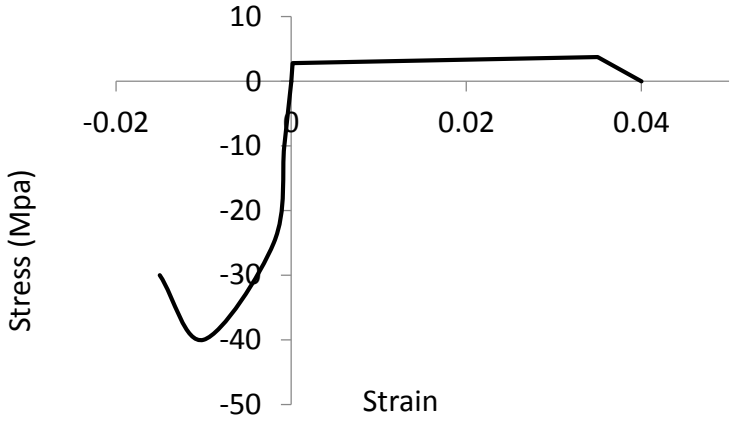

Figure 6.8 Stress-Strain curve describing the behaviour of ECC under uniaxial tension and compression

The validation of the subject model is achieved by comparing the numerical predictions with their experimental counterparts presented in section 3.2.5. For this purpose, a 2-D plane-stress model of the dog-bone specimens, used during testing, is created. The dimensions of the specimens are presented in Figure 6.9. The ECC modelled by the multilinear plastic material and a 100 x 18 4-node mesh is used for the ECC model. A fixed support is assigned to one side of the model. The load is monotonically applied (through the other side of specimen) in the form of displacement increments until failure (see Figure 6.9).

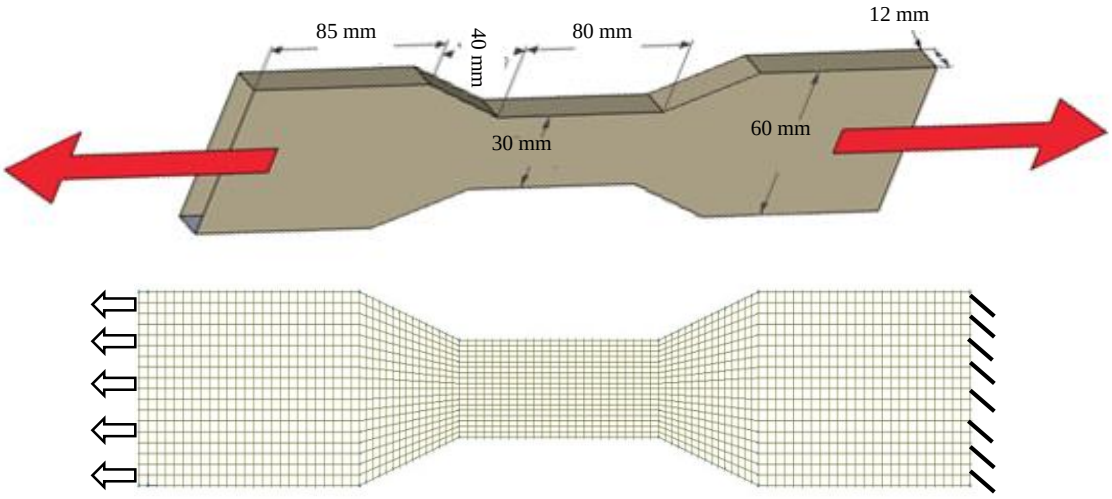

Figure 6.9 FE model of ECC tensile test accompanied by its experiment

Figure 6.10 shows the experimentally and numerically predicted behaviour in the form of stress-strain curves which are in good agreement. Although the plateau part (associated with plastic behaviour) of the experimental stress-strain curves exhibits fluctuations due to the cracking process that the specimens undergo during testing, its counterpart in the multilinear plastic model is assumed to have a uniform gradient.

Figure 6.11a shows the contours of the axial tensile strain developing in the specimen at different levels of loading. The predicated strain distribution is in agreement with the crack pattern observed on the specimen during testing when approaching its ultimate limit state (see Figure 6.11). During test micro-cracks initiate in the central part of dog-bone specimens and then a localized crack developed in the same region. In the FEA models cracking also initiated and developed in central part of the specimen ultimately predicting failure in this region. However, the more uniform strain distribution predicted by the FEA model is associated with the use of the idealised strain curve (characterised by a constant gradient in the plastic region). The model at failure predicts high strain concentrations near the corners of the central portion of the dog-bone sample at which region failure occurred in experiments. However, during testing due to imperfections associated with the specimens or test conditions (i.e. presence of air bubbles in specimens, eccentricity in applied load), failure occurred in the central part but in random places.

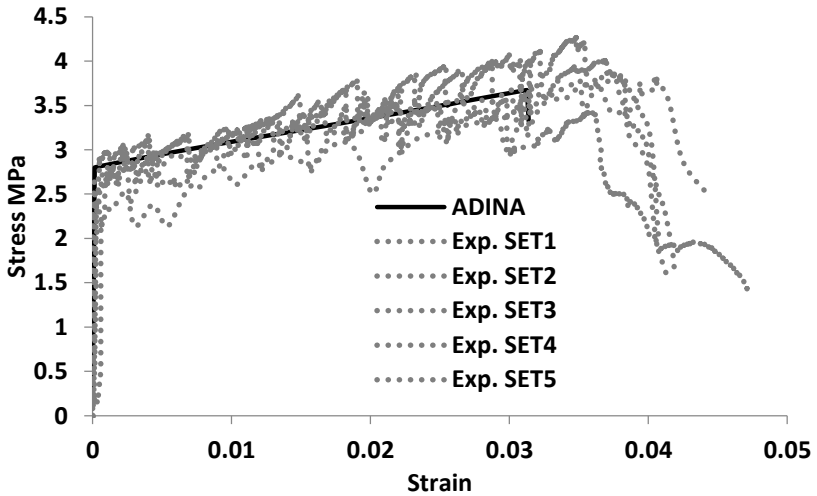

Figure 6.10 Comparison of stress-strain curves predicted numerically and established experimentally for describing the behaviour of the ECC doge-bone under tension

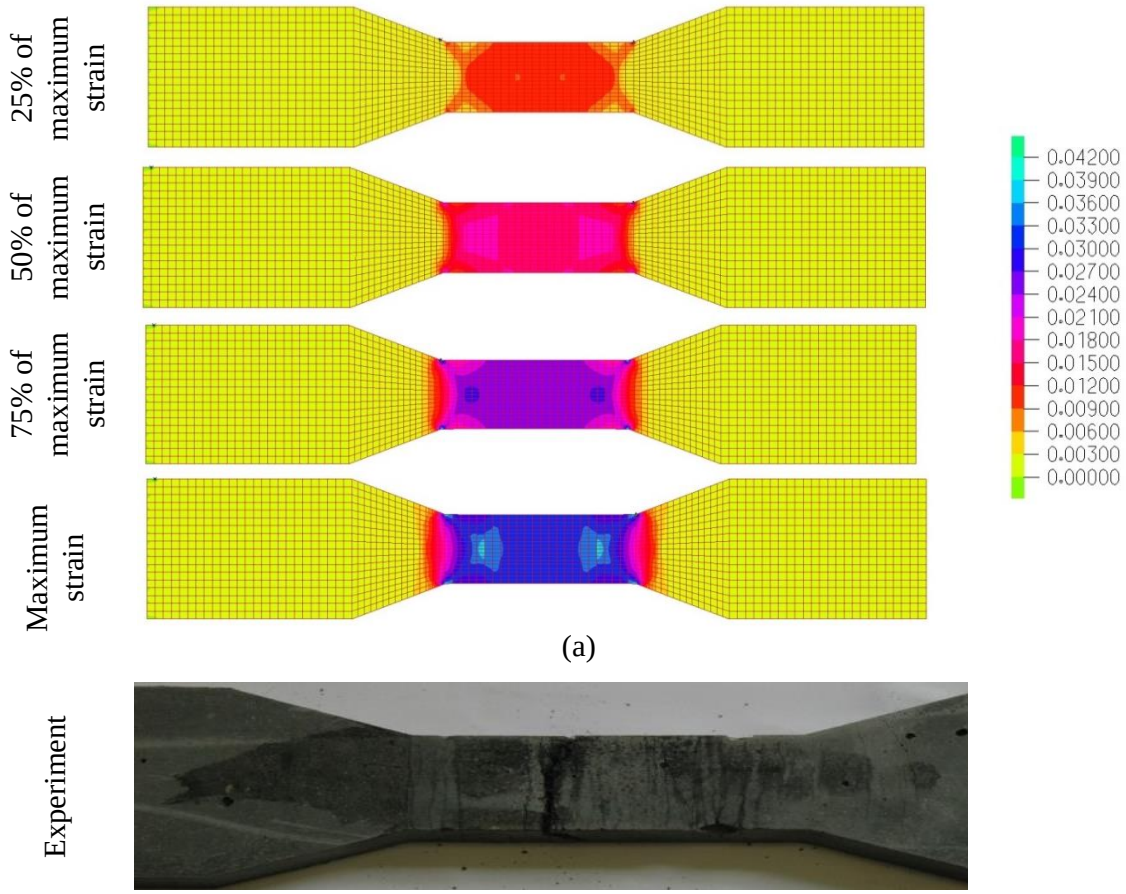

Figure 6.11 Comparison of strain distribution predicted numerically and crack pattern of experiments of the ECC doge-bone under tension

6.2.5 ECC bending behaviour under elevated temperature

ECC (in the MFE model) is modelled as a multi-linear elastic material (ADINA Manual, 2012). The properties of ECC have been established experimentally by conducting a series of flexural tests on ECC prisms previously subjected to elevated temperatures. These tests and the resulting data obtained are presented in Section 3.3. The tensile and compression behaviour of ECC under ambient temperature (20˚C) is described in Section 6.2.4 and Figure 6.8. For H6ECC (hybrid ECC with 6mm steel fibres) and H13ECC (hybrid ECC with 13mm steel fibres) the tensile and compression behaviour under ambient temperature (20˚C) is defined from Tables 3.6 and Table 3.7 respectively. For this purpose, a 2-D plane-stress model of prism specimens, used during testing, is created. The dimensions of the specimens are presented in Figure 6.12. The specimens modelled by a 34 x 4 4-node mesh with dimensions of 4.7 mm x 5 mm is used to model the ECC prismatic specimen. Four steel elements modelled as 4 x 4 mesh of 4-noded brick

elements with dimensions of 9.4 mm x 9.4 mm located at the points at which the load is applied on top of the model and at the supports to avoid localized failure of the model due to the development of high concentatrations in these regions. A pinned support is assigned to the steel elements on one side of the model and a roller to other support. The loads are monotonically applied in the form of displacement increments until failure through the steel elements on top of the model (see Figure 6.12). The validation of the subject model is initially achieved by comparing the numerical predictions with their experimental counterparts under ambient temperature (20˚C) presented in section 3.2.5.

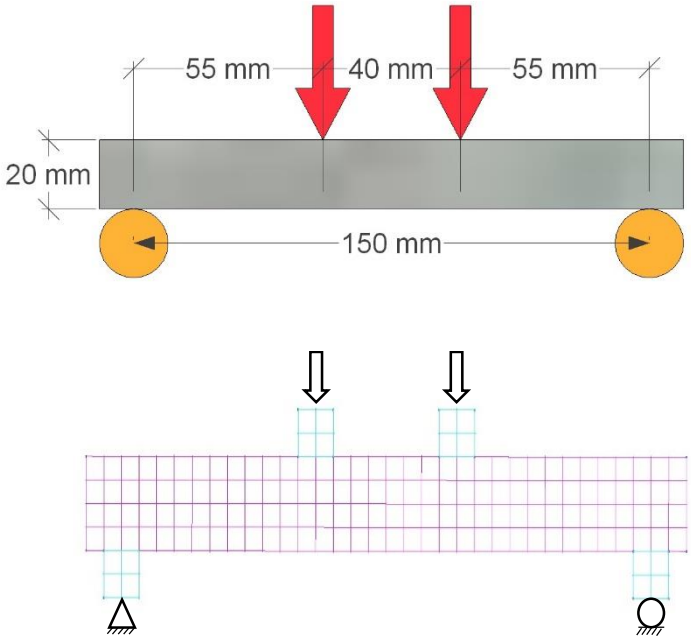

Figure 6.12 FE model for ECC bending test accompanied by the specimen

Figure 6.13 shows the experimentally and numerically predicted behaviour for ECC and hybrid ECCs models at 20˚C in the form load-deflection curves. The presented curves for ECC, H6ECC and H13ECC are in good agreement with their experimental counterparts. However, the elastic branch predicted for MFE load-deflection curve (from start of applying load until initiating the first crack) has a higher gradient compared to that established experimentally. This difference can be attributed to imperfection characterising the experiments associated with the rough faces of specimens caused to non-symmetric loading and supporting condition, and the presence of air bubbles in the actual specimens. In the plateau branch, the experimental load-deflection curves exhibit fluctuations (associated with the ongoing cracking process) which are not accounted for in the numerical predictions due to the use of the idealised stress strain curve for describing ECC behaviour.

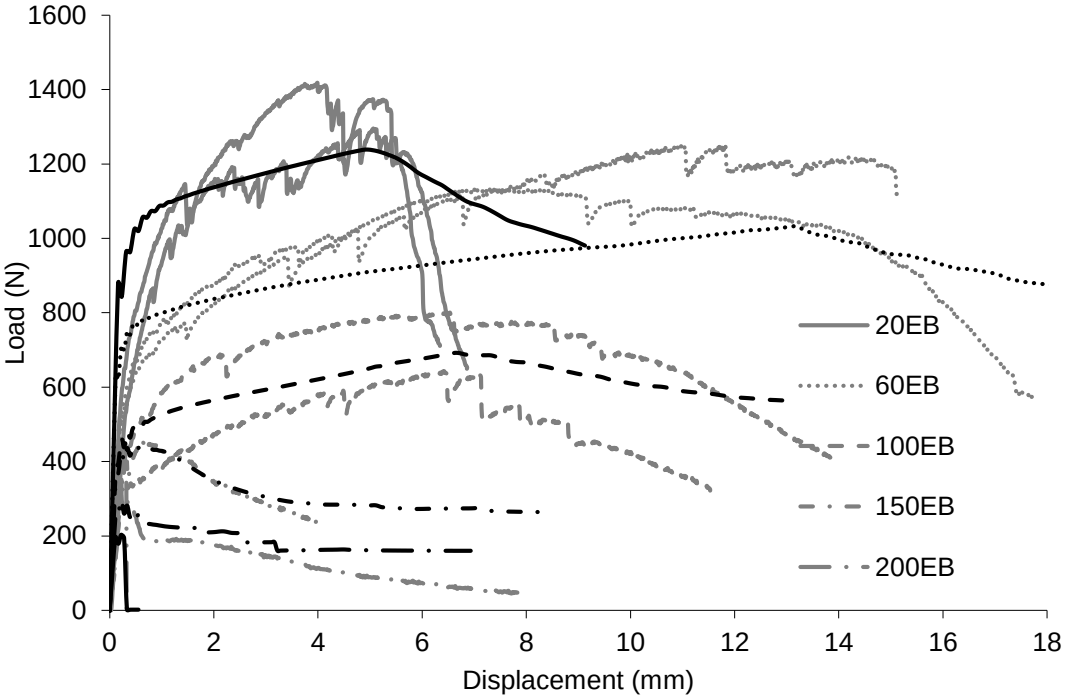
Load (N)
Displacement (mm)
20EB
60EB
100EB
150EB
200EB

a)

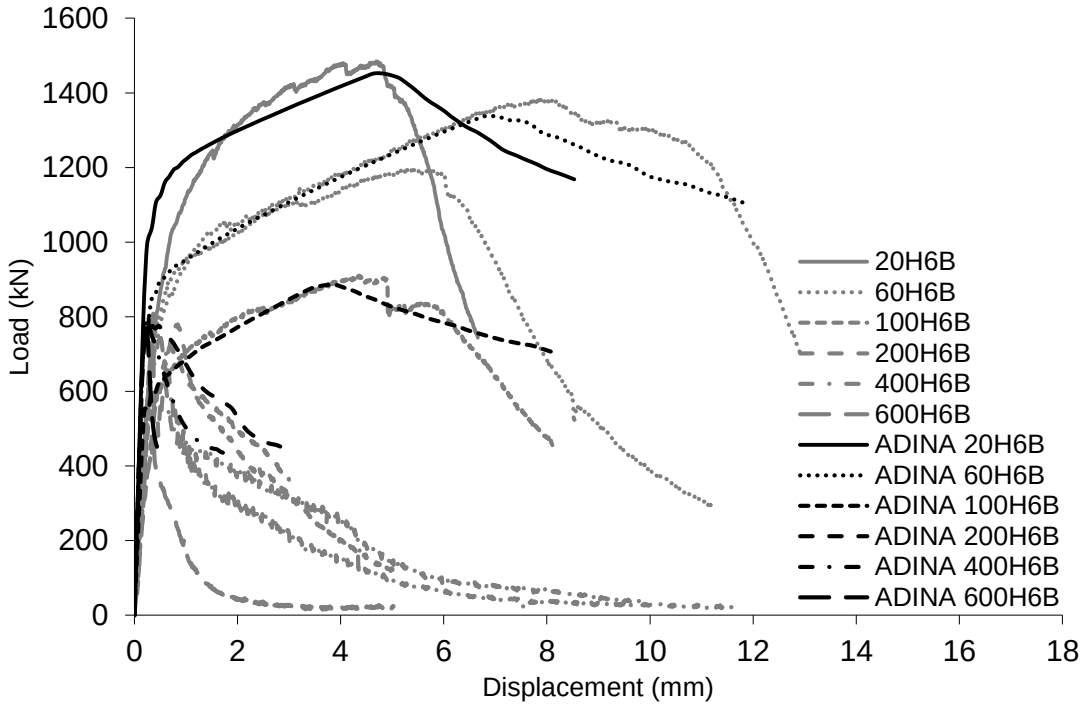
Load (kN)
Displacement (mm)
20H6B
60H6B
100H6B
200H6B
400H6B
600H6B
ADINA 20H6B
ADINA 60H6B
ADINA 100H6B
ADINA 200H6B
ADINA 400H6B
ADINA 600H6B

b)

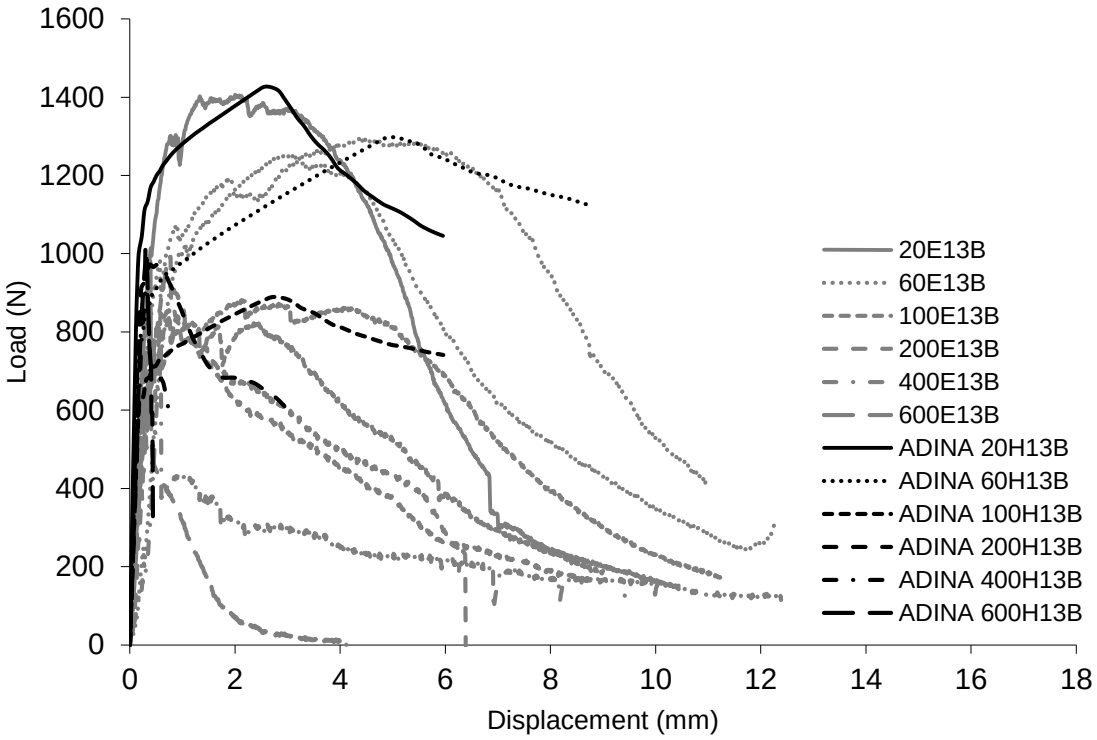

c)

Figure 6.13 Comparison of stress-strain curves predicted numerically and established experimentally for describing the behaviour of the prisms under four point bending test a) ECC b) H6ECC c) H13ECC

To model the compression stress-strain curves of ECC and hybrid ECCs under elevated temperature the results presented in Table 3.7 were used. For models under elevated temperature from 60˚C to 150˚C the compression stress-strain curves obtained at 20 ˚C were used as ECC and Hybrid ECCs presented a very limit change in compression behaviour at 200˚C compare to ambient temperature 20˚C.

For elevated temperatures from 60˚C to 600˚C the stress-strain curves describing ECC and hybrid ECC behaviour under tension were modified in the FEA model so that the predicted load-deflection curves provided a close fit to their experimental counterparts. Table 6.4 presents the predicted behaviour of ECC and hybrid ECCs at elevated temperatures associated with : (i) the initial elastic branch of the load-deflection curve, (ii) the strain hardening branch which initiates after the development of cracking and (iii) the descending (softening branch) which start after the pick load is attained and ultimately resulting in the failure of the specimen (associated with the development of wider localised cracks in the midspan region).

Table 6.4 Predicted results for MFE model under different temperatures

Temperature	First crack strain (%)	First crack stress (MPa)	Maximum strain (%)	Maximum stress (MPa)	Failure strain (%)	Failure stress (MPa)
ECC						
20˚C	0.018	2.8	3.5	3.85	4	0
60 ˚C	0.018	1.95	12	3.75	12.2	0
100 ˚C	0.018	1.1	6	2.1	6.2	0
150 ˚C	0.018	0.8	1	0	NA	NA
200 ˚C	0.018	0.4	0.2	0	NA	NA
400 ˚C	0.018	0.1	0.02	0	NA	NA
H6ECC						
20˚C	0.019	2.89	3	4.36	3.5	0
60 ˚C	0.019	2.01	5	4.21	5.5	0
100 ˚C	0.019	1.18	2.5	2.3	3	0
200 ˚C	0.019	2.17	1	0	NA	NA
400 ˚C	0.019	2.1	0.8	0	NA	NA
600 ˚C	0.019	2	0.42	0	NA	NA
H13ECC						
20˚C	0.018	3.32	2.5	4.71	3	0
60 ˚C	0.018	2.21	4	4.6	4.5	0
100 ˚C	0.018	1.5	2.2	2.5	2.5	0
200 ˚C	0.018	2.9	1	0	NA	NA
400 ˚C	0.018	2.85	0.7	0	NA	NA
600 ˚C	0.018	2.93	0.4	0	NA	NA

Fig 6.14a shows the contours of the tensile strain developing in the ECC specimen under the ambient temperature at different levels of loading. The predicated strain distribution is in agreement with the crack pattern observed on the specimen during testing when approaching its ultimate limit state (see Figure 6.14). In the experiments, the fine cracks initiate in the central part of the prismatic specimens and then larger cracks developed in the same region. In models cracking also initiated and extended in central part resulting in failure being exhibited in this region. However, the more uniform strain distribution observed in the FEA model is associated with the idealized stress-strain curve used for describing ECC behaviour. At failure high strain concentrations are exhibited on the bottom face of the specimen near the mid-span region at which failure ultimately occurred which is agreement with what was observed during testing.

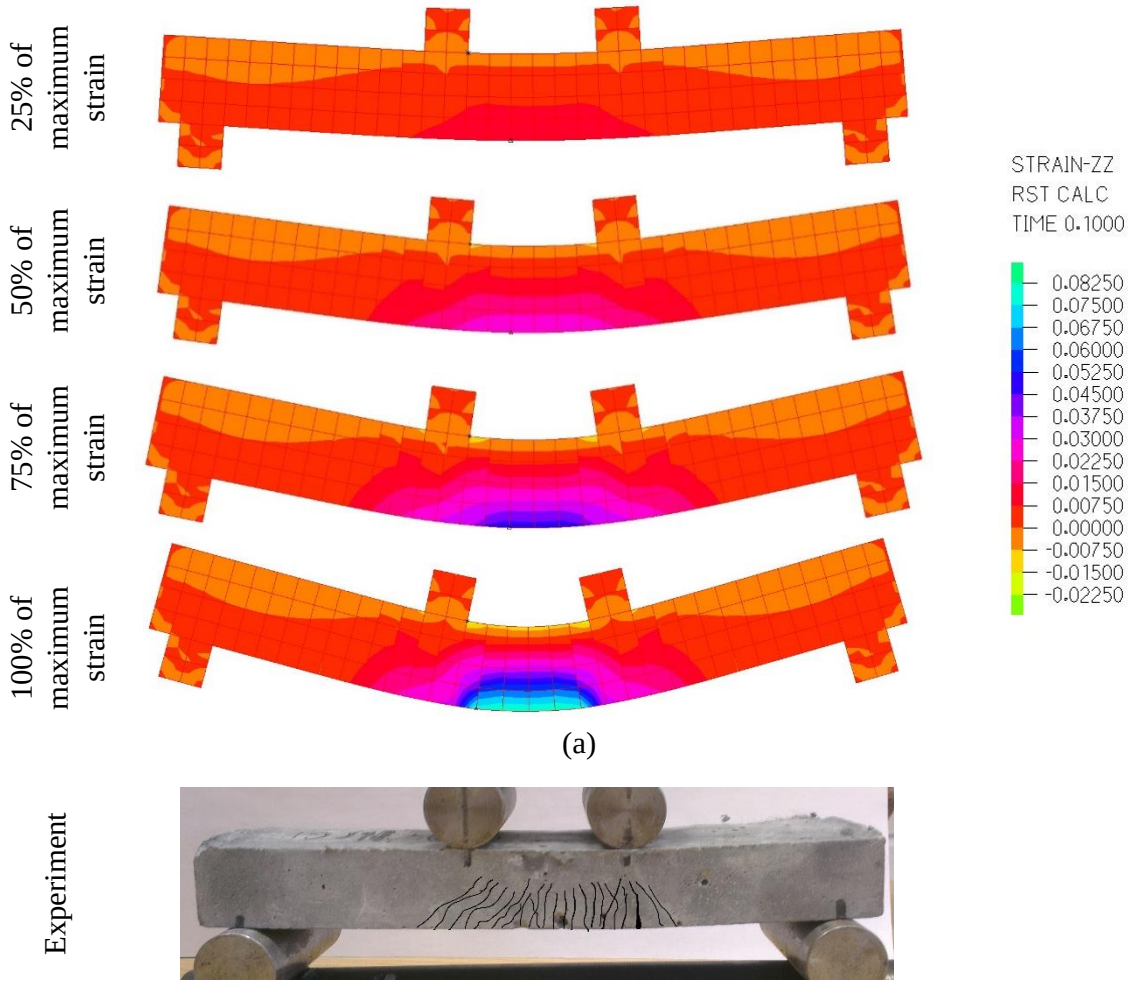

(a)

(b)

Figure 6.14 Comparison of strain distribution predicted numerically and crack pattern of experiments of the ECC prism under four point bending test

6.2.6 Modelling of brick-mortar interface in tension

In order to develop a model capable of describing the behaviour of the brick-mortar interface under tension (ITBM model), a 2-D plane-stress model is used with a thickness of 100mm, representing the specimens tested in section 4.2.3. The model represents two brick units and a mortar layer between them (Figure 6.15). The brick dimensions are 100mm x 65 mm and has a thickness of 100mm. The model presented in section 6.2.1 is employed to describe the material behaviour of the brick units under uniaxial compression and tension. The material model presented in section 6.2.2 is employed for describing mortar material behaviour. Each brick unit is divided into a 2x5 mesh of 4-node finite element mesh with dimensions of 32.5mm x 20mm. The mortar layer is modelled through the use a 1x5 mesh of 4-noded FE mesh with dimensions of 20mm x 5mm.

The cohesive element interface is employed to describe the interface (the bond between mortar and brick) properties. The properties of the cohesive element are chosen so that the model provides a closer fit to the relevant test data presented in section 4.2.3. A tensile strength of 0.5 MPa and shear strength of 0.8 MPa adjusted for the model. A stiffness of $20x10^{11}$ N/m^3 is assumed for cohesive element however the influence of this coefficient is not expected for this test (the displacement of bond cannot be measured in the experiment) and fracture (toughness) of cohesive element assumed at 120% of maximum displacement that simulates a brittle failure for simulation.

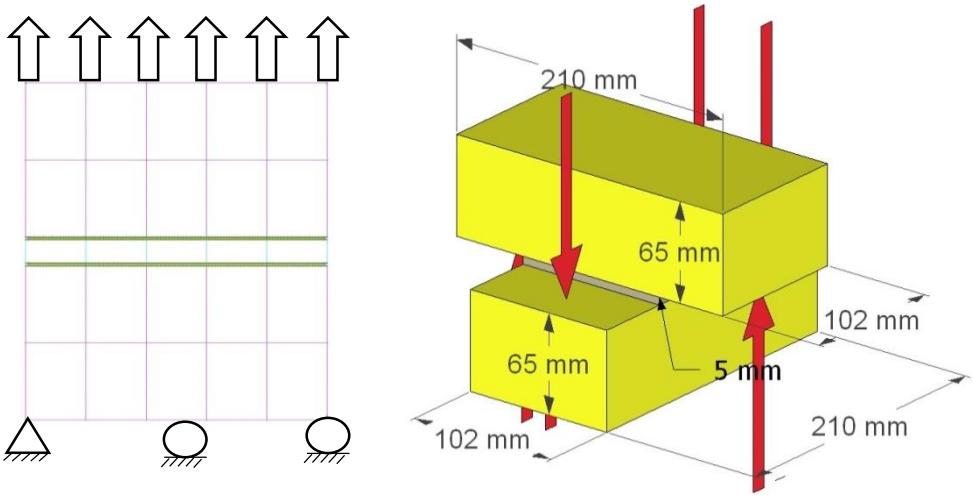

Figure 6.15 FE model for ITBM test accompanied by its experiment

The base of the model is not allowed to move vertically whereas on its upper face is forced to move upwards at a constant rate until failure occurs (See Figure 6.15). The maximum reaction, expressed as stress, developing on the bottom face of the model is 0.5 MPa which is the same as that established experimentally (Figure 6.16). Figure 6.17 shows that failure of the specimen happens in the brick-mortar interface which is also observed during testing.

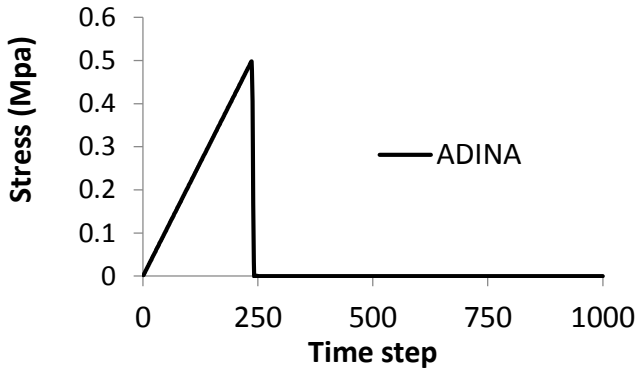

Figure 6.16 The numerically predicted result for ITBM

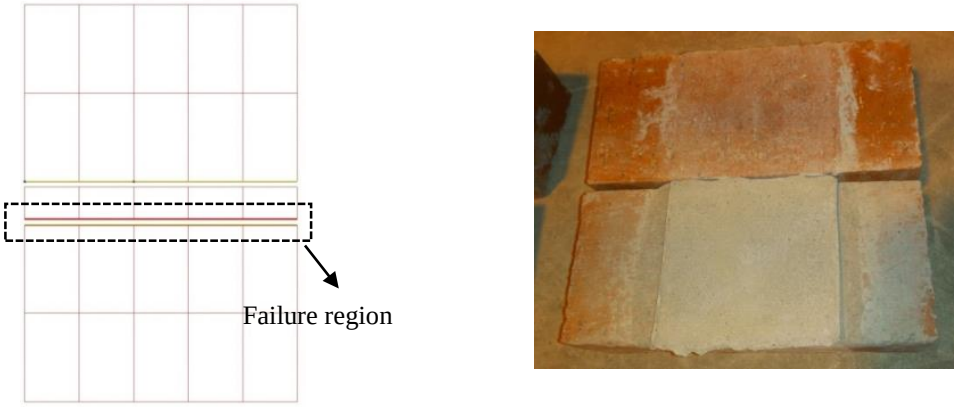

Figure 6.17 Comparison of failure of the ITBM predicted numerically and crack pattern of experiments

6.2.7 Modelling of brick-mortar and brick-ECC interface under shear

In this section two 2-D plane-stress models (ISBM) consisting of three brick units and two mortar layers between bricks and the ISBE consisting of three brick units and two ECC layers between bricks are adopted to simulate the behaviour of shear behaviour of experiments described in section 4.2.2.

For the ISBM model the dimension of each brick was 210 x 65 mm and their thickness is considered equal to 102mm. Each brick is modelled through the use a mesh of 3 x 10 4-node elements with dimensions of 21mm x 21.6mm (see Figure 6.18 a) and their behaviour under uniaxial compression and tension is described by the model presented in section 6.2.2. The behaviour of mortar is described by the material model in section 6.2.3. Each mortar layer is divided into 1x10 mesh of 4-node elements with dimensions of 21mm x 5mm. In the ISBE model, the dimension of each brick was 210 x 102 mm and their thickness is considered equal to 65mm. Each brick is modelled through the use of a mesh of 5 x 10 4-node elements with dimensions of 21mm x 20.4 mm (see Figure 6.18 b). The behaviour of ECC is described by the material model in section 6.2.4. Each ECC layer is divided into 1x10 meshes of 4-node element with dimensions of 21mm x 15mm.

The bond properties between the mortar and brick elements for the case of the ISBM model are described through the use of the cohesive interface element. The cohesive interface is defined between the brick and mortar layer. The tensile properties of the

cohesive interface are obtained from section 6.2.6. A brief parametric study (see Table 6.3) is carried out to investigate the sensitivity of the model. The bond properties between the ECC layer and the brick elements in the case of the ISBE model is also described through the use a cohesive interface element defined between the brick unit and the ECC layer. The tensile properties of the cohesive interface are assumed to be the same as in the case of the mortar–brick interface discussed in section 6.2.6. A brief parametric study (see Table 6.5) is carried out to investigate the sensitivity of the model. A fracture energy of 120% of maximum displacement is assumed for both models to simulate the brittle failure and safeguard of numerical stability of the solution procedure.

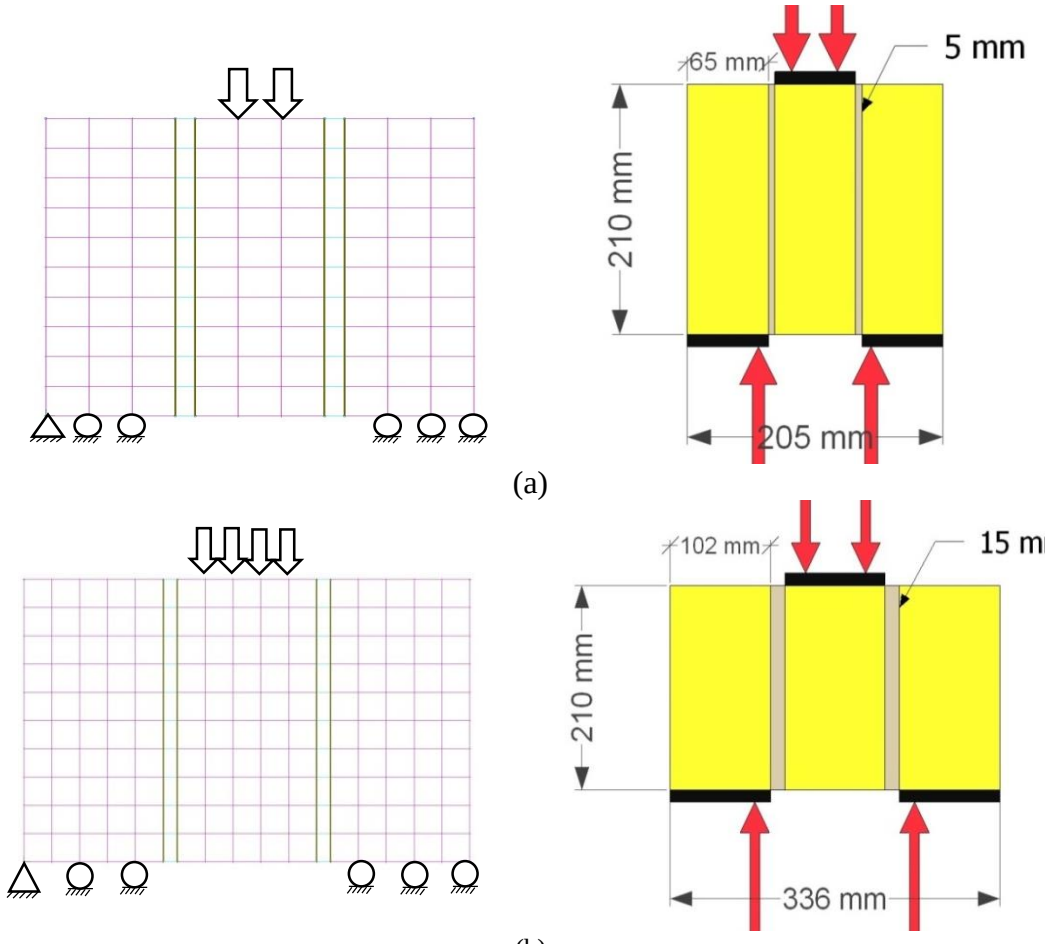

Figure 6.18 FE model accompanied by its experiment a) ISBM model b) ISBE model

Table 6.5: ISBM and ISBE cohesive interface properties

Specimens	ID	Shear strength MPa	Stiffness Pa
ISBM	ISBM1	1.8	10^{11}
	ISBM2	3.6	10^{12}
	ISBM3	12	10^{13}
ISBE	ISBE1	10	10^{11}

	ISBE2	12	10^{12}
	ISBE3	18	10^{13}

For both models, as shown in Figure 6.18, the two bricks on either side of the specimens are not allowed to move along the vertical direction at their base. On the other hand the middle brick is subjected to a distributed load on its upper face. The load is applied monotonically until failure in the form of displacement increments. The numerical analysis predicted that for the ISBM model failure will occur along the interface between the brick units and the mortar. However, the ISBE model predicts that failure will occur along the interface forming between the brick-units and the ECC layer (see Figure 6.20). Both of these predictions are in agreement with the failure mode observed experimentally. The predicted shear strength of ISBM is 0.9 MPa (compared to 0.7MPa established experimentally) and of ISBE is 1.1 MPa (compared to 1.13 measured during testing) which are in agreement with the experimentally established values (Figure 6.19 a). However, the ISBE model appears to underestimate the stiffness. It was found by increasing the stiffness of the cohesive interface more than 10^{13} N/m^3 the failure will happen in the ECC layer rather than the cohesive interface. Thus the aforementioned stiffnesses in Table 6.5 offer the closest result to the experiments (Figure 6.19 b).

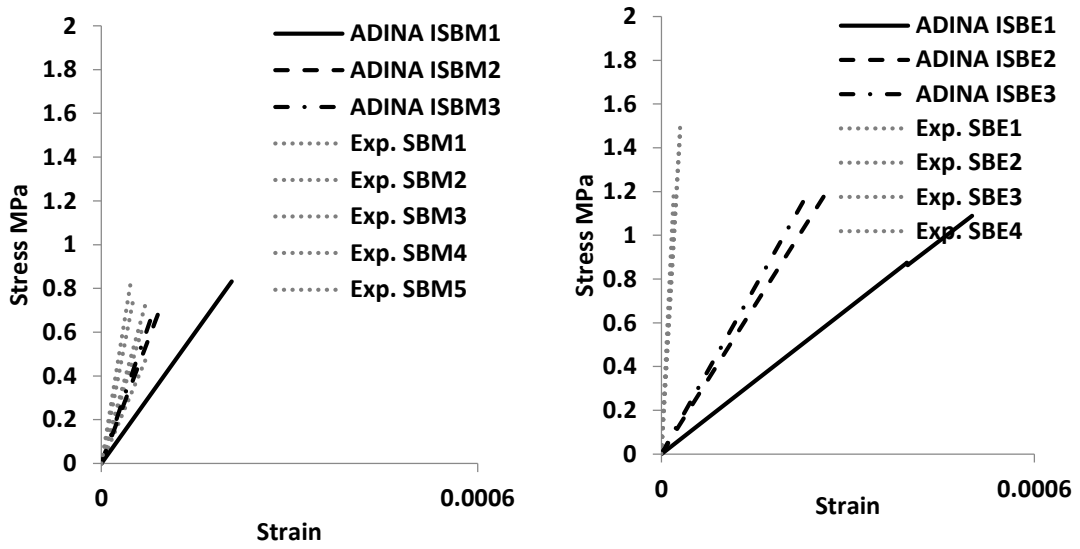

a b

Figure 6.19 Comparison of stress-strain curves predicted numerically and established experimentally for describing the behaviour of a) ISBM model b) ISBE model

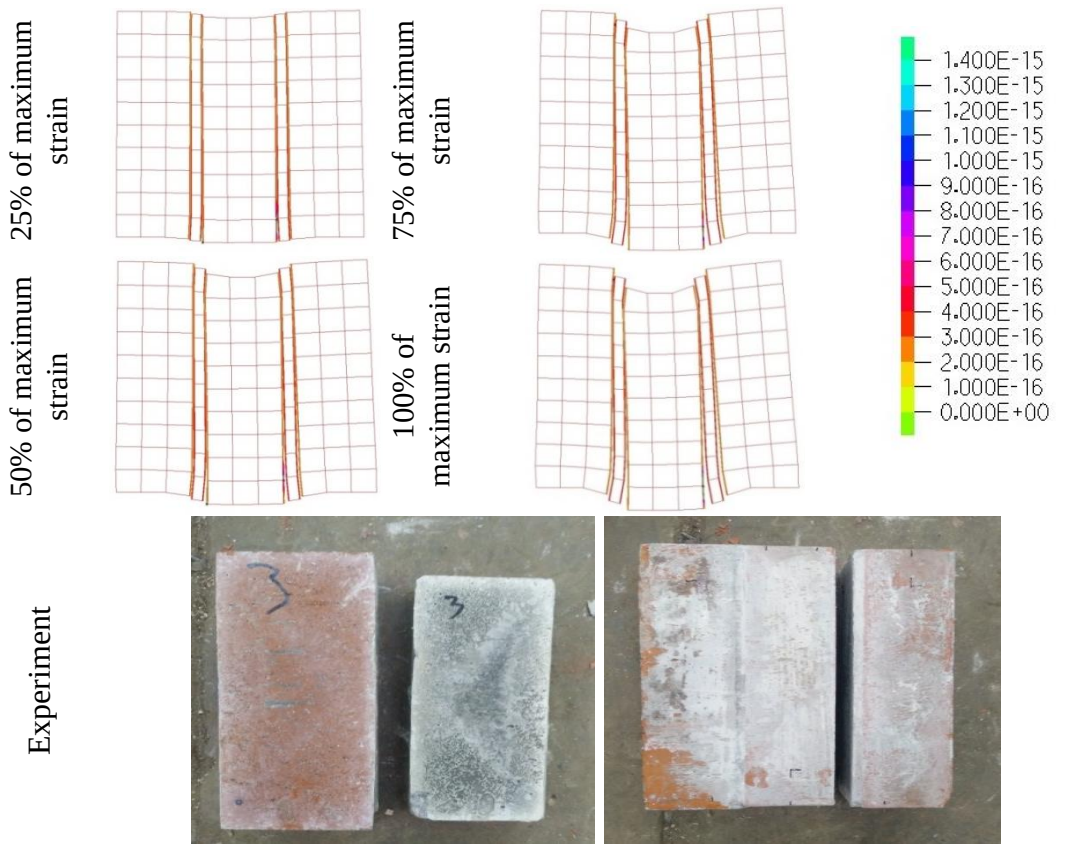

a

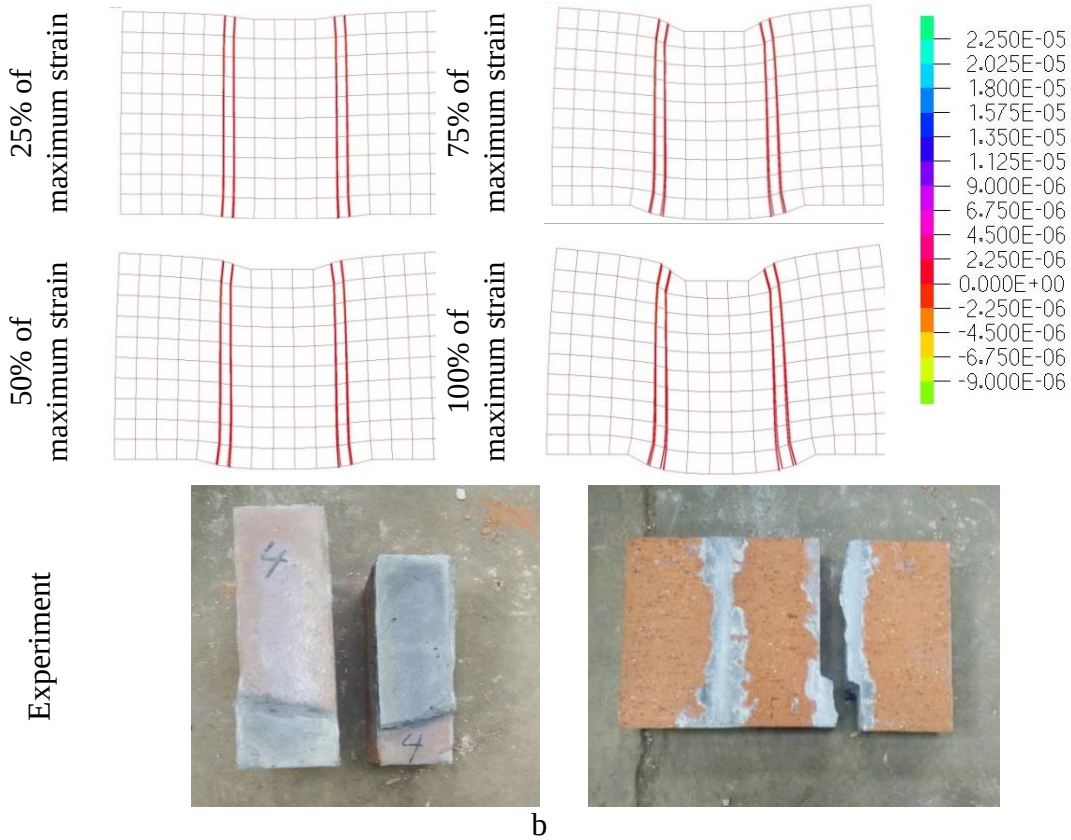

b

Figure 6.20 Comparison of failure predicted numerically and crack pattern of experiments a) ISBM model b) ISBE model

6.2.8 Modelling masonry behaviour under compression

In this model (ICBM) the compression test brickwork (represented by a stack of four bricks connected mortar joints) is simulated as a plane-stress problem. The 2-D model is assumed to have a thickness of 102 mm. Each brick is divided into a mesh of 3x10 4-noded elements with dimensions of 21mm x 21.6mm, whereas each mortar layer is divided into a mesh of 1x10 4-noded elements with dimensions of 21mm x 5mm (see Figure 6.21). The models presented in Sections 6.2.2 and 6.2.3 are employed to describe the behaviour of the brick units and mortar respectively. To define the bond properties at the interface between the mortar and brick interface, cohesive interface were defined between bricks and mortars layer. To calibrate properties of the cohesive element a brief parametric study based on cohesive elements ISBM1, IBSM2 and IBSM3 are developed in Section 6.2.7 (see Table 6.5) is carried. However it found that the cohesive interface do not affect the masonry brickwork behaviour since in all models failure happens in the mortar element. This model was carried out to evaluate results of previous parts.

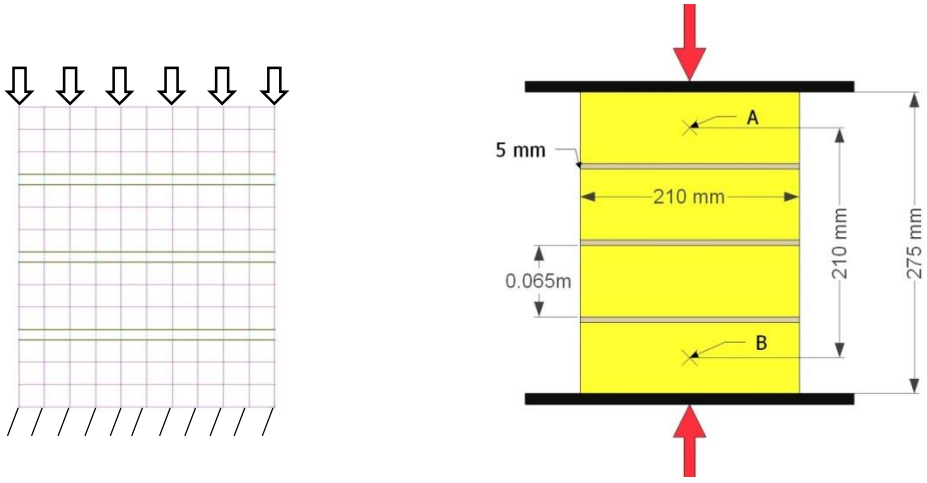

Figure 6.21 FE model accompanied by its experiment for compression test of brickwork

At its base the masonry specimen fixed in the bottom side (Figure 6.21). On the top surface a distributed load was applied monotonically to failure in the form of displacement increments (displacement control). Figure 6.22 shows the result of the ICBM model in the form of stress-strain curves. The maximum compression strength of the model is 25.3MPa compared to 27MPa obtained from the experimental counterpart. The ICBM model prediction tends to overestimate the modulus of elasticity of the specimen. This can be due to the imperfections of experiments including the non-level surface of bricks, capping cement and non-symmetrical samples.

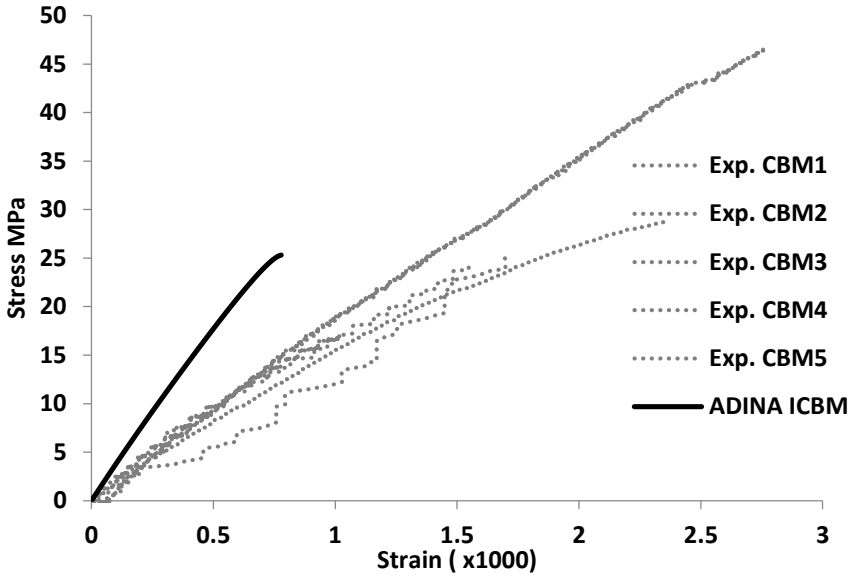

Figure 6.22 Comparison of stress-strain curves predicted numerically and established experimentally for describing the behaviour of the compression test of brickworks

6.3 Part 2- Calibrations of models describing the masonry beam-like specimens

6.3.1 Modelling of plain masonry bending test

The masonry specimen under four-point bending test is considered as a plane-stress problem (the thickness of the specimen is assumed to be 210 mm) and is simulated by two models: a detailed (3-phase) model including brick, mortar and brick-mortrar interface (SDM) and a simplified (2-phase) model (SSM) which substituted the mortar element by brick and only including brick and brick-mortar interface. Due to the symmetry characterising the problem considered only half of the specimen was simulated. The SDM model consists of five bricks and five mortar layers at the joints between the bricks. Each brick unit, which is 102 mm x 65 mm, is modelled as described in section 6.2.2 (see Figure 6.23a) by a mesh of 6x10 4-noded elements with dimensions of 10.2mm x 10.8mm. The mortar layer (defined in section 6.2.3) is 100 mm x10 mm for all joints except for the last layer next to the axes of symmetry which is 100 mm x5 mm. Each mortar layer is divided into a 1 x 10 mesh of 4-node 2-D elements with dimensions of 10.2mm x 5mm. Nine cohesive interfaces elements are defined between bricks and mortars layer.

In the case of the SSM model the mortar layers are substituted by brick units so each brick dimensions are 102mm x 74 mm (see Figure 6.23b). Each brick unit is modelled by a 3 x 5 mesh of 2D 4-node elements with dimensions of 20.4mm x 24.6mm. The density of the

mesh in the SSM model is reduced compared to that employed in the SDM model to decrease the computational resources required by the FE package to solve the problem at hand. In the SSM model five cohesive interface elements are defined between the bricks unit as a boundary condition. The mortar layer is effectively incorporated into the cohesive interface. Due to compatibility reasons (which will be explained in section 6.3.3) a thin layer of material was defined on both sides of the cohesive interface (Figure 6.23). For these reasons one mm of the brick and mortar layer divided from bricks and mortar layers. These layers were divided to 1x51 meshes. These layers from one side were related with the interface element and on the other side were related with the relevent materials (mortar or brick). The meshes size of main part of bricks and this layer is not match to each other. Therefore a glue layer defined between them to uniform the properties of these meshes. Also these layers increased the accuracy of modelling in the cohesive bond.

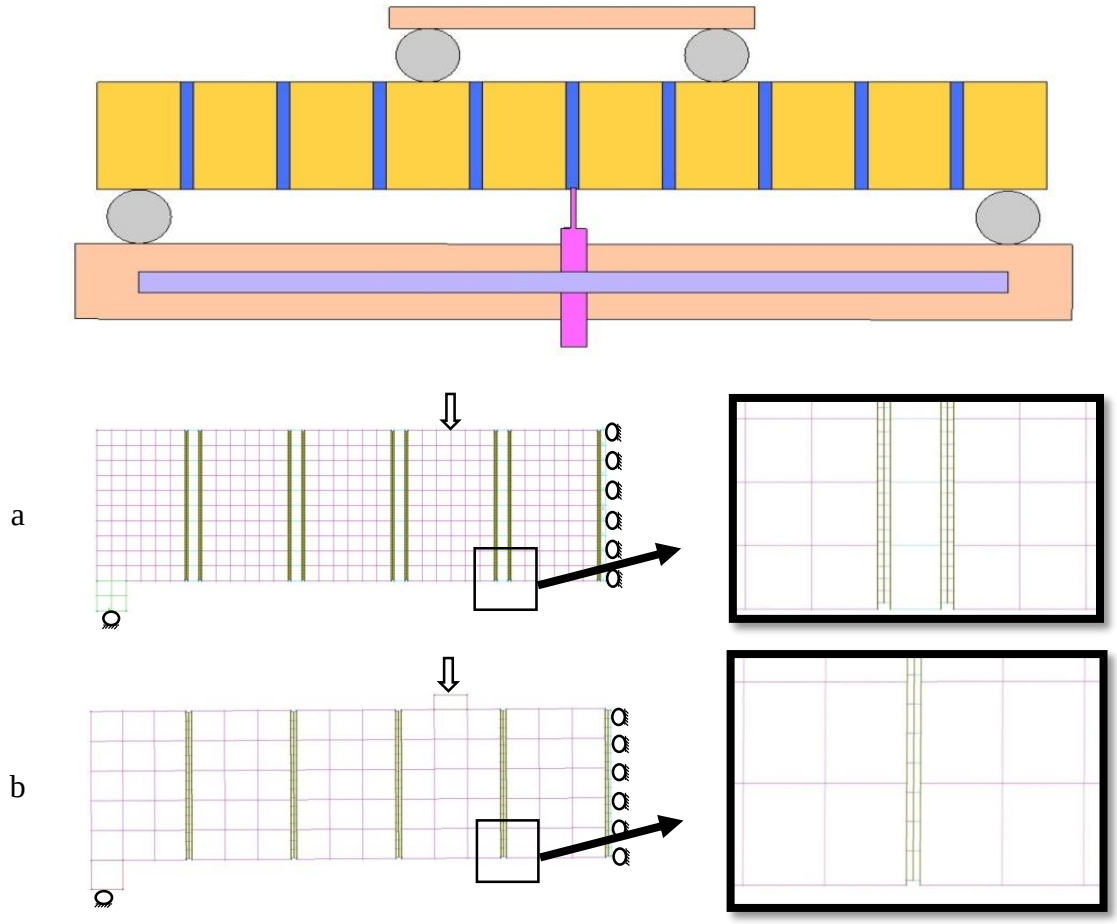

Figure 6.23 FE model accompanied by its experiment for bending test of brickwork a) SDM model b) SSM model

A 20mm x20mm steel element is used to distribute the stresses at the support and avoid premature localised failure. Each steel element was divided into a 2x2 mesh. The support is allowed to rotate and move axially (see Figure 6.23). On the other end the cross-section of the specimen is allowed to only translate vertically due to the symmetry characterising the problem at hand (Figure 6.23). The load is applied monotonically to failure at the middle of fourth brick (Figure 6.23) (from the support) in the form of displacement increments. The load applied monotonically until failure in the form of displacement increments.

For both SDM and SSM models the three different cohesive interface models presented in section 6.2.7 are employed (see table 6.6). The predictions of the models are presented in figure 6.24 in the form of load-displacement curves. Both SDM1 and SSM1 with the same bond properties (ISBM1) provide the closest fit results to the available test data. However, the models overestimate the maximum sustained load providing predictions of 2.1 kN compared to 1.2 kN obtained from the experiments. This difference can be attributed to imperfections associated with the experiments. Also the SSM1 model stiffness is higher than that of the SDM1 model due to smaller number of cohesive interfaces resulting in smaller deformations. Failure in all models happened in the cohesive interface elements within the central span which is in agreement with what was observed during testing (Fig 6.25).

Table 6.6: Brick-mortar cohesive interface properties

Model name	Interface name	Shear strength (MPa)	Toughness (Pa)	Stiffness (Pa)
SDM1	ISBM1	1.8	19.4	10^{11}
SDM2	ISBM2	3.6	7.78	10^{12}
SDM3	ISBM3	12	8.64	10^{13}
SSM1	ISBM1	1.8	19.4	10^{11}
SSM2	ISBM2	3.6	7.78	10^{12}
SSM3	ISBM3	12	8.64	10^{13}

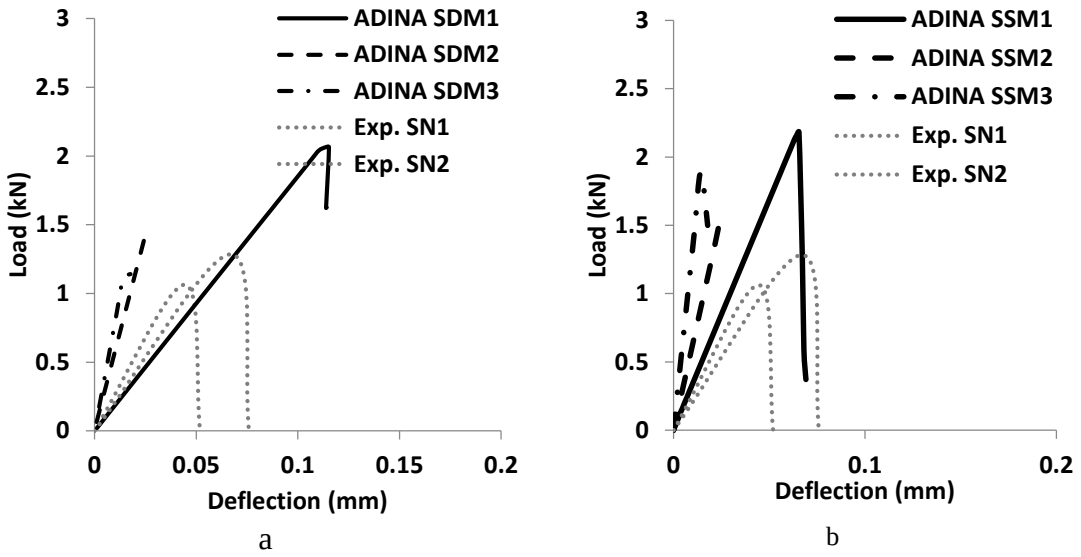

a b

Figure 6.24. Comparison of load-deflection curves predicted numerically and established experimentally for describing the behaviour of a) SDM model series b) SSM model series

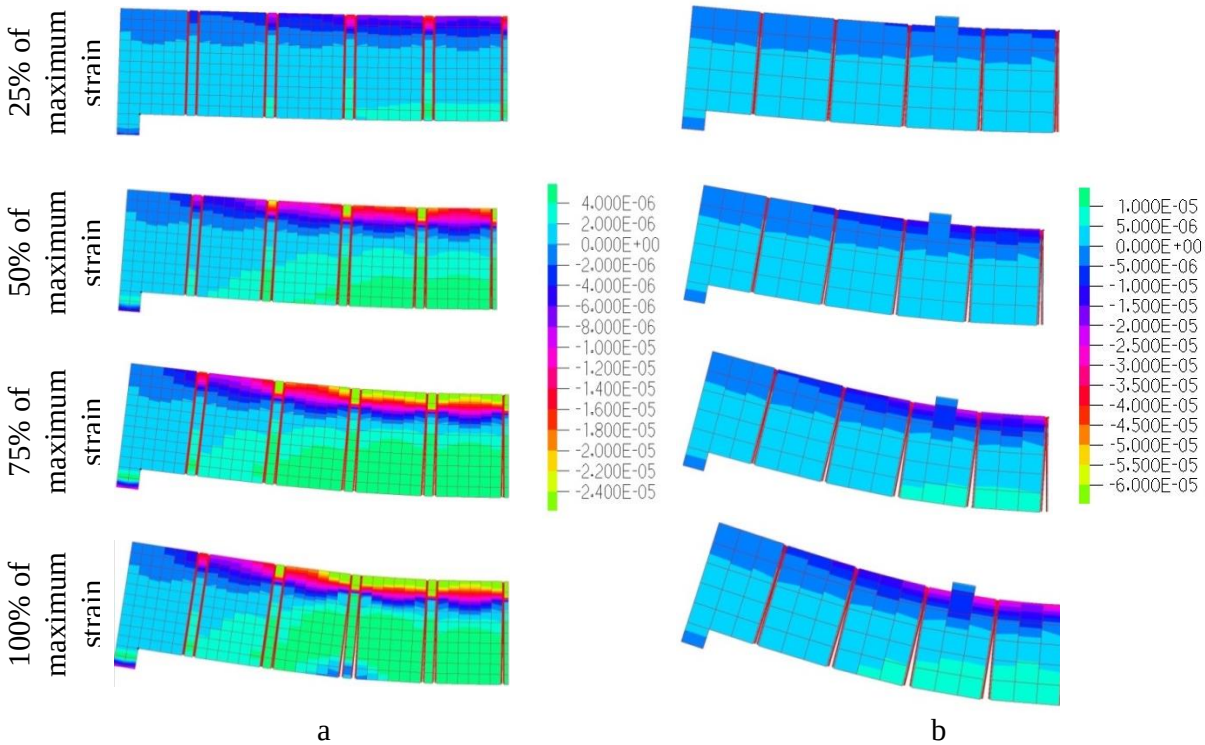

a b

Figure 6.25. Comparison of predicted failure mode and strain distribution of a) SDM and b) SSM model

6.3.2 Modelling of full bond ECC-retrofitted beam under bending test

A detailed (4-phase) model (SDFO) including brick unit, mortar, brick-mortar interface and ECC layer and a simplified (3-phase) model (SSFO) which the mortar is eliminated including brick unit, brick-mortar interface and ECC layer are employed to simulate the

ECC-retrofitted specimens. The same strategies which are applied in Section 6.3.1 for the SDM and SSM models are also applied for the development of the SDFO and SSFO models respectively. In addition an ECC layer (see section 6.2.4) with dimensions of 370x15 mm was attached on the bottom face of the masonry beam. This layer is modelled using a mesh of 4x100 2D 4-node elements with dimensions of 3.7mm x 3.75mm (see Figure 6.26). For the SDFO model, two different cohesive interfaces were defined, the first between the mortar layer and brick surface and the second between the ECC layer and masonry beam (mortar and brick unit). For the SSFO model, two different cohesive interfaces were defined one between the brick surface in masonry beam and other between the ECC layer and brick unit.

In the ADINA software the vertical and horizontal interface element should not meet each other to avoid instability in shared nodes between the two perpendicular interface (Figure 7.26). To overcome this problem a thin layer of brick with 1 mm thickness defined around the interface surfaces of brick. The vertical layer divided to 1x51 meshes. This layer from one side is glued to the brick unit to have same behaviour like main elements and from the other side was related with the interface element. For the horizontal layer a 1x17 mesh was used for this layer. The horizontal layer from one side was glued to the main brick element and from the other side to the interface element. The same action is also taken for the mortar layer. In the vertical case a 51x1 mesh from one side was glued to mortar and from the other side to the interface element. The horizontal layer is divided by 1x2 meshes from one side and glued to mortar and from other side related to the interface element.

A steel element is used for both models to distribute the stresses at the support and avoid premature local failure. The support is allowed to rotate and move axially (see Figure 6.26). On the other end the cross-section of the specimen is allowed only to translate vertically due to the symmetry characterising the problem at hand (Figure 6.26). The load is applied monotonically to failure at the middle of fourth brick (Figure 6.26) (from the support) in the form of displacement increments. The load applied monotonically until failure in the form of displacement increments.

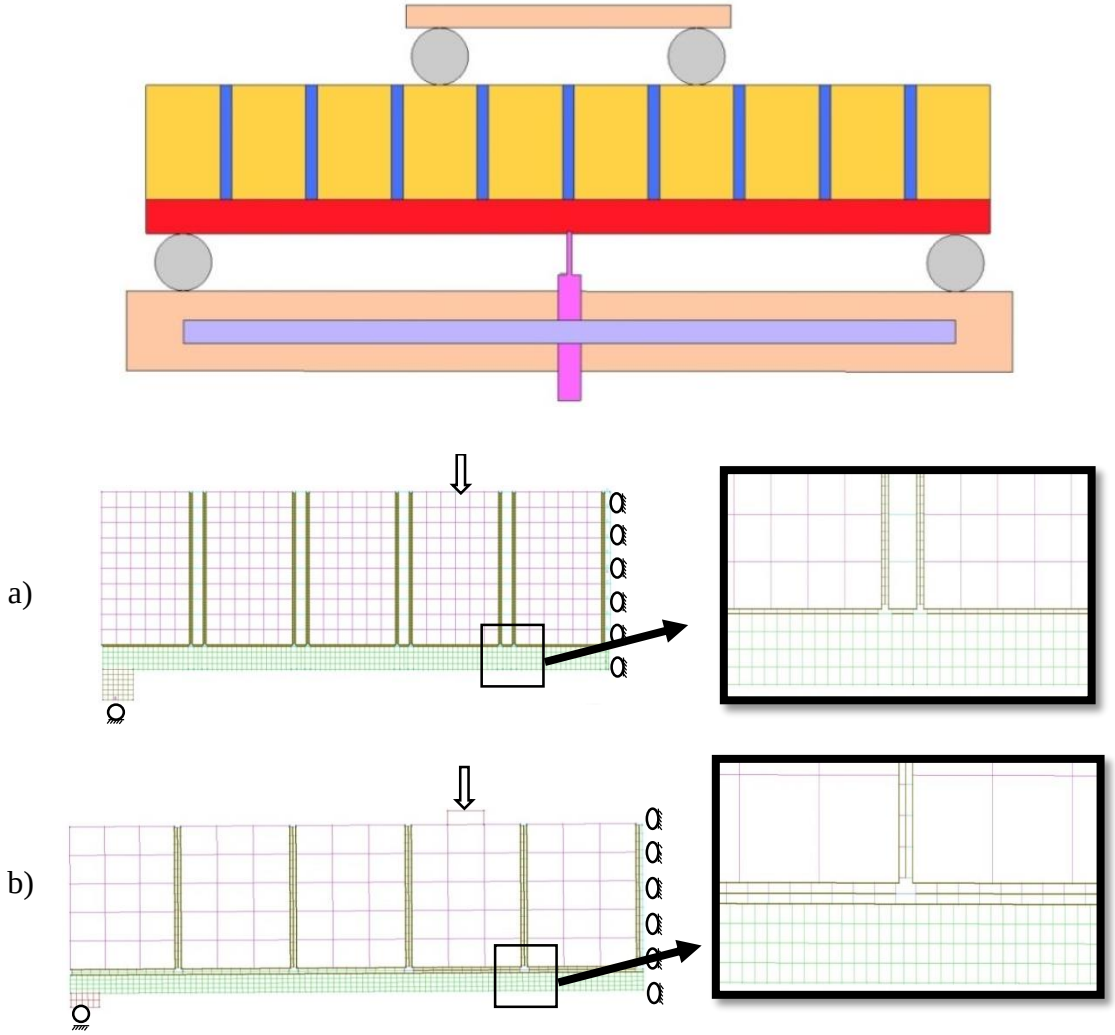

Figure 6.26 FE model accompanied by its experiment for bending test of a) SDFO model b) SSFO model

To calibrate the masonry parts of the SDFO model three different cohesive properties based on Section 6.3.1 are validated on this model (Table 6.7). It is observed that only Penalty stiffness of 10^{11} N/m^3 (SDFO1) is applicable on the model and for cohesive properties with higher values penalty stiffness cannot be run (SDFO2 and SDFO3) due to the instability of the model. Next stiffness of the cohesive interface between brick and ECC was increased by 2 and 20 times to evaluate the effect of this parameter. It observed that the SDFO1 has a more stable result (figure 6.27). For SSFO1 the same cohesive bond as ISBM1 is defined.

Table 6.7 Brick-mortar cohesive interface properties

Model name	Interface name	Shear strength (MPa)	Toughness (Pa)	Stiffness (Pa)
SDFO1	ISBM1	1.8	19.4	10^{11}
SDFO2	ISBM2	3.6	7.78	10^{12}
SDFO3	ISBM3	12	8.64	10^{13}
SDFO4	-	1.8	38.8	10^{11}
SDFO5	-	1.8	388	10^{11}

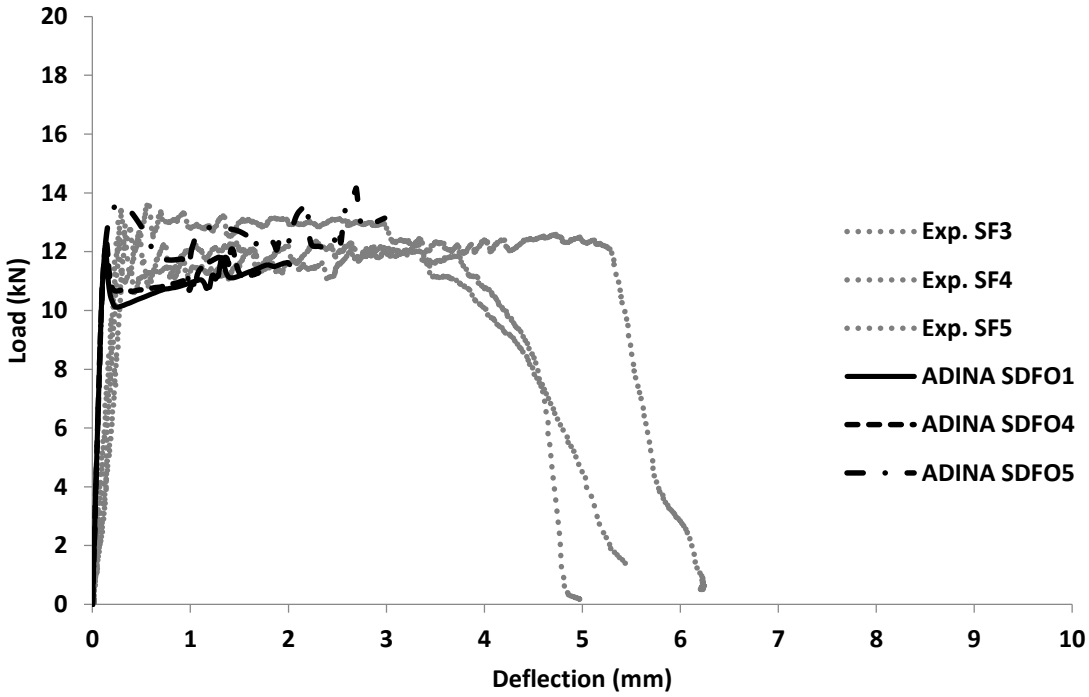

Figure 6.27 Comparison of load-deflection curves predicted numerically and established experimentally for different cohesive interfaces

Table 6.8 presents a parametric study carried out to calibrate the properties of ECC layer for the detailed and simplified models. The strength of ECC was increased by 130%, 145% and 160% s. The results for detailed models are presented in Figure 6.28 a. The maximum load bearing capacity for SDFO1, SDFO6, SDFO7 and SDFO8 are 11.6 kN, 12.9 kN, 13.9 kN and 15.7 kN respectively compared to the experimental counterpart 12.9 kN. The SDFO6 model with 130% enhancement in ECC strength has the best fit results compared to the experimental counterpart whereas the SDFO1 underestimates and SDFO3 and SDFO4 overestimate the experimental results. Figure 6.28 b shows results for simplified models. The SSFO1, SSFO2, SSFO3, and SSFO4 presented maximum

load bearing capacity of 10.71 kN, 12.8 kN, 14.8 kN and 17.1 kN compared to 12.9kN obtained from the experimental counterpart. The SSFO2 model with 130% enhancement in ECC strength presented the best fit the same as the detailed model. The SSO1 results underestimate while the SSFO3 and SSFO4 overestimate the strength obtained from experiments. This can possibly be attributed to the fact that the predictions of the SDFO1 and SSFO1 models underestimate the experimentally established load-carrying capacity by about 10%. This can in turn be attributed to the absorption and evaporation of the water in the ECC layer by the masonry during the curing process resulting in higher strengths in the ECC layer than those anticipated.

The maximum deflection exhibited by the detailed and simplified models are 2.28mm and 2.32mm respectively compared to 3.89mm established experimentally (Figure 6.28). Both models underestimate the maximum displacement recorded during testing. In the experiments, one brick delaminated from the ECC layer and a series of multiple cracks happened beneath that brick increasing the deformability of specimens while in the models this was not captured (Section 4.3.4).

Table 6.8 ECC properties

Model name	Interface name	ECC First crack stress (MPa)	ECC First crack strain	ECC maximum stress (MPa)	ECC maximum strain
SDFO1	ISBM1	2.8	0.00018	3.75	0.035
SDFO6	ISBM1	3.6	0.00018	4.9	0.035
SDFO7	ISBM2	4	0.00018	5.4	0.035
SDFO8	ISBM3	4.5	0.00018	6	0.035
SSFO1	ISBM1	2.8	0.00018	3.75	0.035
SSFO2	ISBM1	3.6	0.00018	4.9	0.035
SSFO3	ISBM2	4	0.00018	5.4	0.035
SSFO4	ISBM3	4.5	0.00018	6	0.035

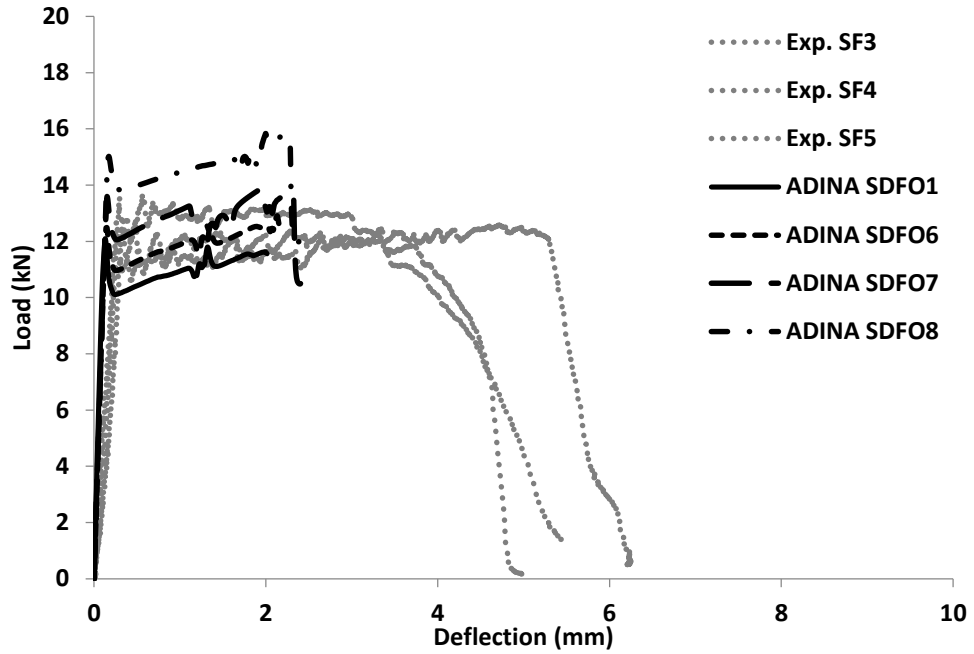

a

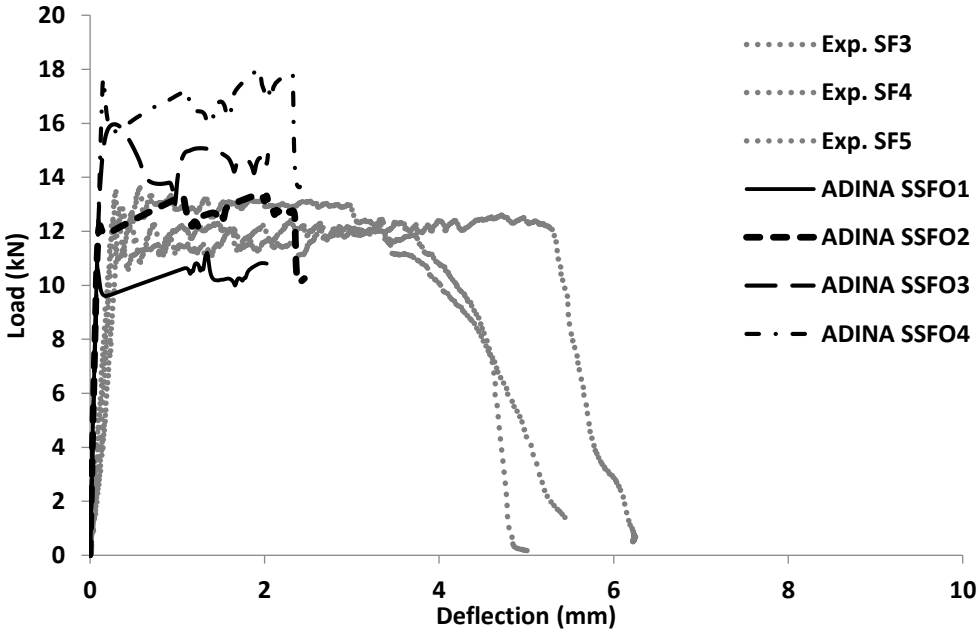

b

Figure 6.28 Comparison of load-deflection curves predicted numerically and established experimentally for describing the behaviour of a) SDFO model series b) SSFO model series

The distribution of strain in the FE model prior to failure can be observed in Figure 6.29. Failure in the model initiated in the brick-mortar interfaces (as in the case of test specimens), later global failure of the specimen happened in the ECC layer. It can be observed that the behaviour of the model is in agreement with the crack patterns recorded during testing.

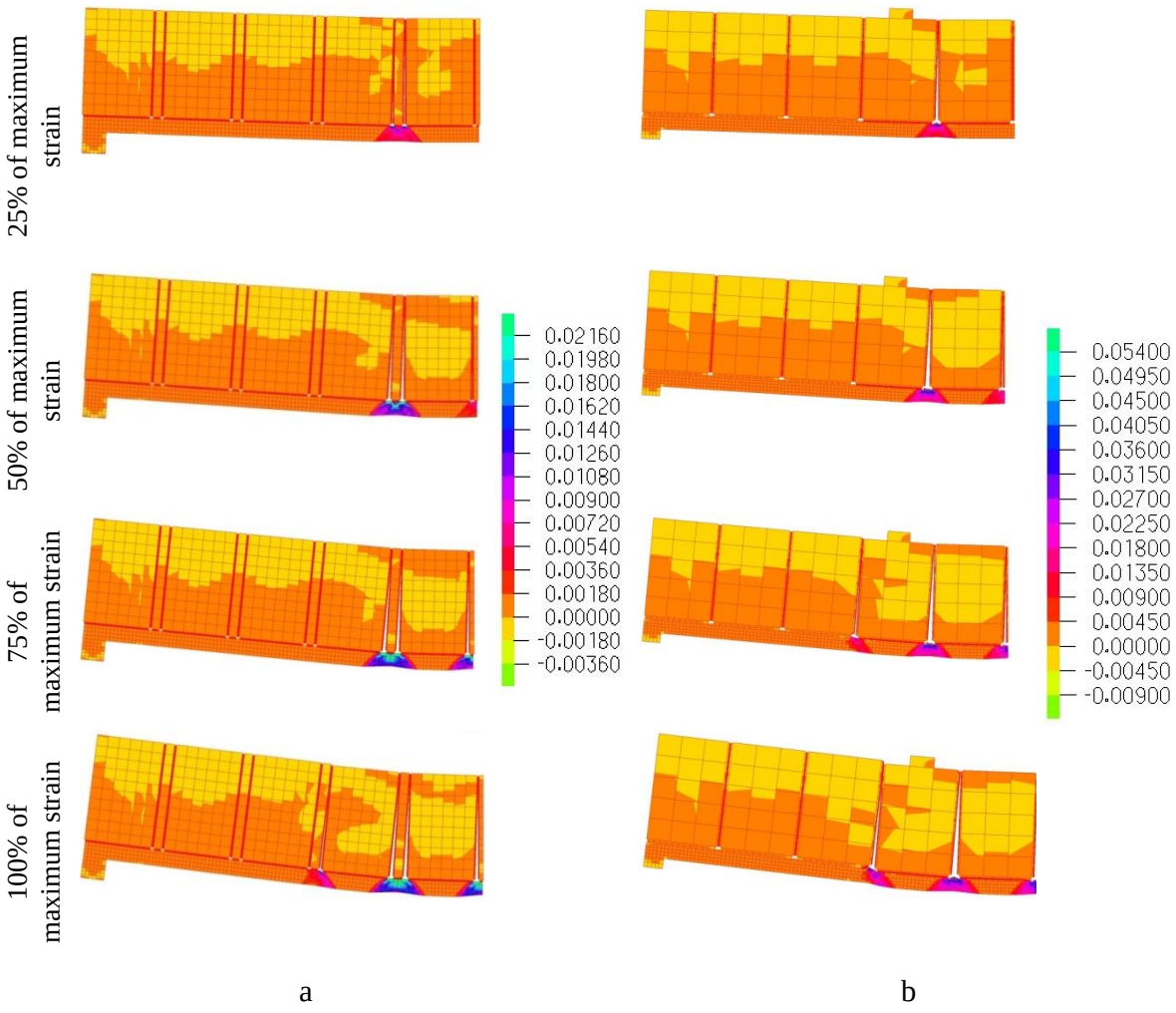

Figure 6.29 Comparison of failure predicted and strain distribution of a) SDFO model b) SSFO model

6.3.3 Modelling of partial bond ECC-retrofitted beam under bending test

A detailed SDPO model and a simplified SSPO model were adopted to simulate the partially bonded ECC-retrofitted beams under four-point flexural tests. For the modelling of the masonry beam-like specimen the strategy presented in section 6.3.1 was used. For the simulation of the ECC layer the method introduced in section 6.3.2 was applied. In order to define the unbonded surface within the central span between the ECC layer and the masonry a contact surface was introduced (very weak bond of 0.05 MPa strength in both tensile and strength has been adopted). In the SDPO model the contact surface connected the two outer bricks and three mortar layers to ECC layer. In SSPO the contact surface connected the two outer bricks (close to the edges of the specimens) and ECC layer. The support and load condition were the same as those applied in the case of the SDFO models in section 6.3.2 (Figure 6.30).

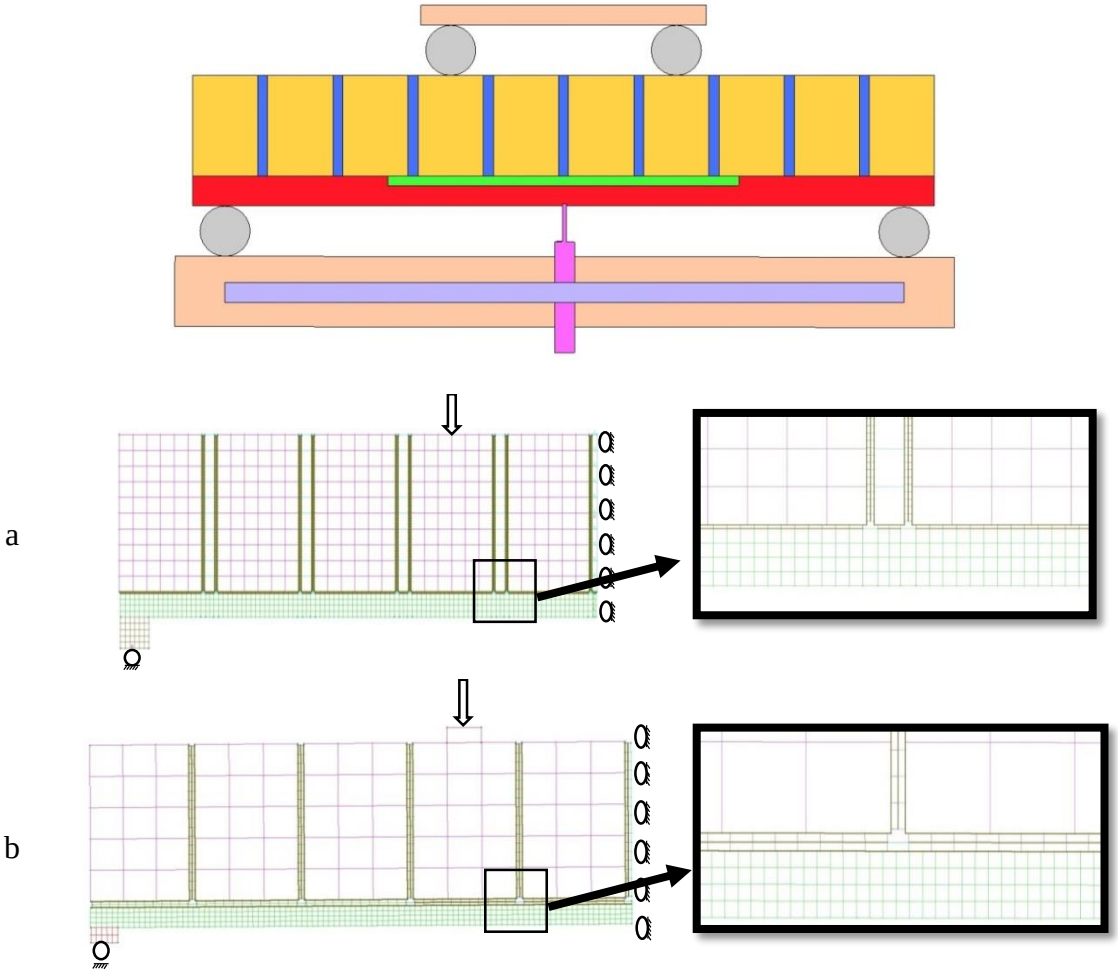

Figure 6.30 FE model accompanied by its experiment for bending test of a) SDPO model b) SSPO model

The cohesive interfaces adapted for both SDPO and SSPO models are based on that employed in the SDFO1 model. The effect of the variation in the mechanical properties of the ECC layer on certain aspects of specimen behaviour is presented in Table 6.9. The first crack stress and maximum stress of ECC layer increased by 130% and 145% compared to results obtained from experiments for the parametric study.

Figure 6.31a presents the results of the parametric study for detailed models. The maximum load bearing capacity for SDPO1, SDPO2 and SDPO3 are 9.81 kN, 12.2 kN and 14.2 kN respectively compared to 10.9kN obtained from the experiment. The predictions of SDFO2 model (with 130% higher ECC strength) provides the best fit to the test data whereas the predictions of model SDFO1 and SDFO3 either underestimate or overestimate the strength obtained from experimental results. Figure 6.28 b presented the predictions of specimen behaviour obtained from the simplified models. Models

SSPO1, SSPO2 and SSPO3, exhibited a maximum load bearing capacity of 10.2 kN, 13.5 kN and 17.1 kN compared to 10.9 kN established experimentally. The predictions of SSPO1 underestimate while those of SSFO2 and SSFO3 overestimate the strength obtained from experiments. A possible reason for this is that the load caring capacity predicted by SDPO1 and SSPO1 models underestimate the experiments counterparts. As is discussed in Section 6.3.2, this can be attributed to the absorption and evaporation of the water in the ECC layer by the masonry during the curing process resulting in higher strengths in the ECC layer than those anticipated.

The maximum deflection predicted by the detailed models are 8.52mm, 9mm and 14.1 mm for SDPO1, SDPO2 and SDPO3 compared to 6.59 mm established during testing (Figure 6.31 a). All predicted deflections overestimated that measured during testing. This is related with the opening of the cracks in all central cohesive interface in the models which increases the deformability of the model. However, during testing only one brick-mortar interface in each joint cracked within the central span.

The maximum deflection predicted by the simplified model are presented in Figure 6.31 b. The SSPO1, SSPO2 and SSPO3 models predicted a maximum deflection of 7mm, 7.59mm and 8.4mm compared to 6.59mm established experimentally. The predicted results for SSPO1 and SSPO2 are close to the experiments while SSPO3 provides higher values of deflection. The reason that the simplified models provide closer predictions to the experimental values compared to the detailed models is due to the reduction of cohesive interface number in the simplified models. In the detailed models, two cohesive interfaces are defied in each joint while in the simplified model only one cohesive interface is defined per joint. Therefore, the number of total cohesive interfaces in the simplified model is half of those in the detailed models. In the experiments also only one brick-mortar interface crack was observed in each joint (see Figure 4.24).

Table 6.9 ECC properties

Model name	Interface name	ECC First crack stress (MPa)	ECC First crack strain	ECC maximum stress (MPa)	ECC maximum strain
SDPO1	ISBM1	2.8	0.00018	3.75	0.035
SDPO2	ISBM1	3.6	0.00018	4.9	0.035
SDPO3	ISBM1	4	0.00018	5.4	0.035
SSPO1	ISBM1	2.8	0.00018	3.75	0.035
SSPO2	ISBM1	3.6	0.00018	4.9	0.035
SSPO3	ISBM1	4	0.00018	5.4	0.035

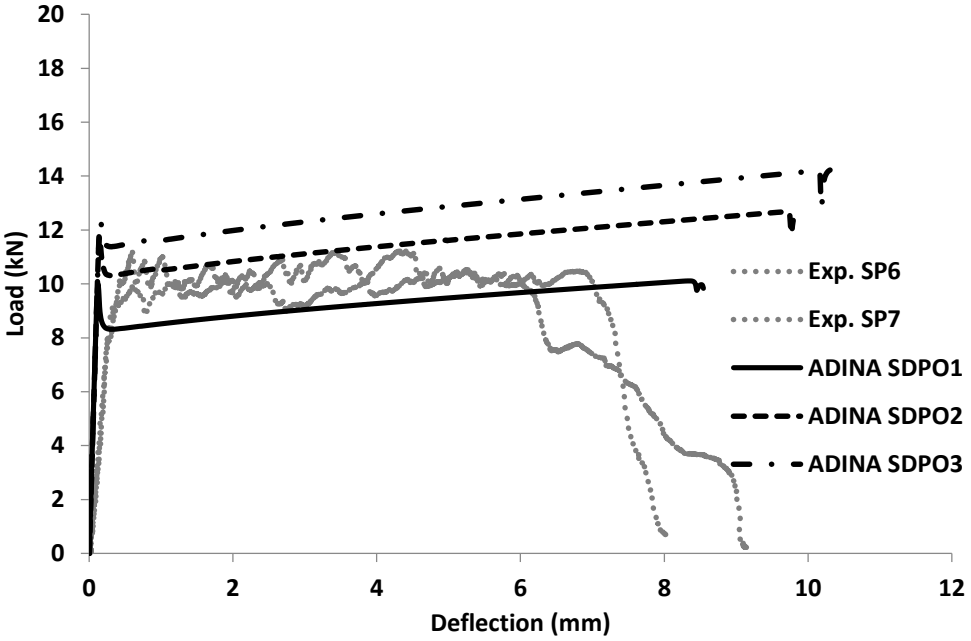

a

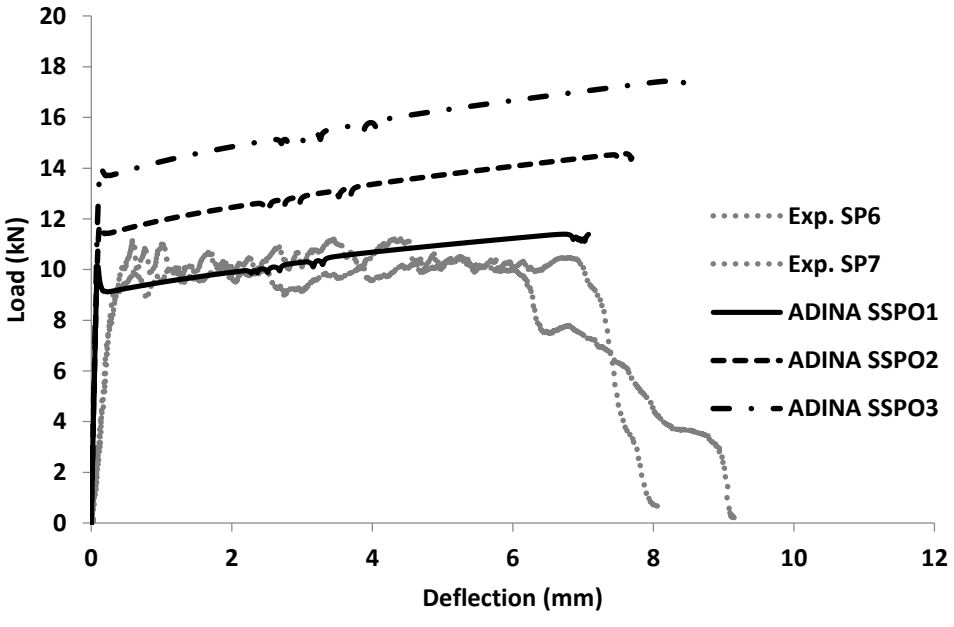

b

Figure 6.31 Comparison of load-deflection curves predicted numerically and established experimentally for describing the behaviour of a) SDPO model series b) SSPO model series

Failure in the model initiated in the brick-mortar interfaces as observed during testing. Then failure occurred in the ECC layer resulting in the collapse of the specimen. The distribution of the strain in the model prior to failure are presented in Figure 6.32. This strain distribution is related to crack pattern in real specimens. It can be observed that the predictions of the model are similar to crack patterns recorded during testing.

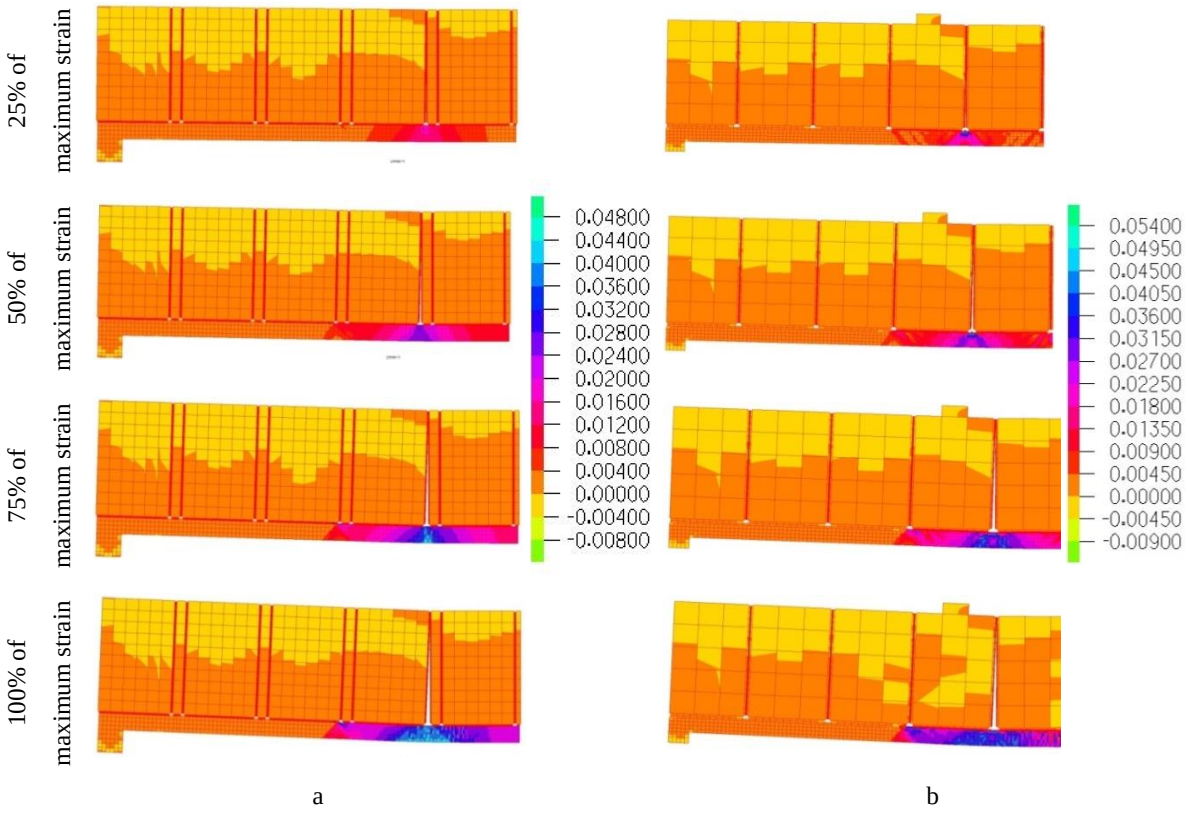

Figure 6.32 Comparison of failure predicted and strain distribution of a) SDPO model b) SSPO model

6.4 Part 3-Parametric study

6.4.1 Modelling the masonry beams retrofitted with two layers ECC

In this section the effect of a series of parameters on the performace of ECC-retrofitted specimens is investigated including the effect of a second layer of ECC on the top of specimens, the boundary conditions imposed, the variation of properties of the materials involved, the geometry of the specimen and the loading rate.

6.4.1.1 The effect of the second layer of the ECC on performance of fully bonded beam under bending test

To model the two layers full bond specimen, the same method as SSFO has been applied. The model (SSFT) was developed based on a simplified model that needs less time for computation (Section 6.3.2). The second layer of ECC is defined on the top of specimens the same as the bottom layer (Figure 6.33).

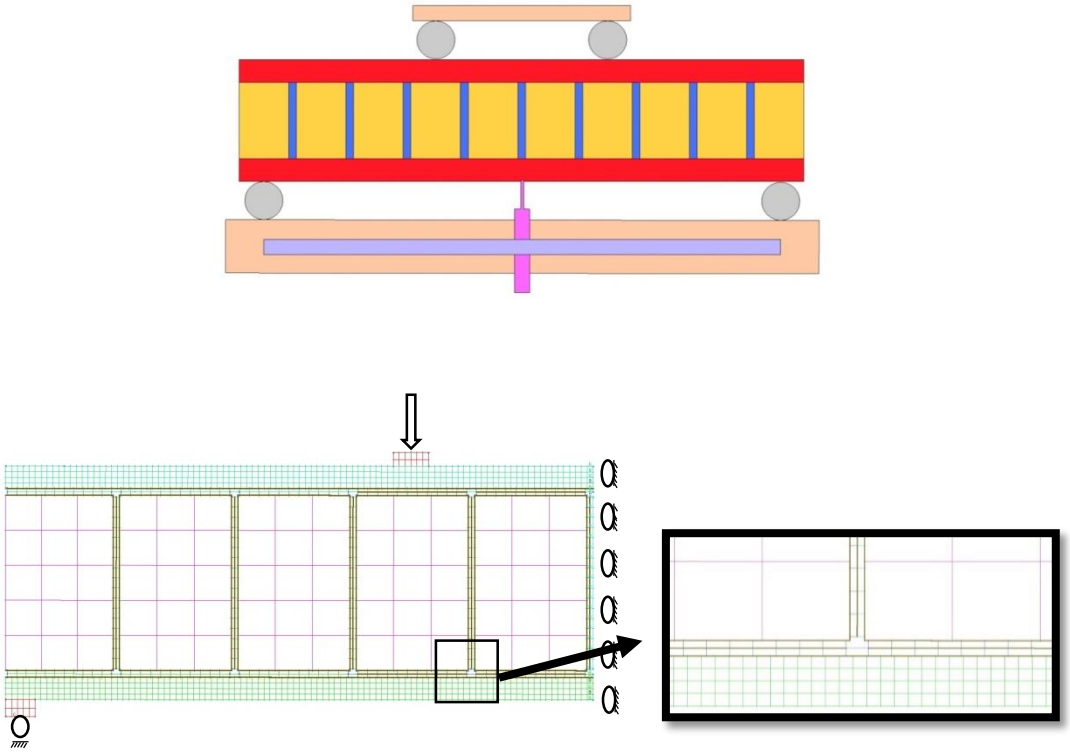

Figure 6.33 FE model accompanied by its experiment for bending test of SDFT model

In all models up to this section the ECC layer was defined as a multi-linear plastic material. However, multi-linear plastic material cannot be used to simulate both tensile and compression properties of ECC properly at the same time. Under impact loading the top ECC layer can be subjected to cyclic loading. Therefore, some new material models, including a multi-linear elastic and a concrete model are defined in order to allow the model to accurately capture the behaviour of this layer. First, a multi-linear elastic material model that can describe ECC behaviour under tension and compression is used. This material can simulate the ECC behaviour realistically under the static loading (Figure 6.34). Next, a concrete model is defined to model the behaviour of the ECC layer subjected to cyclic loads (Figure 6.34). Figure 6.34 presents both material stress-strain

curves. The multi-linear elastic material can simulate the strain hardening tensile behaviour exhibited by ECC while the concrete model can simulate strain softening behaviour. Two different properties assigned to the ECC layer including ECC properties obtained from experiments (see Figure 6.10) and an ECC layer with a 130% higher strength which provided the best fit to the available test data in sections 6.3.2 and 6.3.3 (Table 6.10).

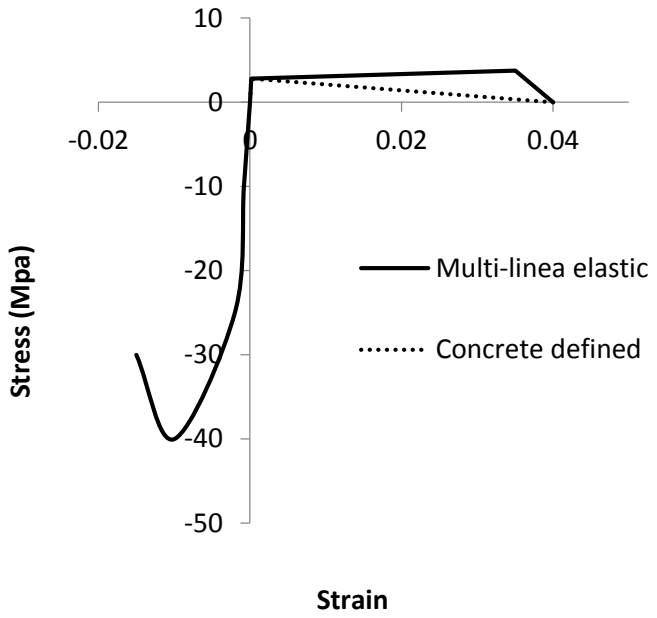

Figure 6.34. Stress-strain curve describing the behaviour of ECC under uniaxial tension and compression

Figure 6.35 shows the predicted results obtained from the models. As relevant test data under static loading is not available for these models, the predictions obtained are compared with their counterparts from models SSFO1 and SSFO2 (with one layer ECC). Both multi-linear elastic and concrete model predict results close to each other. The maximum load carrying capacity of SSFT series are close to those obtained from the SSFO series. For the stronger ECC the load-carrying capacity predicted was 13.9kN and 12.8 kN for SSFT2 and SSFT4 respectively compared to 13.3kN predicted by SSFO2. This shows that the bottom layer of ECC under tension contributes to load bearing capacity and the top layer of the ECC cannot affect the strength of the beam. In the top layer ECC in the SSFT models, the compression strain is about 2 times more than that observed in the top of the bricks in the SSFO models. However, compressive failure is not observed in any model.

The deflections predicted by models SSTF2 and SSTF4 are 2.55mm and 2.74 mm respectively compared to 2.36mm predicted by SSFO2. The results show that for specimens strengthened with fully bonded ECC layers the second layer of ECC on the top face (acting in compression) of the specimens can improve deformability substantially. The top ECC layer can distribute the applied load more uniformly on the masonry beam allow the bottom ECC layer to deform more than in the case of specimens retrofitted with one layer ECC. In the SSFO2 model the ECC layer beneath the joints developed strains up to of 2.3% while in the SSFT2 model the bottom ECC layer the maximum value of strain exhibited was 4.2% strain capacity. This observation presents that in SSFT2 the bottom ECC layer failed in higher level of tension and the top layer undertakes the developing shear while in the SSFO model the bottom ECC layer failed under a combination of tensile and shear forces and only reached a maximum strain value of 2.3% .

Table 6.10 Top layer ECC properties

Model name	Interface name	ECC First crack stress (MPa)	ECC First crack strain	ECC maximum stress (MPa)	ECC maximum strain	ECC material
SSFT1	ISBM1	2.8	0.00018	3.75	0.035	Multi-linear Elastic
SSFT2	ISBM1	3.6	0.00018	4.9	0.035	Multi-linear Elastic
SSFT3	ISBM1	2.8	0.00018	3.75	0.035	Concrete
SSFT4	ISBM1	3.6	0.00018	4.9	0.035	Concrete

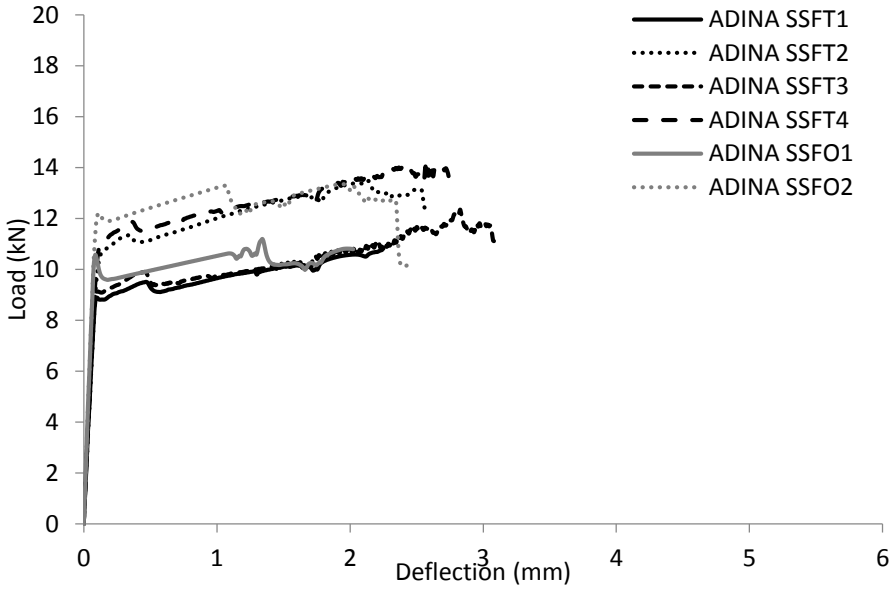

Figure 6.35 Comparison of load-deflection curves predicted numerically for describing the behaviour of SSFT and SSFO series

Failure in the model initiated in the brick-mortar interfaces and then the bottom ECC layer failed in tension. The distribution of stresses in the model prior to failure can be observed in Figure 6.36. This strain distribution is in agreement to crack pattern developing in the specimens during testing.

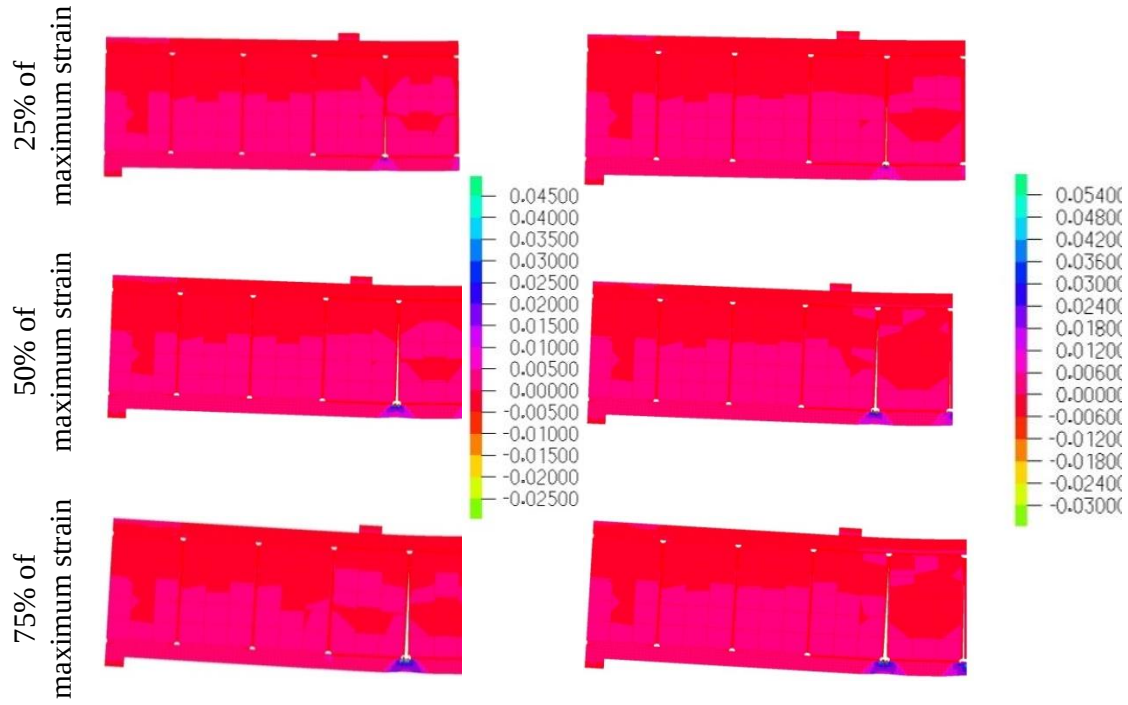

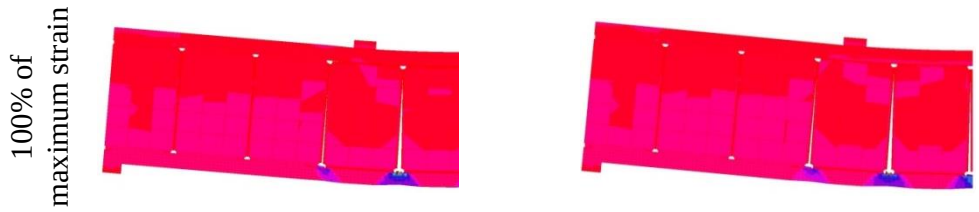

a b

Figure 6.36 Comparison of failure predicted and strain distribution of a) SSFT1 model b) SSFT3 model

6.4.1.2 The effect of the second layer of the ECC on performance of partially bonded beam under bending test

The two layers partially bond specimen (SSPT) is modelled with the same method as SSPO. The model was developed based on a simplified model that needs less time for computation (Section 6.3.3). The second layer of ECC is defined on the top of specimens the same as the bottom layer (Figure 6.37).

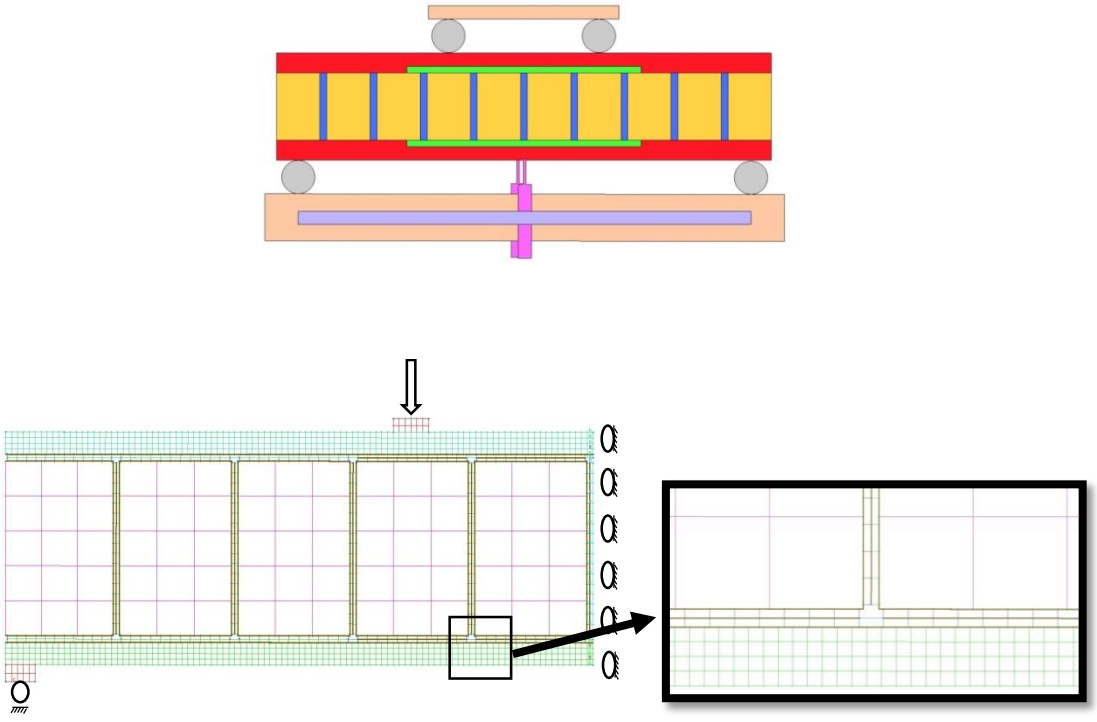

Figure 6.37 FE model accompanied by its experiment for bending test of SSPT model

This is the same as Section 6.4.1.1 where both multi-linear plastic material and a concrete define material are developed for the ECC layer in top of model. Two different properties

are allocated to the ECC layer including ECC properties obtained from experiments (see Section 6.2.4) and the ECC layer with 130% enhancement in strength (Table 6.11).

Figure 6.38 demonstrates the predicted results by models. As the counterpart experiments under quasi-static load are not available for these models, predicted results compared with counterparts results of model with one layer ECC SSPO1 and SSPO2. Both multi-linear elastic and concrete model could predict the results properly. The maximum load carrying capacity and deflection of SSFT series are similar to those exhibited by the SSFO series. In the partially bond specimens bottom ECC layer failed when reached to its maximum tensile strain capacity. Therefore the top layer of ECC cannot increase the deformability of the specimen and the SSFT models deflection is close to SSFO counterparts. The compression strain at the top layer ECC of SSPT is the same as SSPO counterparts. In the SSFO the ECC layer beneath the interfaces reached up to 4.2% strain capacity, the same as the SSFT bottom ECC layer. This observation presents that in SSPT the top layer ECC cannot improve the deflection of the bottom layer ECC.

Table 6.11 Top layer ECC priorities

Model name	Interface name	ECC first crack stress (MPa)	ECC first crack strain	ECC maximum stress (MPa)	ECC maximum strain	ECC material
SSPT1	ISBM1	2.8	0.00018	3.75	0.035	Multi-linear Elastic
SSPT2	ISBM1	3.6	0.00018	4.9	0.035	Multi-linear Elastic
SSPT3	ISBM1	2.8	0.00018	3.75	0.035	Concrete
SSPT4	ISBM1	3.6	0.00018	4.9	0.035	Concrete

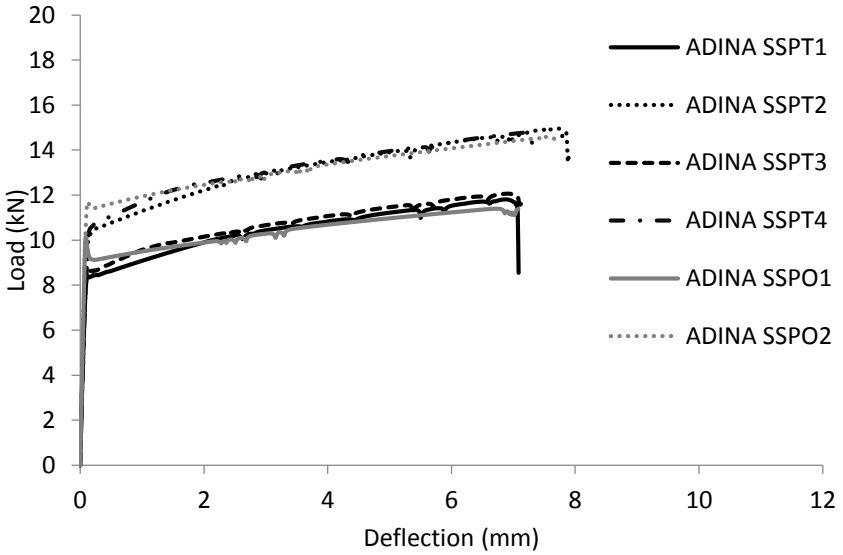

Figure 6.38 Comparison of load-deflection curves predicted numerically for describing the behaviour of SSPT and SSPO series

Failure in the model initiated in the brick-mortar interfaces and then the bottom ECC layer failed in tension. The distribution of stresses in the model prior to failure can be observed in Figure 6.39. This strain distribution is in agreement to crack pattern developing in the specimens during testing.

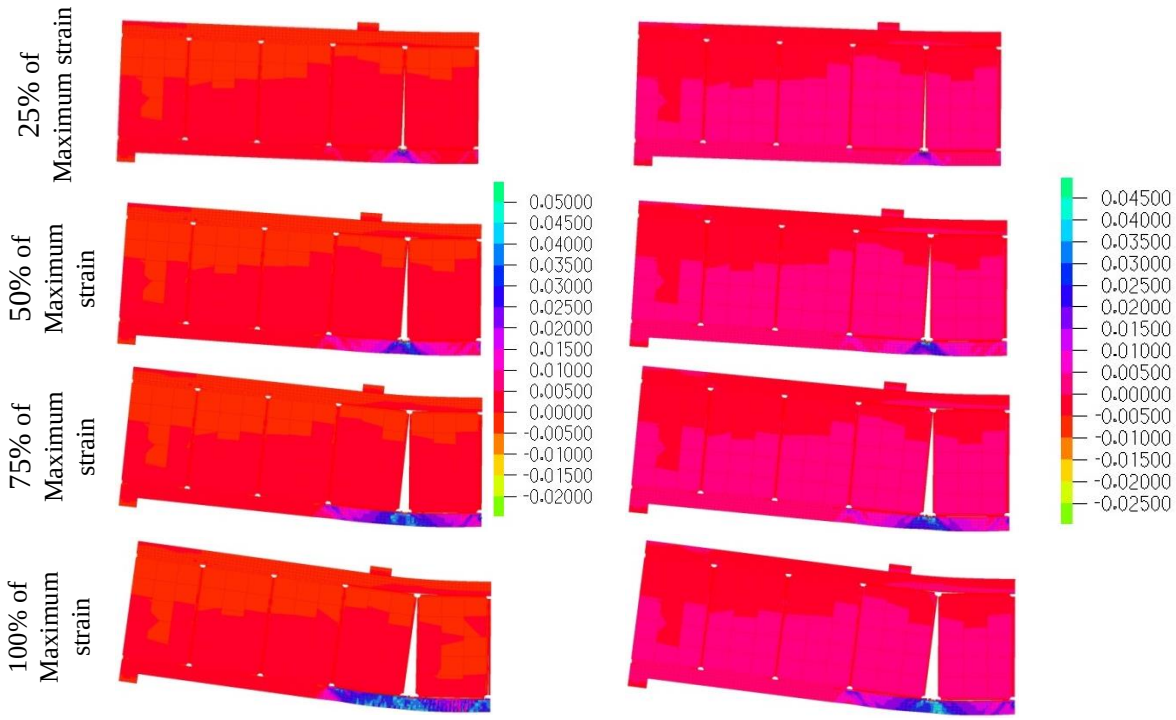

Figure 6.39 Comparison of failure predicted and strain distribution of a) SSPT1 model b) SSPT3 model

6.4.2 Effect of beam length

The experimental and numerical studies presented in chapters 4, 5 and 6 were carried out on specimens with lengths of 800 mm. However, in buildings the height of the walls can be up to 3000 mm. In this section a simply supported masonry beam retrofitted with one layer ECC with a 3000 mm length are simulated in order to assess the effect of ECC retrofitting method on full scale walls.

The model representing the plain masonry long beam (MLB) was developed by adopting the strategy employed in section 6.3.1. The long specimens are considered to consist of a stack of 20 bricks (instead of 5 bricks used in SSM1). Steel elements are used to distribute the stresses at the support which were allowed to rotate and move axially (see Figure 6.40). On the other end the cross-section of the specimen is allowed only to translate vertically due to the symmetry characterising the problem at hand. The load is applied monotonically to failure at the middle of the tenth brick (middle third of span) (Figure 6.40) (from the support) in the form of displacement increments.

For modelling of the fully bonded ECC long beam (FLB) an ECC layer with dimensions of 1493mm x 15 mm was attached on the bottom face of the beam. This layer is modelled using a 4 x 400 mesh of 2D 4-node elements with dimensions of 3.73 mm x 3.75mm (see Figure 6.40). For the case of the long beam strengthened with a fully bonded ECC layer, the cohesive element was adopted as in the case of the SSFO model. To form the unbonded surface in the long beams (PLB) strengthened with an ECC layer a contact surface (between ECC layer and the masonry) was introduced (very weak bond of 0.05 MPa strength is adopted). In the PLB the contact surface initiated from the fourth brick from the support (Figure 6.40). The support and load conditions were the same as those imposed on models SDFO in section 6.3.2 (Figure 6.40).

a)

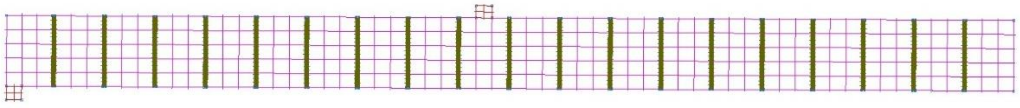

b)

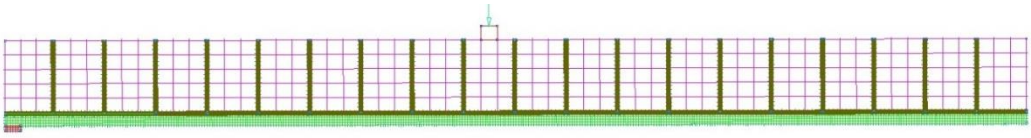

c)

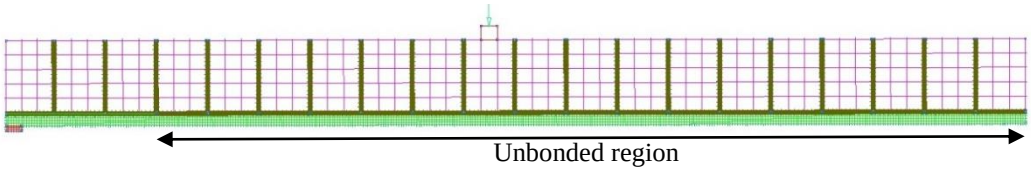

Figure 6.40. FE model for bending test of long models a) plain masonry b) fully bonded beam c) partially bonded beam

Load-deflection results under quasi static load for MLB, FLB and PLB are presented in Figure 6.41. The middle of the partial beam and full bond beam could reach to 174 mm and 98 mm deflection before failure compared to 0.4 mm deflection for the plain masonry long beam. The results show ductile behaviour for both retrofitted beams compared to the plain masonry long beam. The ductility of the beam with the partially bonded ECC layer is about two times higher than that of the full bond beam. Some fluctuations in the load-displacement curves were observed in the case of both retrofitted beams. These fluctuations are due to the sliding of the bricks when the beams reaches 50 mm deflection and deformation of masonry beam reduces the contact surface between the bricks. The load carrying capacity of the FLB and PLB models are 3.1kN and 2.95 kN respectively. As in the case of the experimental and numerical results associated with the shorter beams, the load carrying capacity of the full bonded long beam is higher than the load carrying capacity of partial bonded specimen.

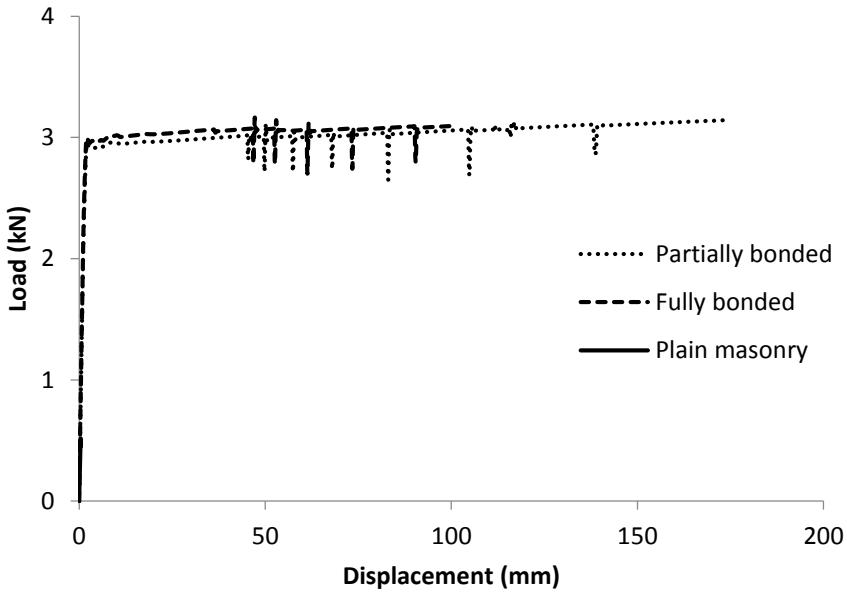

Figure 6.41. Comparison of load-deflection curves predicted numerically for describing the behaviour of MLB, FLB and PLB

Figures 6.42 a, b & c show the strain distribution in MLB, FLB and PLB respectively. The first crack in all beams happened in the brick-mortar interfaces within the central

span. The MLB failed when cracks developed in interfaces which caused a very limited ductility of 0.4 mm. However in the FLB and PLB a series of radial cracks developed in the ECC layer beneath the interfaces. In the FLB the strain in the ECC layer reached to 2% beneath the interfaces when the localized radial cracking was observed resulting in failure of specimen. However in the PLB the cracks developed uniformly up to 2.4% in ECC layer. This uniform distribution of strain in PLB caused to the higher ductility of the specimen.

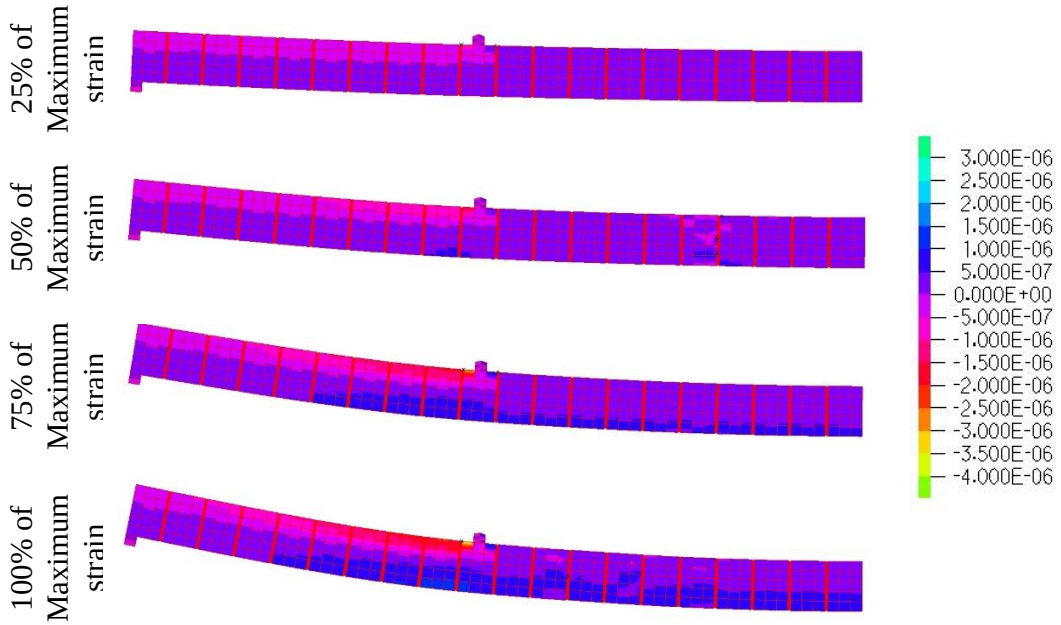

a)

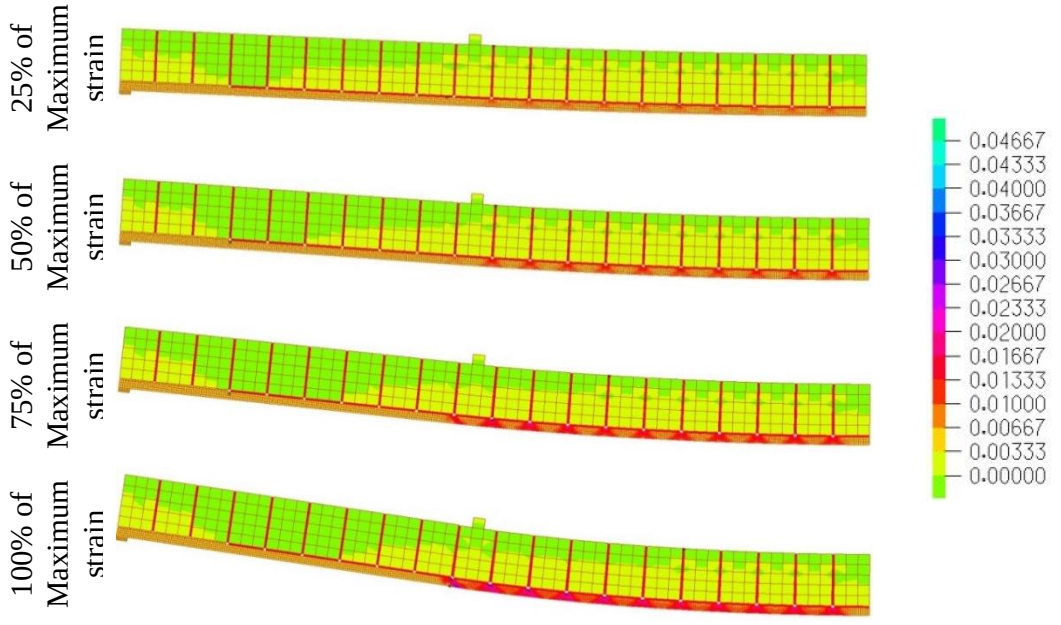

b)

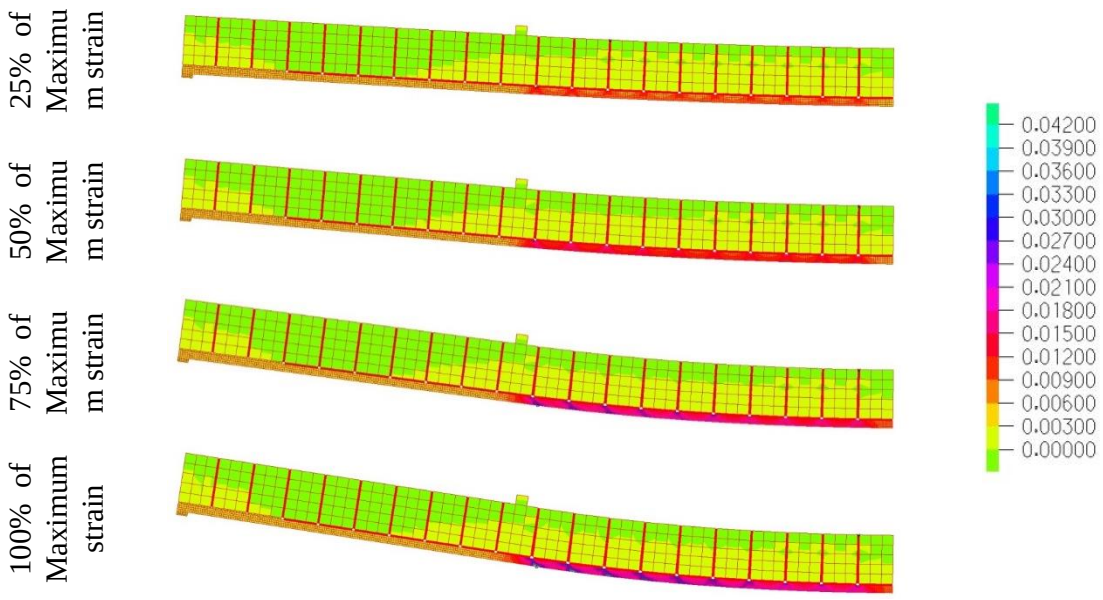

c)

Figure 6.42. Comparison of failure predicted and strain distribution of long specimens a) full bonded b) partially bonded

6.4.3 Effect of variation of mechanical properties of brick, mortar and ECC

In section 6.2.5 it is presented that when ECC and hybrid ECC subjected to elevate temperature their mechanical properties changed drastically. This section investigates the effect of variation in the mechanical properties of ECC and Hybrid ECC on the performance of retrofitted specimens. A big variation also reported on the mechanical properties of masonry walls including brick and mortar. Effects of this variation on the performance of ECC-retrofitted masonry specimens are also studied in the following section.

6.4.3.1 Effect of variation in mechanical properties of ECC on short beams

The mechanical properties of ECC and hybrid ECC can vary at different temperatures. In Section 6.2.5 it presented that the ECC has high variation at elevated temperature compared to hybrid ECCs whereas the behaviour of both H6ECC and H13ECC are more stable at elevated temperatures. Both H6ECC and H13ECC exhibited close behaviour to each other. Therefore only H6ECC behaviour is investigated. This section investigates the effects of variation in mechanical properties of ECC and H6ECC at 20 ˚C, 60 ˚C, 100 ˚C, 200 ˚C and 400 ˚C on the performance of detailed fully bonded (SDFO) and detailed partially bonded (SDPO) models. The same strategy is used in this parametric study for SDFO and SDPO models which are discussed in Sections 6.3.2 and 6.3.3 respectively.

Mechanical properties of brick and mortar are assumed to be constant in all cases, the same as Section 6.2.2 and 6.2.3 respectively. The mechanical properties of ECC and H6ECC under elevated temperatures which are presented in Table 6.4 are introduced to both models.

Figure 6.43 a shows the performance of fully bonded ECC and H6ECC retrofitted specimens (SDFO) at different temperatures. At ambient temperature (20˚C) ECC and H6ECC retrofitted specimens have 12.1 kN and 11.9 kN load bearing capacity and 1.95mm and 1.91 mm deflection respectively. The behaviour of both specimens are close to each other at ambient temperature. At 60 ˚C the ECC and H6ECC specimens have 8.95kN and 9.05kN load bearing capacity and 3.01mm and 5.76mm deflection respectively. This reduction in the load bearing capacity and enhancement of deflection of beams represent the changes of mechanical properties of ECC and H6ECc at 60 ˚C. At 100 ˚C the ECC and H6ECC specimens have 5.55 kN and 6.7 kN load bearing capacity and 2.49mm and 1.64 mm deflection respectively. The decreasing in both loads bearing capacity and deflection is due to the reduction of mechanical properties of both ECC and H6ECC. At 200 ˚C the ECC retrofitted specimen exhibits a brittle failure at 3.48kN with 0.1mm deflection. However the H6ECC retrofitted specimen demonstrates strain softening behaviour with a peak of 6.3 kN and 0.13 mm deflection at peak load. At 400 ˚C the ECC retrofitted specimens suddenly fails at 2.5 kN and 0.1 mm deflection while the H6ECc retrofitted masonry beam presented strain softening behaviour with 7.2 kN peak load and 0.12 mm deflection at peak load.

The performance of partially bonded ECC and H6ECC retrofitted specimens (SDPO) at different temperatures are presented in Figure 6.43 b. At ambient temperature (20 ˚C) ECC retrofitted and H6ECC retrofitted specimens have 10.1 kN and 12.9 kN load bearing capacity and 7.25mm and 8.55mm deflection respectively. The behaviour of both specimens represents the mechanical properties of ECC and H6ECC at ambient temperature where ECC has higher ductility (16%) but lower maximum load bearing capacity (14%) compared to H6ECC. At 60 ˚C the ECC and H6ECC specimens have 9.35kN and 12.8kN load bearing capacity and 24.2mm and 11.2mm deflection respectively. This reduction in the load bearing capacity and enhancement of deflection of beams represent the changes to mechanical properties of ECC and H6ECc at 60 ˚C. At

100 ˚C the ECC and H6ECC specimens have 6.03 kN and 6.7 kN load bearing capacity and 12.8mm and 4.55 mm deflection respectively. The decreasing in both loads bearing capacity and deflection is due to the reduction of mechanical properties of both ECC and H6ECC. At 200 ˚C the ECC retrofitted specimen exhibits a brittle failure at 4.12kN with 0.1mm deflection. However, the H6ECC retrofitted specimen demonstrates strain softening behaviour with a peak of 8.99 kN and 0.13 mm deflection at peak load. At 400˚C the ECC retrofitted specimens suddenly fails at 2.6 kN and 0.08 mm deflection while the H6ECc retrofitted masonry beam presented strain softening behaviour with 7.03 kN peak load and 0.12 mm deflection at peak load.

It is interesting to notice that in all cases the global failure initially happened in the ECC layer not the masonry beam. A tensile failure within the central span is observed in all cases. A clear and proportional relation between the behaviour of ECC/H6ECC and retrofitted beam is noted in all cases. A comparison between the behaviour of fully bonded specimens at elevated temperature (Figure 6.43 a) and partially bonded specimens under elevated temperature (Figure 6.43 b) reveals that partially bonded specimens are more sensitive to changes in mechanical properties of ECC and H6ECC. From 20 ˚C to 100 ˚C the behaviour of fully bonded ECC retrofitted with both ECC and H6ECC are close to each other. However, within the same range of temperature the partially bonded specimens retrofitted by H6ECC exhibited a maximum load bearing capacity about 30% higher and a deflection between 5% to 50 % lower compared to fully bonded counterparts. This reveals that as partially bonded specimens employ the full tensile capacity of the ECC layer are more sensitive to changes in the mechanical properties of the ECC layer.

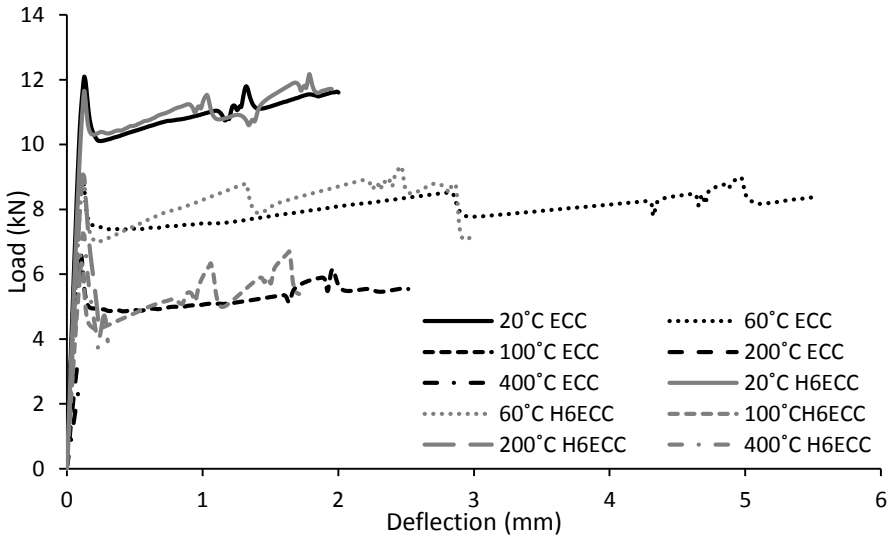

a)

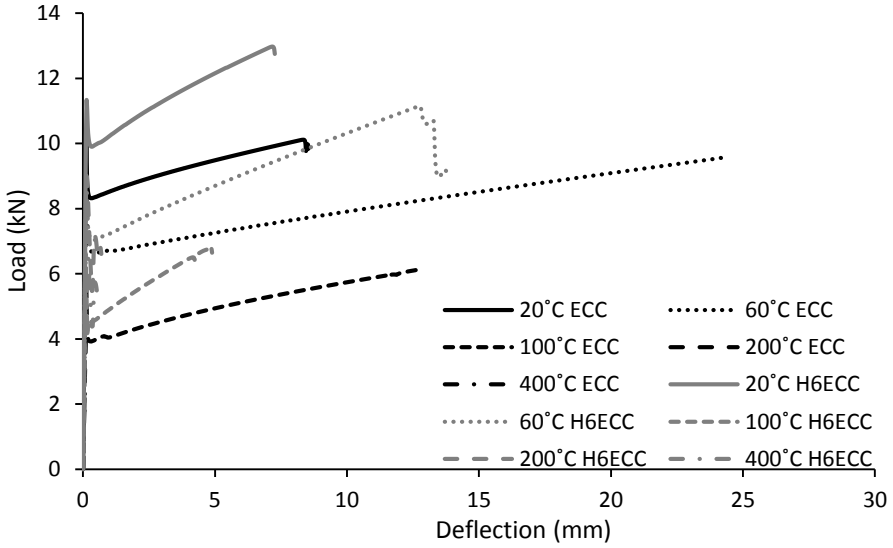

b)

Figure 6.43 Load-deflection curves of ECC and H6ECC retrofitted masonry beams under elevated temperatures a) Full bond specimens (SDFO) b) Partial bond specimens (SDPO)

6.4.3.2 Effect of variation in mechanical properties of ECC on short beams

The mechanical properties of the materials used in masonry walls have a vast range of variation. In this section a parametric study investigates the effects of variation in mechanical properties of brick and mortar on the behaviour of partially bonded ECC masonry walls. As partially bonded specimens presented better performance under flexure load compared to fully bonded specimens, this retrofitting method is selected for this parametric study (SDPO model). The same strategy is used in this parametric study SDPO model which is discussed in Section 6.3.3. Mechanical properties of ECC are assumed to be constant in all cases, the same as Section 6.2.4. Table 6.12 presents the properties of brick and mortar selected for this study. Both brick and mortar used in the experiments have high quality (strength) for brick, a 33%, 66% and 84% reduction in compression strength and for mortar 33% and 66% reduction in compression strength are selected.

Table 6.12: Parametric study on mechanical properties of brick and mortar

ID	Compression strength (MPa)	Modulus of	Tension strength (MPa)

		Elasticity (GPa)	
BC60 E30 (Original beam)	60	30	6
BC40 E30	40	30	4
BC20 E20	20	20	2
BC10 E10	10	10	1
MC22E12 (Original beam)	22	12	2.2
MC14E7	14	7	1.7
MC7E4	7	4	0.7

Figure 6.45 a presents the load deflection results of SDPO model when the mechanical properties of brick changes. The load bearing capacity of BC40E30, BC20E20 and BC10E10 are 9.01kN, 8.73kN and 8.44 respectively compared to 9.7kN load bearing capacity of the original beam. All beams presented the same trend in their behaviour and load bearing capacity close to each other. BC40E30, BC20E20 and BC10E10 exhibited a maximum deflection capacity 4.41mm, 2.5mm 0.87 mm compared to 8.4mm deflection of the original beam. It is interesting to see that the ductility of beams reduced by 48%, 61% and 90% when the strength of bricks reduced by 33%, 66% and 84% respectively, resulting in premature failure at the ECC layer (before reaching the maximum strain capacity). It is noticed that when compression strength of beam reduced to 10MPa ductile behaviour of the specimen was disappearing. This highlights that the compression strength of about 20 MPa for brick is necessary for specimens to exhibit a ductile behaviour.

The effect of variation of mortar strength on the performance of the SDPO model is presented in Figure 6.45b. The load bearing capacity of MC14E7 and MCE4 are 9.01kN and 8.75kN compared to 9.7kN obtained from the original beam. The MC14E7 and MCE4 exhibited a ductility of 5.7mm and 0.22mm respectively compared to 8.4mm deflection of the original beam. Though the load bearing capacity of all beams are close to each other a reduction of 33% and 98% is observed when the strength of mortar reduced by 33% and 66% resulting in premature failure at ECC layer (before reaching the maximum strain capacity). It is noticed that when compression strength of mortar reduced to 7MPa, the ductile behaviour of specimen was disappearing. This highlights that the compression strength of about 14 MPa for mortar is necessary for specimens to exhibit a ductile behaviour.

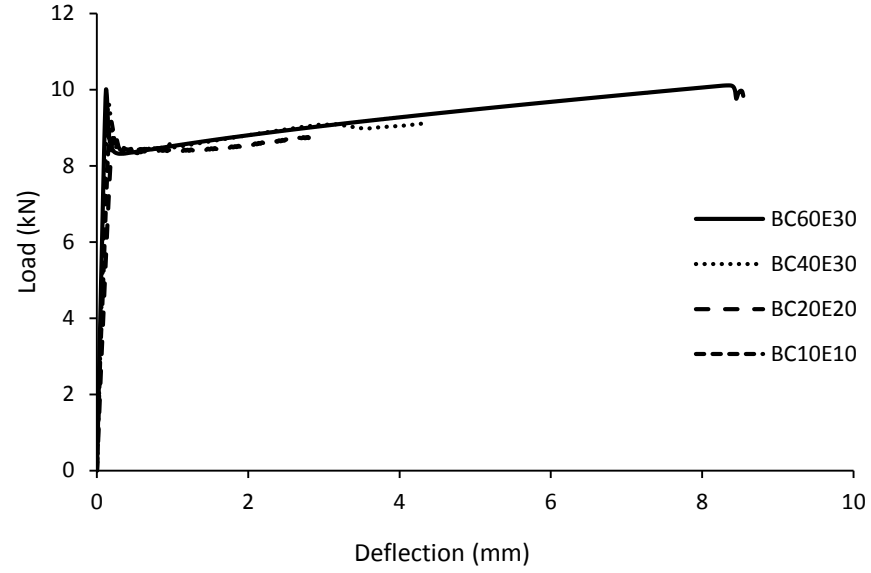

a)

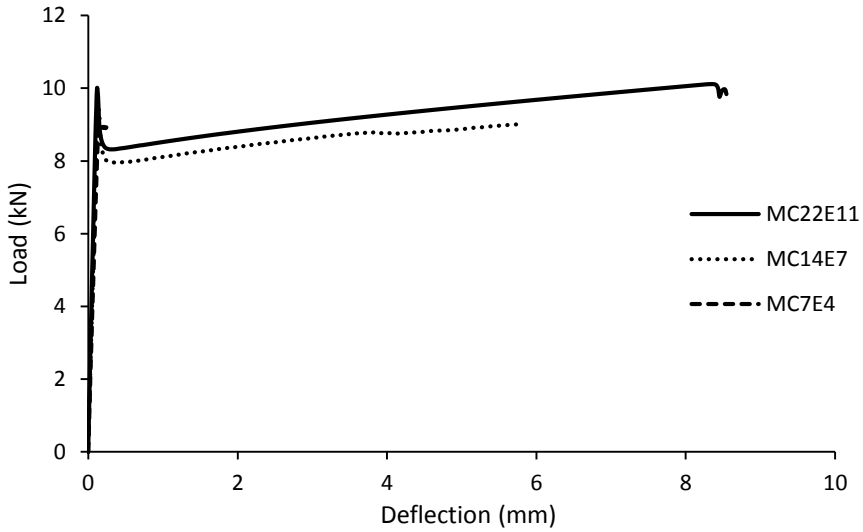

b)

Figure 6.44. Load-deflection curves of ECC retrofitted masonry beams (SDPO) a) variation in mechanical properties of brick b) variation in mechanical properties of mortar

Figure 6.45 demonstrates the strain distribution of beams at failure. By reduction of compression strength in brick it observed that the ECC layer failed at the premature level and before reaching the maximum strain capacity. When the compression strength of brick reduced to 10 MPa (BC10E10) a crack initiated in the fourth brick from the support side. However, the global failure happened in the ECC layer in specimens. In the MC7E4 model a crack developed in the third joint from the support side causing the failure of mortar layer at the top of the third joint. Following by a localized failure in the ECC layer beneath the joint.

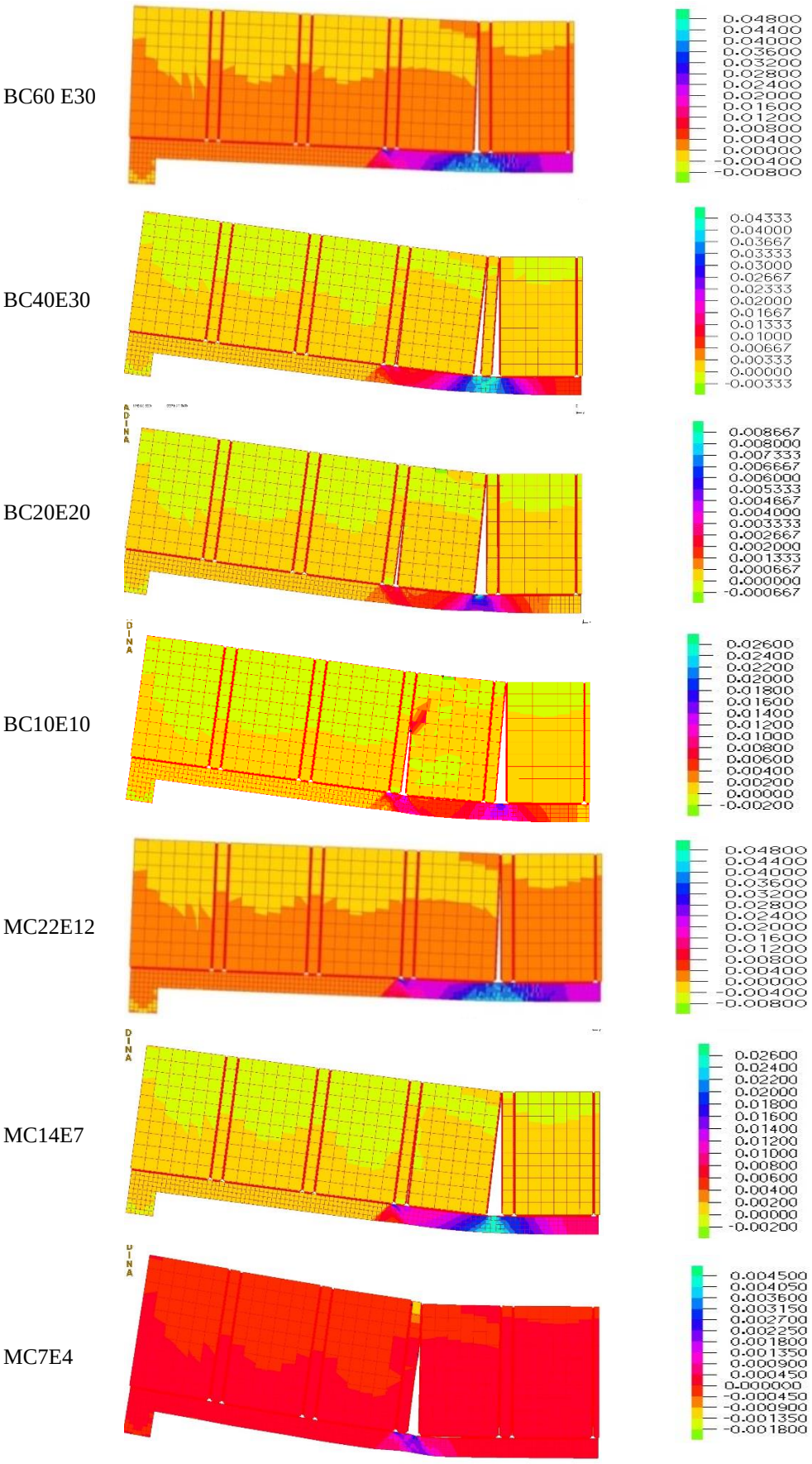

Figure 6.45. Comparison of failure predicted and strain distribution of Specimens

6.4.3.3 Effect of variation in mechanical properties of brick on long beams (PLB)

A brief parametric study which investigates effects of variation in mechanical properties of brick on the behaviour of the partially bonded long beam (PLB model) is presented in this section. The same strategy is used in this parametric study PLB model which is discussed in Section 6.4.2. Mechanical properties of ECC are assumed to be constant in all cases, the same as Section 6.2.4. Table 6.13 presents the properties of brick (mortar material is not available) which reduced a 33%, 66% and 84% in compression strength.

Table 6.13 Parametric study on mechanical properties of brick and mortar

Model name	Compression strength (MPa)	Modulus of elasticity (GPa)	Tension strength (MPa)
BC60 E30 (original beam)	60	30	6
BC40 E30	40	30	4
BC20 E20	20	20	2
BC10 E10	10	10	1

Results of three case studies on the mechanical properties of masonry units are presented in the Figure 6.46. BC40E30, BC20E20 and BC10E10 exhibited 3.1kN , 2.9kN and 2.73 kN load bearing capacity respectively compared to 3.14 kN of original beam and 49mm, 20.4mm and 11.3mm deflection respectively compared to 175mm deflection of the original beam. A 72%, 989% and 945 reductions in the ductility of beams are observed when the strength of brick is reduced by 33%, 66% and 84%. It is interesting to notice that by reducing the compression strength of masonry units the ductility of beams reduced sharply. However the maximum load carrying capacity of beams does not have important change by a reduction in the compression strength of the masonry unit. This is the same as SDPO models when the compression strength of brick reduced to 10MPa the ductility of specimens vanished. This highlights that the same threshold of 20MPa is needed for the long beam to present a ductile performance.

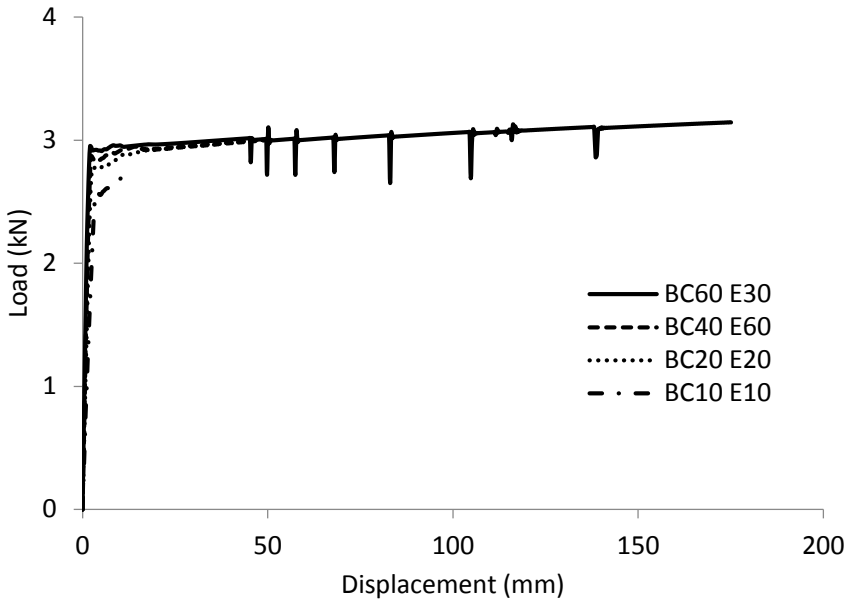

Figure 6.46. Load-deflection curves of ECC retrofitted masonry beams (LPB) with variation in mechanical properties of brick

Figure 6.47 demonstrate the strain distribution of beams at failure. By reduction of compression strength in brick it observed that the ECC layer failed at the premature level and before reaching the maximum strain capacity. These results are in good agreement with the reduction of ductility of beams when brick compression strength is reduced. However, in all cases the brick did not crack during the simulation.

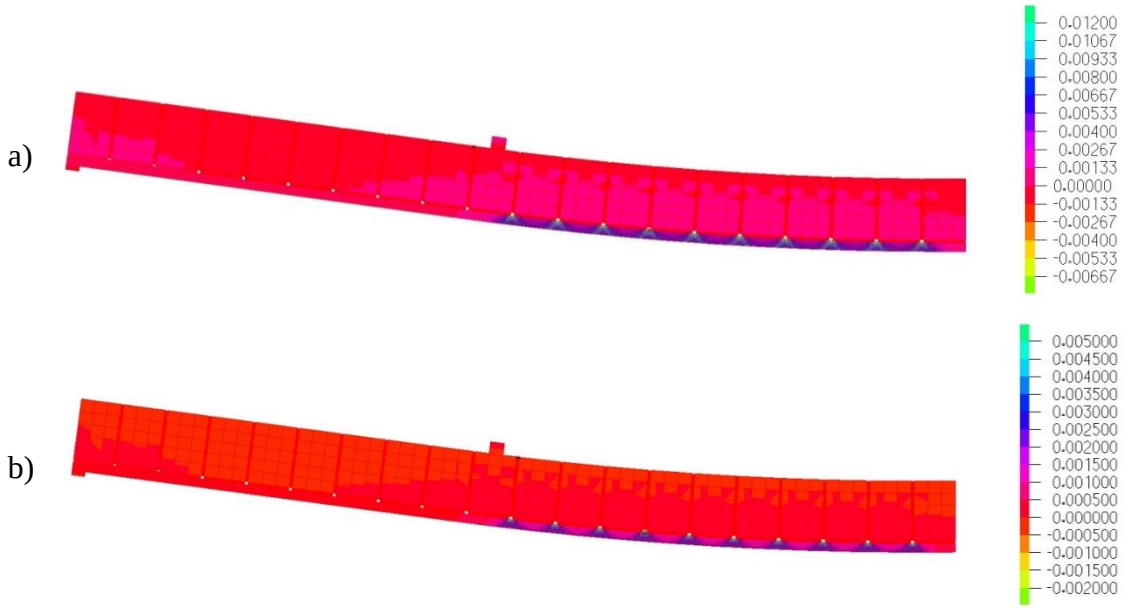

c)

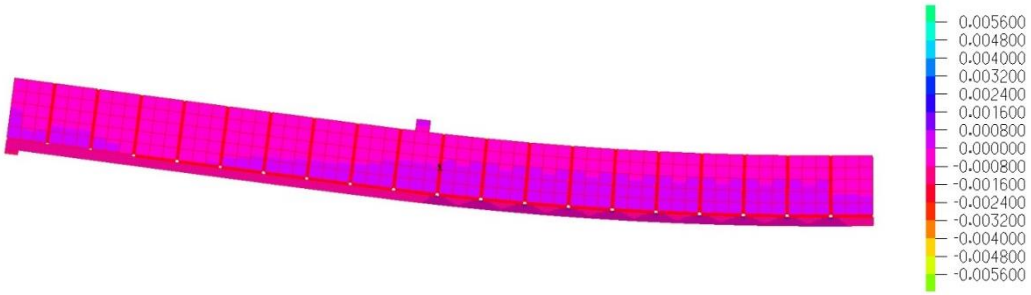

Figure 6.47. Strain distribution in the specimens at failure a) BC40 E30 b) BC20 E20 c) BC10 E10

6.4.4 Effect of support conditions

One of the parameters which affect the masonry walls behaviour is the boundary condition. In the experimental and modelling work presented up to this part all specimens had the roller support. However, other scenarios can happen in the real case for masonry walls. To assess the behaviour of masonry walls under different boundary conditions two other cases of axial movement prevented pinned support with and fixed support are investigated on the fully bonded and partially bonded specimen (FLB and PLB models) (Figure 6.48). The same strategy is used in this parametric study for the PLB model which is discussed in Section 6.4.2. Mechanical properties of ECC, brick and mortar were constant in all cases, the same as Sections 6.2.4, 6.2.2 and 6.2.3 respectively.

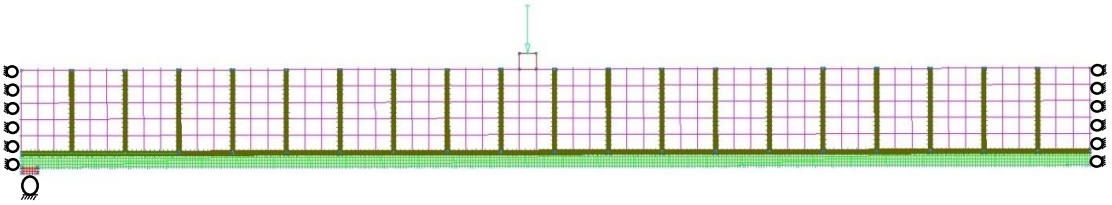

a)

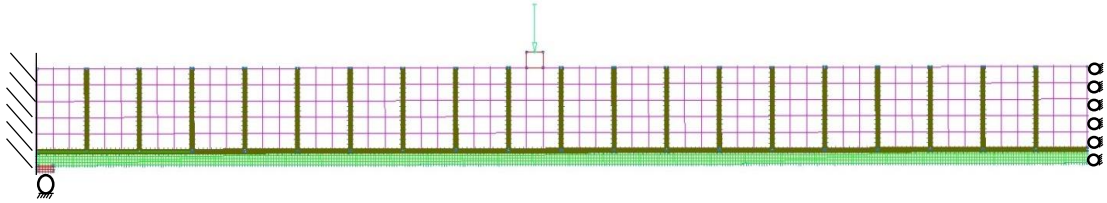

b)

Figure 6.48. FE model for bending test of PLB model a) axial movement prevented on pinned support b) Fixed support

The load-deflection results of both cases are presented in Figure 6.49. The fully bonded and partially bonded specimens presented the same behaviour compared to each other. When the axial movement is prevented in pinned support beam a premature failure happened in the beam. The maximum load capacity was 3 kN and same as roller support beam. However, the deflection of pinned support is 2.5 mm which is several times (between 50-75 times) less than roller support. In the beam with the fixed support the maximum load capacity reached to 18 kN. This load carrying capacity is six times more than a roller and pinned support. However a premature failure after 2.5 mm deflection happened in the axial beam movement is prevented.

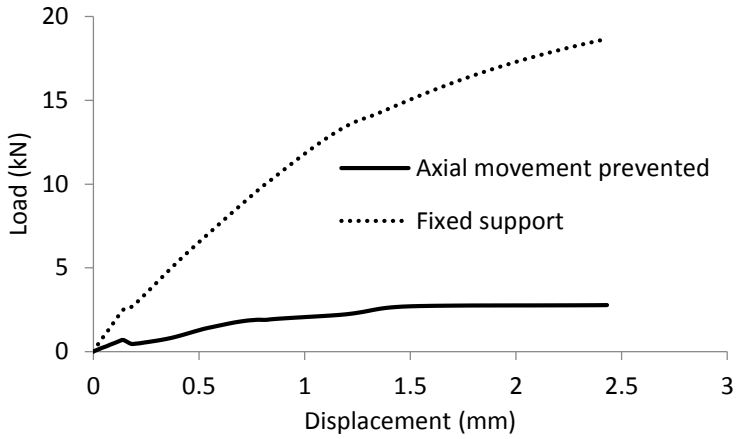

Figure 6.49. Load-deflection curves of bending test of PLB model with different support conditions

Figure 6.50 presents the strain distribution of both beams at failure. A shear failure in both cases happened before reaching to maximum strain capacity. It is observed that the axial movement of roller beam is about 15 mm for the flexural failure mode and if beam is prevented from axial movement by any kind of support the shear failure will occur in the beam.

a)

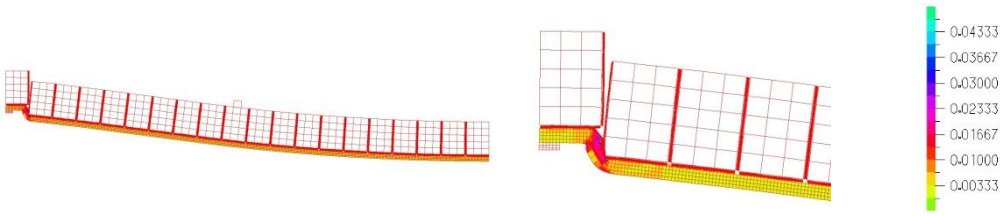

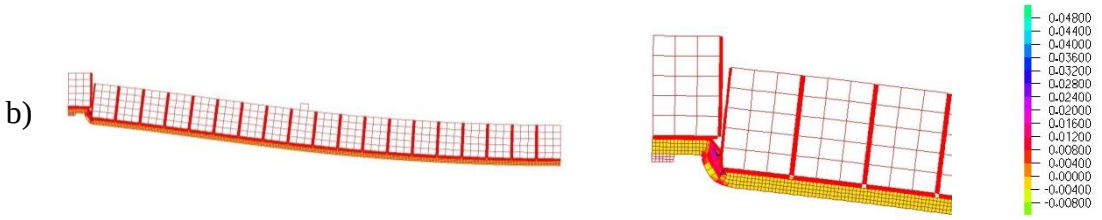

Figure 6.50. Strain distribution in the ECC layer at failure a) axial movement prevented on pinned support b) fixed support

6.4.5 Modelling of full bond ECC bending test under impact load

To simulate the one layer partial bond and full bond specimens under high rate loading an impact pulse measured in experimental tests has been applied on models. The model is developed based on the simplified model SSFO and SSPO which is discussed in Sections 6.3.2 and 6.3.3. The impact load is applied on the load control fashion (Figure 6.51a). The deflection of the model is presented in Figure 6.50 b. Both fully bonded and partially bonded specimens presented the same result which has the same trend with the experiments. However, deflection of the model is about 0.08 mm (12 times) less than the experimental counterpart. The main reasons for this difference can be related by measurement of the loading rate during experiment. As the data measured from impact happened between load cells and load spreader, the real loading rate which applied on the masonry beam can be less than this. Also an initial deflection in the spreader beam is observed during the test that affects the real loading rate.

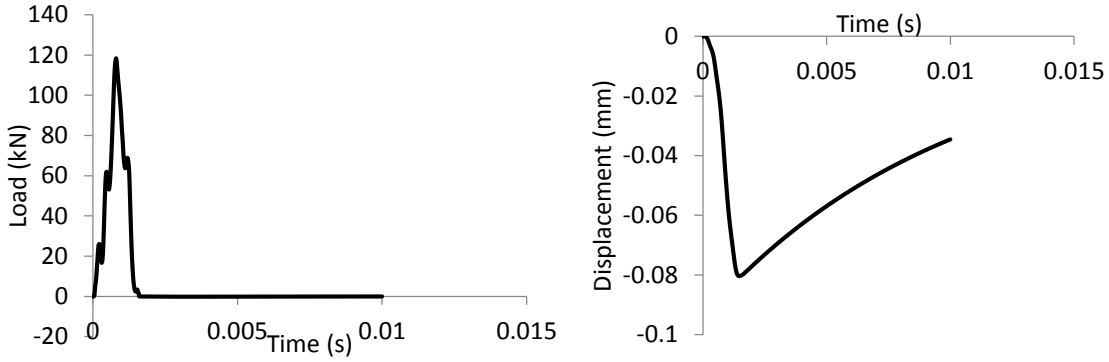

Figure 6.51. a) Time history of impact load obtained from experiments used on the simulation b) Time history of impact load obtained from simulation

To calibrate the model the loading rate reduced by 10 times and the result of deflection is demonstrated in Figure 6.52a. The results of full bond and partial bond specimens have the same trend until maximum deflection and also the simulation results are close to the experimental counterparts. However the pattern for distribution of crack at partial bond model caused to more residual deflection. Also the reaction load in the support is presented in Figure 6.51 c.

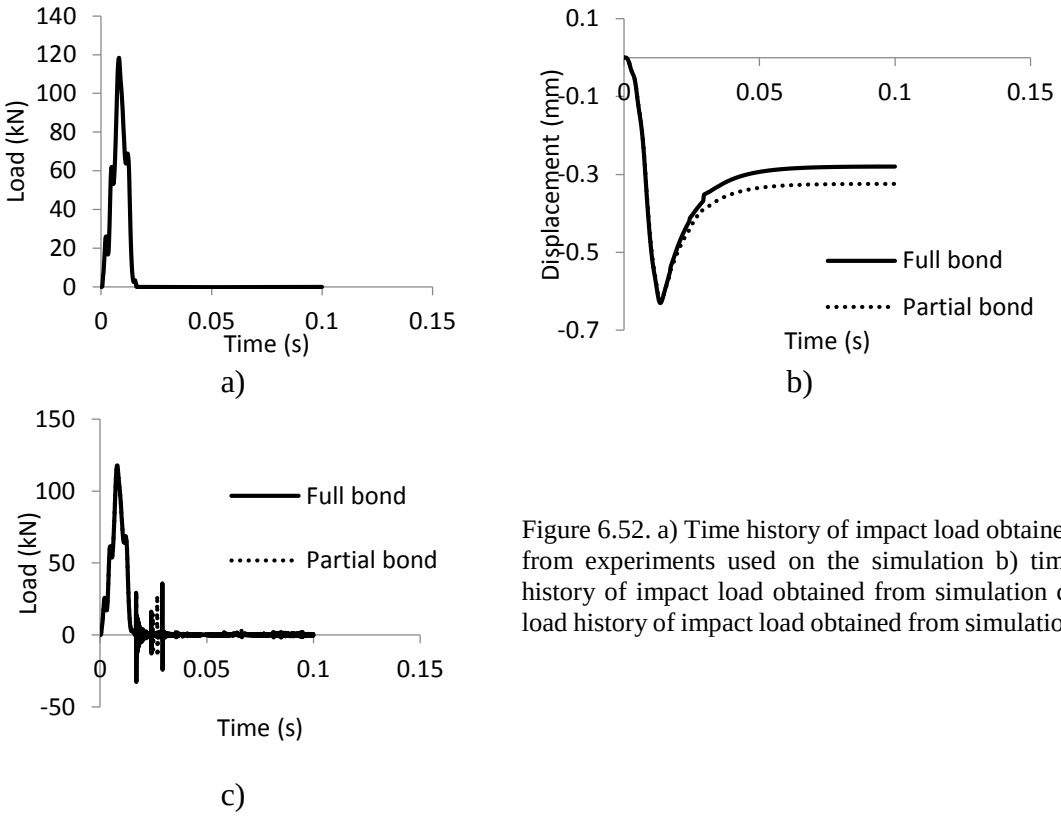

Figure 6.52. a) Time history of impact load obtained from experiments used on the simulation b) time history of impact load obtained from simulation c) load history of impact load obtained from simulation

The failure in the model firstly happened in the cohesive interface I masonry beam and then the stress distributed in the ECC layer. However the global failure under one impact has not happened in both the full bond and partial bond model. The distribution of stress in the model can be observed in Figure 6.53. This strain distribution is related with the crack pattern in real specimens. It can be observed that the behaviour of the model is similar with the crack pattern in experiment tests. However the specimens did not reach to maximum capacity and did not fail under this impact load.

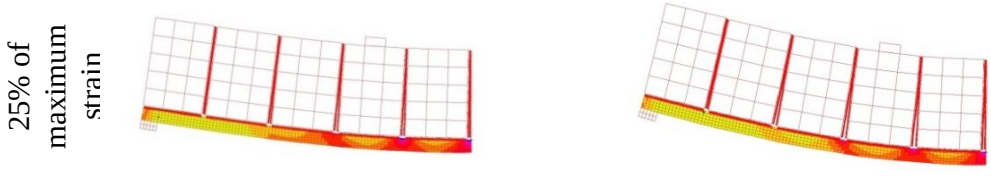

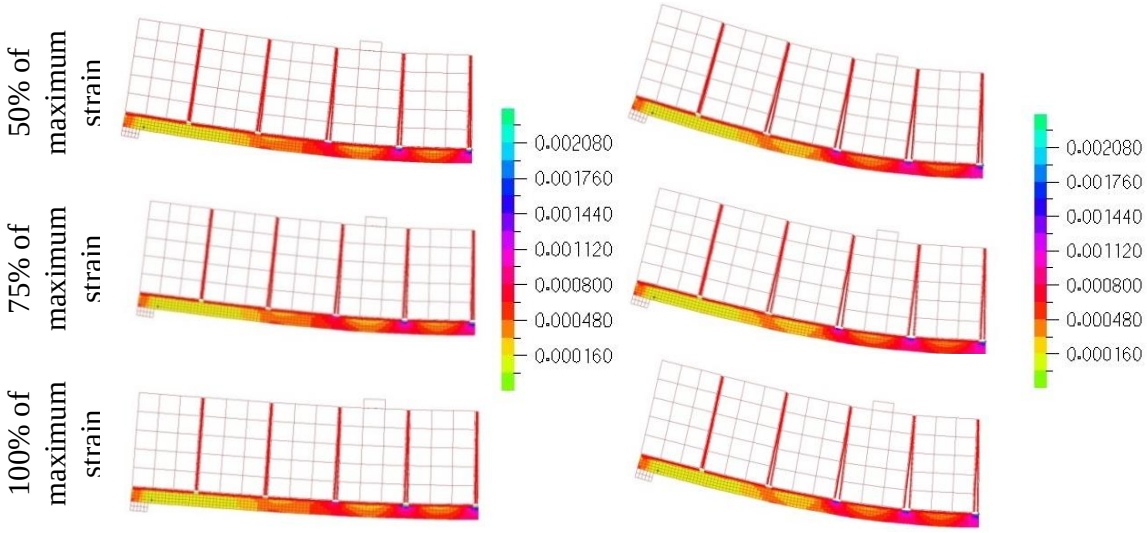

a) b)

Figure 6.53. Strain distribution at failure a) fully bonded (ISFO) and b) partially bonded (ISPO)

6.4.6 Effect of loading rate on the specimens with one layer ECC

After developing the models for the high rate loading, a range of high loading rates are applied on the model. The same strategies which applied in Section 6.4.5 for impact load are applied in these models. The effects of monotonic loading rate on the model are investigated which are presented in Table 6.14. All the loads are applied monotonically until failure of specimen. The rate dependence behaviour of the specimen is presented in Table 6.14. As in all cases the failure happened in the ECC layer beneath the interface of the masonry beam, both the partial bond and full bond specimens have the same performance. It is observed from results that by increasing the loading rate the maximum load carrying capacity of beams increases.

Table 6.14. Performance of beam under monotonic loadings

Loading rate (kN/s)	Fully bonded beam		Partially bonded beam	
	Maximum load (kN)	Maximum deflection (mm)	Maximum load (kN)	Maximum deflection (mm)
1,200,000	6000	15 mm	6000 kN	15 mm
120,000	1933	14 mm	1933 kN	14 mm
12,000	325	7 mm	325 kN	7 mm
1,200	271	12 mm	271 kN	12 mm

Next the behaviour of the model under one pulse of simplified impact load is assessed. This impact load function is consisting of an ascending and descending branch in the same loading rate. To find the maximum load in the simplified impact a reduction factor is applied in maximum monotonic loads (Figure 6.54).

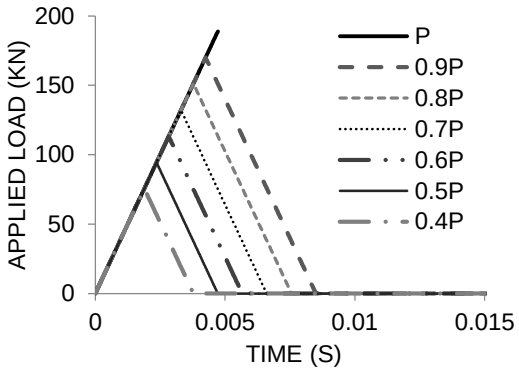

Figure 6.54. One pulse of impact load

The results of beams subjected to one pulse impact are presented in Table 6.14. A reduction on the maximum load compared to monotonic load is observed in all cases. By increasing the loading rate the maximum load capacity increases. However the maximum ductility reduced as the loading rate rises. Both cases of full bond and partial bond have the same behaviour under one pulse impact.

Table 6.15. Performance of beam under one pulse loadings

Loading rate (kN/s)	Fully bonded beam		Partially bonded beam	
	Maximum load (kN)	Maximum deflection (mm)	Maximum load (kN)	Maximum deflection (mm)
1,200,000	2000	3.5	2000	3.5
120,000	700	3.75	700	3.75
12,000	300	5.5	300	5.5
1,200	150	10.5	150	10.5

Finally the maximum capacity of the model subjected by two pulse impact loads is studied. The impact load is applied with the same strategy explained in the last part. The results are presented in Table 6.14. The maximum load capacity of the beam increases by increasing the load capacity. However the deflection of the beam for both full and partial beams is about 5 mm for different loading rates.

Table 6.16. Performance of beam under two pulse loadings

Loading rate (kN/s)	Fully bonded beam		Partially bonded beam	
	Maximum load (kN)	Maximum deflection (mm)	Maximum load (kN)	Maximum deflection (mm)
1,200,000	1800	4.5	1800	4.5
120,000	600	4.5	600	4.5
12,000	200	4.2	200	4.2
1,200	100	7.5	100	7.5

Figure 6.55 shows the values of the applied loading rates considered in the numerical study range from 1,200 to 1,200,000 kN/s for monotonic, one pulse and two pulses loading. From the predicted load bearing results presented in Figure 6.55, it appears that an increase in the loading rate leads to an increase in load-carrying capacity in specimens. A reduction in load bearing capacity of specimens when subjected to pulse loading (not resulting in failure) is observed compared to cases where the load is applied monotonically. These results suggest that the data obtained from impact tests are essentially associated with the post-failure behaviour of specimens. As a result it can be concluded that the true load-bearing capacity of the specimens under impact loading is much lower than the experimentally established values. Furthermore, it is established that the higher the loading rate and intensity of the impact load the larger the latter difference becomes. It is interesting to notice that the results of two pulses loading is close to the one pulse loading results.

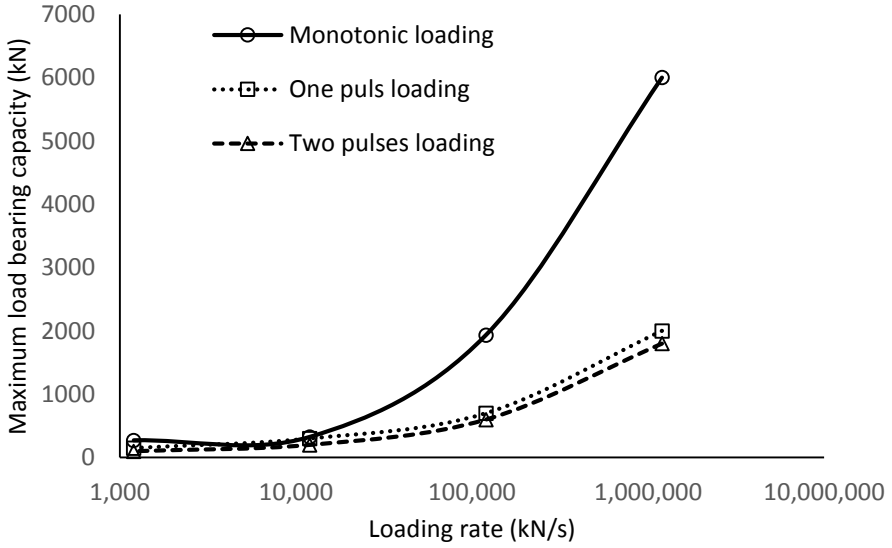

Figure 6.55. Comparison of maximum load bearing capacity under different loading rate

The comparative study between the numerical predictions in this section and their experimental counterparts presented in Chapter 5 reveals that the models employed by ADINA are capable of providing realistic predictions concerning the load bearing capacity of the specimens under increasing rates of impact loading. The predictions obtained confirm the findings of previous published numerical studies (Cotsovos et al., 2008, Cotsovos and Pavlović, 2012) which suggest that effect of loading rate on specimens response reflects the influence of inertia and the nature of the problem at hand: a wave propagation problem within a highly nonlinear medium. However the predicted results for deflection of beam needed more adjustment including calibration of ECC, brick, mortar, brick-mortar interface and brick-ECC interface under impact loading. Further detailed experimental and numerical studies have to be conducted in order to consider the behaviour of materials and interfaces under impact loading. The predictions obtained are presently forming the basis for the development of models for assessing the performance of ECC-retrofitted specimens under impact loading.

6.5 Conclusions

FE models for predicting the response of ECC-retrofitted masonry beams subjected to four-point bending load have been developed in this study. Then the models are used to conduct a series of parametric studies:

- The models developed could realistically describe certain important aspects of the behaviour observed during testing under static load. It is also shown that the modelling has been particularly useful for explaining the different crack patterns when the bond between the masonry and the ECC is altered. In the full bonded case, it is confirmed that cracking occurs due to stress concentrations occurring near the joints in the middle third span, leading to the formation of a radial cracking. In the partial bonded case, the lack of the bond between ECC layer and masonry beam in middle third span is found to lead to the formation of uniform distributed multiple-crack in the middle third span. The same crack pattern was observed experimentally.

- The stress-strain curves of ECC and hybrid ECC at elevated temperature successfully obtained from flexural presented in Chapter 3. It observed that under at 60˚C the strain capacity of ECC and H6ECC and H13ECC increases, namely 12%, 5% and 4%

respectively. At 100 ˚C the strain capacity of ECC increased by 6% while a reduction was observed in the strain capacity of the H6ECC by 2.5% and 2.2% compared to that established under ambient temperatures. Further increasing the temperature resulted in brittle failure in the ECC and changed the behaviour of HECC to strain softening material with limited ductility.

- The retrofitted models with two layers of ECC are adopted for the parametric study. It observed that in the case of fully bonded specimens the second layer of ECC at the compression face can improve the ductility of the specimen. However, the load bearing capacity of the specimens with two layers of ECC was similar to that predicted for the case of the specimens with one layer ECC. The partially bonded model with two layers of ECC exhibited the same load bearing capacity and ductility with their counterparts with one layer ECC.

- A long masonry beam (3000mm) retrofitted with the ECC layer is simulated in the parametric study. The results present a significant enhancement in ductility compared to that observed for the 800mm beam. This increase was 230% for the partially bonded beams and 390% for the fully bonded specimen.

- The effect of the variation in the mechanical properties of ECC, Hybrid ECC, brick and mortar are investigated in the parametric study. It observed that increasing the strain capacity of ECC and Hybrid ECC can improve the ductility of both fully bonded and partially bonded specimens proportionally. It is shown that the reduction of the mechanical properties of the brick on the performance of the 800mm and 3000 mm long beams resulted in a decrease in the ductility of partially bonded beams while the maximum load bearing capacity of beams were not significantly affected. It also observed that the reduction of the mechanical properties of mortar on the performance of 800mm beam resulting in a reduction of the ductility of the partially bonded beams, however, the maximum load bearing capacity of beam were not affected by this parameter.

- The effect of the support condition was investigated through fixed and pinned supports. When the axial displacement is prevented through the use of a fixed support, premature shear failure happened in both fully bonded and partially bonded specimens.

- Behaviour of specimens studied under impact load reveals that the models employed by ADINA are capable of providing realistic predictions concerning load bearing capacity of the specimens. The predictions obtained confirm that effect of loading rate on retrofitted beams response and reflects the influence of inertia. However the predicted results for deflection of the beam needed further calibration.

- It is established that an increase in the loading rate leads to an increase in load-carrying capacity in specimens. A reduction in load bearing capacity of specimens when subjected to pulse loading is observed compared to cases where the load is applied monotonically. These results suggest that the data obtained from impact tests are essentially associated with the post-failure behaviour of specimens. As a result it can be concluded that the true load-bearing capacity of the specimens under impact loading is much lower than the experimentally established values. Furthermore, it is established that the higher the loading rate and intensity of the impact load the larger the latter difference becomes.

6.6 References

BEALL, C. 1993. *Masonry design and detailing: for architects, engineers, and contractors*, McGraw-Hill.

BILLINGTON, S. & YOON, J. 2003. Simulation of cyclically loaded columns made with ductile cement-based composites. *Computational Modeling of Concrete Structures; Proc., EURO-C 2003***,** 881-889.

COTSOVOS, D., STATHOPOULOS, N. & ZERIS, C. 2008. Behavior of RC beams subjected to high rates of concentrated loading. *Journal of structural engineering,* 134**,** 1839-1851.

COTSOVOS, D. M. & PAVLOVIĆ, M. N. 2012. Modelling of RC beams under impact loading. *Proceedings of the Institution of Civil Engineers-Structures and Buildings,* 165**,** 77-94.

ROTS, J. G. 1997. *Structural masonry: an experimental/numerical basis for practical design rules*, AA Balkema.

ADINA Manual. 2012. Theory and modelling guide, Volume 1: ADINA

ADINA. 2014. Finite element analysis version 9.0.1. ADINA R & D Inc.

Chapter 7: Conclusions, design recommendations and suggestions for future work

7.1 Conclusions

This study presents a new technique for retrofitting of masonry infill walls through the use of ECC layers attached on the surface of the masonry when subjected to different loadings rates and temperatures. Chapters 1 and 2 show that the out-of-plane performance of the URM wall is brittle and weak and can be significantly enhanced through the use of an appropriate retrofitting method. Attention is focussed on the use of ECC layers for strengthening URM walls against out-of-plane actions ranging from static loads to earthquakes and high rate loads associated with blast problems which are often coupled with high temperatures. A new methodology is proposed in which the ECC layers are partially bonded onto the masonry wall for further improving the out-of-plane performance of masonry walls by fully utilising the benefits offered by the ECC material mainly in the unbonded regions. Chapter 3 describes the process through which an ECC mixture is developed through the use of materials available in the UK and its mechanical properties are assessed under normal temperatures. This is then followed by a study of the mechanical properties of ECC and hybrid ECC (HECC) when subjected to elevated temperatures. The following conclusions are drawn from Chapter 3:

- The most optimal ECC mix proportions selected were a fly-ash-to-cement ratio of 1.8, a water/binder ratio of 0.28 and fine silica sand to cement ratio of 0.6. The resulting ECC material under uniaxial tension exhibited a strain hardening ductile behaviour with a 3.5% strain capacity under quasi-static loading (1 mm/min). It is observed that for the case of uniaxial tension under increasing values of loading rate (400 mm/min) the strain capacity reduces but the tensile strength increases under increasing levels strain rates. This suggests that the material behaviour of ECC is strain-rate dependent.

- A comparison between the behaviour of ECC and HECC under uniaxial tension (at ambient temperature) reveals that the use of steel fibres can increase the tensile strength while decreasing the ductility of the dog-bone specimens.

- It is observed that for temperatures up to 600 ˚C, the behaviour of ECC and HECC under uniaxial compression are similar. Therefore, steel fibres do not appear to

significantly affect the behaviour of HECC. At 200˚C the compressive strength of the specimens do not show significant changes, whereas at 400˚C and 600˚C a 14% and 25% reduction was observed respectively in the value of the compression strength of the specimens. Considering the weight of the debris produced during testing under uniaxial compression, it is shown that the use of steel fibre can increase the integrity of the specimens resulting in the production of less debris. At 600 ˚C the debris produced by HECCs specimens was to be four times less than that produced by the ECC specimens.

- Due to the use of PVA fibres in ECC and HECC spalling was not observed in the case of the specimens subjected to elevated temperatures of up to 600 ˚C during compression and bending tests.

- During flexural testing under elevated temperatures of up to 100˚C the ductility of ECC, and HECCs increased up to three times compared to that established under ambient temperatures (20 ˚C). It was documented that the enhancement of the ductility of ECC and HECC exhibited for temperatures up to 100˚C is related to the development cracks with larger widths due to the reduction of the modulus of elasticity of the PVA fibres. However, further increasing the temperature, results in brittle failure of the ECC specimens and a change in the behaviour of HECC to strain softening (instead of strain hardening) with limited ductility. The load bearing capacity of all specimens continuously decreased with increasing temperatures up to 100 ˚C and remained constant for higher temperatures. However, the load bearing capacity of HECCs was 100% more than ECC subjected to 100 ˚C to 600 ˚C.

- It is observed under flexural testing at temperatures between 60 ˚C and 100 ˚C the use of steel fibres can limit the crack width exhibited by HECCs specimens by about 500% compared to that observed in the case of ECC specimens. However, steel fibres do not affect the number of cracks developing.

- Under flexural testing it was observed at 150 ˚C the failure mode of PVA fibres changed from '*rupture*' to '*pull out*' resulting in the change of behaviour of the ECC and HECC from strain hardening to strain softening behaviour. At 600 ˚C the steel fibres mode of failure changed from 'pull out' to 'rupture' in the H6ECC and H13ECC specimens.

After developing ECC and HECC materials which exhibited ductile behaviour under normal and elevated temperatures, ECC was used to strengthen masonry beam-like specimens subjected to static four point bending tests. In Chapter 4 the behaviour of a series of masonry beam-like specimens retrofitted using one ECC layer was investigated experimentally under four-point flexural testing. It was observed that the retrofitting of masonry walls with ECC can substantially improve their performance in terms of ductility, stiffness and load carrying capacity. The following conclusions are drawn from Chapter 4:

- Retrofitting of masonry walls with ECC can substantially improve their performance in terms of ductility, stiffness and load carrying capacity. The level of the bond achieved between the ECC layer and the masonry specimens is a very important parameter. The ductility of the masonry beams retrofitted with the partially bonded ECC layer when subjected to static or elevated loading rates is approximately 1.5 to 2 time higher than that established for the case of the fully bonded specimens. This was observed in both cases of loading rate considered: 1mm/min and 200mm/min.

- The partially bonded specimens (subjected to static or elevated loading rates) exhibit ductile behaviour due to the multiple cracking developing in the un-bonded region of the ECC. The cracks in the fully bonded specimens (subjected to static or elevated loading rates) developed near the brick-mortar interface regions (joints) over the centre span of the specimens. In the case of partially bonded specimens, a more uniform crack pattern was observed, indicating a better utilization of the ECC strengthening layer.

- Considering the response of the retrofitted specimens, it is predicted that the strains (and hence the cracking) in the ECC layer in the un-bonded region is more distributed, hence resulting in larger deformations.

- Cracking in the full bonded specimens developed mainly near the brick-mortar interfaces within the central span. The direction of the cracks in the fully bonded specimens is diagonal. Cracking in the partially bond specimens were distributed uniformly in the middle third (un-bonded) span. The direction of the cracks forming in the partially bonded specimens is vertical to the direction of the tensile load applied in the ECC layer. The results of the analytical study reveal that the angle at which the

crack propagates in the fully bonded specimens can increase the first crack load and the peak load by 15%.

- The fully bonded and partially boned beams exhibited an increase in the first cracking load and the maximum load capacity when subjected to elevated loading rates compared to their counterparts recorded under equivalent static loading. This reveals that the load bearing capacity of the specimens under elevated loading rates improved in all cases. It is considered that this change in the recorded behaviour is linked to the strain rate sensitivity of the material properties of ECC.

- The fully and partially bonded beams exhibited a 66% and 35% reduction in deflection when subjected to elevated loading rates compared to their counterparts recorded under static loading. This behaviour presents the strain rate dependency of ECC under increasing loading rate which was discussed in section 3.2.5. However, the fully bonded beams exhibited a reduction of ductility about 3 times higher than that of the partially bonded beams. This shows that the fully bonded beams are more vulnerable when subjected to elevated loading rates. This vulnerability is due to the concentration of stresses near the brick-mortar interface whereas in the case of the partially bonded beams the stress in the ECC layer is distributed uniformly.

- The crack pattern exhibited by the fully bonded and partially bonded specimens had similar characteristics for both cases of loading rates considered. However, the number of cracks developing decreased with increasing loading rates. The same behaviour was observed in the case of the ECC dog-bone specimens.

- The results of the analytical study reveal that in the case of the fully bonded specimens the first crack happens in the interface section of the masonry beams followed by some cracking beneath this interface in the ECC layer. In the case of partially bonded specimens the first crack develops in the interface section of the masonry while at the same time cracking also develops throughout the un-bonded region of the ECC layer.

Studying the behaviour of beam-like specimens under quasi-static and elevated loading rate reveals the ECC can improve the performance of masonry beam-like specimens. However, the strain rate dependent behaviour of ECC affects the retrofitted masonry behaviour. In Chapter 5 the behaviour of a series of masonry beam-like specimens

retrofitted using one or two ECC layers were investigated experimentally under impact load. It was observed that although the behaviour of ECC is strain rate dependant, its use for strengthening the masonry walls improved the response exhibited in terms of ductility, stiffness and load carrying capacity, and integrity under impact load. The following conclusions are drawn from Chapter 5:

- The use of ECC layer(s) resulted in an increase of the specimen's strength, ductility and deformability while prohibiting the generation of debris. The ECC layer essentially acted as a net stopping the production of debris during drop-weight testing.

- It is observed that under high and low intensity impact loading the form of the curve describing the time history of the contact force generated in the impact region is characterised by certain differences depending on the properties of the interface between the impactor and the specimens, the method adopted for applying the ECC layers and the speed with which the impactor strikes the specimen. High intensity impact loads are characterised by a maximum value of 120KN and 80kN for specimens retrofitted with one and two layers of ECC respectively as well as a very short duration of 2 ms. Low intensity impact loads were characterised by a maximum value of 100kN and 80kN for specimens retrofitted with one layer and two layers of ECC respectively as well as very short duration of 4 ms.

- It is interesting to notice that under consecutive drop-tests the impact load generated is largely associated with the impact energy and inertia force and was less affected by the specimen's ability to resist the impact load. On the other hand, the reaction forces generated is associated with the level of damage sustained by the specimen during testing.

- When strengthening the specimens with a second layer of ECC the performance of specimens was significantly enhanced. The dislocation of bricks observed in the partially bonded specimens during impact testing was limited by the top ECC layer and failure of the bricks below the points of loading was not observed. On average 3 impacts were sustained by the specimens with 2 layers of ECC collapsed unlike the specimens strengthened with one layer of ECC which were able to undertake on average 2 impacts. Also the variability observed in the specimens behaviour during

impact testing reduced as the specimens exhibited more consistent performance when the second layer of ECC.

- The level of bond achieved between the ECC layer and masonry surface is an important parameter in the retrofitting of masonry walls against impact loading. The ductility of the specimens retrofitted with a partially bonded ECC layer under impact loading is higher (approximately 40%) compared to that exhibited by the fully bonded specimens. This was observed in both cases of impact loads (high and low intense impact).

- The behaviour of the partially bonded specimens (subjected to high and low intense impact loads) was more ductile due to the multiple and distributed cracking developing in the un-bonded region of the ECC layer. The cracks in the fully bonded specimens (subjected to high and low intense impact) developed near the brick-mortar interface regions (joints) over the centre span of the specimens. In the case of partially bonded specimens, a more uniform crack pattern was observed, indicating a better utilization of the ECC layer.

- It is demonstrated that the strains (and hence the cracking) in the ECC layer in the un-bonded region is more distributed, potentially resulting in larger deformations compared to the fully bonded specimens.

- Strengthening the masonry specimens with one layer of ECC enabled them to undertake levels of applied loading significantly higher than the load-carrying capacity established under equivalent static loading. A comparison between behaviour of specimens exhibited under impact loading and equivalent static loading reveals that the load carrying capacity of the specimens increased by about 4 times while their response exhibits more ductility characteristics. It also allowed the specimens in some cases to undertake more than one drop-tests (blows) before collapsing.

After evaluating the mechanical behaviour of ECC under different loading rates and temperatures and also studying experimentally the behaviour of the ECC retrofitted masonry beam-like specimens under static and impact loading a finite element (FE) analysis is carried out in Chapter 6. The FE models were calibrated against the available test data obtained from the experiments presented in Chapters 3 and 4. The numerical

predictions obtained from the calibrated models were used to explain the mechanics underling behaviour of the beam-like specimens. FE models were also used to predict the effect of various parameters on the behaviour of ECC-retrofitted specimens. The parameters considered include different levels of elevated temperatures, different support conditions, different specimen lengths, the variation of the mechanical properties of the bricks and the mortar as well as the different loading rates. The following conclusions are drawn from Chapter 6:

- The models developed realistically describe certain important aspects of the behaviour exhibited during static testing. It is also shown that the predictions obtained have been particularly useful in explaining the different crack patterns when the bond between the masonry and the ECC is altered. In the full bonded case, it is confirmed that cracking occurs due to stress concentrations occurring near the joints in the middle third span, leading to the formation of a radial cracking. In the partial bonded case, the lack of the bond between the ECC layer and masonry beam in the middle third span is found to lead to the formation of uniform distributed multiple-crack in the middle third span. The same crack pattern was observed experimentally.

- The stress-strain curves of ECC and hybrid ECC at elevated temperatures established numerically from flexural tests are presented in Chapter 3. It observed that at 60˚C the strain capacity of ECC and H6ECC and H13ECC increases, namely 12%, 5% and 4% respectively. At 100 ˚C the strain capacity of the ECC increased by 6% while a reduction was observed in the strain capacity of the H6ECC by 2.5% and 2.2% compared to that established under ambient temperatures. Further increasing the temperature resulted in brittle failure in the ECC and changed the behaviour of HECC to strain softening material with limited ductility.

- The retrofitted models with two layers of ECC adopted for the parametric study revealed that in the case of fully bonded specimens the second layer of ECC (at the top face of the specimen) can improve the ductility of the specimen. However, the load bearing capacity of the specimens with two layers of ECC was similar to that predicted for the case of the specimens with one layer ECC. The partially bonded models with two layers of ECC exhibited the same load bearing capacity and ductility with their counterparts with one layer ECC.

- A long masonry beam (3000mm) retrofitted with the ECC layer was simulated in the parametric study. The results present a significant enhancement in ductility compared to that observed for the 800mm beam. This increase was 230% for the partially bonded beams and 390% for the fully bonded specimen.

- The effects of the variation in the mechanical properties of ECC, Hybrid ECC, brick and mortar are investigated on parametric study. It observed that increasing the strain capacity of ECC and Hybrid ECC can improve the ductility of both fully bonded and partially bonded specimens proportionally. It is shown that the reduction of the mechanical properties of the brick on the performance of the 800mm and 3000 mm long beams resulted in a decrease in the ductility of partially bonded beams while the maximum load bearing capacity of beams were not significantly affected. It also observed that the reduction of the mechanical properties of mortar on the performance of 800mm beam resulting in a reduction of the ductility of the partially bonded beams, however, the maximum load bearing capacity of the beam were not affected by this parameter.

- The effect of the support condition was investigated by adopting fixed and pinned supports. When the axial displacement is prevented through the use of a fixed support, premature shear failure occurred in both fully bonded and partially bonded specimens.

- The behaviour of specimens studied under impact load reveals that the models employed by ADINA are capable of providing realistic predictions concerning load bearing capacity of the specimens. The predictions obtained confirm that the effect of the loading rate on retrofitted beams' response largely reflects the influence of inertia. However, the model developed require further calibration in order to study the effect of the loading rates in all aspects characterising the behaviour of the subject specimen.

- It is established that an increase in the loading rate leads to an increase in the maximum sustained load undertaken by the specimens. The load bearing capacity of the specimens when subjected to pulse loading is significantly lower compared to the maximum sustained load calculated when the load is applied monotonically with the same rate. These results suggest that the data obtained from impact tests do not represent the true load-carrying capacity of the specimen as the peak load recorded during testing is often associated with a specimen physical state characterised by considerable cracking. As a result it can be concluded that the true load-bearing

capacity of the specimens under impact loading is much lower than the experimentally established values. Furthermore, it is established that the higher the loading rate and intensity of the impact load the larger the latter difference becomes.

Finally the experimental and numerical studies carried on in this thesis exhibited that the use of ECC layer to retrofit the URM walls can improve the strength, toughness, ductility and deformability of masonry walls under out-of-plane loads ranging from quasi-static to impact load. The new partially bonding technique introduced in this study resulting in further deformability of specimens compared to the traditional fully bonded ECC layer. This technique also can be employed for other surface retrofitting coating methods.

7.2 Design recommendations

Based on the research carried out in this thesis the following design recommendations for industrial applications are proposed:

1. For retrofitting of structural members (i.e. load bearing masonry walls) which can be exposed to elevated temperatures of up to 60 C due to solar emissions (i.e. building facades) or heat generated inside the building (i.e. walls adjacent to central heater) it is recommended to add 6 mm of steel fibres (see Table 3.5) to the ECC mixture at a ratio of 0.5% by weight. This action does not have any significant effect on the workability of the fresh ECC and the mechanical properties of hardened ECC but it can limit the crack-widths and temperature sensitivity of the mechanical properties of the ECC layer at elevated temperatures (up to 60 ˚C). It is worth mentioning that cracks initiating in the ECC layer at 60 ˚C have a width of about 1 mm compared to 0.2 mm (5 times smaller) in hybrid ECC. The wider cracks expose the PVA fibres to environment weather (erosion) which finally reduce the ECC layer service life.

2. In the case of masonry walls retrofitted with an ECC layer subjected to a combination of high rate loading and high temperature (often associated with explosions) it is recommended to add 6 mm of steel fibres (see Table 3.5) to the ECC mixture by a ratio of 0.5% by weight. The contribution of the steel fibres can improve the performance of the retrofitted members. The steel fibres attribute ductile characteristics behaviour of the walls enabling them to exhibit strain-softening behaviour and safeguarding against brittle forms of failure (the latter being observed in the case of ECC containing only PVA fibres

at temperatures higher than 100 ˚C). Furthermore the use of hybrid ECC at high temperatures results in the production of about 4 time less debris compared to plain ECC thus minimizing the risk of injury from generated debris moving at high speeds (projectiles) during explosions.

3. Based on experiments carried out in chapter three the use of steel fibre longer than 6 mm can reduce the crack widths and the amount of debris produced while improving the ductility of ECC at high temperatures. However, long fibres (13 mm in this study) reduced the ductility and strain hardening performance of hybrid ECC. Therefore, for all applications discussed above in paragraphs 1 and 2 the use of shorter steel fibre (6 mm) is recommended for the production of hybrid ECC.

4. When retrofitting masonry infill walls fabricated by bricks (solid, perforated or frogged) with a minimum compressive strength of 20MPa and a mortar layer with a minimum compressive strength of 7MPa, only one 15mm thick layer of plain or hybrid ECC attached to the face of the wall acting in tension is recommended. However, when using an ECC layer thicker than 15 mm there is a risk that a sudden failure may occur on the face of the masonry wall acting in compression prior to the ECC layer reaching its full tensile capacity. This type of failure is brittle and may result in full or partial collapse of the wall.

5. When retrofitting masonry infill walls fabricated by bricks (solid, perforated or frogged) with a compressive strength less than 20MPa or a mortar layer with a compressive strength less than 7MPa, it is recommended that two layers of ECC (attached to both sides of the masonry walls) is used. The same is recommended for the case of walls with hollow bricks. The minimum thickness of ECC can be 15mm. thicker layers of ECC can be used as there is no danger of brittle compressive failure.

6. In the case of consecutive blast waves, when retrofitting the masonry infill walls it is recommended that hybrid ECC layers are applied on both sides of the walls in order to reduce the risk of dislocation and falling of the masonry units.

7. It is recommended that the partially bonded hybrid ECC layers (see Figure 7.1) are used especially on the face of the of wall acting in tension. Partially bonded ECC layers are more likely to reach their full strain capacity (in tension) compared to fully bonded ECC layers. It is worth mentioning that cracking forming near the joint regions of the masonry walls quickly extend to the fully bonded ECC layers resulting essentially in their premature failure (before reaching their maximum strain capacity). This however does not occur in the case of partially bonded ECC layers.

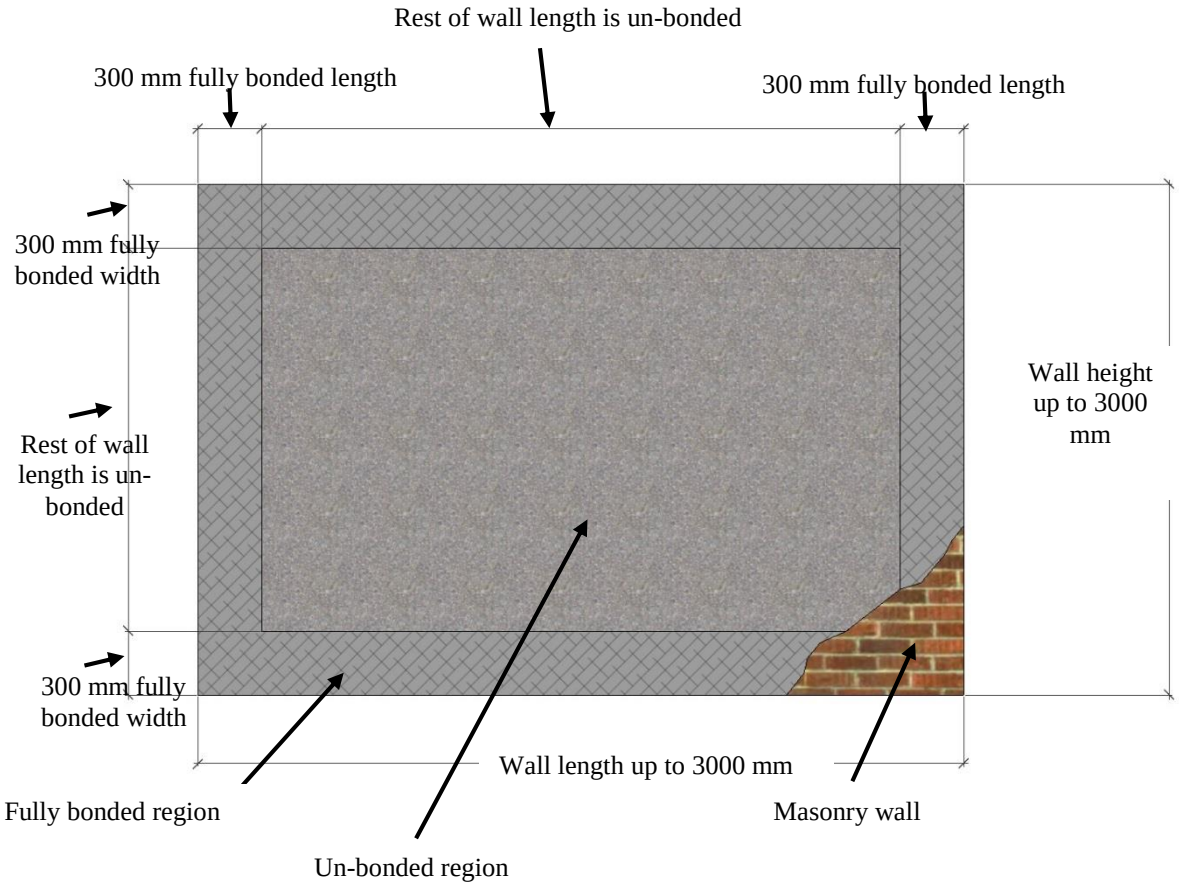

Figure 7.1 Recommended arrangement for partially bonded ECC-retrofitted masonry wall

7.3 Suggestions for future work

Presented work investigates and assesses the possibility to retrofitting of masonry walls using the ECC layer when subjected to different temperature, different loading rate or a combined action including high rating load and temperature. However, during the study some questions were raised and need to be investigated further in the future:

- Further numerical studies are needed to calibrate the behaviour of the ECC retrofitted model under impact loading.

- A 3D model which can represent the behaviour of the retrofitted walls is currently being developed however due to the heavy computational resources are needed to fully calibrate it.
- A series of larger (possibly in real scale) specimens retrofitted with ECC layers should be tested to evaluate the behaviour of the infill masonry walls strengthened through the use of the suggested technique (involving both fully and partially bonded ECC layers).
- The effect of certain parameters on the behaviour of the ECC- retrofitted masonry beam should be investigated including different thicknesses of ECC layer, different shape of bricks, different forms of loading.
- The effect of retrofitting of masonry walls using ECC on the in-plane behaviour of should be studied in more detail.
- The effect of out-of-plane damage on in-plane behaviour of masonry walls should be investigated.
- Assess the contribution of the ECC retrofitted specimens on the behaviour of RC frames under seismic loading and actions associated with more extreme loading conditions (impact, blast, fire).
- The behaviour of specimens retrofitted with hybrid ECC should be investigated under high rate loading.
- The performance of ECC and hybrid ECC retrofitted specimens subjected to a combination of high temperatures and high loading rates should be studied in more detail.